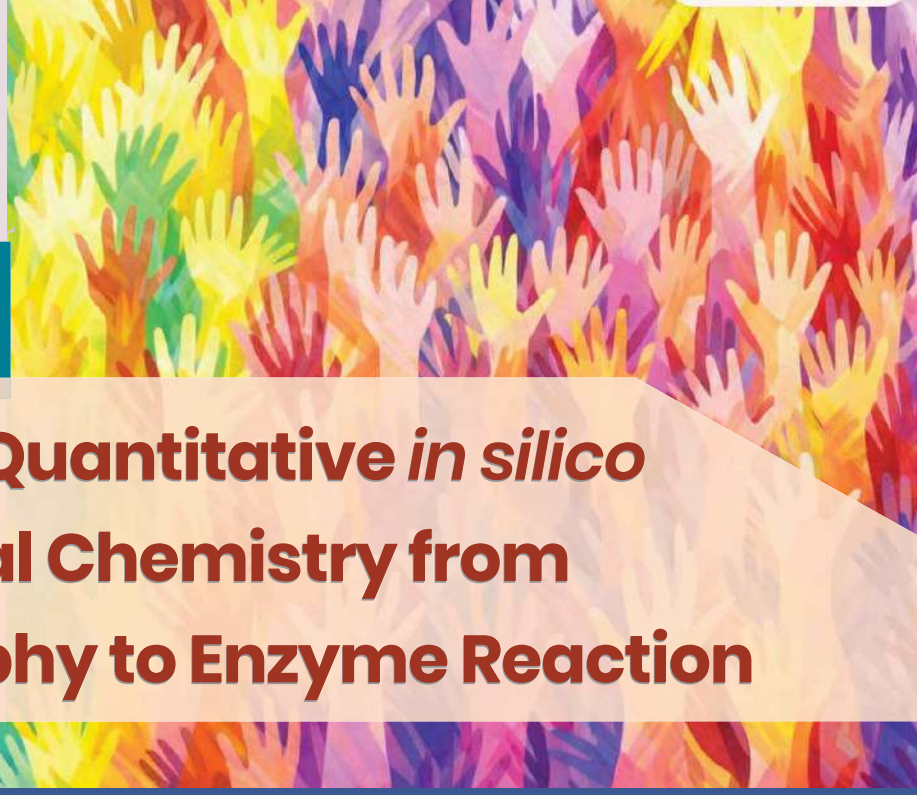
HSPI The Open Access Publisher



Advanced Quantitative *in silico* Analytical Chemistry from Chromatography to Enzyme Reaction

Subject Category: For drug discovery, from chromatography to enzyme selectivity

Toshihiko Hanai*

Yokohama, Japan

Submitted: 28 September 2026 | **Approved:** 15 October 2026 | **Published:** 22 October 2026

Copyright: © 2026 Hanai T. This is an open access article distributed under the Creative Commons Attribution License, which permits unrestricted use, distribution, and reproduction in any medium, provided the original work is properly cited.

DOI: https://dx.doi.org/10.29328/ebook1007

***Corresponding author:** Toshihiko Hanai, PhD. Yokohama, Japan, Email: hanai104@kf7.so-net.ne.jp

Contents - 10 Chapters

Chapter 1: Introduction 8

1.1. Dipole-dipole interaction 9

1.2. Hydrogen bonding 11

1.3. Lewis acidity and basicity 12

1.4. Strong acid-base interaction 13

1.5. Dissociation (ionization) 14

1.6. Prediction of Dissociation Constant 17

1.7. Molecular interaction degree analysis 19

1.7.1. Van der Waals force between n-alkanes 19

1.7.2. Van der Waals force between aromatic compounds 21

1.7.3. Weak Electrostatic Interactions 22

1.7.3.1. Interactor bctween allylethers. 22

1.7.3.2. Interactor bctween allylketones 24

1.7.4. Hydrogen Bonding of alkanol 25

In silico experimental 26

References 27

Chapter 2: Fundamental Molecular Interaction Mechanisms 28

2.1. Van der Waals force (hydrophobic interaction)

2.1.1. Van der Waals force between hexane and aromatic compounds 29

2.1.2. Interaction with alkenes 31

2.1.3. Interactions with a phenyl group. 32

2.2. Hydrogen Bonding 34

2.2.1. Hydrogen bonding with an amino group 34

2.2.2. Hydrogen bonding with a carboxy group 36

2.3. Study the fundamental interaction mechanisms of ion-exchange groups 38

2.3.1. The fundamental activity of carboxy-group 38

2.3.2 The fundamental activity of amino-group 42

2.3.2 The fundamental activity of guanidino-group 45

References 49

Chapter 3: Modeling Analysis of Chromatographic Retention 50

3.1. Solvent Effects in Hydrophobic and Hydrophilic Interaction Liquid Chromatography 50

3.1.1 Contribution of water 51

3.1.2. Contribution of acetonitrile 55

3.2. Solvent effects in ion-exchange liquid chromatography 59

3.2.1. Solvent effect (water) for the binding with ionized carboxy-group 59

3.2.2. Solvent effect (water) for the binding with ionized amino-group 60

3.2.3. Solvent (water) effect for the binding with guanidino-group 61

3.2.4. Solvent (acetonitrile) effect for the binding with ionized carboxy-group 61

3.2.5. Solvent (acetonitrile) effect for the binding with ionized amino-group 62

3.2.6 Solvent effect (acetonitrile) for the binding with guanidino-group ` 63

3.3 Selectivity of sodium and chloride ions for molecular interactions 63

3.3.1 Competition with Na^+ for binding with ionized carboxy-group 63

3.3.2. Competition with Na^+ for binding 65

3.3.3. Competition with Na^+ for binding with guanidino-group 66

3.3.4. Competition with Cl^- for binding with ionized carboxy-group 67

3.3.5 Competition with Cl^{--} for binding with ionized amino-group 69

3.3.6 Competition with Cl^- for binding with guanidino-group 70

References 71

Chapter 4: Quantitative Explanation of Spectra 72

4.1. Titration Analysis 1. Phenolphthalein Color Change 74

4.2 Titration analysis 2 Indicator sulfonephthalein color change 74

4.3. Titration analysis 3. Indicators Methyl-orange and methyl-red color change 76

4.4. Colorimetric analysis of hydrochlorothiazide and creatinine 80

4.5. NMR spectroscopic determination of chemical structures 82

4.6. Chemiluminescence mechanisms and absorption detection mechanisms of bromate in ion- chromatography 87

References 90

Chapter 5: Preparation of model phases Construction of molecules using a computational chemistry program 92
5.1. Modeling graphitized carbon-phase 92
5.2 Construction of silicone-dioxide phases 94
5.3. Preparation of surface modified silica gel phases 98
5.4. Surface modification of model alkyl bonded silica gel 102
5.5. Preparation of model solvent phases 102
5.5.1. Construction of a model methanol phase 103
5.5.2. Construction of a model acetonitrile phase 105
5.5.3. Construction of model water phase 105
5.6. Example of calculation of solvent effects. 108
5.7. Gas chromatography 1. Methyl-silicone phase and the selectivity 111
References 113

Chapter 6: Quantitative explanation of retention mechanisms and solvent effects 114
6.1 Retention mechanisms in normal-phase liquid chromatography 114
6.2 Retention mechanisms in hydrophilic interaction liquid chromatography 116
6.3 Retention mechanisms in hydrophobic interaction chromatography, 118
6.4 Retention mechanisms in ion-exchange liquid chromatography 119
6.5 Selectivity of hydrophobic phases 120
6.5.1 Selectivity of hexyl-phase 121
6.5.2 Selectivity of phenylhexyl-phase 122
6.6 Specificities of fluorocarbon-bonded phases 126
6.6.1. Comparison of fluorocarbon and hydrocarbon substitutes 129
6.6.2. Selectivity of fluorocarbon ligand of bonded silica gel 131
6.6.3 Selectivity of fluorocarbon bonded phase 132
6.7. Selectivity of graphitized carbon-phase 135
6.8. Solvent effect: Interaction between an analyte and a solvent-phase 139
6.8.1 Interactions with a model water-phase 139
6.8.2 Interations with a model acetonitrile-phase 141
6.9 Competitive solvent effects 141
6.9.1 Compututive between pentane and water phase 141
6.10. Column switching and isocratic elution system for fast, sensitive, and reproducible chromatography 143
6.10.1 Methodology 144
6.10.2. Dependent on the Difference in Hydrophobicity of Analytes 145
6.10.3. Dependent on the Difference in Coulombic Force of the Analytes 148
6.10.4. Dependent on the Molecular Sizes of Analytes 148
6.10.5. Dependent on the Steric Hindrance of Analytes 148
6.10.6. Affinity and Enzymatic Reaction 148
6.10.7. Application to Mass Spectrometric Analysis 148
References 149

Chapter 7: Quantitative analysis of the molecular interactions and properties in chromatography 153

7.1 Normal-phase liquid chromatography 153

7.2 Reversed-phase liquid chromatography 153

7.2.1 Phenolic compounds 154

7.2.2 Reversed-phase liquid chromatography for acidic compounds 158

7.2.3 Reversed-phase liquid chromatography for basic compounds 165

7.2.4. Selectivity of Phenylhexyl-bonded siica gel 172

7.3. Bio-mimic ion-exchange groups and chromatography 173

7.3.1. Cation-exchange liquid chromatography 174

7.3.2. Quantitative in silico analysis of acidic drug interactions on a bio-mimic guanidine ion-exchanger 176

7.4. Measurement of Albumin-drug binding affinity (log nK) using liquid chromatography 179

7.5. Chromatography of saccharides 181

7.6. Quantitative in silico analysis of reversed-phase ion-pair chromatography 182

7.6.1. Ion-pair liquid chromatography of free amino acid-copper complex 182

7.6.2. Ion-pair liquid chromatography of Phenylthiohydantoin-amino acids 184

7.6.3 Nitrobenzofurazan-amino acids in reversed-phase ion-pair liquid chromatography 188

7.7. Evaluation of column test methods to study inactivation of chemically bonded silica Gels 192

7.7.1. Experimental 193

7.7.2. Results and discussion 194

7.8. Gas chromatography, Retention mechanisms, Boiling point, and Enthalpy 197

7.8.1. Methyl-silicone phase and the selectivity 197

7.8.2. Boiling point and Enthalpy 201

7.8.3. Ethylene glycol-phase and the selectivity 203

7.8.4. 50% phenylmethyl silicone phase and the selectivity 203

References 212

Chapter 8: Enantiomer Recognition, Introduction of Fundamental Enantiomer Recognition Mechanisms 217

8.1 Introduction of fundamental enantiomer recognition mechanisms 217
8.2 Pirkle type chiral selectors 217
8.3. Enantiomer separation as diastereomers 221
8.4 Chiral derivatization for gas chromatographic analysis 222
8.5 Ligand exchange chiral selector 222
8.6 Crown ether as chiral selector 223
8.7 Cyclodextrin derivatives as chiral selectors 224
8.8 Derivatized polysaccharides as chiral selectors 225
8.8.1. β-D-glucopyranose derivatized chiral selectors 225
8.8.2 Amylose derivatized chiral selectors 228
8.9 Protein as chiral selectors 233
8.9.1 Glycoprotein as chiral selector 233
8.9.2. Cellobiohydrolase 235
8.10 Natural organic compounds 236
8.11 Other enantiomer separation phases 237
8.12 Biological enantiomer selectivity 238
References 238

Chapter 9: Physical biochemistry of enzyme reactions 243

9.1. Alcohol Dehydrogenase 243
9.2. Cinnamyl-alcohol Dehydrogenase (CAD) ELI3-2 249
9.3. Alanine Racemase 253
9.4. Human Serine Racemase 257
9.5. Aspartate Racemase 263
9.6 Glutamate Racemase 264
9.7. Human *D*-Amino acid Oxidase (DAO) 266
9.8. Human acidic *D*-amino acid oxidase (DDO) 270
9.9 Aspartate Oxidase 277
9.10 Glutamate Oxidase 279
9.11 Arginine Oxidase 280
9.12 Lysine Oxidase 283
References 287

Chapter 10: Diagnosis and enzyme activity 292

10.1 Against Chronic Kidney Disease 292

10.1.1. Glycineamidino transferase 293

10.1.2. Guanidinoacetate N-methyltransferase 295

10.1.3. Creatine kinase 297

10.2 Biomarker for senile dementia 299

10.2.1 Human Phenylalanine -4- monooxygenase (phenylalanine hydroxylase) 301

10.2.2. Tyrosine hydrogenase 303

References 305

Chapter 11. Protein-Protein Interactions: SARS-COVID-19 Variants Transmissibility and the Binding Inhibitors 307

11.1 Structure of COVID-19 S-RBD Mutants 308

11.2 Fast Analysis of Transmissibility by Binding Strength between Two Amino Acids 314

11.3 COVID-19 Transmissibility and the Binding Inhibitors 324

11.4 Analysis of Binding Inhibitors as the S-RBD Complexes 327

11.4.1 Properties of Aspirin 327

11.4.2 Lactic acid, performance of ionized carboxyl acid 329

11.4.3 Acidic Compounds as Inhibitor Candidates 329

11.4.4 Natural Polyphenols as Binding Inhibitors 331

11.4.5 Modification of Medicines to Improve the Capability 334

11.4.5.1 Properties of PF 07321332 (Nirumatrelvir) and Molnupiravir 334

11.4.6 Cocktail inhibitors 339

11.4.6.1 Barcitinib, Clofazimine, and Malic Acid Cocktail 339

11.4.6.2 Further Study of Cocktail Applications 342

11.5 Possible Approach to Improve the Known Medicine Activity 343

11.6 Further Proposal of Medicines against COVID-19 346

11.7. Discussion 348

References 350

Chapter 1: Introduction

Analytical chemistry has used various techniques without quantitative explanations of the underlying chemistry. Calorimetric analysis indicated that the hydrogen bonding strength of alkyl alcohols depends on the alkyl chain length, and up to four methylene units can affect the hydrogen bonding strength. This result supported the conclusion that butyl alcohol is a suitable solvent for extracting relatively hydrophobic molecules from water. Color indicators have been the backbone of simple pH tests and titration analyses. The spectrophotometric determination of hydrogen ion concentrations using color indicators was demonstrated [1], and Kolthoff described the dissociation processes in detail [2]. The experimentally measured dissociation of phenolphthalein was explained using four dissociation structures, where the ionization of two phenolic hydroxyl groups converts the neutral molecular form into the red quinoid form. Further, dissociation from the quinoid structure to the alcoholic form eliminates the color. The dissociation mechanisms can also be described using three structures without a transition structure [3]. Furthermore, the mechanisms were quantitatively described by in silico analysis using the chemical structures and the related predicted spectra [4].

NMR spectra of the organic polymer gels were measured in various solvents. The water content outside and inside the resins was related to the ion-exchange capacity, in which water molecules contact the ion-exchange groups [5, 6]. Furthermore, a fundamental study of molecular interactions in chromatography was performed using simple small molecules to analyze the chromatographic behavior of aromatic compounds on an anion-exchange resin with a non-aqueous eluent. The NMR spectra of a model anion exchanger (N,N,N-trimethylammonium ion exchange resin) with aniline or nitrobenzene in a deuterium solvent (ethanol-OD) were measured to investigate chromatographic molecular interactions. The probable signal of a trimethylammonium group shifted toward a high field upon the addition of aniline and toward a low field upon the addition of nitrobenzene. The chemical shift was not observed upon the addition of toluene. The chemical shift is related to electronegativity. The contact conformation in solution may not reflect the chromatographic interactions measured using ion-exchange resins, even if the spectra of ion-exchange resin were broad because the instrument was not used for solid-state NMR. However, the spectra supported chromatographic behavior [7]. Furthermore, electron spectroscopy for chemical analysis (ESCA) was used to measure chemical shifts due to electron localization. The chemical shift of 12C shifted 0.27 eV upon the adsorption of α-hydroxynaphthalene on the anion-exchanger (CR400 Cl form), and that of 12CP shifted -0.26 eV upon the adsorption of 1,8-dinitronaphthalene on the anion-exchanger. The 13C chemical shift of the anion exchanger was -0.08 eV and -0.43 eV for ααα-hydroxynaphthalene and 1,8-dinitronaphthalene, respectively. NMR and ESCA results indicated that the chemical shifts are caused by the interaction between the ion exchangers and the analytes. Although the shifts indicated a positive answer to the strength of molecular interactions, the spectrometric resolution was insufficient at that time [8].

These instrumental analysis results were later quantitatively described using computational chemical (*in silico*) analysis. On the other hand, the quantitative analysis of electron-donor-acceptor intermolecular interactions is a fundamental subject in chemistry. In primary and transient states of numerous chemical reactions, it is the basis of many catalytic processes, determines the specific solvation in solutions, and finally leads to the formation of numerous compounds with different properties [9]. The electron-donor-acceptor approach to molecular interactions provides rationalization and a unified re-interpretation of well-known phenomena in biochemistry [10]. The computationally calculated energy values and fundamental properties follow, and the classical explanations of chromatographic separation and the estimated chromatographic retention (interaction) mechanisms differ from those provided by computational chemical calculations.

Computational chemical calculation: Fundamental properties

Van der Waals energy	Van der Waals force
	Van der Waals mass
	Repulsion
	London's dispersion
	Hydrophobicity related to contact surface area
Hydrogen bonding energy	Hydrogen bonding

Electrostatic energy	Dipole	
Charge transfer		
Coulomb		
	Ion-dipole, interaction	
	Ion-ion interaction	
	Ligand exchange	Electron localization
	Complex formation	Electron localization
No directly related energy	Salting-out	
Steric hindrance		

Van der Waals interaction (hydrophobic interaction) is a combination of van der Waals mass, Repulsion, and London's dispersion. Basically, it depends on the contact surface area of two molecules, and electron localization does not have a significant effect. Dipole is related to electron localization, and dipole-dipole interaction can be explained as part of Lewis acid-base interaction. The difference can be obtained from the electrostatic energy values of molecular interactions. The contact site electron localization can be read from the atomic partial charge (apc) value.

1.1. Dipole-dipole interaction

Dipole moments are commonly used; however, their quantitative explanation is somewhat complicated and difficult to apply to all kinds of compounds. A quantum chemistry method has been developed, and the relevant properties can be readily calculated from the chemical structures [11]; however, dipole-dipole (π-π) interaction cannot be directly calculated, and the phenomenon of electron localization is easily obtained from changes in atomic partial charge values after the contact of two molecules. The fundamental mechanisms of dipole-dipole interaction are explained using simple molecules.

The chloromethane-chloromethane interaction form is considered in three structures. APC values of methane carbon and hydrogen are -0.374 and 0.094 au. The apc values of chloromethane carbon, hydrogen, and chlorine are -0.227, 0.133, and -1.171 au. The methane carbon and hydrogen apc changed plus 0.152 and 0.139 au by replacement of one hydrogen to chlorine. The electron localization is visually displayed in Figure 1 with the apc of methane, chlorine, and chloromethane atoms. Electrophilic superdelocalization is an indicator of the degree to which an electrophile is responsive to a part of a molecule.

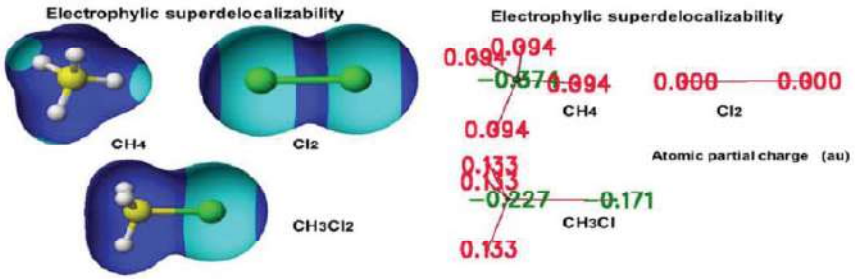


Figure 1: Fundamental properties of methane, chlorine molecule, and chloromethane.

However, the apc values do not change dramatically due to the dipole-dipole interaction of two chloromethane molecules. There are three types of contact, as shown in Figure 2. These molecules do not appear to contact each other, but they are in contact, as shown in Figure 3, which shows the electrostatic potential on the van der Waals surface. The electrostatic potential shows the effect of the electric field of a source charge on the position of another charge within the field.

Changes in the property values of three types of chloromethane pairs are analyzed from changes in atomic partial charge values and molecular interaction (MI) energy value change. The MI energy value is calculated using the MM2 program. MI energy values of the optimized structure (FS), hydrogen bonding (HB), electrostatic interaction (ES), and van der Waals interaction (VW) are obtained using the following equations. The calculated MIHB, MIES, and MIVW values are summarized in Table 1

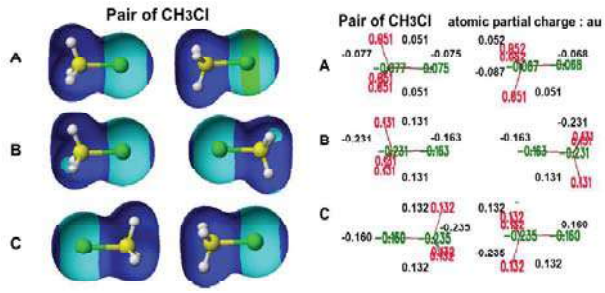


Figure 2: Three types of contact structures of chloromethane

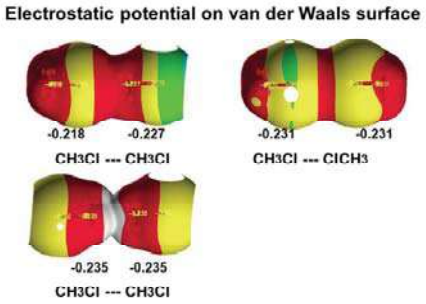


Figure 2: Three types of contact structures of chloromethane

MIFS = 2 x FS (monomer) - FS(dimer)

MIHB = 2 x HB (monomer) - HB (dimer)

MIES = 2 x ES (monomer) - ES (dimer)

MIVW = 2x VW (monomer) - VW (dimer).

Table 1: Molecular Interaction Energy of Chloromethane Pair

Analyte	fs	hb	es	vw	MIFS	MIHB	MIES	MIVW
Monomer	0.1176	0.000	0.000	0.000	–	–	–	–
Complex A	-0.8941	0.000	-0.507	-0.622	1.1293	0.000	0.507	0.622
Complex B	0.2500	0.000	0.384	-0.369	0.0148	0.000	-0.384	0.369
Complex C	-0.2657	0.000	0.550	-1.052	0.5009	0.000	-0.550	1.052

unit: kcal mol^{-1}

The contributions of these properties are analyzed using MIHB, MIES, and MIVW. The MIFS value includes MIHB, MIES, MIVW, and some tension energy values. The tension energy value is affected by changes in molecular shape. Hydrogen bonding does not contribute to the interaction between chloromethane molecules. Van der Waals energy is related to the contact surface area, and the order can be imagined from the structures A, B, and C. Conformation A involves contact between chlorine and methyl. Conformation B involves contact between head to head of chlorine and chlorine, and Conformation B involves contact between methyl and methyl groups. The MIVW values are consistent with these structural considerations. MIES is related to electron localization.

Considering the apc value change at their contact sites, the chlorine apc of conformation A increases by 0. 096 au, apc of conformation B increases by 0. 008 au, and apc of conformation C increases by 0.011 au, but without direct contact. Changes in the methyl carbon apc of conformations A, B, and C are 0.140, -0.004, and -0.008 au. Methyl and methyl do not contact. These simple model experiments clearly explain the contribution of electrostatic interaction and van der Waals force. When two molecules and/or ions come into contact, van der Waals interaction automatically contributes. When molecules have no hydrogen-bonding capability, hydrogen bonding energy values do not appear. The calculated results support the conclusion that structure A is the most obvious possible structure based on dipole-dipole attraction [12]. Speakman described in detail that the negative electronic charge of the chloromethane chlorine and the positively charged carbon contact together. When two polar molecules approach one another, they will tend to do so in an orientation that results in an attractive force between them. For two polar molecules arranged, the attractions between opposite charges exceed the repulsions between like charges. This statement may be confirmed by a simple Coulomb's law calculation based on the bond lengths and van der Waals constant. The above *in silico* calculation using a molecular mechanics program supports his explanation. Furthermore, he described hydrogen bonding in detail in the book.

1.2. Hydrogen bonding

The hydrogen bond is weaker than covalent bonds, and the contribution was observed as a higher boiling point relative to that expected from the molecular mass based on the hydrogen bond. The details were explained using propanoic acid [12]. Here, the properties of the monomer and dimer of acetic acid are analyzed using the calculated molecular interaction energy values and atomic partial charge. The structure and apc of the monomer and dimer are shown in Figure 4, and the molecular interaction energy values are summarized in Table. 2

Table 2: Molecular interaction energy of acetic acid pair.

Analyte	fs	hb	es	vw	MIFS	MIHB	MIES	MIVW
Monomer	-12.5188	-3.400	-6.646	0.399	–	–	–	–
Dimer	-37.1345	-17.560	-15.085	1.338	12.097	10.760	1.793	-0.540

Unit: kcal mol^{-1}

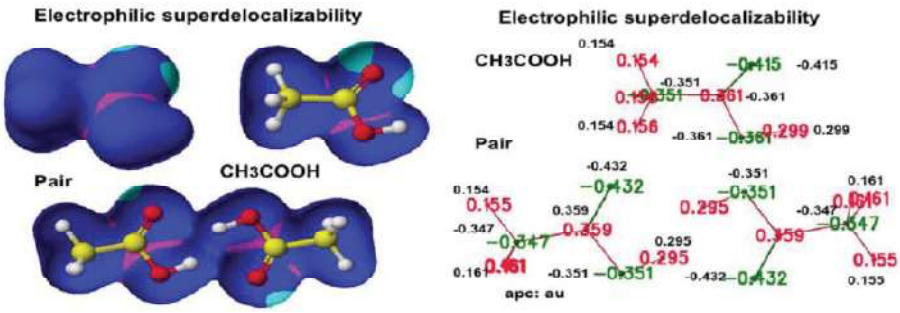


Figure 4: Hydrogen bonding between two acetic acids.

Acetic acid is a molecule capable of hydrogen bonding. The calculated MIHB energy value (10.760 kcal mol^{-1}) indicates that the major interaction is hydrogen bonding, and the carbonyl oxygen electrons contribute a small MIES value. Their condensation reduces van der Waals energy, and the MIVW value is negative. Apc values of hydrogen and carbon change slightly after docking, but apc values of carbonyl and hydroxy oxygens change from -0.415 and - 0.361 to -0.432 and -0.351, respectively. This experiment demonstrates the contribution of hydrogen bonding between two molecules. Furthermore, hydrogen bonding occurs between ions and molecules.

In addition, the contribution of water-molecule hydration of sodium and chloride ions is demonstrated. Cations might bond by the strong ion-dipole force, and anions are usually less hydrated than cations. Probably, they are hydrogen-bonded. The bonding structures between water molecules and chloride and sodium ions are shown in Figure 5. Electron-rich chloride ion may contact the hydrogen of the water molecule, and electron-poor sodium ion may contact the electron-rich oxygen of the water molecule. This classical explanation can be demonstrated using molecular mechanics calculations.

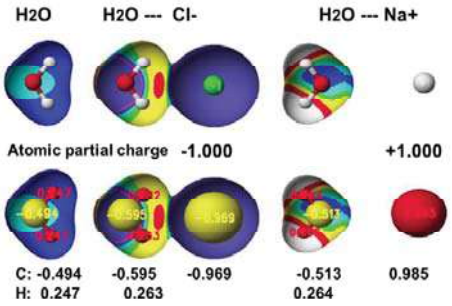


Figure 5: Hydrogen bonding between water and chloride ion and water and sodium ion.

The optimized structure using the molecular mechanics program supports the original explanations. A chloride ion binds between two water molecules' hydrogens, and the apc of the chloride ion increases from -1.000 to -0.969 au, and the apc of the oxygen atom decreases from -0.494 to -0.595 au. On the other hand, the apc of hydrogen increases from 0.247 to 0.263 au. In the case of water and sodium ion contact, the apc of the sodium ion decreases from 1.000 to 0.985 au, and the oxygen apc decreases from -0.494 to -0.513 au. The hydrogen apc increases from 0.247 to 0.264 au. These are examples of hypotheses that may be examined using computational chemical calculations.

1.3. Lewis acidity and basicity

Definition of Lewis acid and base

Acid: any species containing any atom which can accept a share in an electron pair; An acid is an electron-pair acceptor

Base: any species which can share an electron pair with any electron pair acceptors; A base is an electron-pair donor

An acid-base reaction is the sharing of an electron pair with an acid by a base

When the Lewis acid-base reaction is for organic chemistry (change molecule structure), and Lewis acid-base interaction is for chromatography (no change molecule structure). Lewis acid-base interaction can be quantitatively analyzed using model compounds (phases). A simple example is the acetonitrile-benzene interaction. The model structures are shown in Figure 6.

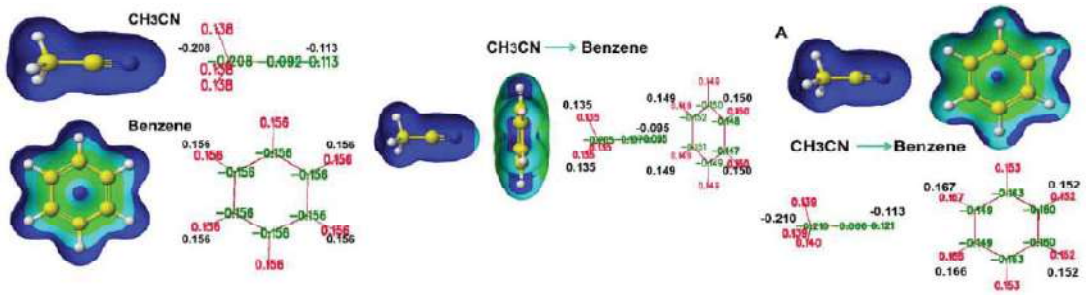


Figure 6: Interaction between acetonitrile and benzene.

After the interaction, the acetonitrile nitrogen apc value increases from -0.113 to -0.095 au. The benzene-ring carbon apc increases, and that of hydrogen decreases due to their Lewis acid-base interaction. It can be explained as a contact charge transfer complex, too. In conformation A, acetonitrile nitrogen faces the center of the benzene ring and the nitrogen faces the side of the ring in conformation B. Conformation B is the favored complex structure based on a comparison of the MI energy values of these complexes. However, the methanol-benzene interaction is based on hydrogen bonding, where the apc value of the methanol hydroxyl hydrogen increases from 0.259 to 0.281 au. A small ES value is not observed for small molecules. The hydrogen bonding is stronger than dipole-dipole interaction (weak electrostatic interaction). The the calculated MI energy values are given in Table 3.

Table 3: Molecular interaction energy of acetonitrile and methanol with benzene

Analyte	fs	hb	es	vw	FS	HB	ES	VW	MIFS	MIHB	MIES	MIVW
Acetonitrile	-0.149	0.000	0.000	-1.151	-9.038	0.000	0.000	2.042	0.812	0.000	0.000	-0.138
Methanol	0.060	0.000	0.000	-0.077	-17.054	-7.670	0.000	1.564	9.038	7.670	0.000	1.364
Benzene	-8.077	0.000	0.000	3.005	–	–	–	–	–	–	–	–

Unit; kcal mol^{-1}

Even interactions between benzene and related compounds do not produce an MIES energy value, but their atoms indicate electron localization. The interaction appears to be governed by van der Waals (hydrophobic) interaction based on the MIVW energy values, as shown in Table 4. There are three types of complex conformations shown in Figure 7 considered between benzene and benzene; however, conformation C is the favorable structure based on the MI energy values. The favorable structure between benzene and toluene is structure D, where a methyl group with a positive inductive effect contacts benzene. In contrast, the phenyl group of chlorobenzene contacts with benzene (conformation A) due to the negative inductive effect of the chlorine group.

Table 4: Molecular interaction energy of benzene, toluene, and chlorobenzene with benzene

Analyte	fs	hb	es	vw	FS	HB	ES	VW	MIFS	MIHB	MIES	MIVW
Benzene	-8.077	0	0	3.003	-19.666	0	0	2.501	3.512	0	0	3.509
Methylbenzene	-8.6	0	0	3.036	-18.735	0	0	3.996	2.857	0	0	2.254
Chlorobenzene	-7.802	0	0	3.214	-17.589	0	0	4.513	1.71	0	0	1.706

Unit; kcal mol^{-1}

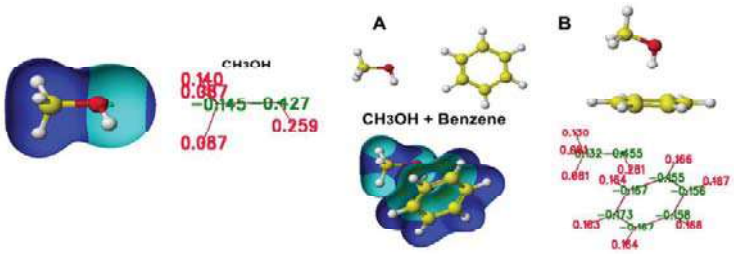


Figure 7: Interaction between methanol and benzene.

1.4. Strong acid-base interaction

The potential of computational chemical analysis of molecular interactions can be understood from the analysis of simple model compounds. Ion–ion interactions were studied for the combination of an ammonium ion (cation) with an acetate ion (anion) by MM2 calculations. The calculated ion-pair formation energy values are as follows. The balance (the MI energy value) after complex (ion-pair) formation indicates the energy contribution of the ion-pair formation. Electrostatic energy contributes mainly to the ion-pair formation between ammonium and acetate ions. The ammonium ion, acetate ion, and the ion-pair structures are shown in Figure 8, where the atomic distance of the ammonium hydrogens has been expanded from 1.0 to 1.3 Å. Their apc values were also calculated using the MOPAC PM5 program, in which the apc of the ammonium hydrogens has been doubled.

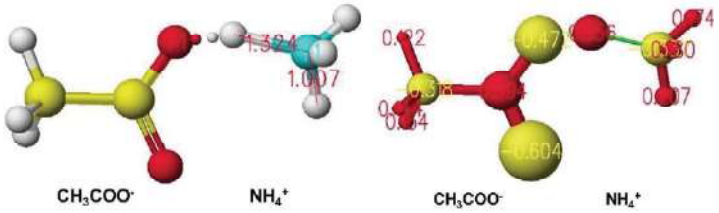


Figure 8: Ion-ion interaction between acetate and ammonium ions, unit: bond length Å, partial atomic charge au.

In proteins, the aspartic and glutamic acid carboxy groups work as a cation-exchange group. The lysine ε-amino group functions as a hydrogen-bonding group and an anion exchanger, and the arginine guanidino group functions as an anion exchanger. Their activity depends on their dissociation, and the dissociation constants of aspartic and glutamic acid carboxy groups are 3.65 and 4.25. The lysine ε-amino and arginine guanidino groups are 10.53 and 12.48, respectively. In general, these amino acids are ionized under physiological conditions. However, the fundamental activity of the carboxy, amino, and guanidino groups was analyzed using simple model compounds considering solvent (water) and ion (sodium and chloride) effects for their molecular interactions with simple model compounds to study ion-ion interaction, hydrogen bonding, and van der Waals interaction. The calculated energy values of strong Lewis acid-base interactions (ion-ion interactions) are represented by electrostatic energy, but the value is much higher than weak interactions such as dipole-dipole and π-π interactions.

1.5. Dissociation (ionization)

Carboxy and phosphoric groups are very common in biological reactions. DNA and RNA are sugar (pentose) phosphate-conjugated nitrogenous bases, and the phosphate binds tightly with basic compounds via ion-ion (anion-cation) interaction. The carboxyl group is present in acidic amino acids (glutamic and aspartic acids), components of proteins. These groups are ionized under biological conditions. The ionization depends on their environmental conditions (pH of the physiological solution). The fundamental mechanism of acid-base interactions is electron transfer and localization, described in detail by C. A. Vanderwerf [13].

The pH of a solution is related to the dissociation constant (pK) of the compound. pKa is the negative logarithm of the acid dissociation constant, and pKb is the negative logarithm of the base dissociation constant Kb. The following equation exhibits the dissociation of acetic acid. Figure 9 shows the electron localization and atomic partial charge for visualization

$CH_3COOH + H_2O = CH_3COO^- + H_3O^+$ p*K*a = 4.24

In pure water and all aqueous solutions, this equilibrium exists and must satisfy the equation:

$\{[H_3O^+]\ [CH_3COO^-] / [CH_3COOH][H_2O]\} = Ka$

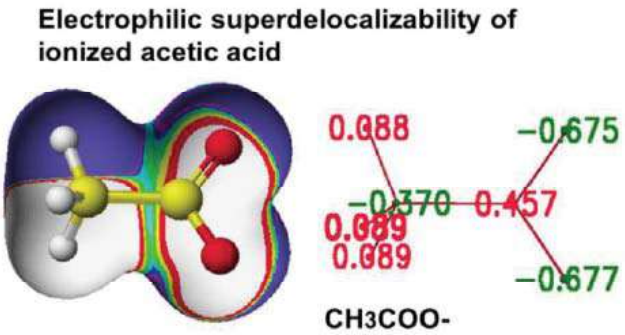


FIgure 9: Ion-ion interaction between acetate and ammonium ions, unit: bond length Å, partial atomic charge au.

The ionization of the carboxyl group reduces the apc value from -0.136 to -0.895 au, and the methyl group apc reduces from 0.115 to -0.104 au. The total apc value reduces from -0.021 to 0.999 au. The calculation of apc values of simple molecules clarifies the electron localization by ionization. The magnitude of the apc value change by ion-ion interactions is large, and that of dipole-dipole interactions is small. The latter phenomenon is called Lewis acid-base interaction. The electrostatic energy value provides the degree of ion-ion interactions and dipole-dipole interactions, although at different magnitudes. Ion-ion interactions exhibit the highest values, followed by hydrogen bonding, dipole-dipole interactions, and van der Waals forces. We have to carefully manage the difference between ion-ion interactions in calculated electrostatic energy values.

On the other hand, lysine ε-amine and arginine guanidino groups of proteins are cations and play crucial roles in binding acidic compounds via ion-ion interaction. Propylamine and propylguanidine are used to demonstrate their ionization. The structures of the molecular and ionized forms of propylamine are shown in Figure 10.

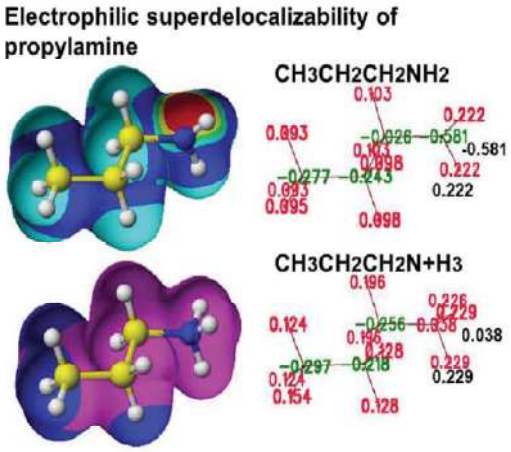


Figure 10: Molecular and ionized form propylamine structures with electrophilic superdelocalization and atomic partial charge.

The total apc values of the molecular form amino group increase from -0.139 to 0.742 au upon ionization. Cationization increases the apc value, and anionization decreases the apc value. The change in apc indicates the electron localization, and the electron-rich group will contact the electron-poor group and neutralize the pair molecules. A guanidino group exhibits both ionized and molecular-form amino groups, and the dissociation constant is high (>12); therefore, it works for hydrogen bonding and ion-ion interaction. This computational chemical drawing cannot show the resonance structure and shows two groups, as shown in Figure 11.

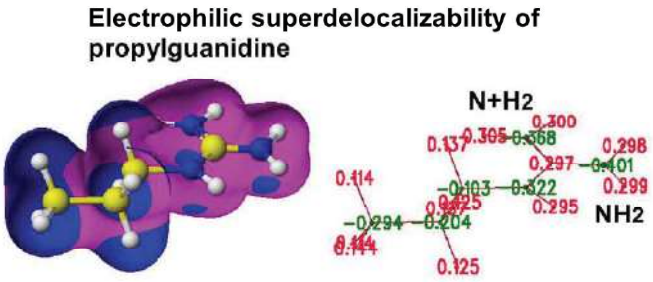


Figure 11: Propylguanidine structures with electrophilic superdelocalization and atomic partial charge.

The total apc values of ionized and molecular-form amino groups are 0.237 and 0.196 au, and the apc value is higher upon ionization. The apc values of the ionized group change by ion-ion interactions. Benzyltrimethylaniline is a simple model of an anion exchanger. The apc of the amino group is changed with a counterion (chloride). Figure 12 shows a part of apc values before and after the attached chloride ion.

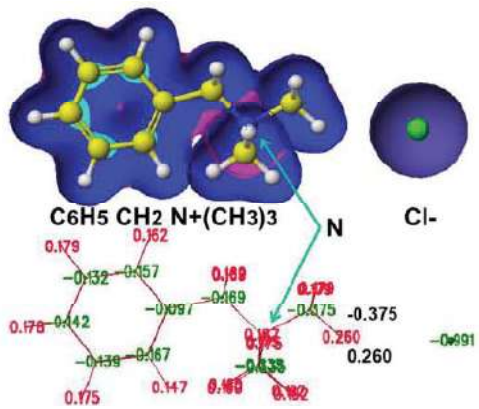


Figure 12: Structure of the *N, N, N*-trimethyaniline chlorine and initial position of aniline.

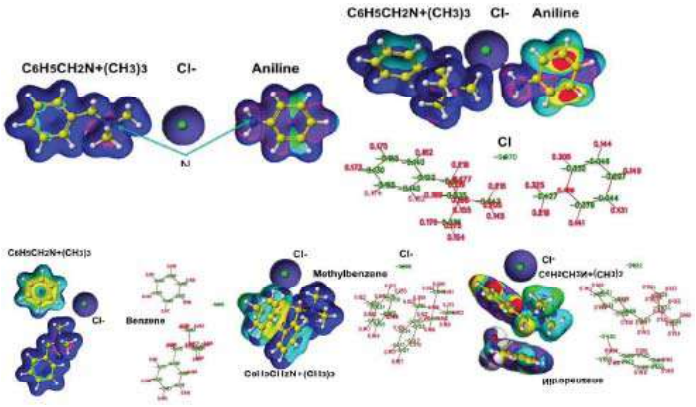


Figure 13: Optimized structures of N, N, N-trimethyaniline chloride with aniline, benzene, methylbenzene, and nitrobenzene..

The model anion exchanger interacts with various compounds, even in non-aqueous solutions. The following analysis demonstrates the feasibility of the ion exchangers as adsorbents. The electron localization and hydrogen bonding capability clearly demonstrate the capability of the ion-exchange group. The in silico analysis was performed using *N,N,N*-trimethylaniline chloride, supported by the atomic partial charge values of the single signal of the *N,N,N*-trimethyl group. The amino group of aniline faced the chloride ion of trimethylammonium. The chloride ion repelled the nitro group of nitrobenzene. Because both nitro- and chloride ions are electron-rich groups or atoms, these small molecules move freely in solution. A weak MIHB contribution is observed for aniline, and a strong MIES contribution is observed for nitrobenzene.

Table 5: Molecular interaction energy of benzene, toluene, and chlorobenzene with benzene

Analyte	fs	hb	es	vw	FS	HB	ES	VW	MIFS	MIHB	MIES	MIVW
Benzene	-8.077	0	0	3.005	-6.113	0	-2.335	9.867	1.205	0	0.022	1.176
Methylbenzene	-8.6	0	0	3.036	-6.718	0	-2.268	9.742	1.288	0	-0.05	1.332
Nitrobenzene	-6.633	0	0	4.17	-6.042	0	-1.797	9.337	2.578	0	-0.516	2.871
Aniline	-6.121	-1.334	0	3.476	-4.191	-1.35	-2.319	10.245	1.239	0.016	0.006	1.209
TMACL	3.17	-2.313	8.038	-	-	-	-	-	-	-	-	-

TMACI: *N, N, N*-trimethylaniline chloride; unit: kcal·mol^{-1}

The molecular interaction causes electron localization. The localized apc values of benzyltrimethylaniline chloride upon contact with benzene, toluene, nitrobenzene, and aniline can be observed through peak shifts in NMR spectra.

Table 6: Totasl atomic partial charge of the *N, N, N*-trimethylaniline chloride

Analyte	Trimethylammonium	Phenyl
Aniline	1.026	-0.039
Benzene	0.923	0.064
Toluene	0.923	0.064
Nitrobenzene	0.483	-0.472

unit: au

The higher the apc value, the greater the shift toward a high field, and the contact with aniline via chloride ion, the peak shifted to a higher field due to the electron localization. The nitrobenzene nitro group is negatively charged and the same as the chloride ion; therefore, the nitrobenzene nitro group was repulsed from benzyltrimethylaniline chloride. The results were obtained when the nitrobenzene phenyl group faced chlorine ion. The single proton peak of trimethylaniline shifted to a higher field upon addition of aniline and shifted to a lower field upon addition of nitrobenzene. The precision of the chemical-shift measurements was high, but that of apc values remains/The apc values of carboxy, hydroxy, and phenyl are negative, that of amino is a little positive, and that of alkyl groups is positive. The apc values and NMR spectra exhibit a certain relationship, but the high-resolution NMR spectra cannot be assigned using current apc values.

NMR was used to measure ion-exchange capacity based on water signals [5, 6]. The higher the ion-exchange capacity, the higher the peak signal intensity. The signal indicates adsorption and molecular interactions between the ion-exchange

resin and the solvent. NMR can be used to measure molecular interactions and may indicate the inductive effect of the interaction; however, we have to manage the chemistry in solution and solid-phase adsorption carefully [14, 15].

1.6. Prediction of Dissociation Constant

Hammett's σ constant was derived from the retention difference of thin-layer chromatography and affects the hydrogen bonding strength of the carboxy group to silica gels. This reflects the inductive effect of substitutes and indicates the localization of electrons. Therefore, dissociation constants can be predicted using Hammett's equation p*K*a = A + BΣo where A and B are constants and σ is Hammett's σ constant. A is the pKa value of non-substituted compounds, and B has to be selected for each series of compounds. There were no standard equations for A and B values. On the other hand, apc values indicate the degree of electron localization. The reference values of dissociation constants were used to predict dissociation constants from apc calculated by the MM/AM1/PM5 program.

The correlation between p*K*a values measured by liquid chromatography and apc of non-substituted aromatic acids, including phenol, was:

$$pKa = -210.485 \times (apc) + 55.797,\ r^2 = 0.994,\ (n = 8). \quad (2)$$

where the reference compounds used for this calculation were benzoic acid, phenylacetic acid, 3-phenylpropionic acid, mandelic acid, trans-cinnamic acid, indole-3-acetic acid, indole-3-butyric acid, and phenol. The constant A of Hammett's equation can be calculated from this equation.

BΣσ of Hammett's equation was:

BΣσ = (-9.356 x p*K*a - 116.314) x Δ(apc of substitute)

where B is (-9.356 **x** p*K*a - 116.314) and Σσ is Δ(apc of substituent). The ortho-effect of p*K*a values of ortho- substituted benzoic acids were 0.618 and 1.356 units for a methyl group and a halogen atom, respectively.

Therefore, p*K*a of benzoic acid derivatives can be predicted from the above equations and ortho-effects. The correlation between predicted and reference p*K*a values for benzoic acid derivatives was as follows:

p*K*a (pred) = 0.991 x p*K*a (ref) -0.017, $r^2 = 0.982$, (n = 22).

The dissociation constants of acidic compounds can be predicted using apc instead of Hammett's constant. [16].

The forces holding two molecules together are similar to those responsible for their dissolution in the solvent. Eight solubility factors are recognized: van der Waals force (a combination of van der Waals volume, repulsion, and London dispersion), dipole-dipole, ion-dipole, Coulombic and repulsion forces, charge-transfer complexation, hydrogen bonding, and hydrogen bonding and coordination bonds. However, some of these are explained as different degrees of dev electron localization; therefore, these forces can be simplified to the van der Waals force, electrostatic interaction, and hydrogen bonding. Consistent with the concept of "like dissolves like, " proposed by Henry Freiser, the molecular interaction (MI) forces between two molecules are the same. The MI of a particular molecule is not due to a single factor but rather to a combination of several factors [17].

If we have to handle a typical reversed-phase liquid chromatography, we shall use the partition coefficient, especially the octanol-water partition coefficient, provides the possible elution order. Computer software for the optimization of chromatographic separation based on the partition coefficient proposed by Hantsch et al. is a common and practical approach for known compounds. However, the application to new types of compounds requires fundamental knowledge of chemistry. The partition coefficient can be measured and obtained from the partition ratio between two liquid phases. We have to understand why such partition occurs and what kinds of molecular interactions occur in solvents [18-20]

A quantitative explanation of donor-acceptor interactions is fundamentally required for learning chromatography as chromatographers but not chromatography operators. The modern instruments run largely automatically after sample bottles have been placed in a holder. The separation condition may be given by someone followed by a published experimental condition. However, the most critically required experiment is sample preparation from various sources. Separation of a mixture of standard samples is a rare case; how to purify samples from a complex matrix requires broad knowledge. Shortening the experiments is possible through an understanding of fundamental principles of chemistry [21, 22].

In silico analyses using simple molecules are described as follows: Hydrophobic interaction was explained using alkanes, which are completely saturated molecules having no specific physicochemical properties except van der Waals volume. They interact via van der Waals forces. Hydrogen bonding interaction was demonstrated using alkyl alcohols. The alkyl-chain length contributes to the hydrogen bonding of alkyl alcohol. The hydrogen bonding of alkyl alcohols depends on alkyl-chain length. Coulombic force (ion-ion interaction) was studied using acetic acid and ammonia. Electrostatic energy is the main contributor to ion-pair formation. Furthermore, steric hindrance was studied using amino acids. Numerous reports using ion exchangers have been published, but molecular interactions of ion-exchange mechanisms and the chemistry have not been quantitatively described [23-25], however, in silico analysis should clarify them. Steric hindrance cannot be directly calculated, but a lower MI energy value indicates lower steric hindrance in a complex. The hydrogen bonding energy values of *R*- and *S*-amino acid complexes are lower than those of *R*- and *R*-complexes or *S*- and *S*-complexes. The typical MI force can be studied using different types of chromatography.

These conclusions provide a basis for quantitatively analyzing enzyme (protein) activities using in silico analysis. Probable molecular interactions (MI) can be quantitatively calculated with a molecular mechanics (MM) program using the chemical structures of two molecules. MI calculations were first applied to simple model compounds, including amino acids. MM calculations can provide hydrophobic interaction, Coulombic interaction, and hydrogen bonding, as well as van der Waals (VW) energy, electrostatic (ES) energy, and hydrogen bonding (HB) energy values. MI sites are indicated by changes in the atomic partial charge (apc) of contact atoms. For example, the Δapc of hydrogen was found to be 0.002 au in hydrophobic interaction between two *n*-hexane molecules while analyzing hydrophobic interaction. The Δapc of oxygen in diethylether was found to be 0.032 au in a study of π−π interaction. The Δapc of hydroxyl hydrogen of pentylalcohol was found to be 0. 013 au when HB was analyzed between two pentylalcohols. When the ion-ion interaction was analyzed between butyric acid and pentylamine, the Δapc values of butyric acid oxygen and pentylamine nitrogen were found to be 0.044 and 0.036 au, respectively [16]. In particular, chiral recognition sites are clearly indicated by Δapc.

These MI energy values (kcal mol^{-1} are the sum of compound A and B energy values minus a complex energy value, calculated as per the following equations [17], where MIHB, MIES, and MIVW are the MI energies of hydrogen bonding (HB), electrostatic (ES), and van der Waals (VW) energy values, respectively.

MIHB = HB (molecule A) + HB (molecule B) – HB (molecule A and molecule B complex),

MIES = ES (molecule A**)** + ES (molecule B) – ES (molecule A and molecule B complex)**,** and MIVW = VW (molecule A) + VW (molecule B) - VW (molecule A and molecule B complex).

The MI in chromatography was analyzed using singly bonded silicon oxides with model ligands such as octyl-, hexenyl-, hexylamine-, and hexylguanidine-bonded trimethoxy-silicones. The HB, ES energy, and VW energy values calculated for MI energy indicate their specific molecular interactions with the analytes [26]. This approach was applied to study the MI mechanisms of ion-exchange liquid chromatography of acidic drugs using hexylamine and hexylguanidine-bonded silica gels [27]. The developed method for quantitative in silico analysis of molecular interaction using the reproducible chromatographic data was applied to the quantitative analysis of various enzyme reactivity. The main interaction site was the ion-ion interaction between a residual amino acid and a counter-ionic group of the analyte. Furthermore, the quantitative analytical method was applied to protein-protein interactions, especially for COVID-19 variants' transmissibility, and designing the binding inhibitors of S-RBD with ACE2 as an application of quantitative ion-ion interaction analysis.

On the other hand, biochemistry has been taught based on molecules and structures. Van Holde proposed the physical part of biochemistry and described: 1. Thermodynamics and biochemistry; 2. Solutions of macromolecules; 3. Chemical equilibrium; 4. Introduction to transport processes; diffusion; 5. Sedimentation; 6. Electric fields; 7. Viscosity; 8. Absorption and emission of radiation; 9. Scattering; 10. Circular dichroism and optical rotatory dispersion; 11. X-ray diffraction. Several of these overlap with instrumental analytical chemistry; however, the textbook explains the fundamental mechanisms in detail. [28]

The practical contribution of computers was recognized and an introductory textbook was written by Breneman and Parker who wrote 25 chapters, and several of them can be used in teaching analytical chemistry. The chapters are 1. Math Basic; 2. Dimensional Analysis; 3. Metric System; 4. Density; 5. Temperature; 6. Molecular Weight and the Mole; 7. Empirical and Molecular formulas; 8. Stoichiometry and Ho Titration; 9. Heat of Reaction from Calorimeter Measurements; 10. Standard Enthalpy from Heats of Formation; 11. Light and Energy; 12. The Hydrogen Atom and Atomic spectra; 13.

Atomic Orbitals; 14. Molecular and rase Hybrid Orbitals; 15. Gas Laws; 16. Gas Kinetic-Molecular Theory; 17. Chemical Kinetics; 18. Chemical Equilibria; 19. Acid-Base Equilibria; 20. Titration Curves; 21. Solubility Products; 22. Entropy and Free energy; 23. Free Energy and Equilibrium; 24. Electrochemistry; 25. Nuclear Chemistry [29]. These texts can be studied using Basic language. Many chapters are prepared for learning general chemistry. These authors mentioned that the book is not a mathematics or computer science book. However, such knowledge is required to learn modern analytical chemistry. Computer-controlled new analytical instruments provide answers without the fundamental understanding of analytical instruments.

Remarks

Electrophilic superdelocalizability: an indicator of the degree to which an electrophile is responsive to a part of a molecule. Superdelocalizability is a quantity that indicates the ability of a molecule's electron density to move from localized to delocalized. The greater the superdelocalizability, the more responsive it is.

The electrostatic potential: a moved unit charge from a reference point to a specific point inside the electric field without producing acceleration. The electrostatic potential shows the effect of the electric field of a source charge on the position of another charge within the field. The SI unit of electrostatic potential: volt.

The details of the computational chemistry program are written by G.D. Purvis, On the use of isovalue surfaces to determine molecule shape and reaction pathways, J. Compt.-Aided Mol. Design, 5 (1991) 55-90.

1.7. Molecular interaction degree analysis

The effect of molecular size of weak interactions is described using simple compounds in this chapter, especially +I effect of alkyl group which has no specific electronic properties; however, atomic partial charge distribution may indicate the contribution of the +I effect. The atomic partial charge values are like Hammett's s constants and indicate the inductive effects. The relative values calculated using computational chemistry may explain the effect quantitatively.

1.7.1. Van der Waals force between n-alkanes: Hydrophobic interaction is an interaction between hydrophobic compounds. Hydrophobic compounds are not wetted by water. An alkane, a completely saturated molecule, is a typical example. Alkanes interact through van der Waals forces; those are a combination of molecular size (van der Waals volume), London dispersion, and repulsion. One example is demonstrated with two molecules of n-pentane (Figure 14). The van der Waals energy (VW) value of a single pentane is 2.138 kcal mol-1, and that of the combined two molecules is -0.070 kcal mol^{-1}. Therefore, the molecular interaction (MI) energy value of the two contacted pentane molecules is 2.138x2 - (-0. 070) = 4.138 kcal mol^{-1}. Pentane is a saturated hydrocarbon and cannot participate in hydrogen bonding (HB) and electrostatic (ES) interaction. Furthermore, electron localization of single and complex pentane is calculated using a molecular orbital package program PM5. Atomic partial charge (apc) indicates electron localization, and the unit is atomic unit (au). The center hydrogen apc is 0. 096, the side hydrogen's apc is 0.093, and the corner hydrogen apc is 0. 095 au. After contacting two pentanes, these apc values are changed to 0.098, 0.092, and 0.094 au. That is, pentane itself is a neutral compound, but the contact produces electron localization (see circled atoms).

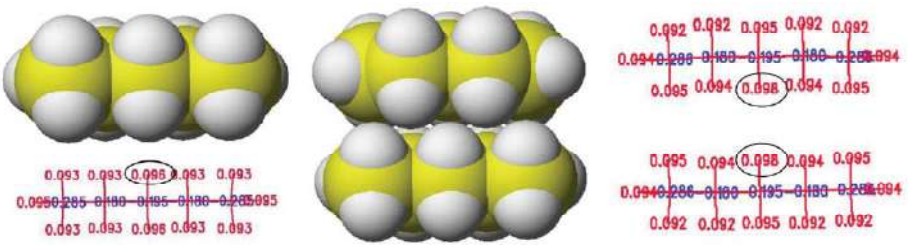


Figure 14: Docking of two pentane molecules.

The second example is the docking of n-hexane (Figure 15). The single molecule VW value is 2.613, and the two molecules VW is -0.145 kcal·mol^{-1}. Therefore, the MIVW energy value is 2.613x2 - (-0.145) = 5.371 kcal mol^{-1}. The center hydrogen apc value is changed from 0.095 to 0.097 au.

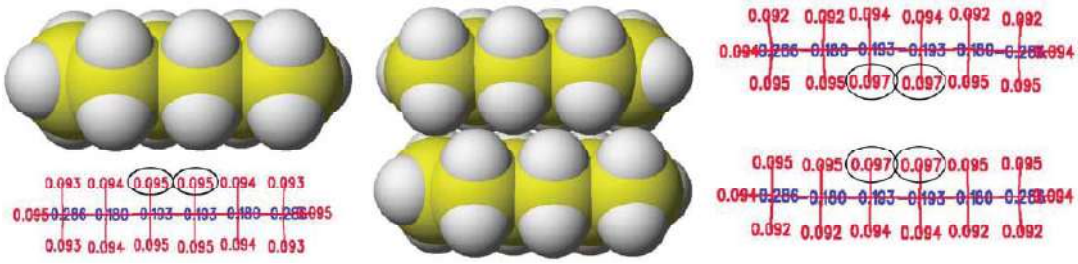


Figure 15: Docking of two hexane molecules.

In n the case of *n*-heptane (Figure 16**),** the single molecule VW value is 3.073, and the two molecules VW is -0.350 kcal mol^{-1}. Therefore, the MIVW energy value is 3.073x2 - (-0.350) = 6.496 kcal mol^{-1}. The center hydrogen apc value is not changed (0.095 au) however, the side hydrogen apc is changed from 0.096 to 0.098. Reading hydrogen apc values indicates their contact center.

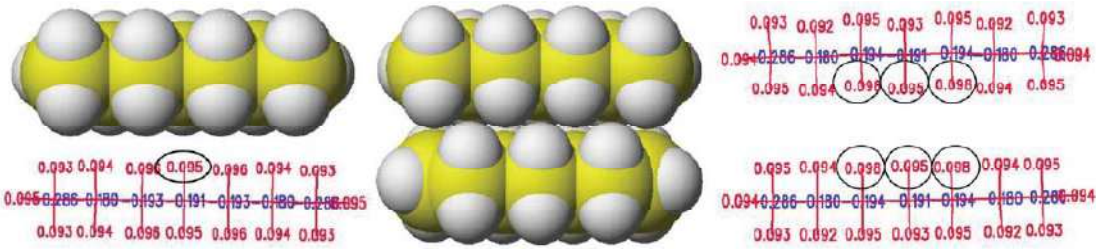


Figure 16: Docking of two heptane molecules.

Octane's MIVW value is 3. 537, and the complex VW is -0.284 kcal mol^{-1}. Therefore, the MIVW energy value is 3. 537 - (-0. 284) = 7.358 kcal mol^{-1}. The center hydrogen apc value is changed from 0.095 to 0.097 au (Figure 17), and the hydrogen apc is changed from 0.095 to 0.096 au.

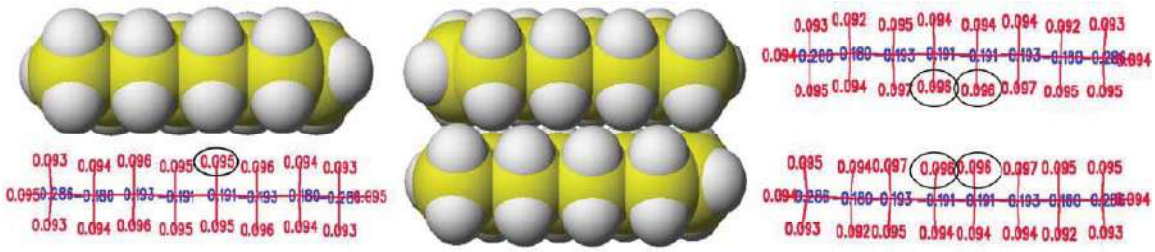


Figure 17: Docking of two heptane molecules.

The calculated molecular interaction energy values are summarized in Table 7. The properties of alkanes clearly show that the molecular interactions are caused by van der Waals force, and electrostatic interactions are not observed even if weak electron localization is observed.

Table 7: Molecular Interaction Energy Values of Polycyclic Aromatic Hydrocarbons Pair

Analyte	HB (Single)	ES (Single)	VW (Single)	HB (Pair)	ES (Pair)	VW (Pair)	MIHB	MIES	MIVW
Pentane	0.000	0.000	2.138	0.000	0.000	-0.070	0.000	0.000	4.346
Hexane	0.000	0.000	2.613	0.000	0.000	-0.145	0.000	0.000	5.371
Heptane	0.000	0.000	3.073	0.000	0.000	-0.350	0.000	0.000	6.496
Octane	0.000	0.000	3.537	0.000	0.000	-0.284	0.000	0.000	7.358

Unit: kcal·mol^{-1}

The calculated MIVW energy values are correlated with the number of carbon atoms in these alkanes (MIVW = 0.997

(number of carbon atoms) – 0. 628). The correlation coefficient is 1.000 (n = 5). These simple experiments show that van der Waals interaction is not caused by neutral electron localization. All molecular interactions are based on electron localization, even if the electron localization is very little by van der Waals interaction (hydrophobic interaction) compared to Lewis acid-base interaction; furthermore, ion-ion interaction is explained later. A little electron localization is observed as a little apc value change at the contact center.

1.7.2. Van der Waals force between aromatic compounds: Alkanes are saturated hydrocarbons and polycyclic aromatic hydrocarbons are hydrocarbons with rich π-electrons; therefore, a complex of two polycyclic aromatic hydrocarbons may produce MIES, based on the expected π–π interaction. The apc of circled carbon and hydrogen changed a little that indicated these two molecules interacted each other as shown in Figures 18-22. However, calculated MI energy value changed little. The MIVW values increase from 3.498 to 12.330 kcal mol^{-1}, and apc value changed a little about 0.005 au. Molecular interaction energy values of a pair of polycyclic aromatic hydrocarbons are summarized in Table 8.

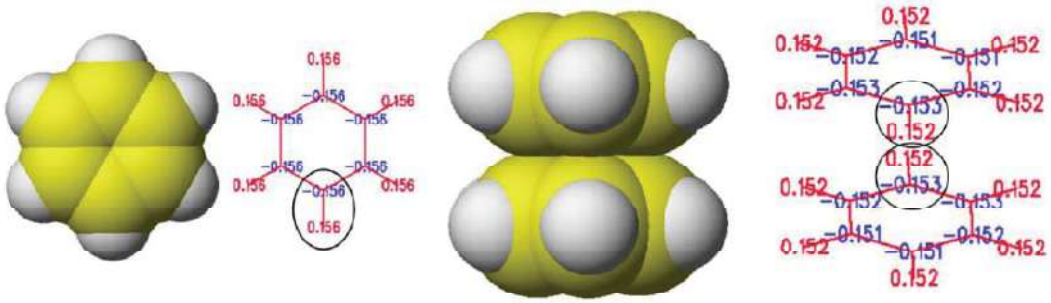


Figure 18: Docking of two benzene molecules with apc values..

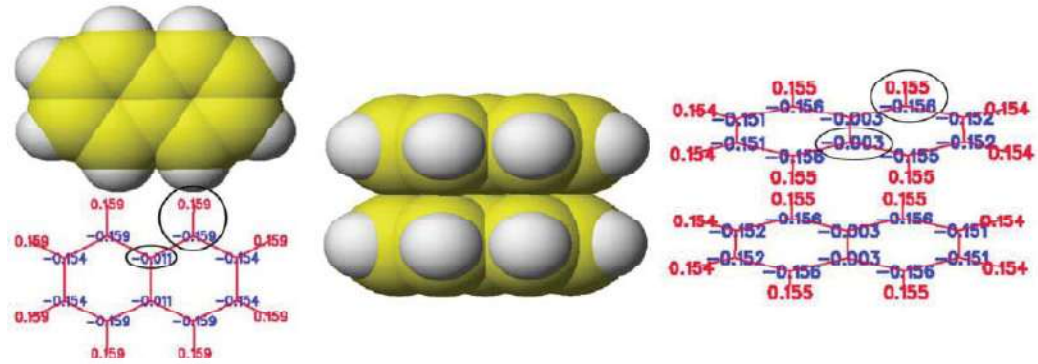


Figure 19: Docking of two naphthalene molecules with apc values.

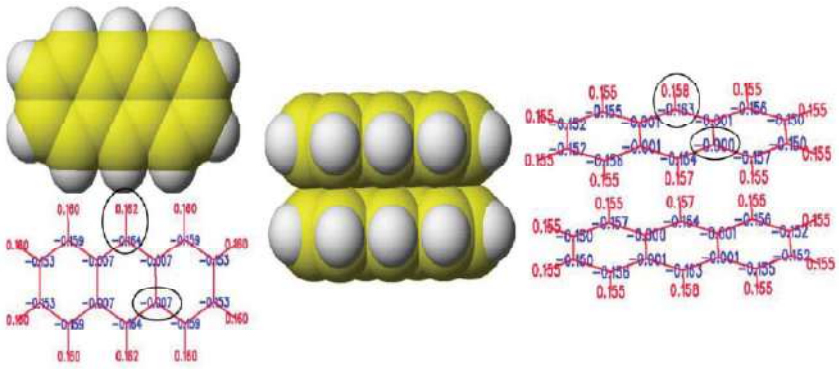


Figure 20: Docking of two anthracene molecules with apc values.

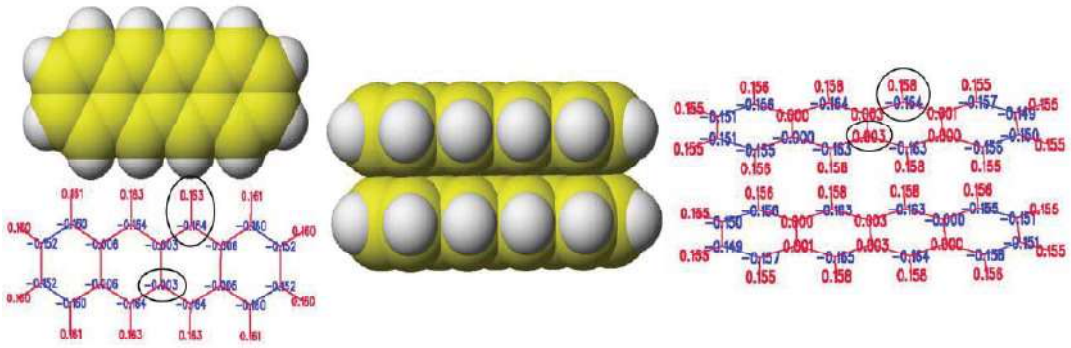


Figure 21: Docking of two tetracene molecules with apc values.

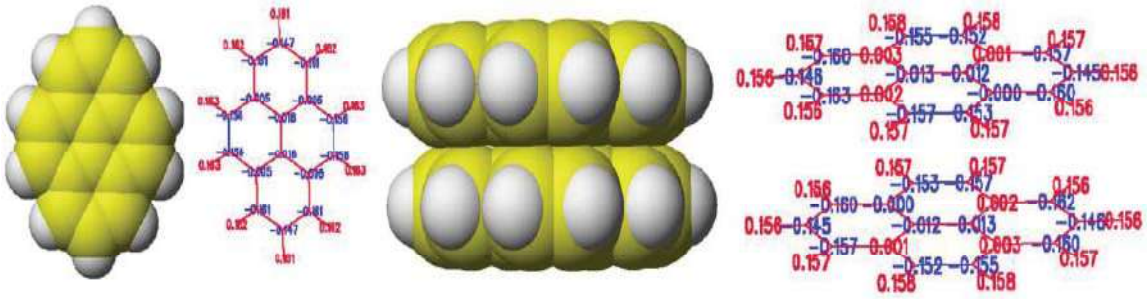


Figure 22: Docking of two pyrene molecules with apc values.

Table 8: Molecular interaction energy values of a pair of polycyclic aromatic hydrocarbons.

Analyte	HB (Single)	ES (Single)	VW (Single)	HB (Pair)	ES (Pair)	VW (Pair)	MIHB	MIES	MIVW
Benzene	0.000	0.000	3.006	0.000	0.000	2.514	0.000	0.000	3.498
Naphthalene	0.000	0.000	5.768	0.000	0.000	5.149	0.000	0.000	6.387
Anthracene	0.000	0.000	8.488	0.000	0.000	7.622	0.000	0.000	9.274
Tetracene	0.000	0.000	11.194	0.000	0.000	10.058	0.000	0.000	12.330
Pyrene	0.000	0.000	10.189	0.000	0.000	9.372	0.000	0.000	11.006

Unit: kcal·mol^{-1}

Usually, interaction mechanism between polycyclic aromatic hydrocarbons is considered π–π interaction. However, these results exhibit the interaction force is van der Waals interaction, and π–π related weak electrostatic interaction is not observed.

1.7.3. Weak Electrostatic Interaction: Dipole-dipole, π–π interaction, contact charge transfer, and weak Lewis acid-base interaction are calculated as electrostatic energy values. The calculated MIES value is smaller than that of ion-ion Interaction, which will be explained in detail later. Saturated hydrocarbons (alkanes) form weak complexes with each other via the van der Waals force. The addition of polar atoms into alkanes adds extra properties to alkanes. Adding oxygen between carbon and hydrogen makes alcohol, whose properties include hydrogen bonding (explain the detail later). Adding oxygen between carbons makes ether, whose properties include π–π, dipole-dipole and charge transfer interaction due to the lone pair electron of oxygen.

1.7.3.1. Interactor bctween allylethers: A complex of two molecules ethylether produces MIES, as demonstrated in Figure 23. The apc of circled hydrogen is changed from 0.088 to 0.098 au. The oxygen enhanced the electron localization. The influence of both sides of the alkyl chain length is studied up to the pentyl group. Their conformations are shown in Figures 23-26. The MIVW values increase from 3.286 to 9.200 kcal mol^{-1}, and MIES values vary by about 0.020 au. The initial and optimized structures of a pair of dipropylether, dibutylether and dipentylether are shown in Figures 17-19. The calculated molecular interaction energy values are summarized in Table 9.

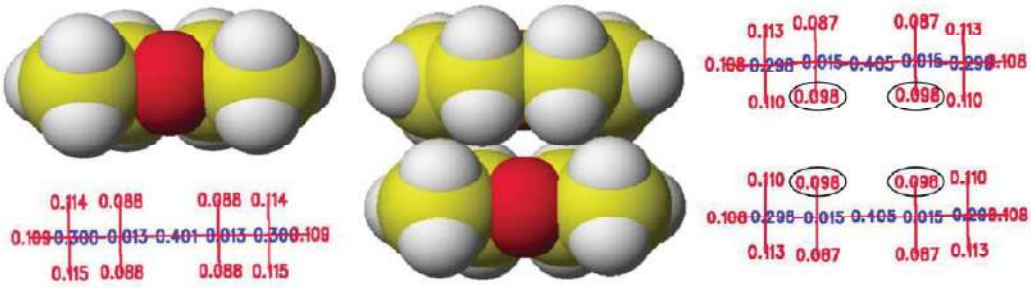


FIgure 23: Docking of two diethylether molecules with apc values..

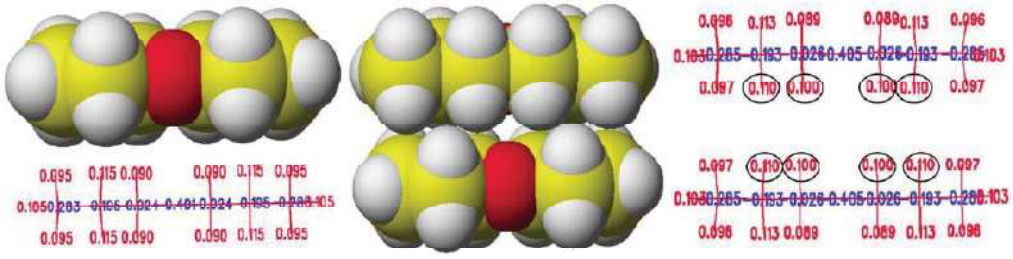


FIgure 24: Docking of two dipropylether molecules with apc values.

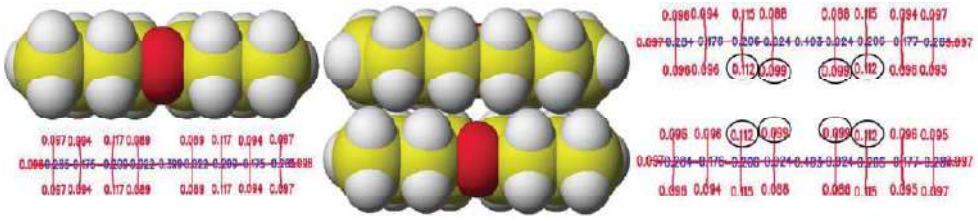


FIgure 25: Docking of two Dipentylether molecules with apc values.

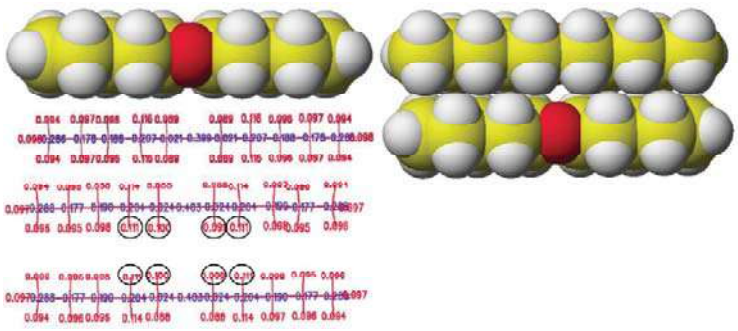


FIgure 26: Docking of two Dipentylether molecules with apc values.

Table 9: Molecular interaction energy values of a pair of alkylethers

Analyte	HB (Single)	ES (Single)	VW (Single)	HB (Pair)	ES (Pair)	VW (Pair)	MIHB	MIES	MIVW
Ethylether	0.000	0.000	2.837	0.000	-0.020	2.388	0.000	0.020	3.286
Propylether	0.000	0.000	3.776	0.000	-0.021	2.193	0.000	0.021	5.359
Butylether	0.000	0.000	4.721	0.000	-0.019	2.401	0.000	0.019	7.041
Pentylether	0.000	0.000	5.654	0.000	-0.021	2.108	0.000	0.021	9.200

unit: kcal·mol^{-1}

The contribution of oxygen of ether is very weak van der Waals force is the main interaction force for ethers.

1.7.3.2. Interactor bctween allylketones: The replacement of hydrogen with oxygen makes ketone. A complex of two molecules acetone produces MIES, as shown in Figure 27. The apc of circled oxygen is changed from -0.393 to -0.425 au. The oxygen enhanced the electron localization. The influence of both sides of the alkyl chain length is studied up to the butyl group. Their conformations are shown in Figures 27-30. The MIVW values increase from 2.179 to 8.167 kcal mol^{-1}, and MIES values vary from 2 to 1.5 au. That is, the contribution of MIES related to the alkyl length is relatively small, but the contribution of MIVW is significant. The electron localization is affected by the +I effect of alkyl length. The +I effect is observed as the stability of alkylalcohol with water. The shorter the alkyl-chain length is the more soluble in water and the longer the alkyl-chain length is the more soluble in gasoline. The calculated molecular interaction energy values are summarized in Table 10.

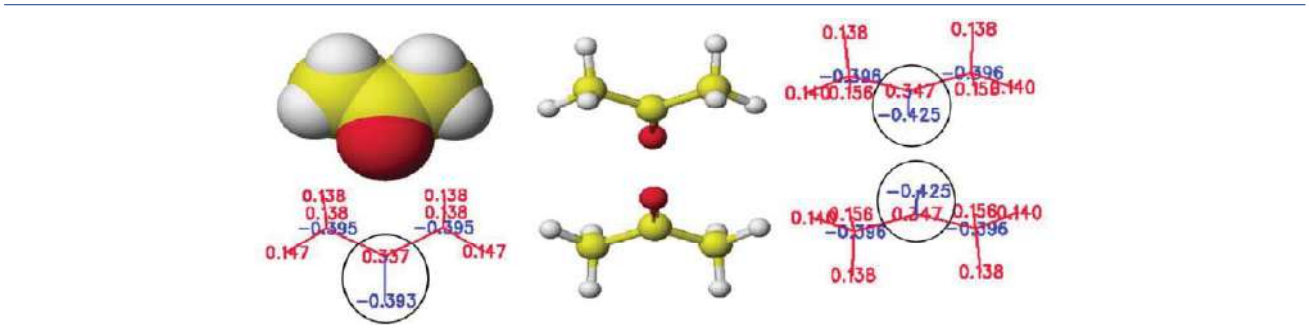


FIgure 27: Docking of two acetone molecules with apc values.



FIgure 28: Docking of two Diethylketone molecules with apc values.

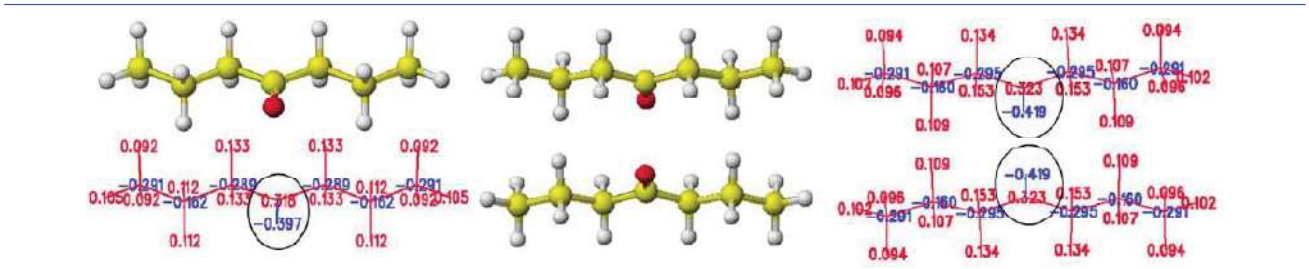


FIgure 29: Docking of two Dipropylketone molecules with apc values.

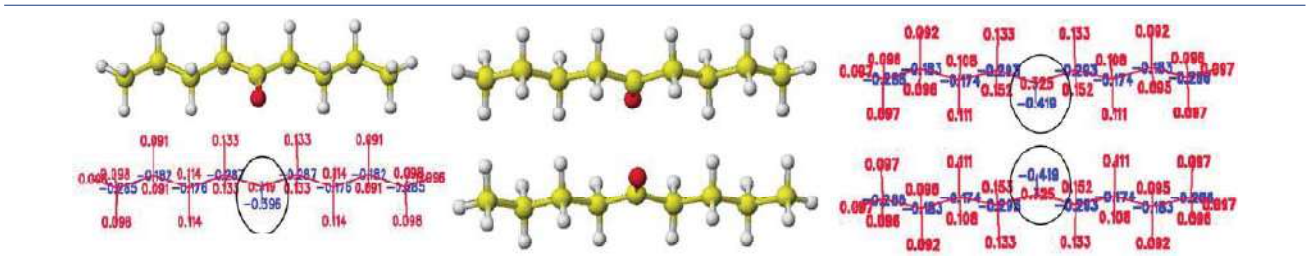


FIgure 30: Docking of two Dibutylketone molecules with apc values.

The cabonyl group demonstrates weak electrostatic interaction, and the π-electron contribution is stronger than ether oxygen; therefore, the electrostatic interaction of carbonyl groups is studied. The alkyl group is from methyl to butyl.

Table 10: Molecular Interaction Energy Values of a Pair of Alkylketones.

Analyte	HB (Single)	ES (Single)	VW (Single)	HB (Pair)	ES (Pair)	VW (Pair)	MIHB	MIES	MIVW
Acetone	0.000	0.000	0.492	0.000	-1.997	-1.186	0.000	1.997	2.179
Ethylketone	0.000	0.000	1.980	0.000	-1.497	-0.293	0.000	1.497	4.253
Propylketone	0.000	0.000	2.909	0.000	-1.354	-0.250	0.000	1.354	6.068
Butylketone	0.000	0.000	3.823	0.000	-1.405	-0.521	0.000	1.405	8.167

Unit: kcal·mol^{-1}

The contribution of carbonyl oxygen is diluted in longer alkyl group ketones. Due to the weak molecular interaction, the contribution is significant only for dimethylketone (acetone). The longer the alkyl chain length decreases the polarity. The carbonyl group contributes to stronger van der Waals force and electrostatic interaction than single ether oxygen. The above simple experiments can explain the solvent strength. The border alkyl chain length between polar (hydrophilic**)** and non-polar (hydrophobic**)** seems to be the butyl group obtained for the alkyl chain +I effect contribution to alkylalcohol hydrogen bonding contribution.

1.7.4. Hydrogen Bonding of alkanol: The hydrogen bonding of alkyl alcohols depends on alkyl-chain length, and up to four methylene units can affect the hydrogen bonding. Alkyl alcohols from methanol to nonylalcohol have been constructed, and individual and identical pair energy values were calculated after optimizing the structures using MM2 calculations. The calculated values are summarized in Table 11, and examples of complexes are shown in Figures 31 and 32.

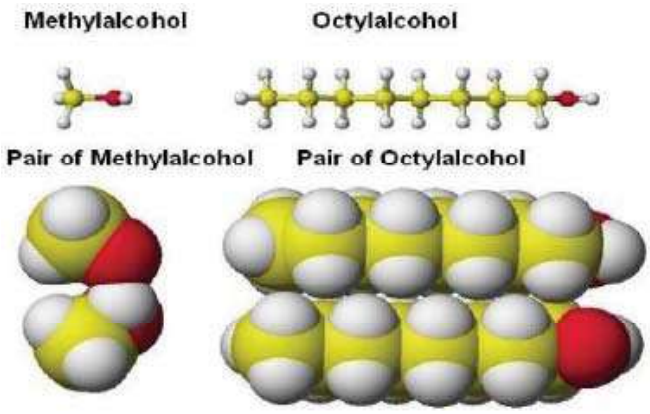


Figure 31: Interaction of a pair of methylalcohol and octylalcohol.

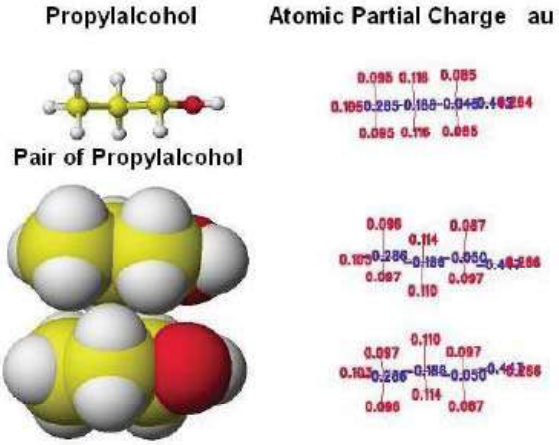


Figure 32: interaction of a pair of propylalcohol and octylalcohol. black, gray, and white balls: oxygen,atomic partial charge, black, gray, and white balls: carbon, and hydrogen, oxygen, carbon, and hydrogen, apc unit: au

Table 11: Complex conformation and MI energy change

	Monomer			Dimer				Molecular interaction	
Compound	hb	es	vw	HB	ES	VW	MIHB	MIES	MIVW
Methylalcohol	0.000	0.000	-0.077	-2.898	-1.216	0.138	2.898	1.216	-0.292
Ethylalcohol	0.000	0.000	0.583	-1.660	-1.268	-0.012	1.660	1.268	1.178
Propylalcohol	0.000	0.000	1.085	-0.102	-0.069	-0.400	0.102	0.069	2.570
Butylalcohol	0.000	0.000	1.565	-0.080	-0.051	-0.439	0.080	0.051	3.569
Pentylalcohol	0.000	0.000	2.034	-0.076	-0.065	-0.479	0.076	0.065	4.547
Hexylalcohol	0.000	0.000	2.580	-0.079	-0.055	-0.565	0.079	0.055	5.725
Heptylalcohol	0.000	0.000	2.961	-0.082	-0.063	-0.632	0.082	0.063	6.554
Octylalcohol	0.000	0.000	3.421	-0.079	-0.057	-0.720	0.079	0.057	7.562

Unit: kcal·mol^{-1}

The complex conformation of two propylalcohol provided MIVW 2.570 and MIHB 0.102 kcal.mol^{-1}. Apc of hydroxy-oxygen was reduced from -0.442 to -0.447 au, and the apc of hydrogen increased from 0.264 to 0.266 au. The contact, contact-charge-transfer complex formation changed a little hydrogen bonding capability. This model analysis is essential to explain hydrogen bonding.

The molecular interaction energy values are plotted against the carbon number of the alkyl alcohol chain, along with the results for alkanes. The energy values of a pair of identical alcohols were smaller than twice the energy of one alcohol. This result indicates that the energy values calculated using the MM2 program can explain the degree of molecular interaction. Increasing the alkyl-chain length decreased hydrogen bonding energy values along with electrostatic energy values by butylalcohol. Their van der Waals energy values indicated their complex formation. Their MIVW energy values increased dramatically with increasing alkyl chain length; then, the value leveled off to a constant. There was a linear increase in the hydrogen bonding energy values up to three carbons. This means hydrogen bonding contributes to molecular interactions for alcohols up to and including three carbon atoms, and van der Waals energy is the main energy for alkyl alcohols with longer chains. However, the corrected energies did not bear a linear relationship to their calculated hydrogen-bonding energies.

In silico analysis

The computational chemistry calculations were performed using desktop computers. The programs used were Versions I–VI of CAChe™ (Fujitsu, Tokyo) and Version 7 (SciGress™, BioCAChe™, Fujitsu, Tokyo). In Version 7, the MM2 program was enhanced with respect to electrostatic and hydrogen-bonding energies; therefore, Version V was mainly used throughout this text to maintain consistency with the previous book, "Quantitative in silico chromatography, computational calculation of molecular interactions" (RSC, Cambridge, 2014, 338 pp.). However, Version 7, which incorporates various programs, was used to identify a suitable program for predicting spectra (Chapter 4). BioCAChe allows the analysis of protein conformations; therefore, BioCAChe™ was used to analyze enzyme selectivity and COVID-19 infection (Chapters 9-11). The programs used are indicated in each chapter, together with keywords from the pull-down menus.

A fundamental difference between the CAChe™ program and other programs is the molecular drawing method. CAChe™ uses freehand drawing, whereas other programs use a Chemintosh™-type method. The free drawing method can be used to prepare four types of monosaccharides easily (α1, 1α, β1, 1β) and various steroids from cholesterol, depending on the user's skill. Therefore, the keywords of pulldown menus are indicated in the text to help users follow these approaches with their own programs. The molecular forms and electron distributions shown were mainly obtained using the MOPAC (molecular orbital package) PM5 program with recommended parameters. Energy values calculated using the MM2 program in CAChe™ Versions 1–6 are identical and may be obtained using ChemDraw™. MM2 was selected instead of MM3 because of its suitability for explaining experimental data. Atomic partial charges were calculated using the MOPAC PM5 program. Selecting suitable programs is a matter of individual judgment when quantitatively explaining one's own experimental data. Computer-based programs developed from experimental data for predicting mass spectra, infrared spectra, and NMR values are not discussed because well-designed operating manuals are available. Log *P* and p*K*a values were mainly obtained from references. Log *P* values obtained through computational chemistry are not included because adequate reference values are available, but a computer science program, Rekker's method, was partly used to analyze retention in reversed-phase liquid chromatography, and a computational chemistry method was partly explored for predicting p*K*a values.

These calculated values are not absolute values and individual computer programs have different operation methods, but similar analysis can be achieved.

References

1. E.R. Brode, The determination of hydrogen-ion concentration by a spectrophotometric method and the absorption spectra of certain indicators, J. Am. Chem. Soc. 1924, 46(3), 581-596.
2. I.M. Kolthoff, Indicator constants, J. Phys. Chem. 1929, 34(7), 1466-1483.
3. Computing across the chemistry curriculum, http://chemed.chem.pitt.edu/ChemEd/ComputingacrosstheChemistryCurriculum.doc
4. T. Hanai, Quantitative evaluation of dissociation mechanisms in phenolphthalein and the related compounds, Journal of Computer Chemistry, Japan, 2016, 15(1), 13-21. Doi 10.2477/jccj.2015-0055.
5. T.W. Creekmore, C.N. Reilley, Nuclear magnetic resonance study of ion-exchange resins. Anal. Chem. 1970, 42, 570-575. Doi: 10.1021/ac60288a014.
6. T.E. Gough, H.D. Sharma, N. Subramanian, Proton magnetic resonance studies of ionic solvation in ion- exchange resins. Part 1. Sulfonated cation-exchange resins. Can. J. Chem. 1970, 48, 917-923. Doi: 10.1139/v70-151.
7. W. Funasaka, T. Hanai, Estimation of adsorption mechanisms using NMR and ESCA, Proceeding of Annual Autumn Symposium of Chubu Kagaku Kanrenkyokai, 1974, IE04.
8. T. Hanai, H. Hatano, N. Nimura, T. Kinoshita, Computational chemical analysis of retention on ion- exchange resin in normal-phase liquid chromatography, H. Hatano, T. Hanai, (Eds) International symposium on chromatography, Jan. 1995, Yokohama, World Sci. Singapore, 1995, pp.97-103.
9. E.N. Gur'yonova, L.P. Gol'dshtein, L.P. Romm, (eds) Donor-acceptor bond, Translated by R. Kondor, D. Slutzkin, 1975, Halsted Press/John Wiley & Son, New York, pp.366.
10. V. Gutmann, The donor-acceptor approach to molecular interactions, 1978, Plenum Press, New York, pp.279.
11. O. Exner, Dipole moments in organic chemistry, 1975, Georg Thieme Pub. Stuttgart, pp. 156, ISBN: 3-13- 523501-7
12. J.C. Speakman, The hydrogen bond and other intermolecular forces, Monographs for teachers, 27, 1975, Chemical Society, London, ISBN 0 85186 919 X
13. C.A. Vanderwerf, Acids, bases, and the chemistry of the covalent bond, 1961, D. Van Nostrand Company, New York.
14. J. Fattori, F.H.S. Rodrigues, J.G.M. Pontes, A.P. Espindola, L. Tasic, Monitoring intermolecular and intramolecular interactions by NMR spectroscopy, Applications of NMR spectroscopy: Volume 2015, 3, 180- 266. https://doi.org/10.1016/B978-1-68108-063-5.50006-0
15. J.M. Lipohock, J.P. Loria, Monitoring molecular interactions by NMR, PMID, 2009, 490, 115-34, doi: 10.1007/978-1-59745-367-7.5
16. T. Hanai, Introduction of in silico chromatography. J. Chromatogr. Sep. Tech. 2016, 7, 1–8, DOI: 10.4172/2157-7064.1000333.
17. T. Hanai, Quantitative in silico chromatography, Computational modeling of molecular interactions, Editor T. Hanai, Royal Society of Chemistry, Cambridge, 2014, 220-236. ISBN: 978-1-84973-991-7.
18. W.J. Dunn III, J.H. Block, R.S. Pearlman, Partition coefficient determination and estimation, 1988, Pergamon Press, ISBN 0-08-033649-3, pp.154.
19. R.F. Rekker, The hydrophobic fragmental constant, 1977, Elsevier Sci. Pub. Amsterdam, ISBN: 0-444-do 41548-3, pp. 389
20. T. Hanai, HPLC, A Practical Guide, 1999, Royal Society of Chemistry, Cambridge, 134.
21. V. Gutmann, The donor-acceptor approach to molecular interaction, 1978, Plenum Press, New York, ISBN 0-306-31064-3, 279
22. E.N. Gur'yonova, I.P. Goldshtein, L.P. Tomm, Donor-accepter bond, 1975, Keter Publishing House Jerusalem Ltd, 1975, New York, ISBN 0-470-33680-3
23. H.F. Walton, Ion-exchange chromatography, Editor Heftman E. Chromatography fundamentals and applications of chromatographic and electrophoretic methods, 1983, Elsevier, Amsterdam, A225-A255, ISBN 0-444-42043-6,
24. O.B. Aikara Ion-exchange chromatography, and its applications, Column chromatography, Chapter 2, Intechopen, London, UK, 2013, 32-58, http://dx.doi.org/10.5772/55744.
25. P.F. Morgan, M. Hanna-Brown, R.J. Flanagan, Characterization of a microparticulate strong anion-exchanger in the HPLC of acidic drugs, Biomed. http://dx.doi.org/10.5772/55744.
26. T. Hanai, Definition of HILIC system and quantitative analysis of retention mechanisms, Current Chromatography, 2018, 5, 43-52, Doi: 10.2174/22132406056661 80207093716
27. T. Hanai T. Polysiliconedioxide phase Fundamental Properties of Packing Materials for Liquid Chromatography, Separation, 2019, 6(2), 1-20, doi:10.3390/separations6010002www.mdpi.com/journal/separations
28. K.E. van Holde, 2.05 Physical Biochemistry, 1971, Prentice-Hall Inc, Englewood Cliffs, NJ, 13-665877-6, p.246)
29. G.L. Breneman, O.J. Parker, Chemistry and Computing, 1989, Prentice Hall, Englewood Cliffs, NJ, pp. 197).

Chapter 2: Fundamental Molecular Interaction Mechanisms

Various terms have been used to describe molecular interactions in different fields, such as van der Waals forces, repulsion, London dispersion, hydrophobic interactions, dipole-dipole interactions, charge-transfer interactions, hydrogen bonding, Coulombic interactions (ion-ion and ion-dipole), ligand exchange, complex formation, salting-out, and steric effects. However, in silico analyses simplify these interactions into three categories: van der Waals, hydrogen bonding, and electrostatic interactions. Therefore, these three interactions are described here using simple molecules and energy values calculated with a molecular mechanics program.

A molecular interaction involving only van der Waals forces is called a hydrophobic interaction. Saturated aliphatic hydrocarbons are commonly used to collect various compounds from aqueous solutions and air. However, the recovery varies depending on the properties of the target compounds. The simplest model experiment is the calculation of the interaction between two aliphatic compounds, and any other properties should not affect the interactions. Substituent effects are demonstrated by differences in the interactions of various aromatic compounds with n-hexane as a model hydrophobic molecule. The interaction energy values are obtained as differences in van der Waals energy.

The electron localization induced by an interaction is called a Lewis acid-base interaction. The introduction of polar atoms into hydrocarbon molecules causes dynamic electron localization. The simplest examples involve interactions between alkyl-ethers and alkyl-ketones. The alkyl-chain length affects the degree of electron localization. Substituent effects are analyzed through the molecular interactions of various aromatic compounds. Weak Lewis acid-base interactions are represented by weak electrostatic energy values in molecular mechanics calculations.

Various compounds are adsorbed on alkane phases in aqueous solutions. The interaction forces are studied using simple aromatic compounds with model ligands. The model ligand is n-hexane, and the structure and atomic partial charge (apc) values are given in Figure 2.1. The chemical structures of the solutes (analytes) are shown in Figure 2.2 and their properties are summarized in Table 2.1. Molecular distance and apc value changes after optimization of complex structures are used to explain the selectivity of molecular interactions in the following discussion.

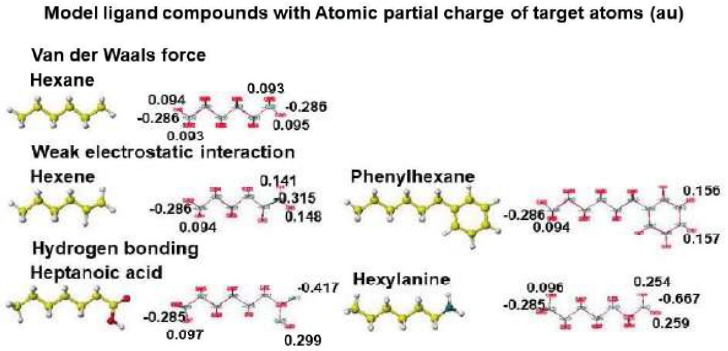


Figure 2.1: Chemical structures of model ligands with their atomic partial charge (apc) values.
Large white (gray), blue (dark gray), red (black) and white small balls are carbon, nitrogen, oxygen, and hydrogen.

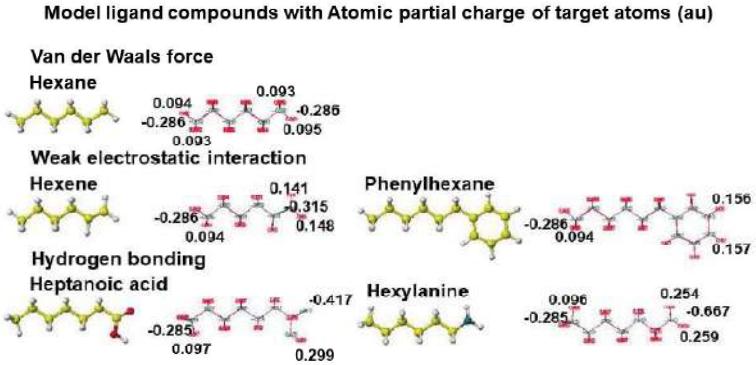


Figure 2.2: Structure of standard compounds with atomic partial charge.
Yellow, red, blue, green and small white balls: carbon, oxygen, nitrogen, chlorine, and hydrogen

Table 2.1: Molecular properties of model ligands and standard compounds

Chemicals	FS	HB	ES	VW
n-Hexane	3.472	0	0	2.613
Hexene	3.8036	0	0	2.103
Phenylhexy	−4.1934	0	0	5.909
Heptanoic acid	−4.6924	−3.418	−6.671	3.905
Hexylamine	7.4859	−0.606	−4.332	3.864
Hexylguanidine	−14.3406	0	−21.981	4.994
Benzene	−8.0770	0	0	3.006
Methylbenzene (toluene)	−8.6003	0	0	3.037
Chlorobenzene	−7.8015	0	0	3.214
Phenol (M)	−10.2088	−1.463	0	2.957
Phenol (I)	−7.6759	0	0	2.986
Benzoic acid (M)	−13.9182	−3.455	−6.669	4.877
Benzoic acid (I)	−2.5494	0	0	4.742
Aniline (M)	−6.1214	−1.334	0	3.416
Aniline (I)	−1.0477	0	0	3.497

Unit: kcal mol^{-}

2.1. Van der Waals force (hydrophobic interaction)

2.1.1 Van der Waals force between hexane and aromatic compounds: First, an analyte is placed 5 Å from the edge of n-hexane, and the distance is gradually shortened by 0.5 Å until the molecules contact each other after optimization using molecular mechanics (MM2) calculations. Figure 2.3 shows a conformation of hexane and benzene at a distance of 3.532 Å as an example; The optimized distance of these molecules is based on the molecular properties of an analyte and the direction toward a ligand. After optimization of the molecular conformation, n-hexane contacts benzene at a distance of approximately 3 Å, forming the complex structure shown in Figure 2.3. Both n-hexane and benzene have no HB or ES energy values, and n-hexane and benzene have VW energies of 2.613 and 3.006 kcal mol^{-1}. The VW energy of the complex is 4.453 kcal mol^{-1}. Therefore, their MIVW energy is 1.166 kcal mol^{-1}. The other analytes include methylbenzene (toluene), chlorobenzene, phenol, benzoic acid, aniline, ionized phenol, ionized benzoic acid, and ionized aniline and are initially positioned as shown in Figures 2.3. The optimized complex structures are shown in these figures. The calculated MI energy values are summarized in Table 2.2.

Table 2.2: Molecular interaction (MI) energy values of complexes of *n*-hexane and standard compounds.

Chemicals	Right				Left			
	IP	MIHB	MIES	MIVW	IP	MIHB	MIES	MIVW
Benzene	2.987	0	0	1.166	-	-	-	-
Methylbenzene	3.042	0	0	1.143	3.741	0	0	1.101
Chlorobenzene	3.022	0	0	4.346	4.021	0	0	1.847
Phenol	3.036	0.001	0	1.126	3.058	0.003	0	0.575
Benzoic acid	3.029	0.003	0.002	1.198	4.601	0.003	-0.002	0.741
Aniline	3.022	0	0	1.153	3.201	0.001	0	0.825
Ionized phenol	3.012	0	0	1.638	2.762	0	0	0.367
Ionized benzoic acid	3.023	0	0	1.2	3.968	0	0	0.655
Ionized aniline	3.015	0	0	1.166	3.789	0	0	0.857

Right or Left: direction of analytes (left or right side in Figures); IP: initial distance before optimization; MIHB, MIES, and MINW: molecular interaction (MI) energy values of hydrogen (HB), electrostatic (ES) and van der Waals (VW) interaction; unit: kcal mol^{-1}.

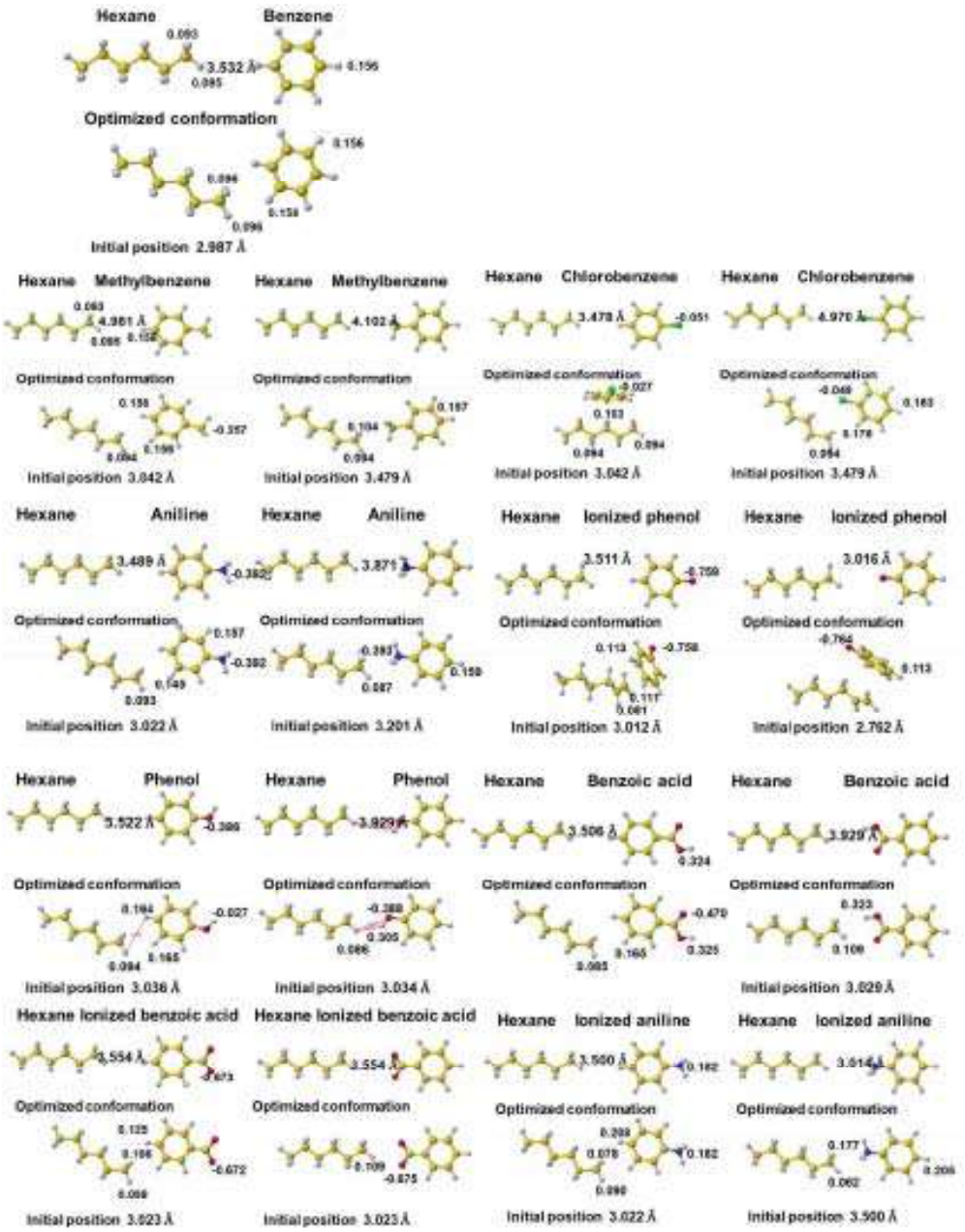


FIgure 2.3: Molecular interaction between n-hexane and standard compounds.

The initial position (IP) distance indicates that the terminal hydrogen atom of hexane faces a phenyl group hydrogen or substituent atom. In general, the terminal hydrogen of hexane faces the phenyl hydrogen of an analyte with A, and then these molecules form complexes through van der Waals forces. The inductive effect of polar groups causes the analyte to move into direct interaction with the alkyl chain of *n*-hexane and causes higher MIVW values, and the calculated MIVW energy values depend on induced electron localization. This phenomenon is used for hydrophobic liquid extraction and solid-phase adsorption. The interaction site can be inferred from the apc value change before and after complex formation shown in these figures. As expected, in these analytes' structures, their fundamental interaction force is van der Waals forces, and the polar substituents reduce the MIVW values. The apc value of the end hydrogen of n-hexane is about 0.095 au, and the value changes little when it contacts with a phenyl group; however, the hydrogen apc value varies from 0.062 au with aniline amino group nitrogen (Figure 2.3) to 0.160 au in ionized phenol oxygen (Figure 2.3), but the electron localization does not appear as MIES value changes. The apc values of the analyte substituents are about the same except methylbenzene methyl group due to direct hydrophobic interaction and the chlorine atom of chlorobenzene due to direct contact of the phenyl group with the *n*-hexane chain (Figure 2.3, MIVW 4.346 kcal mol^{-1}). The absolute value difference

between apc and MIVW is not obtained by the difference in their initial position, which is affected by their interaction and repulsion force. This simple model experiment suggests that even relatively polar compounds interact with alkyl groups longer than a butyl group. The sections on weak electrostatic interactions and hydrogen bonding will later describe the effect of alkyl chain length on polarity.

2.1.2. Interaction with alkenes: The contribution of a double bond was studied using *n*-hexene with the same analytes instead of vinyl groups, whose molecular size is too small for a docking study. Hexenyl-bound silica gels can be used to analyze the specificity of the vinyl group in chromatography. The molecular interaction between a vinyl group and benzene was examined, as shown in Figure 2.4. where molecular properties (HB, ES, and VW energy values of the single and complex molecule are given in the figure together with apc values. The vinyl group and benzene are located about 3 Å apart, and then the structures were optimized. Benzene comes into contact with the vinyl group, and these molecules interact through van der Waals forces with an MIVW value of 2.858 kcal mol^{-1}. The apc value of the vinyl end carbon and hydrogen changed from -0.315 and 0.148 to -0.309 and 0.141 au.

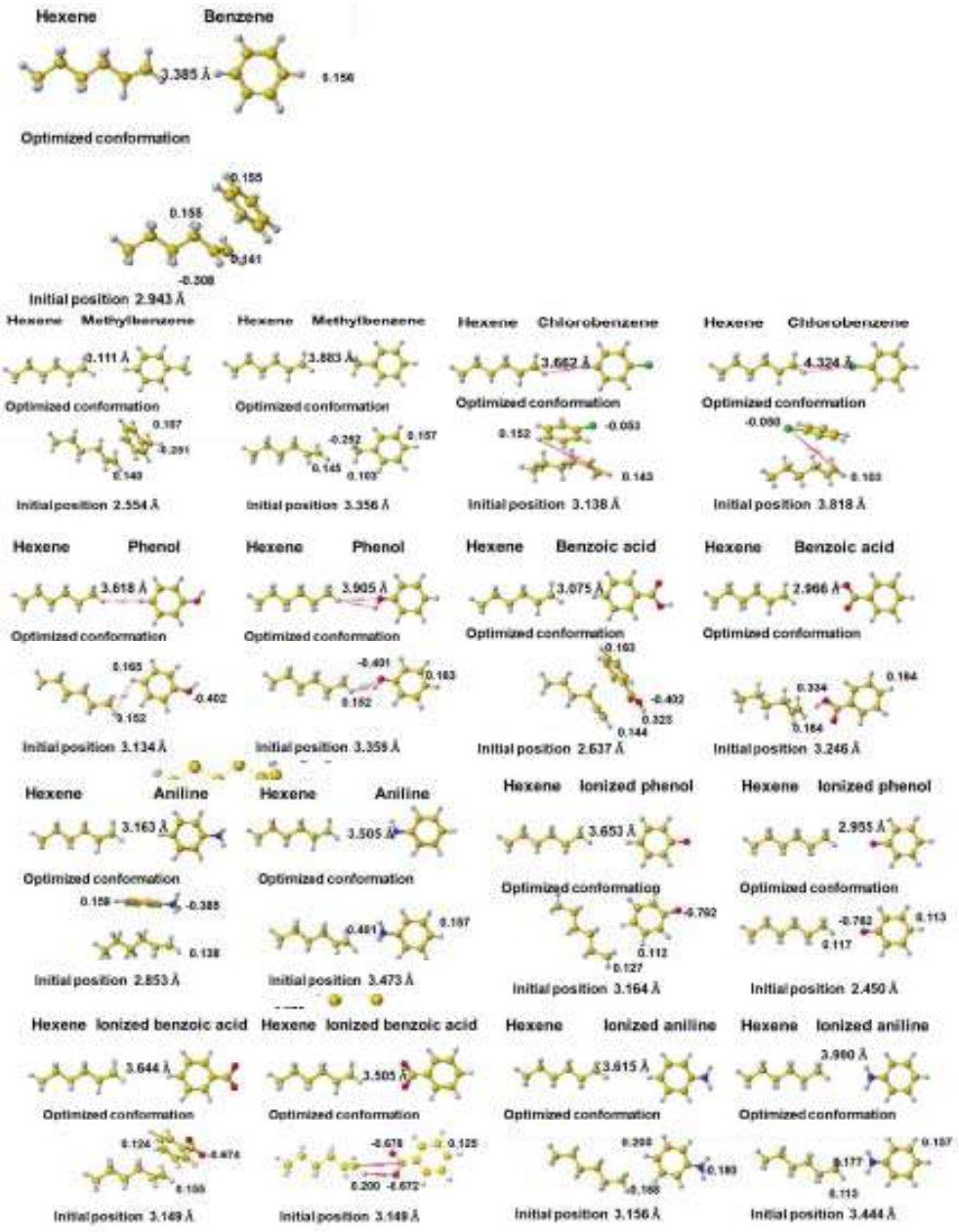


Figure 2.4: Molecular interaction between hexene and standard compounds.

Similar interaction analysis is performed for methylbenzene, chlorobenzene, phenol, benzoic acid, aniline, ionized phenol, ionized benzoic acid, and ionized aniline. These analyte substituents may cause selectivity; therefore, the substituent groups are oriented directly toward the vinyl group, and the reference conformation is designed to study mainly van der Waals interaction. The conformations before and after optimization are shown in Figures 2.4. The MIHB, MIES, and MIVW values are summarized in Table 2.3.

Table 2.3: Molecular interaction (MI) energy values of complexes of *n*-hexene and standard compounds.

Chemicals	Right				Left			
	IP	MIHB	MIES	MIVW	IP	MIHB	MIES	MIVW
Benzene	2.943	0	0	2.858	-	-	-	-
Methylbenzene	2.554	0	-0.001	0.431	3.356	0	0.006	0.747
Chlorobenzene	3.138	0	-0.049	4.348	3.818	0	-0.029	3.742
Phenol	3.134	2.297	0.075	2.093	3.359	2.328	0.067	1.345
Benzoic acid	2.637	-0.108	0.026	3.512	3.246	2.343	0.015	1.179
Aniline	2.853	0.281	-0.021	3.16	3.473	1.031	0.028	1.589
Ionized phenol	3.164	0	-0.019	2.973	2.45	0	0.105	3.005
Ionized benzoic acid	3.149	0	-0.019	3.258	4.505	0	-0.132	0.561
Ionized aniline	3.156	0	0.047	3.642	4.612	0	0.109	0.769

Right or Left: direction of analytes (left or right side in Figures); IP: initial distance before optimization; MIHB, MIES, and MINW: molecular interaction (MI) energy values of hydrogen (HB), electrostatic (ES) and van der Waals (VW) interaction; unit: kcal mol^{-1}.

The molecular interaction force of methylbenzene is weak, and these two molecules have to be located within 3 Å (Figure 2.4). When the phenyl group faces the vinyl group, the required initial distance is 2.6 Å, and when the methyl group faces the vinyl group, the required initial distance is 3.4 Å. The aps value of the end vinyl hydrogen is 0.140 and 0.145 au. The contact center is the vinyl group.

For chlorobenzene, the chloro group is recognized by the vinyl group, and the distance is 3.8 Å (Figure 2.4). The hydroxy group of phenol contributes to molecular recognition, and these molecules are recognized at a distance of 3.4 Å (Figure 2.4). The apc value of the hydroxy group hydrogen changes from 0.305 to 0.316 au. The result indicates that the hydroxy group is the contact center. The complex formation of benzoic acid with the vinyl group requires 2.6 Å between the phenyl group and the vinyl group (Figure 2.4). However, the distance of 3.3 Å is sufficient to bring the carboxy group with the vinyl group. The contribution of MIHB (2.343 kcal mol^{-1}) is greater than MIVW (1.179 kcal mol^{-1}). The apc value of the carboxy hydrogen changes from 0.324 to 0.334 au, and that of the vinyl group hydrogen changes from 0.148 to 0.164 au. The aniline amino group exhibits similar behavior to the carboxy group (Figure 2.4); the contribution of MIHB is weak (1.031 kcal mol^{-1}) compared with an MIVW value of (1.589 kcal mol^{-1}). The apc value of the amino group nitrogen changed from -0.392 to -0.401, and that of the vinyl group hydrogen changed from 0.148 to 0.152 au.

The ionization of the substituent group eliminates hydrogen-bonding capability but enhances electrostatic interaction capability. When the phenyl group of ionized phenol faces the vinyl group (Figure 2.4), MIVW (2.973 kcal mol^{-1}) contributes to their interaction, the oxygen of ionized phenol faces the vinyl group, the contribution of MIES (0.105 kcal mol^{-1}) is obtained. The carboxy group of ionized benzoic acid demonstrates a negative contribution of MIES (-0.132 kcal mol-1) (Figure 2.4). These two molecules are located close to each other but do not come into contact. Aniline interacts strongly MIVW (3.642 kcal mol^{-1}) via the phenyl group, and the amino group exhibits the weak MIES (0.109 kcal mol^{-1}) (Figure 2.4). The apc value of the vinyl hydrogen changes from 0.148 to 0.113 au. These results indicate that the contact center is the vinyl group.

2.1.3. Interactions with a phenyl group: Further study of π-electron contribution is studied using phenylhexane A phenyl group has more p-electron effect than a vinyl group. How does it affect the molecular interactions of these compounds being studied? The phenyl group of phenylhexane recognizes benzene within **3Å** with weak MIVW (0.456 kcal mol^{-1}). The apc of the phenyl group hydrogen changes little from 0.156 to 0.155 au (Figure 2.5). The substitute methyl group affects the interactions between the phenyl group and methylbenzene. The phenyl-phenyl Interaction occurs at 3Å distance with MIVW (0.469 kcal mol^{-1}), and the Phenyl-methyl Interaction occurs at 4A with MIVW (0.772 kcal mol^{-1}) and produces weak MIES (0.003 kcal mol^{-1}) (Figure 2.5). That is, the interaction force is not via p-p but van der Waals force. The apc values of the phenyl group hydrogen are identical due to the weak contact

charge transfer complex. The -I effect is analyzed using chlorobenzene. The phenyl-phenyl Interaction causes MIVW (0.468 kcal mol^{-1}) at 3Å, and the phenyl and chloro interaction causes MIVW (0.505 kcal mol^{-1}) in Figure 2.5. The phenyl-phenyl Interaction is a normal phenomenon, and the phenyl and chloro interaction may not occur. The apc of phenyl group hydrogen changes little with methylbenzene and increases to 0.159 au with chlorobenzene.

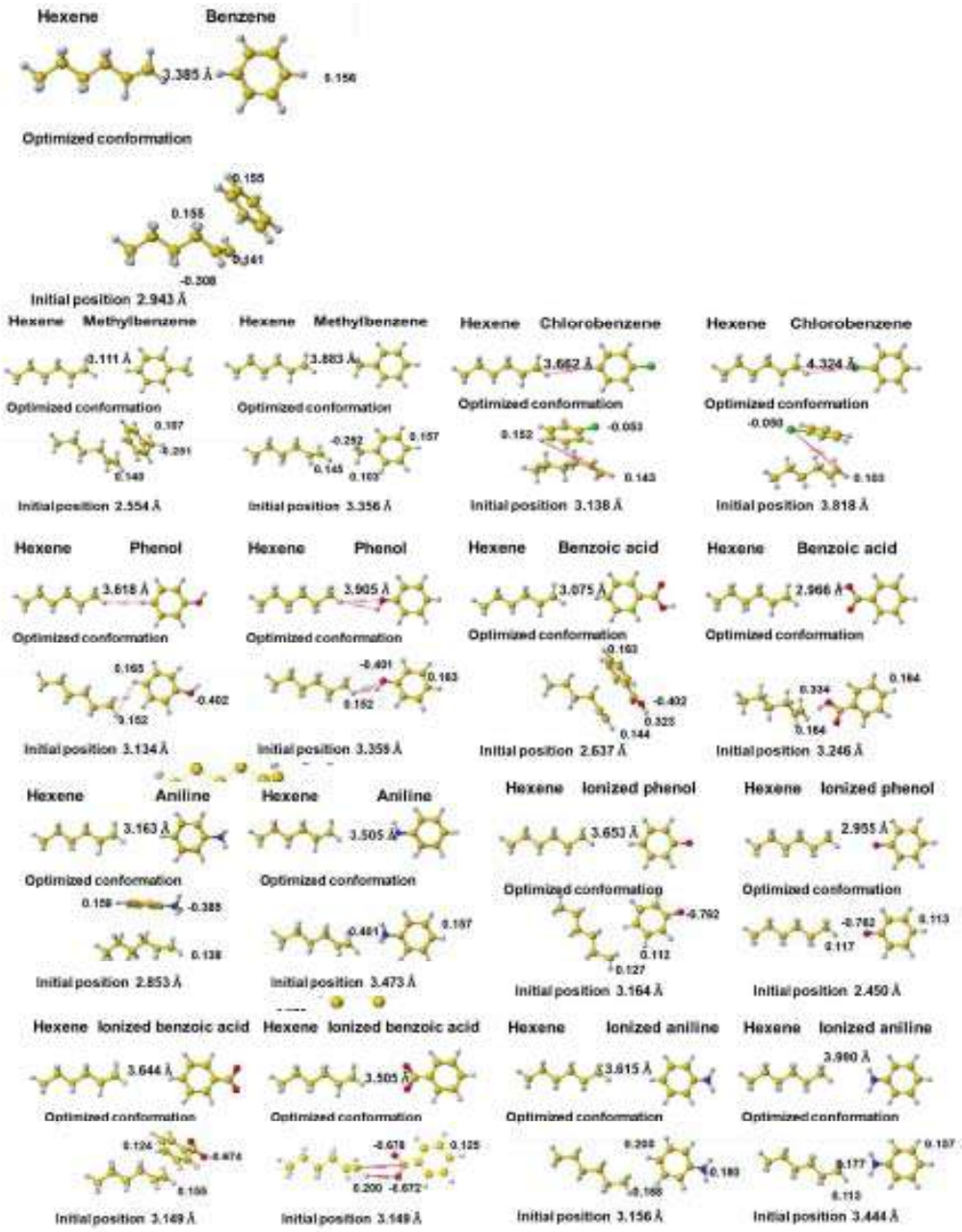


FIgure 2.5: Molecular interaction between phenylhexyl and standard compounds.

The behavior of phenol with hydrogen bonding capability should differ from methyl- and chlorobenzene (Figure 2.5). The phenyl-phenyl interaction occurs within 3 Å by MIVW (0.461 kcal mol^{-1}), and the phenyl and hydroxy group contacts at 3.5 Å by MIVW (2.453) and MIHB (6.934 kcal mol^{-1}). The hydrogen bonding between the phenyl group and the hydroxy group contributes to the strong molecular interactions. The apc value of the hydroxy-group hydrogen changes from 0.305 to 0.330 au. The results of benzoic acid are similar to those obtained for phenol (Figure 2.5). The phenyl-phenyl interaction causes 0.476 kcal mol^{-1} MIVW. The phenyl-carboxy group interaction causes 2.324 kcal mol^{-1} MIVW and 6.934 kcal mol^{-1} MIHB. The apc value changes from 0.158 to 0.148 through phenyl–phenyl interaction; however, it changes from 0.324 to 0.347 au through phenyl–hydroxy interaction.

The behavior of aniline is similar to that of phenol, but the MI energy values are very small (Figure 2.5). The phenyl-phenyl interaction causes about the same MIVW value (0.467 kcal mol^{-1}) to those of the other compounds, and the phenyl-amino group interaction causes 0.450 kcal mol^{-1} MIVW and 0.290 kcal mol^{-1} MIHB. The apc value is 0.157 au through phenyl–phenyl interaction, and the value is approximately the same as that obtained for the above aromatic compounds. However, the contact with the amino group reduces to 0.143 au. These results indicate that the contact may occur via the amino group even if the interactions are weak compared with those of phenol and benzoic acid.

Furthermore, the ionization effect of analytes is studied using phenol, benzoic acid, and aniline. The effect of ionizations are observed when these ionized substituents face the phenyl group. Phenol's phenyl- phenyl interaction causes weak MIVW (0.465 kcal mol^{-1}), and phenyl-oxygen interaction produces weak MIVW (0.338 kcal mol^{-1}) (Figure 2.5). Benzoic acid's phenyl-phenyl interaction produces MIVW (0.489 kcal mol^{-1}), and the phenyl-carboxy group interaction produces MIVW (0.608 kcal mol^{-1}) and MIES (-0.086 kcal mol^{-1}). The negative MIES value indicates that two molecules are once contacted but repulsed. This phenomenon opposes the results obtained by the molecular form of benzoic acid (Figure 2.5), but the difference is supported by the apc value difference that the apc value increases for ionized benzoic acid but decreases for the molecular form of benzoic acid. For aniline, the MIVW value is 0.714 kcal mol^{-1}, and the MIES value is 0.069 kcal mol^{-1}. The interactions are caused by hydrophobicity (Figure 2.5). The substituent effect occurs when the substitute contacts the phenyl group, and the evidence can be understood from the apc value changes comparing the little changes of the apc value by phenyl and phenyl interaction. These molecular interaction energy values are summarized in Table 2.4.

Table 2.4: Molecular interaction energy values of phenylhexane and standard compounds.

Chemicals	Right				Left			
	IP	MIHB	MIES	MIVW	IP	MIHB	MIES	MIVW
Benzene	3.001	0	0	0.456	-	-	-	-
Methylbenzene	3.117	0	0	0.469	4.012	0	0.003	0.772
Chlorobenzene	3.017	0	0.005	0.468	4.201	0	-0.014	0.505
Phenol	3.015	0.001	-0.001	0.461	3.517	6.937	0.09	2.458
Benzoic acid	2.769	0.005	0.005	0.476	4.498	6.934	0.055	2.324
Aniline	3.051	0.002	0	0.467	3.615	0.29	0	0.45
Ionized phenol	3.045	0	-0.019	0.465	2.706	0	-0.063	0.338
Ionized benzoic acid	3.034	0	-0.008	0.489	4.016	0	-0.086	0.608
Ionized aniline	3.006	0	0.013	0.474	3.963	0	0.069	0.714

Right or Left: direction of analytes (left or right side in Figures); IP: initial distance before optimization; MIHB, MIES, and MINW: molecular interaction (MI) energy values of hydrogen (HB), electrostatic (ES) and van der Waals (VW) interaction; unit: kcal mol^{-1}.

2.2. Hydrogen Bonding

Hydrogen bonding is also due to electron localization; however, the existence of hydrogen causes strong interactions, and the effect depends on the surrounding structures. The hydrogen bonding effect of alkyl alcohols depends on the alkyl-chain length [2]. The hydrogen bonding effects are described using n-hexylamine and heptanoic acid as model molecules and the same analytes used before. The chemical structures of heptanoic acid and hexylamine with atomic partial charge values are shown in Figure 2.1.

2.2.1. Hydrogen bonding with an amino group: Benzene located at a distance of 3 Å forms a complex with the amino group (Figure 2.6). The MIVW and MIHB energy values are 2.955 and 3.057 kcal mol-'. Hydrogen bonding contributes to their interactions. The apc value of the amino hydrogen changes from 0.251 to 0.215 au, and the nitrogen apc changes from -0.655 to -0.553 au. These values support the contribution of hydrogen bonding and the contact center in their molecular interactions.

For methylbenzene, the amino and phenyl interaction energy value is approximately the same as that obtained for benzene; however, the amino group and methyl group interaction is based on MIVW (1.560 kcal mol-1), and the contributions of MIHB and MIES are small (Figure 2.6). The apc value of amino group hydrogen changes from 0.212 and -0.575 au by the amino group and phenyl group contact, and that does from 0.222 and -0.584 au by the amino group and methyl group contact. These values suggest that the interaction occurs between the amino and phenyl groups.

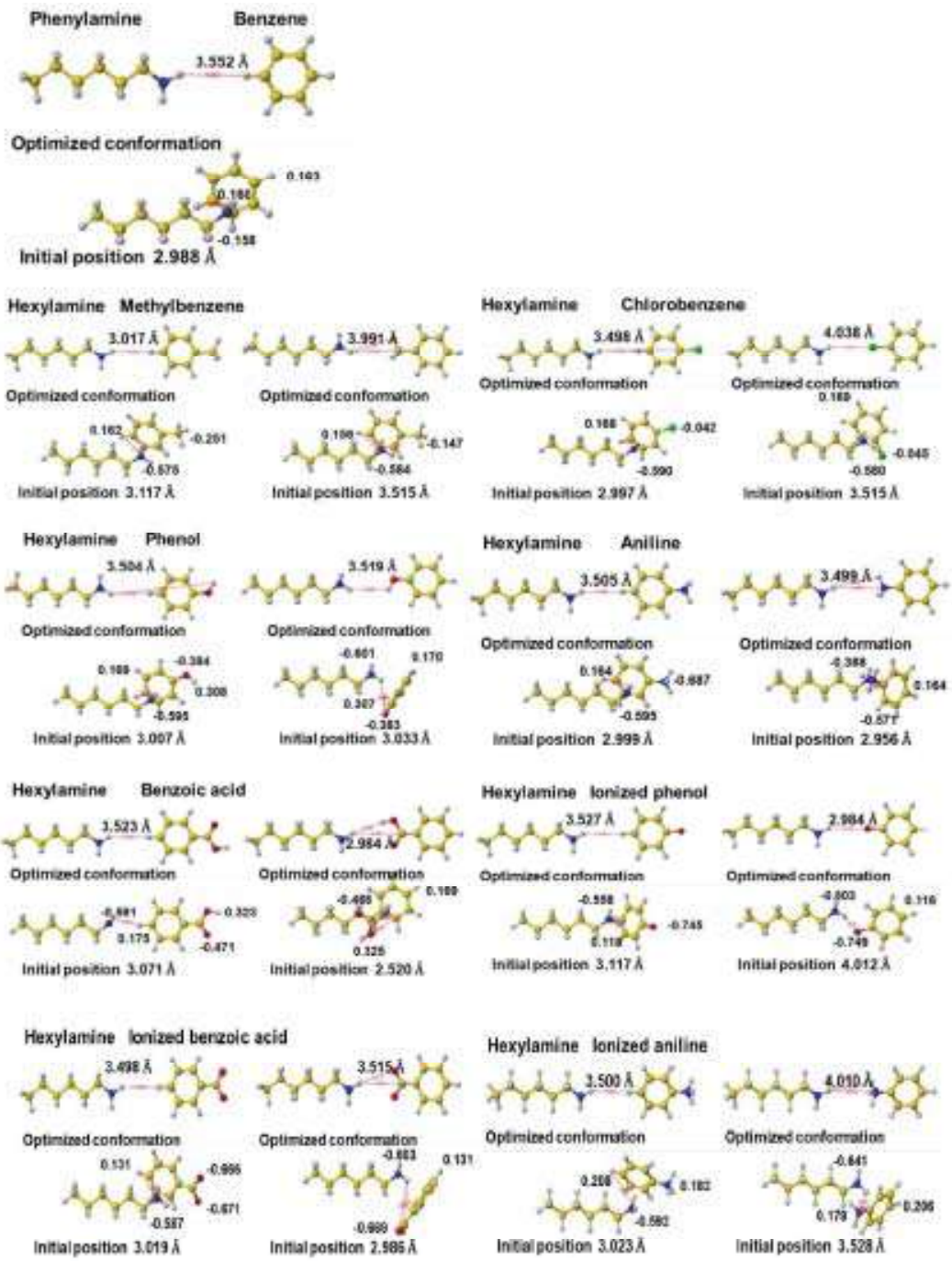


FIgure 2.6: Molecular interaction between phenylhexyl and standard compounds.

Chlorobenzene does not differ from the initial conformation (Figure 2.6). The contribution of MIHB is greater than that of MIVW. However, the apc values differ depending on their initial locations. The apc value of the amino group hydrogen and nitrogen at the chloro and amino interaction are 0.219 and -0.590 au, and those at the phenyl and amino interaction are 0.243 and -0.601 au. This result suggests that the center of interaction is the phenyl group.

For phenol, the results are similar to those obtained for methylbenzene (Figure 2.6). The contribution of MIHB is greater than that of MIVW. The hydroxy group of phenol does not directly contribute to the interaction. However, the apc values indicate the favorable initial location. In the face-to- face position of the amino group and the hydroxy group, the apc values of the amino group hydrogen and nitrogen are 0.217 and -0.591 au, and in that of the amino group and

the phenyl group, those values are 0.243 and -0.601 au. This result suggests that facing both polar groups may interact favorably.

Benzoic acid demonstrates slightly different behavior (Figure 2.6). The facing amino group and the phenyl group exhibit a similar result to the phenol result with stronger MIVW. However, when the carboxy group faces the amino group, benzoic acid moves and forms contact through van der Waals interactions. The amino group hydrogen and nitrogen apc values are 0.225 and -0.591 au by facing the amino and carboxy groups and 0.215 and -0.579 au by facing the amino and phenyl groups. Using aniline as an analyte demonstrates results similar to chlorobenzene and phenol (Figure 2.6). The apc values of the amino group hydrogen and nitrogen indicate that the phenyl group is the center of interaction. The apc values of the amino group hydrogen and nitrogen are 0.217 and -0.595 au facing the amino and amino group and 0.211 and -0.571 au facing the amino and phenyl groups.

The ionization of these analytes reduces the MIVW contribution and increases the MIES contribution when the amino group faces its polar substituents. When it contacts with ionized phenol (Figure 2.6), the apc values of the amino group hydrogen and nitrogen are 0.258 and -0.558 au, and these values are 0.303 and -0.603 au when the amino group faces the phenol phenyl group. In the case of ionized benzoic acid, the values are 0.240 and -0.587 au and 0.257 and -0.603 au when facing the ionized carboxy and phenyl groups (Figure 2.6). The behavior is the same for the ionized aniline. The apc values of the amino group hydrogen and nitrogen change to 0.221 and -0.592 au by facing the ionized amino group, and those change to 0.226 and -0.641 au by facing the phenyl group, respectively. The optimized initial conformations are shown in these Figures, and the details of molecular interaction energy values are summarized in Table 2.5.

Table 2.5: Molecular interaction energy values of hexylamine and standard compounds.

Chemicals	Right				Left			
	IP	MIHB	MIES	MIVW	IP	MIHB	MIES	MIVW
Benzene	2.998	3.057	0	2.956		-	-	-
Methylbenzene	2.749	3.22	0.011	2.977	3.515	0.057	0.058	1.56
Chlorobenzene	2.997	3.166	-0.043	2.975	3.515	3.424	0.083	2.779
Phenol	3.007	3.103	0.009	2.932	3.033	3.119	0.023	2.382
Benzoic acid	3.028	0.23	0.022	1.212	3.976	3.157	-0.006	3.888
Aniline	2.997	3.026	-0.047	3.07	3.263	3.169	0.027	3.32
Ionized phenol	3.007	3. 558	-0.104	1.872	2.984	1.552	0.137	1.132
Ionized benzoic acid	3.019	3.292	-0.032	2.834	3.497	3.096	0.208	2.822
Ionized aniline	3.023	2.996	0.302	3.008	3.882	3.017	0.21	2.426

Right or Left: direction of analytes (left or right side in Figures); IP: initial distance before optimization; MIHB, MIES, and MINW: molecular interaction (MI) energy values of hydrogen (HB), electrostatic (ES) and van der Waals (VW) interaction; unit: kcal mol^{-1}.

2.2.2. Hydrogen bonding with a carboxy group: The hydrogen of the molecular-form carboxy group forms a hydrogen bond with a phenyl group. Benzene contacts the carboxy hydrogen from a distance of 3.5 Å (Figure 2.7). The contribution of hydrogen bonding (MIHB 6.832 kcal mol^{-1}) is greater than that of van der Waals force (2.038 kcal mol^{-1}). The carboxy hydrogen and oxygen apc values change from 0.298 to 0.323 au and -0.358 to -0.387 au, respectively. The center of interaction is the hydrogen atom.

For methylbenzene, the direction of the methyl group affects the contribution of hydrogen bonding (Figure 2.7). The MIHB value is 6.811 when the phenyl group faces the carboxy group in the initial configuration. The apc values of the hydroxy hydrogen and oxygen change from 0.322 and 0.024 au and -0.382 and 0.027 au, respectively. The contribution is weak (MIHB 2.131 kcal mol^{-1}) when the methyl group faces the carboxy group. The main interactions occur between the carboxy group and the phenyl group.

The results of chlorobenzene are similar to those of methylbenzene (Figure 2.7); however, the contribution of MIES is observed. The MIES values are 0.319 and -0.402 kcal mol-^{1}, depending on the orientation of the chloro group. The contact of the carboxy group with chloro produces a positive MIES value

The phenol hydroxy group is capable of forming hydrogen bonds (Figure 2.7); therefore, orienting the hydroxy group toward the carboxy group produced strong hydrogen bonding (MIHB 9.982 kcal mol^{-1}) but weak MIES (0.180 kcal mol^{-1}) contribution compared with the carboxy group and the phenyl group contact (MIES 1.175 kcal mol^{-1}). The results of benzoic acid are similar to those of phenol (Figure 2.7). The contribution of hydrogen bonding is particularly strong. However, the apc value changes less in these polar group interactions than in the polar and non-polar group interactions.

The former values are 0.302 and -0.359; the latter are 0.311 and -0.386 au. The location of the aniline amino group does not show any difference (Figure 2.7), and the MIHB values are 6.897 and 6.863 kcal mol^{-1}. The apc values of the carboxy group hydrogen and oxygen are 0.330 and -0.385 au and 0.330 and -0.391 au.

The phenyl groups of the ionized compounds bind the heptanoic acid carboxyl group with mainly hydrogen bonding, and the acidic polar groups are repulsed from the carboxy group (Figure 2.7). The ionized amino group forms tight contact with the carboxy group with MIHB (6.762) and MIES (2.084 kcal mol^{-1}) (Figure 2.7). The results obtained for the carboxy group contribution are summarized in Table 2.6. The dissociation constant of the heptanoic acid is 4.9; therefore, the carboxy group is ionized in aqueous solutions. The ionization effect is explained in the chapter on ion-ion Interaction.

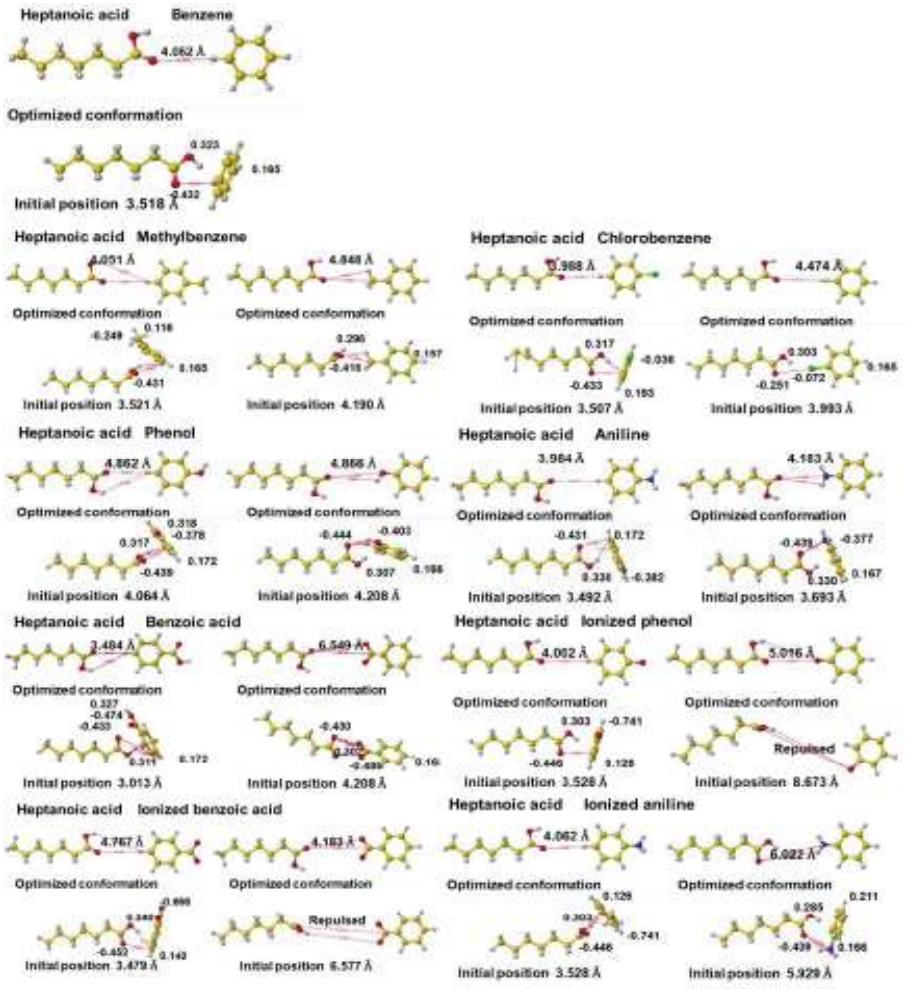


Figure 2.7: Molecular interaction between heptanoic and standard compounds.

Table 2.6: Molecular interaction energy values of heptanoic acid and standard compounds.

Chemicals	Right				Left			
	IP	MIHB	MIES	MIVW	IP	MIHB	MIES	MIVW
Benzene	3.518	6.832	-0.081	2.038	-	-	-	-
Methylbenzene	3.521	6.811	0.005	2.726	3.515	0.086	0.012	2.137
Chlorobenzene	3.507	6.955	-0.402	2.23	3.993	0.835	0.319	1.356
Phenol	4.064	7.699	0.18	2.276	4.208	9.982	1.176	1.605
Benzoic acid	3.013	7.163	0.623	2.215	4.924	11.73	1.682	0.47
Aniline	3.492	6.863	-0.09	2.108	3.693	6.897	-0.248	2.165
Ionized phenol	3.528	7.163	0.361	2.015	4.543	-0.012	-0.06	1.072
Ionized benzoic acid	3.479	6.838	-0.242	2.246	6.577	-0.019	-0.089	1.119
Ionized aniline	3.528	6.758	2.083	2.304	5.929	6.762	2.084	2.038

Right or Left: direction of analytes (left or right side in Figures); IP: initial distance before optimization; MIHB, MIES, and MINW: molecular interaction (MI) energy values of hydrogen (HB), electrostatic (ES) and van der Waals (VW) interaction; unit: kcal mol^{-1}.

2.3. Study the fundamental interaction mechanisms of ion-exchange groups

The fundamental interactions of carboxy-, amino-, and guanidino groups of various compounds, such as drugs, are easily described using simple model compounds to understand their interaction mechanisms. These groups were attached to a hexyl group, and the analytes were toluene, benzene, phenol, benzoic acid, aniline, and their ionized forms. In the following Figures 2.8, gray (yellow), black (red), dark gray (blue), and small white balls are carbon, oxygen, nitrogen, and hydrogen atoms. Green (light gray) is chlorine, and large white balls represent sodium atoms. The calculated molecular properties are given in Table 2.1.

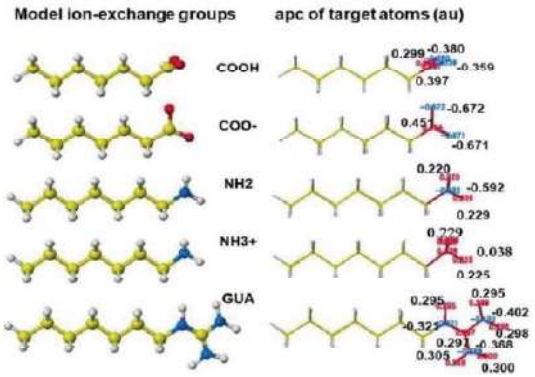


FIgure 2.8: Properties of model phase ligands with atomic partial charge.

2.3.1. The fundamental activity of carboxy-group: A carboxy group consists of hydroxy and carboxyl groups, demonstrating hydrogen bonding and electrostatic energy values. However, the carboxy group is ionized under physiological conditions. An amino group did not show hydrogen bonding energy value because no bond is formed. A guanidino group has weak hydrogen bonding, but electrostatic energy was predominant. In the initial position, benzene was located about 3.07Å apart from the carboxy group and optimized the structure. Benzene contacted the carboxy group and formed a contact charge transfer complex, and the atomic partial change indicated the contact site.

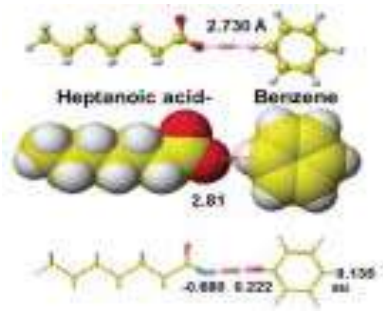


FIgure 2.9: Molecular interaction between ionized heptanoic acid and benzene.

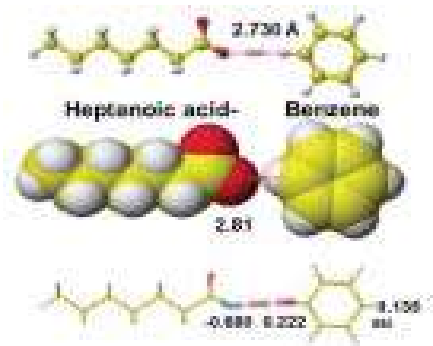


FIgure 2.10a and b: Docking of ionized heptanoic acid with methylbenzene and apc.

Electron localization was studied by adding methyl and chlorine groups. The methyl +I effect can be analyzed by docking the carboxy group and either phenyl or methyl groups of methylbenzene. At the initial position, the methyl group faced toward the carboxy group, and the conformation was then optimized. The complex structures are shown in Figures 2.10a and b. In Figure 2.10a, these compounds interacted through weak van der Waals forces (2.131 kcal mol^{-1}). In Figure 7b, the interaction energy values were high, and these molecules formed contact through hydrogen bonding (MIHB 6.811 kcal mol^{-1}). Carboxy oxygen apc changed from -0.671 to -0.679 and -0.680 au, respectively, and the phenyl p-hydrogen apc changed from 0.157 to 0.220 au (Figure 2.10a). The methyl carbon apc changed from -0.251 to -0.261 au (Figure 2.10b) due to their electron localization by their contact. Figure 7b should be a possible conformation even if the MI energy value was small.

Chlorobenzene with the -I effect of chlorine was also docked via hydrogen bonding between the carboxy group and the phenyl group via hydrogen bonding (MIHB 6.955 kcal mol^{-1}). The apc values of carboxy oxygen did not change significantly (-0.674 and -0.670 au) (Figure 2.11a), but chlorine apc values clearly changed from-0.051 to -0.097 (Figure 2.12) and -0.046 au (Figure 2.13). These differences indicate their contact or repulsion. In Figure 8b, these two molecules came into contact, and the phenyl *p*-hydrogen apc value changed from 0.163 to 0.134 au (Figure 2.11a). The primary interaction was van der Waals force (MIVW 1.660), higher than MIES 1.137 kcal mol^{-1} value. The repulsion increased their atomic distance to 6.62 Å, and the apc values of key atoms did not change significantly (Figure 2.11b). The actual conformation should be that shown in Figure 2.11a.

In the case of phenol, the phenolic hydroxy group is tightly docked with the carboxy group via electrostatic interaction (MIES 2.217 kcal mol^{-1}). However, hydrogen and oxygen apc values were changed like in the case of benzene, and hydrogen and oxygen apc values changed from 0.305 and -0.386 to 0.376 and -0.120 au, respectively (Figure 2.12b). The phenyl group docked with the carboxy group, but the oxygen apc value did not change significantly, but phenyl p-hydrogen apc changed from 0.163 to 0.228 kcal mol^{-1} indicated their contact (Figure 2.12a). Figure 2.12 should be the actual conformation.

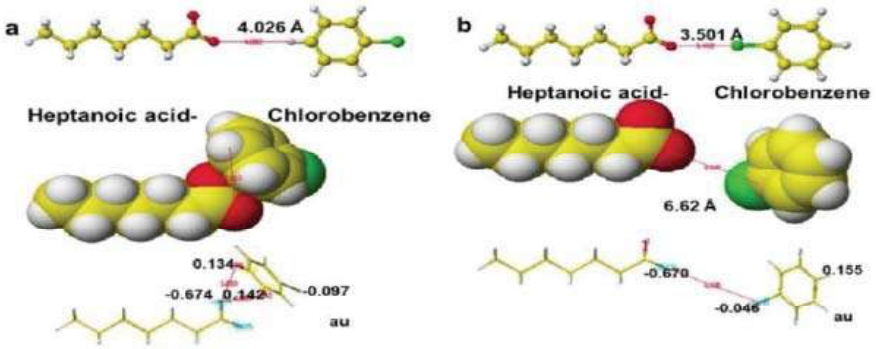


Figure 2.11a and b: Docking of ionized heptanoic acid with chlorobenzene and the atomic partial charge.

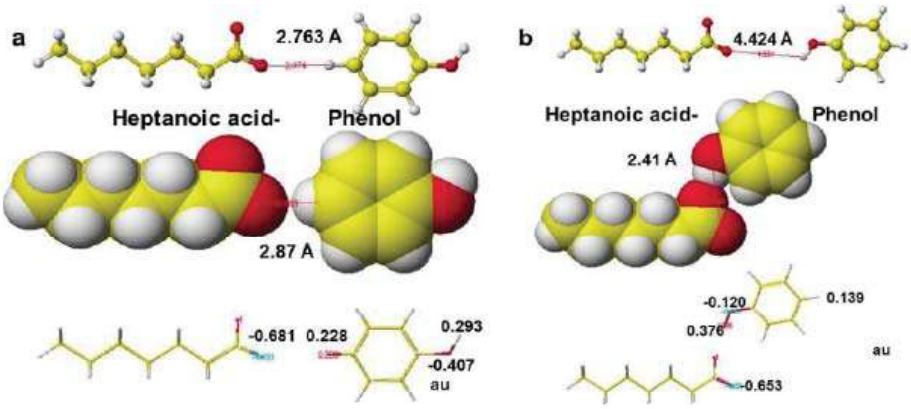


Figure 2.12a and b: Docking of ionized heptanoic acid with phenol and the apc values.

Benzoic acid demonstrated similar behavior to phenol. The benzoic acid located 3.54 Å from the heptanoic acid carboxyl group formed a tight complex via MIES (2.150 kcal mol^{-1}). Even the phenyl group faced the carboxy group (Figure 2.13a); they formed a complex via MIVW, and the smooth complex formation between carboxy groups did not demonstrate clear apc change, but the conformation of Figure 2.13b showed clear changes in apc values. The apc values of hydrogen and oxygen in Figure 2.13a were 0.228 from 0.164 and -0.687 from -0.671, respectively. That in Figure 2.13b was 0.374 and -0.363 au, respectively. Figure 2.13b should be the actual conformation.

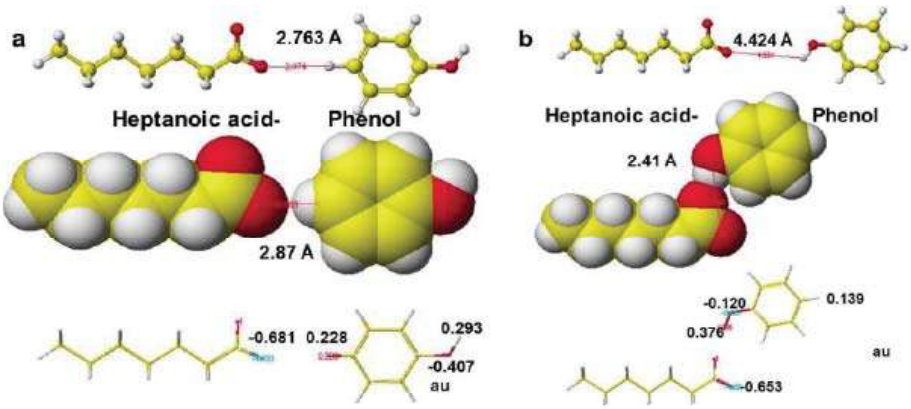


FIgure 2.12a and b: Docking of ionized heptanoic acid with benzoic acid and the apc values.

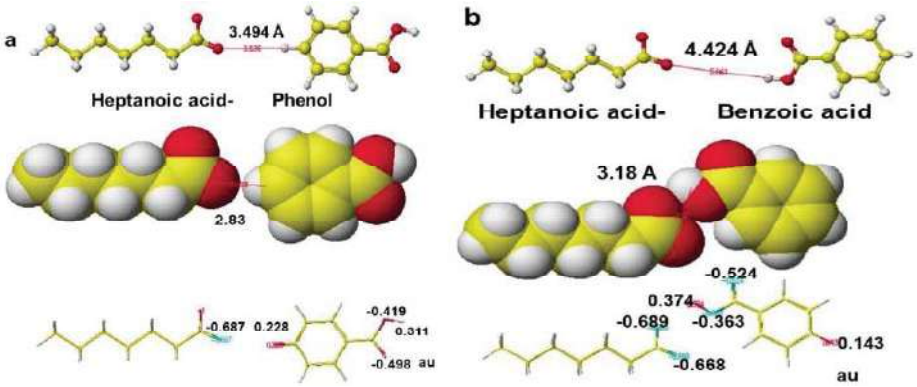


FIgure 2.13a and b: Docking of ionized heptanoic acid with benzoic acid and the apc values.

For aniline, an acid-base interaction was expected, and an interaction between the amino and carboxy groups was observed via electrostatic interaction (MIES 0.424 kcal mol^{-1}). However, the MIVW value was 0.807 kcal mol^{-1}. The hydrophobic interaction was stronger than the electrostatic interaction. The apc values of hydrogen and oxygen in Figure 2.14a and Figure 2.14b were 0.226 and -0.677 and 0.317 from 0.220 and -0.691 from -0.672 au, respectively. The molecular form amine should not interact tightly with ionized carboxy groups.

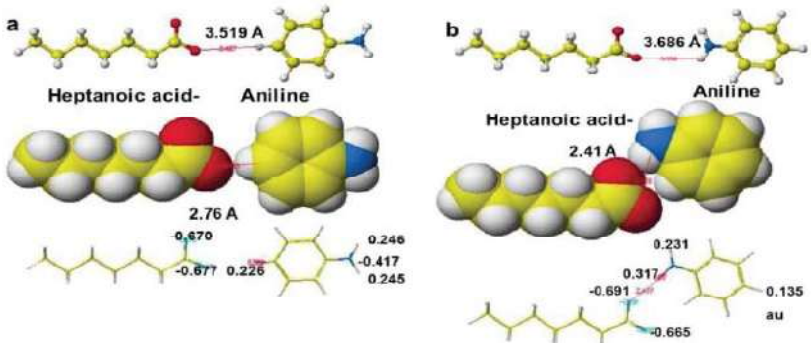


FIgure 2.14a and b: Docking of ionized heptanoic acid with aniline and the apc values.

The molecular interactions between heptanoic acid and ionized phenol are shown in Figures 2.15a and b. Especially, benzoic acid was bound with the carboxy group via hydrogen bonding, and the apc values of carboxy oxygen changed from 0.112 to 0.176 au. The apc values of the carbonyl oxygen did from -0.671 to -0.646 au (Figure 2.15a). The initial atomic distance expanded from 2.68 to 2.81 Å; the MIES was negative (-1.310 kcal mol^{-1}). The ionized phenol was repelled from the carboxy group, and this phenomenon should occur in a very high pH location. These similarly charged negative ions repelled each other and expanded their molecular distance to 13.04 Å in Figure 2.15b.

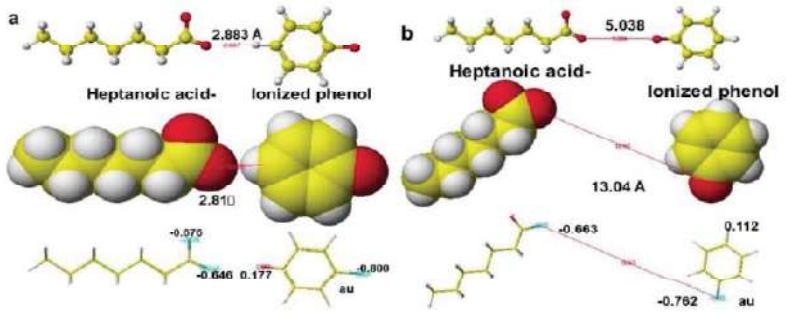


FIgure 2.15a and b: Docking of ionized heptanoic acid with ionized phenol and the apc values.

Ionized benzoic acid was repelled from the carboxylate ion; however, the hydrophobic site may contact via weak MIVW (0.693 kcal mol^{-1}). Fundamentally, the ionized carboxy compound was repelled from the carboxy group, and the negative MIES values and longer atomic distances clearly provided evidence in Figures 2.16a and b.

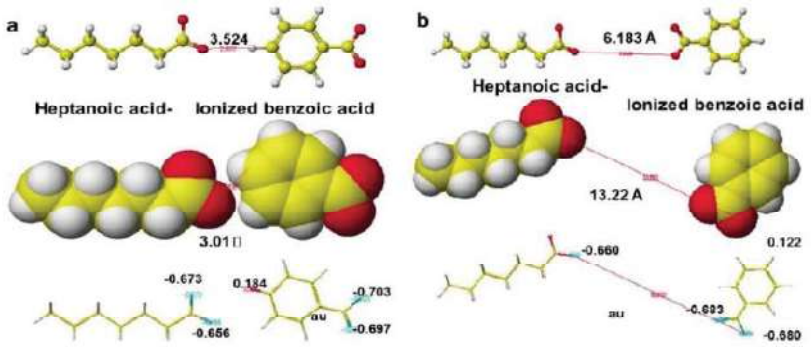


FIgure 2.16a and b: Docking of ionized heptanoic acid with ionized benzoic acid and the apc values.

The ionized amino group tightly contacted the carboxy group even when the amino group was located on the opposite side of the carboxy group (Figure 2.17a). These conformations demonstrated high MIES values (over 7 kcal mol^{-1}), and the carboxy oxygen apc values were -0.720 and -0.698 from -0.671 au. The amino hydrogen apc values were 0.209 and 0.269 from 0.219 au. A strong ion-ion interaction was observed for their opposite ions (Figure 2.17b). The molecular interaction energy values are summarized in Table 2.7, and the conformations are indicated as their Figure number.

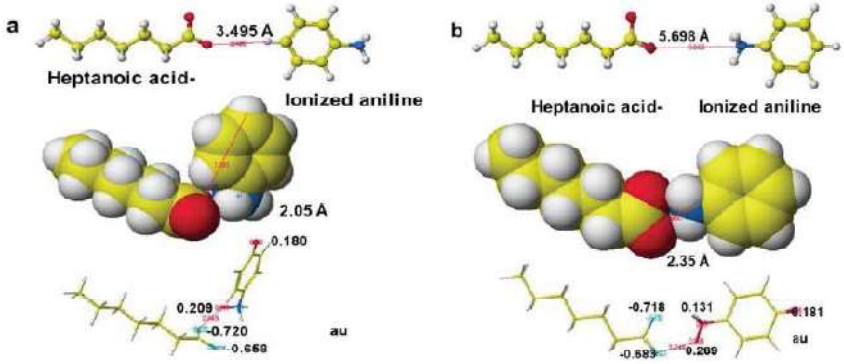


FIgure 2.17a and b: Docking of ionized heptanoic acid with ionized aniline and the apc values.

Table 2.7: Molecular interaction energy values of heptanoic acid and standard compounds.

Chemicals	Right				Left			
	IP	MIHB	MIES	MIVW	IP	MIHB	MIES	MIVW
Benzene	2.73	0	0	0.368	-	-	-	-
Methylbenzene	2.733	0	-0.063	0.382	4.202	0	0.244	0.538
Chlorobenzene	4.026	0	1.137	1.66	3.511	0	0.048	0.08
Phenol	2.763	0.003	-0.04	0.371	4.424	0.003	1.137	1.66
Benzoic acid	3.494	0	0.048	0.371	5.045	0.003	2.217	0.48
Aniline	3.519	0.007	0.222	0.386	3.686	-0.199	2.15	0.424
Ionized phenol	2.883	0.001	0.03	0.374	5.038	-0.002	0.424	0.807
Ionized benzoic acid	3.524	0	-1.31	0.347	6.183	0	-0.638	0
Ionized aniline	3.495	0	-0.696	0.693	5.698	0	7.261	0.923

Right or Left: direction of analytes (left or right side in Figures); IP: initial distance before optimization; MIHB, MIES, and MINW: molecular interaction (MI) energy values of hydrogen (HB), electrostatic (ES) and van der Waals (VW) interaction; unit: kcal mol^{-1}.

2.3.2 The fundamental activity of amino-group: The molecular form of the amino group exists in solutions above pH 12 where water contains OH^- and H_3O^+ ions. However, amino group behavior was analyzed in ionized form to clarify its hydrogen-bonding and ionic capabilities. Therefore, the binding of ionized hexylamine with the same analytes used for studying the carboxyl group activities was examined in this study.

The benzene aromatic ring is capable of hydrogen bonding. However, when benzene was located at a distance of 3 Å, benzene docked with the amino group after conformational optimization with an MIVW value of 0.621 kcal mol^{-1}. The amino hydrogen apc changed from 0.225 to 0.232 au. The benzene hydrogen apc changed from 0.156 to 0.093 au. This result also supports the contact site (Figure 2.18). Due to the weak molecular interaction, methylbenzene also bound with the amino group when it was initially located 3 Å away. The MIVW energy values were 0.983 and 0.760 kcal mol-1, respectively, shown in Figures 2.16a and b. Initially orienting the amino group toward the phenyl group produced higher apc change than orienting it toward the methyl group. The apc value of amino-hydrogen was 0.230 au (Figure 2.19a) and 0.228 au (Figure 2.19b), respectively. Their contact also induced the electron localization of other atoms. respectively..

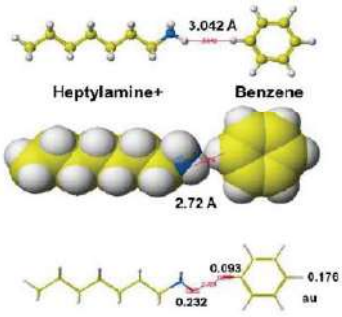


FIgure 2.19: Docking of ionized heptylamine with benzene and the apc..

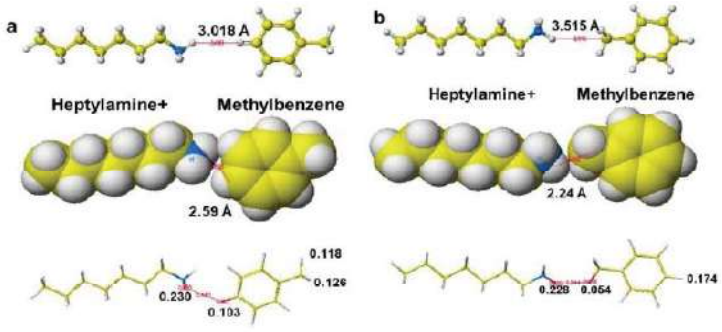


FIgure 2.17a and b: Docking of heptylamine with methylbenzene and the apc values.

When the chlorine of chlorobenzene faced the amino group at a 5 Å distance, they docked together with MIVW 1.156 kcal mol^{-1} (Figure 17b). The MIES was 0.651, but MIHB was zero kcal mol^{-1}, and the electron localization was induced by the contact. The chlorine apc changed from -0.051 to -0.113 au. The contact between the amino group and the phenyl group induced the electron localization (Figure 2.21a); however, the actual docking is expected to occur between the amino group and the chlorine.

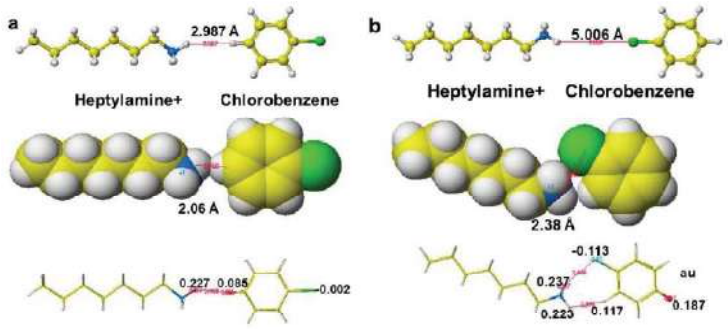


FIgure 2.21a and b: Docking of heptylamine with chlorobenzene and the apc values.

Docking with phenol was based on van der Waals forces (MIVW) 0.955 and 0.943 kcal mol^{-1}, respectively, in Figures 2.16a and b). Contact of the amino group with the acidic hydroxy group produced an MIES value of 0.547 kcal mol^{-1}(Figure 18b). The contact strength can be inferred from changes in apc values. The amino hydrogen apc of Figures 2.22a and b were 0.228 and 0.246 from 0.225 au. The phenolic oxygen apc changed from -0.386 to -0.436 kcal mol^{-1}. The actual docking is expected to occur between the amino group and the hydroxy group, as shown in Figure 18b. The benzoic acid docking was similar to that of phenol. The docking of the amino group with the benzoic acid carbonyl group produced a high MIES value (2.575 kcal mol^{-1}). The carbonyl oxygen apc changed from 0.470 to-0.573 au, as shown in Figure 19a. The change was little when the amino group contacted the phenyl group (Figure 2.23a), and van der Waals forces contributed to the contact (MIVW 0.938 kcal mol^{-1}). The actual docking should occur like Figure 2.23b.

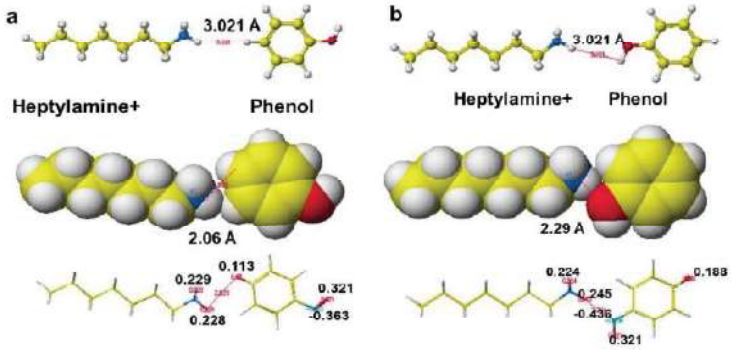


FIgure 2.22a and b: Docking of heptylamine with phenol and the apc values.

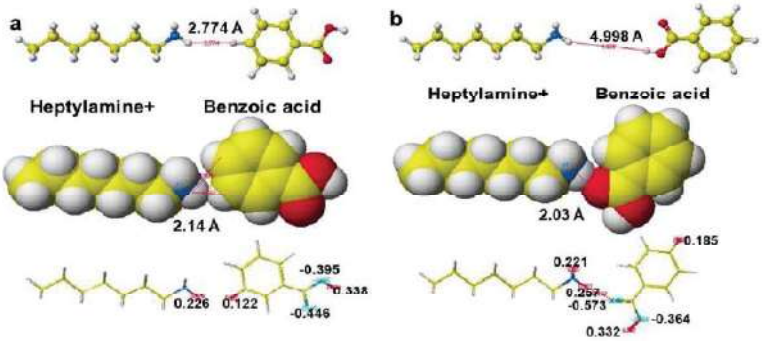


FIgure 2.23a and b: Docking of heptylamine with phenol and the apc values.

The docking of the amino group with aniline was weak, and the main interaction was van der Waals force. The MIVW values were 0.626 and 0.686 kcal mol^{-1}, respectively (Figures 2.20a and b). The aniline nitrogen apc changed from 0.182 to -0.447 au. The Figure 20b form should be the actual conformation.

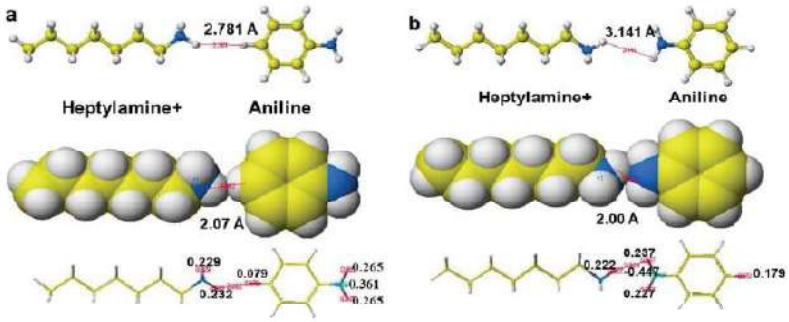


FIgure 2.24a and b: Docking of heptylamine with aniline and the apc values.

The docking of ionized phenol produced the electrostatic force. Their MIES values were 1.288 and 4.010 kcal mol^{-1}, respectively (Figures 2.25a and b). Even though these molecules were separated 6 Å apart, the oxygen apc changed from -0.759 to -0.813 au. The p-hydrogen apc changed from 0.112 to 0.141 au. The higher apc value change compared with the above molecules indicated the binding strength.

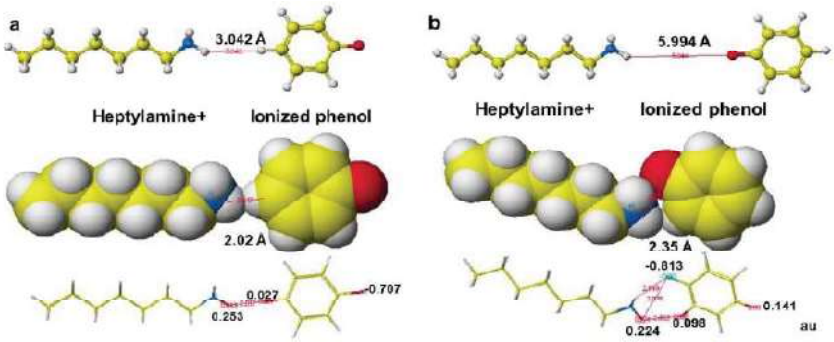


FIgure 2.25a and b: Docking of heptylamine with ionized phenol and the apc values.

Docking with ionized benzoic acid produced a strong electrostatic force. Their MIES values was 6.972 kcal mol^{-1}, (Figures 2.26b). Even when these molecules were separated by 5 Å; the strong interaction bound together. The oxygen apc changed from -0.759 to -0.695 au. The *p*-hydrogen apc changed from 0.112 to 0.146 au. The docking between the amino group with the phenyl group (Figure 2.26a) was possible due to the van der Waals force (MIVW 0.839 kcal mol^{-1}). MIES (0.838 kcal mol^{-1}) indicated the contribution of electrostatic interaction.

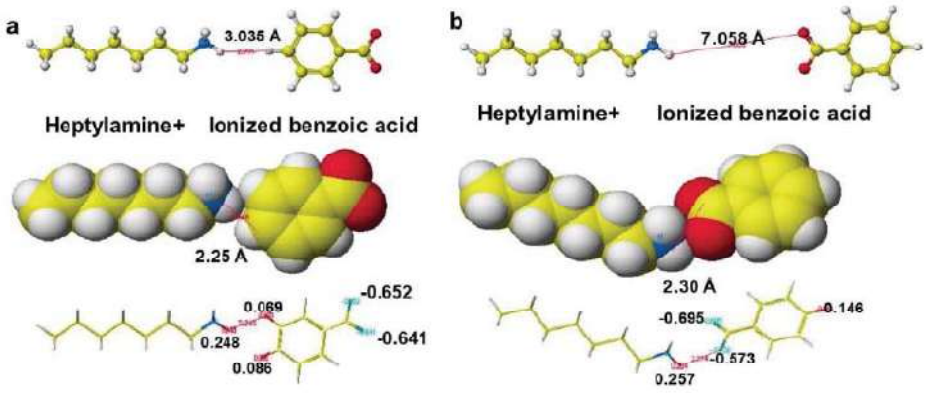


FIgure 2.26a and b: Docking of heptylamine with ionized benzoic acid and the apc values.

Contact with the similarly charged ionized aniline was unfavorable from the amino group (Figure 2.27b). The phenyl group contacted the amino group through van der Waals forces (Figure 2.27a). The amino group hydrogen apc changed from 0.225 to 0.205 au, and phenyl *p*-hydrogen apc changed from 0.206 to 0.153 au. The latter result indicates a possible contact of ionized amino compounds. The molecular interaction energy values docking with the heptylamines are summarized in Table 2.18.

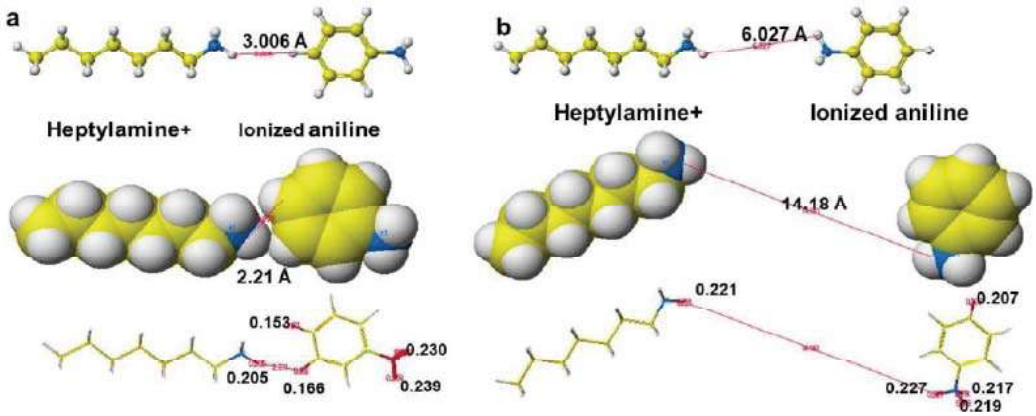


FIgure 2.27a and b: Docking of heptylamine with ionized aniline and the apc values.

Table 2.18: Molecular interaction energy values after docked ionized heptylamine and standard compounds.

Chemicals	Right				Left			
	IP	MIHB	MIES	MIVW	IP	MIHB	MIES	MIVW
Benzene	3.042	0	0	1.258	-	-	-	-
Methylbenzene	3.018	0	0.06	1.263	3.575	0	-0.186	1.305
Chlorobenzene	2.987	0	-0.303	1.249	5.006	0	1.039	1.211
Phenol	3.021	-0.002	0.101	1.495	3.021	0.016	0.467	1.538
Benzoic acid	2.774	-0.006	-0.059	1.592	4.998	-0.031	2.611	1.144
Aniline	2.781	0	-0.025	1.259	3.141	0	-0.011	5.603
Ionized phenol	3.042	0	3.793	1.848	5.944	0	4.024	1.398
Ionized benzoic acid	2.771	0	0.813	1.494	7.058	0	6.961	1.059
Ionized aniline	3.006	0	-1.019	1.254	6.027	0	-0.807	0.625

Right or Left: direction of analytes (left or right side in Figures); IP: initial distance before optimization; MIHB, MIES, and MINW: molecular interaction (MI) energy values of hydrogen (HB), electrostatic (ES) and van der Waals (VW) interaction; unit: kcal mol^{-1}.

2.3.2 The fundamental activity of guanidino-group: The following analysis demonstrates the hydrogen-bonding capability observed for a guanidino phase used for saccharide recognition. The guanidino group consisted of amino and ionized amino groups as a computational model rather than as a resonance structure; therefore, it demonstrates hydrogen bonding and ion-ion interaction capability. When the guanidino group faced the phenyl group (Figure 2.25a), hydrogen bonding was the primary interaction (MIHB 4.487 kcal mol^{-1}), and van der Waals force contributed to the interaction (MIVW 1.438 kcal mol^{-1}). The guanidino hydrogen atoms involved in contact apc values changed from 0.311 and 0.323 to 0.298 and 0.300 au. The nitrogen apc changed from -0.402 and -0.368 to -0.414 and -0.386 au (Figure 2.28). Contact of the guanidino group with the methyl group (Figure 2.29b) was weak, and the MI energy values were small. The guanidino hydrogen apc was 0.300 from 0.298 au. The methyl hydrogen apc values were 0.087 and 0.088 from 0.105 and 0.108. Therefore, the contact conformation should be like Figure 2.29a.

The initial position did not affect the MI energy values, but the guanidino group and chlorine interaction were strong even though they were separated by 5 Å. The hydrogen bonding was the main force, and MIHB value was 4.509 kcal mol^{-1}. Van der Waals interaction also contributed, and the MIVW value was 1.569 kcal mol^{-1}. The guanidino hydrogen involved in contact apc changed from 0.298 to 0.316 or 0.315 au (Figure 2.30).



FIgure 2.28a and b: Docking of heptylguanidine with benzene and the apc values.

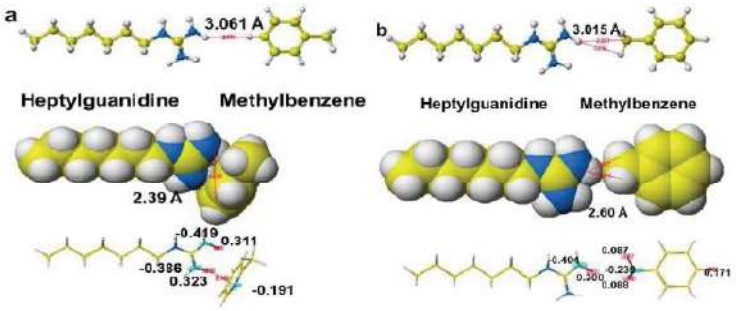


FIgure 2.29a and b: Docking of heptylguanidine with methylbenzene and the apc values.

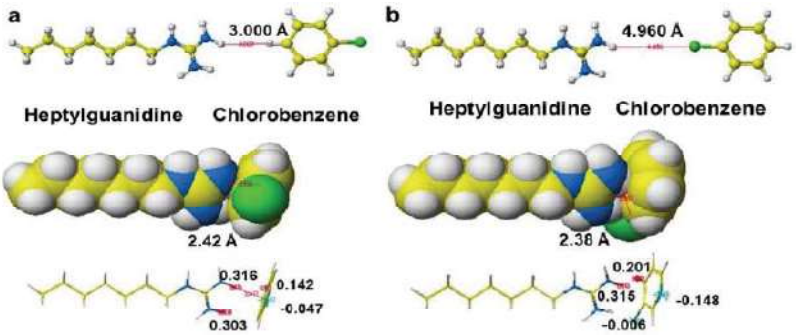


FIgure 2.30a and b: Docking of heptylguanidine with chlorobenzene and the apc value.

The complex conformation with phenol was similar to that of chlorobenzene. The primary interaction force is hydrogen bonding. The MIHB values of Figures 2.31a and b were 4.811 and 1.040 kcal mol^{-1}, and MIVW values indicated the contribution of van der Waals force. The results suggest that the guanidino group directly interacted with the phenyl group.

The conformation of the guanidino group complexes with the benzoic acid was similar to those of the other analytes. The guanidino group contacted the phenyl group and produced an MIES value of values. The guanidino hydrogen apc change indicated the contact center, and the value changed from 0.305 to 0.316 au. The benzoic acid-hydroxy oxygen apc changed from -0.410 to -0.399 au (Figure 2.32).

The conformation of the complex with aniline was slightly different from acidic compounds. The guanidino group contacted the phenyl group (Figure 33a) and produced an MIES value of energy (0.125 kcal mol^{-1}). However, the guanidino group contact with the amino group was weak, and MIES and MIVW values were small (MIES and MIVW, 0.031 and 0.544 kcal mol^{-1}).

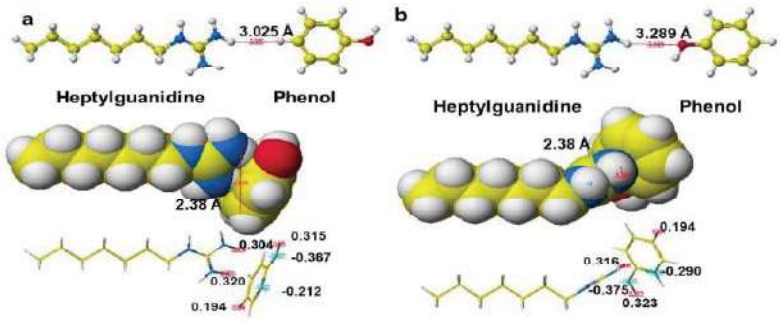


FIgure 2.31a and b: Docking of heptylguanidine with phenol and the apc values.

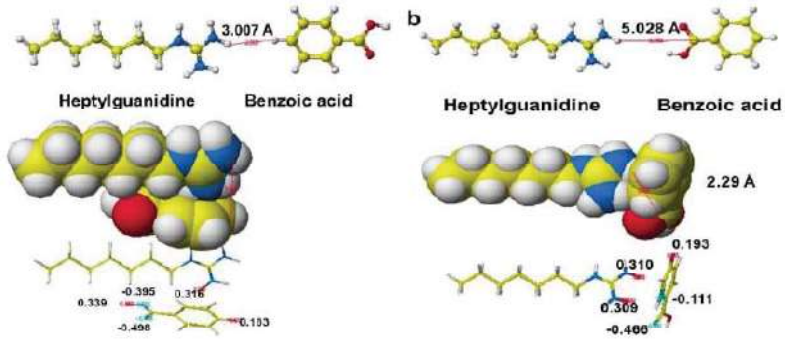


FIgure 2.32a and b: Docking of heptylguanidine with benzoic acid and the apc values.

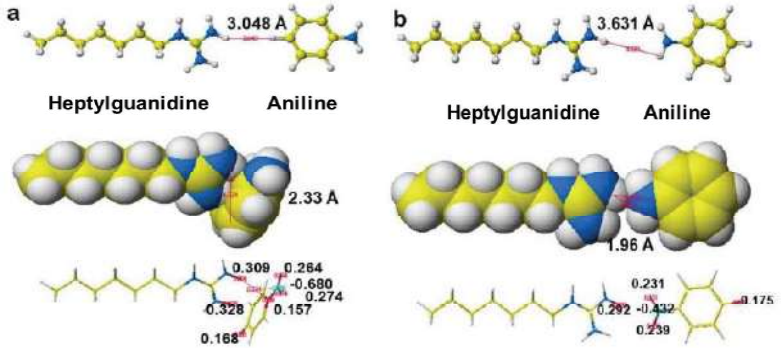


FIgure 2.33a and b: Docking of heptylguanidine with aniline and the apc values.

Th The contribution of MIES played an important role in the complex formation of the guanidino group with ionized phenol; although this phenomenon occurs in very high pH solutions due to the high pKa values of phenol. The MIES values of Figures 34a and b were 4.683 and 2.545 kcal mol^{-1}. The phenolic oxygen apc changed from -0.759 to - 0.721 and -0.717, and the guanidino hydrogen apc values were 0.342 and 0.356 from 0.305 and 0.295 in Figures 34a and b.

The ionized benzoic acid conformation differed from that of ionized phenol. The ion-ion interaction (electrostatic interaction) was essential in Figure 35b. The MIES energy (5.937 kcal mol^{-1}) supported the conclusion. The oxygen apc values changed from -0.673 to -0.689 and -0.724 au (Figure 2.35b), and the guanidino hydrogen apc was 0.360 from 0.3 au. The apc changed a little in Figure 2.35a conformation. These results indicate that the actual conformation should be Figure 2.35b.

Binding with similarly charged ionized aniline was different from that of acidic compounds. The ionized amino group was repelled from the guanidino group (Figure 2.36b). The possible interaction was with the phenyl group as observed with acidic compounds via hydrogen bonding (Figure 2.36a). The calculated molecular interaction energy values for heptylguanidine docking are summarized in Table 2.19.

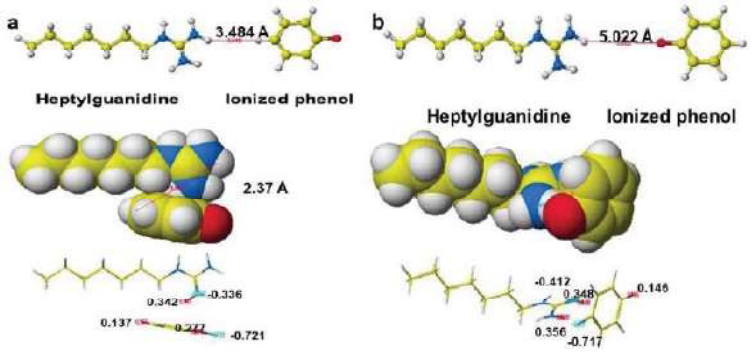


FIgure 2.34a and b: Docking of heptylguanidine with ionized phenol and the apc values.

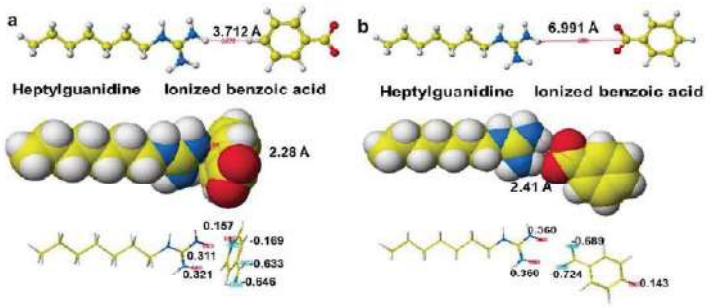


FIgure 2.35a and b: Docking of heptylguanidine with ionized benzoic acid and the apc values.

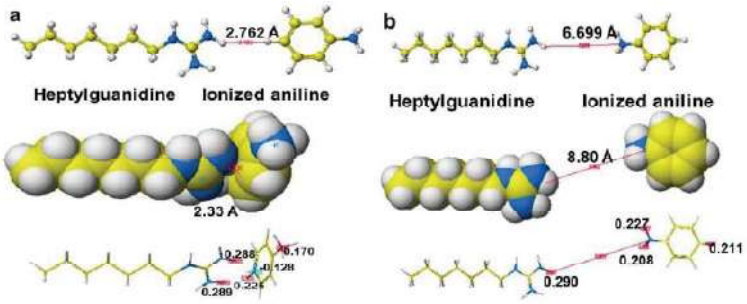


FIgure 2.36a and b: Docking of heptylguanidine with ionized aniline and the apc values.

The direct molecular interactions of ion-exchange groups were investigated using simple molecules. Quantitative analysis should clarify the qualitative speculation of molecular interactions of various compounds with proteins. Although actual compounds contain various functional groups; the simple experience can estimate the fundamental mechanisms.

Table 2.19: Molecular interaction energy values after docked heptylguanidine and standard compounds.

Chemicals	Right				Left			
	IP	MIHB	MIES	MIVW	IP	MIHB	MIES	MIVW
Benzene	3.043	4.487	-0.01	1.438	-	-	-	-
Methylbenzene	3.019	4.499	0.226	1.545	3.269	0.07	-0.25	0.704
Chlorobenzene	2.789	4.509	-1.195	1.567	5.019	0.718	1.813	0.464
Phenol	3.02	4.811	0.531	1.351	3.667	1.04	0.137	2.87
Benzoic acid	3.024	4.592	3.782	1.644	3.227	1.62	7.623	0.636
Aniline	3.203	3.282	0.125	2.448	3.123	0.229	0.031	0.544
Ionized phenol	3.502	4.683	5.937	1.173	5.518	2.545	7.545	-0.153
Ionized benzoic acid	3.712	4.153	3.116	1.677	6.991	0.114	10.24	0.233
Ionized aniline	2.762	0.213	-1.815	0.425	6.999	0	-1.126	-1.013

Right or Left: direction of analytes (left or right side in Figures); IP: initial distance before optimization; MIHB, MIES, and MINW: molecular interaction (MI) energy values of hydrogen (HB), electrostatic (ES) and van der Waals (VW) interaction; unit: kcal mol^{-1}.

The direct molecular interactions of ion-exchange groups were quantitatively investigated using simple molecules. The in silico analysis using model compounds clarifies qualitative interpretations of molecular interaction mechanisms of ion-exchange chromatography. Furthermore, binding mechanisms of various compounds with proteins can be estimated from these analyses. Although actual substituents interact with various groups, this simple model can be further applied for protein-substitute binding mechanisms in later chapters.

The simple modeling analysis of molecular interactions provides the fundamental mechanisms of molecular interactions. The weakest interaction force is van der Waals force, and hydrophobic interactions are observed when hydrophobic sites of molecules approach to a distance of about 3 Å. Ion-ion interactions, represented by strong electrostatic energy values calculated with a molecular mechanics program, are observed even when two molecules are separated by more than 5 Å, whereas repulsion occurs between compounds with the same charge. These experiments can be performed using an economical computational chemistry program.

References

1. T. Hanai, Introduction of in silico chromatography, Journal of Chroma\tography, Separation technique, 2016, 7 (5) pp.8, DOI: 10.4172/2157-7064.1000333

2. T. Hanai, Quantitative in silico chromatography, Computational modeling of molecular interactions, 2014, RSC, Cambridge, pp. 338, (ISBN: 978-1-84973-991-7) .

Chapter 3: Modeling Analysis of Chromatographic Retention

Chromatography is an excellent analytical method for measuring molecular interactions (MI) with high reproducibility, and retention mechanisms relate to solubility; therefore, quantitatively explaining molecular interaction mechanisms is a fundamental subject in analytical chemistry. Chromatography is based on repeated (continuous) distribution of analytes between two phases. One phase that carries analytes is called the mobile phase (eluent), and another phase that holds the analytes is called the stationary phase. However, the stationary phase structure is complex. Solid or non-movable polymers are basically stationary phases. However, when used in liquid, the solid or non-movable polymer is coated with mobile-phase components, and these solvent-coated phases are the real stationary phases. In general experimental conditions, complete removal of the coated liquid is impossible. However, building a realistic model of stationary phases in silico is difficult; therefore, model phases must be simplified to study molecular interactions in chromatography. Chromatographic relative retention time (capacity ratio)were correlated with calculated molecular interaction (MI) energy values using a variety of model phases suitable for the analyte's molecular properties and the chromatographic conditions. The MI energy value was calculated by subtracting the complex energy from the sum of the analyte and model-phase energies. The energy value change after complex formation is considered as the MI energy value and comprises the final (optimized) structure (MIFS), hydrogen bonding (MIHB), electrostatic (MIES), and van der Waals (MIVW) forces. The MIHB and MIVW indicate the contribution of hydrogen bonding and molecular size effects, respectively. The calculated MI energy values were correlated with the log k values of the analytes. For example, to predict retention time using MIFS = a x log k + b (a and b are constants), all groups' slope a and constant b should be the same for an ideal system.

Instrumental development of chromatography techniques has been well achieved. No more dynamic instrumental development seems exciting; however, the chemistry of chromatography has not been well developed. The most popular phase is chemically modified silica gels. Bonded silica gels synthesized from pure silica gel (more than 99.999% pure) are chemically stable and permit long-term operation to study molecular interactions.

However, calculated MI energy values are not absolute, must consider as describe the relative selectivity because all computer software is updating. The properties of different bonded silica gels were described using simple model ligands and model analytes to explain the interaction mechanisms quantitatively. Analytes repeatedly interact with a ligand, are solvated with solvent (eluent components), and move toward the exit of the column filled with bare or ligand-bonded packing materials. This simple model analysis uses eight model ligands (hexyl, hexenyl, phenylhexyl, heptanoic acid, hexylamine, ionized heptanoic acid, ionized hexylamine, and guanidyl-bonded silicone tetraoxides. However, the chromatographic eluent is the main driving force and a mixture of solvents, buffer components, surfactants, and ion-pair reagents used to manage chromatographic purification processes. The solvent and ion effects are described using simple methods.

The selected solvents are water (proton acceptor and donor solvent) and acetonitrile (proton donor solvent). Methanol is also a proton acceptor and donor solvent, but its properties are similar to water, and the difference is due to the solubility degree due to the cluster structure. The competitive interaction of an analyte was analyzed with either the bonded ligand or a solvent molecule using several models; the ligand and solvent molecule are aligned linearly, with a distance of 15Å between the edge of the ligand and the solvent molecule. A silicon atom of the silicon oxide and hydrogen of water or the methyl carbon of acetonitrile are locked to fix their initial positions. The details of their locations are shown in the following Figures. The same method is also used to analyze competitive ion interactions. The selected ions are sodium and chloride.

Electron localization contributes to molecular and ionic interactions, like inductive effects in organic reactions. Electrostatic interaction varies from strong ion-ion to weak π–π (dipole-dipole) interaction; however, it can be easily explained as Lewis acid-base interaction. The substituent's inductive effect affects the strength of the interaction center. Molecular mechanics calculations also identify hydrophobic (van der Waals) interactions and hydrogen bonding as major contributions. Therefore, several ligands and popular compounds are selected to simplify the explanation in this chapter.

3.1. Solvent Effects in Hydrophobic and Hydrophilic Interaction Liquid Chromatography

Solvents, especially organic modifiers, generally control the solvation of packing materials and analytes in reversed-phase liquid chromatography, where hydrophobic alkyl- and phenyl-ligand-bonded silica gels are common. Polar ligands are used for hydrophilic interaction liquid chromatography (HILIC); however, the retention mechanisms are similar

to normal-phase liquid chromatography. Both hydrogen bonding and weak electrostatic interactions contribute to the retention. The retention mechanisms in reversed-phase liquid chromatography are attributed to hydrophobic interaction. If hydrophobic interaction is eliminated from the retention mechanisms in liquid chromatography, hydrogen-bonding and electrostatic interactions remain. On the other hand, the partition mechanism is used qualitatively to explain elution-time differences in liquid chromatography, where an analyte moves between the stationary phase and the eluent. When an analyte remains in the eluent, it moves faster; when the analyte remains on the bonded-phase surface, it moves more slowly. The affinity level is visualized in the following experiments with atomic partial charge as the indicator of electron localization.

3.1.1 Contribution of water: The selected bonded phases are dimethyl-trihydroxy-silane-bound hexyl-, hexenyl-, phenylhexyl-, heptylcarboxy-, and hexylamino-bonded silica gels. We use only one ligand to simplify the explanation. We compare solvent effects using atomic partial-charge changes and molecular interaction energies, where hydrogen-bonding and electrostatic energy values reflect specific interactions. The first selected solvent is water, a hydrogen-bonding solvent. Initially, the ligand edge, the water, and the hydrogen atom are kept at 15Å, and the water and silicon are kept at 15Å, to prevent ligand movement and maintain their initial distances. An analyte is placed between the ligand edge and water hydrogen; then, the initial conformation is optimized as shown in the figures.

The visually optimized structures indicate possible interaction points between two molecules, and the interaction center is clearly indicated. The hexyl ligand did not exhibit strong interaction with aromatic compounds. The polar substituents interacted with water molecules, moved toward them, and contacted them closely via hydrogen bonding; ionization of the substituents weakened this hydrogen bonding. Electron localization changed their original apc values. MI energy values indicate the main interaction mechanism and the degree of affinity. Electron-rich- π–π type repulsion, but not interaction, was also quantitatively demonstrated. A typical example is chlorobenzene, where the electron-rich chlorine is bonded with a water molecule. The strong MIHB supports strong binding and a negative MIVW energy value; the apc value of chlorine changed from -0.051 to -0.033 au. The apc value of the water molecule hydrogen was changed from 0.247 to 0.275 au. Benzoic acid showed a similar result to chlorobenzene due to the carbonyl oxygen, and its hydrogen-bonding capability increased the MIES value (1.899 kcal m^{-1}). However, ionized benzoic acid did not show such action. Ionized aniline did not move, and the amino group repelled water molecules, showing zero MIVW and positive MIES value (0.445 kcal mol^{-1}). Figure 3.1 shows the optimized conformation of the hexyl ligand, the analyte, and a water molecule, and Table 3.1 summarizes the molecular interaction energy value.

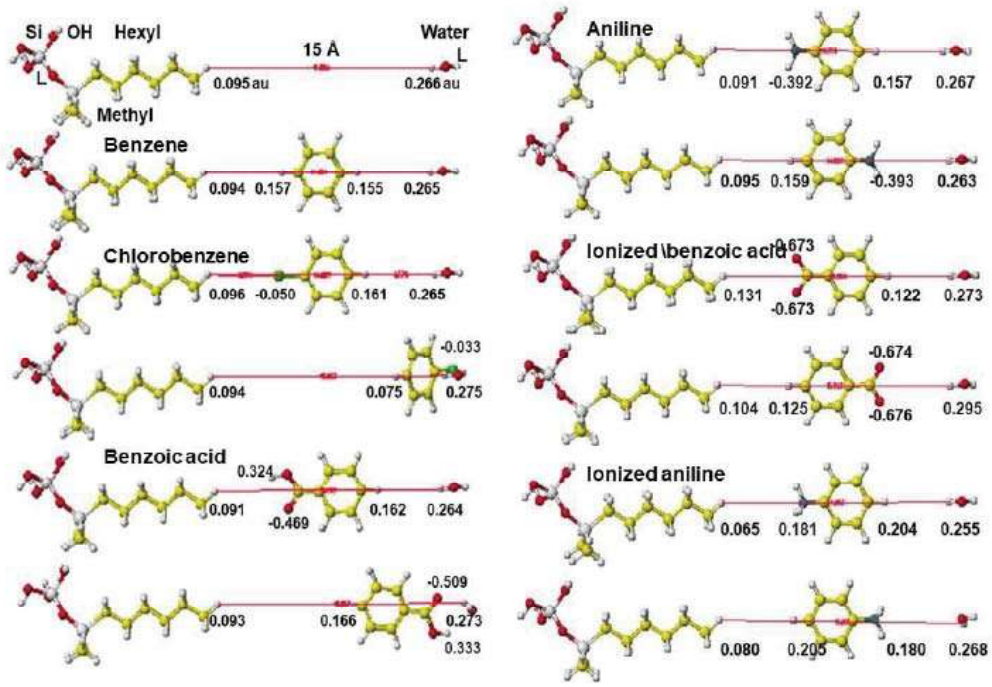


Figure 3.1: Compete interaction of hexyl ligand and water molecule.

Table 3.1: Compete for molecular interaction between hexyl-ligand and water.

Chemicals	Right			Left		
	MIHB	MIES	MIVW	MIHB	MIES	MIVW
Benzene	0.03	0.005	0.071	-	-	-
Chlorobenzene	15.789	-0.31	-1.258	0.061	-0.017	0.167
Benzoic acid	10.232	1.899	-1.062	0.061	-0.017	0.167
Aniline	0.021	-0.007	0.102	0.041	-0.009	0.098
Ionized benzoic acid	-0.001	0.411	0.45	0.053	-0.04	0.143
Ionized aniline	0.012	0.445	0	0.048	0.031	0.099

Right or Left: direction of analytes (left or right side in Figures); IP: initial distance before optimization; MIHB, MIES, and MINW: molecular interaction (MI) energy values of hydrogen (HB), electrostatic (ES) and van der Waals (VW) interaction; unit: kcal mol^{-1}.

The hydrophobic hexyl ligand did not show any strong positive interaction, as indicated by the MIVW energy values. The positive contribution was actually a negative contribution due to binding of an analyte with the water molecule. We studied the contribution of the π electron using hexenyl and phenylhexyl ligands. The optimized conformations are shown in Figures 3.2 and 3. The molecular interaction energy values are summarized in Tables 3.2 and 3.

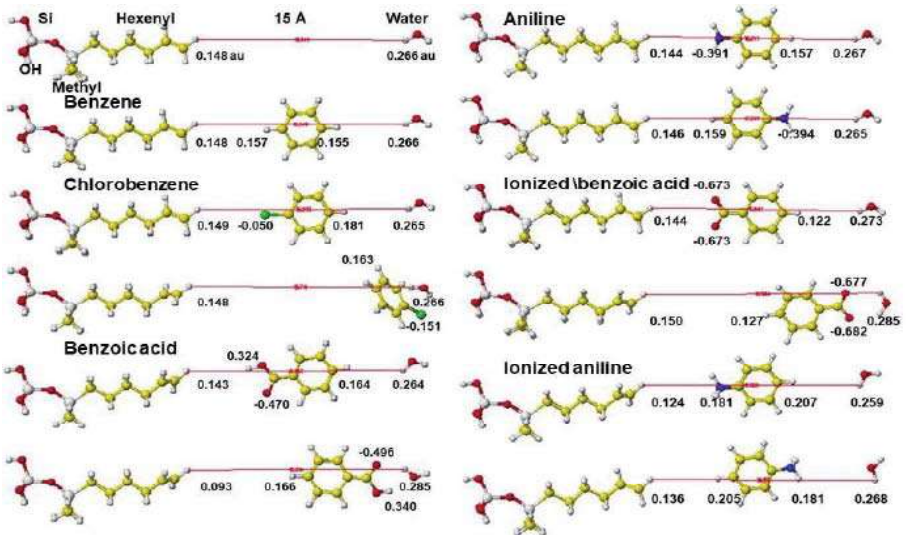


FIgure 3.2: Compete for molecular interaction between hexenyl-ligand and water.

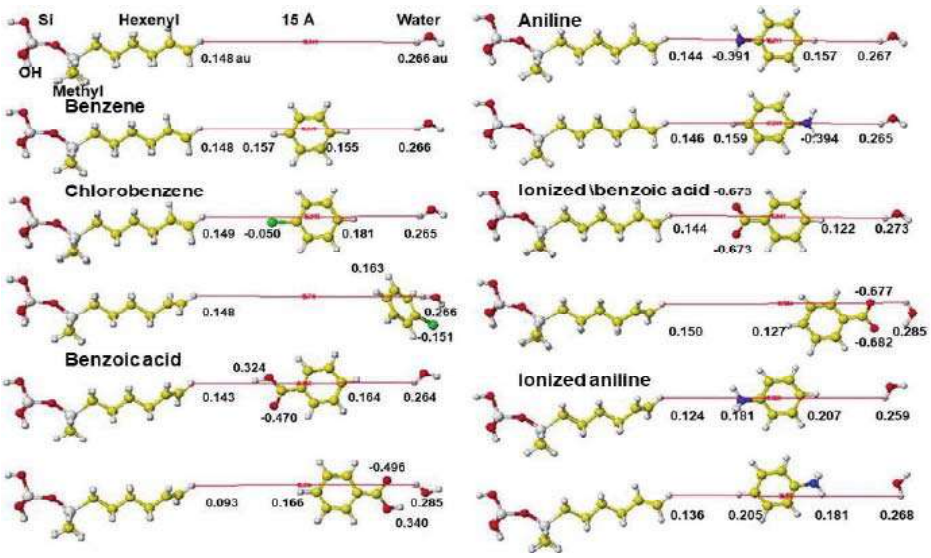


FIgure 3.3: Compete for molecular interaction between phenylhexyl-ligand and water.

Table 3.2: Compete for molecular interaction between hexenyl-ligand and water.

Chemicals	Right			Left		
	MIHB	MIES	MIVW	MIHB	MIES	MIVW
Benzene	0.026	0	0.063	-	-	-
Chlorobenzene	15.788	-0.308	-1.27	0.037	-0.024	0.155
Benzoic acid	6.889	2.123	0	0.087	0.042	0.084
Aniline	0.022	0.003	0.076	0.044	0	0.074
Ionized benzoic acid	0.207	2.543	0.158	0.041	-0.098	0.123
Ionized aniline	0.012	0.436	0.075	0.029	0.097	0.065

Right or Left: direction of analytes (left or right side in Figures); IP: initial distance before optimization; MIHB, MIES, and MINW: molecular interaction (MI) energy values of hydrogen (HB), electrostatic (ES) and van der Waals (VW) interaction; unit: kcal mol^{-1}.

Table 3.3: Compete for molecular interaction between phenylhexyl-ligand and water.

Chemicals	Right			Left		
	MIHB	MIES	MIVW	MIHB	MIES	MIVW
Benzene	0.026	0	0.088-	-	-	
Chlorobenzene	15.783	-0.311	-1.256	0.008	-0.005	0.75
Benzoic acid	10.233	1.894	-1.045	0.116	-0.025	0.172
Aniline	0.029	0.004	0.107	0.059	0	0.094
Ionized benzoic acid	11.11	-0.406	-0.556	0.045	-0.046	0.189
Ionized aniline	0.008	0.383	0.139	0.032	0.096	0.119

Right or Left: direction of analytes (left or right side in Figures); IP: initial distance before optimization; MIHB, MIES, and MINW: molecular interaction (MI) energy values of hydrogen (HB), electrostatic (ES) and van der Waals (VW) interaction; unit: kcal mol^{-1}.

The contribution of π - electron of the ligand was not significant; however, the phenylhexyl ligand's phenyl π-electron contributed more to molecular interactions than that of the vinyl group, as expected. The actual π-electron contribution cannot be determined from the results using a single ligand because the vinyl ligand has a higher density than the phenyl ligand due to steric hindrance from the larger molecular size of the phenyl group. Instead, the water-molecule contributions from binding to polar substituents clearly indicated the hydrogen-bonding contribution of the phenylhexyl ligand (> 10 kcal mol^{-1} MIHB values). The optimized structure shows strong hydrogen bonding of point-to-face interaction but not point-to-point interaction. The apc value of the contacted chlorine was changed from -0.051 to -0.151 au. The benzoic acid carbonyl oxygen apc value changed from -0.470 to -0.495 au for the vinyl ligand and from -0.470 to -0.504 au. Ionized aniline amino group contributed a little. The water molecule was twisted (repulsed), which was supported by MIES values for both vinyl and phenyl ligands.

The hydrogen-bonding effects of heptanoic and hexylamine ligands were studied and the optimized conformations are shown in Figures 3.4 and 3.5. The optimized molecular interaction energy values are summarized in Table 3.4.

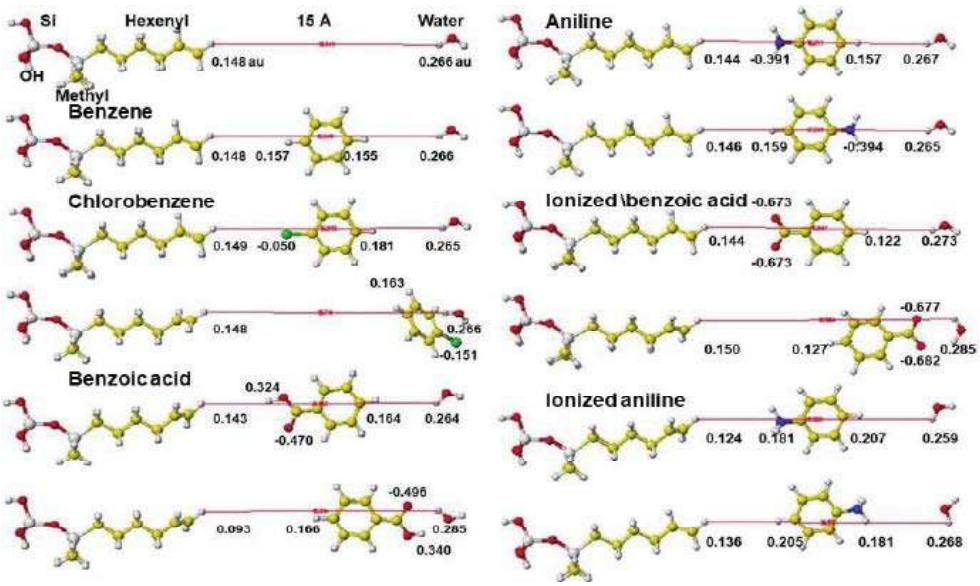


FIgure 3.3: Compete for molecular interaction between heptylcarboxy-ligand and water.

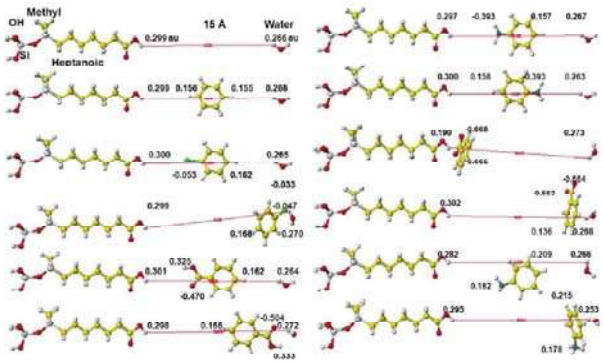


FIgure 3.4: Compete for molecular interaction between heptylcarboxy-ligand and water.

Table 3.4: Compete for molecular interaction between heptylcarboxy-ligand and water

Chemicals	Right			Left		
	MIHB	MIES	MIVW	MIHB	MIES	MIVW
Benzene	0.037	0	0.042	-	-	-
Chlorobenzene	14.699	-0.002	-1.703	0.055	0.062	0.105
Benzoic acid	10.236	1.898	-1.053	0.144	-0.119	0.106
Aniline	0.037	0	0.056	0.049	-0.001	0.059
Ionized benzoic acid	11.253	-0.335	-0.639	6.826	-0.267	1.384
Ionized aniline	11.264	0.159	-0.749	0.039	0.213	0.064

Right or Left: direction of analytes (left or right side in Figures); IP: initial distance before optimization; MIHB, MIES, and MINW: molecular interaction (MI) energy values of hydrogen (HB), electrostatic (ES) and van der Waals (VW) interaction; unit: kcal mol^{-1}.

Only the ionized carboxyl group was pulled to the ligand carboxy group. Ionized benzoic acid bound tightly to water molecules via van der Waals forces. Strong hydrogen bonding occurred between ligand carboxyl group and ionized benzoic acid (MIHB 6.826 kcal mol^{-1}). All electron-rich groups were pulled toward water molecules via hydrogen bonding observed between the water molecule and the analyte substituents, such as ionized benzoic acid and aniline, via point-to-face hydrogen bonding. The apc value of the water molecule changed from 0.266 to 0.288 and 0.253 au. These positive and negative changes reflect Lewis acid-base interactions. The positively charged amino group was repelled by the carboxyl group and bound to a water molecule, and the amino group was repelled directly by the water molecule. The evidence was read from apc values, which were derived from atomic partial charge values.

Another hydrogen-bonding-capable ligand is the amino group. A chemically stable hexylamine-bonded silica gel was synthesized; therefore, its properties were studied as in other ligand models. The in silico analysis results are summarized in Figure 3.5 and Table 3.5.

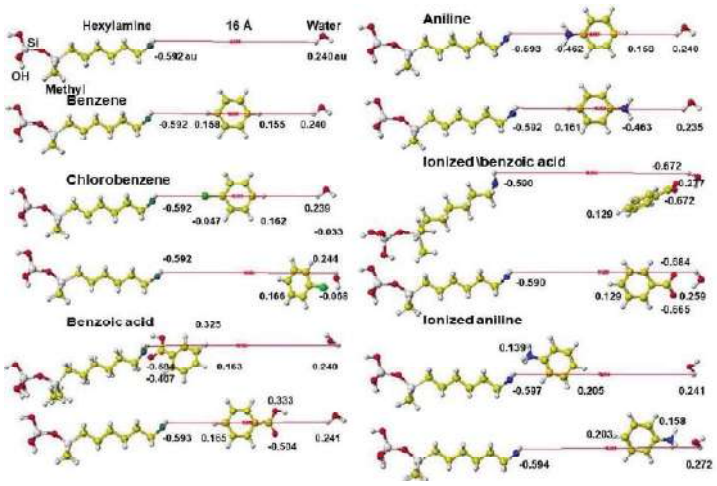


FIgure 3.5: Compete for molecular interaction between hexylamino-ligand and water.

Table 3.5: Compete for molecular interaction between hexylamino-ligand and water.

Chemicals	Right			Left		
	MIHB	MIES	MIVW	MIHB	MIES	MIVW
Benzene	0.011	0	0.035	-	-	-
Chlorobenzene	4.846	0.552	0.209	0.014	-0.154	0.117
Benzoic acid	0.103	0.205	0.06	4.846	0.552	0.219
Aniline	0.058	-0.001	0.051	0.031	0.02	0.045
Ionized benzoic acid	14.85	10.662	-0.807	18.759	10.283	-1.913
Ionized aniline	10.601	10.711	-1.989	0.206	5.87	0.601

Right or Left: direction of analytes (left or right side in Figures); IP: initial distance before optimization; MIHB, MIES, and MINW: molecular interaction (MI) energy values of hydrogen (HB), electrostatic (ES) and van der Waals (VW) interaction; unit: kcal mol^{-1}.

The amino phase is used for saccharide analysis in aqueous acetonitrile; however, glucose recovery is poor due to rapid glycosylation. The retention mechanism is hydrogen bonding. The benzoic acid carboxy group and ionized aniline amino groups were directly bound with the hexylamine amino group (MIHB 4.846kcal mol^{-1}). The large hydrogen bonding energy values of ionized benzoic acid was obtained from the ionized carboxy group and water molecule. Such evidence was also observed for chlorobenzene and ionized aniline. The ionized benzene carboxy group was repelled and bound directly to a water molecule. The tight binding produced high MIES energy values and negative MIVW energy values. The bonding point was visualized, and the key element's apc values support the phenomenon. The apc value of the water-molecule hydrogen changed from 0.240 to 0.244, 0.259, and 0.272 au for chlorobenzene, ionized benzoic acid, and ionized aniline, respectively. Electrostatic interactions and the twisted water molecule supported this evidence. Atomic partial charge indicated the direct binding sites,

3.1.2. Contribution of acetonitrile: Acetonitrile has a similar dipole moment to that of water. The dipole moments of acetonitrile and water are 2.44 and 2.55, respectively, and they showed a good linear relationship between log k and log P (octanol-water partition coefficient). Therefore, acetonitrile was used to study the solvent effect. The experimental conditions were the same as those for the studied contribution of the water molecule,

Table 3.6: Compete for molecular interaction between hexyl-ligand and acetonitrile.

Chemicals	Right			Left		
	MIHB	MIES	MIVW	MIHB	MIES	MIVW
Benzene	-0.002	-0.006	0.107	-	-	-
Chlorobenzene	-0.001	-0.461	0.198	-0.002	0.108	0.266
Benzoic acid	-0.122	1.944	0.01	0.005	0.051	0.255
Aniline	0	-0.014	0.15	-0.007	-0.015	0.15
Ionized benzoic acid	-0.001	0.416	0.299	-0.001	-0.152	0.249
Ionized aniline	0	4.733	-0.044	-0.001	0.277	0.159

Right or Left: direction of analytes (left or right side in Figures); IP: initial distance before optimization; MIHB, MIES, and MINW: molecular interaction (MI) energy values of hydrogen (HB), electrostatic (ES) and van der Waals (VW) interaction; unit: kcal mol^{-1}.

The clear direct binding between the hexyl group and these analytes was not observed because the interaction is weak and driven by van der Waals (hydrophobic) forces. The benzoic acid carboxyl and ionized aniline amino groups bound directly with water molecules via electrostatic interactions. The MIES values are 1.944 and 4.733kcal mol^{-1}. The apc value of acetonitrile nitrogen changed from -0.113 to -0.149 and -0.308 au by benzoic acid and ionized aniline, respectively. The electron-rich ionized carboxyl group was repelled by the electron-rich acetonitrile cyano group. The apc value of acetonitrile nitrogen was changed from -0.113 to -0.136 au.

Further, the ligand π-electron contribution was studied using single hexenyl and phenylhexyl ligand models. The results are summarized in Figures 3.7 and 3.8 and Tables 3.7 and 3.8. The direct binding of the hexenyl ligand vinyl group was unclear, but acetonitrile bound to the benzoic acid carboxylate and ionized aniline amino groups; electrostatic interactions: the EPC value of acetonitrile nitrogen was changed from -0.113 to -0.184 and -0.310 au by benzoic acid and ionized aniline, respectively. We further studied the π-electron contribution using the phenylhexyl ligand.

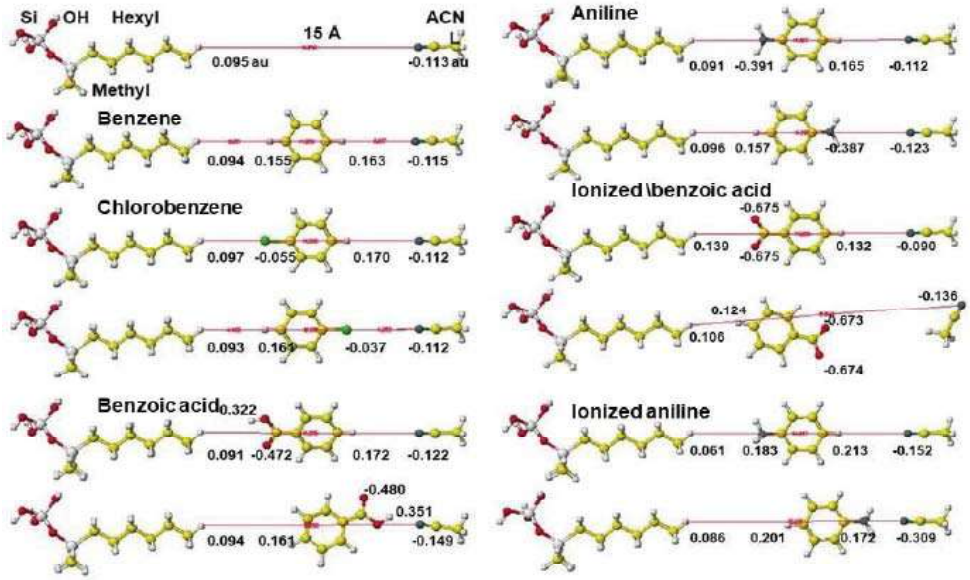


FIgure 3.6: Compete for molecular interaction between hexyl-ligand and acetonitrile.

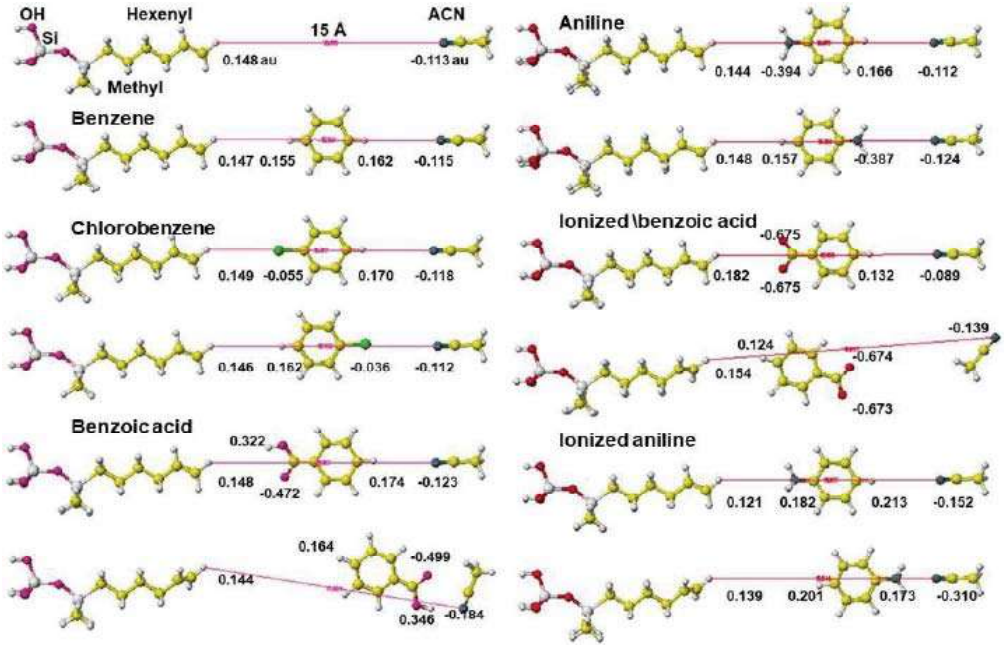


FIgure 3.7: Compete for molecular interaction between hexenyl-ligand and acetonitrile.

Table 3.7: Compete for molecular interaction between hexenyl-ligand and acetonitrile

Chemicals	Right			Left		
	MIHB	MIES	MIVW	MIHB	MIES	MIVW
Benzene	-0.002	-0.001	0.087	-	-	
Chlorobenzene	-0.001	-0.489	0.176	0	0.088	0.187
Benzoic acid	-0.142	3.527	0.22	0.029	0.062	0.186
Aniline	-0.001	-0.004	0.121	0.011	0.011	0.113
Ionized benzoic acid	0.001	0.437	0.15	0.001	-0.331	0.177
Ionized aniline	-0.004	4.753	-0.034	-0.002	0.418	0.136

Right or Left: direction of analytes (left or right side in Figures); IP: initial distance before optimization; MIHB, MIES, and MINW: molecular interaction (MI) energy values of hydrogen (HB), electrostatic (ES) and van der Waals (VW) interaction; unit: kcal mol^{-1}.

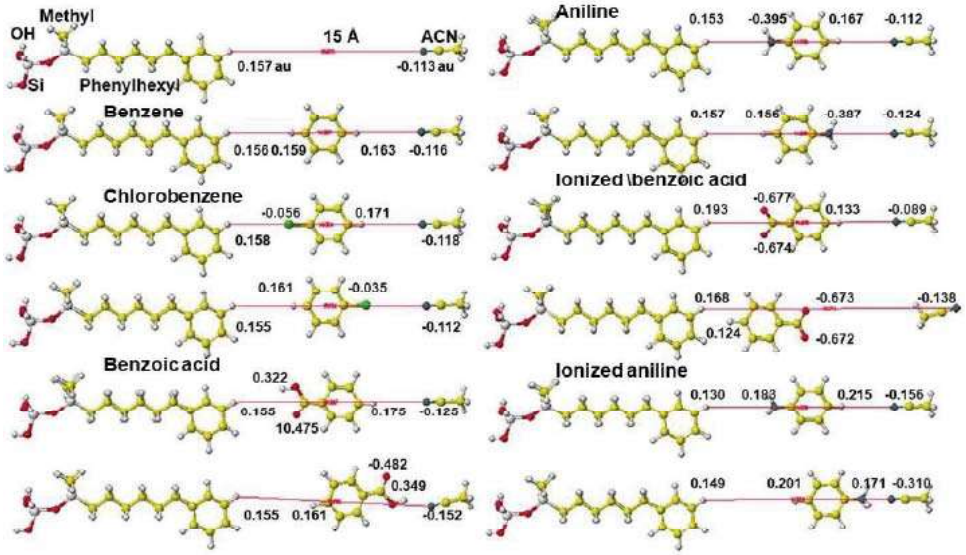


Figure 3.8: Compete for molecular interaction between phenylhexyl-ligand and acetonitrile.

Table 3.8: Compete for molecular interaction between phenylhexyl-ligand and acetonitrile.

Chemicals	Right			Left		
	MIHB	MIES	MIVW	MIHB	MIES	MIVW
Benzene	0	0	0.116	-	-	
Chlorobenzene	0	-0.531	0.232	-0.001	0.102	0.277
Benzoic acid	-0.106	2.098	0.1	0.046	0.06	0.249
Aniline	-0.001	-0.007	0.167	0.021	0.013	0.15
Ionized benzoic acid	0	0.44	0.877	-0.002	-0.193	0.255
Ionized aniline	0	4.756	-0.036	0	0.316	0.182

Right or Left: direction of analytes (left or right side in Figures); IP: initial distance before optimization; MIHB, MIES, and MINW: molecular interaction (MI) energy values of hydrogen (HB), electrostatic (ES) and van der Waals (VW) interaction; unit: kcal mol^{-1}.

The phenylhexyl ligand exhibited properties similar to those of the hexenyl ligand. Weak van der Waals interaction (MIVW 0.255 kcal mol^{-1}) may be caused by repulsion between the ionized carboxy group and acetonitrile. Repulsion of both molecular and ionized carboxyl groups was significant, especially because the carboxy and cyano groups are in the same electron-rich category. are repelled like a magnet. Hydrogen bonding and van der Waals forces did not contribute to these interaction analyses. These results reflect the π-electrons of vinyl and phenyl groups. However, actual chromatography may not directly support the above results because the bonding density of vinyl and phenyl ligands is not the same. The vinyl ligand can have much denser bonding than the phenyl ligand due to steric hindrance.

The ligand's hydrogen-bonding capability was studied using molecular forms with heptylcarboxy and hexylamino groups. The results are summarized in Figures 3.9 and 10 and Table 3.9 and 10.

Table 3.9: Compete for molecular interaction between heptylcarboxy-ligand and acetonitrile.

Chemicals	Right			Left		
	MIHB	MIES	MIVW	MIHB	MIES	MIVW
Benzene	0.006	0	0.055	-	-	
Chlorobenzene	0.006	-0.158	0.085	1.141	19.367	0.589
Benzoic acid	5.885	1.188	0.207	0.178	-0.075	0.144
Aniline	0.07	0.077	0.074	0.056	0.004	0.083
Ionized benzoic acid	-0.008	2.369	0.095	2.221	7.716	-0.188
Ionized aniline	3.432	21.703	-2.795	2.614	20.66	-1.926

Right or Left: direction of analytes (left or right side in Figures); IP: initial distance before optimization; MIHB, MIES, and MINW: molecular interaction (MI) energy values of hydrogen (HB), electrostatic (ES) and van der Waals (VW) interaction; unit: kcal mol^{-1}.

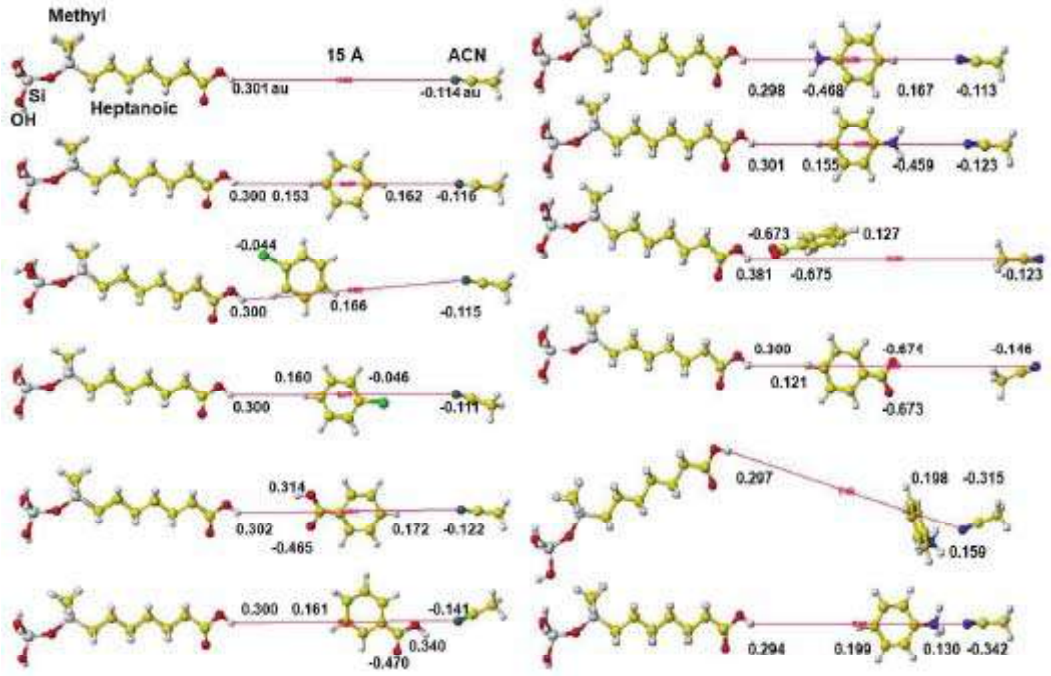


FIgure 3.9: Compete for molecular interaction between heptylcarboxy-ligand and acetonitrile.

Direct binding of heptanoic-carboxy was observed with chlorobenzene, chlorine, and ionized benzoic acid carboxy groups via electrostatic interaction. The MIES values were 19.367 and 7.716 mol^{-1}, respectively. The high MIES value of ionized aniline resulted from direct interaction with acetonitrile, and the MIVW value was negative. The apc value of acetonitrile nitrogen changed from -0.114 to -0.342 au. Acetonitrile strongly repelled the ionized benzoic acid carboxyl group. This was evidenced by the rotation of acetonitrile, whose carbon was locked and could not rotate. The ionized aniline amino group was repelled by the heptanoic acid carboxyl group and bound to acetonitrile via electrostatic interactions involving the phenyl and cyano groups. We identified the interaction center from changes in atomic partial charges. The apc value of the acetonitrile nitrogen was changed from -0.114 to -0.315 au. Acidic carboxy group exhibited selectivity compared to hydrophobic ligand and π-electron rich ligand. We studied basic amino-group specificity using a hexylamino ligand.

Table 3.10: Compete for molecular interaction between hexylamino-ligand and acetonitrile.

Chemicals	Right			Left		
	MIHB	MIES	MIVW	MIHB	MIES	MIVW
Benzene	-0.217	-0.021	0.066	-	-	-
Chlorobenzene	-0.216	-0.455	0.143	-0.088	-1.247	0.281
Benzoic acid	5.849	1.797	0.156	3.567	0.641	0.548
Aniline	-0.044	-1.123	0.215	-0.203	0.009	0.095
Ionized benzoic acid	-0.106	8.695	0.246	-0.105	8.855	0.247
Ionized aniline	3.434	22.143	-2.829	0.924	22.143	-2.829

Right or Left: direction of analytes (left or right side in Figures); IP: initial distance before optimization; MIHB, MIES, and MINW: molecular interaction (MI) energy values of hydrogen (HB), electrostatic (ES) and van der Waals (VW) interaction; unit: kcal mol^{-1}.

The dynamic interaction was found for benzoic acid and ionized aniline via hydrogen bonding for benzoic acid (MIHB 3.567 kcal mol^{-1}), and electrostatic interaction for ionized aniline (22.143 kcal mol^{-1}). The apc value of the carboxy hydrogen changed from 0.324 to 0.312 au, and that of the ionized amino group nitrogen changed from 0.182 to 0.134 au. However, the ionized carboxyl group was repelled toward acetonitrile and bound with the rotated acetonitrile. The initial ionized carboxyl group moved to acetonitrile without repulsion and bound to the positive side of acetonitrile. The ionized aniline amino group was bound together via electrostatic interaction; however, the ionized aniline amino group moved smoothly to the acetonitrile cyano group and bound via electrostatic, like Lewis acid-base interaction.

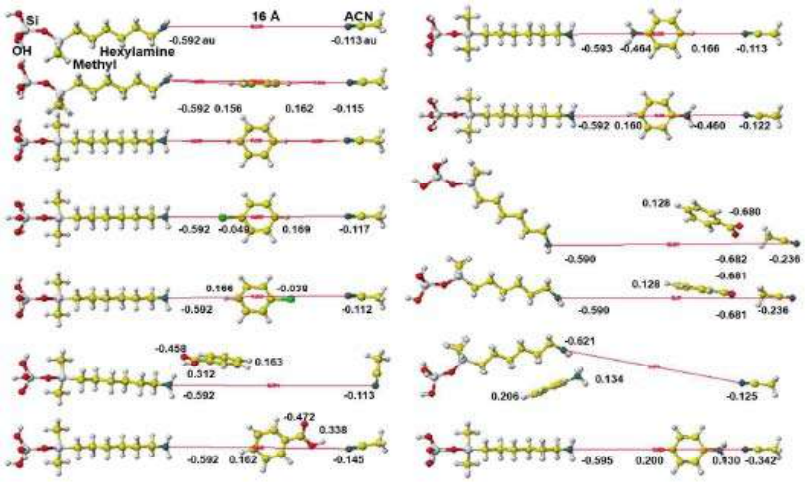


FIgure 3.10: Compete for molecular interaction between hexylamino-ligand and acetonitrile.

This simple study of solvent effects provides a fundamental mechanism for the retention and desorption of various compounds. Actual analysis must be performed using model phases, not a single ligand. However, this pinpoint interaction analysis makes chromatographic retention mechanisms clear. Actual chromatographic retention mechanisms are complex because analytes are multifunctional. Model phase analysis is demonstrated in later chapters.

3.2. Solvent effects in ion-exchange liquid chromatography

3.2.1. Solvent effect (water) for the binding with ionized carboxy-group: Molecular interactions usually occur in aqueous physiological conditions. The solvent is water containing buffer components. Water molecules contribute critically to the solubility and binding of molecules with proteins. Hydrophobic analytes are repelled by water molecules and bind to proteins, while hydrophilic analytes are solvated by water molecules. The following experiments are the simplest experiment. The contribution of water can be analyzed by a competitive interaction between an ionized group and a water molecule.

An analyte was located at the center of an ion-exchange group, and a water molecule was located 15Å away, as shown in the following figures. Then, we optimized the initial conformations to determine whether the analyte should contact the ion-exchange group or the water molecule. Strong contact or repulsion depends on the molecular properties of the analytes, as discussed in previous chapters. The optimized conformations are summarized in Figure 3.11 and calculated molecular interaction energy values are summarized in Table 3.11. Analytes that interact weakly with the carboxyl group did not show clear movement, such as benzene. Benzoic acid directly contacts the carboxyl ligand via electrostatic interaction (MIES 1.749 kcal mol^{-1}). The apc values of the carboxy hydrogen and carbonyl oxygen changed from 0.324 and -0.470 to 0.362 and -0.525 au. However, the high-electron-density chlorine was repelled from the carboxy group, and the chlorine and p-hydrogen apc values changed slightly from -0.051 and 0.163 to -0.040 and 0.175 au, respectively. Chlorine contacted the water molecule with a high MIHB (14.697 kcal mol^{-1}). The atomic distance expanded to 16.19 Å. The ionized aniline amino group contacted the carboxylate ligand via ion-ion interaction (MIES 7.892 kcal mol^{-1}). The apc of the amino-group hydrogen and carboxyl oxygen changed from 0.215 and -0.670 to 0.134 and -0.734 au. Repulsion of electron-rich groups of ionized benzoic acid was observed. Such π−π repulsion was not observed for the molecular form of the heptylcarboxy ligand. This experiment exhibited a fundamental chemical phenomenon.

Table 3.11: Compete for molecular interaction between ionized heptylcarboxy-ligand and water.

Chemicals	Right			Left		
	MIHB	MIES	MIVW	MIHB	MIES	MIVW
Benzene	0.027	0.003	0.091		-	-
Chlorobenzene	14.697	0.073	-1.701	15.789	-0.226	-1.257
Benzoic acid	0.101	0.166	0.15	-0.117	1.749	0.652
Aniline	0.024	0.031	0.076	0.033	-0.003	0.098
Ionized benzoic acid	0.017	-0.293	0.139	11.135	-0.6	-0.583
Ionized aniline	0.012	1.319	0.116	0.007	7.892	0.22

Right or Left: direction of analytes (left or right side in Figures); IP: initial distance before optimization; MIHB, MIES, and MINW: molecular interaction (MI) energy values of hydrogen (HB), electrostatic (ES) and van der Waals (VW) interaction; unit: kcal mol^{-1}.

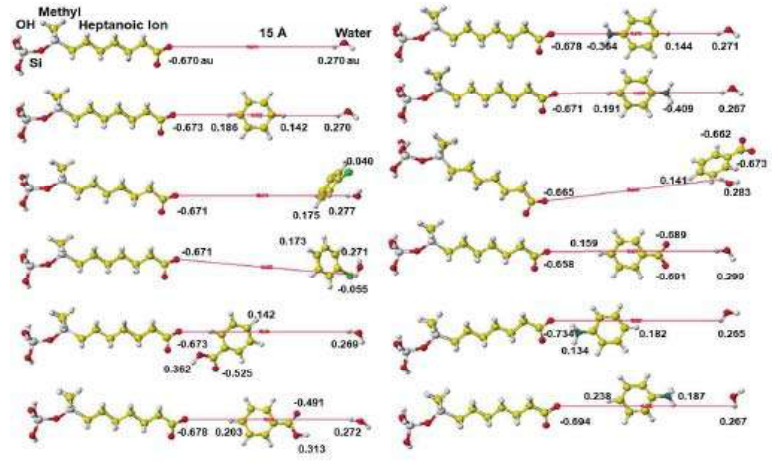


FIgure 3.11: Compete for molecular interaction between ionized heptylcarboxy-ligand and water.

3.2.2. Solvent effect (water) for the binding with ionized amino-group: The ionized amino group of the ligand showed specificity. The hexylamino ligand directly interacted with chlorobenzene, benzoic acid, and ionized benzoic acid. The main interaction force is electrostatic interaction, and MIES values were 1.126, 2.661, and 7.792 kcal mol^{-1}. Ionized aniline repelled and bound with a water molecule via hydrogen bonding (MIHB 11.361 kcal mol^{-1}). These optimized structures exhibited the binding and repulsion of polar substitutes from the ionized heptylcarboxy ligand and the binding conformation of these analytes with a water molecule.

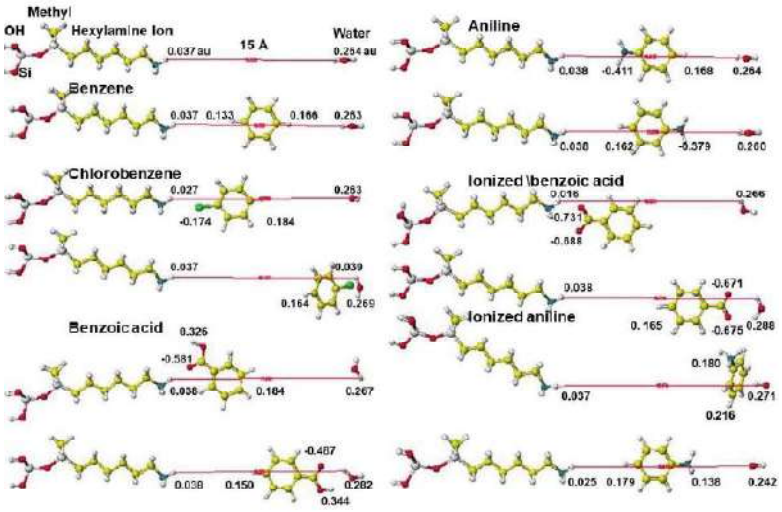


FIgure 3.12: Compete for molecular interaction between ionized hexylamino-ligand and water.

Table 3.12: Compete for molecular interaction between ionized hexylamine-ligand and water.

Chemicals	Right			Left		
	MIHB	MIES	MIVW	MIHB	MIES	MIVW
Benzene	0.028	0.002	0.055	-	-	-
Chlorobenzene	14.696	-0.062	-1.707	0.004	1.126	0.541
Benzoic acid	6.893	2.068	0.008	-0.03	2.661	0.497
Aniline	0.024	-0.007	0.072	0.036	0.004	0.065
Ionized benzoic acid	0.204	2.947	0.221	-0.014	7.792	0.687
Ionized aniline	0.01	-0.307	0.066	11.361	-0.558	-0.739

Right or Left: direction of analytes (left or right side in Figures); IP: initial distance before optimization; MIHB, MIES, and MINW: molecular interaction (MI) energy values of hydrogen (HB), electrostatic (ES) and van der Waals (VW) interaction; unit: kcal mol^{-1}.

3.2.3. Solvent (water) effect for the binding with guanidino-group: The guanidino group of arginine (a biological ion-exchange group) can engage in hydrogen bonding and ion interactions under physiologic conditions; this property was was analyzed from chromatographic behavior. The analyzed data are summarized in Figure 3.13 and Table 3.13.

The molecular form and ionized benzoic acid directly contacted the guanidino substituent via electrostatic interaction (MIES 4.296 and 10.055 kcal mol^{-1}). The apc values of the carboxyl hydrogen and benzoic acid carbonyl oxygen changed from 0.324 to 0.303 and -0.470 to -0.733 au, respectively. Ionized aniline was repulsed from the guanidino substituent and bound to a water molecule via hydrogen bonding (MIHB 11.285 kcal mol^{-1}). The apc value of water hydrogen was changed from 0.264 to 0.252. Chlorobenzene was bound to a water molecule via hydrogen bonding (15.783kcal mol^{-1}).

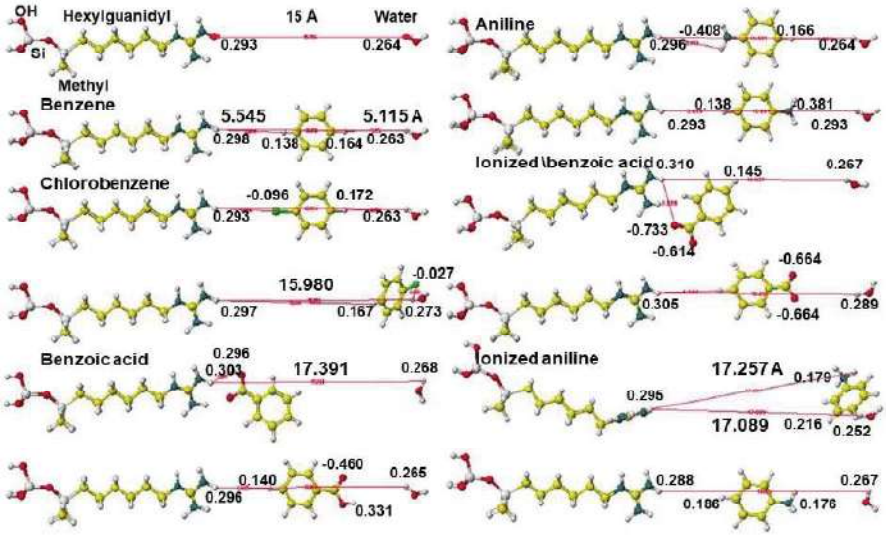


Figure 3.13: Compete for molecular interaction between hexylguadinine-ligand and water.

Table 3.13: Compete for molecular interaction between hexylguanidine-ligand and water.

Chemicals	Right			Left		
	MIHB	MIES	MIVW	MIHB	MIES	MIVW
Benzene	0.034	-0.001	0.02	-	-	-
Chlorobenzene	15.783	-0.447	-1.255	0.693	1.897	0.474
Benzoic acid	10.232	1.797	-1.079	1.513	4.296	0.714
Aniline	0.033	-0.015	0.05	0.044	0.012	0.06
Ionized benzoic acid	0.206	3.38	0.193	0.116	10.055	0.306
Ionized aniline	0.175	0.936	-0.038	11.285	-1.147	-0.839

Right or Left: direction of analytes (left or right side in Figures); IP: initial distance before optimization; MIHB, MIES, and MINW: molecular interaction (MI) energy values of hydrogen (HB), electrostatic (ES) and van der Waals (VW) interaction; unit: kcal mol^{-1}.

3.2.4. Solvent (acetonitrile) effect for the binding with ionized carboxy-group: Chlorobenzene bound to acetonitrile via hydrogen bonding, and the ionized molecule bound to water via hydrogen bonding, but the ionized aniline bound to a water molecule. The benzoic acid carboxy group bound to the ionized amino group (Lewis acid-base interaction) and hydrogen-bonded with water molecules. The ionized benzoic acid carboxyl group bound with the ionized amino group and water molecule via electrostatic interaction. The ionized aniline amino group was repelled and bound to a water molecule via hydrogen bonding.

Benzoic acid and ionized aniline contacted the carboxylate ligand directly via electrostatic interaction (MIES 3.738 and 8.095 kcal mol^{-1}), and the apc values of the benzoic acid carboxy hydrogen and carbonyl oxygen changed from 0.324 and -0.470 to 0.384 and -0.508 au. Chlorobenzene was repelled by the carboxy group and contacted acetonitrile via electrostatic interaction (MIES 0.527 kcal mol^{-1}). Benzoic acid contacted acetonitrile via electrostatic interaction (MIES 2.006 kcal mol^{-1}). The apc of the carboxy hydrogen was changed from 0.324 to 0.341 au. Ionized aniline contacted with acetonitrile via electrostatic interaction (MIES 8.095: kcal mol^{-1}).

Table 3.14: Compete for molecular interaction between ionized heptylcarboxy-ligand and acetonitrile.

Chemicals	Right			Left		
	MIHB	MIES	MIVW	MIHB	MIES	MIVW
Benzene	-0.003	-0.009	0.101	-	-	-
Chlorobenzene	0	0.527	0.187	0	0.396	1.722
Benzoic acid	-0.137	3.738	0.369	-0.173	2.006	0.385
Aniline	-0.001	0.026	0.133	-0.005	0.009	0.14
Ionized benzoic acid	-0.001	0.081	0.199	-0.001	3.71	0.898
Ionized aniline	0.001	5.507	0.005	0.001	8.095	0.249

Right or Left: direction of analytes (left or right side in Figures); IP: initial distance before optimization; MIHB, MIES, and MINW: molecular interaction (MI) energy values of hydrogen (HB), electrostatic (ES) and van der Waals (VW) interaction; unit: kcal mol^{-1}.

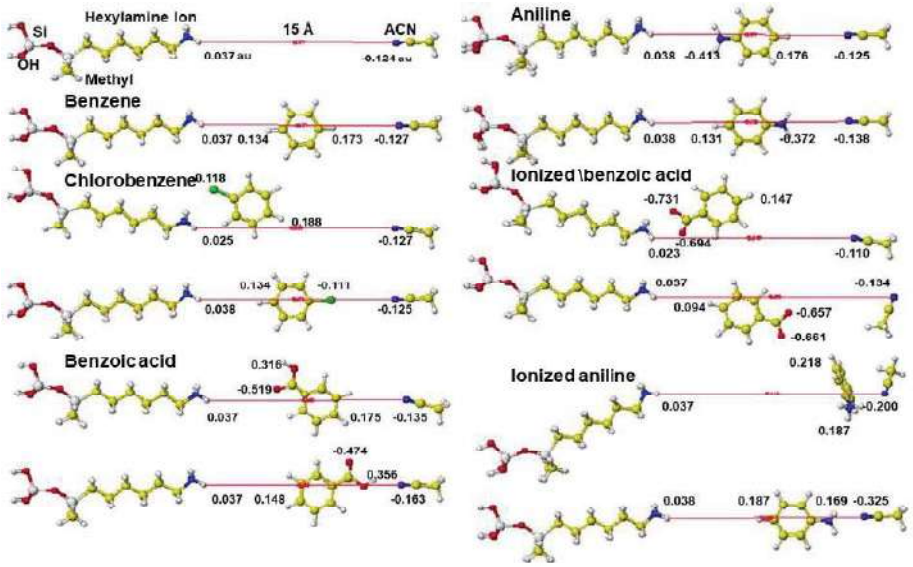


FIgure 3.15: Compete for molecular interaction between ionized amino-ligand and acetonitrile.

3.2.5. Solvent (acetonitrile) effect for the binding with ionized amino-group: The ionized amino group lacks hydrogen bonding capability. No clear evidence was observed for benzene. The chlorine apc changed from -0.051 to -0.118 au. However, chlorine contacted the amino group via hydrogen bonding (MIHB 14.696 kc l mol^{-1}). The chlorine apc changed from -0.051 to -0.174 au, and electron localization increased the p-hydroxy hydrogen apc from 0.163 to 0.184 au. Benzoic acid carbonyl contacted the amino group via hydrogen bonding and electrostatic interaction (MIHB 14.696 and MIES 2.068 kcal mol^{-1}). The carbonyl oxygen charge changed from -0.470 to -0.571 au. The contact site was clear, and ionized amino groups should trap ionized carboxy compounds via electrostatic interaction (MIES 7.792 kcal mol^{-1}). The apc of the amino hydrogen and carboxy oxygen changed from 0.037 and -0.673 to 0.023 and -0.731 au. Electron localization of aniline was observed, but the contact did not occur.

Table 3.15: Compete for molecular interaction between ionized hexylamine-ligand and acetonitrile.

Chemicals	Right			Left		
	MIHB	MIES	MIVW	MIHB	MIES	MIVW
Benzene	0.028	0.002	0.055	-	-	-
Chlorobenzene	14.696	-0.062	-1.707	0.004	1.126	0.541
Benzoic acid	6.893	2.068	0.008	-0.03	2.661	0.497
Aniline	0.024	-0.007	0.072	0.036	0.004	0.065
Ionized benzoic acid	0.204	2.947	0.221	-0.014	7.792	0.687
Ionized aniline	0.01	-0.307	0.066	11.361	-0.558	-0.739

Right or Left: direction of analytes (left or right side in Figures); IP: initial distance before optimization; MIHB, MIES, and MINW: molecular interaction (MI) energy values of hydrogen (HB), electrostatic (ES) and van der Waals (VW) interaction; unit: kcal mol^{-1}.

3.2.6 Solvent effect (acetonitrile) for the binding with guanidino-group: The molecular form and ionized benzoic acid directly contacted the guanidino substituent via electrostatic interaction (MIES 4.296 and 10.055 kcal mol^{-1}). The APC values of the carboxyl hydrogen and benzoic acid carbonyl oxygen changed from 0.324 to 0.303 and -0.470 to -0.733 au, respectively. Ionized aniline was repulsed from the guanidino substituent and bound to a water molecule via hydrogen bonding (MIHB 11.285 kcal mol^{-1}). Apc value of water hydrogen was changed from 0.264 to 0.252. Chlorobenzene was bound to a water molecule via hydrogen bonding (15.783kcal mol^{-1}).

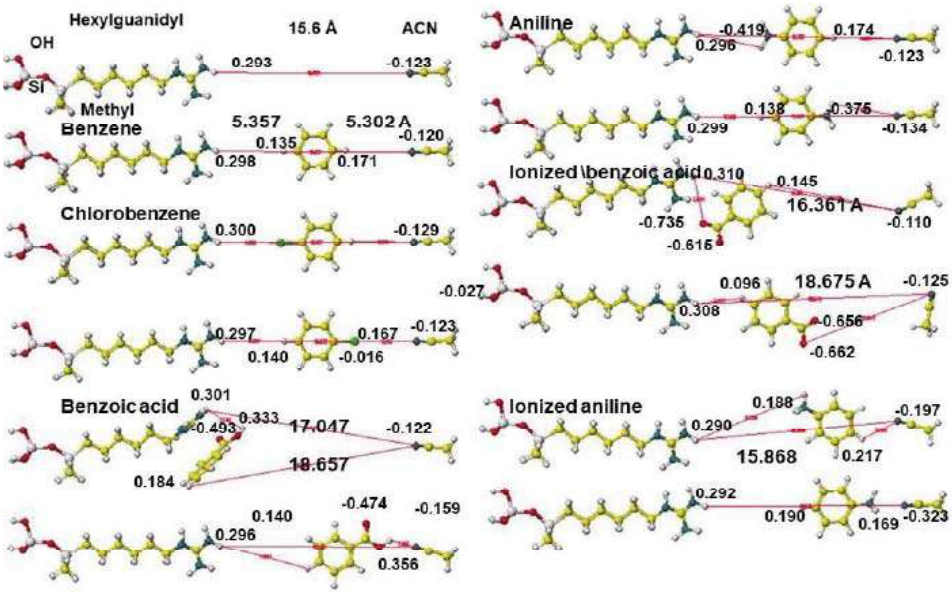


Figure 3.16

Table 3.16: Compete for molecular interaction between hexylguanidine-ligand and water.

Chemicals	Right			Left		
	MIHB	MIES	MIVW	MIHB	MIES	MIVW
Benzene	0.034	-0.001	0.02	-	-	-
Chlorobenzene	15.783	-0.447	-1.255	0.693	1.897	0.474
Benzoic acid	10.232	1.797	-1.079	1.513	4.296	0.714
Aniline	0.033	-0.015	0.05	0.044	0.012	0.06
Ionized benzoic acid	0.206	3.38	0.193	0.116	10.055	0.306
Ionized aniline	0.175	0.936	-0.038	11.285	-1.147	-0.839

Right or Left: direction of analytes (left or right side in Figures); IP: initial distance before optimization; MIHB, MIES, and MINW: molecular interaction (MI) energy values of hydrogen (HB), electrostatic (ES) and van der Waals (VW) interaction; unit: kcal mol^{-1}.

Compete for molecular interaction between hexylguadinine-ligand and acetonitrile

The binding capability of the guanidino ligand was higher than that of ionized hexylamine, and the degree can be evaluated from MIHB and MIES values. The ion-exchange capability can be estimated from the MIHB and MIES values. However, the molecular interaction energy values are low in competitive interaction with acetonitrile. The solubility of hydrophobic compounds is high in acetonitrile. This in silico analysis supports fundamental knowledge about solubility.

3.3 Selectivity of sodium and chloride ions for molecular interactions

3.3.1 Competition with Na^+ for binding with ionized carboxy-group: Sodium ion was placed instead of a water molecule and studied the positive charged ion effect for the competitive binding. The sodium ion was locked. The carboxy group and sodium ion induced electron localization in the analytes, but these neutral compounds (benzene and methylbenzene) did not bind with either the carboxy group or the sodium ion. The chlorine atom of chlorobenzene shifted toward the sodium ion via electrostatic Interaction (MIES 0.790 kcal mol^{-1}). The chlorine apc changed from -0.051 to -0.163 au, and the p-hydrogen apc also changed from 0.163 to 0.208 au (Figure 3.17). The carboxyl group repulsed the chlorine toward the sodium ion, and the phenol oxygen contacted the sodium ion in a Lewis acid-base interaction.

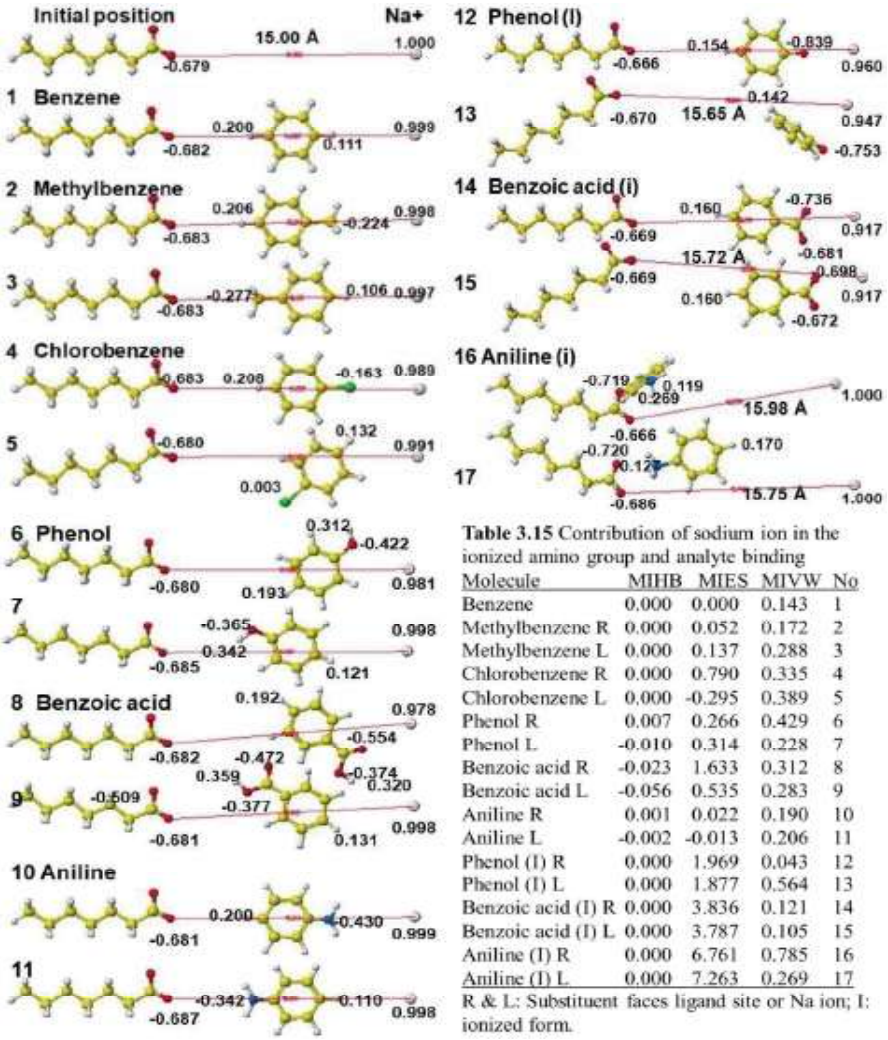


Table 3.15 Contribution of sodium ion in the ionized amino group and analyte binding

Molecule	MIHB	MIES	MIVW	No
Benzene	0.000	0.000	0.143	1
Methylbenzene R	0.000	0.052	0.172	2
Methylbenzene L	0.000	0.137	0.288	3
Chlorobenzene R	0.000	0.790	0.335	4
Chlorobenzene L	0.000	-0.295	0.389	5
Phenol R	0.007	0.266	0.429	6
Phenol L	-0.010	0.314	0.228	7
Benzoic acid R	-0.023	1.633	0.312	8
Benzoic acid L	-0.056	0.535	0.283	9
Aniline R	0.001	0.022	0.190	10
Aniline L	-0.002	-0.013	0.206	11
Phenol (I) R	0.000	1.969	0.043	12
Phenol (I) L	0.000	1.877	0.564	13
Benzoic acid (I) R	0.000	3.836	0.121	14
Benzoic acid (I) L	0.000	3.787	0.105	15
Aniline (I) R	0.000	6.761	0.785	16
Aniline (I) L	0.000	7.263	0.269	17

R & L: Substituent faces ligand site or Na ion; I: ionized form.

FIgure 3.17.1-17: Contribution of a sodium ion.

The electron localization was observed from the p-hydrogen apc change (0.164 to 0.193 au). The phenolic oxygen appeared to be rejected by the carboxyl group, but no significant electron shift in the oxygen was observed. The benzoic acid carbonyl oxygen contacted the sodium ion, like the phenolic oxygen, through electrostatic interaction (MIES = 1.633 kcmol^{-1}).The apc changed from -0.470 to -0.554 au (Figure 3.17-8).The benzoic acid carboxyl group was also repulsed from the carboxy group (Figure 3.17.9). Aniline was like a neutral compound even though the electron was localized (Figure 3.17-10).

The ionized phenol was kicked off dynamically from the carboxyl group and caught by the sodium ion (Figure 3.17.13). The phenolic oxygen contacts the sodium ion via electrostatic interaction (MIES 1.999 kcal·mol^{-1}). The oxygen apc changed from -0.759 to -0.839 au, and the sodium ion apc changed from 1.000 to 0.960 au (Figure 3.17.12). The p-hydrogen apc also changed from 0.112 to 0.154 au. Ionized benzoic acid behaved like ionized phenol, and the ionized carboxyl was repelled from the carboxyl group and captured by the sodium ion (Figure 3.17.15). The oxygen and p-hydrogen apc changed from -0.673 and -0.124 to - 0.698 and 0.160 au. In Figure 3.17.14, ionized benzoic acid oxygen contacted the sodium ion, and the oxygen and p-hydrogen apc changed from -0.673 and -0.124 to -0.403 and 0.160 au. The primary Interaction was the electrostatic force; the MIES values were 3.836 (Figure 3.17.15) and 3.787 (Figure 3.17.14) kcal·mol^{-1}). The positively charged ionized aniline was repelled from the sodium ion and contacted the carboxyl group (Figure 3.17-16). The nitrogen apc changed from 0.182 to 0.119, and the hydrogen apc changed from 0.219 to 0.269 au. The primary force was electrostatic interaction (6.761 kcal mol^{-1}). In Figure 3.17.17, the positively charged amino group contacted the carboxylate via electrostatic interaction (MIES 7.263 kcal·mol^{-1}). The nitrogen and hydrogen apc changed from 0.182 and 0.219 to 0.127 and 0.271 au. Table 3.17 summarizes the calculated molecular interaction energy values.

3.3.2. Competition with Na^+ for binding with ionized amino-group: The ionized heptylamine and sodium ion are positively charged. Ionic strength should affect competitive Interaction with analytes. Both the ionized amino group and the sodium ion induced their electron localization; the analytes benzene, methylbenzene, phenol, and aniline did not contact either the ionized heptylamine or the sodium ion. Chlorobenzene shifted toward the sodium ion with a weak electrostatic Interaction (MIES 0.521 kcal mol^{-1}). The chlorobenzene contacted the heptylamine with weak electrostatic interaction and van der Waals forces (MIES 0.549 and MIVW 1.072 kcal·mol^{-1}). Their key atoms' apc values did not change significantly (Figure 3.17.22). Benzoic acid carbonyl oxygen contacted the sodium ion (MIES 1.390 kcal·mol^{-1}), and the apc changed from -0.470 to -0.527 au (Figure 3.17.25). Such electrostatic Interaction was observed between the carboxyl oxygen and heptylamine MIES 2.5866 kcal mol-1), and the oxygen apc changed from -0.470 to -0.570 au (Figure 3.17.26). The electron-rich ionized phenolic oxygen bound with both cations via electrostatic Interaction (MIES 3.663 and 4.618 kcal·mol^{-1}) in Figures 3.17.29 and 30. The oxygen apc changed from -0.759 to -0.808 and -0.803 au. The p-hydrogen apc also changed from 0.124 to 0.111 and 0.130 au. Ionized benzoic acid behaved similarly to ionized phenol. The ionized carboxyl oxygen contacted the sodium ion and heptylamine via electrostatic Interaction (MIES 5.033 and 7.542 kcal·mol^{-1}). The ionic oxygen apc changed from -0.673 to -0.685 and -0.723 au (Figures 3.17.31 and 32). The sodium ion apc also changed from 1.000 to 0.931. The positively charged aniline amino group was repulsed by the sodium ion and the heptylamine. Their MIES values were negative. In Figure 3.17-33, the kicked aniline contacted the heptylamine alkyl group via van der Waals force (MIVW 5.132 kcal·mol^{-1}). Table 3.18 summarizes the calculated molecular interaction energy values.

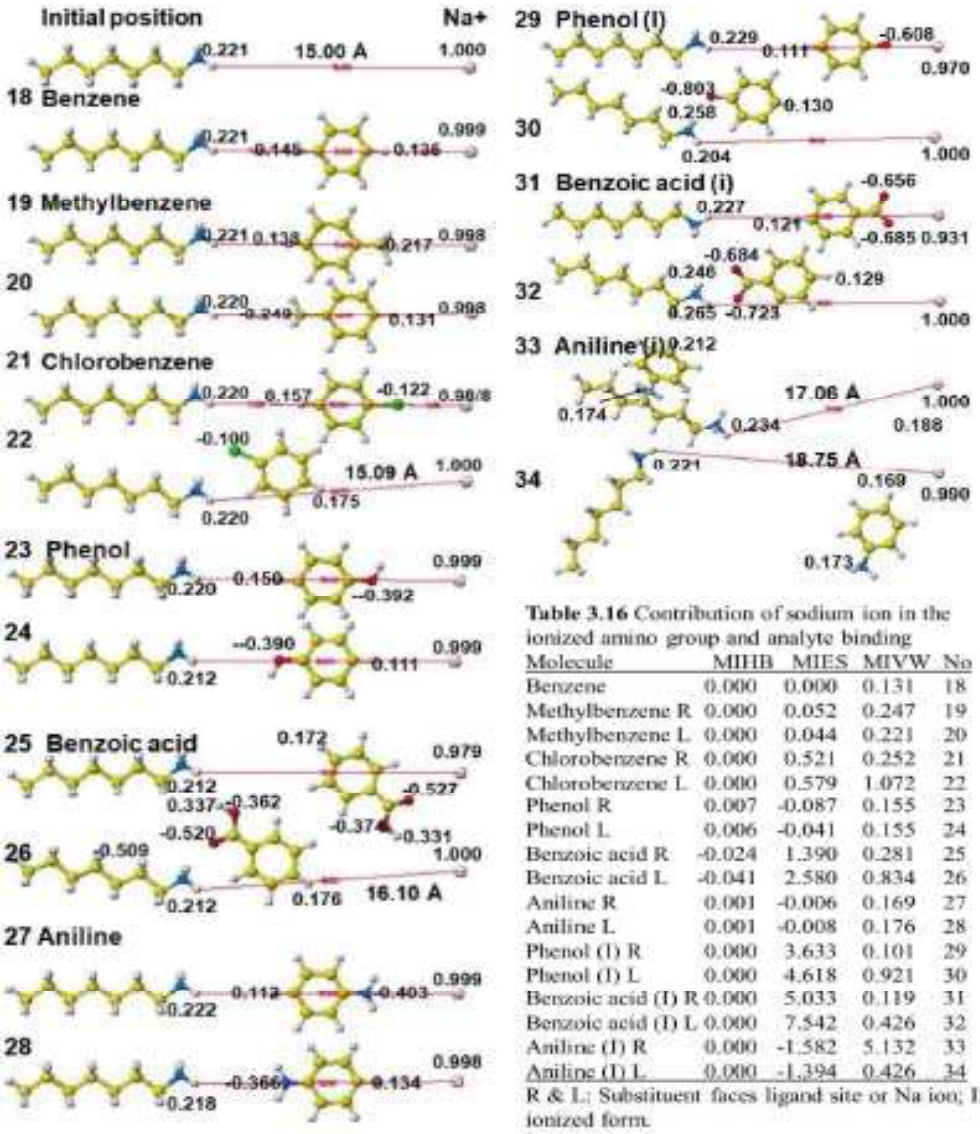


Table 3.16 Contribution of sodium ion in the ionized amino group and analyte binding

Molecule	MIHB	MIES	MIVW	No
Benzene	0.000	0.000	0.131	18
Methylbenzene R	0.000	0.052	0.247	19
Methylbenzene L	0.000	0.044	0.221	20
Chlorobenzene R	0.000	0.521	0.252	21
Chlorobenzene L	0.000	0.579	1.072	22
Phenol R	0.007	-0.087	0.155	23
Phenol L	0.006	-0.041	0.155	24
Benzoic acid R	-0.024	1.390	0.281	25
Benzoic acid L	-0.041	2.580	0.834	26
Aniline R	0.001	-0.006	0.169	27
Aniline L	0.001	-0.008	0.176	28
Phenol (I) R	0.000	3.633	0.101	29
Phenol (I) L	0.000	4.618	0.921	30
Benzoic acid (I) R	0.000	5.033	0.119	31
Benzoic acid (I) L	0.000	7.542	0.426	32
Aniline (I) R	0.000	-1.582	5.132	33
Aniline (I) L	0.000	-1.394	0.426	34

R & L: Substituent faces ligand site or Na ion; I: ionized form.

Figure 3.17.18-34: Contribution of a sodium ion in the ionized amino group and analyte binding.

3.3.3. Competition with Na^+ for binding with guanidino-group: The competitive sodium-ion effect on the molecular Interaction of the guanidino group with these analytes was basically the same as that of the amino group. Benzene, methylbenzene, phenol, and aniline did not contact the guanidino group or the sodium ion. The high-electron-density chlorine in chlorobenzene moved toward the guanidino group; however, the phenyl group contacted the guanidino group via hydrogen bonding (MIHB 4.529 kcal·mol^{-1}). The electron density of the benzoic acid oxygen contacted the sodium ion via electrostatic interaction (MIES 1.362 kcal mol^{-1}). The oxygen apc changed from -0.470 to -0.524 au, and the sodium ion apc changed from 1.000 to 0.976 au (Figure 3.17.42). In Figure 3.17.43, the benzoic acid tightly contacted the guanidino group via hydrogen bonding (MIHB 4.622 kcal·mol^{-1}); however, the carbonyl oxygen and hydroxy hydrogen apc changed slightly from -0.470 and 0.374 to -0.462 and 0.371 au. This result indicated that the guanidino group contacted the phenyl group. The MIVW (2.257 kcal·mol^{-1}) supported the interaction site.

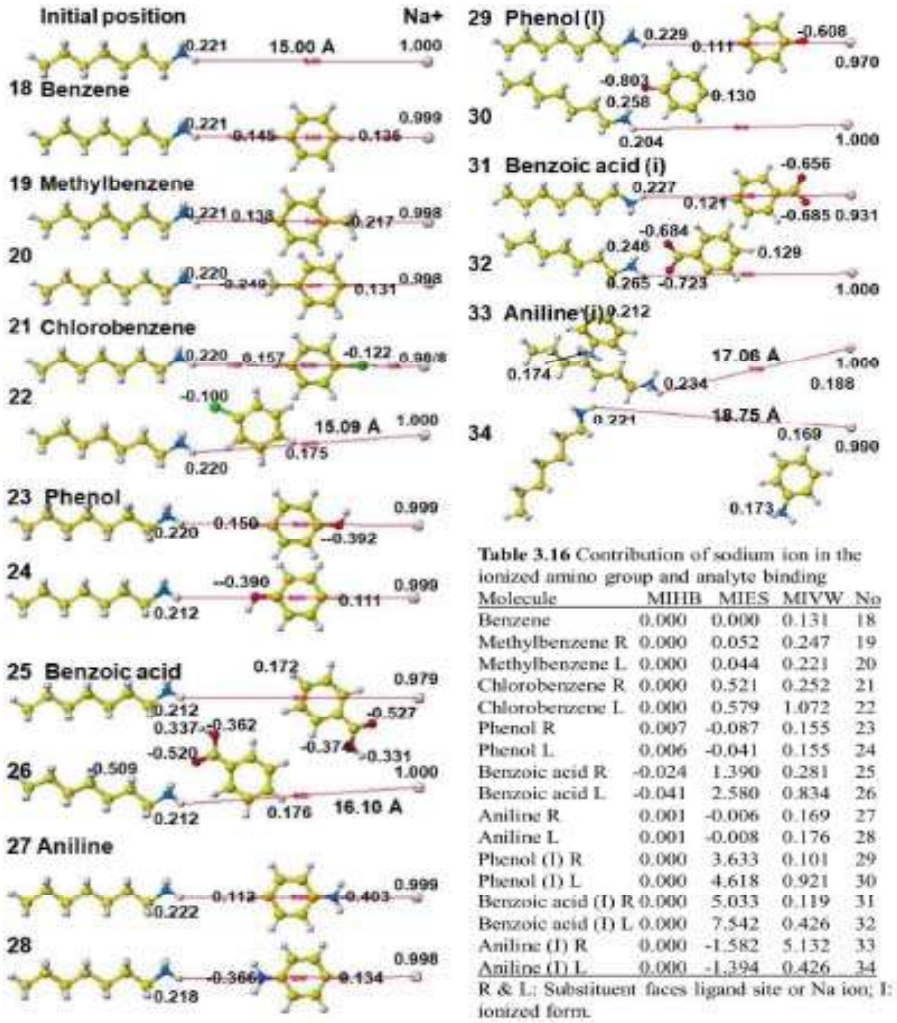


Table 3.16 Contribution of sodium ion in the ionized amino group and analyte binding

Molecule	MIHB	MIES	MIVW	No
Benzene	0.000	0.000	0.131	18
Methylbenzene R	0.000	0.052	0.247	19
Methylbenzene L	0.000	0.044	0.221	20
Chlorobenzene R	0.000	0.521	0.252	21
Chlorobenzene L	0.000	0.579	1.072	22
Phenol R	0.007	-0.087	0.155	23
Phenol L	0.006	-0.041	0.155	24
Benzoic acid R	-0.024	1.390	0.281	25
Benzoic acid L	-0.041	2.580	0.834	26
Aniline R	0.001	-0.006	0.169	27
Aniline L	0.001	-0.008	0.176	28
Phenol (I) R	0.000	3.633	0.101	29
Phenol (I) L	0.000	4.618	0.921	30
Benzoic acid (I) R	0.000	5.033	0.119	31
Benzoic acid (I) L	0.000	7.542	0.426	32
Aniline (I) R	0.000	-1.582	5.132	33
Aniline (I) L	0.000	-1.394	0.426	34

R & L: Substituent faces ligand site or Na ion; I: ionized form.

Figure 3.17.18-34: Contribution of a sodium ion in the ionized amino group and analyte binding.

The minus-ion phenol oxygen contacted the sodium ion via electrostatic interaction (MIES 3.497 kcal·mol^{-1}), and the oxygen and sodium ion apc changed from -0.759 and 1.000 to -0.807 and 0.969 au, respectively (Figure 3.17.46). The ionized oxygen was pulled to the guanidino group and tightly bound via hydrogen bonding and electrostatic Interaction (MIHB 4.734 and MIES 4.111 kcal·mol^{-1}). The oxygen and p-hydrogen apc changed from -0.759 and 0.112 to -0.713 and 1.444 au, and the guanidino hydrogen apc changed from 0.295 to 0.346 au. The results indicated that the phenyl group was the contact center. The van der Waals force also contributed to the contact (MIVW 1.195 kcal·mol^{-1}). The ionized benzoic acid carboxyl group contacted both the sodium ion and the guanidino group (Figures 3.17.34, 48 and 49), and the primary interaction force was electrostatic interaction (MIES 4.972 and 5.890 kcal·mol^{-1}).

In Figure 3.17.34.48, the oxygen and sodium apc changed from -0.673 and 1.000 to -0.686 and 0.931 au. The oxygen

and the guanidino hydrogen apc changed from -0.673 and 0.295 to -0.715 and 0.356 au. The positively charged amino group repelled from the sodium ion and contacted the guanidino group via hydrogen bonding (MIHB 4.472 kcal·mol^{-1}) in Figure 3.17.34.50, and the amino nitrogen and p-hydrogen apc changed from 0.182 and 0.206 to 0.175 and 0.234 au. The positively charged aniline and the guanidino group should not contact via electrostatic Interaction, but hydrogen bonding and van der Waals interaction (MIVW 1.564 kcal·mol^{-1}) were possible interaction mechanisms. The calculated interaction energy values are summarized in Table 3.19. The sodium ion acted as a positively charged ion. The following experiment demonstrated the contribution of a negatively charged chloride ion.

3.3.4. Competition with Cl$^-$ for binding with ionized carboxy-group: The sodium ion was replaced with a chloride ion, and the effect of the negatively charged ion was studied for competitive binding. The chloride ion was locked. The carboxy group and chloride ion induced electron localization in the analytes, but benzene, methylbenzene, and aniline did not bind with either the carboxy group or the chloride ion; even electron localization was induced in their molecules. The electron-rich chlorine was repulsed from the carboxyl group (Figure 3.18.5), and the chlorine and p-hydrogen apc changed from -0.051 and 0.163 to -0.095 and 0.204 au. In Figure 3.18-7, the ionized heptanoic acid oxygen contacted the phenol hydroxyl group via electrostatic interaction (MIES 2.083 kcal mol^{-1}). The hydroxy oxygen apc changed from -0.386 to -0.428 au (Figure 3.18.7). The benzoic acid carboxy group contacted the chlorine via weak hydrogen bonding and electrostatic interaction (MIHB 0.379, MIES 0.974 kcal·mol^{-1}). In Figure 3.18.9, the benzoic acid carboxy group contacted the heptanoic acid oxygen via electrostatic interaction (MIES 2.320kcal·mol^{-1}), and the contact-site oxygen apc changed from -0.664 and -0.470 to -0.657 and -0.379 au (Figure 3.18-9).

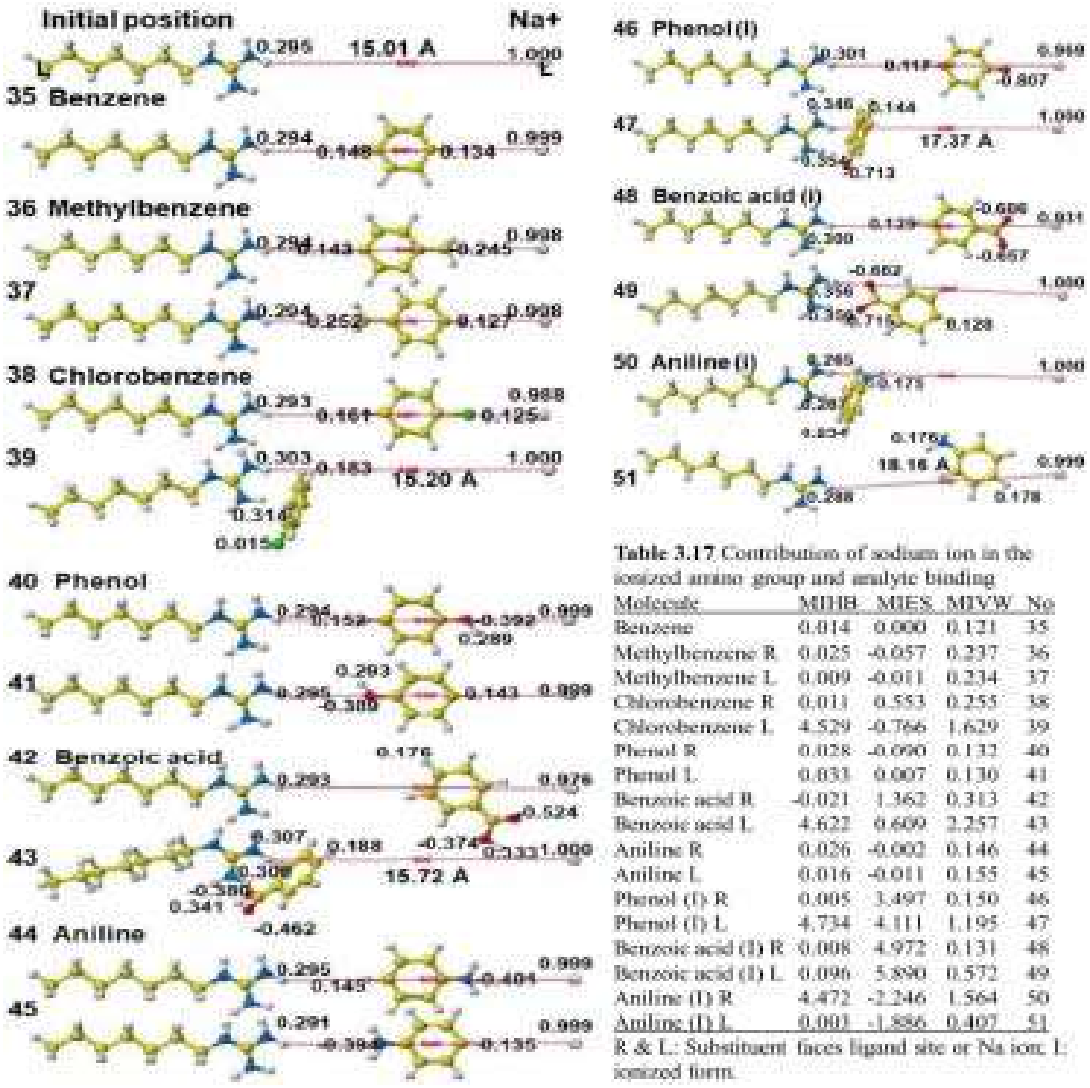


Table 3.17 Contribution of sodium ion in the ionized amino group and analyte binding

Molecule	MIHB	MIES	MIVW	No
Benzene	0.014	0.000	0.121	35
Methylbenzene R	0.025	-0.057	0.237	36
Methylbenzene L	0.009	-0.011	0.234	37
Chlorobenzene R	0.011	0.553	0.255	38
Chlorobenzene L	4.529	-0.766	1.629	39
Phenol R	0.028	-0.090	0.132	40
Phenol L	0.033	0.007	0.130	41
Benzoic acid R	-0.021	1.362	0.313	42
Benzoic acid L	4.622	0.609	2.257	43
Aniline R	0.026	-0.002	0.146	44
Aniline L	0.016	-0.011	0.155	45
Phenol (I) R	0.005	3.497	0.150	46
Phenol (I) L	4.734	4.111	1.195	47
Benzoic acid (I) R	0.008	4.972	0.131	48
Benzoic acid (I) L	0.096	5.890	0.572	49
Aniline (I) R	4.472	-2.246	1.564	50
Aniline (I) L	0.003	-1.886	0.407	51

R & L: Substituent faces ligand site or Na ion. L: ionized form.

FIgure 3.17.35-51: Contribution of a sodium ion in the ionized amino group and analyte binding.

The negatively ionized phenolic oxygen was kicked off the chlorine ion and trapped by heptanoic acid via van der Waals forces (MIVW 4.010 kcal·mol^{-1}) near the heptanoic acid alkyl group (Figure 3.18.12). The ionized phenol was also kicked off from the heptanoic acid (Figure 3.18.13). The ionized benzoic acid phenomena were the same as those of ionized phenol, and the ionized benzoic acid carboxy group was kicked off from both the chloride ion and the heptanoic acid (Figures 3.18.14 and 15), and the heptylcarboxylic acid alkyl group caught the phenyl group (MIVW 2.418 kca ·mol^{-1}) in Figure 3.18.14. The positively charged aniline contacted both the chloride ion and the heptanoic acid (Figures 3.18.16 and 17) via electrostatic Interaction (MIES 4.495 and 8.531 kcal·mol^{-1}). The contact center nitrogen pc changed from 0.182 to 0.121 and 0.137 au. The chlorine (Figure 3.18.16) and the oxygen (Figure3.18.17) apc changed from-1.000 and -0.664 to -0.981and-0.658 au. Table 20 summarizes the calculated molecular interaction energy values.

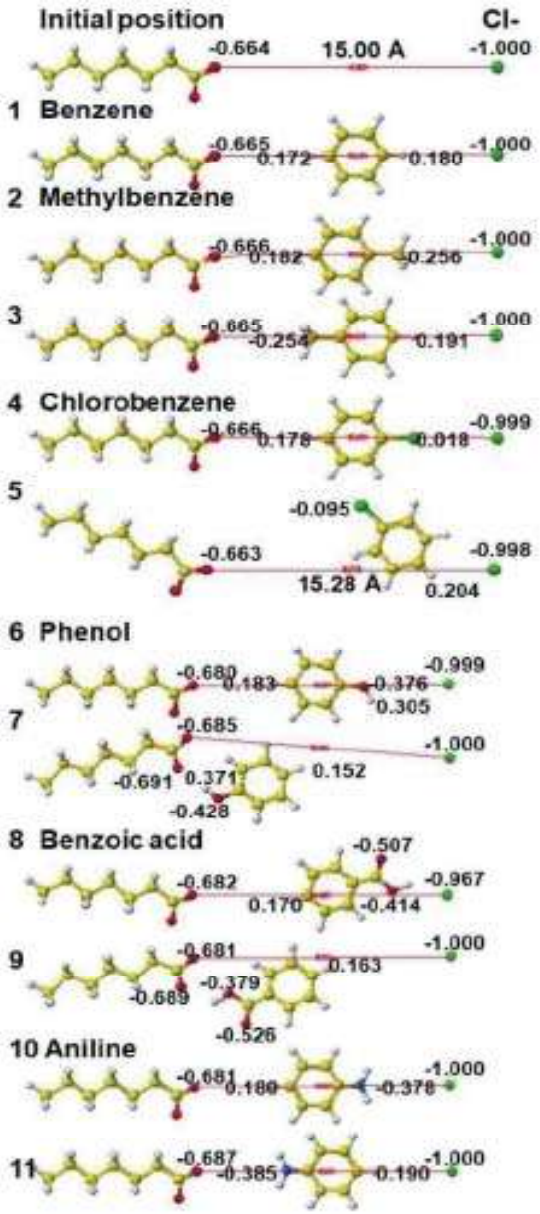


Table 3.18 Contribution of chloride ion in the ionized amino group and analyte binding

Molecule	MIHB	MIES	MIVW	No
Benzene	0.000	0.000	0.135	1
Methylbenzene R	0.000	0.037	0.258	2
Methylbenzene L	0.000	0.065	0.254	3
Chlorobenzene R	0.000	-0.362	0.345	4
Chlorobenzene L	0.000	0.315	0.631	5
Phenol R	0.009	0.072	0.155	6
Phenol L	-0.002	2.083	0.599	7
Benzoic acid R	0.379	0.974	0.227	8
Benzoic acid L	-0.181	2.320	0.364	9
Aniline R	0.012	0.009	0.157	10
Aniline L	-0.001	0.012	0.195	11
Phenol (I) R	0.000	-0.981	4.010	12
Phenol (I) L	0.000	-1.546	0.579	13
Benzoic acid (I) R	0.000	-0.855	2.418	14
Benzoic acid (I) L	0.000	-0.934	0.709	15
Aniline (I) R	0.000	4.495	0.366	16
Aniline (I) L	0.000	8.534	0.136	17

R & L: Substituent faces ligand site or Cl ion; I: ionized form.

FIgure 3.18.1-17: Contribution of a chlorine ion in the ionized carboxy group and analyte binding

3.3.5. Competition with Cl^- for binding with ionized amino-group: Analytes were located between the positively charged heptylamine and the negatively charged chlorine to their competitive effect. The clear movement of benzene, methylbenzene, and aniline was observed, and electron localization was induced. Chlorobenzene chlorine interacted with the heptylamine via electrostatic and van der Waals forces (MIES 0.716 and MIVW 1.194 kcal·mol^{-1}), and the chlorine apc changed from 0.051 to -0.128 au (Figure 3.18.22). The phenol hydroxy contacted the chlorine ion via electrostatic and van der Waals forces (MIES 0.860 and MIVW 0.513 kcal·mol^{-1}). The chlorine ion apc changed from -1.000 to -0.981 au (Figure 3.18.23). The hydroxyl group was kicked off from the heptylamine (Figure 3.18.24). The benzoic acid carboxylate contacted both the chloride ion and the heptylamine via electrostatic Interaction (MIES 0.878 and 2.734 kcal.mol^{-1}). The hydroxy hydrogen and carbonyl oxygen apc changed from 0.324 and -0.470 to 0.404 and -0.587 au.

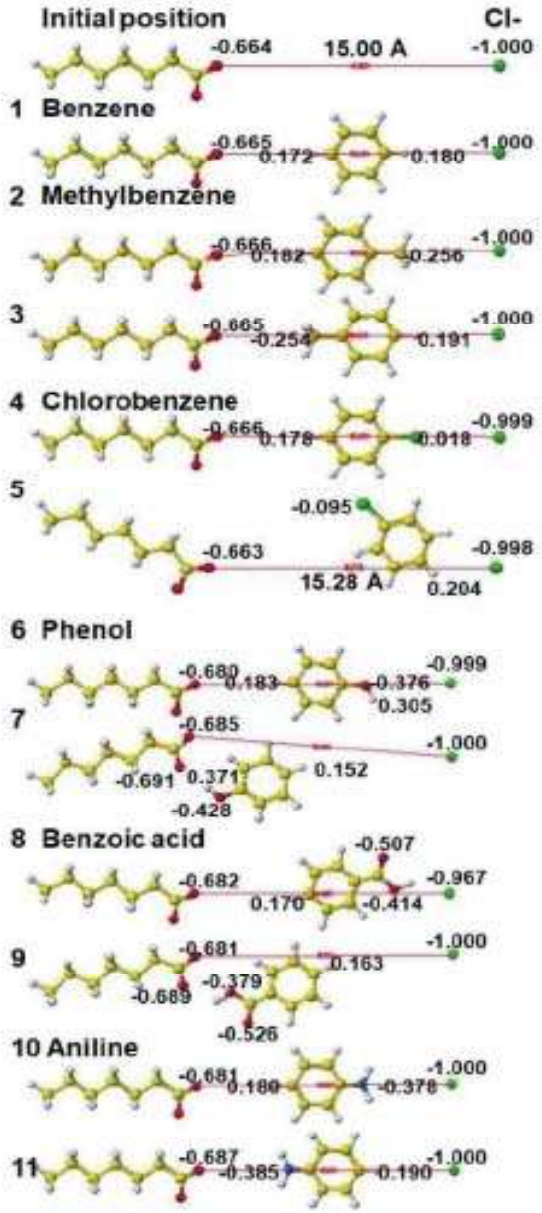


Table 3.18 Contribution of chloride ion in the ionized amino group and analyte binding

Molecule	MIHB	MIES	MIVW	No
Benzene	0.000	0.000	0.135	1
Methylbenzene R	0.000	0.037	0.258	2
Methylbenzene L	0.000	0.065	0.254	3
Chlorobenzene R	0.000	-0.362	0.345	4
Chlorobenzene L	0.000	0.315	0.631	5
Phenol R	0.009	0.072	0.155	6
Phenol L	-0.002	2.083	0.599	7
Benzoic acid R	0.379	0.974	0.227	8`
Benzoic acid L	-0.181	2.320	0.364	9
Aniline R	0.012	0.009	0.157	10
Aniline L	-0.001	0.012	0.195	11
Phenol (I) R	0.000	-0.981	4.010	12
Phenol (I) L	0.000	-1.546	0.579	13
Benzoic acid (I) R	0.000	-0.855	2.418	14
Benzoic acid (I) L	0.000	-0.934	0.709	15
Aniline (I) R	0.000	4.495	0.366	16
Aniline (I) L	0.000	8.534	0.136	17

R & L: Substituent faces ligand site or Cl ion; I: ionized form.

Figure 3.18.18-34: Contribution of a chlorine ion in the ionized amino group and analyte binding.

The ionized phenol was kicked off from the chlorine ion and contacted the heptylamine via electrostatic interaction (MIES 3.158 kcal·mol^{-1}), and the oxygen apc changed from -0.459 to -0.791 au (Figure 3.18.29). In Figure 3.18-35.30, the phenolic oxygen directly contacted the heptylamine via electrostatic Interaction (MIES 3.298 kcal.mol^{-1}), and the apc changed from -0.759 to -0.809 au. Ionized benzoic acid behaved the same as ionized phenol. The carboxyl group was kicked off from the chloride ion and contacted the heptylamine via electrostatic Interaction (MIES 6.447 kcal mol^{-1}), and the oxygen apc changed from -0.673 to -0.695 and -0.736 au (Figure 3.18.31). The carboxy directly contacted the heptylamine via electrostatic interaction (MIES 6.461 kcal·mol^{-1}), and the oxygen apc changed from -0.673 to -0.737 au (Figure 3.18.32). The ionized aniline directly contacted the chloride ion via electrostatic interaction (MIES 3.045 kcal mol^{-1}), and the nitrogen apc changed from 0.182 to 0.119 au (Figure 3.18.33). The amino group kicked off the heptylamine and was caught by the chloride ion via electrostatic interaction (MIES2.943 kcal.mol^{-1}), and the nitrogen apc changed from 0.182 to 0.112 au (Figure 3.18.34). Table 3.21 summarizes the calculated molecular interaction energy values.

3.3.6 Competition with Cl$^-$ for binding with guanidino-group: The heptylguanidine action was similar to that of heptylamine, and benzene, methylbenzene, phenol, and aniline did not contact either the guanidino group or the chloride ion; even electron localization was induced. The electron-rich chlorobenzene chlorine was repelled by the chloride ion and trapped by the guanidino group via hydrogen bonding and van der Waals interactions (MIHB 4.694, MIVW 1.545 kcal·mol^{-1}). The chlorine apc changed from 0.051 to -0.012 au (Figure 3.18.39). The benzoic acid contacted the chloride ion via electrostatic Interaction and hydrogen bonding (MIES 0.917, MIHB 0.372 kcal·mol^{-1}), and the hydroxy hydrogen and chloride ion apc changed from 0.324 and -1.000 to 0.403 and -0.962 au (Figure 3.18.42). However, the benzoic acid carboxyl group was repulsed from the guanidino group.

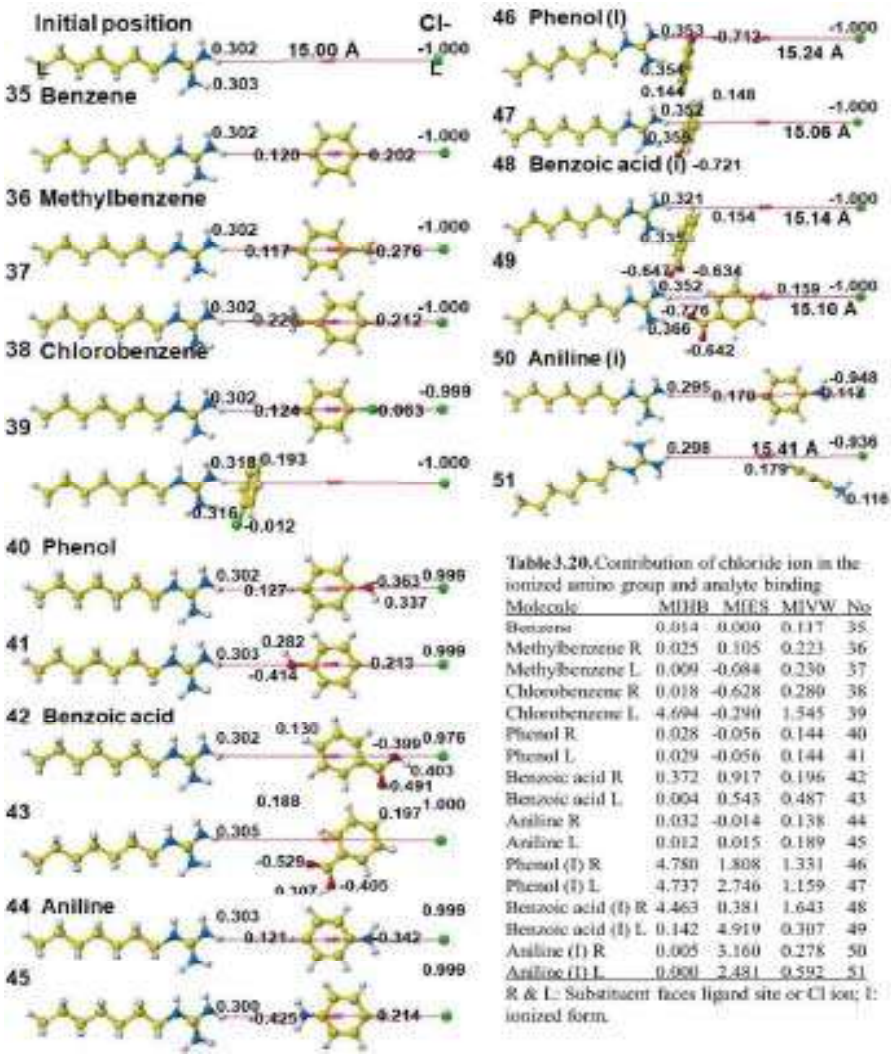


Table 3.20. Contribution of chloride ion in the ionized amino group and analyte binding.

Molecule	MIHB	MIES	MIVW	No
Benzene	0.014	0.000	0.117	35
Methylbenzene R	0.025	0.105	0.223	36
Methylbenzene L	0.009	-0.084	0.230	37
Chlorobenzene R	0.018	-0.628	0.280	38
Chlorobenzene L	4.694	-0.290	1.545	39
Phenol R	0.028	-0.056	0.144	40
Phenol L	0.029	-0.056	0.144	41
Benzoic acid R	0.372	0.917	0.196	42
Benzoic acid L	0.004	0.543	0.487	43
Aniline R	0.032	-0.014	0.138	44
Aniline L	0.012	0.015	0.189	45
Phenol (I) R	4.780	1.808	1.331	46
Phenol (I) L	4.737	2.746	1.159	47
Benzoic acid (I) R	4.463	0.381	1.643	48
Benzoic acid (I) L	0.142	4.919	0.307	49
Aniline (I) R	0.005	3.160	0.278	50
Aniline (I) L	0.880	2.481	0.592	51

R & L: Substituent faces ligand site or Cl ion; I: ionized form.

Figure 3.18.35-51: Contribution of a chlorine ion in the guadinino group and analyte binding.

The ionized phenol oxygen was repelled by the chloride ion and captured by the guanidino group via hydrogen bonding, electrostatic interaction, and van der Waals forces (MIHB 4.780, MIES 1.808, and MIVW 1.331 kcal mol^{-1}). The conformation was observed by changes in their apc values. The phenolic oxygen, p-hydrogen, and guanidino hydrogen apc changed from -0.759, 0.112, and 0.302 to -1.712, 0.144, and 0.353 au (Figure 3.18.46). The phenol directly contacted the guanidino group; however, the electron-rich oxygen contacted the electron-poor hydrogen (MIHB 4.737, MIES 2.746, and MIVW 1.159 kcal·mol^{-1}), and the phenolic oxygen and the guanidine hydrogen apc changed from -0.759 and 0.000 to -0.721 and 0.000 au (Figure 3.18.47). Ionized benzoic acid showed similar behavior: the ionized carboxyl group was repelled by the chloride ion and trapped by the guanidino group (Figure 3.18.48) via hydrogen bonding and van der Waals forces (MIHB 4.463, MIVW 1.643 kcal mol^{-1}). The carboxyl oxygen and the guanidino nitrogen apc changed from 0.673 to 0.640 and but the p-hydrogen and the other guanidino hydrogen apc changed from 0 .124 and 0.302 to 0.321 and 0.321au. The result indicated that the contact center was the phenyl group. The ionized carboxyl directly contacted the guanidino group via electrostatic interaction (MIES 4.919 kcal.mol^{-1}), and the oxygen and the guanidino hydrogen apc changed from -0.673 and 0.000 to -0.776 and 0.000 au (Figure 3.18.49). The ionized aniline contacted the chloride ion via electrostatic interaction (MIES 3.160 kcal mol^{-1}), and the nitrogen and chlorine apc changed from 0.182 and -1.000 to 0.117 and -0.948 au (Figure 3.18-50). The ionized amino group was repelled by the guanidino group and trapped by the chloride ion via electrostatic interaction, and the nitrogen and the chloride ion apc changed from 0.182 and -1.000 to 0.116 and -0.936 au (Figure 3.18.51).

The simple model analysis of biologically active ion-exchange groups provided the fundamental action of ion-exchange groups to various substitutes. Ion-exchange groups interact with molecules through ion-ion interactions, hydrogen bonding, and van der Waals forces; molecular mechanics calculations quantitatively described these interactions. This fundamental knowledge provided basic approaches for analyzing specific protein (enzyme) properties.

References

1. T. Hanai. HPLC, A Practical Guide, 1999, RSC, Cambridge.ISBN:0-85404-515-5
2. T. Hanai, Quantitative in silico chromatography, Computational modeling of molecular interactions, 2014, RSA, Cambridge, pp. 338, (ISBN: 978-1-84973-991-7)
3. T Hanai, Fundamental Properties of Packing Materials for Liquid Chromatography, Separation, 2019-01-05, 6(2), 1-20, doi: 10.3390/separations6010002 www.mdpi.com/journal/separations
4. T. Hanai, International Journal of Analytical Techniques, 2018, 4(1), 1-6. IJAT-17-RA-121, DOI: 10.15226/2577-7831/4/100115,https://symbiosisonlinepublishing.com/chromatographic- science/articlesinpress.php

Chapter 4 Quantitative Explanation of Spectra

Current computational chemistry enables quantitative explanation of fundamental mechanisms in spectral analysis. Computational chemistry calculations can predict absorption spectra; however, these programs do not include solvents and buffers. Therefore, feasibility is assessed using color indicators. Furthermore, the application is used for colorimetric analysis. NMR improves the determination of protein stereo structure. Therefore, a combination of NMR spectroscopic analysis and computational chemical analysis becomes an attractive tool in protein chemistry. Molecular interactions are measured using NMR. However, predicting NMR spectra of small molecules is straightforward using database-based computer programs in computational chemistry. Therefore, the feasibility of proton nuclear magnetic resonance (1H-NMR) and carbon nuclear magnetic resonance (13C NMR) is described using relatively simple molecules for the easy understanding. However, some spectroscopic analytical methods are not included: Infrared spectra predicted using computational chemistry are too broad, and those predicted using database computer programs exhibit too sharp spectra; Mass spectra can be predicted using a database computer program (computer science program) without computational chemistry. The previous book [1] described mechanisms for highly sensitive detection (chemiluminescence mechanisms, absorption detection of bromate in ion chromatography, and derivatization for highly sensitive detection).

4.1. Titration Analysis 1. Phenolphthalein Color Change

Color indicators have been the backbone of simple pH tests and titration analyses. The spectrophotometric determination of hydrogen ion concentrations by using color indicators was described [1]. Kolthoff described the dissociation processes in detail [2]. The experimentally measured dissociation of phenolphthalein is described using four dissociation structures, where the ionization of two phenolic hydroxyl groups converts the neutral molecular form into the red quinoid form. Further dissociation from the quinoid structure to the alcoholic form eliminates the color. The dissociation mechanisms can also be described using three structures without a transition structure [3].

Phenolphthalein (PP) is a trendy indicator in titration analysis. The color changes to light red following the titration process. It then turns red (red shift) at the neutralization point. As the FA titration continues, the color shifts back (blue shift). The phenomena are spectroscopically measured. The initial spectrum shifts to the longer wavelength, then returns to the shorter wavelength. Figure 4.1 shows the original structure of isobenzofuran, including phenolphthalein. The properties of these indicators are summarized in Table 4.1.

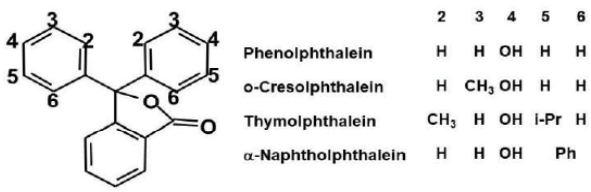


Figure 4.1: Structure of isobenzofuran.

Table 4.1: Specificity of indicators.

Indicators	pH range	color	p*K*a	Absorption wavelength nm					apc
				measured				ref	au
			p*K*ap	A	B	C	D		
Phenolphthalein	8.2 – 10.0*1	C→Pk	9.50	230	549	-	553	553*2	-1.538
	8.0 – 10.6*2							552*3	
o-Cresolphthalein	8.2 – 9.8	C→R	9.04p	-	-	-	-	586*4	-1.539
Thymolphthalein	9.3 – 10.5	C→B	9.19p	-	-	-	-	598*2	-1.544
αNaphtholphthalein	7.3 – 8.7*1	C→B	7.90p	-	-	-	-	-	-1.501

Increasing the pH of a phenolphthalein solution causes electron transfer in phenolphthalein and shifts the double-bond position, forming a conjugated double bond (Figure 4.2) and shifting a shift in the absorption wavelength toward a higher wavelength (redshift) (Figure 4.3 PP3). Further titration breaks the conjugated double bond (Figure 4.4), and the solution color disappears (Figure 4.4 PP4). These processes are analyzed *in silico*. First, draw these molecules and optimize the structures. The electron distribution is obtained from the calculations using the MOPAC **PM3** program. Further, the spectra of these structures are visualized using the **ZIND** program and **Visualizer** menu. The obtained spectra are shown in Figure 4.3, where PP1 – PP4 are related to structures 1-4 in Figure 4.2. The HOMO and LUMO electrons are shown in Figure 4.4.

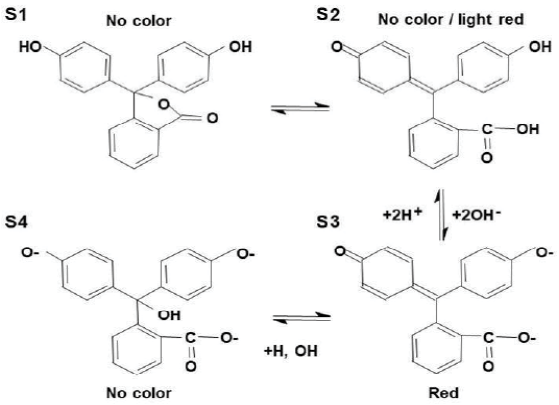


FIgure 4.2: Dissociation of phenolphthalein.

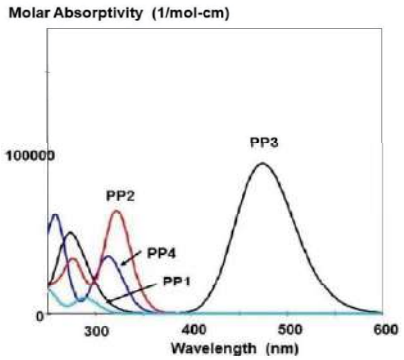


FIgure 4.3: Predicted absorption spectra.

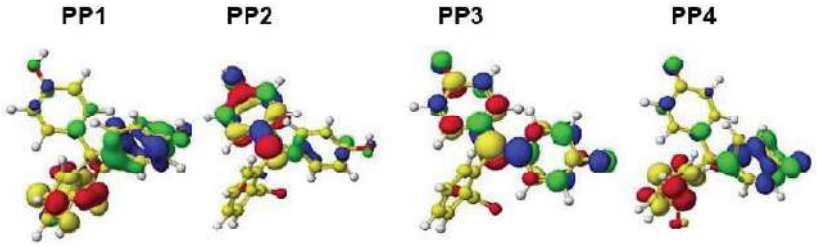


FIgure 4.4: HOMO & LUMO electron distribution followed the titration.

Structure 3 (PP3) shows conjugated double bonds at the central carbon, with an absorption spectrum showing a maximum wavelength of 480 as shown inn in Figure 4.3. The HOMO indicates the blue and green color, and the LUMO indicates the red and yellow color. Further titration damages the conjugated double bond, and the absorption spectrum shifts to a lower wavelength.

The predicted spectra obtained *in silico* are not precisely the same. *In silico* analysis does not include a solvent for the calculation; however, the study's spectra changed due to the structural change and can be followed. This analytical method helps to design new molecules. The measured maximum wavelength of phenolphthalein is 552 nm. The predicted nearest spectrum can be obtained from advanced programs such as MO-SPDDG/MNDO using RPA/MNDO geometry, MO-SMNDP using C1 ar MNDO geometry, MO-SPDDG/MNDO using RPA at PDDG/MNDO geometry, and MO-SPDDG/PM3 using RPA at PDDG/PM3 geometry [5].

o-Cresolphthalein: 3,3-bis(4-hydroxy-3-methylphenyl) -isobenzofuran-1(3*H*)-one

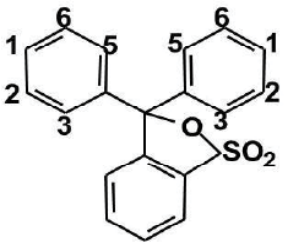
α-Naphtholphthalein: 3,3-bis(4-hydroxynaphthalene-1-yl)-2-benzofuran-1-one Phenolphthalein: 3,3-bis(4-hydroxyphenyl)isobenzofuran-1(3*H*)-one

Thymolphthalein: 3,3-bis(4-hydroxy-2-methyl-5-propane-2-yl-phenyl)-2-benzofuran-1-one

PM3: Parametric Model 3; Reparametrization of MNDO with core-core repulsion terms similar to those of ZINDO

4.2 Titration analysis 2 Indicator sulfonephthalein color change

Several sulfonephthalein-related compounds are used as specific indicators. Slight differences in chemical structure give them specific colors at different pH values. Figure 4.5 shows the fundamental structures, and Table 4.2 summarizes their properties. The mechanisms of color change related to their structures are the same as those demonstrated for phenolphthalein, as shown in Figure 4.6. Table 4.3 summarizes their predicted spectra' maximum wavelengths.



	1	2	3	5	6
Bromocresol green	OH	Br	CH_3	H	Br
Bromocresol purple	OH	CH_3	H	H	Br
Bromophenol blue	OH	Br	H	H	Br
Bromothymol blue	OH	i-Pr	H	CH_3	Br
Chlorophenol red	OH	H	H	H	Cl
Cresol purple	OH	H	CH_3	H	H
Cresol red	OH	CH_3	H	H	H
Phenol red	OH	H	H	H	H
Thymol blue	OH	i-Pr	H	CH_3	H

FIgure 4.5: Chemical structure of sulfonephthalein Table 1. Specificity of indicators.

Table 4.2: Specificity of indicators 2

Indicators	pH range	color	p*K*a	Absorption wavelength nm	ref wl		apc							
							measured		ref		au			
				p*K*ap		A	B	C	D					
Bromocresol	3.8 - 5.4	Y→B	4.9		415	619	619	619	615*[5]		-1.392			
Green							-411	-409	-400					
Gromocresol	5.2 - 6.8	Y→P	6.40 -		-	-	-	591*[2]				-1.451		
purple	4.8 - 7.5*[2]			6.30*[2]										
Promophenol	3.0 - 4.6	Y→B	4.10-		-	-	-	592*[2,6,7]						
blue	2.4 - 5.6*2		4.05*[2]					427-592*6	-1.386					
			404*6											
Bromothymol	6.0 - 7.0	Y→B	7.3	434	614	441	619	617	-1.458					
Blue	5.8 – 8.4		7.1	-415		-400								
Chlorophenol	5.0 – 6.6	Y→R	6.25	435	574	441	574	560	-1.459					
Red				-441	-574									
Cresol purple	1.2 – 2.8	R → Y	1.51	-	-	-	-	434						
	7.4 - 9.0	Y → R	8.46					578	-1.532					
Cresol red	-0.2 – 1.8	R → Y	1.59					519-434						
	7.2 – 8.8	Y → R	8.46					572	-1.526					
	6.8 – 9.6		8.2					519						
			8.06					434-573						
Phenol red	6.8 – 8.4	Y → R	8	-	-	-	-	558	-1.525					
	6.2 – 9.2		7.9	-	-	-	-	432-558						
			7.72	-	-	-	-							
Thymol blue	1.2 – 2.8	R → Y	1.65	-	-	-	-	544						
	1.2 – 3.4		1.75	-	-	-	-							
	8.0 – 9.6	Y → B		-	-	-	-	596	-1.531	7.4 – 10.2		8.9	-	-

pH range, color, p*K*a from ref. 4.5, p*K*ap: predicted p*K*a, apc: atomic partial charge of oxygen of structure S3, unit: au; C: clear (no color); Pk: pink; R: red; B: blue; Y: yellow; P: purple; A: 0.05M H_3PO_4; B: 0.05M Na_2HPO_4; C: H2O; D: 0.01M NaOH; ( ): second wavelength

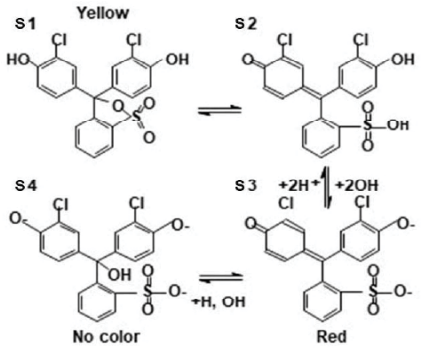


FIgure 4.6: Dissociation of chlorophenol red.

Table 4.3: Predicted absorption spectra of dissociated structures.

Indicators	S1	S20	S3	S4
Phenolphthalein	292	578	660	307
o-Cresol phthalein	290	577	630	315
Thymol phthalein	302	489 > 414	621	308
a-Naphthol phthalein	323	600	650	343
Bromocresol green	280	585	617	320
Bromocresol purple	283	453	684	311
Bromophenol blue	266	548	676	309
Bromothymol blue	290	570	670	315
Chlorophenol red	277	364	478	318
Cresol purple	197>	592	515	340
Cresol red	282	546	515	318
Phenol red	282	556	675	323
Thymol blue	286	593	746	325

S1, S2, S3, S4: structure 1-4 in Figure 4.6, Double peaks are indicated based on the absorption strength (>).Program: ZINDO CI MM2,

Their color change is not dynamic like that of phenolphthalein. Phenolphthalein's color changes from non-color to red; however, sulfonephthalein-related compounds change from the original color to different colors. Therefore, the calculation program requires precision.

Indicator color changes can be studied quantitatively using *in silico methods based on* spectra. Chemical structure changes related to electron distribution are used to study reaction mechanisms and designs in organic chemistry. Analytical chemists should consider the chemical structures of analytes using a computational chemical method like an analytical instrument. However, current computational chemistry programs are not perfectly developed or up to date. We can use the computational chemistry programs, but we should use the mass spectrometer results, as we use references for all analytical processes,

o-Cresolphthalein: 3,3-bis(4-hydroxy-3-methylphenyl) -isobenzofuran-1(3*H*)-one

α-Naphtholphthalein: 3,3-bis(4-hydroxynaphthalene-1-yl)-2-benzofuran-1-one Phenolphthalein: 3,3-bis(4-hydroxy-phenyl)isobenzofuran-1(3*H*)-one

Thymolphthalein: 3,3-bis(4-hydroxy-2-methyl-5-propane-2-yl-phenyl)-2-benzofuran-1-one

Bromocresolgreen;2,6-Dibromo-4-[7-(3,5-dibromo-4-hydroxy-2-methyl-phenyl)-9,9-dioxo-8-oxa-9λ6-thiabicyclo[4.3.0] nona-1,3,5-triene-7-yl]-3-methylphenol

Bromocresol purple: 4,4'-(1,1-dioxido-3*H*-2,1-benzoxathiole-3,3-diyl)bis(2-bromo-6-methylphenol) Bromophenol blue: 4,4'-(1,1-dioxido-3*H*-2,1-benzoxathiole-3,3-diyl)bis(2,6-dibromophenol)

Bromothymol blue: 4,4'-(1,1-dioxido-3*H*-2,1-benzoxathiole-3,3-diyl)bis(2-bromo-6-isopropyl-3-methylphenol)

Chlorophenol red: 2-chloro-4-[3-(3-chloro-4-hydroxyphenyl)-1,1-dioxobenzo(χ)oxathiol-3-yl]phenol Cresol red: 4,4'-(1,1-dioxido-3*H*-2,1-benzoxathiole-3,3-diyl)bis(2-methylphenol)

Cresol purple: 4,4'-(1,1-dioxido-3*H*-2,1-benzoxathiol-3-yldine)bis(3-methylphenol) Phenol red: 4,4'-(3H-2,1-benzoxathiole-3-ylidene)bisphenol

Thymol blue: 4-[9-(4-hydroxy-2-methyl-5-propane-2-yl-phenyl)-7,7-dioxo-8-oxa-7 λ 6 thiabicyclo[4.3.0]nona-1,3,5-trien-9-yl]-5-methyl-2-propane-2-yl-phenol

4.3 Titration analysis 3. Indicators Methyl-orange and methyl-red color change

Titration analysis is the simplest quantitative analytical method for acidic and basic medicines; however, most are weakly acidic and basic compounds. Precise determination of the titrated volume is critical t, as it is determined by eye; therefore, a spectroscopic determination is encouraged. Various indicators have been developed for adjusting the dissociation of medicines and the indicator color change.

Methyl orange (MO)dissociation constant is 3.4; its color below pH3.1 is red and yellow above pH4.4. The color is orange between pH 3.1 and 4.4. The nitrogen of MO is ionized; the chemical structure is either the benzoyl (MO2) or quinoid (MO3) form. The equilibrium of MO2 and MO3 produces a red color. The MO2 and MO3 structures are shown in Figure 4.7. Figure 4.8 shows the predicted spectra from three programs (MM2, PM3, and MNDOd).

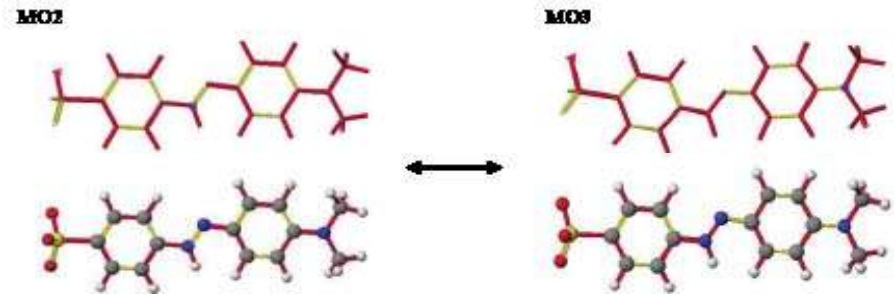


FIgure 4.7: Equilibration of methyl-orange benzenoid and quinoid structures. Red and yellow bonds: single and double bonds; Red (black), yellow (light gray), white, blue (dark gray), gray: oxygen, sulfur, hydrogen, nitrogen, and carbon atoms.

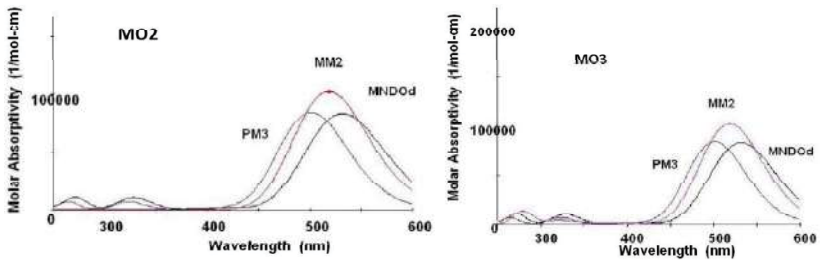


FIgure 4.8: Predicted spectra of methyl-orange benzenoid (MO2) and quinoid (MO3) structures in an acidic solution

The optimized equilibrium structures of MO2 and MO3 contact charge-transfer complexes are shown in Figure 4.9, and the predicted spectra are shown in Figure 4.10.

The programs used for optimization are MM2**2, PM3, and MNDOd**.The ZINDO demonstrates the spectra. The optimized structure using **PM3** is like two arcs by repulsion of center molecules, and the optimized complex structures using **MM2** and **MNDOd** are parallel complexes. The PM5 version of **PM3** also showed a similar structure. As observed in the analysis of phenolphthalein spectra, PM3 predicts a lower maximum absorption wavelength, while **MM2 predicts a** higher one than the characteristic wavelength. The combination of **MNDOd** and **ZINDO** programs produces the characteristic wavelength experimentally measured.

Further, in a higher pH solution, the structure becomes the yellow-colored benzenoid form. Figures 4.11 and 12 show the chemical structure and the predicted spectra. The two-molecule complex exhibits a tan-orange color with high molar absorptivity. The single-molecule solution is red with about half the molar absorptivity. The maximum wavelength of methyl orange is slightly higher than the characteristic wavelength; however, this program can study the methyl orange color change.

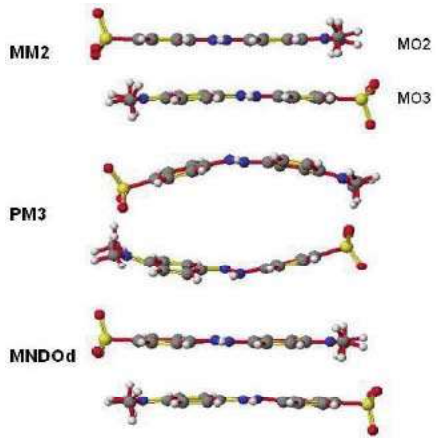


FIgure 4.9: Equilibrated three complex structures.

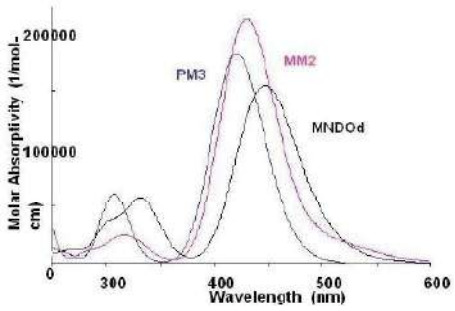


FIgure 4.10: Predicted three methyl-orange complex spectra.

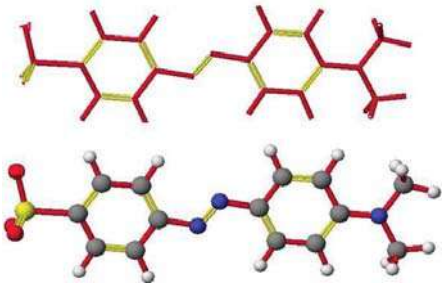


FIgure 4.11: Methyl-orange structure in high pH solution.

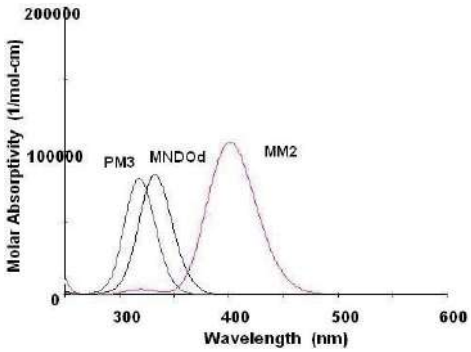


FIgure 4.12: Predicted methyl-orange spectra in high pH solution.

The dissociation constant of methyl red (MR) is 4.95. The quinoid structure shows red in a less than pH 4.4 solution, and the benzenoid structure in a higher than pH 6.2 solution is yellow. The color is orange between these pH solutions.

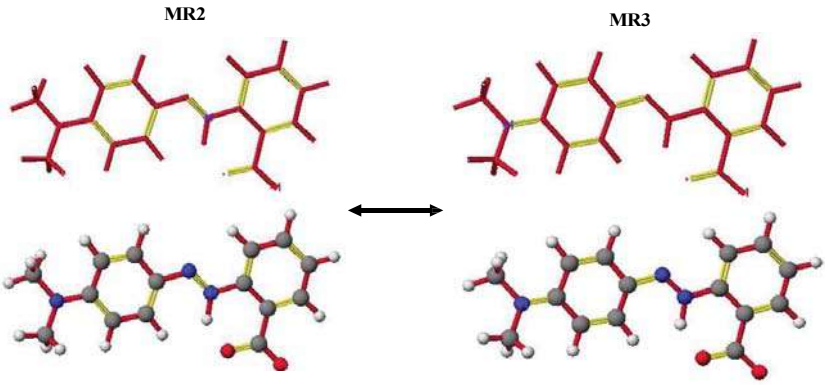


Figure 4.13: Equilibration of methyl-red benzenoid and quinoid structures. Red and yellow bonds: single and double bonds; Red (black), yellow (light gray), white, blue (dark gray), gray: oxygen, sulfur, hydrogen, nitrogen, and carbon atoms.

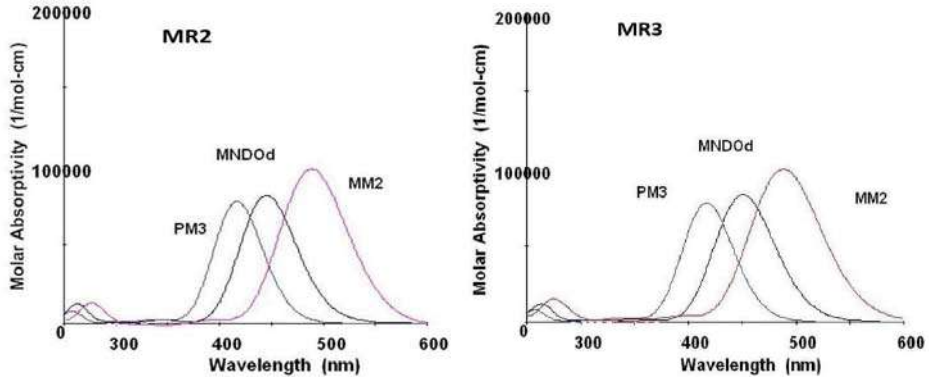


Figure 4.14: Predicted methyl-red benzenoid (MR2) and quinoid (MR3) spectra in acidic solution.

The analysis method of the behavior of methyl orange is applied to analyze methyl red behavior. The benzenoid (MR2) and quinoid (MR3) structures are shown in Figure 4.13, and the predicted spectra are shown in Figure 4.14. These MR2 and MR3 exist as a balanced complex. The possible structures optimized using MM2, PM3, and MNDOd are shown in Figure 4.14, and their spectra are given in Figure 4.15.

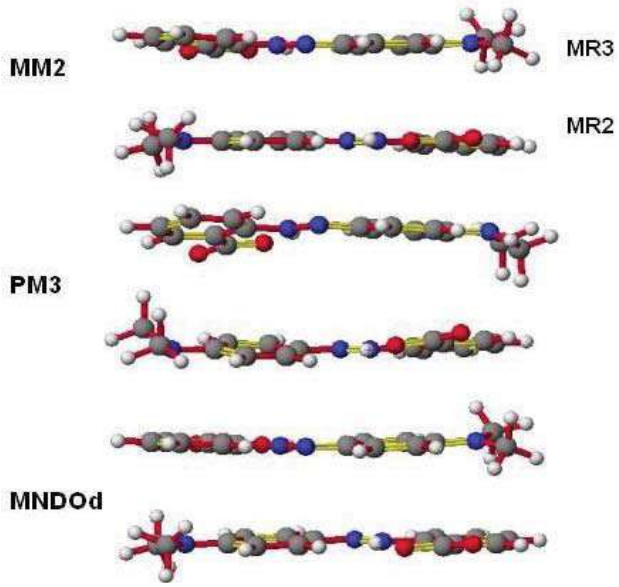


Figure 4.15: Equilibrated three complex structures.

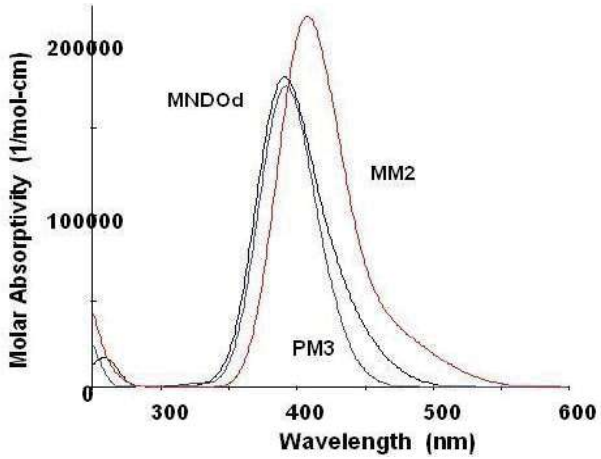


FIgure 4.16: Predicted absorption spectra of the complexes.

The properties of their complex structures and spectra are similar to those of methyl orange. The only difference is that the predicted spectra by PM3 and MNDOd are identical. In a higher pH solution, the MR structure is a yellow-colored benzenoid (MR3). The chemical structure and predicted spectra are shown in Figures 4.17 and 8.

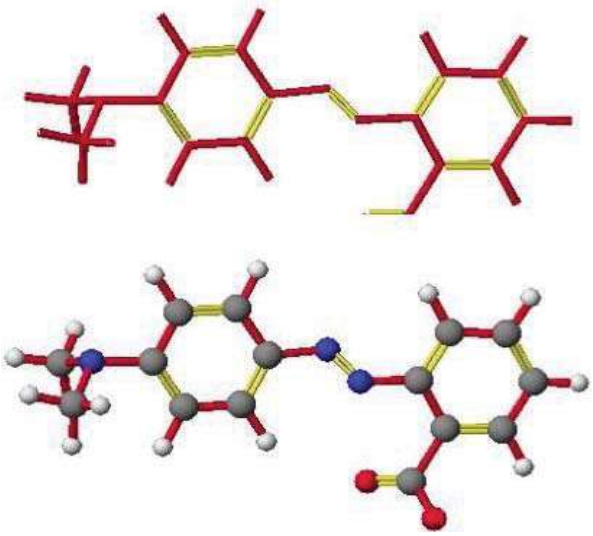


FIgure 4.17: Methyl-red structure in high pH solution.

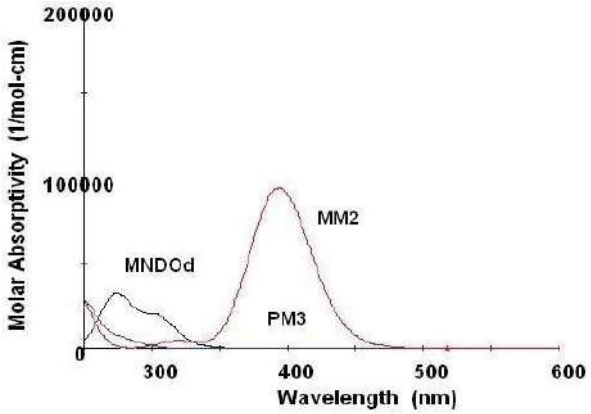


FIgure 4.18: Predicted methyl-red spectra in high pH solution.

The predicted spectra maximum wavelength (MWL) and molar absorptivity (MA) are summarized in Table 4.4.

Table 4.4: Predicted spectra of methyl-orange and methyl-red.

Program	MNDO-ZINDO		PM5-ZINDO		MM2-ZINDO	
MS	MWL	MA	MWL	MA	MWL	MA
MO1	278.9	39712	336.1	81005	420.7	108086
MO2	334.7	86000	334.9	80140	401.3	106360
MO3	539.9	70120	522.7	83300	535.4	92125
MO2+MO3	427.3	163600	412.4	139240	461.5	136585
MR1	299.2	62170	321.5	68140	417.2	2078
MR2	303.1	64754	334.8	70400	394.1	93682
MR3	302.5	65596	337.7	71810	495.7	95068
MR2+MR3	407.3	123820	407.7	131795	455.5	61116

MS: molecular structure; MO1-3: methyl orange 1-3 in Figure 4.7 ans 10; MR1-3: methyl red 1-3 in Figure 4.13 and 16; MO2+MO3 and MR2+MR3: resonance forms in Figure 4.15 and 16; MWL: maximum wavelength (nm): MA: molecular absorptivity (1/mol-cm)

These predicted spectra are not exactly the same as those experimentally measured because the computational chemical calculation does not account for solvent effects. However, this approach shows that chemical structure changes affect the indicator co-change; furthermore, it supports the development of colorimetric analysis analyte derivatization [36].

4.4 Colorimetric analysis of hydrochlorothiazide and creatinine

Quantitative analysis of 4-amino-6-chlorobenzene-1,3-disulfonamide is a possible impurity of hydrochlorothiazide, which is one of the thiazide diuretics, is performed using colorimetric analysis. The absorption spectra of 4-amino-6-chlorobenzene-1,3-disulfonamide and hydrochlorothiazide are identical; therefore, 4-amino-6-chlorobenzene-1,3-disulfonamide is derivatized with *N*-(1-naphthyl) 9-*N, N*-diethylethylenediamide to produce a compound with absorption in the visible region. Figure 4.19 shows the reaction scheme and these chemical structures, and Figure 4.20 shows their predicted spectra.

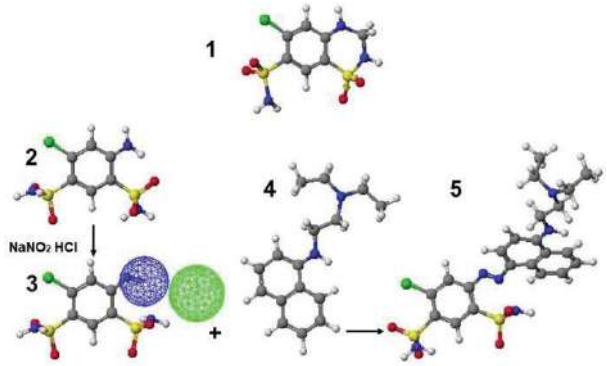


FIgure 4.19: Reaction detection scheme of 4-amino-6-chlorobenzene-1,3-disulfonamide.

In Figure 4.19, caged atoms are positively charged nitrogen (blue) and negatively charged chloride ion (yellow-green). These ions interact through ion-ion interactions. Spectra predicted using MM2 and MNDOd are similar; however, spectra predicted using PM3 show no visible absorption.

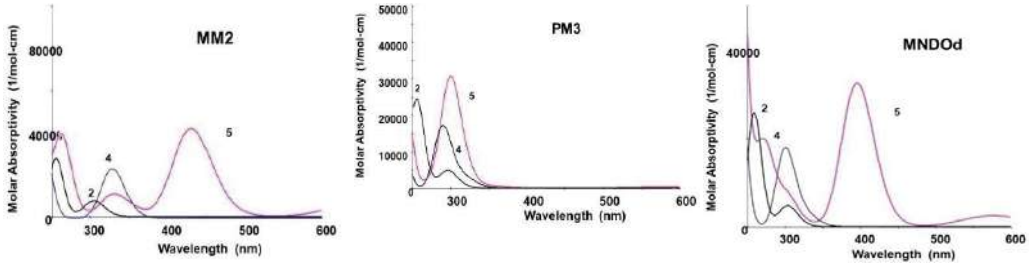


FIgure 4.20: Predicted absorption spectra optimized using MM2, PM3, and MNDOd.

Creatinine is creatine's dehydration product, an amino acid derivative, and is naturally produced in the human body from glycine and arginine. Creatine is an endogenous amino acid derivative produced by vertebrate animals and occurring primarily in muscle cells. Creatine is essential for energy storage. Creatinine is an indicator to determine the condition of chronic renal failure. Therefore, creatinine is analyzed in general clinical analysis. Creatinine (A) reacts with picric acid (B) and produces compound (C), which has a spectrum with a maximum wavelength of 490 nm by the Jaffe reaction. Figures 4.21 and 4.22 show the reaction scheme and spectra.

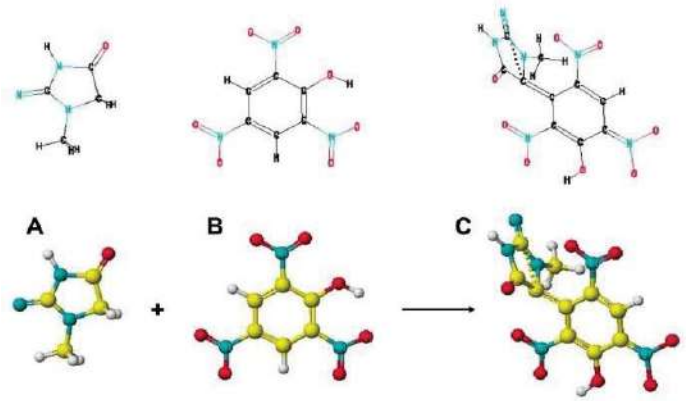


FIgure 4.21: Reaction scheme of creatinine detection.

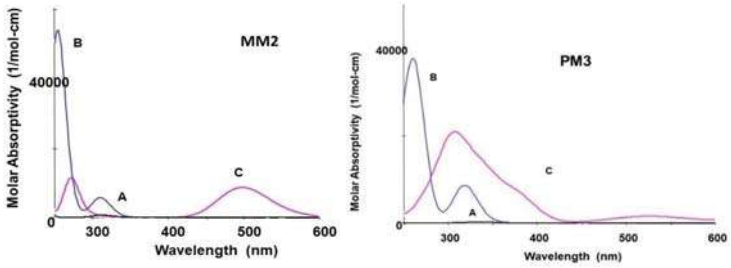


FIgure 4.22: Predicted absorption spectra optimized using MM2 and PM3.

MM2 program produced the best spectra. PM3 produced broad spectra, and MNDOd showed an error message; the MNDOd program may not recognize the picric acid nitro group.

Abbreviations of computational chemical programs

The following programs are listed in CAChe™ (SciGress™) programs; however, the selection guide is not available. First, we mainly optimized the constructed structures with MM2; then we calculated their spectra using the following programs.

ADF: Amsterdam Density Functional (DFT-Density Functional Theory- for molecules, heavy elements, transition metals) [8]

AM1: Austin Model 1-semi-empirical method for the quantum calculation of molecular electronic structure in computational chemistry based on NDDO [9-11].

CEO: Collective Electronic Oscillators [11, 12]

CI: Configuration Interaction [13, 14]

CNDO: Complete Neglect of Differential Overlap [15-19]

CNDO/S: CNDO for Spectroscopy

DFT: Density Functional Theory [20, 21]

DFT B88: DFT Becke88- pure GGA [22, 23]

GGA: Generalized Gradient Approximation [22, 24,25]

LYP: GGA correlation functional from Lee, Yang and Parr functional [22, 23]

INDO: Intermediate Neglect of Differential Overlap [12-14, 26]

INDO/S: INDO for Spectroscopy [12,27]

MNDO: Modified NDDO; does not take intra-account delocalization effect, uses only s and p orbital sets [8,10,28-30].

MNDO/d: MINDO with d-orbital [31]

MINDO/3: version up product of INDO; Modified Neglect of Diatomic Differential Overlap [14, 26, 31]

MO-S: Molecular Orbital package to calculate Spectroscopic properties of a molecule [SciGress, Fujitsu]

NDDO: Neglect of Diatomic Differential Overlap [10, 14]

PDDG: Pairwise Distance Directed Gaussian modification of NDDO provides good description of the van der Waals attraction between atoms [28].

PM3: Parametric Model 3; Reparametrization of MNDO with core-core repulsion term similar to those of AM1 [9,10, 28].

PM5: Parametric Model 5; Version-up program of PM3 [10]

PM6: Version-up program of PM5, however, PM6 can handle more elements compared to PM5 according to James Stewart [10, 32].

PW91: Perdew-Wang 1991 functional [22-25, 32]

RM1: Recife Model 1, Semi-empirical methods, Reparametrization of AM1 for H, C, N, O, P, S, F, Cl, Br, and I [10, 32, 33].

RPA: reference [11]

SAOP: Statistical Average of Orbital Potentials [32]

TZP: Triple-Z quality augmented by one set of Polarization functions [22]

ZINDO: reference [13]

ZORA: Zero-Order Regular Approximation [32]

Necessity unit: atomic unit (au) = 627.50955 kcal·mol^{-1} = 27.2116 eV

1 eV = 23.06 kcal·mol^{-1}; Enthalpy (ΔH) = kcal·mol^{-1}; HOMO, LUMO = eV

4.5 NMR spectroscopic determination of chemical structures

Nuclear magnetic resonance (NMR) is a powerful, relatively non-selective analytical tool that enables the ascertainment of molecular structure, including relative and absolute configurations and intermolecular interactions. Improving NMR resolution by developing high-power magnets enables structural analysis of proteins. In particular, the feasibility of protein-ligand binding stereostructure determination accelerates drug discovery. The stereostructures measured in solution provide much better information about protein-ligand binding conformation than stereostructures obtained by X-ray crystallography. On the other hand, computational chemical analysis provides the actual stereo structure in detail, including enantiomers. The stereostructure of proteins can be determined from amino acid sequence data *in silico.* The combination of NMR and computational chemical analysis is a powerful analytical tool for studying drug discovery,

NMR is not only used to determine the conformation between two molecules but also to determine binding strength. Generally, spectra shift to low fields by increasing the electron negativity of molecules. One example: the single signal

of trimethyl of benzyltrimethylammonium chloride shifted to higher field upon addition of aniline and to lower field upon addition of nitrobenzene in hexadeuteriumethyl alcohol (deuterated ethanol). The ape values of carboxy, hydroxy, and phenyl are negative; that of amino is a little positive, and that of alkyl groups is positive. The optimized structures of benzyltrimethylammonium chloride with aniline and nitrobenzene are shown in Figures 4.23 and 4.24**.** Figure4.24.B shows the repulsion of nitrobenzene from the chloride ion.

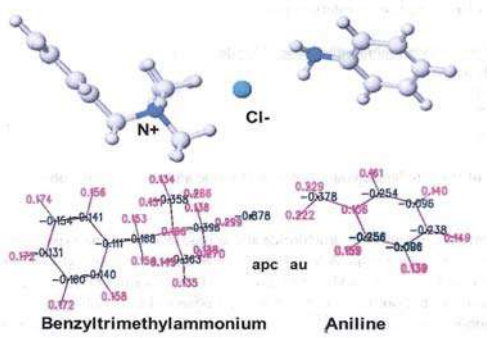


FIgure 4.23: Optimized conformation of benzyltrimethylammonium chloride with aniline.

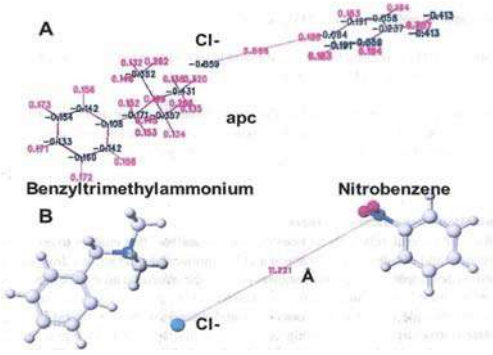


FIgure 4.24: Benzyltrimethylammonium chloride with nitrobenzene.

Table 4.5: Molecular interaction energy of benzene, toluene, and chlorobenzene with benzene.

Analyte	fs	hb	es	vw	FS	HB	ES	VW	MIFS	MIHB	MIES	MIVW
Benzene	-8.077	0	0	3.005	-9.147	0	-1.908	8.831	1.859	0	0.015	1.719
Toluene	-8.6	0	0	3.036	-20.416	0	-2.148	2.651	12.605	0	0.255	8.03
Nitrobenzene -6.633	0	0	3.214	-12.415	0	-2.585	6.19	6.882	0	0.692	4.669	
Aniline	-6.121	-1.334	0	3.416	-17.528	-1.58	-2.354	3.763	12.197	0.246	0.461	7.298
TMACl	0.79	0	-1.893	7.648								

TMACl:'*N, N,* N-trimethylammonium chloride; unit: kcal mol^{-1}

Table 4.5 summarizes the calculated ape values of the trimethylammonium and phenyl groups. The initial single signal at 220 Hz was not shifted by the addition of toluene and chlorobenzene. The low-resolution NMR spectra also allowed analysis of molecular interactions in solution.

Table 4.6: Signal (Hz) of trimethyl group of benzyltrimethylammoniuim chloride.

	Amount (mL)	Aniline	Nitrobenzene	
	0		220	220
	25		220	227
	50		217	29
	75		213	232

The sample solution is a mixture of 50 mg of trimethylammoniumbenzene chloride and aniline or nitrobenzene in 500 µL hexadeuterium ethanol

Similar results were obtained using mixtures of aniline hydrochloride and aniline. The experiment supported the

results of the properties of anion-exchange resin. The absorption spectrum of the anion exchanger (CG400-1(Cl^-)) at 300 Hz shifted to a higher magnetic field in the presence of aniline in C2H5OD and shifted to a lower magnetic field within nitrobenzene. Such an absorption spectrum was not observed for a polystyrene gel and was weak for a polystyrene gel with low ion-exchange capacity. The ap values of the carboxyl, hydroxy, and phenyl groups are negative, and that of the amino group is positive; however, predicting NMR spectra is still difficult, like predicting dissociation constants. Therefore, the following experiments use a program that predicts NMR spectra mathematically, calculated from measured data as part of computational chemistry.

The electrons around a nucleus circulate in a magnetic field and create a secondary induced magnetic field. This field opposes the applied field, as stipulated by Lenz's law, and atoms with higher induced fields (i.e., higher electron density) are therefore called shielded, relative to those with lower electron density. Electron-donating alkyl groups, for example, increase shielding, whereas electron-withdrawing substituents such as nitro groups deshield the nucleus. Substituents also create local induced fields. Bonding electrons can also lead to shielding and deshielding effects. A striking example of this is the p bonds in benzene. Circular current through the hyperconjugated system causes a shielding effect at the molecule's center and a deshielding effect at its edges. Chemical shift trends are explained by the degree of shielding or deshielding. Nuclei resonate over a wider range to the left (or more to the right) of the internal standard. When a signal is found with a higher chemical shift:

- the applied effective magnetic field is lower, if the resonance frequency is fixed (as in old traditional CW spectrometers)
- the frequency is higher, when the applied magnetic field is static (normal case in FT spectrometers)
- the nucleus is more deshielded
- the signal or shift is downfield or at low field or paramagnetic

Conversely, a lower chemical shift is called a diamagnetic shift; it is upfield and more shielded

Two-dimensional NMR spectroscopy has become increasingly important for assigning complex NMR spectra and determining new molecular structures. In this chapter, we study spectroscopic analysis using proton nuclear magnetic resonance (^{1}H-NMR) and carbon nuclear magnetic resonance (^{13}C-NMR) to identify and study molecular structures. The NMR spectral prediction program is Spartan'18. First, draw chemical structures or transfer, previously prepared and saved structures in SMILES format, and optimize them using the Build menu; then prepare NMR using the pull-down menu.

Draw chemical structures using the pull-down menu: Select then **New** Build Key. Obtain a drawing board: select an atom or a chemical structure in the data bank. Then double-click at the center of the board to produce the selected atom or molecule. Select an atom or a molecule and click at the target atom or molecule, and continuously build the target molecule. If it is necessary, change bonds and charge. Finally, select the optimization key and optimize the target molecule; then, save it.

After obtaining the optimized target compound, select the Setup button and open the calculation menus. Select NMR spectrum and click calculation. The calculation begins, and the process appears, showing the time elapsed until completion; select the Spectrum button and the spectrum selection menu, which appears and shows the completed data list. Select the target molecule, and the spectrum appears. The calculation takes time; therefore, batch calculation is recommended.

Example 1: Identification of spectra of compounds C3H6Cl2, C3H7NO2, and C8H8O2.

One spectrum exhibits an aromatic ring, and one indicates a typical methyl group. Imagine the location of methyl groups. Prepare dichloropropane, nitropropane, and *p*-methoxybenzaldehyde based on these speculations, and obtain their spectra. The calculated ^{1}H and 13C spectra are shown as two-dimensional NMR in Figures 2.25-27. Figure 2.26 shows a methyl signal, where the 1.03 ppm signal corresponds to the 1,2,4-hydrogens of nitropropane. The carbon 10.5 mm signal corresponds to these hydrogens. The aromatic ring 1,3-hydrogen signal is 7.90 ppm, and that of the 4,5-hydrogens is 6.80 ppm in *p*-methoxybenzaldehyde in Figure 2.27. The corresponding 13C signals are 133.1 ppm for the 1,3-carbons

and 113.3 ppm for the 4,6-carbons. 1,3-dichloropropane is a symmetrical molecule; therefore, the spectrum is simple and has few signals. Identifying the chemical structure seems difficult, but it is relatively easy. The number of ^{13}C signals is only two, and the 33.7 and 37.6 ppm signals correspond to the 2-carbon and 1,3-carbons.

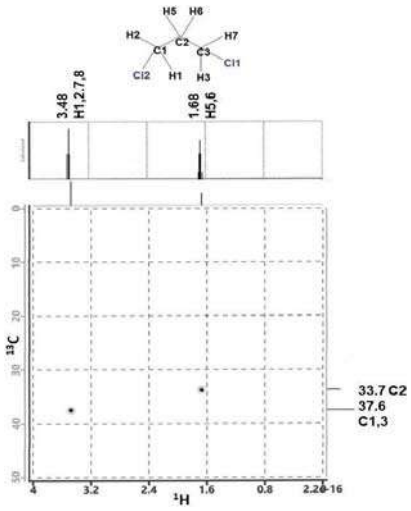


Figure 4.25: 1,3-dichloropropane.

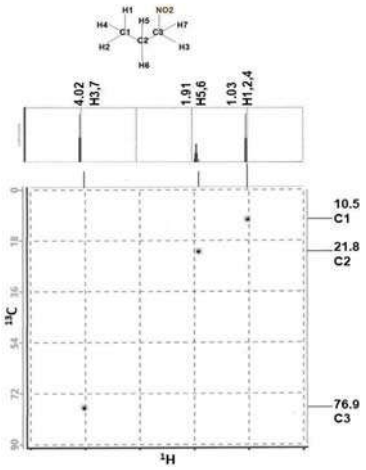


Figure 4.26: 3-nitropropane.

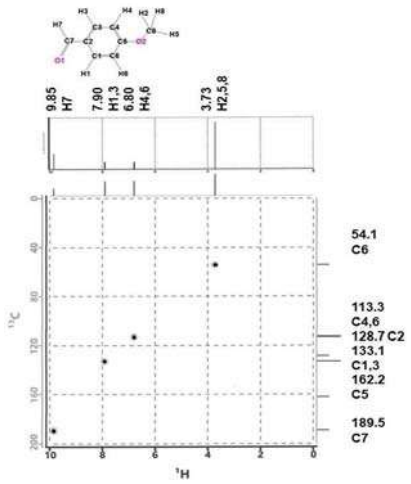


Figure 4.27: *p*-methoxybenzaldehyde.

In Figure 2.26, 3,7-Hydrogen of nitropropane signal shifts to 4.02 ppm, and the ^{13}C signal also shifts to 76.9 ppm, affected by the nitro group. In Figure 2.27, the ^{13}C signal of p-methoxybenzaldehyde shifts to 189.5 ppm. The corresponding hydrogen signal is observed at 9.85 ppm, and 2,5,8-Hydrogen of the methyl group is 3.73 ppm. ^{13}C of carbonyl signal is not provided. These predicted spectra are very identical to their measured spectra. The replacement learns the substitute effect to the chemical shift of substitutes.

Example 2: Identification of ^{13}C signal of C4H8Br2

The proposed structure and predicted ^{1H} and ^{13}C spectra are summarized in Figure 2.28. The hydrogen signals of C1 and C2 are 1.12 ppm and 1.34 and 2.32 ppm. The hydrogen signal of 3-carbon is 3.73 ppm due to the bromine. 9-Hydrogen signals of 4-carbon are 3.53 and 3.54 ppm, and 10-hydrogen signals of 4-carbon are 3.27 and 3.24 ppm. Determining chemical structures using ^{1}H is tedious; however, HSQC (^{1}H-^{13}C COSY) makes it easy to identify.

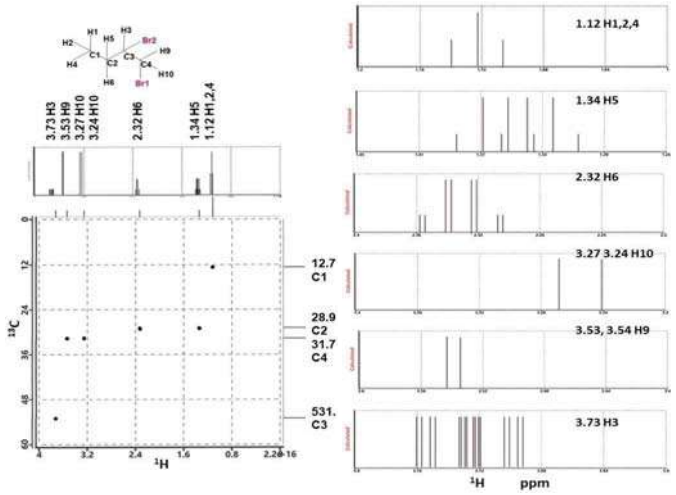


FIgure 4.28: 1,2-dibromobutane.

Example 3: Determination of butylic acid ethylester chemical structure

^{1}H-^{1}H COSY and ^{13}C-^{1}H COSY (HSQC) spectra of butylic acid ethylester are shown in Figure 4.29. The cross COSY signals in Figure 4.29A are eliminated for a clear demonstration. The methyl ^{13}C signal of 1-carbon is 13.1 ppm, corresponding to the 1,2,4-hydrogen signal is 0.99 ppm. The methylene ^{13}C signal of 2-carbon is 18.2 ppm, corresponding to 5,6-hydrogen signals are 1.61 ppm. The methylene ^{13}C signal of 3-carbon is 34.6 ppm, corresponding to 3,7-hydrogen signals is 2.15 ppm. The methyl ^{13}C signal of 5-carbon is 60.0 ppm, corresponding to 8,10 hydrogen signals are 4.05 ppm. The methyl 13C signal of 6-carbon is 14.0 ppm, corresponding to 9,11,12-hydrogen signals are 1.19 ppm. 1H COSY in Figure 4.29A indicates neighbor hydrogens.

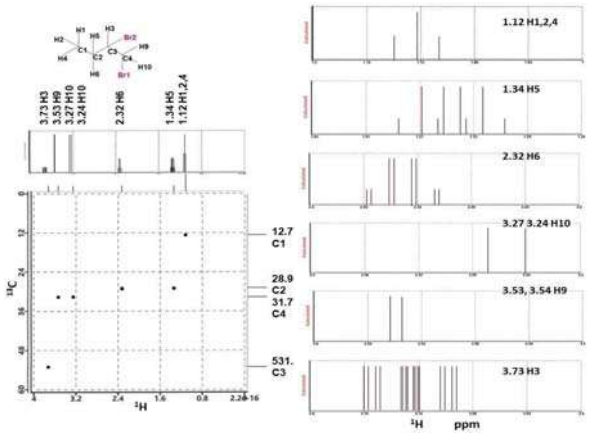


FIgure 4.29A: Butylic acid ethylester ^{1}H-^{1}H COSY.

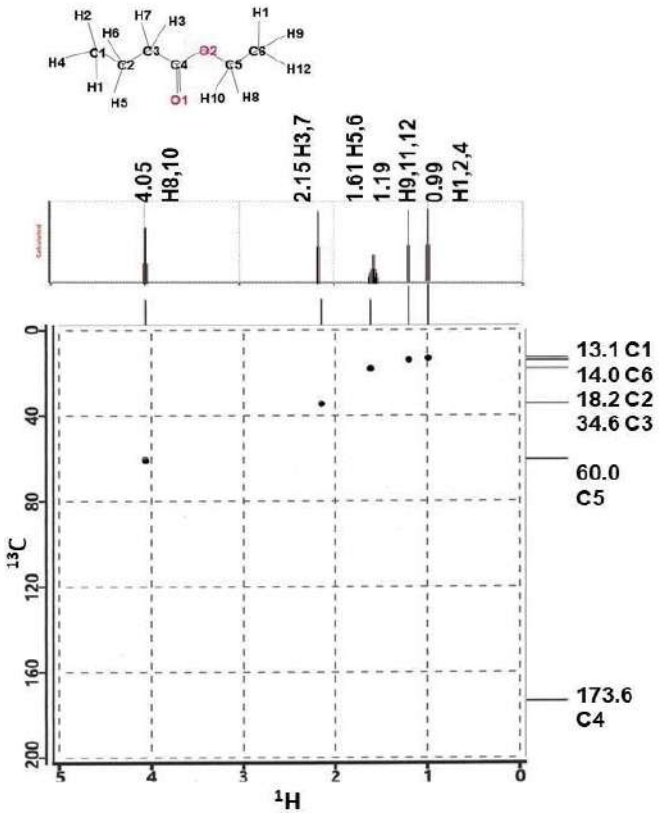


Figure 4.29B: Butyric acid ethylester ^{13}C-^{1}H COSY (HSQC).

COSY(correlationspectroscopy)techniquemakeseasytheidentificationofNMRsignals.This method helps to identify neighboring ^{1}H. Geminal coupling is the coupling of two hydrogen atoms bound to the same carbon atom (Ha-C-Hb). Vicinal coupling is the coupling of two hydrogen atoms bound to two adjacent carbon atoms (Ha-X-Y-Hb).Figure4.29 demonstrates the spectra of butylic acid ethylester. The HSQC (Heteronuclear Single Quantum Coherence) experiment determines proton-carbon single-bond correlations, where the protons lie along the observed F2 (X) axis and the carbons along the F1 (Y) axis. The following figures indicate 1H and 13C spectra, where corresponding atoms and predicted wavenumbers (ppm) are shown. However, the atom numbering is not actual chemical names and is assigned by the programs. The above examples show predicted spectra from chemical structures, and everyone can analyze them through in silico analysis.

4.6 Chemiluminescence mechanisms and absorption detection mechanisms of bromate in ion-chromatography

Chemiluminescence detection is a highly sensitive method used in gas chromatography, liquid chromatography, supercritical fluid chromatography, capillary electrophoresis, chip analysis, flow-injection analysis, and immune assays. It is also a selective detection method; it detects glycated albumin-containing albumin in liquid chromatographic effluent. It selectively detects reducing organic compounds such as reducing sugars, ascorbic acid, uric acid, steroids, glutathione, and cysteine. Radicals (superoxide, reactive oxygen species) produced by the keto-enol conversion are detected by collecting them with luminescence reagents such as luminol and lucigenin. Therefore, the feasibility of keto-enol conversion is related to the luminescence intensity. Different luminescence reagents have been developed for rapid analysis or continuous luminescence. The 17th Carbon of the steroid is the reaction center, and luminescence intensity relates to steroid toxicity.

Figure 4.30 shows the reaction scheme. An alkali solution drives the keto-enol conversion, producing radicals that are trapped by the luminescence reagent luminol or lucigenin, which produces luminescence. The reaction mechanism is considered the same as the firefly action, and the luminescence intensity depends on the reaction feasibility and the luminescence reagent.

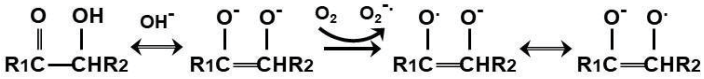


FIgure 4.30: Reaction scheme of luminescence.

One example: Conversion of the carbonyl at the 7th carbon of phenacyl alcohol to an alcohol produces radicals. The apc value (unit: au) change of the 7th Carbon is related to the luminescence intensity and further, the phenacylalcohol toxicity (r^2 = 0.970, n = 5). The reaction scheme is shown in Figure 4.31.

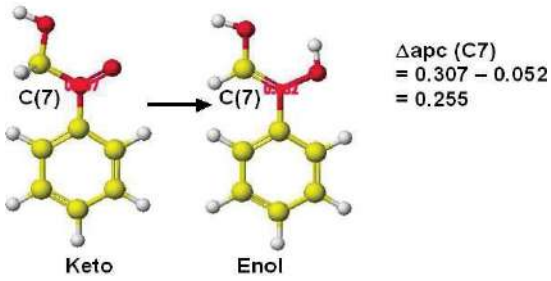


FIgure 4.31: Reaction scheme of phenacylalcohol.

The structure of steroids is like an open hand, but the actual structure is like a fat cigar. A carbonyl oxygen or alcohol substitute exists at one end, and various substituents exist at the other end. The reaction center is the 33rd Carbon carbonyl group. The conversion to the enol form produces radical [35]. The carbonyl and enol structures are shown in Figure 4.32.

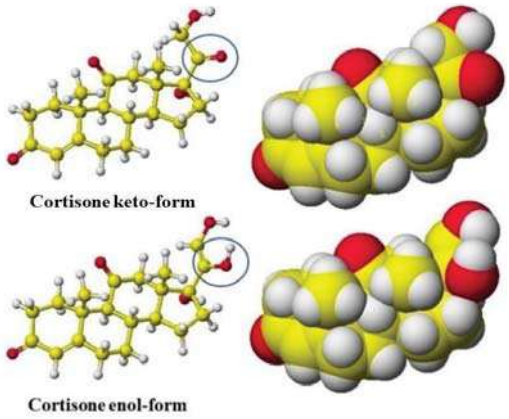


FIgure 4.32: Superoxide production mechanisms of Cortisone.

high sensitivity of uric acid is related to the three carbonyl groups. Figure 4.33 shows the structural change from the lactam to the urate form.

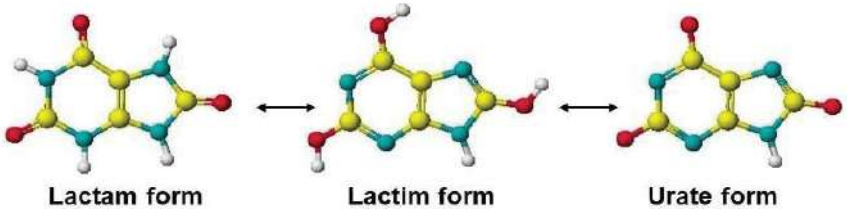


FIgure 4.33: Dissociation of uric acid in basic solution.

Glycosylation of proteins produces Amadori-type compounds that generate radicals. Conjugation of albumin lysine with glucose makes glycated albumin produce radicals in our body; therefore, we should avoid overeating sugars [36]. Figure 4.34 shows the reaction scheme.

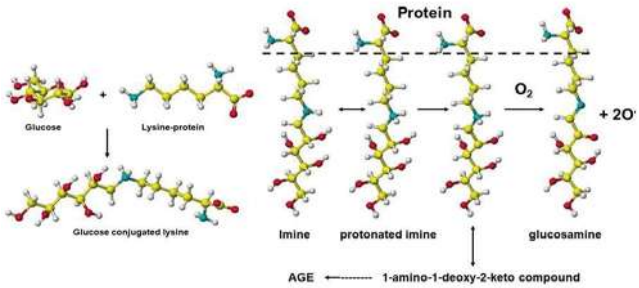


FIgure 4.34: Superoxide production from glycated albumin.

Several luminescence reagents have been developed. AkaLumine is used for *in vivo monitoring* because its absorption wavelength is 403 nm and its luminescence wavelength is 677 nm; these wavelengths avoid noise from other compounds [37]. This specificity differs from luminol and lucigenin, whose absorption wavelength is in the ultraviolet region. Figure 4.35 shows the predicted reaction mechanism and spectra.

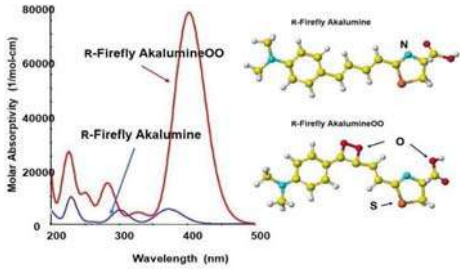


FIgure 4.35: AlaLumine and the reaction scheme.

The fundamental problem in handling chemiluminescence analysis is the lack of standard compounds. Peroxywater is a popular compound, but the quality is not guaranteed. We purified albumin to make the standard compounds; however, it was an arduous process, and we determined purity using liquid chromatography. Amadori-rearranged compounds are sensitive to luminescence analysis; therefore, the simple Amadori-rearranged compound was synthesized from glucose and *p*-toluidine. The synthesized 1-deoxy-1-p-toluidine-D-fructose is a stable white powder that allows easy preparation of the standard solution [36].

Superoxide is related to toxicity. The LD50 (mg.kg-1) of phenacylalcohol was calculated using TOPKAT@ and correlated to the apc of keto-enol 7th Carbons (r = 0.949, n = 5). The apc of the 33rd Carbon of steroids correlated with their endocrine activity (r = 0.873, n = 23) and blood vessel contraction index (r = 0.724724, n = 19) [38]. These results indicate that chemiluminescence measurements may predict toxicity; combining chemical experiments with computational chemical prediction is a method for drug development. Combining retention-time measurements in liquid chromatography with log *P* (octanol-water partition coefficient) prediction is also a practical approach to drug development. The details are demonstrated later.

When synthesizing reaction products is difficult, the spectra of predicted compounds support highly sensitive detection. Bromate is detected in the ultraviolet region in ion chromatography [39]. Figure 4.36 shows the predicted chemical structure and spectrum.

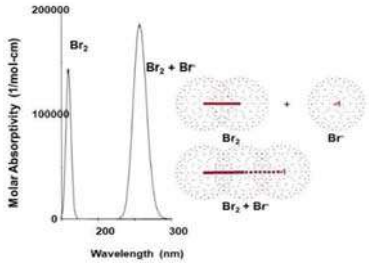


FIgure 4.36: High-sensitive detection of bromine, the complex structure, and predicted spectrum.

Computational chemistry can help analyze and understand the chemistry behind spectroscopic analysis, even when compounds are not synthesized. This is practical analysis based on fundamental chemistry. However, artificial intelligence approaches cannot replicate this type of reasoning.

References

1. T. Hanai, Quantitative in silico analytical chemistry, Computationall modeling of molecular interactions, 2014, RSC, Cambridge, ISBN:
2. E.R. Brode, The determination on hydrogen-ion concentration by a spectrophotometric method and the absorption spectra of certain indicators, J. Am. Chem. Soc. 1924, 46(3), 581-596.
3. I.M. Kolthoff, Indicator constants, J. Phys. Chem. 1929, 34(7), 1466-1483.
3. Computing across the chemistry curriculum, http://chemed.chem.pitt.edu/ChemEd/ComputingacrosstheChemistryCurriculum.doc
4. T. Hanai, Quantitative evaluation of dissociation mechanisms in phenolphthalein and the related compounds, Journal of Computer Chemistry, Japan, 2016, 15(1), 13-21. Doi 10.2477/jccj.2015-0055.
4. T. Hanai, Quantitative evaluation of dissociation mechanisms in methylorange and methylred, International Journal of Chemistry, Mathematics and Physics (IJCMP), 2018, 2 (3), p.23-26, https://dxc.doi.org/10.22161/ijcmp.2.3.1DOI: www.aipubliucations.com/ijcmp
5. T. Kinoshita, Absorption analysis in T. Kinoshita (ed) Instrumental analysis for pharmaceutical students, 1997, Hirokawa Pub. Tokyo, p. 22, ISBN 4-567-25560-7
6. M.J.S. Dewar, E.G. Zoebisch, E.F. Healy, J.J.P. Stewart, AM1: A new general purpose quantum mechanical molecular model, J. Am. Chem. Soc. 1985, 107, 3902-3909.
7. K. Kahn, Semi-empirical quantum chemistry, http://web.chem..ucsb.edu/~kalju/chem226/public/semiemp_intro.html
8. J.J.P. Stewart, Optimization of parameters for semi-empirical methods V: modification of NDDO approximations and application to 70 elements, J. Mol. Model, 2007, 13, 1173-1213.
9. T.D. Bouman, A.E. Hansen, K.L. Bak, T.B. Pedersen, R.A. Kirby, Random phase application/semi-empirical computations of electronic structure of extended organic molecules, Recent Research Developments in Physical Chemistry, 1996, 1-24.
10. S. Tretiak, A. Saxena, R.L. Martin, A.R. Bishop, CEO/semi-empirical calculations of UV-visible spectra in conjugated molecules, Chem. Phys. Lett., 2000, 331, 561-568.
11. W.P. Anderson, W.D. Edwards, M.C. Zerner, Calculated spectra of hydrated ions of the first transition-metal series, Inorg. Chem. 1986, 25, 2728-2732.
12. R.C. Bingham, M.J.S. Dewar, D.H. Lo, Ground states of molecules. XXV. MINDO/3. An improved version of the MINDO semi-empirical SCF-MO method, J. Am. Chem. Soc. 1975, 97, 1285-1293.
13. J.A. Pople, D.P. Santry, G.A. Segal, Approximate self-consistent molecular orbital theory. 1. Invariant procedure, J. Chem. Phys., 1965, 43, S129-S135.
14. J.A. Pople, G.A. Segal, Approximate self-consistent molecular orbital theory II. Calculations with complete neglect of differential overlap. J. Chem. Phys. 1965, 43, S136-S146.
15. J.A. Pople, G.A. Segal, Approximate self-consistent molecular orbital theory. III. CNDO results for AB2 and AB3 systems. J. Chem. Phys. 1966, 44, 3289-3298.
16. J.A. Pople, D.L. Beveridge, P.A. Dobosh, Approximate self-consistent molecular-orbital theory. V. Intermediate neglect of differential overlap. J. Chem. Phys. 1967, 47, 2016-2023.
17. S.P. Bhattachcharyya, M. Chowdhury, A method for calculating CNDO-MO bonding parameters. 2. Preliminary applications, J. Phys. Chem. 1967, 81, 1602-1604.
18. R.E. Stratmann, R.E. Scuseria, M.J. Frisch, An efficient implementation of time-dependent density-functional theory for the calculation of excitation energies of large molecules, J. Chem. Phys. 1988, 109, 8218-8224.
19. M.E. Casida, C. Jamorski, K.C. Casida, D.R. Salahub, Molecular excitation energies to high-lying bound states from time-dependent density-functional response theory: Characterization and correction of the time-dependent local density approximation ionization threshold, J. Chem. Phys. 1998, 108, 4439-4449.
20. M. Swart, M. Sola, F.M. Bickekhaupt, Energy landscapes of nucleophilic substitution reactions: A comparison of density functional theory and coupled cluster methods, J. Compt. Chem., 2007, 28, 1551-1560.
21. R. Rivelino, V. Ludwig, E. Rissi, S. Canuto, The orbital studies of hydrogen bonding in water-cyanides and in the base pair Gu-Cy, J. Mol. Struct., 2002, 615, 257-266.
22. J.P. Perdew, K. Burke, M. Ernzerhof, Generalized gradient approximation made simple, Phys. Rev. Lett., 1996, 77, 3865-3868.
23. J.P. Perdew, Y. Wang, Acute and simple analytic representation of the electron-gas correction energy, Phys. Rev. B, 45, 13244 (1992).
24. M.C. Zerner, G.H. Loew, R.K. Kirchner, U.T. Mueller-Westerhoff, An intermediate neglect of differential overlap technique for spectroscopy of transition-metal complexes. Ferrocene, J. Am. Chem. Soc., 102, 589-599 (1980).

25. S. Tretiak, V. Chernyak, S. Mukamel, Two-dimensional real-space analysis of optical excitations in acceptor-substituted carotenoids, J. Am. Chem. Soc., 119, 11408-11419 (1997).

26. M.J.S. Dewar, W. Thiel, Ground states of molecules. 38. The MNDO method. Approximations and parameters, J. Am. Chem. Soc., 99, 4899-4907 (1997).

27. M.P. Repasky, J. Chandrasekhar, W.L. Jorgensen, PDDG/PM3 and PDDG/MNDO: improved semi-empirical methods, J. Compt. Chem., 16, 1601-1622 (2002).

28. M.R. Silva-Junior, W. Thiel, Benchmark of electronically excited states for semi-empirical methods: MNDO, AM1, PM3, OM1, OM2, OM3, INDO/S, and INDO/S2, J. Chem. Theory Compt. 6, 1546-1564 (2010).

29. M.J. Dewar, W. Thiel, Ground states of molecules. 39. MNDO results for molecules containing hydrogen, carbon, nitrogen, and oxygen, J. Am. Chem. Soc. 99, 4907-4917 (1997).

30. A.S. Goncalves, T.C.C. Franca, J.D. Figueroa-Villar, P.G. Pascutti, Conformational Analysis of Toxobonine, TMB-4 and HI-6 using PM6 and RM1 Methods, J. Braz. Chem. Soc., 21, 179-184 (2010).

31. G.T. Velde, F.M. Bickelhaupt, E.J. Baerends, C.F. Guerra, S.J. Van Gisbergen, J.G. Snijders, T. Ziegler, Chemistry with ADF, J. Compt. Chem., 22, 931-967 (2001).

32. G.B. Rocha, R.O. Freire, A.M. Simas, J.J.P. Stewart, Computational Chemistry - Semi-empirical Methods, J. Compt. Chem. 27, 1101-1111 (2006).

33. T. Hanai, Quantitative computational chemical analysis of the sensitivity of chemiluminescence detection. J. Liq. Chromatogr. Rel. Technol. (2002), 25(16), 2425-2431.

34. T. Hanai, M. Uchida, M. Amao, C. Ikeda, K. Koizumi, T. Kinoshita, Selective chemiluminescence analysis of Amadori form of glycated human serum albumin. J. Liq. Chromatogr. Rel. Technol (2000), 23(20), 3119-3131.

35. T. Kuchimaru, S. Iwano, M. Kiyama, S. Mitsumata, T. Kadonosono, H. Niwa, S. Maki, S. Kizaka-Kondoh, A luciferin analogue generating near-infrared bioluminescence achieves highly sensitive deep-tissue imaging, Nature Communications 7 (2016) 11856, Doi: 10.1038/ncomms 11856.

36. T. Hanai, T. Tachikawa, Quantitative analysis of chemiluminescence intensity and toxicity in silico, Akio Tsuji, Masakatsu Matsumoto, Masako Maeda, Larry j. Kricka, Philip E. Stanley (Eds) Bioluminescence & Chemiluminescence, Progress and Perspectives, World Scientific, 2005, Singapore, 397-400.

37. T. Hanai, Y. Inoue, T. Sakai, H. Kumagai, Computational Chemical Analysis of the Highly Sensitive Detection of Bromate in Ion Chromatography. J. Chem. Info. Comp. Sci. (1998), 38(5), 885-888.

Chapter 5: Preparation of model phases

Construction of molecules using a computational chemistry program

The first step in quantitatively studying analytical chemistry is constructing target molecules using a computational chemistry program. Then, select a program from the pull-down menus to calculate the necessary properties. Several methods are available for drawing molecules on a computer screen. A popular program provides many predefined structures. Therefore, we can select and combine them to construct target molecules. Similar programs include Chemintosh, Chem3D, and ChemDraw. Another program is a freehand drawing program where you select and connect atoms; it optimizes hand-drawn structures for bond strength, bond angle, and atomic orbitals. The free-hand drawing method is recommended instead of picking parts from the database because it requires knowledge of atomic orbitals. Aromatic and aliphatic carbons have sp^2 and sp^3 atomic orbitals, respectively. Confusing sp^2 with sp^3 (or vice versa) produces strange structures. Automatically connecting six carbon atoms usually produces cyclohexane. Therefore, select three even or odd carbon-carbon bonds and fix the atomic orbitals before optimizing the six-carbon ring to produce benzene. Users may find it difficult to draw asymmetric rings like those in the data bank, but the program adjusts the shape to either cyclohexane or benzene. To prepare pyridine, select a carbon atom in benzene, then choose nitrogen and replace the carbon with nitrogen. In a freehand drawing program, prepare a target molecule using only carbon atoms, and replace carbon atoms with the desired atoms. This approach is faster than selecting each atom and drawing it step by step. However, careful selection of atomic orbitals is necessary. For example, carbonyl carbon and oxygen are sp2-orbital atoms.

5.1. Modeling graphitized carbon-phase

The chromatographic retention time difference has been qualitatively explained [1]. However, a quantitative explanation is necessary to understand the phenomenon. A quantitative explanation requires the digitalization of molecular properties. Computational chemistry methods can help solve these problems [2]. Hammett's constants help explain reactivity, but they can be replaced with electron localization calculated using a computational chemistry program. Video visualizations of electron-localization phenomena are used to teach organic chemistry. Electron localization and electron transfer are necessary for organic chemistry, but a quantitative explanation of electron localization is necessary for chromatographic phenomena.

In gas chromatography, analytes contact solid or liquid phases and leave by vaporization (related to boiling point), moving toward the column outlet. Generally, non-polar gases such as helium, nitrogen, and argon are used as the carrier gas. In chemical gas chromatography, ammonia or formic acid is doped in the carrier gas. In this case, we have to consider the contribution of these polar compounds to the retention mechanisms.

In liquid chromatography, the properties of both packing materials and eluents affect the retention mechanisms. Eluents contribute significantly; however, their quantitative explanation is complicated because solubility is difficult to control in chromatography. Eluent is challenging in the mobile phase; however, the definition of stationary phase is not simple. The stationary phase is an adsorbent in adsorption liquid chromatography, and the absolute stationary phase is packing materials coated with some eluent components. In reversed-phase mode, the amount of organic solvent coated on the surface of the organic phase depends on the organic solvent concentration in the eluent-containing water [3]. Therefore, constructing an actual model stationary phase is difficult. Here, we use the terms "packing material" and "eluent" to simplify the explanation. The present program cannot calculate molecular interactions with an eluent; therefore, we calculate molecular interactions with a single solvent.

In model chromatography experiments, the actual structures of packing materials are unknown; therefore, we construct simple, speculative model phases and use them to quantitatively analyze chromatographic retention. The simplest model phase is a graphitized carbon phase, and graphitized carbon is a large polycyclic aromatic hydrocarbon (PAH). We have to manage the double-bond positions carefully. As the first experiment, construct a polycyclic hydrocarbon larger (19PAH) than coronene (Figure 5.1).

First, draw a ring carbon using sp^2 carbon, fix the double bonds, select the pull-down menu "Ring," and build a benzene ring. Or correct the benzene ring from a structure database. Then, connect the required number of aromatic rings and build a size-appropriate flat PAH phase. Carefully correct the double bonds; otherwise, the arrangement of double bonds may become incorrect. When sp^3 carbon is found, fix sp^3 carbon for further study. The PAH size depends on the analyte's molecular size, and the analyte should be located inside the PAH phase. Finally, optimize the constructed

model phase structure using the MM2 program in the pull-down menu. The optimized structure provides final structure (FS), Hydrogen bonding (HB), and electrostatic energy (ES) values. Other calculated properties include bond stretch, bond angle, dihedral angle, and improper torsion; however, these properties are not generally used to explain retention. Memorize the calculation time for a batch calculation.

An optimized PAH structure should be flat, not bent. However, the horizontal-to-vertical ratio is not unity; the optimized structure may be bent. How to build a flat model? To build a flat model, select Duplicate (Ctrl+D) or Copy & Paste the original model, keep these two models in parallel before optimization, lock one phase, and optimize the structures. We can obtain two parallel flat phases. There are two approaches for calculating molecular interaction (MI) using these phases. One method is "Keep one phase free, and another phase is locked," or use only one locked phase after one unlocked phase is erased.

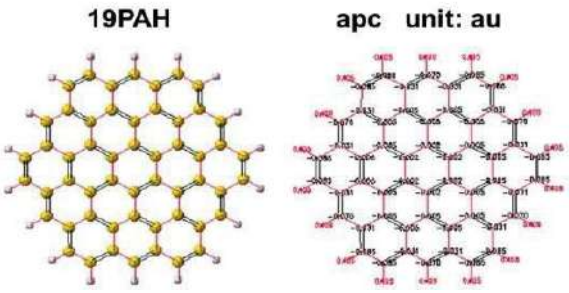


Figure 5.1: Structure of 19PAH and atomic partial charge.

Once you prepare a model graphitized carbon phase (a large PAH), use the MOPAC (Molecular Orbital Package) program to obtain the electron distribution. The fast, straightforward calculation is HOMO & LUMO calculation. The results indicate a relatively homogeneous electron distribution. Select Partial Chg & Calc. Bond Order from a pull-down menu, showing carbon atoms' apc. For example, the apc of the 19PAH center carbon is -0.002 au, and the absolute apc value becomes more significant for the peripheral carbon atoms. The apc of the second from the center is -0.005 au, then -0.031 au; the outermost carbon's apc is -0.085 au.

On the other hand, the apc of outside hydrogen is +0.105 au. The center has a negative charge, and the outside has a positive charge. The electron distribution and apc depend on the shape (vertical and horizontal ratio of the PAH. To study the electron distribution, we construct an unsymmetrical PAH by removing 6 rings from 19PAH. Figure 5.2 shows the structure.

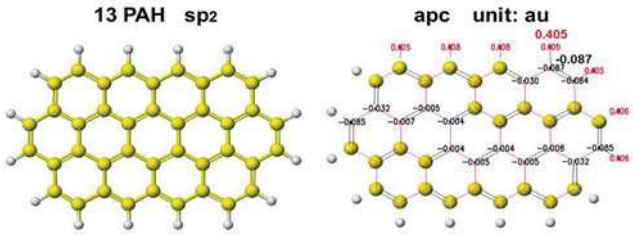


Figure 5.2: Structure of 13PAH and apc.

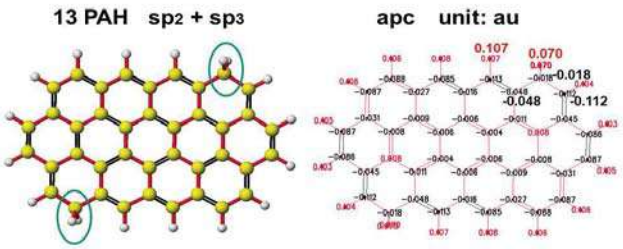


Figure 5.3: Structure of 13PAH (sp^3) and apc.

The apc of the 13PAH center carbons is -0.004 and -0.005 au, and that of the peripheral carbon atoms is -0.073 and -0.085 au. This result indicates that the electron distribution depends on molecular shape. Figure 5.3 shows a 13PAH constructed by missing the order of the double bon**ds**. Two sp^3 carbons (circled carbon) exist in the structure. The apc of hydrogen is 0.070 au. The molecule is not a perfect PAH. Figure 5.4 shows the electron distribution calculated using the HOMO & LUMO program for these molecules. These figures help explain electron localization.

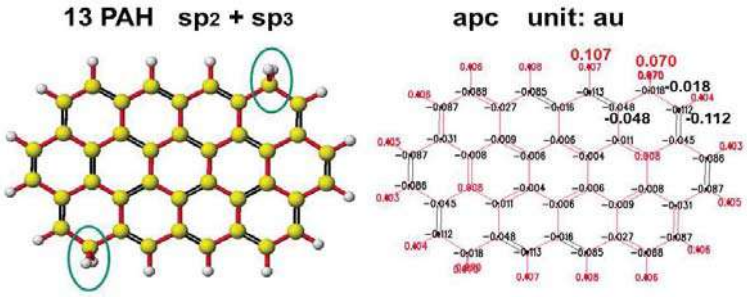


FIgure 5.4: HOMO & LUMO electron of model PAHs.

Constructing different molecular shapes and optimizing structures can help explain electron distribution based on shape and size. In analytical chemistry, we always use comparison values to clarify results. Therefore, reference selection is fundamentally required, and the approach is the same in computational chemical analysis. Attention: this program cannot handle the resonance structure of benzene; therefore, carefully select sp^2 or sp^3 carbon. When sp^2 and sp^3 carbons are mixed, the molecule is not flat because of the bond angle. The atomic angle of sp^2 and sp^3 atoms are 120 ° and 109°, respectively [4, 5].

5.2 Construction of silicone-dioxide phases

Use a silicon atom and draw a silicon chain, then fix the atomic distance and angle. Select an oxygen atom and replace an even or odd silicon atom with oxygen. Select the geometry menu and set the silicon-oxide chain. The silicon oxide builds an arc structure as shown in Figure 5.5a.

Next, change the oxygen atomic orbital from sp^3 to sp^2, then optimize the geometry. The oxygen moves from outside to inside the arc, as shown in Figure 5.5b. After optimizing these structures using the molecular mechanics (MM2) program, these rings are changed to arc structures. However, the size is not the same because sp^2 and sp^3 oxygen have different bond angles. The bond angles of sp^2 and sp^3 oxygens are 120 and 109°, respectively. While constructing large molecules, we may forget this correction and get an unusual structure, especially in protein analysis.

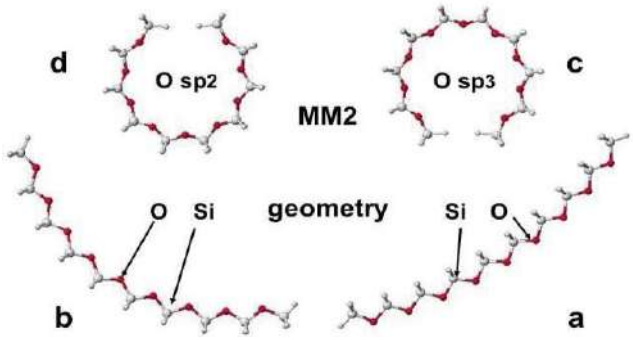


FIgure 5.5a, b: Structure of oligo silicone dioxide.

Silica gels and surface-modified ones are the most popular packing materials. Silica gel is a polymer of silicon dioxide and is used as a liquid in synthesis processes. Impurities in highly pure silica gels synthesized from gaseous organic silicones come from solvents used in the synthesis processes. The careful synthesis process provides over five-nines purity (> 99.999 %) products. Pure silica gels make easy surface modifications, and the final products are chemically stable. Preparing model silica gels is necessary to quantitatively analyze reproducible retention times measured using chemically stable packing materials.

Figure 5.5 shows fiber-like polysilicon dioxide. When kneaded together, the fibers do not produce homogeneous porous silica gels, and the physical strength of the end products is not guaranteed. One of the fundamental structures for preparing the stereo structure is a ring consisting of three silicon dioxide units shown in Figure **5.6,** where oxygen can be; polymerization is included. Further polymerization of the three-membered silicon dioxide ring builds different structures shown in Figures 5.7 and 5.8. Further polymerization does not provide a physically strong structure because of the limited number of active silanol groups.

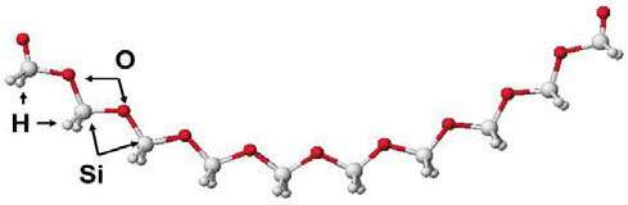


FIgure 5.5: Silicon-oxide oligomer.

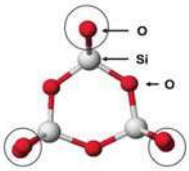


FIgure 5.6: Three-membered silicon-oxide ring, bondable oxygen in circle.

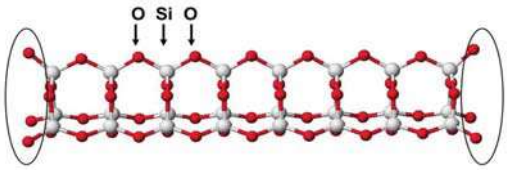


FIgure 5.7: Vertically connected three-membered silicon-oxide rings.

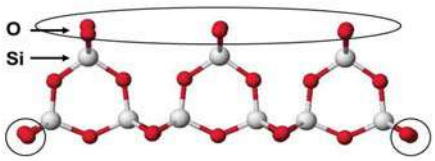


FIgure 5.8: Horizontally connected three-membered silicon-oxide rings.

This ring can build a large pore silicon dioxide ring shown in Figure 5.9. Further polymerization builds a sizeable flat structure shown in Figure 5.10. However, the polymerization in a different direction has limitations due to the lack of active silanol groups, as shown in Figure 5.11.

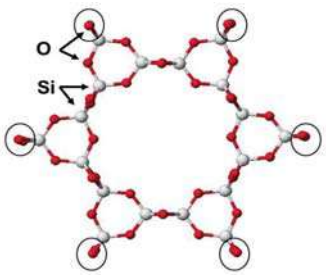


FIgure 5.9: Connected to build a large pore.

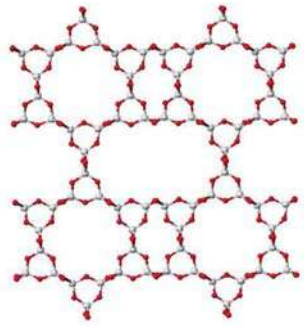


FIgure 5.10: Horizontally connected three-memberedsilicon-oxide ring.

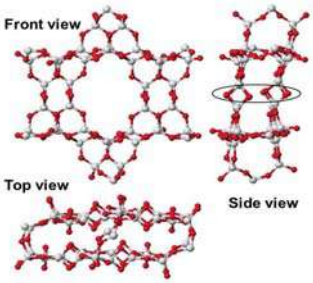


FIgure 5.11: Vertically connected three-membered silicon-oxide ring.

Another possible fundamental structure consists of six silicon dioxides shown in Figures 5.12 and 5.13. The preparation follows a model graphitized carbon phase and prepares an expansive flat phase by binding the structure shown in Figure 5.13. Make two 19-ring structures shown in Figure 5.14 and set them parallel, as shown in Figure 5.15. Lock one phase and optimize the structures. The optimized structure shown in Figure 5.16 indicates that the center groups stand homogeneously, but the outer groups are bent. Prepare a large phase and use the center for analyzing chromatographic retention.

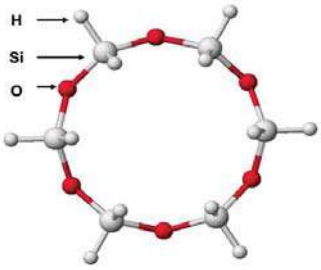


FIgure 5.12: Six-membered silicon-oxide ring .

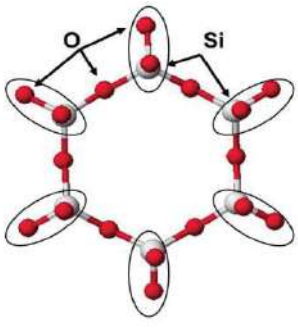


FIgure 5.13: Optimized Figure 8 structure.

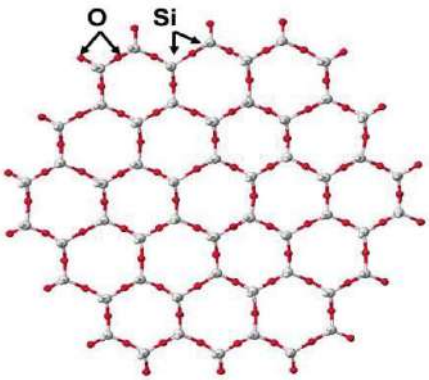


Figure 5.14: Horizontally connected six-membered.

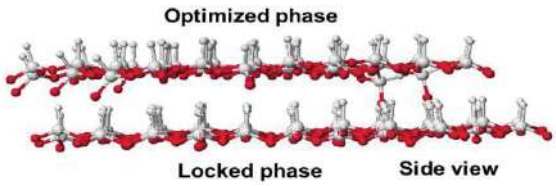


Figure 5.15: Optimized Figure 5.14 structure silicon-oxide ring.

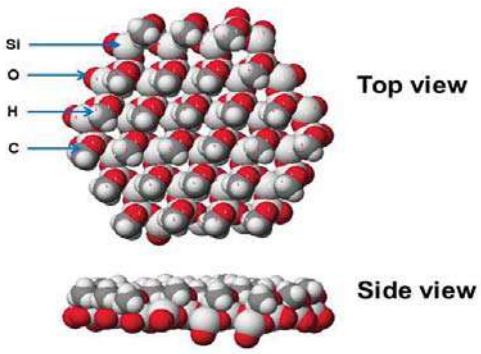


Figure 5.16: Methylated silanol groups of an optimized Figure 5.15 structure.

The parallel phases connect at even or odd sp3 silicon atoms via silanol oxygen on the upper or lower surface of the flat phase. The repeated processes can build a physically strong 3D silica gel structure. That is, 50% of silicon atoms produce silanol groups on the surfaces, and the remaining 50% bind the two phases; the remaining silanol groups can be used for further chemical bonding.

The shape of silica gels varies depending on the reaction processes; however, model porous silica gels have a homogeneous surface for describing average retention mechanisms. The atomic distance between the chlorides and alkoxy oxygen atoms of silyl reagents is 3.429 Å and 3.005 Å, respectively. The optimized model silica gel phase consists of two types of 6-membered silicon dioxide rings. The silicon atomic distance is 4.6 – 5.6 Å (n = 6), and the oxygen atomic distance is 4.7 – 5.7 Å (n = 6). These atomic distances are critical in designing the chemically bonded phases. Considering the trichlorosilane reaction, can all three chlorine atoms bind with three silanol groups existing on the silica gel surface? However, the atomic distance between chlorine and oxygen atoms permits only one bond, and the other two chlorine atoms do not involve bonding. This physical measurement of atomic distances suggests that the general reaction schemes are inaccurate, and the chemically bonded structures do not describe the actual structures. The molecular dimensions of silyl reagents exceed the interatomic distances; less than 50% of silanol groups are used for surface modification. The necessity of 2nd silylation (end-capping) is applied to synthesize chemically stable bonded silica gels. The 2nd silylation does not significantly increase the carbon content, but liquid chromatographic measurements support the necessity [2,6].

5.3. Preparation of surface modified silica gel phases

As demonstrated in Section 5.2, there are two types of silicon-oxide rings. The distance between two reactive silicon atoms is 4.6–5.6 Å (n = 6), and that of reactive oxygen atoms is 4.7–5.7 Å (n = 6). The atomic distances are not the same; therefore, the constructed polymer structure is not homogeneous. Constructing a homogeneous structure using sp3 atoms has limitations; therefore, we constructed a flat structure using sp2 atoms and then converted the initial atom to silicon. The atomic distance between lutetium atoms in the six-membered rings is 5.56 Å, about the same as the distance between two silicon atoms in silicon oxide. Using lutetium, we prepare a graphitized carbon phase. Figure 5.17 shows an optimized double phase constructed using 1221 lutetium atoms.

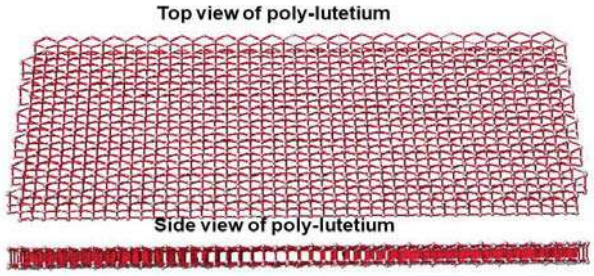


FIgure 5.17: Flat lutetium phase.

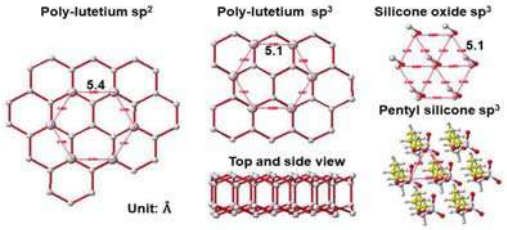


FIgure 5.18: Creation of alkylsilane bonded phase model from polylutetium phase.

Figure 5.19 shows the stereo structure of a model silica-gel-based pentylsilane-bonded silica gel, demonstrating that alkylsilanes are highly dense and contain no silanol groups, making them an ideal model phase for analyzing optimal retention mechanisms in liquid chromatography. If silanol groups exist, unpredictable retention occurs, especially for basic compounds, and makes it difficult for quantitative analysis of retention mechanisms. An sp^3-atom polymer is not flat, unlike benzene and like polycyclohexane. A side-view structure shows the actual structure. Lutetium is converted to silicon dioxide; then the silyl-reagent silicon atoms are placed at the silanol-hydrogen positions. Before cutting the bonds to optimize the structure, lock silicon atoms to keep their positions. Add carbon atoms to the silicon positions intended for the silyl reagents. Replace the hydrogen atoms on sp^3 positions step by step with carbon atoms. Figure 5.19 shows the example of a pentyl-bonded silica gel.

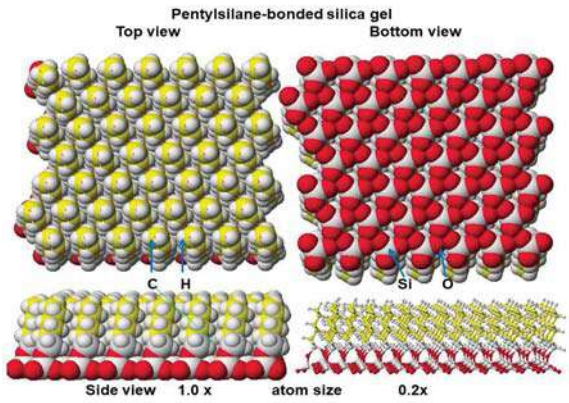


FIgure 5.19: Structure of model pentylsilane-bonded silica gel.

The sp^2 lutetium atoms are converted to sp^3 silicon, then hydrogen atoms are added using the Valence function. Lock silicon and hydrogen; then, cut the silicon-silicon bond. Converting hydrogen to sp^2 oxygen produces a flat silicon tetraoxide phase. Lock the lower three oxygen atoms, and use the remaining upper oxygen to further bond the two phases. Adding hydrogen to the remaining oxygen produces a silanol phase. The model silanol phase is shown in Figure 5.20.

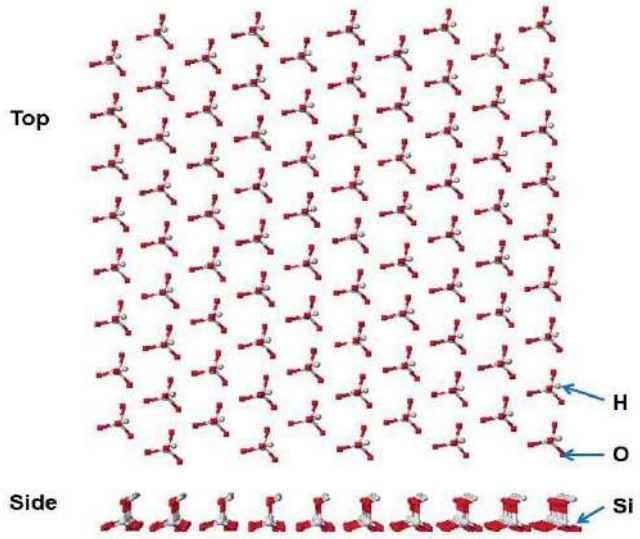


FIgure 5.20: Model silanol phase, red (black), large and small white balls: oxygen, silicon, hydrogen.

Piling up the single-layer can build a model of mechanically robust silica gel. First, adding a silicon atom connects three lower oxygen atoms and a neighboring silicon tetraoxide oxygen. Then, using the Geometry function, it creates the same bond distance in the newly connected bonds. Repeating this process produces a double-layer silicon oxide phase. Duplicate this double-layer silicon oxide and stack and connect the upper and lower double-layers. In this process, oxygen atoms of the lower double-layer silicon oxide connect to silicon atoms of the upper double-layer. Remove extran oxygen atoms from the upper double-layer. Connecting sp3 silicon with one sp2 oxygen produces a connected double-layer where half the silicon atoms are used for the connection. A model tetra-layer silica gel is shown in Figure 5.21.

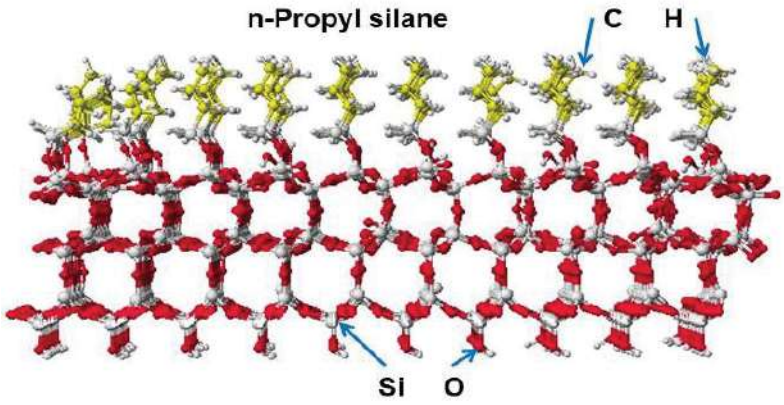


FIgure 5.21: Model tetra-layer silica gel bonded propyl groups. red (black), yellow (gray), large and small white balls: oxygen, carbon, silicon, hydrogen.

The center of the model layer was uniform, but the atoms at the edges were free to move. The bonded propyl groups stand nearly upright. The silicon atoms on the silica gel surface are sp3; therefore, the propyl groups slant, as shown in Figures 5.22A and B. Docking the analyte using the rhombic phase produces a complex molecule in which the analyte rests on top of the alkyl layer but does not enter between the alkyl chains. Therefore, these alkyl group-bonded silicon tetraoxide groups rotate to form vertical alkyl groups. Figures 5.22A, 4B, and 4C are dimethylpentyl-bonded, dimethylsilyl-bonded, and vertical dimethyloctyl-bonded silica gel models.

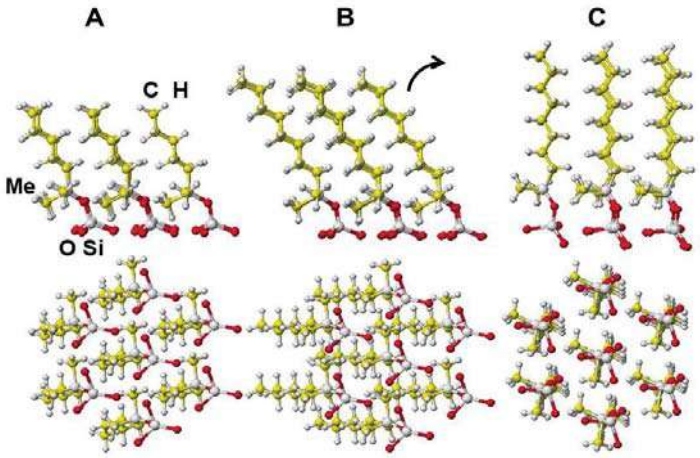


FIgure 5.22: Model alkyl-bonded silica gels. A: dimethylpentyl-bonded, B: dimethyloctyl-bonded, C: vertical dimethyloctyl-bonded silica gel model, red (black), yellow (gray), large and small white balls: oxygen, carbon, silicon, hydrogen.

Another challenge is modeling low-density alkyl-bonded phases because alkyl groups contact each other. Figure 5.23 shows the optimized structures of pentyl- and octyl-bonded models. The pentyl groups stand straight (A), but the octyl groups bend (B). These model trimethylsilane-treated silica gels include trimethylsilane. These model phases can be used for flat docking molecules.

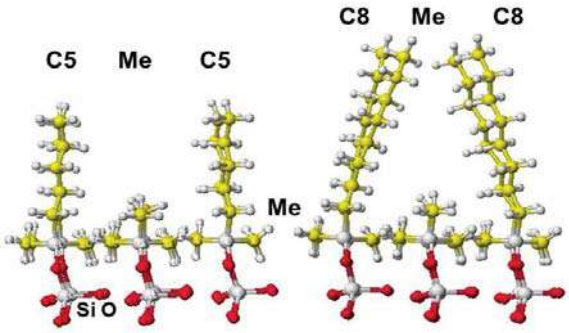


FIgure 5.23: Model dimethylalkyl-bonded silica gels. A: pentyl-bonded, B: octyl-bonded silica gels, Atoms: see Figure 5.22..

The feasibility of model phases was studied using two dense pentyl-bonded (Figure 5.24) and octyl-bonded (Figure 5.25) silica gels and a sandwich-type dodecyl-bonded silica gel (Figure 5.26). The analyte was phenol, a planar molecule. A pentyl group was used to avoid the influence of silica gel oxygen in the sandwich-type dodecyl-bonded silica gel model.

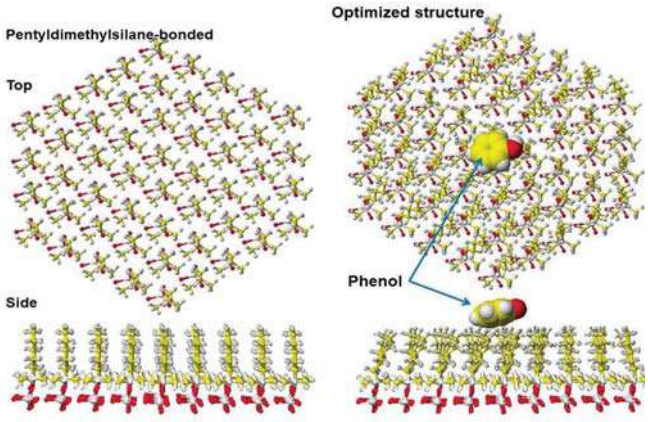


FIgure 5.24: Model pentyl-bonded silica gel (A) and the optimized structure after docking phenol, Atoms: see Figure 5.22.

The pentyl groups that stood straight before optimization (Figure 5.24A) bent after optimization and became a dense structure (Figure 5.24B). Phenol contacted the surface of the densely packed pentyl and octyl phases (Figures 5.24B and 25B).

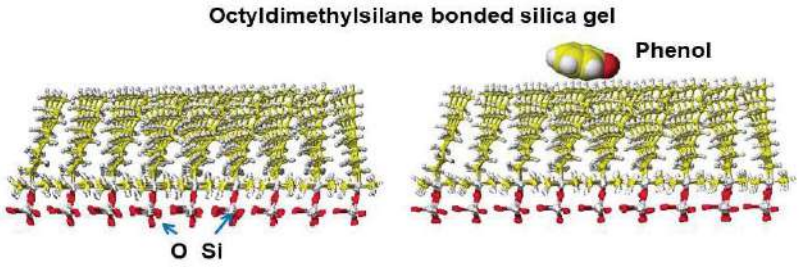


Figure 5.25: Model octyl-bonded silica gel. A: Initial structure, B; optimized structure with phenol. Atoms: see Figure 5.22.

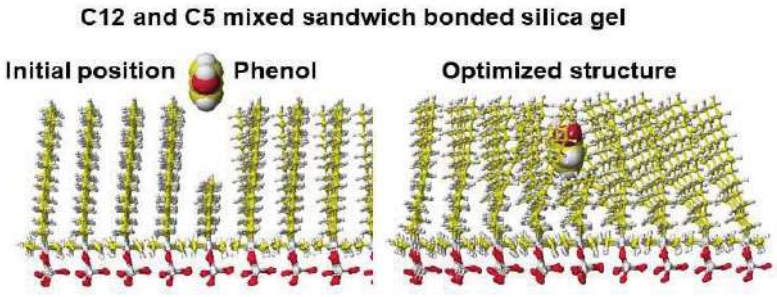


Figure 5.26: Model dodecyl-pentyl bonded silica gel of initial conformation, and optimized conformation with phenol, Atoms: see Figure 5.22..

A densely packed alkyl-bonded phase can be used for quantitative analysis of retention of planar molecules in which one side of the molecules contacts the bonded phase. One-sided interaction is half of the total interaction, and the interaction energy values reflect the relative interaction. However, this model is not practical for non-flat molecules; therefore, a sandwich-type model is better, even though it is not perfect for general analysis of molecular interactions. Packing materials are porous, and their surfaces are not flat. The actual retention model represents a form of partial solvation rather than complete solvation. One possible model is like a cone shape; however, constructing such a model is not easy using current computational programs, and a valley-type solvent wall is prepared, and model phases are shown later.

Considering the retention mechanisms in ion exchangers, ion-ion interaction, which is the strongest molecular interaction, and other interactions like van der Waals interaction and hydrogen bonding are not significant. Therefore, a flat model of the ion exchanger is built, and Figure 5.27 shows the contact of scoporamin with the model phase, with four types of structures.

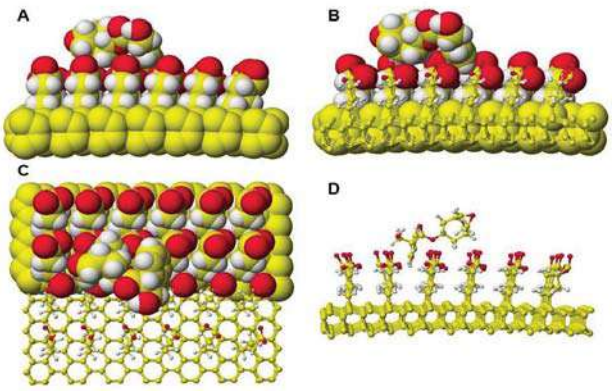


Figure 5.27: Model structure of scopolamine retains on a carboxy-phase.

Sugar is separated using chromatography with anion exchangers using aqueous ethanol and acetonitrile. The retention mechanism is hydrogen bonding; the structure is relatively flat; the positions of the hydroxyl groups are critical in determining differences in retention time. Figure 5.28 shows a model guanidine phase.

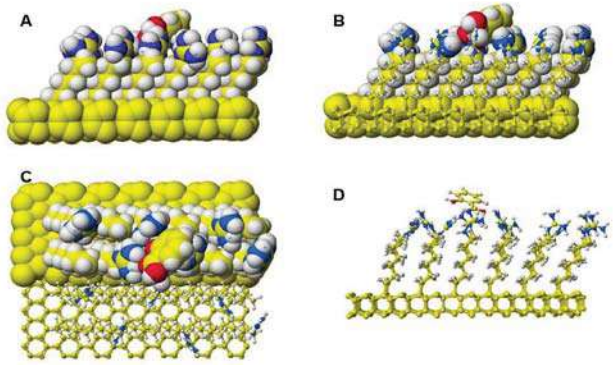


FIgure 5.28: Retention of mannose on a model guanidine-phase.

Model phases are updated as computer hardware improves and experimental evidence emerges. These simple models are sufficient to study direct interactions in reversed-phase liquid chromatography, but they must be refined to better represent actual systems. [7-9].

5.4. Surface modification of model alkyl bonded silica gel

Various models of surface-modified, chemically bonded silica gel are constructed from dimethylhexyl-bonded silica gel. Figure 5.29 shows the modification processes.

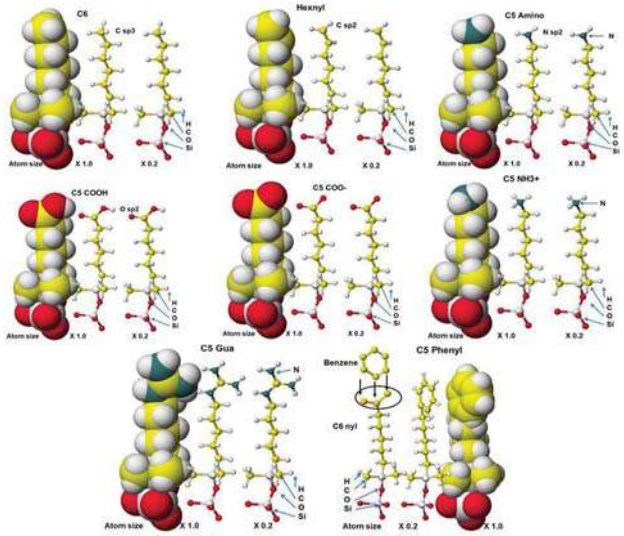


FIgure 5.29: Preparation of various bonded-phase models.

The phenyl ligand is prepared after superimposing benzene on the modified vinyl group, as shown in the Figure. This method is tedious, but it allows practical construction of the proposed ligands. These three molecules are part of the hexynyl phase, and all ligands are tightly bound and usually bent toward the outside of these model phases after optimization using MM2; therefore, the outside ligands are locked before optimization if necessary. Chapter 7 shows the practical applications of these model phases.

5.5. Preparation of model solvent phases

One approach is to modify graphitized carbon (a large polycyclic hydrocarbon). A graphitized carbon phase exhibits a homogeneous carbon layer. Therefore, carbon atoms are locked and cut bonds. After converting the atomic orbitalss of individual carbon atoms from sp2 to sp3, add hydrogen atoms to satisfy valence. These carbon atoms become methane

molecules; then, one hydrogen atom is converted to an oxygen atom. The methane molecules are converted into methanol molecules. The hydroxyl groups face upward or downward. This high-density methanol layer is ready to study molecular interaction (solvent effect) with various molecules. Another approach is to select an sp2 atom and prepare a polycyclic molecule. Figure 5.30 shows a a polycyclic nitrogen compound. Then, the nitrogen atoms are converted to sp2 silicon, as shown in Figure 5.31.

5.5.1. Construction of a model methanol phase: One approach is a modification of graphitized carbon (large polycyclic hydrocarbon). A graphitized carbon phase exhibits a homogeneous carbon layer. Therefore, carbon atoms are locked and cut bonds. After fixing atomic orbital of individual carbon from sp^2 to sp^3, add hydrogen atoms using val**ance.** These carbon atoms become methane molecules, then, one hydrogen atom is converted to an oxygen atom. The methane molecules are converted into methanol molecules. The hydroxyl groups face upward or downward. This high-density methanol layer is ready to study molecular interaction (solvent effect) with various molecules. Another approach is to select an sp^2 atom and prepare a polycyclic molecule. Figure 5.30 shows a polycyclic nitrogen compound. Then, the nitrogen atoms are converted to sp^2 silicon shown in Figure 5.31.

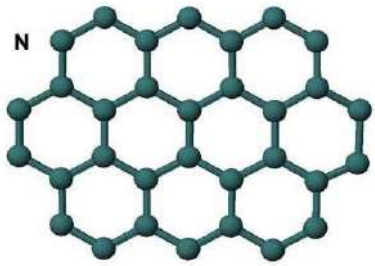


FIgure 5.30: Polycyclic nitrogen molecule.

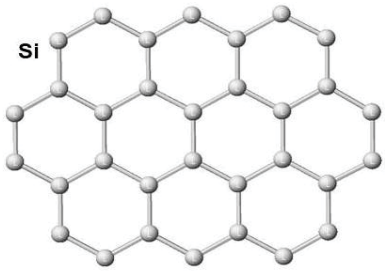


FIgure 5.31: Polycyclic silicone molecule. “L” indicates the locked atom.

Before further modification, the two layers are bound to avoid deforming the flat layer shown in Figure 5. 32. After optimization of this double-layer molecule using the MM2 program, add hydrogen and cut the bonds between the upper and lower layers shown in Figure 5.33, where the top and side view structures are exhibited. Select one optimized molecule (Figure 5.34) and convert hydrogen to oxygen to produce a hydroxyl group (Figure 5.35).

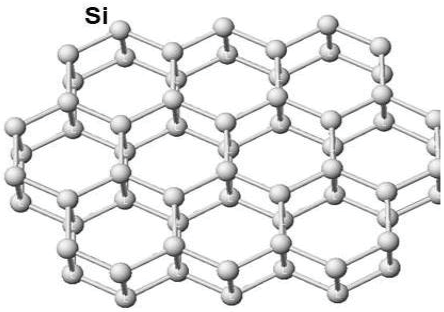


FIgure 5.32: Double layer structure of polycyclic silicone molecule. “L” indicates the locked atoms. All silicone atoms of lower layer are locked.

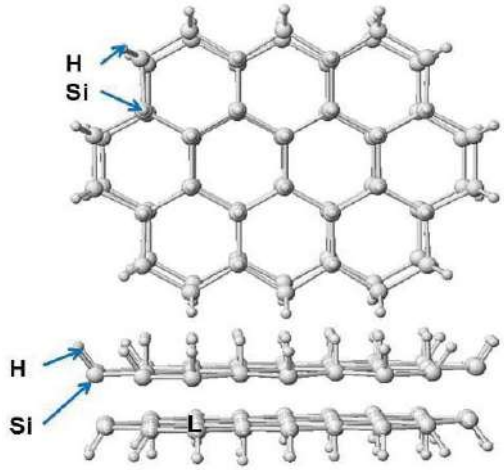


Figure 5.33: Optimized and erased binding bonds of Figure 32 structure. "L" indicates the locked atoms and all silicone atoms of lower layer are locked..

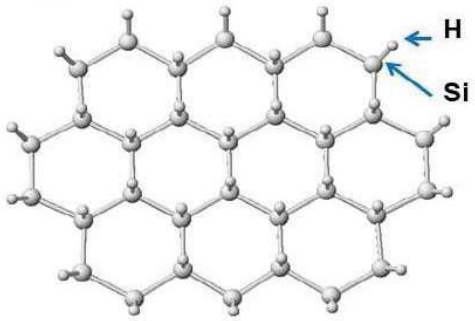


Figure 5.34: Corrected one layer of the optimized structure of polycyclic silicone compound with hydrogen atoms.

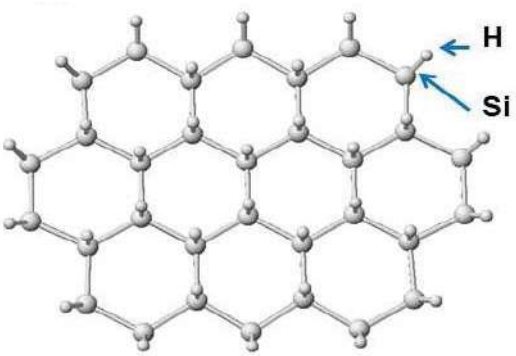


Figure 5.35: Structure of hydrogen converted oxygen.

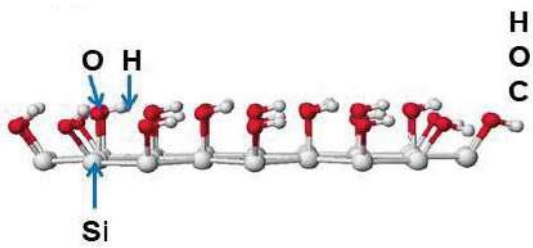


Figure 5.36: Produced silanol groups.

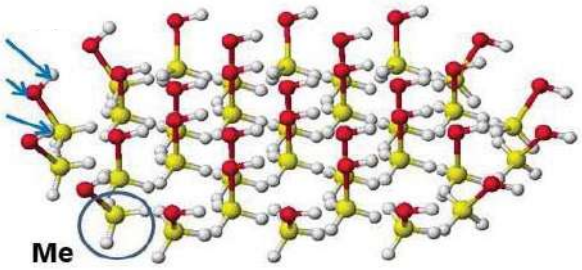


FIgure 5.37: Methanol layer where methyl carbons are locked..

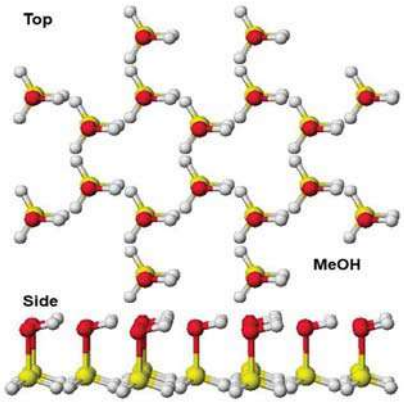


FIgure 5.38: Final structure of methanol phase where methyl carbons are locked.

5.5.2. Construction of a model acetonitrile phase: Once the methanol phase is available, the acetonitrile phase is easy to prepare. First, replace the methanol oxygen atom with a carbon atom, and change the hydrogen atoms to nitrogen atoms. Then, oxygen-hydrogen single bonds are converted to triple bonds (Figure 5.39). The final structure is ready after fixing the atomic orbitalss and bond lengths. Figure 5.39 shows the top and side views of the acetonitrile phase where all methyl groups are locked.

Figure 5.39A. Structure of the converted cyano group from hydroxyl group, where "L" indicates the locked atoms. Figure 5.39B. Final structure of the acetonitrile phase after optimized atomic orbital where "L" indicates the locked atoms.

5.5.3. Construction of model water phase: Construct a water phase from a polycyclic silicone structure shown in Figure 5.40. Replace silicone atoms with oxygen atoms, look at the oxygen atoms, and cut the silicone bonds. Add hydrogen atoms, keep the water molecules with hydroxyl groups horizontal, and remove the other water molecules. Then, lock the upper hydrogen atoms and unlock the oxygen atoms. Now, the hydroxyl groups can freely contact an analyte. Figure 5.40 shows the top and side views of a water phase before erasing extra water molecules.

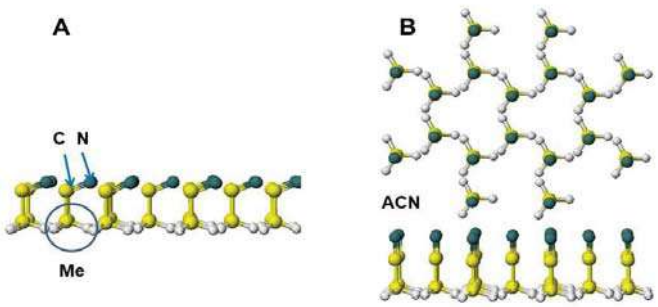


FIgure 5.39: A. Structure of the converted cyano group from hydroxyl group, where "L" indicates the locked atoms. Figure 5.39B. Final structure of the acetonitrile phase after optimized atomic orbital where "L" indicates the locked atoms..

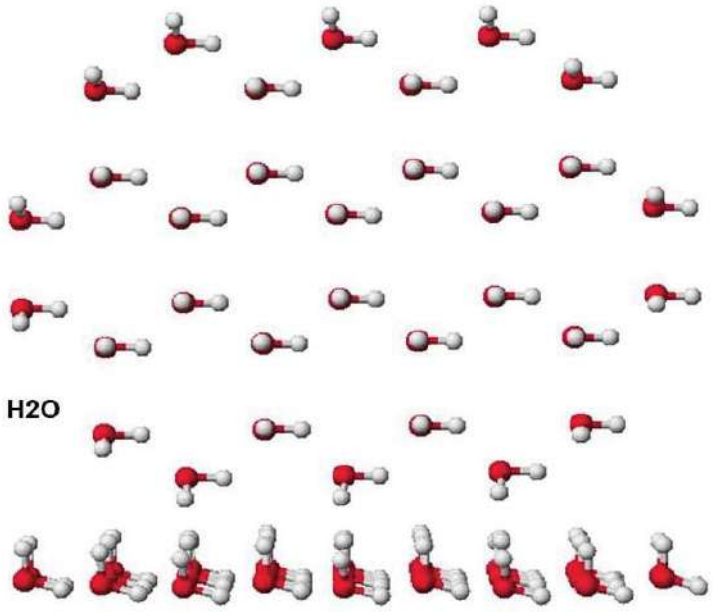


FIgure 5.40: Water layer constructed from polycyclic silicone phase.

Figure 5.41 shows the top and side views of an actual flat acetonitrile phase, and Figure 5.42 shows a partly converted acetonitrile-methanol mixed phase for easy comparison. Figure 5.43 shows side views of actual flat methanol and water phases. Figure 5.44 shows the side view of V-shaped water, acetonitrile, and methanol model phases. These V-shaped models are used for drug analysis because they require steric hindrance.

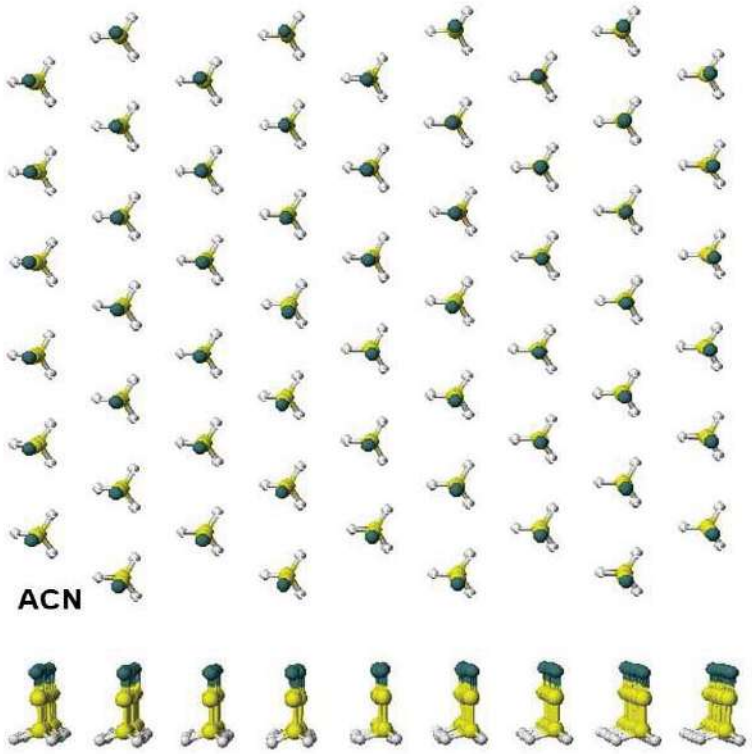


FIgure 5.41: Top and side views of a flat acetonitrile-phase.

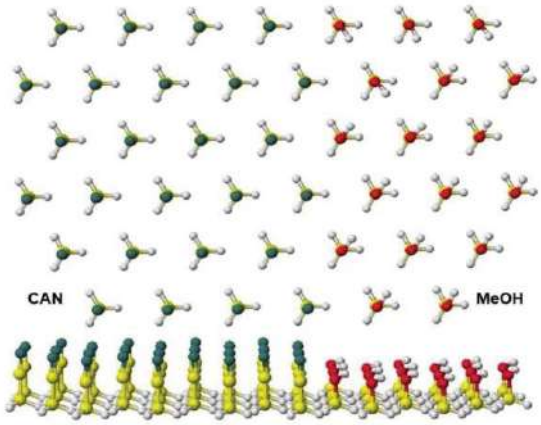


Figure 5.42: A partly converted acetonitrile and methanol phase.

These V-shaped solvent phases are used for molecules that are not flat and require more contact surface area because of steric hindrance. Increasing the contact surface area improves the precision of calculated molecular interaction energy values. The ideal shape is a cone-shaped valley, but the current program cannot create such a structure. When a solubility prediction program using computational chemistry is available, precision should be improved.



Figure 5.43: Side views of methanol and water phases.

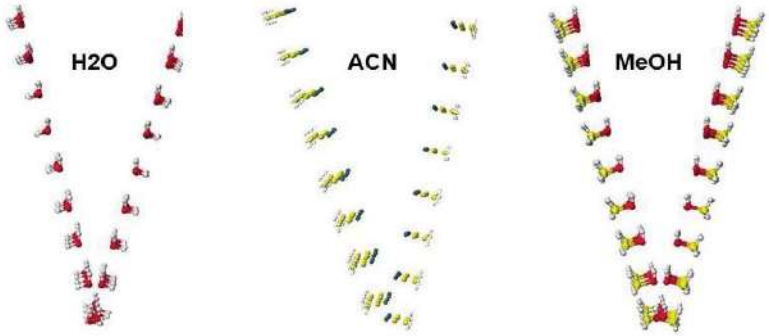


Figure 5.44: Actual V-shape water, acetonitrile and methanol model phases.

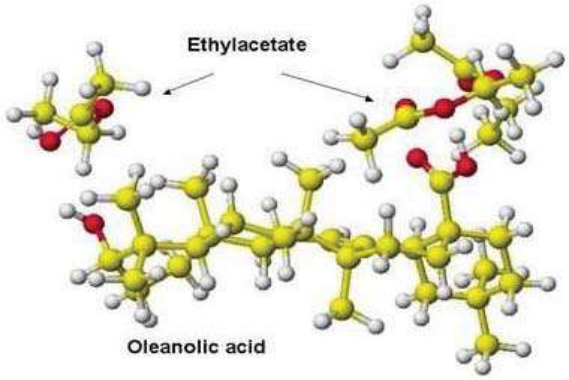


Figure 5.46: Oleanolic acid and ethylacetate (1+3) complex.

5.6. Example of calculation of solvent effects

Quantitative analysis of adsorption (retention) and desorption requires a quantitative explanation of molecular interactions between analytes and the packing materials (stationary phase) and analyte's solvation. Desorption mechanisms include solvation and ion exchange, as well as salting-out and ligand exchange. The actual modeling of the solvation is intricate; therefore, an analyte and a model solvent phase interaction are studied.

Operating molecular dynamics (MD) programs seemed ideal; however, the optimized conformations of an analyte and solvent molecules were not reproducible. Therefore, we calculated MI between an analyte and a model solvent phase using an MM2 program. Chapter 3 demonstrated the fundamental MI between an analyte and a model solvent phase. The contribution of MIVW, MIHB, and MIES depended on the properties of analytes, solvents, and model phases. When analyzing flat molecules, a flat model solvent phase provides a quantitative explanation of analyte-model phase interactions. Generally, drug stereo structures are complicated and require three-dimensional model solvent phases. A corn-type model is used to explain silica gel pores. A current program cannot build a large solvent core; therefore, a V-shaped solvent wall is constructed and provides an analyte-sandwich-type contact with solvent molecules. Analyte contact with solvent molecules occurs at both the polar and non-polar sites of solvent molecules; therefore, the density of solvent molecules should be considered when preparing a solvent phase.

Prepare a flat silicon phase and use it to prepare a methanol phase. Change the hydrogen atoms on the upper surface to an oxygen atoms, then, add hydrogen to prepare silanol. Then change silicon-carbon atoms, lock carbon, and add hydrogen using Valence. Now, a flat methanol phase is ready for further use. The acetonitrile phase is prepared by replacing the hydroxyl group with the cyano group, and the water phase is prepared from the methanol phase. Change the methanol carbon hydrogen, lock the hydrogen, and erase the three hydrogens. The two phases form a V-shape with a 3° angle. The angle was experimentally determined for various shape medicines.

Figure 5.46 exhibits the solvation of oleanolic acid with ethyl acetate molecules. Ethyl acetates contacted the oleanolic hydroxy group, but the alkyl group did not contact ethyl acetate. Additional ethyl acetate molecules did not form a solvent cage structure. I am not sure whether this is a limitation of the computer program. The MIHB and MIES energy values were -10.959 and 4.294 kcal mol-1, respectively.

The calculated results indicate that hydrogen bonding is the primary interaction. In contrast, MD conformation analysis did not show reproducible solvation structures, which should show contact between the analyte polar group and the polar group of solvent molecules, and between the non-polar group and the non-polar side of solvent molecules. Therefore, a simple but not ideal solvent-phase model is used to further demonstrate solvation.

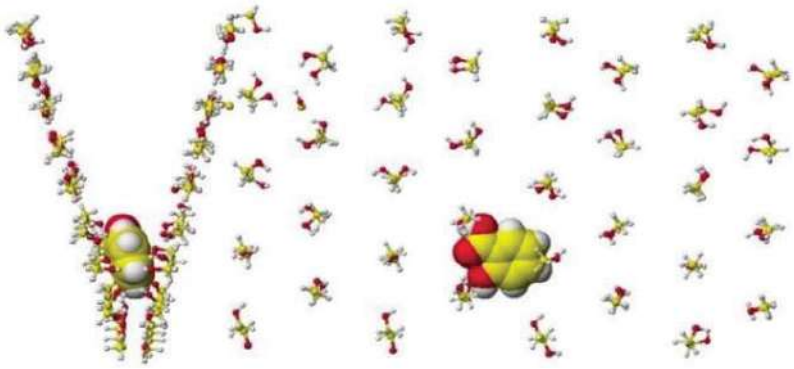


FIgure 5.47: *p*-Hydroxybenzoic acid and methanol- phase.

Figure 5.47 shows the MI of *p*-hydroxybenzoic acid (log *P* 1.00) with a methanol phase. Place *p*-hydroxybenzoic acid at the center of the V-shaped methanol-phase; then, optimize the structure. The front view shows *p*-hydroxybenzoic acid trapped between methanol molecules. The side view clearly indicates the contact conformation where a methanol hydroxy group contacts the *p*-hydroxybenzoic acid hydroxyl group, and another methanol hydroxyl group hydrogen contacts the *p*-hydroxybenzoic acid oxygen. The calculated MIHB, MIES, and MIVW energy values are 23.210, 2.384, and 2.628 kcal·mol^{-1}, respectively.

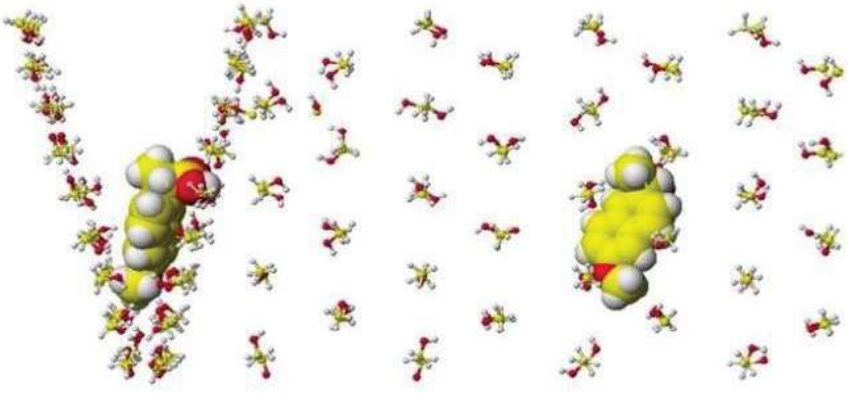


FIgure 5.48: Salicylic acid and methanol-phase phase.

Figure 5.48 shows that methanol hydroxyl-group hydrogens contact salicylic acid (log *P* 2.19) oxygen and the phenyl group. Hydrogen bonding contributes to a complex conformation. The calculated MIHB, MIES, and MIVW energy values are 22.265, 2.889 and 3.997 kcal·mol^{-1}, respectively. The primary interaction is hydrogen bonding, but the VW interaction contribution cannot be neglected.

The methanol hydroxy group's hydrogens contact both the polar and phenyl groups of relatively hydrophobic naproxen (log *P* 2.82) and or mefenamic acid (log *P* 5.34) in the optimized structures (Figures 5.49 and 5.50). Their MIHB, MIES, and MIVW energy values are 22.714, 3.485, and 4.597 for naproxen and 20.918, 3.021 and 11.515 kcal mol^{-1} for ketoprofen·mol^{-1}, respectively. Hydrogen bonding contributes most, and van der Waals interactions depend on analyte hydrophobicity.

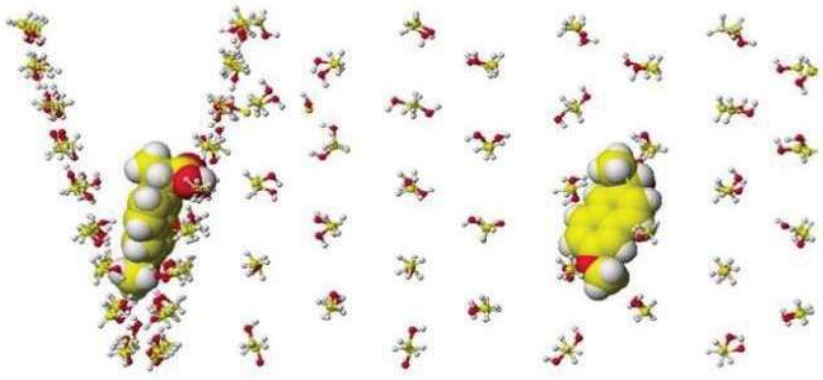


FIgure 5.49: Naproxen and methanol-phase.

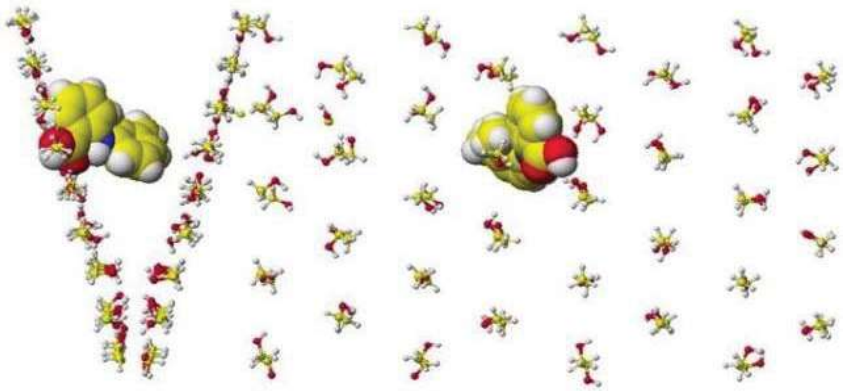


FIgure 5.50: Mefenamic acid and methanol-phase.

The MI structures for basic drugs are the same as those obtained for acidic drugs. The methanol hydroxyl group forms hydrogen contacts with both the basic-drug polar group and the phenyl group; that is, hydrogen-atom contacts with lone-pair electrons. These basic drugs are ionized in an acidic solution; therefore, the docking is performed in their ionized forms. Acidic drugs are ionized in a high-pH solution (pH 10); solvation in the methanol phase indicates that electrostatic interactions contribute to the primary interaction force, based on MIHB and MIES energy values. However, hydrogen bonding contributes to retaining basic ionized drugs in the methanol phase. The MIHB, MIES, and MIVW of theophylline (log *P* = -0.25, Figure 5.51) and atropine (log *P* = 1.32, Figure 5.52) are 15.781, 5.488, 8.067 and 23.344, 4.418, and 12.217 kcal mol^{-1}. Hydrogen bonding contributes significantly, and van der Waals forces are not negligible.

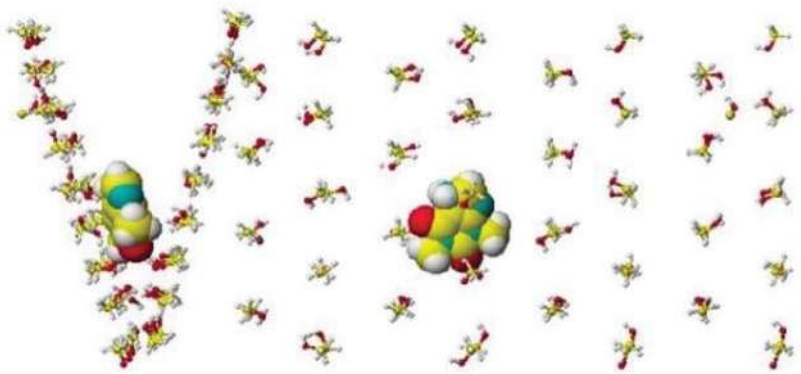


FIgure 5.51: Theophylline and methanol phase.

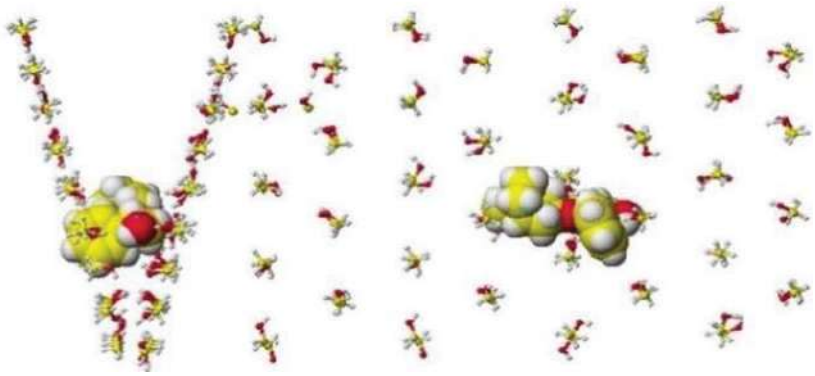


FIgure 5.52: Atropine and methanol phase.

Lidocaine (log*P*1.98, Figure 5.53) and diazepam (log*P* 3.19, Figure 5.54) were docked ,and obtained the MI energy values. Their MIHB, MIES, and MIVW energy values are 22.064, 3.183, and 11.293 for lidocaine, and 29.963, 12.512, and 7.024 for diazepam (kcal mol^{-1}), respectively. Hydrogen bonding contributes strongly, and van der Waals forces are not negligible.

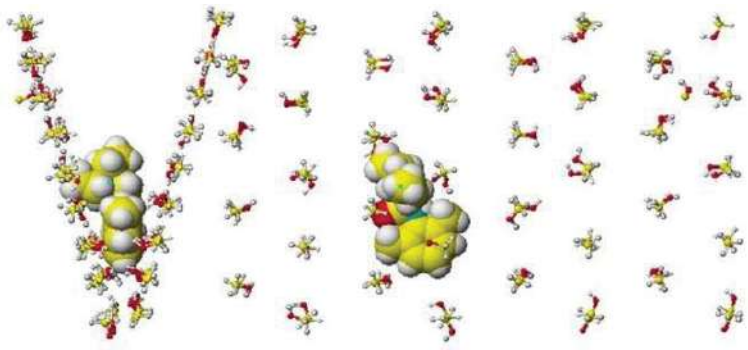


FIgure 5.53: Lidocaine and methanol phase.

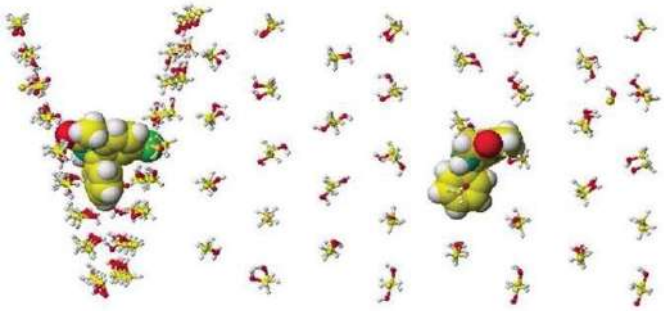


FIgure 5.54: Diazepam and methanol phase.

Here, log *P* values are used for relative comparison; they are for molecular-form compounds, not ionized-form compounds. The log *P* used for ionized-form comparisons does not reflect the reflectivity. A program that predicts retention time in reversed-phase liquid chromatography has a fundamental error because it defines the log *P* values of ionized-form compounds as zero.

This computational chemistry program cannot handle an absolute solvation conformation; however, MI energy values calculated using the solvent phase improve the relationship between measured log *k* values and calculated molecular interaction energy values. The following chapters demonstrate several examples.

5.7. Gas chromatography 1. Methyl-silicone phase and the selectivity

In gas chromatography, an inert gas serves as the mobile phase (carrier) and delivers gaseous molecules (analytes) to the column exit. The moving speed is delayed by contact between the analytes and a liquid phase (stationary phase). Retention time depends on the analyte (solute) volatility and the interactions between the analyte and the stationary phase.

The methyl silicone phase is inert; therefore, analyte interactions are van der Waals forces. The elution order depends on the volatility ofthe analytes. Conversely, analyte boiling points can be predicted from retention time using a calibration curve of standard compounds. A model methyl silicone phase is constructed using methyl silicone fibers. Figure 5.55 shows the chemical structure of polymethyl silicone.

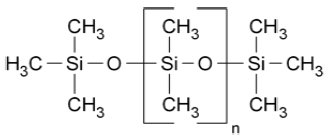


FIgure 5.55: Chemical structure of poly-methylsilicone.

Increasing **n** produces an arc structure of methyl silicone fiber shown in Figure 5.56a. Optimization using the MM2 program is shown in Figure 5.56b. These structures can produce a polymer phase; however, the prepared polymer phase does not reflect the methyl silicone phase's properties because analytes can contact polar oxygen atoms. Analytes should contact the methyl group; therefore, a methyl-covered phase is constructed based on a previously constructed PAH phase.

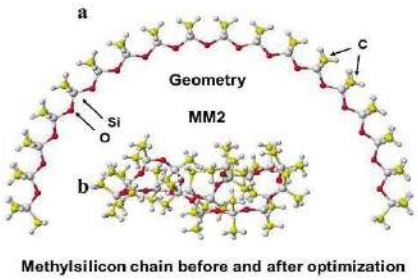


FIgure 5.56: Preparation of methylsilicone phase.

Connect 6 sp2 silicon atoms to form a ring, then fix the ring shape using Ring in the pull-down menu. Then, increasing the number of rings makes a phase whose size depends on the molecular size of the analytes. Figure 5.57 shows the example.

The structure in Figure 5.57a was prepared using sp^2 silicon as a combined four-block system; therefore, the surface is not flat, and the connected lines appear as a step. Figure 5.57b was prepared using sp3 silicon and optimized, and this approach produced a flat model phase. The optimized structure using the MM2 program exhibits a twisted shape, as shown in Figure 5.58a. Changing sp^2 silicon to sp^3 silicon in Figure 5.56, then optimizing the structure using the MM2 program, produces a flat phase shown in Figure 5.57.

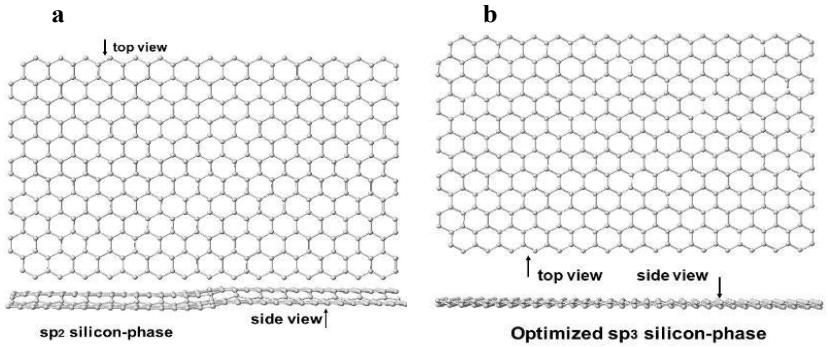


FIgure 5.57: a and b prepared using sp2 and sp3 silicon. 3b was optimized using the MM2program..

To prepare a flat silicone phase, duplicate the model phase of Figure 5.57; then, move one phase to the parallel position to make a double layer. Then, connect an even number of silicone layers between the upper and lower flat phases. Optimizing the the connected double layer produces a flat silicone phase. The intermediate structure is shown in Figure 5.58b.

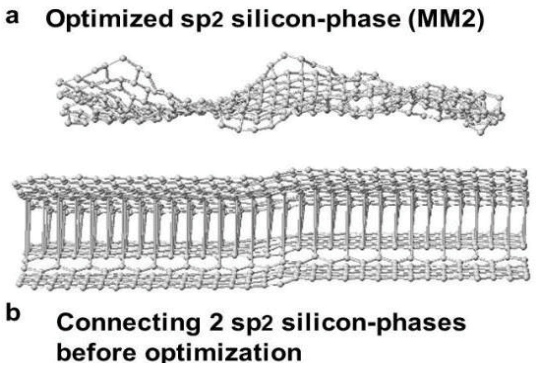


FIgure 5.58: Preparation of model silicone phase.

Add hydrogen to the optimized double-layer silicone phase; then, change the hydrogen to sp^3carbon. Finally, construct a flat methyl-silicone phase. This phase can be used to obtain molecular interaction energy values by docking with analytes. The least necessary as a model phase is the flatness, and the shape affects the docked energy values. The optimized model methyl-silicone phase using the MM2 program produced the arc structure shown in Figure 5.59a. This structure cannot be used for further study because the contact surface with analytes depends on the analyte's shape. How to build a flat phase? One approach is to lock the lower silicone layer and erase it after optimizing the structure using the MM2 program. The optimized structure is shown in Figure 5.59b, where the methyl-silicone groups are highly condensed. The 2nd approach is to cut the lower silicone phase and lower the location, then optimize the structure. The optimized structure is shown in Figure 5.59c, where the center of the methyl-silicone phase is flat, and the edge is bent. The 3rd method, as shown in Figure 5.54/3b, connects an even number of silicone upper and lower phases. Change the hydrogen of the upper phase to the methyl group. Then, optimize the structure using the MM2 program. The optimized structure is shown in Figure 5.59d, which is slightly bent due to the different sizes of the methyl group and a silicon atom. Reference 2 used the last structure, where the silicone phase was locked in advance of optimization.

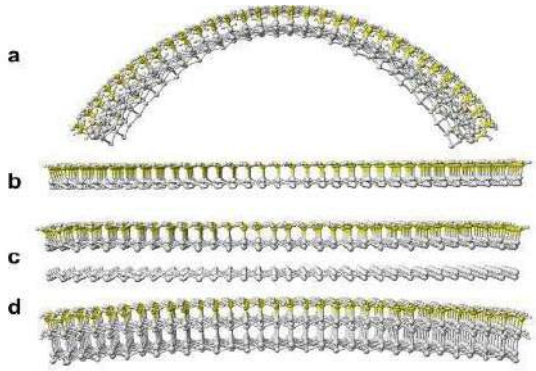


Figure 5.59: Preparation of model methylsilicone phase.

Chapter 5 describes the preparation methods of model phases. Quantitative analysis of chromatographic retention time requires model molecular interaction phases. Constructing stationary phases is complicated because the structures of coated liquids are unknown and generally a combination of solvents and ionic molecules. The thickness of the coated liquid depends on the surface material's properties and the mixture ratio of components. The model phases are prepared without adsorbed liquid. The previous book described the details of the gas chromatographic phases.

References

1. T. Hanai, HPLC, A Practical Guide, Royal Society of Chemistry, 1999, Cambridge, UK, (ISBN: 0-85404-515-5, 1-134.
2. T. Hanai, Quantitative *in silico* chromatography: Computational modeling of molecular interactions, Royal Society of Chemistry, 2014 May, Cambridge, UK, (ISBN: 978-1-84973-991-7), 1-338
3. E. Kovats, 15th Int. Symp. Chromatgr. 1984, Nurnberg, Oct. 1-5.
4. T. Hanai, Analysis of the mechanism of retention on graphitic carbon by a computational chemical method. J. Chromatogr. A 2004, **1030**(1-2), 13-16.
5. T. Hanai, Quantitative *in silico* analysis of the specificity of graphitized (graphitic) carbons, Advances in Chromatography, 2011, **49**, 257-290.
6. T. Hanai, New developments in liquid-chromatographic stationary phases. Advances in Chromatography (New York) 2000, **40l**, 315-357.
7. T. Hanai, Quantitative explanation of retention mechanisms in reversed-phase mode liquid chromatography, and utilization of typical reversed-phase liquid chromatography for drug discovery, Current Chromatography, 2019, **6**, 52-64. DOI: 10.2174/2213240606666190619120733.
8. T. Hanai, Fundamental Properties of Packing Materials for Liquid Chromatography, Separation, 6(2), 2019-01-05, 1-20, DOI: 10.3390/separations6010002, www.mdpi.com/journal/separations
9. T. Hanai, Quantitative explanation of basic compound retention mechanisms in reversed-phase mode liquid chromatography, Separations, 2020, **7**, 61 (30 October 2020), doi:10.20977/preprints 202009.007.v1

Chapter 6 Quantitative explanation of retention mechanisms and solvent effects

6.1 Retention mechanisms in normal-phase liquid chromatography

Normal-phase liquid chromatography is used to be called adsorption liquid chromatography, and the appearance of reversed-phase liquid chromatography changed the name to balance the naming. More precisely, it should be called non-aqueous liquid chromatography, without water as a component of the eluent. Actually, a small amount of aqueous ammonia or formic acid is added to the eluent. Generally, silica gel and alumina are used as adsorbents. Basically, water is not a component of the eluent. The primary retention mechanism is hydrogen bonding; therefore, analytes are retained by hydrogen-bonding capability [1].

Silica gel is a polymer of silicon dioxide and constructing a model flat layer of such a polymer is complicated. Silica gel retains analytes through hydrogen bonding with silanol groups on its surface. Therefore, follow the approach used to construct a gas chromatographic phase. First, draw a six-ring using sp^2 silicon, increase the number of rings, and fix the shape flat using **Geometry**. (Figure 6.1a) Next, change the sp^2 silicon to sp^3 silicon, then, optimize the structure. Now, the flat silicon phase is ready for further modification. Add hydrogen using **Valence** on the top phase (Figure 6.1b). Change the hydrogen to sp^2 oxygen and add hydrogen using **Valence**. This yields a silanol-phase, as shown in Figure 6.1c. In addition, you can prepare an amino-phase using the same method. Using nitrogen instead of hydrogen, Figure 6.1d shows the structure of an amino phase.

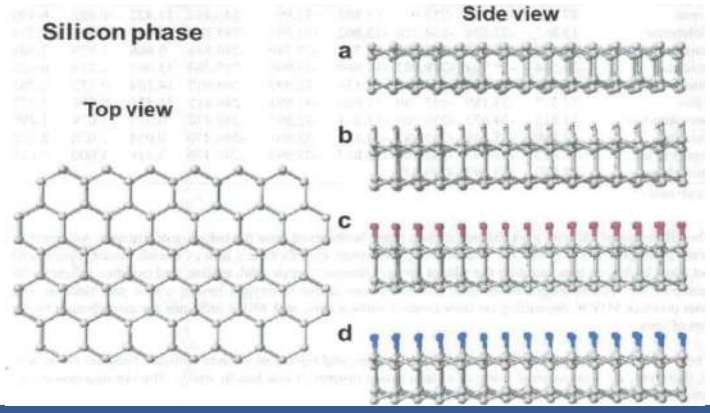


FIgure 6.1: A model phase was constructed using silicon. a: side view; b: addition of hydrogen (white) at the upper position; c: conversion from hydrogen to oxygen (red, black); d: conversion from hydrogen to nitrogen (blue, dark gray).

The size of a silanol phase depends on the size of the analytes. Figure 6.2 shows the optimized complex structures with various analytes used for 32PAH. Table 6.1 summarizes the calculated energy values of the complexes (HB, ES, VW) and the molecular interaction (MI) energy values (MIHB, MIES, MIVW).

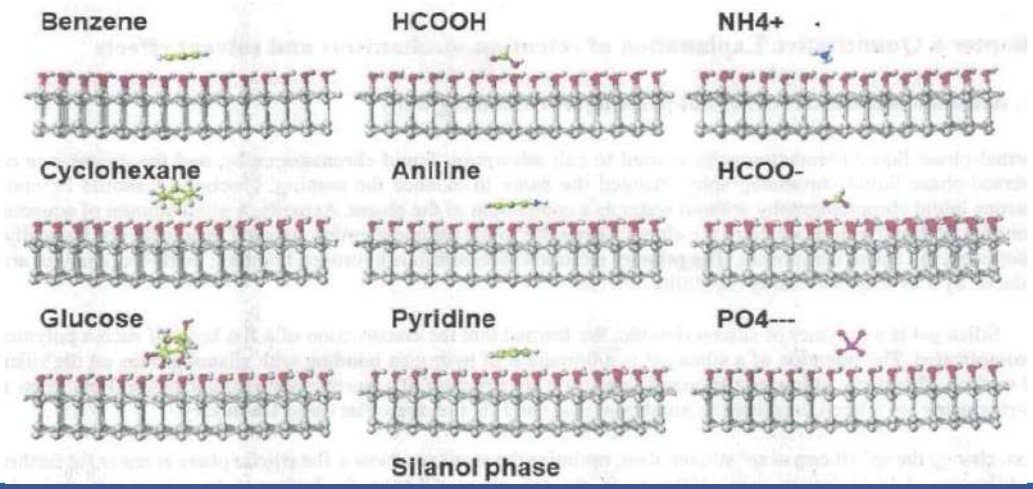


FIgure 6.2: Retention of standard compounds on the model silanol-phase

Table 6.1: Properties of standard compounds and the molecular interaction energy values.

Analyte	HB	ES	VW	hb-13.802	es-32.993	vw-249.470	MIHB	MIES	MIVW
Benzene	-27.624	-32.911	-252.954	-13.802	-32.993	-246.464	13.822	-0.082	6.49
Cyclohexane	-13.863	-33.036	-254.35	-13.802	-32.993	-245.836	0.051	0.043	8.514
Glucose	-27.402	-27.675	-252.352	-17.735	-24.746	-244.848	9.666	2.929	7.504
Formic acid	-29.534	-39.987	-249.987	-14.469	-37.99	-249.364	15.065	1.754	0.623
Aniline	-29.3	-32.841	-253.316	-15.136	-32.993	-246.053	14.164	-0.152	7.263
Pyridine	-25.373	-33.189	-252.389	-13.802	-32.993	-246.612	11.571	0.196	5.777
Ammonium ion	-13.812	-34.072	-250.969	-13.802	-32.993	-249.47	0.01	1.079	1.499
Formic ion	-13.86	-35.619	-251.987	-13.802	-32.993	-249.47	0.058	2.626	2.517
Phosphoric ion	-17.013	-35.993	-252.508	-13.802	-32.993	-249.47	3.211	3	3.038
Silanol-phase	-13.802	-32.993	-249.47						

Unit: kcal. mol^{-1}

The difference in MI with a graphitized carbon phase is observed from the behavior of benzene. An aromatic ring forms hydrogen bonding with the silanol group. However, cyclohexane's lack of double bonds (π-electrons) does not show hydrogen bonding with the silanol group. Glucose, formic acid, aniline, and pyridine interact via hydrogen bonding. Hydrogen bonding in the phosphate ions arises from oxygen lone pairs; even ions produce MIVW depending on their contact surface area, and MIES indicates their contribution to retention

The simple silanol phase has condensed silanol groups and rejects analyte entrance between the silanol groups; therefore, the fundamental study of silanol group properties can be handled easily. The construction of the actual model silica gel is explained later. Hydrophilic interaction liquid chromatography (HILIC) is a keyword to search related publications. Hydrophilic interaction includes all interactions except hydrophobic interactions, combining hydrogen bonding, dipole-dipole, π−π interactions, and ion-ion interactions. Therefore, it is called aqueous normal-phase liquid chromatography. The interaction is obtained as MIHB and HIES by in silico analysis.

How does it differ from traditional normal-phase liquid chromatography? In general, HILIC uses packing materials with polar surface groups. Silica gel can be used,, but eluents containing water are unstable and unsuitable for this purpose. Chemically bonded silica gels and organic polymer gels are generally used for HILIC. Adding a small amount of water to the eluent is a specific method. Historically, the origin of HILIC is traced to a chromatography developed by Samuelson, who analyzed saccharides using an ion-exchange resin and aqueous ethyl alcohol. Therefore, an amino phase is prepared from the silanol phase. Replace oxygen with nitrogen, and use Valence to add hydrogen. Figure 6.1 shows the process. The optimized structures of complexes are shown in Figure 6.3.

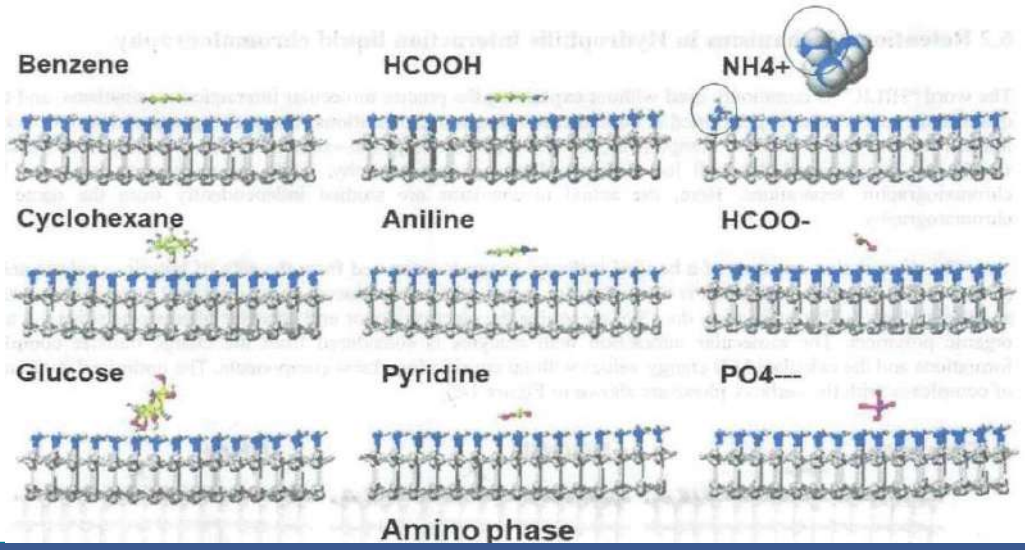


Figure 6.3: Retention of standard compounds on the amino-phase.

Table 6.2 summarizes the calculated data. The retention behavior of these analytes is similar to that obtained with the silanol phase, and only ammonium ions demonstrated a different phenomenon. The ammonium ion is located at the center of the amino phase; however, it moved to the corner and was retained by electrostatic interaction, as indicated by a circle in Figure 6.3.

The amino-phase is basic, and the silanol phase is acidic. These differences can be understood from the relative MIHB values based on the interaction. The ammonium ion shows slightly more complex behavior, contacting the corner via electrostatic interaction. benzene. The MIHB energy indicates that the hydrogen bonding strength of aniline and pyridine is less than that observed using the silanol phase; inversely, the hydrogen bonding strength of formic acid is more potent with the silanol phase. Acidic ions interact with the amino group by electrostatic interactions

Table 6.2: Retention of standard compounds on the amino-phase.

Analyte	HB	ES	VW	hb-29.027	es-1.269	vw-272.847	MIHB	MIES	MIVW
Benzene	-36.915	-1.135	-276.416	-29.027	-1.269	-269.841	7.888	-0.134	6.575
Cyclohexane	-29.153	-1.275	-278.375	-29.027	-1.269	-269.213	0.126	0.006	9.162
Glucose	-53.785	5.383	-273.847	-32.961	6.978	-268.225	20.834	1.593	5.622
Formic acid	-33.792	-7.219	-274.855	-29.694	-6.266	-272.741	4.098	0.953	2.114
Aniline	-39.082	-1.227	-276.465	-30.361	-1.269	-269.43	8.721	-0.042	7.035
Pyridine	-35.397	-1.19	-276.027	-29.027	-1.269	-269.989	6.37	0.079	6.185
Ammonium ion	-29.105	-4.229	-274.081	-29.027	-1.269	-272.847	0.078	2.96	1.234
Formic ion	-29.127	-1.362	-275.177	-29.027	-1.269	-272.847	0.1	3.093	2.33
Phosphoric ion	-31.337	-8.804	-275.968	-29.027	-1.269	-272.847	2.31	7.535	3.121
Amino-phase	-29.027	-1.269	-272.847						

Unit: kcal. mol^{-1}

6.2 Retention mechanisms in hydrophilic interaction liquid chromatography

The term " HILIC" is commonly used without explaining the precise molecular interaction mechanism, and the quantitative explanation is performed under limited chromatographic conditions. The packing material surface is not ionized without buffer-solution components, acid, and alkali except ion exchangers; ion-exchange mechanisms should not be observed. We call it ion-exchange liquid chromatography, while ion exchangers are used for chromatographic separations. Here, we study the mechanisms independently of the chromatography. We estimate the dissociation constant of a bonded carboxyl group from the p*K*a of butyric – valeric acids (4.83–4.89). The carboxyl group is in the molecular form in acidic eluents and the ionized form in neutral and basic eluents. Molecular interactions with the analyte are considered based on charge-transfer complex formation and calculated MI energy values, without considering eluent components. Figure 6.4 shows the optimized structures of complexes with the carboxy-phase.

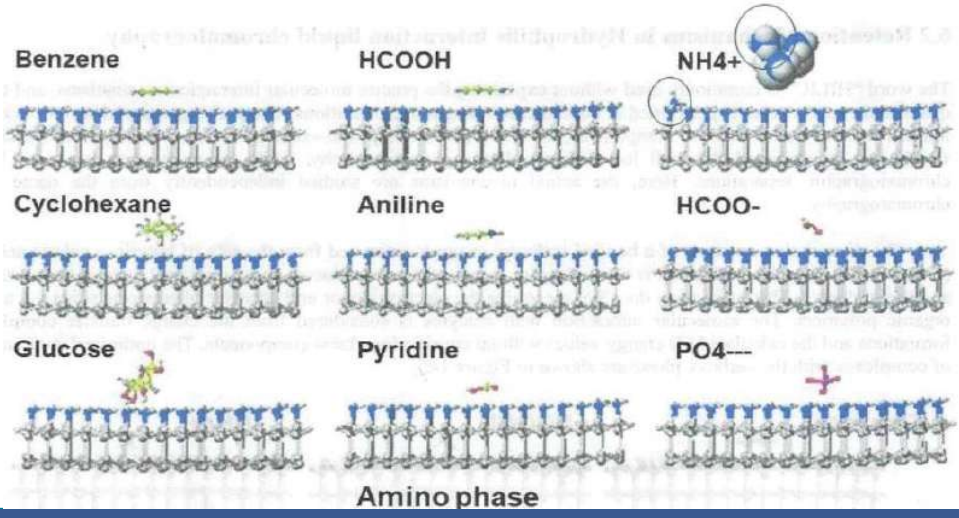


Figure 6.4: Retention of standard compounds on a carboxy-phase.

The ionized formic acid was repelled to 5.52Å position, and the phosphoric ion was located at the edge and held by hydrogen bonding. MIHB contributed to the retention of benzene, glucose, aniline, pyridine, and formic acid, and MIES contributed to the retention of phosphoric and ammonium ions. These results explain that various analytes are retained in the carboxy-phase without an ionic eluent. The phenomenon is the retention mechanism of known ion-exchange liquid chromatography.

Table 6.3: Selectivity of carboxy-phase.

Analyte	FS	HB	ES	VW	MIFS	MIHB	MIES	MIVW
Benzene	-869.4113	-269.795	-308.892	-271.82	19.636	13.775	0.554	5.557
Cyclohexane	-843.5121	-256.384	-308.365	-273.609	8.3722	0.364	0.027	7.974
Glucose	-868.2922	-305.172	-301.073	-265.045	41.9606	45.218	0.982	0.398
Formic acid	-867.6285	-275.551	-315.857	-268.488	20.1456	18.864	2.522	-0.675
Aniline	-868.3549	-271.904	-308.488	-272.452	20.5352	14.55	0.15	6.6
Pyridine	-863.32	-267.872	-308.85	-271.452	17.2748	11.852	0.512	5.041
Ammonium ion	-845.726	-256.82	-312.165	-270.397	5.6525	0.8	3.827	1.128
Formic ion	-841.0073	-255.78	-307.601	-269.577	-0.631	-0.24	-0.737	0.308
Phosphoric ion	-845.0736	-281.468	-316.268	-269.875	82.159	25.448	7.93	0.606
Carboxy-phase	-841.6983	-256.02	-308.338	-269.269				

Unit: kcal. mol^{-1}

While water is present in the eluent, the carboxy group may ionize; therefore, we optimized complexes of the ionized carboxy-phase with various analytes, and the conformations are shown in Figure 6.5. Table 6.4 summarizes the molecular interaction energy values.

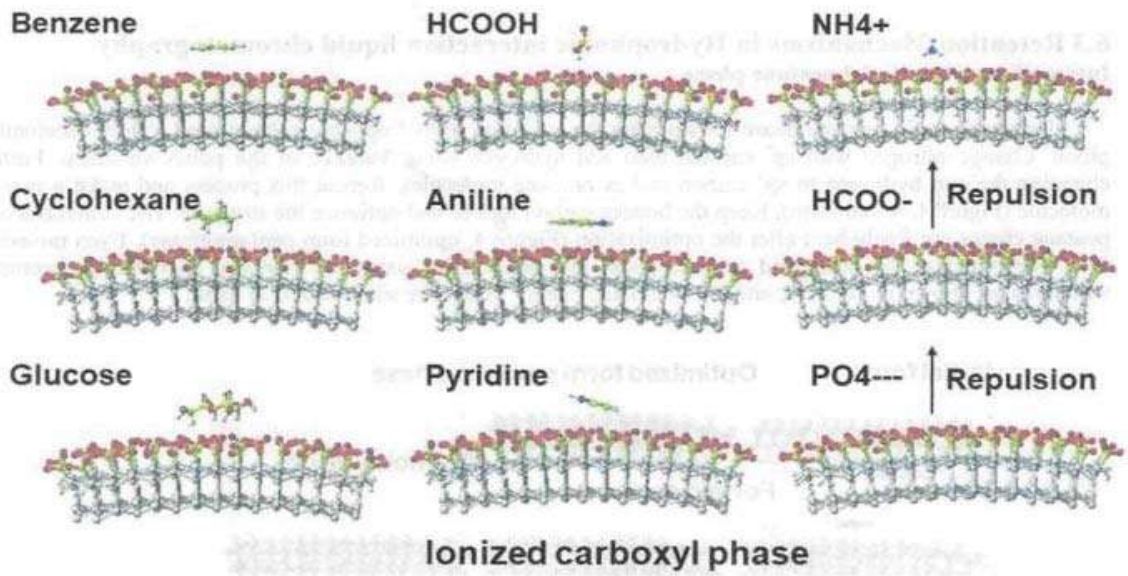


Figure 6.5: Retention of standard compounds on an ionized carboxy-phase.

The anions of formic and phosphoric ions was repulsed and disappeared from the computer screen. In actual liquid chromatography, these ions are eluted before the solvent peak by ion exclusion. In reverse, a cation-like ammonium ion is tightly held *via* MIES. Hydrogen bonding generally does not contribute to the ionized carboxy-phase. Glucose retention seemed strong; however, this experiment describes only the difference in retention mechanisms, not the difference in retention time. Glucose retention time depends on water concentration in the eluent; glucose is retained in a highly concentrated organic-modifier eluent, and benzene elutes quickly. This retention mechanism was applied for the liquid chromatography of saccharides, where highly concentrated ethylalcohol was used before and uses acetonitrile instead of ethylalcohol at present. This type of experiment clarifies vague retention mechanisms.

Table 6.4: Selectivity of ionized carboxy-phase.

Analyte	FS	HB	ES	VW	MIFS	MIHB	MIES	MIVW
Benzene	788.9048	0	841.569	-297.098	6.0087	0	-1.171	6.263
Cyclohexane	801.5345	0	841.59	-295.615	6.0144	0	-1.192	6.408
Glucose	798.3	-3.542	840.088	-297.969	18.0572	-0.392	8.557	8.75
Formic acid	783.0932	-0.654	827.086	-295.863	12.1127	-0.013	8.315	2.128
Aniline	788.1506	-1.336	841.59	-297.476	6.7185	0.002	-1.192	7.052
Pyridine	790.3815	0	840.515	-296.863	6.2621	0	-0.117	5.88
Ammonium ion	751.719	0	796.06	-295.333	50.8963	0	-3.235	0.389
Formic ion	803.1933	0	843.633	-294.23	-2.1428	0	-3.235	0.389
Phosphoric ion	838.8274	0	846.9	-293.717	40.9468	0	-6.502	-0.124
Ionized carboxy-phase	800.9905	0	840.398	-293.841				

Unit: kcal. mol^{-1}

6.3 Retention mechanisms in hydrophobic interaction chromatography

To prepare a pentane-phase for studying the solvation of a hydrophobic solvent, use a model acetonitrile-phase. Change nitrogen to sp^3 carbon, then, add hydrogen using Valence of the pull-down menu. Further, change the terminal hydrogen to sp^3 carbon to make a propane molecule. Repeat this process and make a pentane molecule (Figure 6.6, initial form). Keep the bottom carbon locked and optimize the structure. The straightforward pentane chains bend freely after optimization (Figure 6.6, optimized form, pentane-phase). Even molecules love freedom. Use the optimized pentane-phase and calculate MI using the standard analyte. Figure 6.6 shows the complex structures, and Table 6.5 summarizes the calculated energy values.

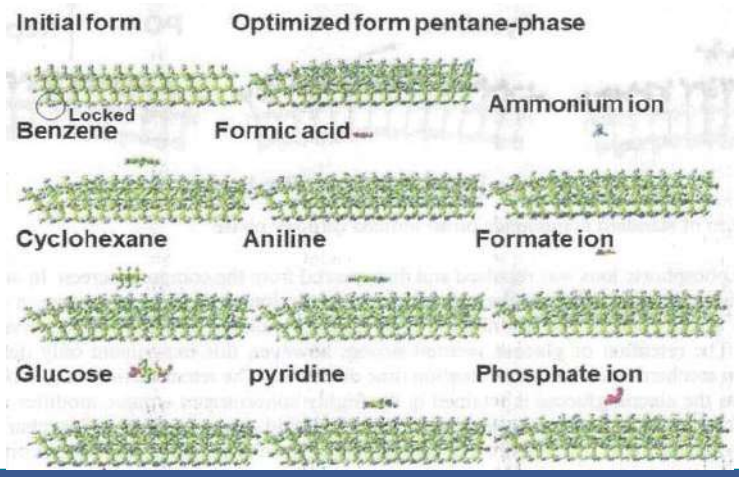


Figure 6.6: Retention of standard compounds on a penyl-phase.

Table 6.5: Selectivity of pentyl-phase.

Analyte	FS	HB	ES	VW	MIFS	MIHB	MIES	MIVW
Benzene	293.2954	0	0	-21.091	7.1674	0	0	7.056
Cyclohexane	314.7039	0	0	-13.816	0.3943	0	0	0.409
Glucose	323.4453	-3.934	8.248	-12.888	0.4612	0	-0.001	0.469
Formic acid	302.5669	-0.667	-4.997	-17.166	0.1883	0	0	0.231
Aniline	294.023	-1.334	0	-21.938	8.3954	0	0	8.314
Pyridine	297.3733	0	0	-20.873	8.3954	0	0	6.69
Ammonium ion	310.0388	0	0	-17.174	0.1258	0	0	0.133
Formic ion	308.4452	0	0	-17.204	0.1548	0	0	0.163
Phosphoric ion	325.124	0	0	-21.003	62.1995	0	0	3.962
Pentyl-phase	308.5398	0	0	-17.041				

Unit: kcal. mol^{-1}

Polar glucose, formic acid and ions do not come into contact with the non-polar pentane phase. However, a strong basic phosphate ion contacts the non-polar phase via van der Waals forces based on the MIVW value. This selective solvation of the model pentane phase helps study the specificity of reversed-phase in later chapters.

6.4 Retention mechanisms in ion-exchange liquid chromatography

The propylamine ~ heptylamine dissociation constant is 10.60 ~ 10.67; therefore, hexylamine is considered the ionic form in aqueous eluents. Hexylamine is the ionized form in eluents containing buffer components. In physiological conditions, the p*K*a of lysine is 10.69, and that of arginine is 12.48. We quantitatively analyzed the retention mechanism of various analytes on the ionized amino and guanidino phases using MI energy values. The experimental method is the same as previously performed.

The ammonium ion, the same cation as the amino phase, was repelled and disappeared from the screen. The MIHB values indicate that hydrogen bonding does not contribute to retention, but electrostatic interactions (MIES) do. The molecular form of formic acid is retained, and MI energy explains the mechanism. Ionization indicates the contribution of MIES, but it does not directly relate to the strength of molecular interactions. MIES arises from both Lewis acid-base (dipole-dipole) and ion-ion interactions. The higher MIES value indicates ion-ion interactions. A typical example is the behavior of phosphate ions. The calculated MIES demonstrates the electron-density differences and supports charge transfer, dipole-dipole, π-π, and ion-ion interactions, and different scientific groups use these words. We use only electrostatic interactions for *in silico* chromatography. Figure 6.7 shows the results, and Table 6.6 summarizes them.

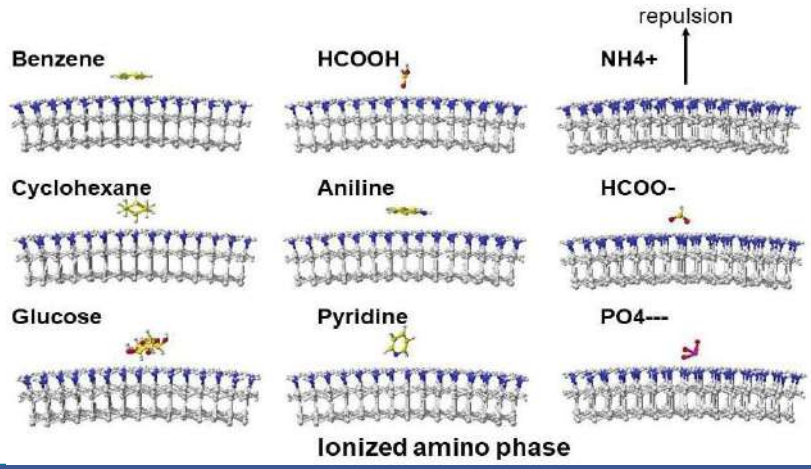


FIgure 6.7: Retention of standard compounds on an ionized amino-phase.

Table 6.6: Selectivity of an ionized amino-phase.

Analyte	FS	HB	ES	VW	MIFS	MIHB	MIES	MIVW
Benzene	701.5595	0	893.778	-260.256	7.2379	0	-0.724	7.44
Cyclohexane	714.9636	0	893.602	-260.916	8.4692	0	-0.548	8.725
Glucose	710.2064	-3.599	888.72	-260.794	22.0347	-0.335	12.581	9.591
Formic acid	696.8772	-0.651	876.973	-258.202	14.2126	-0.016	11.084	2.483
Aniline	702.7897	-1.335	893.414	-260.614	7.9633	0.001	-0.36	8.206
Pyridine	705.072	0	890.878	-258.014	7.4555	0	2.176	5.047
Ammonium ion	719.8086	0	894.341	-255.82	-1.3094	0	-1.287	-0.005
Formic ion	650.9086	0	831.641	-258.178	66.0258	0	61.413	2.353
Phosphoric ion	586.2172	0	740.431	-258.691	209.4409	0	152.623	2.866
Ionized amino-phase	716.8744	0	893.054	-255.825				

Unit: kcal. mol^{-1}

The results for the guanidine phase are the same as for the ionized amino phase. The ammonium ion was repelled, the phosphate ion was tightly held by ion-ion interaction, and the ionized formic acid was also held. Figure 6.8 shows the results, and Table 6.7 summarizes the calculated energy values.

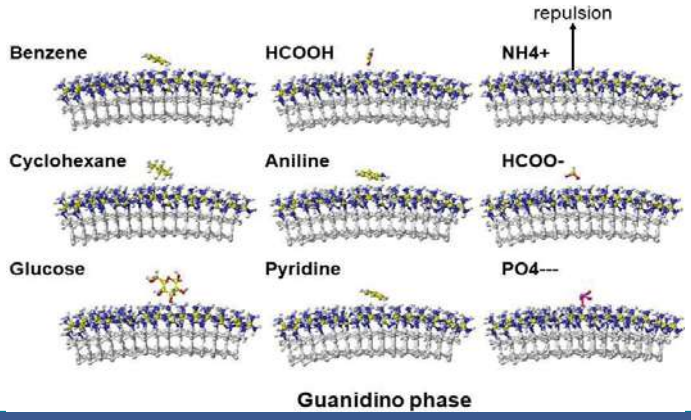


Figure 6.8: Retention of standard compounds on a guanidine-phase.

Table 6.7: Selectivity of a guanidine-phase.

Analyte	FS	HB	ES	VW	MIFS	MIHB	MIES	MIVW
Benzene	37.8387	-59.774	72.495	-291.968	13.135	8.241	-0.771	6.621
Cyclohexane	58.0552	-51.531	-71.996	-292.867	7.5539	-0.002	-0.272	8.148
Glucose	55.4601	-61.201	71.011	-287.837	19.9573	5.734	8.86	4.106
Formic acid	39.2259	-54.836	56.65	-289.836	14.247	2.636	10.077	1.589
Aniline	39.7228	-60.648	72.448	-292.082	13.2065	7.781	-0.724	7.146
Pyridine	43.2546	-58.603	72.801	-291.811	11.4492	7.07	-1.077	6.316
Ammonium ion	62.4207	-51.508	73.378	-288.382	-1.7452	-0.025	-1.654	0.029
Formic ion	4.8874	-52.062	21.302	-289.805	54.353	0.529	50.422	1.422
Phosphoric ion	-46.4059	-58.385	-38.078	-284.398	184.2403	6.852	109.802	-3.955
Guanidino-phase	59.0507	-51.533	71.724	-288.353				

Unit: kcal. mol^{-1}

The discussion using the data obtained for both the carboxy- and amino-phases clarifies the retention mechanism and can correctly write the chromatographic name. We can write reports precisely and transfer the results without doubt. The *in silico* analysis of chromatographic retention mechanisms using model phases permits the natural chromatographic phenomena. In chromatography, adsorption and desorption are repeated from the inlet to the outlet of columns. The next chapter studies desorption mechanisms using model solvent phases.

6.5. Selectivity of hydrophobic phases

A dimethyl-alkyl mono-chlorosilane-bonded phase was constructed as a model phase. The alkyl groups produced a tightly dense phase. Porous silica gels did not yield such a bonded-phase. However, we used such phases to analyze indirect interactions between an analyte and a model phase. The model hexyl-, phenylhexeyl-, and hexenyl-phases are shown in Figures 6.9A - C, where aniline contracted with these phases. The bottom groups were allowed to contact the analyte. We placed the analyte at a certain distance from the end of the bonded group. Thereafter, the pair of compounds was optimized to obtain a complex form, and the value of the molecular interaction (MI) energy was calculated.

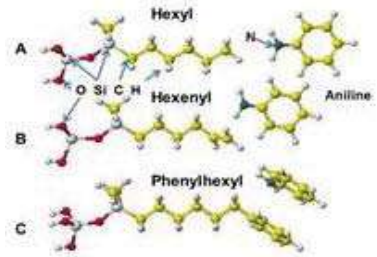


Figure 6.9: Model hexyl-, phenylhexyl-, and hexenyl-phases White small, large black ball, black ball, white, and black balls: hydrogen, carbon, oxygen, silicone and nitrogen .

The simple study used simple analytes and one alkyldimethylsilicone-bonded silicon trioxide. Table 6.8 summarizes the properties of the analytes.

Table 6.8: Properties of analytes.

Benzene	Hammett's	apc of group	apc of	apc of	apc of	log *P*	p*Ka*
Substitute	s constant	unit: au head atom	balance	*p*-hydrogen			
p-Amino	-0.57	0.18	H 0.255	0.041	0.159	1.03	4.69
p-Amino (I)	-	0.809	H 0.229	0.893	0.207	-	-
p-Hydroxy	-0.38	-0.081	H 0.305	0.245	0.164	1.54	10.02
p-Methyl	-0.14	0.066	H 0.107	0.092	0.158	2.59	-
Hydrogen	0	0.156	H 0.156	0	0.156	2.06	-
p-Fluoro	0.06	-0.198	F -0.198	0.365	0.167	2.28	-
p-Chloro	0.24	-0.051	Cl -0.051	0.214	0.163	2.83	-
p-Carboxy	0.44	-0.105	H 0.324	0.269	0.164	1.79	4.2
p-Carboxy (I)	-	-0.808	H -0.647	0.931	0.123	-	-

The retention order of these benzene derivatives in the reversed-phase mode liquid chromatography employing an octadecyl-bonded phase in 50% aqueous ethyl alcohol was benzoic acid (log P = 1.79) < phenol (log P = 1.54) < benzene (log P = 2.06) < chlorobenzene (log P = 2.81) < ethylbenzene (log P = 3.12). The different elution of benzoic acid and phenol may be due to ionization of benzoic acid in the aqueous eluent; ionization reduces hydrophobicity, and retention is weakened in reversed-phase liquid chromatography employing alkyl-bonded phases.

6.5.1. Selectivity of hexyl-phase: The atomic partial charge (apc) of the head of the bonded phase silica gel was negative except in ionized amino. However, that of the end hydrogen was positive. Table 6.9 shows the calculated apc of the head of the substituents.

Table 6.9: Atomic partial charge of head substitute of model hexyl bonded silica gels.

Substitute	apc au	substitute	apc au	substitute	apc au
Ionized amino	0.718	Vinyl	-0.061	Ionized carboxy	-0.888
Methyl	-0.005	Carboxy	-0.13		
Phenyl	-0.028	Amino	-0.138	apc unit: au	

No simple relation existed between the substituent apc value of the analyte and those of the model phases. The apc value of the molecular interaction between an analyte and a model bonded phase indicates the degree of contribution.

The aniline recognition of this model phase was also studied. We placed the amino or phenyl group of aniline against three model phases within a certain distance and obtained the MI energy values by optimizing the complex using a molecular mechanics program. The apc indicated that electron localization was obtained using the MOPAC PM5 program. The distance between the analyte and the model phase varies with MI strength. This distance indicates MI strength. The reference molecules were benzene, methylbenzene, chlorobenzene, phenol, and benzoic acid. The calculated MI energies were the hydrogen bonding (HB), electrostatic (ES), and van der Waals (VW) energy values. These individual energy values indicated the specificity of the MI mechanisms. The charge of apc values indicated the MI center and the strength of electron localization, as summarized in Table 6.10.

Table 6.10: Calculated properties of analytes with different model phase.

Analyte	MIHB	MIES	MIVW	apc	apc	Atomic distance
		Kcal mol^{-1}	au	au	A	
Hexyl-phase				**CH3**		**Atom or group**
Aniline	0	-0.011	0.766	-0.037	0.208 H	3
Aniline (I)	0	0.144	0.808	-0.069	0.840 NH3	3.5
Benzene	0	-0.026	0.985	-0.007	0.158 H	3
Methylbenzene	0.02	0.02	-2.155	-0.008	0.069 CH3	3.5

Chlorobenzene	0.001	-0.006	2.399	0	contact face ClBz	4
Phenol	0	-0.031	0.988	-0.009	0.166 H	3
Benzoic acid	0.005	-0.023	1.006	-0.012	0.166 H	3
Benzoic acid (I)	0	-0.189	0.675	0.059	-0.860 COO-=	3.5
Phenylhexyl-phase				Ph		
Aniline	0.292	-0.027	5.367	-0.06	Total	3.5
Aniline (I)	0	0.189	1.04	-0.108	0.844 NH3	3.5
Benzene	0	0.009	0.783	-0.076	0.156 H	3.5
Methylbenzene	0	0.014	1.116	-0.076	0.068 CH3	3.5
Chlorobenzene	0	-0.022	0.751	-0.074	-0.053 Cl	4.0
Phenol	6.922	0.085	2.723	-0.067	-0.084 OH	3.5
Benzoic acid	6.914	0.03	2.313	-0.062	-0.108 COOH	3.0
Benzoic acid (I)	0	-0.193	0.745	-0.04	-0.864 COO-	3.5
Hexenyl-phase				Vinyl		
Aniline	-0.056	-0.031	1.732	-0.051	0.267 H/NH2	3.5
Aniline (I)	0.001	0.169	3.319	-0.06	0.159 Ph	3.5
Benzene	0.002	-0.026	2.881	-0.051	0.000 Bz	3
Methylbenzene	0.001	-0.019	0.908	-0.058	0.071 CH3	4
Chlorobenzene	0.003	0.05	3.565	-0.058	0.056 Ph	4
Phenol	2.305	0.071	2.187	-0.055	-0.084 OH	3.5
Benzoic acid	2.324	-0.008	1.222	-0.055	-0.110 COOH	3.5
Benzoic acid (I)	0.001	-0.195	3.328	-0.061	-0.136 Ph	3.5
Apc of CH3, Ph, and Vinyl: apc of head atom of model phase: apc of atom or group: contact atom or group of analytes						

All analytes contacted the model hexyl phase via the VW force. Chlorobenzene, which exhibited strong electron localization, recognized the model hexyl phase at a longer distance (4 Å) than the others and showed a strong MI with VW energy of 2.4 kcal mol^{-1}. No specific indication of aniline retention was observed. The selectivity of the hexyl phase was unclear except for chlorobenzene. This indicates that retention in the alkyl phase is not selective but is based on analyte hydrophobicity.

The phenylhexyl-phase is expected to be the selective bonded phase in an aqueous eluent and demonstrated HB capability. The hydrogen of the phenol hydroxyl, benzoic acid carboxyl, and aniline directly contacted the phenyl ring of the model phenylhexyl- phase. The ionized aniline showed slight ES interaction, and the VW interaction force was significant compared with the others. The chloro group of chlorobenzene showed similar properties to those of the others. The chloro group of chlorobenzene, which possessed similar properties like the phenyl group did not support the strong VW interaction. The behavior of the phenol and benzoic acid was similar but different from that of aniline. The phenylhexyl-phase should maintain the retention with HB in a non-aqueous and highly concentrated organic modifier eluent. The contribution of the ES interaction was minimal.

The hexenyl-phase was also expected to demonstrate selectivity because of the double bond. The HB contribution was insignificant, as observed in the phenylhexyl-phase, but its contribution of VW force was greater than those of the others. In particular, the behavior with ionized aniline was specific compared with the others. These results suggested the phase selectivity for aniline.

6.5.2. Selectivity of phenylhexyl-phase: The relation between MIVW calculated MIVW calculated using a model pentyl-phase and log *k* values measured using a pentyl-phase [**1]** indicated that MIVW of PAHs was larger than that of alkylbenzene (AlBz) even though the log *k* values of AlBz were larger than those of PAHs was larger than that of as shown in the following equations. The difference in the slopes of these equations indicated the selectivity of the pentyl- phase. The slope for PAHs was about twice that for AlBz. The results indicated that alkyl compounds are retained more strongly in the pentyl-phase than PAHs. Fundamentally, increasing the contact surface area increases MIVW. The contribution of MIES and MIHB was negligible, with MIHB = 0 and MIES very small, as summarized in Table 6.11.

MIVW (AlBz) = 8.499 log k + 4.024, r = 0.997, n = 10,

MIVW (PAH) = 17.089 log k + 1.154, r = 0.985, n = 15.

In contrast, no such difference was observed for the phenylhexyl-phase. The relation between log k [1] and MIVW of PAHs and AlBzs was similar. The slopes were 11.375 and 10.632, respectively, as shown in the following equations. MIES and MIHB contributions were not observed, as summarized in Table 6.11.

MIVW (AlBz) = 11.375 log k + 3.393, r = 0.996, n = 10,

MIVW (PAH) = 10.632 log k + 1.154, r = 0.993, n = 16.

The selectivity of the pentyl-phase can be quantitatively explained by "like dissolves like". However, it is unknown why the phenylhexyl-phase lacks selectivity. If the π−π interaction is predominant in the phenyl-phase, the contribution of MIES should be observed, but is not observed. MIVW is generally related to the contact surface area; therefore, MIVW is related to the van der Waals volume (VWV). The relation between MIVW and VWV of AlBz and PAH for the pentyl-phase is given by the following equations.

MIVW (AlBz) = 0.061 (VWV) + 0.378, r = 0.996, n = 10,

MIVW (PAH) = 0.059 (VWV) + 0.263, r = 0.995, n = 16.

The slope difference was 3%. The contact surface area of ALBz and PAH did not differ significantly. On the other hand, these relations for the phenylhexyl-phase indicated selectivity. AlBz demonstrated a higher contact surface area than PAH. The difference in slope was 28% (0.075:0.084/AlBz:PAH) compared to a difference of 7% (11.375:10.632/AlBz:PAH) for the pentyl-phase. If π−π interaction contributes to the retention of the pheny-phase, MIVW of PAH should demonstrate a higher value than that of AlBz, even if the VWV is used as a standard value. PAH demonstrated less contact surface and showed similar retention to AlBz, but the contribution of MIES was negligible.

The log k values of PAH were smaller than those of AlBz, and this may be due to the solvation degree of the pentyl- and phenylhexyl-phases. This would be the case if PAH solubility in acetonitrile, the main eluent solvent, is higher than that of AlBz. Therefore, we calculated the molecular interaction energy values of PAH and AlBz using a model acetonitrile phase consisting of 72 molecules, a modification of the phase reported in reference [**2**]. We analyzed the solvation degree of these model phases.

We locked the methyl group of acetonitrile to prevent acetonitrile molecules from forming clusters. The silicone trioxide of the pentyl and phenylhexyl groups was locked to prevent contact **de** and acetonitrile. Because these bonded phases did not show a silanol effect, the solvent molecule should not interact with silicone oxide.

The MIES values for pentyl- and phenylhexyl-phases were 1.478 and 1.318 kcal min^{-1}, respectively, and the MIVW values of pentyl- and phenylhexyl-phases were 1.267 and 0.918 kcal mol^{-1}. respectively. The contributions of MIES and MIVW of the pentyl- and phenylhexyl-phases were similar. The pentyl group demonstrated stronger contact with the acetonitrile phase. This may support the weak retention of PAH in the pentyl-phase but not support the stronger retention of PAH in the phenylhexyl-phase.

One probable reason why MIES did not contribute to the retention is the contact formed between PAH and this model phenylhexyl-phase. PAH was located above the condensed phenyl groups, but no face-to-face contact was observed. Therefore, the effect of the localization of the phenyl-group electrons in the phenylhexyl-phase was studied. Figure 6.10 shows a phenylhexyl pair optimized with the MM2 program**,** where the phenyl groups are parallel; however, they twist after optimization with the MOAC program.

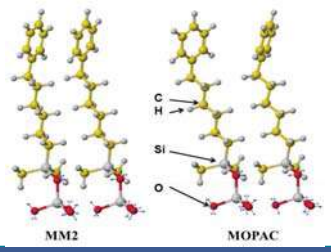


Figure 6.10: Optimized structure of a pair of phenylhexyl silicon oxides.

We increased the number of phenylhexyl groups and calculated the molecular interaction energy to study the effect of phenyl-group condensation on MIES. As a result, MIES contributed little to molecular interactions compared with MIVW. The degree of contribution of MIVW and MIES can be determined from the following equations, where x is the number of phenylhexyl groups.

MIES = $0.144x^2 - 0.658x + 0.315$, $r = 0.998$, x: 1-20

MIVW = $0.965x^2 + 88.861x - 87.428$, $r = 0.999$, x: 1-20.

The same analysis was achieved for the pentyl-phase. x is the number of penyl goups.

MIES = $0.147x^2 - 1.152x + 1.440$, $r = 0.999$, x: 1-19,

MIVW= $0.064x^2 + 6.369x - 8.163$, $r = 1.000$, x: 1-19.

While MIES did not play a significant role, MIVW made a major contribution to these molecular interactions, with the condensation of the phenyl groups not clearly affecting their electron localization. This result was also confirmed by MOPAC calculations of a pair of phenylhexyl and pentyl groups. The above equations demonstrated a higher correlation using the secondary equation. The linear equations provided lower correlation coefficients for MIES (48.10 and 426 for phenylhexyl and pentyl, respectively). The phenyl-phenyl interaction is also due to strong VW compared to ES force.

The electron localization for a pair of phenylhexyl groups was analyzed using MOPAC calculations. The atomic partial charge (apc, unit: au) of the two phenyl groups in Figure 6.10 is shown in Figure 6.11. Indeed, the apc of these phenyl groups was not homogeneous, and electron localization was clearly observed. Therefore, the phenyl group in the real-bonded phenyl-phase was neither condensed nor homogeneously distributed. Part of the phenyl group may interact with PAH molecules, and although MIES between one PAH molecule and the model phase is small, one-to-one interaction should be significant enough to allow strong retention of PAH on a phenyl phase.

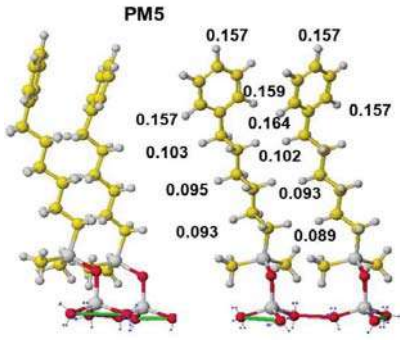


Figure 6.11: Atomic partial charge values of selected atoms..

Table 6.11: Calculated molecular interaction energy and measured log *k* values of alkylbenzene and polycyclic aromatic hydrocarbons on phenylhexyl- and pentyl-phases.

Chemical	Phenylhexyl-phase	Pentyl-phase					
		Log *k*	MIVW	MIES	log *k*	MIVW	MIES
Methylbenzene	0.326	7.614	-0.001	0.312	6.49	-0.001	
Ethylbenzene	0.428	7.952	0	0.417	7.629	-0.003	
Propylbenzene	0.538	9.539	0.001	0.537	8.857	-0.003	
Butylbenzene	0.653	10.304	0.001	0.653	9.809	-0.002	
Pentylbenzene	0.758	11.783	0	0.771	10.487	-0.002	
Hrexylbenzene	0.871	13.441	-0.002	0.894	11.655	-0.002	
Heptylbenzene	0.985	14.984	0.003	1.019	12.343	-0.01	
Octylbenzene	1.095	16.096	0.004	1.144	13.442	0	
Nonylbenzene	1.204	16.889	0.004	1.271	14.721	-0.002	
Nonylbenzene	1.204	16.889	0.004	1.271	14.721	-0.002	

Decylbenzene	1.313	18.281	0.005	1.4	16.357	-0.002	
Benzene	0.23	5.81	-0.001	0.209	5.45	-0.001	
Naphthalene	0.47	8.335	0	0.41	7.656	0.01	
Acenapohthylene	0.521	9.088	0.001	0.45	8.951	0.008	
Acenaphthene	0.616	9.752	0.003	-	9.293	0.001	
Fluorene	0.602	10.008	0	0.527	9.693	0.006	
Phenanthrene	0.655	10.42	0	0.538	10.322	0.001	
Anthracene	0.679	10.75	0.002	0.562	10.09	0.001	
Pyrene	0.778	10.848	0	0.614	11.653	0.002	
Fluoranthene	0.746	10.947	0.001	0.599	11.179	0.001	
Chrysene	0.869	13.076	0.001	0.673	12.672	0.001	
Benzo(a)anthracene	0.878	13.17	0.001	0.692	12.774	0.001	
Benzo(b)fluoranthene	0.97	13.504	-0.001	0.741	14.753	0.001	
Benzo(k)fluoranthene	0.982	14.113	0	0.741	14.093	0.001	
Dibenzo(a,h)anthracene	1.071	14.809	0.001	0.803	15.713	0.002	
Benzo(g,h,i)perylene	1.118	15.3	0	0.822	14.565	0.001	
Indeno(1,2,3-c,d)pyrene	1.102	14.822	-0.234	0.822	15.023	-0.237	
Eluent: 70% aq. Acetonitrile at 40°C [4]							

Quantitative *in silico* analysis of the chromatographic behavior of alkylbenzene and polycyclic hydrocarbons in reversed-phase liquid chromatography using phenylhexyl-bonded silica gel indicated that van der Waals forces were the major molecular interaction, with negligible electrostatic contributions. However, hydrogen bonding contributed weakly to the retention of acidic drugs. The selectivity of phenylhexyl-bonded silica gel was shown in the chromatography of compounds with similar hydrophobicity but different hydrogen-bonding and electrostatic interactions, such as the separation of tolbutamide and tolazamide. Separating these compounds was difficult with alkyl-bonded silica gels, even with an octadecyl-bonded silica gel. Actual bonded phases showed an island structure; therefore, the space between ligands should demonstrate more stereoselectivity for compounds such as acidic drugs. However, although this expected model phase cannot be constructed using *in silico* analysis, a general rule of retention mechanism can be defined using ligand-saturated model phases.

The measured log k_s of 15 basic drugs using a pentyl-bonded silica gel in pH10 eluent were correlated to those measured using an octyl-bonded phase with r = 0.998 (n = 15). These pentyl- and octyl-bonded silica gels show no selectivity, and the octyl-bonded silica gel has a higher retention capacity than the pentyl-bonded silica gel. The retention capacity of the pentyl-bonded silica gel is about 91% of the octyl-bonded silica gel.

The correlation coefficient of log k values and MIVW calculated using the octyl-phase model was 0.760 (n = 15). Adding MIES, calculated using the methanol-phase model, to the MIVW improved the r value to 0.891 (n = 15). Eliminating theophylline, whose log k value was very small (log k -1.644), improved these r values to 0.812 and 0.933 (n = 14).

The correlation coefficient between log k values and MIVW calculated using the pentyl-phase model was 0.677 (n = 15). Adding MIES calculated using the methanol-phase model to MIVW improved the r value to 0.702 (n = 15). Eliminating theophylline, whose log value was very small (log k =- 1.644), improved these r values to 0.931 and 0.933 (n = 14).

The chemical stability of the pentyl-bonded silica gel is equivalent to that of the octyl-bonded silica gel. The chemically stable pentyl-bonded silica gel requires less organic modifier. That is, it is an environmentally friendly way to use such a stable bonded-phase silica gel. We studied feasibility by comparing acidic drug log k values measured using octyl-bonded silica with calculated MIVW values using the model pentyl-phase. The r value between log k and MIVW values was 0.602, and adding MIES values calculated using the methanol phase improved it to 0.916 (n = 19). Eliminating the mefenamic acid value improved the r value to 0.645 and 0.953 (n = 18). The results were the same as those calculated using MIVW values calculated using the octyl-phase model. However, a large molecule can be partly covered by longer alkyl groups; this may cause poor correlation. Such a model pentyl-phase provides an answer within a short hour and supports further discussion. The log k value of basic drugs measured in a pH 10.0 eluent does not guarantee whether we

are discussing chromatographic behavior of the molecular form. Generally, basic drugs have dual ionic groups; therefore, the actual molecular form at pH 10.0 is unclear. The log *k* value at pH 13.0 is necessary to improve the theoretical analysis of chromatographic behavior

Various packing materials with quantitatively known retention capability permit building a quick separation system using a multi-column switching method with a single eluent instead of gradient elution methods. The multi-column and single-eluent systems provide fast analysis with a stable baseline. A highly sensitive electrochemical detector can be applied, such as for chromatography of guanidyl compounds and catecholamine-related compounds. These log *k* values were measured using pentyl- and octyl-bonded silica gel columns. The eluent was 50 % methanol containing 50 mM sodium phosphate (pH 2 – 10) at 40 °C.

6.6. Specificities of fluorocarbon-bonded phases

Florine was produced from fluorite, and the fluorite might be used to prepare a specific tea bowl "YONBA TENMOKU CHAWAN (extremely rare pottery for tea ceremony)". Synthesized organic compounds containing fluorine demonstrate thermal stability. One example is Teflon® (tetrafluoroethylenepolymer).Fluorine is a member of the halogen group, but it shows specific properties; the fluoro group shows properties like the methoxy group but not the chloro group. Fluorine tightens the chemical structure of fluorine compounds, making them chemically stable. Various fluorine-containing group-bonded silica gels were synthesized, and their specificities were reviewed [3]. However, the qualitative explanation of these bonded-phase silica gels was difficult due to the lack of fundamental properties of these packing materials, such as actual surface area, bonding density, chemical stability, and inertness related to silanol activity. We need chemically stable. And similar bonded-density bonded-phase silica gels from pure silica gels. We can only describe the relative selectivity qualitatively. The following explanation is based on data reported and demonstrated using hydrocarbon- and fluorocarbon-bonded silica gel in the same chromatographic conditions. The bonded phases are believed to be suitable for fluorine-containing compounds. Fluorinated compounds differ from related hydrocarbons. Figure 6.12A shows the structure of fluoropentane. The atomic partial charge (apc) indicates the difference from hydrocarbon pentane (Figure 6.**12**). Fluorine is negatively charged, and carbon is positively charged. The electron localization is different from that of hydrocarbon pentane, where the carbon is negatively charged, and hydrogen is positively charged.

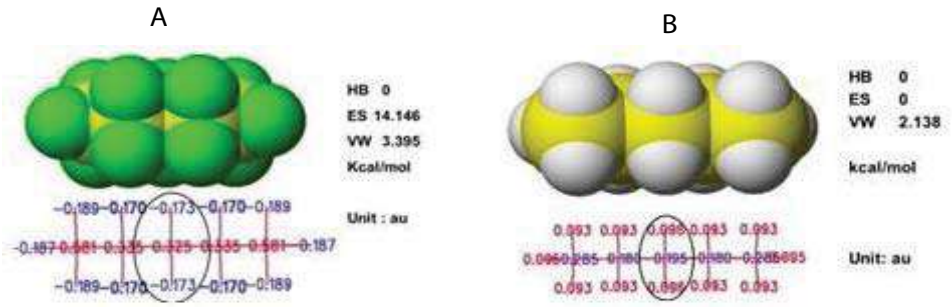


Figure 6.12: Chemical structure of perfluoropentane (A) and pentane (B) with the properties and atomic partial charge.

The primary molecular interaction force between two perfluoropentanes (A) is the van der Waals force, and weak electrostatic interactions contribute to the interaction compared with the result obtained for two pentanes (B), shown in Figure 6.13; the shift of apc is demonstrated in Figure 6.14A and B.

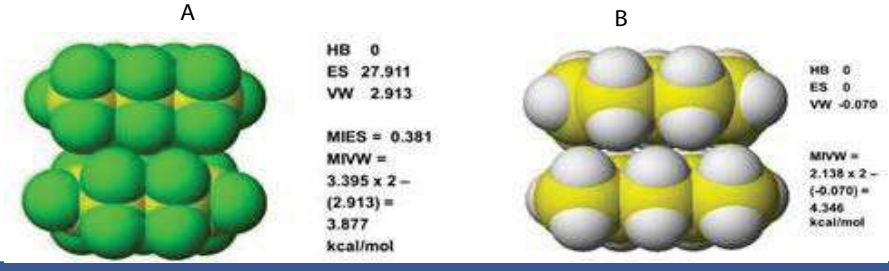


Figure 6.13: Perfluoropentane (A) and pentane (B) complex with the properties.

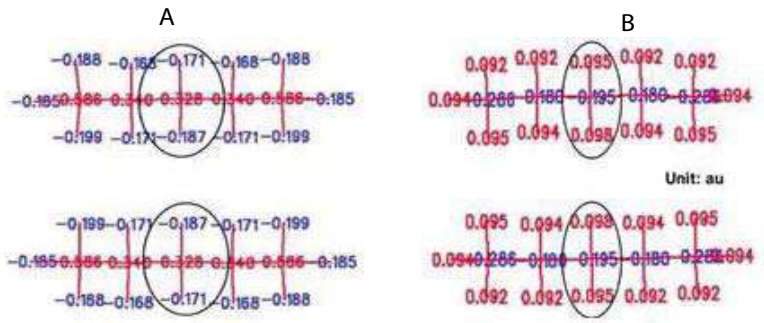


FIgure 6.14: Atomic partial charge of the perfluoropentane complex and the pentane complex.

The perfluoropentane complex bound by van der Waals force (MIVW=3.877 kcal.mol^{-1}) and electro static interaction(MIES=0.371kcal·mol^{-1}) did not contribute to the interaction.The MIVW of the pentane complex was 4.346 kcal mol^{-1}, and van der Waals interaction was the primary binding force. The interaction center of apc is indicated in the Figures. The structures of the perfluorohexane and hexane complexes were prepared, and the calculated properties and apc are shown in Figures 6.15-17.

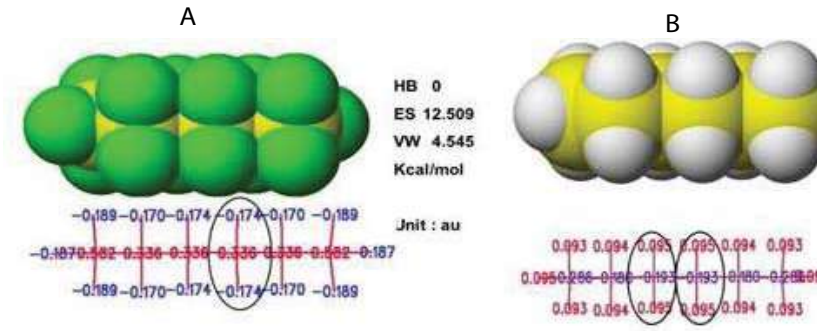


FIgure 6.15: Chemical structure of perfluorohexane (A) and hexane (B) with the properties and apc.

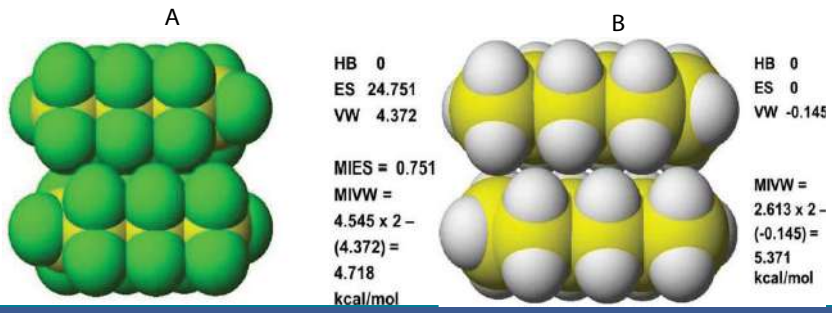


FIgure 6.16: Perfluorohexane (A) and hexane (B) complex with the properties.

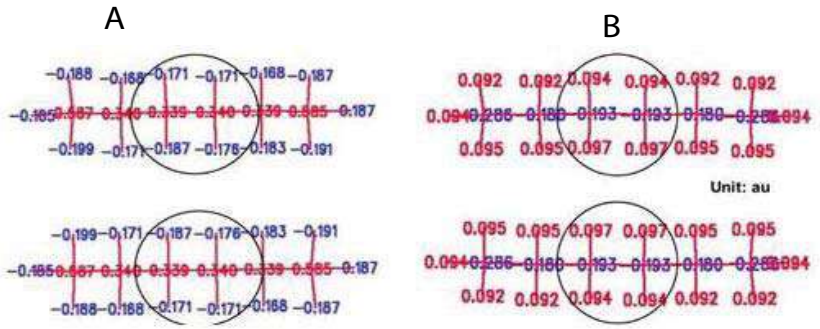


FIgure 6.17: Perfluorohexane (A) and hexane (B) complex with apc.

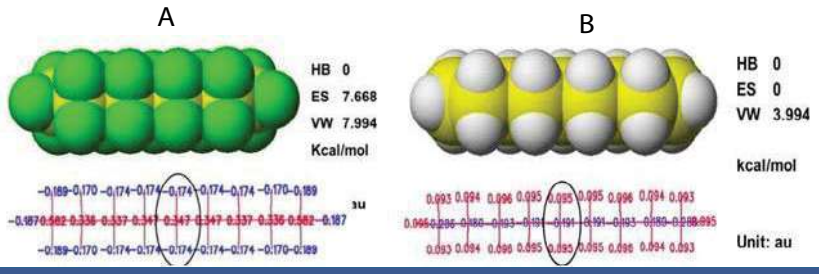


FIgure 6.18: Chemical structures of perfluorononane (A) and nonane (B) with properties and apc.

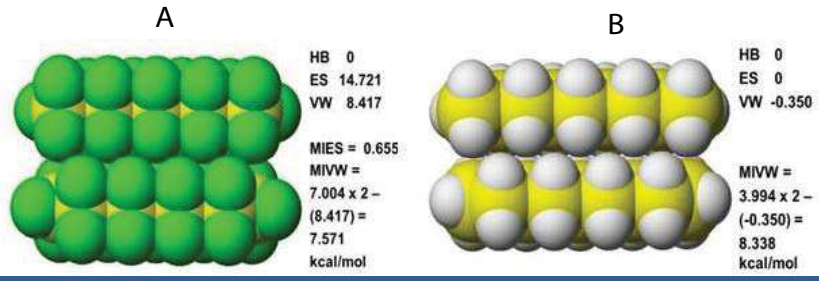


FIgure 6.19: Perfluoronanone (A) and nonane (B) complexes with the properties.

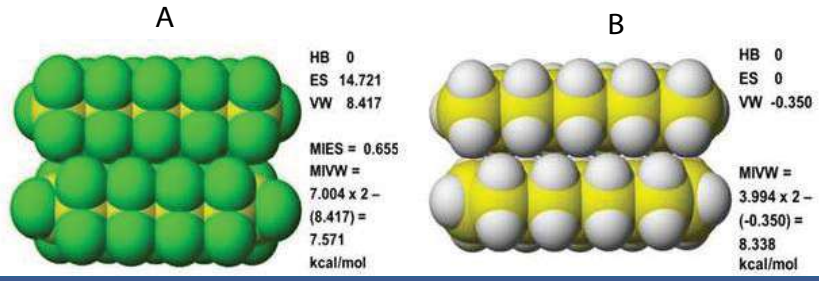


FIgure 6.20: Atomic partial charge of the perfluorononane (A) and nonane (B) complexes.

The MIVW energy values of these complexes increased from 3.877 to 7.5711 kcal mol^{-1} (from pentane to nonane in Figures 6.13, 15, and 18), and MIES increased from 0.38 to 0.66 kcal mol^{-1}. The apc of the contact-center fluorine decreased from -0.173 to -1.187 (perfluoropentane) and from -0.174 to -0.188 au (perfluorononane). It changed only 0.002 au for alkanes. The atomic partial charge differences should affect reversed-phase liquid chromatography, as the bonded phases.

Figure 21 summarizes the MIVW energy values of two identical molecule complexes: ethylether ~ pentyl ether, acetone ~ butyl ketone, benzene ~ propylbenzene, chlorobenzene ~ trichlorobenzene, and perfluoropentane ~ perfluorononane. The MIVW of each group of compounds was linearly related to their heavy-atom (excluding hydrogen) numbers. This small difference is due to atomic size and contact conditions. For example, fluorine's atomic size is smaller than carbon's, and benzene's molecular size is smaller than cyclohexane's.

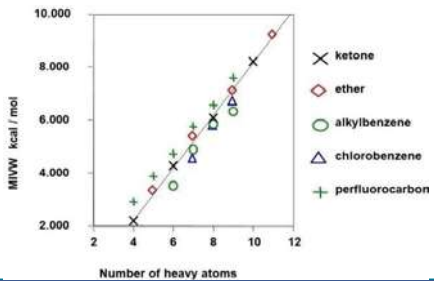


FIgure 6.21: Relation between MIVW and the number of atoms.

The contribution of electrostatic interaction was 0.020 and 0.003 kcal mol^{-1} for ethylether and alkylbenzene. That of dimethyl ketone was -1.997, and that of ethyl-, propyl-, and butyl-ketone was about -1.4 kcal mol^{-1}. That of chlorobenzene changed from 0.103 to 0.923 kcal mol^{-1} due to its position on the benzene ring. The difference in electrostatic energy contribution at the position is the same as that learned in organic chemistry as Hammett's equation: ortho, meta, and para position contribution. Computational chemical calculations provide this electrostatic contribution. The electrostatic energy of perfluorocarbons increases with molecular size from 0.381 to 0.655 kcal mol^{-1} from pentane to nonane. The change in atomic partial energy indicates the molecular interaction site due to molecular interaction strength.

6.6.1. Comparison of fluorocarbon and hydrocarbon substitutes: The alkyl-chain length affects the retention capability of different form analytes; dodecane was proposed as the standard alkyl-chain length; however, a popular alkyl-chain length is octadecane. The minimum alkyl-chain length was proposed due to the chemical stability of the bonded-silica gel phase. Shorter chain lengths increased electron localization by the silicon dioxide matrix. Therefore, the electron localization of fluorocarbon-chain length was calculated and compared with that of hydrocarbon-chain length. Figure 6.22 summarizes the electron localization of this model-bonded silicone oxide for fluorocarbons, and the reference hydrocarbons are summarized in Figure 6.**22**. Table 6.12 summarizes the calculated properties (es, vw energy values, and apc of the end carbon and fluorine). The nucleophilic susceptibility exhibits the electron distribution (low – high: red-purple-magenta-blue-green-yellow-white) for visually understanding the bonded ligand differences.

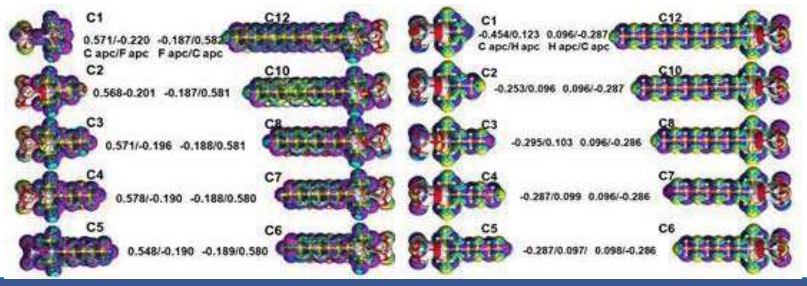


Figure 6.22: Chain length affected the apc of the head of bonded ligands of perfluoro-ditrifluoromethyl silicon trioxide and alkyl-dimethylsilicontrioxide; nucleophilic susceptibility exhibits the electron distribution (low – high: red-purple-magenta-blue-green-yellow-white).

Table 6.12: Carbon-chain length effect of model fluorocarbon and hydrocarbon bondedsilicon groups.

	Fluorocarbon				Hydrocarbon			
Cn	es	vw	apc C	apc F	es	vw	apc C	apc H
1	-104.23	-4.073	0.571	-0.22	-2.922	-3.524	-0.454	0.123
2	-54.079	-4.02	0.568	-0.201	-2.921	-2.16	-0.253	0.096
3	-60.283	-3.079	0.571	-0.196	-2.921	-2.767	-0.295	0.103
4	-63.4	-2.063	0.578	-0.19	-2.919	-2.385	-0.287	0.099
5	-65.025	-0.955	0.578	-0.19	-2.92	-1.903	-0.286	0.097
6	-66.617	-0.173	0.58	-0.189	-2.931	-1.423	-0.287	0.098
7	-68.223	**1.327**	0.58	-0.188	-2.931	-0.962	-0.286	0.096
8	-69.837	2.48	0.581	-0.188	-2.931	-0.505	-0.286	0.096
9	-71.447	3.628	0.581	-0.187	-2.931	-0.039	-0.286	0.096
10	-73.058	4.786	0.581	-0.187	-2.93	0.421	-0.286	0.096
11	-74.657	5.927	0.582	-0.187	-2.93	0.876	-0.286	0.096
12	-76.275	7.095	0.582	-0.187	-2.93	1.339	-0.286	0.096

Both fluorocarbon and hydrocarbon do not have hydrogen bonding energy; however, fluorocarbon exhibit strong electrostatic energy values, and the van der Waals energy value indicates the contribution of the molecular interaction with analytes. The apc of fluorocarbon is opposite from that of hydrocarbon mentioned in the last chapter. An interesting property is van der Waals energy, and the value becomes positive after heptyl for fluorocarbon and decyl for hydrocarbon. These differences may help to design a new bonded phase. These apc values also suggested the contribution of the silicone-dioxide matrix to the electron localization of these carbon chains. The border carbon chain of fluorocarbon is pentyl, and that of hydrocarbon is propyl. The electron distribution of ligands is presented in Figures 6.23A and B. The

unbalanced of electrons was observed at the head of ligands, and the center of ligands was relatively neutral as obtained for binary complexes of polyfluoro and hydrocarbons. Analytes contact at the top of ligands for high-density bonded phases. The electron distribution should affect the retention, and the apc values indicated that the perfluorocarbon ligand exhibited a larger apc unbalance (0.768 au in Figure 6.23A). The value of hydrocarbon ligand was about a half (0.384 au in Figure 6.23B). As a result, electrostatic interaction should contribute to perfluorocarbon phases.

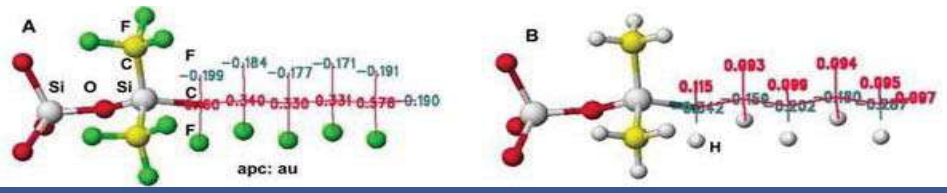


FIgure 6.23: A and B. apc distribution of perfluoropentyl and pentyl ligands.

The same analysis was applied to study the chain-length effect in phenyl phases.in Figures 24A and B, the structures are shown, and Table 6.13 summarizes the calculated properties.**13**.

Table 6.13: Carbon-chain length effect of model phenyl bonded-silicone groups.

	Fluorocarbon				Hydrocarbon			
Cn	es	vw	apc C	apc F	es	vw	apc C	apc H
1	-92.893	-1.192	0.2	-0.137	-2.288	-1.788	-0.154	0.163
2	-76.182	0.652	0.209	-0.135	-3.574	-0.019	-0.167	0.158
3	-75.809	1.818	0.21	-0.134	-2.712	0.447	-0.169	0.158
4	-77.744	2.974	0.211	-0.133	-2.935	0.936	-0.168	0.158
5	-79.351	4.179	0.212	-0.133	-2.938	1.421	-0.169	0.158
6	-80.979	5.361	0.212	-0.133	-2.923	1.839	-0.169	0.158

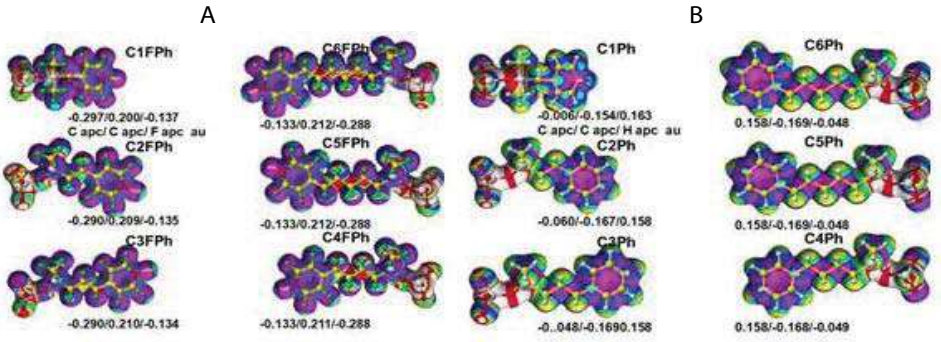


FIgure 6.24: Chain length affected the apc of the head of phenyl-bonded ligands. A: perfluoro-fluorodimethyl silicon trioxide, B: alkyl-dimethyl silicon trioxide; nucleophilic susceptibility exhibits the electron distribution (low – high: red-purple-magenta-blue-green-yellow-white).

The electron localization of the perfluorophenyl ligand was larger than that of the phenyl ligand. This electron localization should further contribute to molecular interactions in the perfluorophenyl phase, as shown in Figure 6.25.

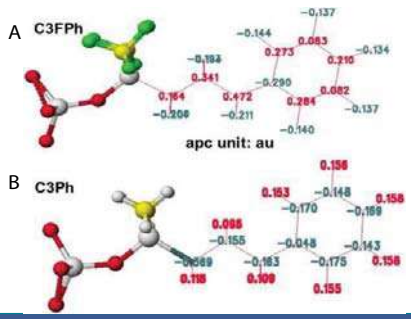


FIgure 6.25: A and B. apc distribution of perfluoro-structures.

6.6.2. Selectivity of fluorocarbon ligand of bonded silica gel: The selectivity of fluorocarbon-bonded silica gel was analyzed using perfluorooctyl and octyl-dimethylsilicone-tetraoxide, as shown in Figures 6.26A and B. Table 6.13 lists the selected analytes. Figures 6.27A and B show structures of n-hexane and n-perfluorohexane-bound ligands as examples. Table 6.14 summarizes the calculated MI energy values between these model ligands and analytes.

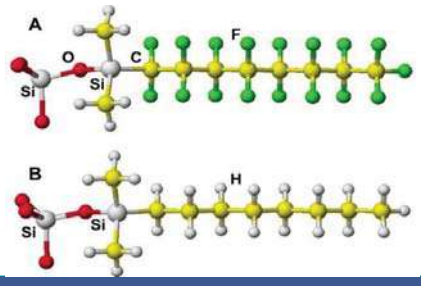


FIgure 6.26: A and B. dimethylperfluorooctyl pheyl and phenyl-propyl ligands and octyl.

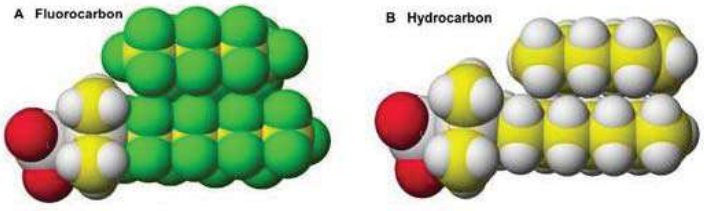


FIgure 6.27: A and B. Structures of n-hexane and n-perfluorohexane bound octane-ligands.

Table 6.14: Molecular interaction energy values between the model ligand and analytes.

Model ligands	Octylfluorocarbon			Octyhydrocarbon		
Analytes	MIHB	MIES	MIVW	MIHB	MIES	MIVW
Water	3.224	0.449	0.165	0.001	0.003	1.292
Methanol	2.071	0.456	1.47	0	-0.012	2.044
Ethanol	1.929	0.722	2.101	0	-0.016	2.553
Acetonitrile	0	1.195	2.395	0	0.057	2.912
n-Hexane	0	0.051	6.01	0	-0.023	6.42
n-Fluorohexane	0	0.902	6.132	0	-0.034	4.322
Cyclohexane	0	0.062	4.494	0	-0.013	3.981
Cyclofluorohexane	0	0.062	4.494	0	-0.034	4.322
Benzene	0	0.036	5.156	0	-0.014	5.604
Hexafluorobenzene	0	0.242	5.279	0	0.047	6.304
Toluene	0	0.054	6.237	0	-0.016	6.583
Fluorobenzene	0	0.218	5.337	0	0.026	5.571
Chlorobenzene	0	0.145	6.075	0	-0.006	6.367
Phenol	0.432	0.305	5.135	0.002	-0.012	5.805
Benzoic acid	0.184	0.969	5.866	0.003	-0.005	6.896
Aniline	0.329	0.333	5.485	0	-0.013	6.297
Ionized phenol	0	0.778	5.335	0	-0.021	5.673
Ionized benzoic acid	0	1.568	5.917	0	-0.01	6.595
Ionized aniline	0	0.383	5.392	0	-0.002	6.413

The primary molecular interaction force is van der Waals interaction for both hydrocarbon and perfluorocarbon ligands. Hydrogen bonding and electrostatic interactions are negligible in the retention mechanisms of hydrocarbon ligands. However, electrostatic interactions contribute to the retention mechanism of fluorocarbon ligands. The degree of contribution depends on the analytes. Hydrogen bonding contribution depends on the hydroxy-group of analytes.

Hydrocarbons repel water, but polar compounds retain on the fluorocarbon surface. The results indicate that solvation of the perfluorocarbon phase should be considered for quantitative analysis of retention time. Acetonitrile was a wettable solvent. This means analyte retention times are shorter than in the hydrocarbon phase due to easy replacement in reversed-phase liquid chromatography. Fluorocarbon has a capability similar to that of a phenyl ligand, and its hydrophobic interaction force is weaker than that of a hydrocarbon. Chromatographic retention time on a fluorocarbon phase should be shorter than on a hydrocarbon phase and should show selectivity for analytes with π-electrons. Analytes should ionize and show selective retention in the fluorocarbon phase, while total retention remains similar to that in the hydrocarbon phase.

6.6.3 Selectivity of fluorocarbon bonded phase: The selectivity of fluorocarbon was studied by docking with severals simple compounds used for the evaluation of several hydrocarbon ligands. Usually, the elution order relates to the analyte's log P, or relative hydrophobicity, in reversed-phase liquid chromatography using hydrocarbon-bonded silica gel phases. However, the elution order is reversible in reversed-phase liquid chromatography using perfluorocarbon-bonded silica gel phases. Berendsen et al. [4] demonstrated the performance of a fluorocarbon-bonded phase compared to the results obtained using a hydrocarbon-bonded phase. The elution order of trifluoroethanol, pentafluorophenol, toluene, α,α,α-trifluorotoluene, and octanol was related to their van der Waals molecular interaction energy values using a hydrocarbon-bonded silica gel (MIVW in Table 6.14). However, the elution order was not related to their van der Waals molecular interaction energy values (MIVW in Table 6.14). Even the combined MI energy values (MIHB+MIES+MIVW) did not support their elution order. The elution order was related to additional solvent effects, such as MI energy values in water (H_2O; MIHB+MIES+MIVW) and methanol (MeOH; MIHB+MIES+MIVW) phases. The relatively high wettability of the perfluorocarbon-bonded phase demonstrated a significant difference from hydrocarbon-bonded phases; therefore, the total elution time is shorter than that of the hydrocarbon-bonded phase. Fluorocarbon compounds retained longer than hydrocarbon compounds, such as pentafluorophenol, which retained longer than phenol, and trifluoromethylbenzene, which retained longer than toluene. However, the elution order was related to their log *P* values. The higher resolution with the fluorocarbon-bonded phase seems due to physical factors rather than differences in molecular interactions (chemical factors). The longer retention of octanol than trifluoromethyl benzene on the decyl-bonded phase, compared with their log *P* values, likely reflects poor solvation in methanol. Therefore, the selectivity of the fluorocarbon-bonded phase was not clearly explained. The log *P* values calculated using the Cache™log *P* program and molecular interaction energy values are summarized in Table 6.14. Monde et al. also demonstrated the performance of a fluorocarbon-bonded silica gel [**5**]. The fluorocarbon-bonded phase reversed the elution order of hexafluorobenzene, ethylbenzene, and anthracene. The elution order opposed their log *P* values (Table 6.14), even though the MIVW values calculated using both hydrocarbon and perfluorocarbon phases were similar; however, the MIVW values did not support the elution order from the perfluorocarbon-bonded phase. Finally, the elution order from the perfluorocarbon-bonded phase was supported by the addition of MI values calculated using the water phase. The reversed elution order on fluorocarbon-bonded silica gel was expected to show greater solvation of the fluorocarbon-bonded phase with methanol. Perfluorooctyl- and octyl-bonded model phases are shown in Figures 6.28A and B. Figure 6.29 shows the structure of the molecular interaction with a water phase is shown in Figure 6.29.

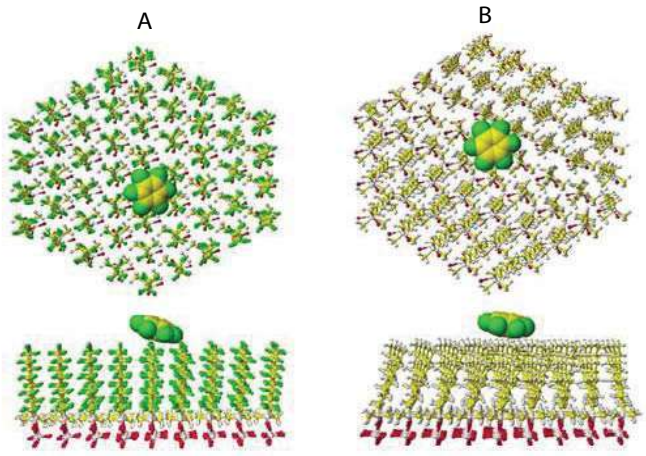


FIgure 6.28: A and B. Model-phases with an adsorbed analyte..

Table 6.15: Molecular properties of analytes and their molecular interaction (MI) values measured using model phases.

Analytes			C8F	Solvation	C8
	log *P*	MIHB	MIES MIVW	MI(solvent)	MIVW
Chromatogram A [**4**]		*1			*2
Trifluoroethanol	0.71	3.224	23.589 3.606	7.357	5.406
Phenol	1.762	0.783	23.378 6.293	7.249	7.23
Pentafluorophenol	2.46	0.804	24.008 6.827	7.442	8.168
Toluene	2.514	0	23.061 7.484	7.39	8.253
a,a,a-Trifluorotoluene	2.929	0	23.378 7.457	8.393	8.698
Octanol	2.527	0	23.568 12.442	7.876	12.435
Chromatogram B [**5**] Hexafluorobenzene		*3			*4
	2.884	0	0.800 6.624	5.155*2	8.1
Ethylbenzene	2.91	0	-0.013 9.145	4.394	10.089
Anthracene	4.051	0	-0.137 9.875	1.034	12.332
*1: MI=(MIHB+MIES+MIVW)-0.2xH2O(MIHB+MIRS+MIVW)-0.15xMeOH(MIHB+MIES+MIVW)					
*2: MI=MIVW, *3:MI=(MIHB+MIES+MIVW)-0.47xH2O(MIHB+MIES+MIVW), *4: MI=MIVW					
Eluent: Chromatogram A (70% aqueous methanol), Chromatogram B (65% aqueous methanol					

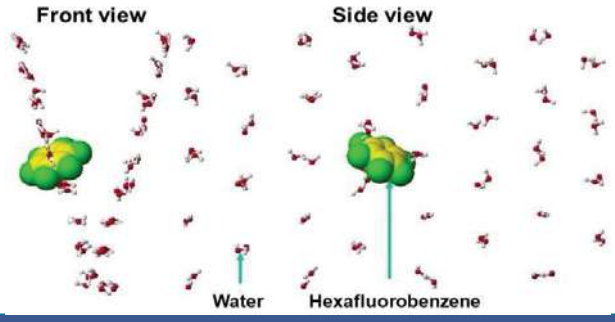


Figure 6.29: Interaction of perfluorobenzene with a model water phase.

The elution order of methyl benzoate, toluene, triphenylene, *o*-terphenyl, and hexafluorobenzene was not simply related to their log *P* values, even using a hydrocarbon-bonded phase. Additional water-phase solvation effects were required to support the elution order. Further additional solvent effects calculated in the water phase were required to explain the elution order measured using the perfluorocarbon-bonded phase. In addition, *o*-terphenyl changed the molecular shape dramatically and altered the original molecular properties. *Ortho*-terphenyl is a flat molecule, but the structure flexibility affected the calculated molecular interaction energy values. The elution order of methyl benzoate, toluene, triphenylene, *o*-terphenyl, and hexafluorobenzene followed their log *P* values in reversed-phase liquid chromatography using an octadecyl-bonded silica gel column, and the retention of triphenylene and *o*-terphenyl was too long to be observed on the chromatogram compared to the chromatogram measured using a perfluorocarbon column. However, the elution order was unrelated to their log *P* values on a perfluorocarbon column. The solvation degree of these compounds demonstrated a significant role in their elution order. Triphenylene and *o*-terphenyl eluted before hexafluorobenzene, even though their log *P* values differ by more than two.

Table 6.16. Molecular properties of analytes and their molecular interaction (MI) values measured using model phases

Analytes		C8F	C8F	Solvation	C8	Solvation
	log *P*	MIES	MIVW	MI(solvent)	MIVW	MI(solvent)
Chromatogram C [**6**]			*1			*2
Methylbenzoate	1.777	-0.193	9.037	0.32	10.416	6.017
Toluene	2.514	0.092	6.998	0.876	8.253	6.232
Triphenylene	5.053	-0.261	13.776	1.553	15.992	7.315
o-Terpheyl	5.415	0.175	13.34	2.118	14.463	10.22
Hexafluorobenzene	2.884	0.794	6.749	2.249	8.1	6.9
Chromatogram D [**7**]	2.047	0.403	11.615	10.459	11.569	5.023
Fluorobenzene	2.186	1.058	11.4	10.742	13.154	5.946
o-Difluorobenzene	2.326	0.649	14.353	12.812	14.319	6.921

m-Difluorobenzene	2.326	-0.736	15.517	12.829	16.332	8.133
p-Difluorobenzene	2.326	-1.203	14.895	11.267	13.303	4.915
*1: MI=MIES+MIVW-0.26xH2O(MIHB+MIES+MIVW)						
*2: MI=MIVW-0.24xH2O(MIHB+MIES+MIVW)-0.015xMeOH(MIHB+MIES+MIVW)						
*3: MI=MIES+MIVW-0.1xH2O(MIHB+MIES+MIVW)						
***4: MI=MIES+MIVW-0.43xH2O(MIHB+MIES+NIVW)-0.15xMeOH(MIHB+MIES+MIVW)** **Eluent: Chromatogram C (60% aqueous methanol), Chromatogram D (60% aqueous methanol) [6]**						

The difficulty of the above approach was found in the quantitative analysis of the chromatography of difluorobenzene isomers. The molecules are flat, and the surface area is identical; therefore, their calculated complex formation and calculation of molecular interaction energy values using model phases were required. Table 6.17 summarizes the calculated MI energy values for the water and methanol phases.

Table 6.17: Interaction energy with solvent.

Analytes		Water			Methanol	
	MIHB	MIES	MIVW	MIHB	MIES	MIVW
Trifluoroethanol	7.119	4.728	1.089	7.237	3.879	2.38
Phenol	22.303	-0.16	1.997	19.858	-0.134	4.849
Pentafluorophenol	23.945	2.559	0.566	23.467	3.227	2.927
Toluene	23.192	0.021	0.689	19.077	0.061	5.761
a,a,a-Trifluorotoluene	26.016	-0.163	0.625	16.928	-0.696	5.057
Octanol	-0.278	3.802	8.399	1.97	2.334	9.2
Hexafluorobenzene	16.377	4.896	-0.913	20.586	3.612	4.357
Ethylbenzene	20.815	0.077	4.443	19.107	-0.181	7.926
Anthracene	42.744	-3.081	2.44	31.505	-0.806	8.312
Methylbenzoate	27.784	1.176	3.826	19.98	1.12	7.37
Triphenylene	43.128	-0.981	3.86	32.185	-0.785	10.811
o-Terphenyl	40.388	-0.22	3.665	36.246	-1.604	11.761
Benzene	14.502	0.385	0.699	16.869	0.551	4.523
Fluorobenzene	15.41	0.599	1.153	20.293	-0.968	5.144
o-Fifluorobenzene	16.981	-0.175	0.809	16.325	0.571	4.175
m-Difluorobenzene	18.649	0.445	0.428	19.064	-1.449	5.18
p-Difluorobenzene	19.105	0.603	0.263	16.213	0.313	4.545

The specificity of perfluorocarbon-bonded silica gel phases is the solvation in reversed-phase mode liquid chromatography. Table 6.14 summarizes the fundamental solvation. The contribution of MIHB and MIES was negligible for the hydrocarbon phase, and MIVW is the primary interaction force; however, MIHB and MIES contributed to the analyte's selective elution order. Some groups showed a reversed elution order from the hydrocarbon phase due to solvation. Solvation in the perfluorocarbon phase reduced the elution time of these compounds. We may reduce the organic modifier consumption.

The resolution difference between a fluorocarbon and a hydrocarbon phase may depend on their bonded-phase density difference, the properties of silica gels, and their chain-length difference [**7**]; however, the shorter elution time in the fluorocarbon phase is a specificity of the fluorocarbon phase described above. The longer retention of polar compounds may reflect MIHB between the perfluoro group and the analyte's polar substituents. A linear solvation energy relationship describes the selectivity of perfluorocarbon-bonded phases [8]. However, the synthesis used normal (not pure) silica gels, and the end-capping was not completed. Furthermore, they did not demonstrate chemical stability and inertness. Therefore, evaluating the conclusion for polar analytes, as mentioned in solute size and hydrogen-bonding capability, is not easy. If they used longer ligands (more than a butyl chain) for bonding, the difference between perfluorocarbon- and hydrocarbon-bonded phases is clear. The alkyl-chain length effect was determined by synthesizing a stable phenyl-bonded phase based on fundamental observations from calorimetric analysis of the alkyl-chain length effect on hydrogen bonding in alkyl alcohols. The final product is a popular phenylhexyl-bonded silica gel [9].

The difference in wettability of fluorocarbon and hydrocarbon phases was measured using contact angle [10]. On hydrocarbon-bonded surfaces, the contact angles of benzene and hexafluorobenzene increase with increasing carbon chain length of the silylation agents, and on fluorocarbon-bonded surfaces the contact angles of these compounds increase with increasing carbon chain length of the silylation agents. This observation is supported by the atomic partial charges of silyl reagents described in the previous chapter. Furthermore, characterization of perfluorocarbon-bonded phases using supercritical fluid chromatography indicated that ionic interactions and dipole-dipole interactions are necessary to describe the properties of perfluorocarbon-bonded phases [11]. The observation can be quantitatively explained by electrostatic interaction (MIES) observed in the quantitative analysis of chromatographic retention of several compounds using the model phases model phases. In addition, perfluorocarbon-bonded phases were applied for the chromatography of fluorine-containing pharmaceuticals. The separation of fluorine-containing and desfluoro analogs was better than that observed using octadecyl-bonded silica gel [12]. The observation demonstrated the specificity of perfluorocarbon-bonded phases with shorter retention times. The specific property of fluorocarbon was applied to the purification of biological compounds, especially peptides. The fluoro-derivatized peptides bound non-covalently to the fluorinated phases; non-fluorinated compounds were not retained on the fluorinated phases, and the retained fluorinated compounds were selectively purified. The approach was applied for lipid and nucleic acid purifications [13]. A dual-grafted fluorinated hydrocarbon amine weak anion-exchange polymeric resin was synthesized to remove perfluorooctanoic acid from water. The fluorinated polymer's purification capability was twice that of the related non-fluorinated polymer and six times that of activated carbon. The adsorption mechanisms were proposed to be hydrophobic and electrostatic interactions [14]. The above *in silico* analysis using model compounds supports the proposed adsorption mechanisms. Furthermore, several functionalized carbon-based materials with perfluoropolyether moieties were described. The high thermal and chemical stability, along with the fluorous effect, could enable certain applications in chromatography, especially for separating different fluorinated mixtures [15]. Fluorinated reactions with carbon demonstrated the possibility of synthesizing a different type of packing material for chromatography. A perfluorooctyl-functionalized paper was developed for solid-phase extraction of perfluorinated compounds in water and determined using electrospray ionization-tandem mass spectrometry [16]. Use fluorocarbon-bonded silica gels for reversed-phase LC if chemical stability is guaranteed.

6.7. Selectivity of graphitized carbon-phase

Graphitized carbon is a very stable packing material, but it is very hydrophobic, and it is challenging to remove most adsorbed compounds. Graphitized carbon can be used for chromatography and very polar compounds. The specific mechanisms are quantitatively analyzed by docking various compounds with a graphitized model phase (19PAH). Preparation of analyte structures: glucose can be prepared from cyclohexane by replacing one carbon with oxygen; then, hydrogens are converted to hydroxy groups. Add hydrogen by selecting the valence menu in Beautify, then the pull-down menu. Correct the location of the hydroxyl groups; then, optimize the structure using the MM2 program. If the hydroxyl hydrogen is oriented incorrectly, change the oxygen to sp^3 carbon, add sp^3 carbon and add valence using the **Valence** menu, erase unwanted hydrogens, then switch the carbon to sp^2 oxygen. If glucose is in the library, select it from the library for easier preparation. The docking MI study uses three previously prepared PAHs (19PAH, 13PAH, and 13PAH (sp^3)). The analytes are benzene, cyclohexane, glucose, formic acid, aniline, ammonium ion, ionized formic acid, and phosphate; these were selected to create the molecular model and assess the effects. Figure 6.30a shows the pre-docking location, and Figure 6.30b shows the complex after docking.

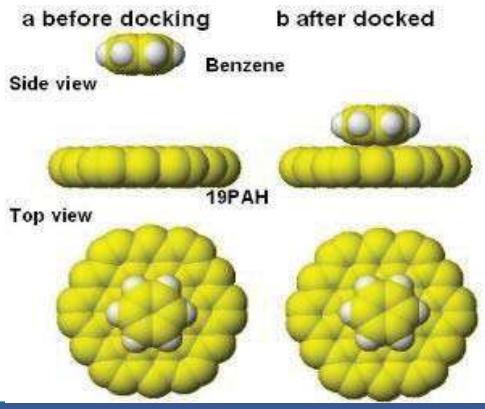


Figure 6.30: Structures of before and after docking of benzene onto 19PAH.

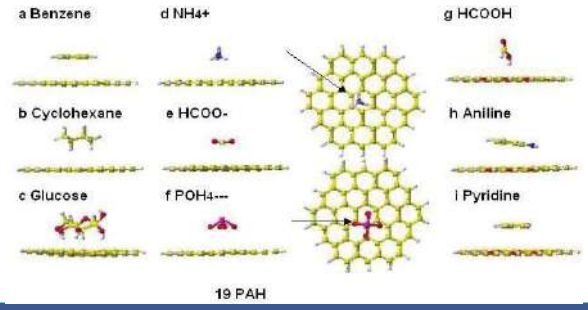


Figure 6.31: Complex structures of various analytes with 19PAH. White, yellow, blue, red, and purple balls are hydrogen, carbon, nitrogen, oxygen, and phosphate atoms..

Figure 6.31 shows the complex conformation of benzene (a), cyclohexane (b), glucose (c), ammonium ion (d), formic ion (e), and phosphate ion (f). The top view of ammonium and phosphate ion complexes is also shown.

The MI strength is calculated using the MM2 program. MI energy values of hydrogen bonding (HB), electrostatic interaction (ES), and van der Waals interaction (VW) are summarized in Table 6.18.

Table 6.18: Selective interaction of standards analytes with 19PAH.

Analyte	HB	ES	VW	MIHB	MIES	MIVW
Benzene	0	0	32.903	0	0	8.652
Cyclohexane	0	0	34.175	0	0	8.008
Glucose	-41.12	11.459	36.839	29.482	-2.003	6.332
Formic acid	-10.357	-4.982	36.293	9.69	-0.015	2.648
Aniline	-4.344	0	33.853	3.01	0	8.417
Pyridine	0	0	33.289	0	0	8.404
Ammonium ion	0	0	35.342	0	0	3.207
Formic ion	0	0	35.392	0	0	3.157
Phosphoric ion	0	0	34.463	0	0	4.086
Model 19PAH	0	0	38.549			

Unit: kcal. mol^{-1}

The primary MI with a graphitized phase is the van der Waals force (MIVW). MIHB contributes to saccharide retention. The retention of ions can be understood from the apc values of 19PAH. A positively charged ammonium ion remains at the center, and the negatively charged formate ions do not contribute to retention and are retained by MIVW. Further analysis is carried out using 13PAH, whose complex structures are shown in Figure 6.32. The calculated MI energy values are summarized in Table 6.19.

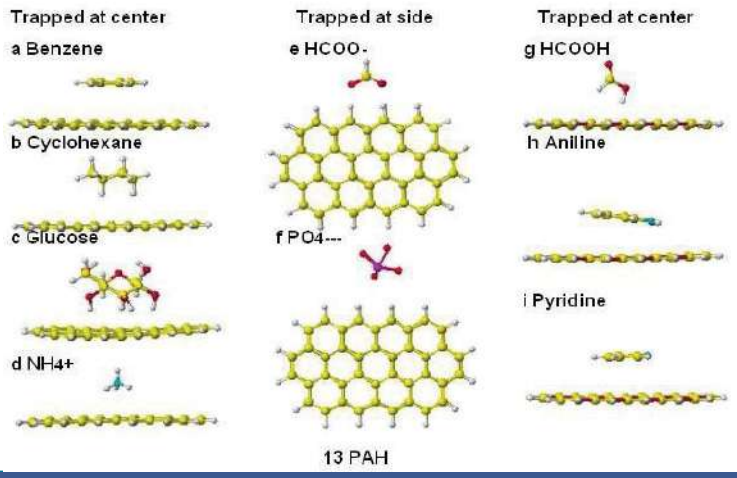


Figure 6.32: Interaction of unlocked 13PAH and standard analytes.

Table 6.19: Retention of standard analytes on unlocked model 13PAH.

Analyte	HB	ES	VW	MIHB	MIES	MIVW
Benzene	0	0	22.873	0	0	8.085
Cyclohexane	0	0	24.097	0	0	7.489
Glucose	-32.445	10.815	26.669	28.511	-2.568	5.905
Formic acid	-10.229	-4.983	25.831	9.562	-0.013	2.227
Aniline	0	0	23.789	2.913	0.001	7.58
Pyridine	0	0	23.216	0	0.001	7.594
Ammonium ion	0	0	24.905	0	0	3.047
Formic ion	0	0	27.076	0	0	0.876
Phosphoric ion	0	0	26.411	0	0	1.541
Model 13PAH	0	0	27.952			
Unit: kcal. mol^{-1}						

Formic and phosphate ions are repulsed from the center of 13PAH and held at the edge of 13PAH.Glucose is held at the center of 13PAH by hydrogen bonding. The complex shows a dish-like structure of 13PAH due to hydrogen bonding. Basically, the result for 13PAH is the same as that of 19PAH. However, the 13PAH structure is distorted; therefore, 13PAH is locked, and the same analysis is performed. Figure 6.33 shows these complex structures, and Table 6.20 summarizes the molecular interaction energy values. The comparison of data listed in Tables 6.14 and 15 indicates that the flexibility of the model phase attracts ion adsorption.

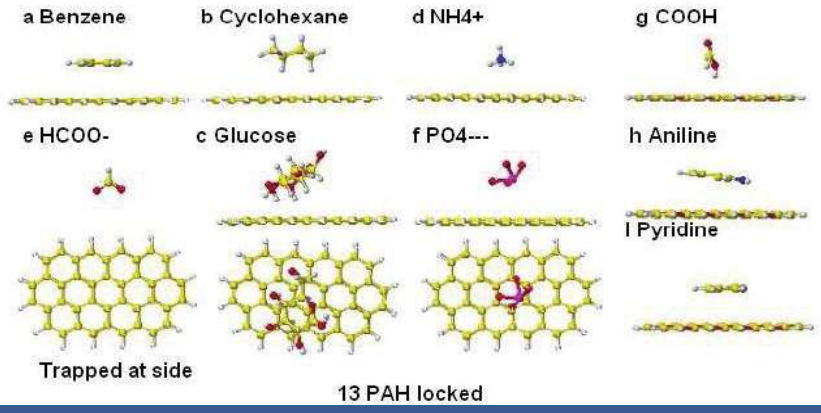


Figure 6.33: Interaction of locked 13PAH and standard analytes.

Table 6.20: Retention of standard analytes locked model 13PAH.

Analyte	HB	ES	VW	MIHB	MIES	MIVW
Benzene	0	0	22.943	0	0	7.315
Cyclohexane	0	0	24.179	0	0	6.707
Glucose	-30.249	10.623	26.158	26.315	-2.376	5.716
Formic acid	-10.186	-4.984	25.807	9.519	-0.013	1.551
Aniline	-3.96	0	33.279	2.626	0	-3.079
Pyridine	0	0	23.279	0	0	6.831
Ammonium ion	0	0	24.901	0	0	2.351
Formic ion	0	0	24.947	0	0	2.305
Phosphoric ion	0	0	24.122	0	0	3.13
Model 13PAH	0	0	27.252			
Unit: kcal. mol^{-1}						

Furthermore, the influence of sp^3 carbon is studied using 13PAH (sp^3). The structures of complexes are shown in Figure 6.34, and the calculated MI energy values are summarized in Table 6.21.

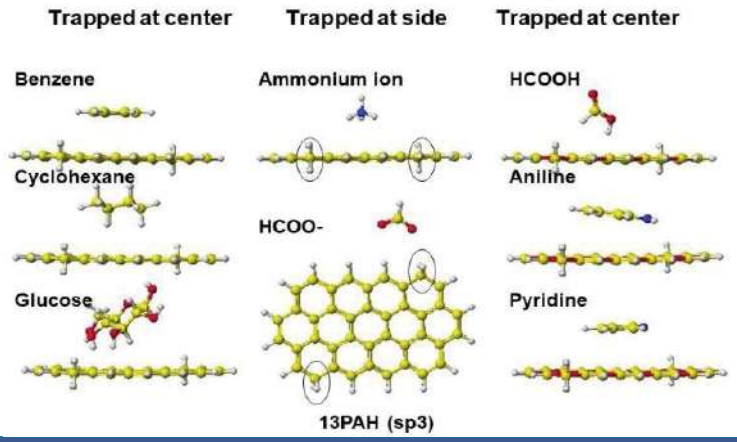


Figure 6.34: The structures of complexes with 13PAH (sp3).sp3 carbons are circled with two hydrogens.

The existence of sp3 carbons produced electron localization, and ES energy was found in the model phase. This electron localization induces MIES, and this phenomenon can be observed in the electron localization of electrodes.

Table 6.21: Retention of standard analytes unlocked model 13PAH(sp^3).

Analyte	HB	ES	VW	MIHB	MIES	MIVW
Benzene	0	0.001	21.779	0	0	8.134
Cyclohexane	0	0.001	22.998	0	0	7.543
Glucose	-30.783	8.564	27.072	26.849	-0.316	-4.457
Formic acid	-10.19	-5.098	24.763	9.523	0.102	2.25
Aniline	-4.163	0.009	22.135	2.829	-0.008	7.688
Pyridine	0	0.005	22.135	0	0.004	7.63
Ammonium ion	0	-0.11	23.863	0	0.111	3.044
Formic ion (top)	0	0.067	23.888	0	-0.066	3.019
Formic ion (side)	0	0.402	25.881	0	0.403	1.026
Phosphoric ion	0	0.31	23.029	0	0.309	3.878
Model 13PAH(sp^3)	0	0.001	26.907			

Unit: kcal. mol^{-1}

The difference between flexible and locked 13PAH indicates the apc values of the center six carbons. These apc values are similar in these complexes with benzene (Figure 6.35b). In the complex with the ammonium ion, the apc values decrease about 10 times. The complex with a formic ion at the side of 13PAH doubles the apc of hydrogen, and the apc of carbon decreases by half. In complexes with locked 13PAH, the apc of the complex with benzene does not change; the apc of the complex with ammonium ion becomes one-tenth. When a form is located at the side of 13PAH, the apc becomes positively charged.

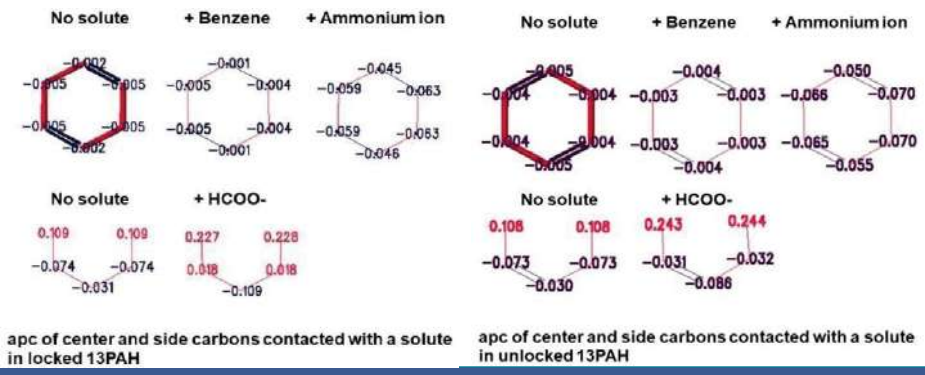


Figure 6.35: apc of contact center of locked and unlocked 13PAHs.

As shown, PAH forms a contact charge-transfer complex with the molecules. The interaction strength is described using MIHB, MIES, and MIVW, calculated using the MM2 program. This approach can be applied to quantitatively explain chromatographic retention. The individual MI energy value supports selectivity. The degree of apc values at the contact site explains the centralization of localization effects and further interactions beyond the fundamental, supporting further study of chromatographic retention with model phases.

The hydrophobicity of graphitized carbon is essential, and the interaction with hydrophobic compounds is too strong to remove. This property was applied for the fast chromatographic analysis of guanidine compounds. The system was assembled with three types of columns, including one graphitized column and one eluent. The compounds weakly retained on an octadecyl-bonded silica gel were separated on a graphitized carbon column. This system was applied to identify different types of kidney diseases [17]. A similar system was used for the fast analysis of aromatic amino acid metabolites (catecholamines) [18]. Further, liquid chromatography using a graphitized carbon column clarified the chromatographic behavior of cis-fatty acids [19]. Graphitized carbon synthesized from a silica gel matrix retains silica gel's properties; therefore, unexpected retention was observed [20].

6.8. Solvent effect: Interaction between an analyte and a solvent-phase

The solvent contribution is significant in liquid chromatography. An analyte contacts the phase's surface, is replaced by solvent molecules, and leaves the location. The one-step adsorption and desorption process is defined as one theoretical plate number based on the physical part of chromatography. More repeated processes increase the theoretical plate number; therefore, the system's purification (separation) power improves. As a solid phase's selectivity (affinity) is important, that of a solvent, generally we call the solvent eluent as a mixture of solvent and ions, is the key factor of the purification (separation) process. The simplest model analysis is demonstrated for targeting the most common liquid chromatography system, reversed-phase liquid chromatography, using a simple model phase.

6.8.1 interactions with a model water-phase: The comprehensive capability of liquid chromatography comes from unlimited solvent selection. However, no systematic selection guide exists; therefore, handling liquid chromatography is difficult. The long-time experiment helps the solution. Previously, the molecular interaction between the analytes and the model phases was studied. This chapter describes solvent effects using models of solvent phases, as explained, in relation to analytes and model solid phases. The fundamental problem in handling solvent effects is that no solubility prediction method is available. Therefore, this approach provides the initial information about solvent effects in liquid chromatography but does not provide the absolute answer.

The best condition to describe solvent effects is that solvent molecules completely cover an analyte. The model experiment can be done using a molecular dynamics program; however, the optimized conformations by molecular dynamics do not show a reproducible structure. Therefore, we apply a flat model phase to obtain basic information about solvent effects.

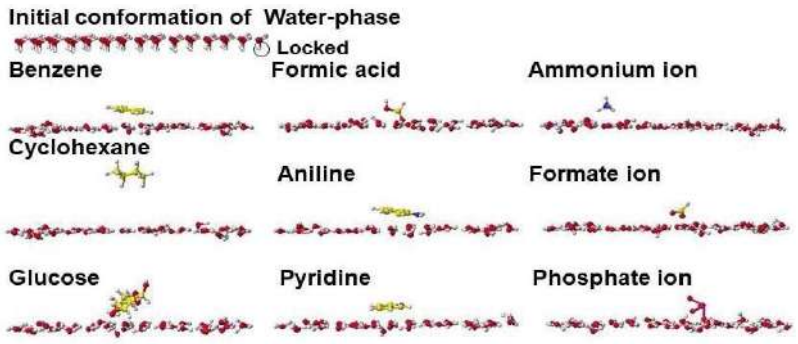


Figure 6.15-: Retention of standard compounds on a water phase.

The simplest method to create a solvent phase is to modify the silanol phase prepared in Chapter 5. Change silicones to carbons; then, cut bonds between carbons. Now you have a model methanol phase containing 43 methanol molecules to study solvent effects. However, lock carbon atoms to avoid forming clusters after optimizing the structure. The structure of the model methanol phase is given in the homework. Converting the methyl group of methanol to hydrogens makes a model water-phase shown in Figure 1. The surface hydrogens are free, and the bottom hydrogens are locked. This model

does not produce clusters, but water molecules can move freely. Locate analytes at the center of the model phase (8 Å); then optimize the structures. The resulting conformations are shown in Figure 1. Molecules and ions have hydrogen-bonding capability and are contact-adsorbed with the model water phase. Cyclohexane is inert and has no hydrogen-bonding capability; it does not move and stays at the initial position. The calculated energy values are summarized in Table 6.12.

Table 6.12: Selectivity of the water phase.

Analyte	FS	HB	ES	VW	MIFS	MIHB	MIES	MIVW
Benzene	-179.851	-131.621	-59.621	20.635	26.7843	31.238	27.373	-1.467
Cyclohexane	-139.072	-99.754	-61.273	17.945	0.6401	-0.16	29.025	1.851
Glucose	-148.699	-119.474	-57.961	21.173	19.076	15.626	33.96	-0.389
Formic acid	-168.056	-119.786	-67.998	18.599	17.2814	19.205	30.763	-2.331
Aniline	-176.829	-128.96	-59.819	18.872	25.7179	27.712	27.571	0.707
Pyridine	-172.487	-124.487	-61.949	20.068	24.0477	24.573	29.701	-1.048
Ammonium ion	-150.08	-103.904	-65.737	16.84	6.7153	3.99	33.489	-0.678
Formic ion	-150.775	-95.807	-88.9	12.91	5.845	-4.107	36.652	3.252
Phosphoric ion	-128.555	-102.555	-72.333	14.513	61.9747	2.641	40.085	1.649
Water-phase	-144.9898	-99.914	-32.248	16.162				

Unit: kcal. mol^{-1}

The MIHB values of benzene, glucose, formic acid, aniline, and pyridine contribute to the interactions. The high MIES value of cyclohexane is not due to cyclohexane itself; it is caused by water molecules. This information suggests that MIES values for other analytes may not be produced from their analytes. The above analysis was performed without pre-optimizing the model water phase. Following the discussion, the optimized model water phase uses the MM2 program to study the effect of experimental processes. Figure 16 shows the complex conformations optimized using the analytes and the pre-optimized model water phase, and Table 13 summarizes the calculated energy values.

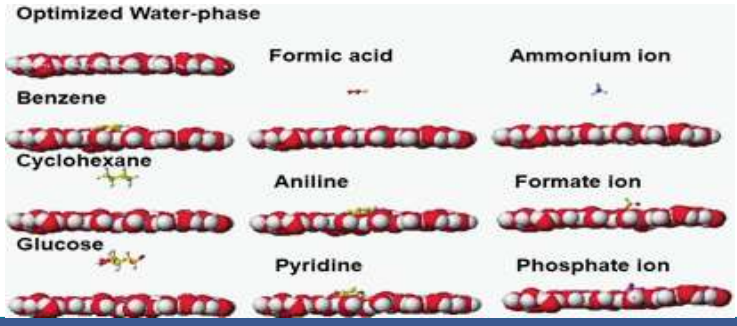


FIgure 6.16-: Retention of standard compounds on an optimized water phase.

Table 6.13: Selectivity of a water phase 2.

Analyte	FS	HB	ES	VW	MIFS	MIHB	MIES	MIVW
Benzene	-181.969	-131.83	-32.903	22.384	28.9024	31.916	0.655	-3.216
Cyclohexane	-138.814	-99.404	-62.609	19.28	0.3822	-0.51	30.361	0.516
Glucose	-129.319	-103.319	-54.276	20.229	0.3126	-0.529	30.275	0.555
Formic acid	-172.658	-122.806	-69.47	18.553	21.8835	22.225	32.225	-2.285
Aniline	-181.175	-130.579	-64.608	20.852	30.0641	29.331	32.36	-1.273
Pyridine	-175.792	-127.581	-61.928	19.984	26.4553	27.667	29.68	-0.964
Ammonium ion	-151.093	-103.328	-67.726	17.14	7.728	3.414	35.478	-0.978
Formic ion	-153.293	-100.22	-69.024	14.64	8.363	0.308	36.776	1.552
Phosphoric ion	-138.293	-110.867	-76.365	16.722	72.087	10.953	44.117	-0.58
Water-phase	-144.9898	-99.914	-32.248	16.162				

Unit: kcal. mol^{-1}

Comparing the MIH and MIES values in Tables 12 and 13 for benzene and glucose clarifies the focus of this experiment. While the hydroxyl groups of the model phase are free, hydrogen bonding with the analyte forms easily. The benzene MIES value (0.655) in Table 6.13 supports that benzene retention did not occur via electrostatic interaction. The unexpected MIES contribution is due to water-molecule clustering, which can be observed using molecular dynamics analysis. Not producing clusters is fundamentally required to cancel MI energy values within solvent molecules. A straightforward approach is to keep a certain distance between solvent molecules.

6.8.2 Interations with a model acetonitrile-phase: AAcetonitrile, classified as a donor solvent, is commonly used in liquid chromatography. Liquid chromatography is analyzed using a model phase. One approach to preparing a model acetonitrile phase is to use the silanol phase, replace oxygen with carbon and hydrogen with nitrogen, and change the single bond between oxygen and nitrogen to a triple bond. The second approach uses the methanol phase and converts oxygen and hydrogen to carbon and nitrogen, then the single bond to a triple bond. The optimized structure is shown in Figure 17, and the calculated energy values are summarized in Table 14.

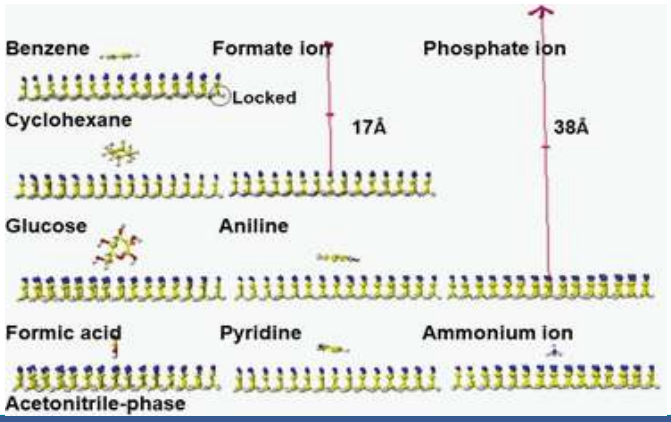


Figure 6.17-: Retention of standard compounds on an acetonitrile-phase.

Table 6.14: Selectivity of acetonitrile phase.

Analyte	FS	HB	ES	VW	MIFS	MIHB	MIES	MIVW
Benzene	257.7384	0	334.093	-97.567	3.5625	0	-10.036	5.187
Cyclohexane	271.8651	0	334.024	-97.413	3.9612	0	-9.987	0.517
Glucose	277.5917	-3.964	339.065	-95.606	7.0429	0.03	-6.761	2.021
Formic acid	258.2153	-0.666	325.646	-98.075	5.268	-0.001	-6.586	3.931
Aniline	258.4916	-1.334	333.646	-97.999	4.6549	0	-9.589	0.997
Pyridine	261.4156	0	333.912	-97.46	3.5054	0	-9.855	0.458
Ammonium ion	255.5602	0	321.569	-98.066	15.3325	0	2.488	1.064
Formic ion	271.6021	0	336.096	-96.987	-2.2742	0	-12.039	-0.015
Phosphoric ion	302.6401	0	336.573	-96.99	45.4115	0	-12.516	-0.012
Acetonitrile-phase	269.2679	0	334.057	97.002				

Unit: kcal. mol^{-1}

The specificity of donor solvent acetonitrile is easily estimated from Figure 3. Anions are repelled from the surface: the formate ion is repelled to 17 Å, and the phosphate ion to 38 Å, depending on their ionic strength. Glucose and formic acid are trapped with weak hydrogen bonding, and the ammonium ion is trapped by electrostatic interaction.

6.9 Competitive solvent effects

6.9.1 Compututive between pentane and water phase: The movement of analytes toward either the packing surface or eluent is adsorption or desorption in liquid chromatographic processes. We studied an analyte's affinity for either the packing material surface or the solvent phase using parallel phases of the model phases. As shown in Figure 18, an analyte was placed at the center of two phases separated by 13 Å; the structure was then optimized. The first trial was the selectivity of the water and pentane phases. The conformations of these analytes are shown in Figure 18.

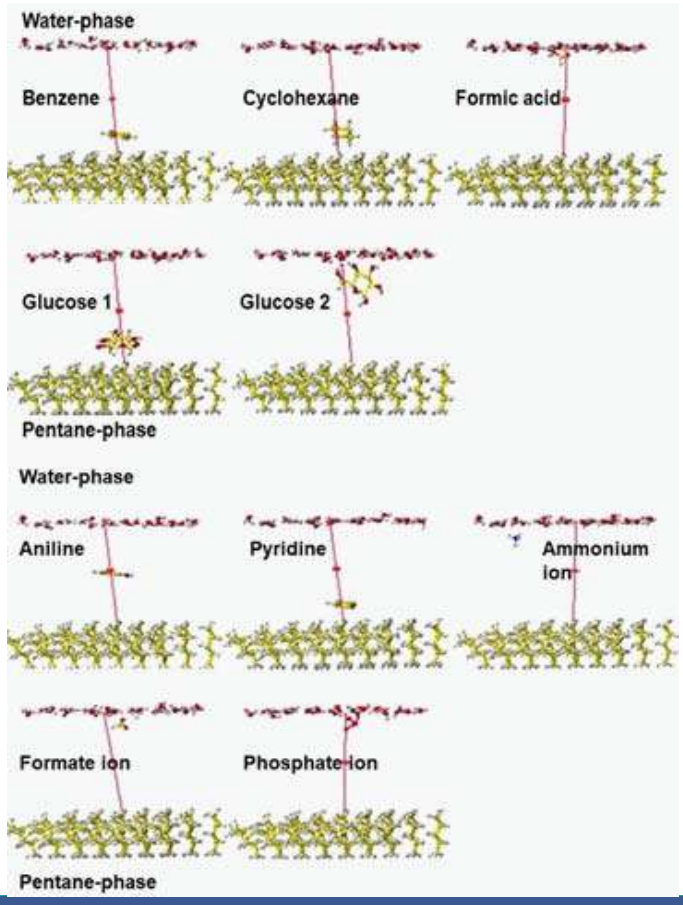


FIgure 6.18-: Competitive interaction between water and pentane phases.

Benzene was shown before; hydrogen bonding with the water phase shifted toward the pentane phase. The hydrophobic compound cyclohexane also moved toward the pentane phase. Polar formic acid and ions moved toward the water phase. Aniline stayed in its initial position, and pyridine moved toward the pentane phase. Glucose demonstrated unpredictable behavior. The hydroxyl group's initial position was critical, and it had an affinity interaction with the water phase. Aniline's initial position was also critical; a slight shift toward the pentane phase caused aniline to move toward it. The location of substituents was also critical for the interaction. The hydroxyl groups were repelled from the pentane phase, and the hydrophobic groups were repelled from the water phase. The calculated MI energy values are summarized in Table 15.

Table 6.15: Selective retention between water and pentane phases.

Analyte	FS	HB	ES	VW	MIFS	MIHB	MIES	MIVW
Benzene	149.3265	-100.615	-60.861	-4.617	2.4024	-3.301	-2.329	7.727
Cyclohexane	157.2978	-105.607	-64.037	-2.618	9.0665	1.691	0.847	6.356
Glucose	164.6207	-110.833	-55.136	-2.218	10.5519	2.983	0.193	6.944
Glucose 2	158.0259	-123.431	-59.404	6.462	17.1367	15.581	4.461	-1.736
Formic acid	133.9	-124.314	-69.996	1.459	20.1209	19.731	1.809	-1.249
Aniline	154.6837	-104.112	-62.19	2.396	-0.9992	-1.138	-1	1.125
Pyridine	148.5933	-102.839	-63.559	-4.468	6.8657	-1.077	0.369	7.43
Ammonium ion	157.5873	-104.842	-66.158	0.314	3.8434	0.926	2.968	-0.21
Formic ion	160.3589	-97.791	-66.523	-2.092	-0.493	-6.125	3.333	2.196
Phosphoric ion	173.0288	-108.161	-75.372	-1.079	65.5608	4.245	12.182	1.183
Water-pentane phase	159.8059	-103.916	-63.19	0.104				

Unit: kcal. mol^{-1}

The contact of hydrophobic compounds (benzene, cyclohexane, pyridine) with the pentane phase is dependent on MIVW. Polar compounds (glucose2, formic acid) are retained due to MIHB. The contact of ions (ammonium ion, formic ion, phosphate ion) is due to MIES. Figure 19 shows the competitive interactions between acetonitrile and pentane.

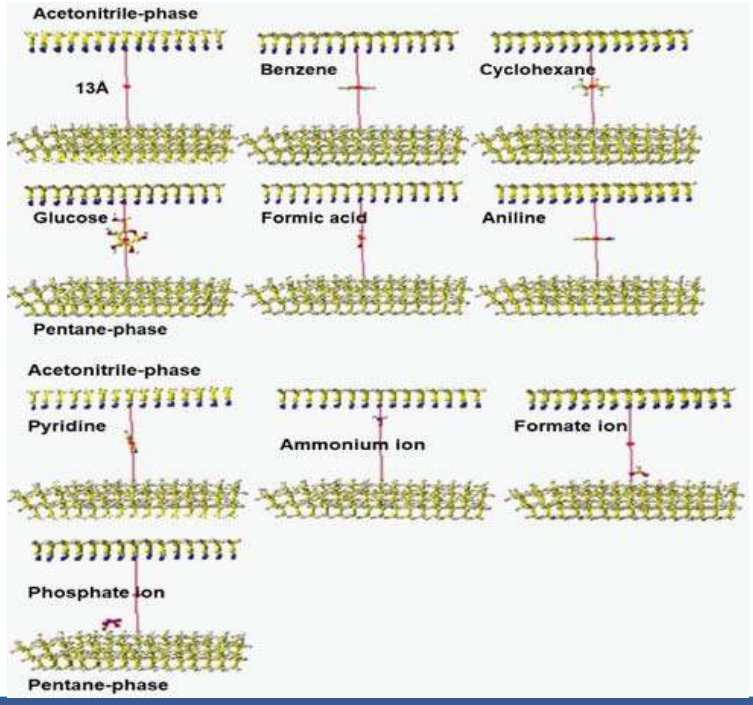


FIgure 6.19-: Competitive interaction between acetonitrile and pentane phases.

Benzene, cyclohexane, and aniline stayed at their initial positions. Glycose was rotated and moved toward the acetonitrile phase, and the formic acid hydroxyl group moved toward the acetonitrile phase. The phosphate ion has a hydrogen-bonding hydroxyl group, but an oxidative group moved toward the pentane phase. The calculated MI energy values are summarized in Table 16.

Table 6.16: Competitive interaction between acetonitrile and pentane.s

Analyte	FS	HB	ES	VW	MIFS	MIHB	MIES	MIVW
Benzene	569.3681	0	334.036	-111.46	0.7483	0	-0.002	0.746
Cyclohexane	563.6934	0	334.032	-111.155	21.0584	0	0.002	1.069
Glucose	588.162	-3.991	340.305	-111.998	5.3981	0.057	1.976	2.9
Formic acid	569.3197	-0.663	326.876	-113.946	3.0891	-0.004	2.161	0.332
Aniline	571.2678	-1.334	334.025	-111.174	0.8042	0	0.09	0.871
Pyridine	572.522	0	333.673	-111.724	1.3245	0	0.361	0.862
Ammonium ion	564.4817	0	321.621	-114.763	15.3365	0	12.413	1.043
Formic ion	578.6614	0	337.273	-116.713	-0.408	0	-3.239	2.993
Phosphoric ion	619.9288	0	347.387	-117.884	37.0483	0	-13.353	4.164
Acetonitrile-pentane phase	578.1934	0	334.034	-113.72				

Unit: kcal. mol^{-1}

Analytes contact with the acetonitrile phase with MIES. Formic acid and phosphate ion contact the pentane phase with weak MIVW. This simple experiment does not demonstrate the absolute solvation conformation; however, it helps explain the contribution of solvents.

6.10. Column switching and isocratic elution system for fast, sensitive, and reproducible chromatography

The applications of High-pressure, high-flow-rate separation is not ideal for obtaining stable, sensitive, and

reproducible results. Gradient elution is commonly used for fast separation. Gradient elution is fast, but it requires re-equilibration and is generally not suitable for highly sensitive detection. A column-switching method is complicated because of the instrumentation needed. Once a system is established, however, a stable, reproducible, and highly sensitive chromatography can be achieved.

Column-switching separation, based on the selectivity and retention capacity of packing materials, is an ideal chromatographic condition for obtaining reproducible, highly sensitive results. A column-switching system is used for trace enrichment, sample clean-up, and the so-called heart-cut, where target fractions from the first column are transferred online to a second column with different properties for further separation. The second method is also called two dimensional chromatography. This method can be applied to multi-column switching methods (multi-dimensional chromatography). Applications are classified based on differences in hydrophobicity, Coulombic force, molecular size, steric hindrance of analytes, affinity, and enzyme reactions, and on application to spectrophotometric analysis. The typical and selected references are given.

A double-column amino acid analyzer is considered the first column-switching instrument. Once the same sample had been applied to columns of anion and cation exchange resins, acidic and basic amino acids were separated in parallel and detected. The system was modified for a single injection using a switching valve, column switching are classified into two types: the use of a short column for trace enrichment in environmental analyses and for sample clean-up in biomedical analyses; and the so-called heart-cut, where target fractions from the first column are transferred, online, to a second column with different properties for further separation. The second method is also called two-dimensional chromatography. The fast, two-dimensional chromatographic system is built around gas chromatography, and with the addition of a mass spectrometer, is called three-dimensional chromatography. Typical examples of heart-cut are enantiomeric separation and ionic separation. Furthermore, the same category of compounds is continuously separated using the different retention powers of packing materials. This article describes a methodology for preparing a successful column-switching system based on analyte properties.

6.10.1 Methodology: The success of column switching depends on the molecular properties of analytes and packing materials. A packing material can selectively separate a group of compounds from other analytes. Packing-material selection depends on retention factors in chromatography. These factors are the same as solubility parameters, such as van der Waals forces, Coulombic forces, and steric hindrance. Hydrogen bonding and charge-transfer interactions, such as Lewis acid-base interactions, can be included as weak Coulombic forces [l]. These molecular properties are calculated *in silico* as van der Waals, hydrogen bonding, and electrostatic energy values. The electrostatic energy includes Lewis acid-base, charge-transfer, and Coulombic forces; these terms are used by different fields of chemists. Column-switching separation is classified as follows

I. Dependent on the difference in hydrophobicity of analytes.

2. Dependent on the difference in Coulombic force of analytes.

3. Dependent on the molecular size of analytes.

4. Dependent on the steric hindrance of analytes.

5. Affinity and enzyme reactions.

6. Application to mass spectrophotometric analysis.

A separation is described by the following equation, which indicates the degree of resolution between two peaks in a chromatogram. R_s. A complete separation requires $R_s > 1.2$ units.

$$R_s = [\{(a - 1)/a\}\sqrt{N}]/4$$

Resolution can be improved by increasing the column plate number (physical parameter), *N,* and/or the separation factor; selectivity of packing materials and the ratio of the capacity factors of two compounds. *N* is the physical parameter and α is the chemical parameter for the separation [1].

Column switching uses the selectivity, α, of packing materials, but not the column's theoretical plate number.

Understanding the chemistry of the retention in liquid chromatography is the key to preparing a column-switching system. Reference [21] provides details on packing materials and structure. A diagram of the system is shown in Figure 42. A variety of compounds have been effectively analyzed using column switching.

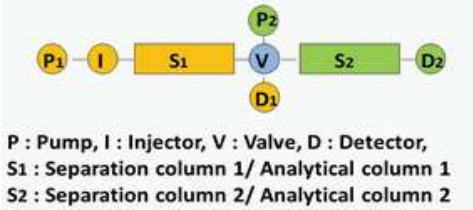


Figure 6.42-: Column-switching systems using two columns

6.10.2. Dependent on the Difference in Hydrophobicity of Analytes: Pre-concentration on a hydrophobic cartridge is a commonly used pretreatment in trace analyses. A variety of pre-columns have been used in reversed-phase liquid chromatography for online pre-filtration and pre-concentration. A small column for solid-phase extraction is used to pre-concentrate trace amounts of relatively hydrophobic compounds, especially in environmental analyses. Trace metals are derivatized and concentrated in a hydrophobic phase, then transferred to a separation column [22]. Peptides, drugs, and relatively hydrophobic compounds in environmental water samples were also concentrated in a hydrophobic phase and separated on a separation analytical column. The choice of packing material allows selective concentration of a specific range of hydrophobic compounds. Biological samples require deproteinization before applying the sample solution for a chromatographic analysis. A variety of chemicals in urine, serum, and tissues can be concentrated on a hydrophobic phase after deproteinization, and then separated in an analytical column. Numerous reports have been published on the concentration of trace compounds. Some modifications to packing materials for solid-phase extraction have been made for the direct injection of biological samples without deproteinization. Preconcentration approaches for trace compounds in biological samples [23] and trace substances in surface waters [24] were applied.

Restricted access packing materials (RAMS) have both hydrophobic and hydrophilic sites.[18] Also called internal-surface reversed-phase packing materials, RAMs have two functions: the surfaces of particles (the end-groups of bonded phases) are polar to reflect the adsorption of, e.g., proteins, while the surfaces within the pores (the inner compartment of bonded phases) are relatively non-polar to support the hydrophobic adsorption of, e.g., drugs. Such a solid phase (packing material) is also called a shielded hydrophobic phase, mixed functional phase, or dual-zone phase. This type of material can be prepared by coating proteins and cellulose. Relatively polar organic porous polymers are also used for this purpose. New bonded phases have been developed. The hydrophilic phase of the particle surface prevents protein adsorption, while the hydrophobic site adsorbs hydrophobic compounds. The hydrophobicity is designed using different ligands. A column packed with inner hydrophobic packing materials is used for online prefiltration of proteins in biological samples. Relatively hydrophobic compounds are trapped inside of the hydrophobic sites of the packing material and transferred to an analytical column for further separation. Inserting a low-concentration column before the second analytical column is useful for trace analysis.

Table 6.27: Properties of basic compounds.

	Basic drugs	log *P*	p*Ka*
1	Theobromine	-0.78	9.9
2	Allopurinol	-0.55	9.4
3	Caffeine	-0.07	14
4	Theophylline	-0.02	8.6
5	Scopolamine	0.98	7.75
6	Triamterene	0.98	6.2
7	Homatropine	1.45	9.9
8	Carbamazepine	1.98	13.9
9	Procain	2.14	8.11
10	Lidocaine	2.26	7.9
11	Quinine	3.44	4.1

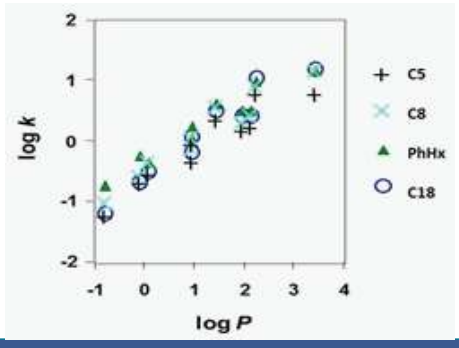


FIgure 6.43-: Retention strength of column based on hydrophobicity of basic drugs. Column size: 50 x 3.0 mm I.D., Eluent: 50% methanol containing 10 mM ammonium formic acid (pH 10.2), Flow rate: 0.40 mL min-1, at 40°C.

For quantitative analysis, how to precisely calculate peak area is the key factor, and the time constant of the integration reduces peak recognition from peak fronting and tailing; however, the time constant cannot be used to calculate the actual peak area obtained in gradient elution. One solution is applying isocratic elution with a column-switching system. One example demonstrates chromatograms measured in the same analysis time. Elution order in reversed-phase liquid chromatography of basic drugs is also based on hydrophobicity (log *P*: octanol-water partition coefficient) [**21, 25, 26**]. We correlated log *P* values with log *k* values measured in an eluent containing 50% methanol and 10 mM ammonium formate (pH 10.2). The slope and intersection demonstrated the selectivity of these bonded-phases. Figure 39 summarizes the relationship. The properties of these basic drugs are collected in **Table 27**. Here, relative hydrophobicity (log P) is used to compare selectivity and to achieve fast isocratic separation of basic compounds. (log P) is used to compare the selectivity and exhibits fast isocratic separation of basic compounds.

The strength of hydrophobicity of these bonded phases for these compounds was column-dependent. The correlation between log *P* and log *k* values was 0.97 (PhHx), 0.97 (C18), 0.97 (C8), and 0.95 (n = 10). The low correlation coefficient compared with acidic drugs is because these basic drugs were not in their ionized form based on their p*K*a values and the eluent used for LC-MS. The log *k* values measured using the C18 column were similar to those measured on the C8 column. This means these compounds did not require longer alkyl-chain bonded phases because of their molecular size. The requirement differs from that of carotenoids whose molecule shape is quite long.

The correlation coefficient between results obtained using octadecyl (C18)-bonded silica gel columns and those obtained using either pentyl (C5)- or octyl (C8)-bonded silica gel columns was1.00 (n = 10). The result indicated that these three columns have no specific selectivity. The difference lies in hydrophobicity strength. When a shorter analytical time is required, increasing the organic modifier concentration or using a shorter column is used. However, this approach is called the accordion effect, and resolution becomes poor. One solution to achieve shorter analysis times is to construct an isocratic-elution and column-switching system. Figure 44 shows example chromatograms. Basic drugs having longer retention times due to their log *P* values were separated using a short (50 mm) C5 column, and those weakly retained on the C5 column due to their low log *P* values were separated using a combined 50 cm C5 column and a 150 cm C18 column. These mixtures were separated within 15 min.

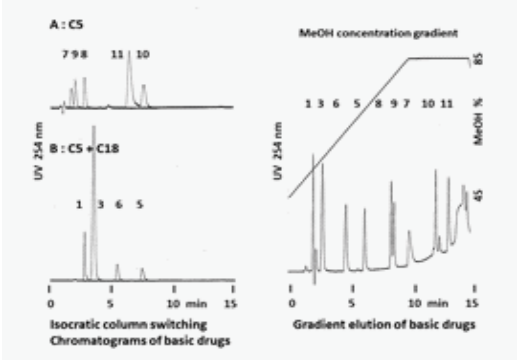


FIgure 6.44-: Quick separation of basic drugs using isocratic and column switching elution. Column A: C5 50 x 3.0 mm I.D., Column B: C18 150 x 3.0 mm I.D.; eluent: 45% methanol containing pH 10.2 ammonium formate; flow rate: 0.40 mL min-1 at 40oC; peak number: see Table 24.

Isocratic isocratic-elution and column-switching separation: Column, C5: 50 x 3.0 mm I.D., C18: 150 x 3.0 mm I.D.; Eluent: 47% MeOH containing10mM $HCOONH_4$ (pH 9.00); Gradient chromatogram: Column, C18 150 x 3.0 mm ID; Eluent: 45 - 85% MeOH containing10mM $HCOONH_4$ (pH 10.20); Flow rate: 0.40 mL min^{-1}; Column temp: 40ºC; Peak number: see Table **27**. Basic compounds are separated within 15 min. One uses two columns (A and B), and the other uses gradient elution. The column-switching method's capability is clearly visible, and the reproducibility is summarized in Table 28.

Table 6.28: Reproducibility (standard deviation: SD) of retention time (RT) and peak area.

Basic drugs	Isocratic			Gradient		
No	RT min	SD %	Area SD %	RT min	SD %	Area SD %
6	5.464	0.01	0.16	4.828	0.22	0.8
5	7.455	0.03	0.18	6.357	0.5	0.85
7	1.687	0.18	0.44	8.531	0.44	0.46
9	2.009	0	0.02	8.772	0.43	0.98
8	2.744	0.08	0.18	10.07	0.12	0.42
11	6.423	0.03	0.16	12.22	0.34	0.94
10	7.561	0.19	0.21	13.32	0	0.79

The standard deviation (SD) values of retention time and peak area clearly indicate higher reproducibility in the isocratic elution system than in the gradient elution system, due to the flat baseline. Furthermore, isocratic elution permits the use of a highly sensitive electrochemical detector. Skilled chromatographers should develop column-switching and isocratic elution systems for reliable qualitycontrol analysis. Furthermore, gradient elution requires column reconditioning time to re-equilibrate columns, but isocratic elution permits continuous injection for short analysis time. The preparation of eluent is also simplified, too.

The combination of isocratic elution and a column-switching system with a narrow inter-diameter (3 mm) column demonstrated reproducible retention time and peak area. Furthermore, it achieved a shorter analysis time than gradient elution. In gradient elution, it requires skill to read peak area because of baseline change. However, the baseline is flat in isocratic elution. Continuous injection can be performed in isocratic elution, but gradient elution requires a re-equilibration interval. The larger the organic modifier concentration change, longer the re-equilibration interval. Consider a combination of isocratic elution and a column-switching system to perform reproducible, short-analysis-time chromatography for your regular chromatographic work. This technique also offers advantages for easy LC system maintenance and troubleshooting.

These factors improve separation factors and selectivity for purification (separation) of target compounds. The above example shows differences in hydrophobicity, selection of different hydrophobic bonded-phase silica gels, and balancing organic modifier concentration. A slightly complex column-switching system is used to separate amino acids and guanidine compounds. The system can be applied in practice for large-scale purification processes without highly theoretical plate-number columns. In particular, we cannot use theoretically high-plate-number columns for purification processes, and we must carefully manage the selectivity of packing materials and solvents. Water is a terrible solvent. Removal is costly, and high temperatures damage chemicals. Freeze-drying is not suitable for large-scale operation.

Biological samples are injected directly, and drugs and their metabolites are analyzed: for example, loxoprofen in human serum for pharmacokinetic study [27], propiverine in human plasma [28], rabeprazole for a bioequivalence study [29], phenols in animal feed [30], organophosphorus esters in human plasma [31].DNA fragments [32] and benzodiazepine in urine [33]. A longer first column is also used to purify target compounds, and the fractions are transferred to a second column to further separate drugs in blood and urine. Baicalein, rhein, and berberine in rat plasma [34] and amoxicillin in human plasma.[35]. A two-column system was used to analyze radio ligands and their metabolites in plasma [36].

The major application of column switching is sample clean-up using a small column. A combination of different hydrophobic columns in parallel permits fast separation of a variety of hydrophobic mixtures with isocratic elution. Free amino acids include very polar, polar, and hydrophobic amino acids. These three groups were separated in parallel using three types of hydrophobic columns by forming a copper complex online [37]. Very polar compounds such as guanidino compounds, were also separated by reversed-phase ion-pair liquid chromatography using a hydrophobic packing material, a carbon column [37]. Catecholamine-related compounds, metabolites of hydrophobic aromatic amino acids, were also effectively separated using a combination of different hydrophobic packing materials [18].

6.10.3. Dependent on the Difference in Coulombic Force of the Analytes: Biological sample matrices are very complicated. Therefore, selective concentration of target compounds has been performed using ion-exchange trap columns. Sample components are separated into three groups, i.e., acidic, basic, and neutral. Further separation is carried out using reversed-phase liquid chromatography or ion-exchange liquid chromatography, with a longer ion-exchange column. Conversely, the first separation is carried out using reversed-phase liquid chromatography, and then further separation is performed by ion-exchange liquid chromatography. Using ion exchangers expands the capability of a simple clean-up. Ion exchange separated proteins [38] and peptides in human blood [39]. Piritramide in human plasma [40]. Ion exchange was used to analyze vancomycin in plasma [41], acidic compounds in plasma [42], nutrients in high chloride concentration [43], and inorganic selenium [44].

Ionized compounds were eluted rapidly from a reversed-phasecolumn. Thus, reversed-phase ion-pair liquid chromatography was used to separate a mixture of hydrophobic and ionic compounds. The column-switching method for reversed-phase ion-pair liquid chromatography is the same as for reversed-phase liquid chromatography. A very common application, due to Coulombic force, is sample pretreatment. Removing ionic compounds for the analysis of neutral compounds, such as saccharides ,is an example. The separation of acidic and basic drugs is another example.

6.10.4. Dependent on the Molecular Sizes of Analytes: This approach has been applied to separating polymers, oligomers, and monomers. Each fraction is then further separated using a suitable separation method. One example is the separation of saccharides in exploded wood [45, 45a]. Proteins, peptides, and amino acids were analyzed, step by step, and automated column-switching separation was studied. However, protein separations do not compete with those achieved by two-dimensional electrophoresis.

A size-exclusion column is also used for sample pretreatment in biomedical analyses. Mainly, larger molecules like proteins are eluted within the exclusion limit. Then, small molecules, the target molecules, are further separated by either reversed-phase liquid chromatography or ion-exchange liquid chromatography. Proteins and non-target fractions are eluted, and the target fraction is transferred to an analytical column. This system was applied to a pharmacokinetic study of omeprazole and rabeprazole [46] and an automated determination of 5-fluorouracil and its metabolites [47]. A variety of newly developed restricted access packing materials has partly replaced size-exclusion columns.

6.10.5. Dependent on the Steric Hindrance of Analytes: The molecular size effect is used in size-exclusion liquid chromatography. The steric effect, a difference in molecular shape, is mainly applied to normal-phase liquid chromatography. Enantiomeric separation is usually carried out with normal-phase liquid chromatography, using specially designed packing materials such as the Pirkle type [48] and modified cyclodextrins[49]. Natural polymers with steric selectivity are also used for enantiomeric separation, using the natural form or a modified form, like α-1-acid glycoprotein [50], amylase *tris* (3,5-dimethylphenylcarbamate) [51], and ovomucoid [52.]. Enantiomeric separation columns have limited separation power, as indicated by the theoretical plate number. First, the mixtures are separated using reversed-phase liquid chromatography, then the target fraction is transferred from the reversed-phase to the enantiomeric separation column.

The difficulty in the transfer from the reversed-phase to the separation column is due to unmatched eluent components. Some technical solution is required to establish this system. When an aqueous eluent is used for the first column, a small amount of aqueous solution should be miscible in the non-aqueous eluent of the enantiomeric column. Another solution is to use a small trap column to reduce the excess aqueous solution, then backflush into an enantiomeric separation column using a suitable solvent (eluent).

6.10.6. Affinity and Enzymatic Reaction: Proteins attract molecules selectively. Selectivity and affinity were used after immobilizing proteins on packing materials. Affinity is not 100 percent effective; therefore, the affinity-based mixtures were further purified using a second column. Polyclonal antibodies [53], monoclonal antibodies [54] and β-cyclodextrin [55] were immobilized for specific purifications. The immobilization technique is applied to immunoassays, even if the precision of the quantitative analysis is less than that of liquid chromatography. Man-made affinity polymers, molecularly imprinted packing materials, have been developed for the selective concentration of targeted compounds. The key compounds are 17β-estradiol [56], bisphenol [57], atropine, propranolol, naproxen, and ibuprofen [58]. The difficulty of synthesizing a suitable imprinted polymer stems from the molecular shape of the target compounds during packing and extraction from the sample solution.

Quantitative analysis of enzyme reactivity is performed using an immobilized enzyme column. Given the difficulty of obtaining a relatively large amount of enzyme and retaining enzymatic activity after immobilization, several reaction columns have been synthesized, such as monoamine oxidase [59], β-glucuronidase [60], lipase [61], phenylethanolamine *N*-methyltransferase [62], horse liver alcohol dehydrogenase [63], and nicotinic acetylcholine receptor [64]. An enzyme column was developed for online trypsin digestion to analyze protein components [65]. An inorganic catalytic Pt/Rh alumina column was used to determine nitropyrene metabolites with chemiluminescence detection [66]. These online sample treatments improve quantitative analysis of targeted compounds and enable automated analysis.

6.10.7. Application to Mass Spectrometric Analysis: A mass spectrometer is a powerful tool for identifying analytes; however, a direct, free connection between liquid chromatography and a mass spectrometer is not permitted. At the very least, inorganic salts should be eliminated prior to the use of mass spectrometer. One approach is to collect the target fraction in a small trapped column, then wash out interfering components before introduction to the mass spectrometer. Even if one uses a small column with volatile salt, one must wash the mass chamber very often to maintain its sensitivity.

Polar compounds are separated using ion-exchange liquid chromatography; however, the inorganic salt should be eliminated before mass spectrometric analysis. The targeted fraction is collected on a small trap column, then the salt is removed with a volatile ion-pair reagent, and the compounds are introduced into the mas spectrometer [67]. A miniaturized separation column with a volatile eluent and a desalting column are ideal when using a mass spectrometer as a detector. We have seen how column switching can expedite separation of substances of interest, using techniques that take advantage of dependence on the differences in hydrophobicity of analytes; dependence on the differences in Coulombic force of analytes; dependence on the molecular size of analytes; dependence on the steric hindrance of analytes; affinity and enzymatic reactions; and application of mass spectrophotometric analysis.

Major advances have been made in the design and development of bonded phases made from silica gels. These bonded phases combine the advantages of silica and organic polymers (i.e., high mechanical strength and extended pH stability). Selecting columns allowed measurement of albumin-drug binding affinity without albumin [68]. Computational chemistry is a useful tool for designing new materials, for studying molecular interactions, and for predicting molecular properties [68]. Combining computational chemical analysis with chemical and physical analyses will enhance the development of packing materials, improve effectiveness, and facilitate chromatographic analysis. This computational approach is based on modeling analysis of chromatography and can be applied to enzyme reactivity by replacing model phases with enzymes. Such *in silico* analysis also supports drug discovery [69].

References

1. T. Hanai, Quantitative in silico chromatography, Computational modeling of molecular interactions, Royal Society of Chemistry, Cambridge, 2014, pp. 338. ISBN: 978-1-84973-991-7
2. T. Hanai, Quantitative in silico analysis of mammalian serine racemase activity, Intern. J. Chem. Math. Phys. (IJCMP), 2018, 2 (6), 53-58, https;// dx.doi.org/10.22161/ijcmp.2.6.1
3. T. Hanai, T. Quantitative in silico analysis of D-amino acid oxidase reactivity and inhibition, Current Bioactive Compounds, 2016, 13, 312-317. doi: 10.2174/1573407212666161014133246
4. G.E.Berendsen, K.A. Pikaart, L-de. Galan, C. Olleman, C. (Heptadecafluorodecyl)dimethylsilyl bonded phase for reversed-phase liquid chromatography, Anal. Chem. 1980, 52, 1990-1993. https://doi.org/10.1021/ac50062a056
5. T. Monde, T. Kamiusuki, T. Kuroda, K. Mikumo, T. Ohkawa, H. Fukube High-performance liquid chromatographic separation on a fluorocarbon-bonded silica gel column, J. Chromatogr. A, 1996, 722, 273-280, https://dor.org/10.1016/0021-9673(95)00436-X
6. Wakopak catalog page 51, Wako product information-Chromatography-8th edition.
7. K. Jinno, H. Nakamura, Retention characteristics of fluorinated bonded silica phase in reversed-phase liquid chromatography, Chromatographia 1994, 39, 285-293. https://doi.org/10.1007/BF02274515
8. M. Reta, P.W, Carr, P.C. Sadek, S.C. Rutan, Comparative study of hydrocarbon, fluorocarbon, and aromatic bonded RP-HPLC stationary phases by linear solvation energy relationships, Anal. Chem., 1999, 71, 3484-3496. Doi: 10.1021/ac990081l
9. T. Hanai, New developments in liquid-chromatographic stationary phases. Adv. Chromatogr. 2000, 40l, 315-357. ISBN: 0-8247-0018-X
10. T. Kamiusuki, T. Monde, N. Nakamura, K. Yano, T. Toko, T. Konakahara, Interaction between a solute molecule and a fluorocarbon bonded layer in reversed-phase high-performance liquid chromatography, J. Coll. Inter. Sci., 1999, 220, 123-127. https://doi.org/10.1016/jcis.1999.6518
11. C. West, E. Lemasson, S. Khater, E. Lesellier, An attempt to estimate ionic interactions with phenyl and pentafluoro[henyl stationary phases in supercritical fluid chromatography, J. Chromatogr. A, 2015, 1412, 126-138. https://doi.org/10.1016/j.chroma.2015.08.009

12. E. Regalado, A.A. Makarov, R. McClain, M. Przybyciel, C.J. Wilch, Search for improved fluorinated stationary phases for separation of fluorine-containing pharmaceuticals from their difluoro analogs, J. Chromatogr, A, 2015, 1380, 45-54. https://di.org/10.1016/j.chroma.2014.12.025

13. N.C. Yoder, D. Yuksel, L. Dafik, K. Kumar, Bioorthogonal noncovalent chemistry: fluorous phases in chemical biology, Cur. Opin. Chem. Bio. 2006, 10, 576-583. https://doi.org/10.1016/j.cbpa.2006.10.007

14. R. Xie, L. Zhou, A.E. Smith, C.B. Almquist, J.A. Berberich, N.D. Danielson, A dual grafted fluorinated hydrocarbon amine weak anion exchange resin polymer for adsorption of perfluorooctanoic acid from water. J. Haz. Mat. 2022, 431, 128521. Doi.org/10.1016/j.jhaxmat.2022.128521.

15. M. Sansotera, M. Gola, W. Navarrini, Perfluoropolyether-functionalized carbon-based materials and their applications, NewFluorinated Carbons: Fundamentals and applications. 2017, 361-392. http://dx.doi.org/10.1016/B978-0-12-803479-8.00015-2.

16. X. He, Y. He, S. Huang, Z. Fang, J. Liu, M. Ma, B. Chen, Fluoro-functionalized paper-based solid-phase extraction for analysis of perfluorinated compounds by high-performance liquid chromatography coupled with electrospray ionization-tandem mass spectrometry, J. Chromatogr. A, 2019, 1601, 79-85. https://doi.org/10.1016/j.chroma.2019.06.019

17. T. Hanai, Y. Inamoto, S. Inamoto, Chromatography of guanidine compounds, J. Chromatogr. B. Biomedical Sciences and Applications, 2000, 747, 123-138.

18. T. Hanai, K. Kaneko, H. Homma, Semi-micro liquid chromatography of aromatic amino acid metabolites using isocratic elution and Column switching, Biom. Chromatogr., 03 September 2002, https://doi.org/10.1002/bmc.176Digital Object Identifier (DOI)

19. K. Gaudin, T. Hanai, P. Chaminade, A. Baillet, Retention behavior of polysaturated fatty acid methyl esters on porous graphitic carbon, J. Chromatogr. A. 2007, 1157, 56-64.

20. T. Hanai, H. Homma, Quantitative in silico analysis of the selectivity of graphitic carbon synthesized by different methods, Anal. Bioanal. Chem. 2008, 390, 369-375.

21. T. Hanai, Selection of chromatographic method for biological materials, Advanced Chromatographic and Electromigration Methods in Biosciences, J. Chromatogr. Library, 60, Elsevier, Amsterdam, 1998, p. 1-51.

22. Z. Chen,G-Y. Yang,I.S. Wang, I.L. Li, Q. Su, Simultaneous determination of tin, nickel, lead, cadmium and mercury in tobacco and tobacco additives by microwave digestion and RP-HPLC followed by on-line column enrichment, J. Chin. Chem. Soc. 2004, 51, 71-77.

23. C. Cruz, I. Donizeti de Souza, C.F. Grecco, E.C. Figueiredo, Recent advances in column switching high-performance liquid chromatography for bioanalysis, Sustainable Chemistry and Pharmacy, 2021, 21, 100431, https://doi.org/10.1016/j.scp.2021.100431

24. K. Kochale, R. Cunha, T. Teutenberg, T. C. Schmidt, Development of a column switching for direct online enrichment and separation of polar and nonpolar analytes from aqueous matrices, Journal of Chromatography A, Date: 11 January 2024, 10.1016/j.chroma.2023.46455T.

25. Hanai, Optimization of liquid chromatography for biomedically important compounds, in T.Hanai, (ed) Liquid Chromatography in Biomedical Analysis, Journal of Chromatography Library 50, Elsevier, Amsterdam, 1991, 21-46.

26. T. Hanai, HPLC, A Practical Guide, Royal Society of Chemistry, Cambridge, 1999, pp 134. (ISBN: 0-85404-515-5)

27. H-Y. Cho, C-H. Park. Y-B. Lee, Direct and simultaneous analysis of loxoprofen and its diastereomeric alcohol metabolites in human serum by on-line column switching liquid chromatography and its application to a pharmacokinetic study, J. Chromatogr. B.2006,835, 27-34.

28. I.E. Ban, J-E. Maeng, J.S. Woo, C-K. Kim, Sensitive column-switching high-performance liquid chromatography method for determination of propiverine in human plasma, J. Chromatogr. B. 2006, 831, 230-235.

29. S.S. Singh, M. Jain, H. Shah, S. Gupta, P. Thakker, R. Shah, B.B. Lohray, Direct injection, column switching-liquid chromatographic technique for the estimation ofrabeprazole in bioequivalence study, J. Chromatogr. B. 2004, 813, 247-254.

30. I.M. Kawaguchi, S. Takahashi, F. Seshimo, I.N. Sakui, N. Okanouchi,R. Ito, K. Inoue, Y. Yoshimura, S. Izumi, T. Makino, H. Nakazawa, Determination of 4-tert.-octylphenol and 4-nonylphenol in laboratory animal feed sample by stir bar sorptive extraction followed by liquid desorption and column-switching liquid chromatography-mass spectrometry with solid-phase extraction, J. Chromatogr. A. 2004, 1046, 83-88.

31. I.N. Amini, C. Crescenzi, Feasibility of an on-line restricted access material; liquid chromatography tandem mass spectrometry method in the rapid and sensitive determination of organophosphorous triesters in human blood plasma, J. Chromatogr. B. 2003,795, 245-256.

32. A. Brink, U. Lutz, W. Voelkel, W.K. Lutz, Simultaneous determination of 6-methy1-2'-deoxyguanosine, 8-oxo-7,8-dihydro-2'-deoxyguanosine, and l,N6-etheno-2'-deoxyadenosine in DNA using on-line sample preparation by HPLC column switching coupled to ESI-MS-MS, J. Chromatogr. B. 2006, 830, 255-261.

33. A. Miki, M. Tatsuno, M. Katagi, M. INishikawa, H. Tsuchihashi, Simultaneous determination of eleven benzodiazepine hypnotics and eleven metabolites in urine by column-switching liquid chromatography-mass spectrometry J. Anal. Toxicol. 2002,26, 87-93.

34. L. Yi, J-P. Gao, X. Xu, L. Dai, Simultaneous determination of baicalein, rhein and berberine in rat plasma by column-switching high-performance liquid chromatography, J. Chromatogr, B.2006, 838, 50-55.

35. Q.B. Cass, R.F. Gomes, S.A. Calafatti, J. Pedrazolli, Determination of amoxicillin in human plasma by direct injection and coupled-column high-performance liquid chromatography, J. Chromatogr. A. 2003, 987, 235-241.

36. N. Vasdev and T. L. Collier, Design and Prototype of an Automated Column-Switching HPLC System for Radiometabolite Analysis, Pharmaceuticals, 2016, 9(3), 51; https://doi.org/10.3390/ph9030051

37. M. Hirukawa, M. Maeda, A. Tsuji, T. Hanai, Separation of free amino acids by reversed-phase ion-pair chromatography with column switching and isocratic elution, J. Chromatogr,. 1990, 507, 95-101.

38. I.M. Pepaj, S.R. Wilson, K. Novotna, E. Lundanes, T. Greibrok, Two-dimensional capillary liquid chromatography: pH gradient ion-exchange and reversed-phase chromatography for rapid separation of proteins, J. Chromatogr. A. 2006, 1120, 132-141.

39. E. Machtejevas, H. John, K. Wagner, L. Standker, G. Marko-Varga, W-G. Forssmann, R. Bischoff, K.K. Unger, Automated multi-dimensional liquid chromatography: sample preparation and identification of peptides from human blood filtrate, J. Chromatogr. B. 2004, 803, 121-130.

40. R. Kahlich, C.H. Gleiter, S. Laufer, B. Kammerer, Quantitative determination of Piritramide in human plasma and urine by off- and on-line solid-phase extraction liquid chromatography coupled to tandem mass spectrometry, Rapid Comm. Mass Spectrom. 2006, 20, 275-283.

41. M. Saito, T. Santa, M.Tsunoda, H. Hamamoto, N. Usui, An automated analyzer for vancomycin in plasma samples by column-switching high-performance liquid chromatography with UV detection, Biomed. Chromatogr. 2004, 18, 735-738.

42. O. Rbeida, B. Christiaens, Ph. Hubert, D. Lubda, K-S. Boos, J. Crommen, P.C. Chiap, Evaluation of a novel anion-exchange restricted-access sorbent for on-line sample clean-up prior to the determination of acidic compounds in plasma by liquid chromatography, J. Chromatogr. A 2004,.1030, 95-102.

43. P. Bruno, M. Caselli, G. De Gennaro, B. De Tommaso, G. Lastella, S. Mastrolitti, Determination of nutrients in the presence of high chloride concentrations by column-switching chromatography, J. Chromatogr. A.2003, 1003, 133-141.

44. J.L. Gomez-Ariza, D. Sanchez-Rodas, M.A. Caro de la Torre, L. Giraldez , E. Morales, Column-switching system for selenium speciation by coupling reversed-phase and ion-exchange high-performance liquid chromatography with microwave-assisted digestion-hydride generation-atomic fluorescence spectrometry, J Chromatogr. A.2000, 889, 33-39.

45. R.H. Marchessault, S. Coulombe, T. Hanai, H. Morikawa,. Monomers and oligomers from wood. Transactions of the Technical Section (Canadian Pulp and Paper Association), 1980, 6(2), TR52-TR56.

45a. T. Hanai, Liquid chromatography of carbohydrates, Adv. Chromatogr. 1986, 25, 278-307

46. M. Shimizu, T. Uno, T. Niioka, N. Yaui-Furukoshi, T. Takahata,, K. Sugawara, T. Tateishi, Sensitive determination of omeprazole and its two main metabolites in human plasma by column-switching high-performance liquid chromatography: application to pharmacokinetic study in relation to CYP2C19 genotypes, J. Chromatogr. B. 2006, 832, 241-248.

47. T. Maeda, S. Sumi, K. Hayashi, K. Kidouchi, T. Owaki, H. Togari, S. Fujimoto, Y. Wada, Automated determination of 5-fluorouracil and its metabolite in urine by high-performance liquid chromatography with column switching IJ. Chromatogr. B. 1999, 731, 267-273.

48. M. Faraoni, A. Messina, C.M. Polcaro, Z. Aturki, M. Sinibaldi, Chiral separation of pesticides by coupled-column liquid chromatography I Application to the stereoselective degradation of fenvalerate in soil. J. Liq. Chromatogr. Rel. Technol. 2004, 127, 995-1012.

49. A. Motoyama, A. Suzuki, I. Shirota, R. Namba, Direct determination of pindolol enantiomers in human serum by column-switching LC-MS&MS using a phenylcarbamate-β-cyclodextrin chiral column. J. Pharm. Biomed Anal. 2002, 28, 97-106.

50. D. Whittington, P. Sheffels, E.D. Kharasch, Stereoselective determination of methadone and the primary metabolite EDDP in human plasma by automated on-line extraction and liquid chromatography mass spectrometry, J Chromatogr. B.2004, 809, 313-321.

51. Q.B. Cass, V.V. Lima, R.V. Oliveira, N.M. Cassiano, A.L.G. Degani, J. Pedrazzoli, J. Enantiomeric determination of the plasma levels of omeprazole by direct plasma injection using high-performance liquid chromatography with achiral-chiral column-switching , J. Chromatogr. B .2003, 798, 275-281.

52. V.K. Boppana, W.H. Schaefer, M.J. Cyronak, High-performance liquid chromatographic determination of warfarin enantiomers in plasma with automated on-line sample enrichment, J. Biomed. Biophys. Meth. 2002, 54, 315-326.

53. I.M. Itoh, G. Kominami, On-line extraction followed by high-performance liquid chromatography and radio immunoassay for a novel retinobenzoic acid, AM-80, in human plasma, J. Immunoassay Immunochem. 2001.22, 213-223.

54. C.K. Holtzapple, L.H. Stanker, Affinity selection of compounds in a fluoroquinoline chemical library by online immune affinity deletion coupled HPLC, Anal. Chem.1998. 70, 4817--4821.

55. K. Lshimura, K. Fukunaga, T. Irie, K. Uekama, T. Ohta, H. Nakamura, Application of a beta-cyclodextrin sulfate-immobilized precolumn to selective online enrichment and separation of heparin-binding proteins by column-switching high-performance liquid chromatography, J. Chromatogr. A. 1997, 769, 209-214.

56. Y. Watanabe, T. Kubo, T. Nishikawa, T. Fujita, K. Kaya, K. Hosoya, Fully automated liquid chromatography-mass spectrometry determination of 17β-estradiol in river water, J. Chromatogr. A. 2006, 1120, 252-259.

57. Y. Watanabe, K. Hosoya, N. Tanaka, T. Kondo, M. Morita, T. Kubo, LC-MS determination of bisphenol A in river water using a surface-modified molecular-imprinted polymer as an on-line pretreatment device, Anal. Bioanal. Chem. 2005, 381, 1193-1198.

58. M. Nakamura, M. Ono, T. Nakajima, Y.. Ito, T. Aketo, J. Haginaka, Uniformly sized molecular imprinted polymer for atropine and its application to the determination of atropine and scopolamine in pharmaceutical preparations containing Scopolia extract, J. Pharm. Biomed. Anal. 2005, 37, 231-237.

59. N. Markoglou, R. Hsuesh, I.W. Wainer, Immobilized enzyme reactors based upon the flavoenzymes monoamine oxidase A and B. J. Chromatogr. B.2004,804, 295-302.

60. E. Calleri, G. Marrubini, G. Massolini, D. Lubda, S.S. De Fazio, S. Furlanetto, W. Wainer, L. Manzo, G. Caccialanza, Development of a chromatographic bioreactor based on immobilized beta-glucuronidase on monolithic support for the determination of dextromethorphan and dextrorphan in human urine, J. Pharm. Biomed. Anal. 2004, 35, 1179-1189.

61. E. Calleri, C. Temporini, S. Furlanetto, F. Loiodice, G. Fracchiolla, G. Massolini, Lipases for biocatalysis: development of a chromatographic bioreactor, J. Pharm. Biomed. Anal. 2003, 32, 715-724.

62. N. Markoglou, I.W. Wainer, Biosynthesis in an on-line immobilized-enzyme reactor containing phenylethanolamine N-methyltransferase in single-enzyme and coupled-enzyme formats, J. Chromatogr. A. 2002, 948, 249-256.

63. V. Sotolongo, D.V. Johnson, D. Wahnon, I.W. Wainer, Immobilized horse liver alcohol dehydrogenase as an online high-performance liquid chromatographic enzyme reactor for stereoselective synthesis, Chirality, 1999, 11, 39-45.

64. M.T. Baynham, S. Patel M.R. Sharvil, I.W. Wainer, Multidimensional on-line screening for ligands to the a3 neuronal nicotinic acetylcholine receptor using an immobilized nicotinic receptor liquid chromatographic stationary phase, J Chromatogr. B.2002, 772, 155-161.

65. E. Calleri , C. Temporini, E. Perani, C. Stella, S. Rudaz, D. Lubda, G. Mellerio, J. Veuthey, G.ICaccialanza, G. Massolini, Development of a bioreactor based on trypsin immobilized on monolithic support for the on-line digestion and identification of proteins, J Chromatogr. A.2004, 1045, 99-109.

66. K. Hayakawa, C. Lu, S. Mizukami, A. Toriba, N. Tang, Determination of 1-nitropyrne metabolites by high-performance liquid chromatography with chemiluminescence detection, J. Chromatogr. A. 2006, 1107, 2006, 286-289.

67. H. Yoshida, T. Mizukoshi, K. Hirayama, H. Miyano, On-line desalting-mass spectrometry system for the structural determination of hydrophilic metabolites, using a column switching technique and a volatile ion-pairing reagent, J. Chromatogr. A.2006, 1119, 315-321.

68. T. Hanai, Basic properties of a molecular mechanics program and the generation of unknown stereo structures of proteins for quantitative analysis of enzyme reactions, in Watkins (ed) Molecular Mechanics and Modeling, Nova Science, New York, 2015, 25-48.

69. T. Hanai, Chromatography and computational chemical analysis for drug discovery. Current Medicinal Chemistry, 2005, 12, 501-525. doi:10.2174/0929867310504050501

Chapter 7: Quantitative analysis of the molecular interactions and properties in chromatography

The most important step in studying molecular interaction mechanisms in chromatography is constructing an ideal model phase. We used a large polycyclic aromatic hydrocarbon as a model graphitized carbon phase to clarify molecular interaction mechanisms. We studied retention mechanisms in gas chromatography with high precision using polymer models because solvent effects can generally be neglected in gas chromatography. Adding HOMO and LUMO energies improved precision. Three-dimensional structures of packing materials made docking analysis difficult. Modeling liquid chromatography retention is not simple, even though modeling the chiral recognition phase is relatively simple. Modeling ion-exchange liquid chromatography is simpler than reversed-phase liquid chromatography because of strong ion-ion interactions and simplified desorption mechanisms. However, modeling reversed-phase liquid chromatography is very difficult because it lacks a molecular interaction center.The main interaction mechanism is van der Waals forces, but the interaction center is unclear. The contact surface Area contributes to the retention force. A suitable phase for each molecule can be prepared; however, this approach does not guarantee general applicability to retention mechanisms. The bonded phases are considered homogenate reaction products. Pore shape and size may cause different densities of bonded phases at pore sites. This type of question may be neglected for non-porous silica gel-based bonded phases. This type of phase may neglect steric hindrance, so we must design the bonded phase to introduce steric hindrance and improve selectivity. The computational chemical (in silico) analysis for quantitative molecular interactions has been applied in different types of chromatography, such as ion-exchange separations [1, 2], enantiomer separation [1, 3-10], and affinity separations [1, 11-21], furthermore chromatography detection mechanisms, human serum albumin binding affinity, enthalpy, and boiling point [1]. These simple model studies indicate that present computational chemical calculation programs are far from perfect. The above results will help improve the precision of such programs because chromatographic measurements of molecular interactions are highly reproducible. Precision should improve if quantitative solubility prediction becomes available.

7.1 Normal-phase liquid chromatography

Normal-phase liquid chromatography, also known as adsorption liquid chromatography, is less common now; however, preparative applications remain a popular purification technique for both large- and small-scale work. The small-scale operation is commonly used for preparation. Although reversed-phase mode has strong separation power, removing water from the total process water takes time and energy;ergy, therefore, normal-phase systems using organic solvents are preferred for large-scale operation. Normal-phase systems use polar adsorbents and non-polar eluents. The relative polar and nonpolar relationship applies to normal-phase liquid chromatography, and the main molecular interaction mechanisms are hydrogen bonding and Lewis acid-base interactions; therefore, this interaction is also called hydrophobic interaction. The original normal-phase liquid chromatography is now active as hydrophilic interaction liquid chromatography (HILIC) using eluents containing a small concentration of water. The original HILIC mode separation was performed for saccharide separation. Therefore, we classify it as either non-aqueous or aqueous normal-phase liquid chromatography.

Because silica gel columns are stable and reproducible, quality control systems today do not use non-aqueous normal-phase liquid chromatography. Even popular thin-layer liquid chromatography also uses reversed-phase systems. Normal-phase liquid chromatography uses surface-modified silica gels and organic polymer packing materials. Normal-phase liquid chromatography is especially effective for enantiomer separations because of its primary molecular recognition mechanisms.

7.2 Reversed-phase liquid chromatography

Retention in reversed-phase liquid chromatography was quantitatively analyzed using the octanol-water partition coefficient (log *P*) and the dissociation constant (p*K*a) because log *P* values include solvent effects that must be considered when studying the reversed-phase liquid chromatographic behavior of analytes. Experimental log *P* values for ionized compounds have not been reported, and researchers have used zero log P values to predict the retention times of partly ionized compounds. However, the log *P* values predicted by computational chemistry methods are not satisfactory; hence, prediction methods based on measured log *P* values are used in practice. Indeed, the precision of predicted log *P* values is not satisfactory for new types of compounds. If accurate log P values, especially for ionized compounds, could be calculated, they could be used to study retention behavior in reversed-phase liquid chromatography [22]. Therefore, we studied a new approach.

Chromatography is an excellent analytical method to study molecular interactions (MIs). Chromatographic retention has been quantitatively analyzed via computational chemistry calculations. However, building an in silico model of the stationary phase *is difficult*; therefore, chromatography studies of MIs require a simplified stationary-phase model [1]. The retention times measured in a variety of chromatographic techniques, from gas chromatography to liquid chromatography, including affinity liquid chromatography, were quantitatively analyzed *in silico*; the calculated MI energy values between the analyte and a model phase were related to the measured logarithmic capacity-ratio (log *k*) values. Furthermore, the retention times could be predicted if standard compounds for column calibration, such as alkanes in gas chromatography and alkylbenzenes in reversed-phase liquid chromatography for phenolic compounds, were available.

The chromatographic behavior of ionizable compounds depends on the eluent pH used. The pH at which retention behavior changes is called the dissociation constant, pKa. The relative retention time (capacity ratio, retention ratio) *k* relates the dissociation constant p*K*a to the eluent pH. Pietzyk et al. [23] proposed the following equation.

$k = (k_m + k_i(Ka/[H^+])/(1 + (Ka/[H^+])$ where k_m and k_i are the capacity ratios of the molecular and ionized analytes, respectively; *K*a is the dissociation constant of the analytes, and $[H^+]$ represents the hydrogen ion concentration in the eluent. The p*K*a values depend on the organic modifier used and its concentration. Therefore, we must clearly describe how we measured pH and the buffer components. We modified the equation to predict retention time using molecular interaction (MI) energy values calculated with model phases. We replaced k_m and k_i with the molecular interaction energy of the ionized compound (MIi) and the molecular form (MIm), respectively, because MIi values were higher than MIm values. The dissociation constants can be predicted from atomic partial charge (apc) that is used like Hammett's σ σ constant [22]. Various chromatographic data were quantitatively analyzed *in silico*, and the results were summarized in a book format [1].

7.2.1 Phenolic compounds: An initial study to classify the selectivity of pentyl- and octyl-bonded silica gels was based on the chromatographic behavior of four phenolic compounds (phenol, 44-chlorophenol, 2,4-dichlorophenol, and 2,4,6-trichlorophenol) measured in reversed-phase liquid chromatography using model phases. The methanol concentration for the octyl-bonded and pentyl-bonded silica gel columns was 50 and 33%, respectively. The log *k* values measured in these columns are identical, and the correlation coefficient was 0.997 (n = 4). The columns differed in strength, and no selectivity was observed; the only technical difference in the in silico analysis was the calculation time. The calculation times of the pentyl- and octyl-phases were 10 and 90 min, respectively. Calculation time was exponentially related to the number of heavy atoms (excluding hydrogen). The choice of model alkyl-bonded phase depends on alkyl-chain length. Longer alkyl groups support selectivity, while shorter alkyl groups help quickly understand chromatographic behavior. Preparing a homogeneous longer alkyl-bonded phase may introduce human error when determining the initial analyte position. Therefore, a short alkyl group not affected by the silica gel oxygen model is suitable for general purposes.

Phenol log *k* values measured using pentyl-bonded silica gel were correlated with calculated MI energy values using model structures of pentyl- and octyl-phases. The correlation coefficient between log *k* measured using the pentyl- and octyl-bonded silica gel and MIVW was 0.990, 0.969, 0.997, 0.991, and 0.987, 0.982, 0.983, 0.998 kcal mol^{-1}. Van der Waals forces help retain phenolic compounds in these model phases. This result supports using a model pentyl-bonded silica gel for rapid analysis [24].

The dissociation constant of phenolic compounds is higher than 10; therefore, these compounds are usually chromatographed as their molecular form. However, halogenated phenols have a dissociation constant less than 10, and their retention times are shorter than expected in high-pH eluents; still, retention-time prediction for phenolic compounds across different pH eluents is not a major problem, and the error is small compared with that for acidic and basic compounds. We measured longer retention times because standard compounds were available, and we used them to validate the retention-time prediction process in high-pH-controlled eluents.

The retention times of phenolic compounds measured by reversed-phase liquid chromatography were quantitatively analyzed *in silico* using a dodecyl- and pentyl-mixed bonded silica gel model phase. We used alkylbenzenes as calibration standards for phenolic compounds, as alkanes were used in gas chromatography. The main molecular interaction force between the hydrophobic surfaces and analytes was hydrophobicity, calculated as the van der Waals energy values. Desorption resulted from solvation of the analytes by an organic modifier. Solvation was analyzed as a molecular interaction between a model acetonitrile phase and the analytes. The latter interaction is mainly related to the electrostatic energy values from log *k* values measured in aqueous acetonitrile,

The phase is dodecyl-pentyl-bonded silica gel, and analytes cannot contact the silica gel; free silanol groups do not affect analyte retention. We dock molecules and ionized phenolic compounds, then calculate MI energy values. Figure 7.1 shows the complex of 2,3,4,5-tetrachlorophenol and the model phase. We summarize the molecular properties of the phenolic compounds and complexes, along with their log *k* values measured in reversed-phase mode using acetonitrile as the organic modifier. The properties are the final (optimized) structure (fs, FS), hydrogen bonding (hb, HB), electrostatic (es, ES), and van der Waals (vw, VW) energies. We also collected their molecular interaction energy values with an acetonitrile phase (aMIHB, aMIES). The standard calibration compounds are alkylbenzenes.

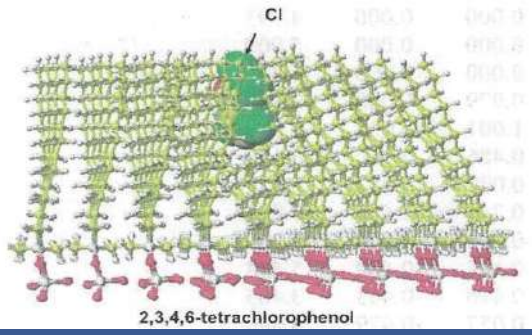


FIgure 7.1: Docked penta-chloro phenol into a dodecyl-pentyl bonded silica gel.

The correlation coefficient (*r*) is 0.348 (N = 54) between log *k* and MIVW. Adding the hydrogen-bonding interaction energy (MIHB) improved the correlation coefficient to 0.865. Further improvement was minimal (*r* = 0.867) with the addition of the solvent effect (aMIHB). The calculated equations follow, excluding 2,5- and 2,6-dinitrophenol due to the ortho effect,

log *k* = MIVW, *r* = 0.348, n = 52,

log *k* = MIVW – 7xMIHB, *r* = 0.865, n = 52,

log *k* = MIVW – 7xMIHB – 2xaMIHB, *r* = 0.867, n = 52,

The contribution of hydrogen energy value was high for phenolic compounds; therefore, the correlation was recalculated based on hydrogen energy values.

log *k* = MIHB, *r* = 0.794, n = 52,

log *k* = MIHB + 0.2 MIVW, *r* = 0.857, n = 52,

log *k* = MIHB + 0.2MIVW + aMIHB, *r* = 0.863, r = 52,

The addition of MIES and aMIHB did not affect the correlation significantly. The correlation of MIVW – 7xMIHB – 2xaMIHB is shown in Figure 7.2.

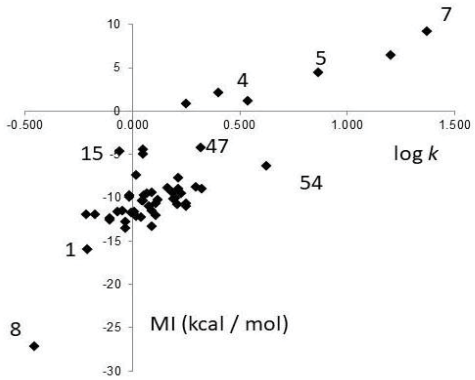


FIgure 7.2: Relation between log k and molecular interaction energy values. Numbers beside symbols: see Table 7.1.

The solvation of the hydroxyl group in acetonitrile alone can be studied quantitatively, but quantitative analysis of total solvation is difficult, especially for nitro-substituted compounds, particularly ortho-nitrophenols. Their different behaviors from alkyl- and halogenated phenols cannot be explained using molecular properties such as HOMO and LUMO energies, entropy, enthalpy, ionization potential, heat of formation, and MI energy values (kcal mol^{-1}) between an analyte and acetonitrile.

The retention times of phenolic compounds measured in reversed-phase liquid chromatography were quantitatively analyzed in silico using molecular mechanics, and solvent effects were quantitatively analyzed in silico using a model solvent phase and model complexes between an analyte and solvent molecules. The correlation coefficient between the combined molecular interaction energy and solvent-effect values calculated in silico and log k was about 0.86. The log k values in reversed-phase liquid chromatography can be quantitatively predicted using an ideal model phase and a solubility prediction method. These results show that this new approach to quantitatively analyzing chromatographic retention time in reversed-phase liquid chromatography is possible. Precision should improve when solubility can be predicted. We measured these log k values using an octyl-bonded silica gel with 70% aqueous acetonitrile at pH 2.0 and 40°C. We measured retention times on an octadecyl-bonded silica gel column (150 x 4.6 mm ID) with 70% aqueous acetonitrile containing 20 mM phosphoric acid at 40°C. Molecular modeling and molecular interaction energy values were calculated using the Cache™ V7.5 program (Fujitsu, Japan).

Table 7.1: Properties of phenolic compounds.

No	Compound	log *k*	fs	hb	es	vw
1	Phenol	-0.208	-8.1266	0.514	0	2.93
2	Benzene	0.25	-8.077	0	0	3.006
3	Methylbenzene	0.4	-8.6003	0	0	3.036
4	Ethylbenzene	0.54	-6.7841	0	0	4.053
5	Butylbenzene	0.868	-5.4673	0	0	4.993
6	Hexylbenzene	1.202	-4.1933	0	0	5.909
7	Heptylbenzene	1.373	-3.5548	0	0	6.368
8	1,3-Dihydroxybenzene	-0.456	-8.2571	0.979	0	2.859
9	1,4-Dihydroxybenzene	-0.52	-8.2657	1.001	0.027	2.89
10	Naphtol	0.057	-17.1861	0.486	0	6.176
11	2-Bromophenol	-0.032	-6.0651	0.039	1.857	3.513
12	2-Chloro-6-methylphenol	0.053	-4.9263	0.381	2.562	3.991
13	2-Chlorophenol	-0.066	-6.0025	-0.098	2.076	3.366
14	E-Ethylphenol	0.067	-3.0928	0.163	-0.469	5.454
15	2-Methylphenol	-0.06	-8.46	0.416	-0.463	3.465
16	2-Nitrophenol	0.041	-8.7597	0.057	-0.479	4.68
17	3-Bromophenol	0.009	-7.8272	0.509	-0.117	3.233
18	3-Chlorophenol	-0.032	-7.9748	0.512	-0.124	3.151
19	3-Ethylphenol	0.017	-6.8406	0.521	0.025	3.949
20	3-Methylphenol	-0.102	-8.62	0.53	0.025	2.959
21	3-Nitrophenol	-0.174	-8.8466	0.501	-0.188	4.082
22	4-Bromophenol	-0.004	-7.8036	0.52	-0.09	3.21
23	4-Chloro-4-methylphenol	0.111	-8.6415	0.517	-1.323	4.493
24	4-Chloro-3,5-dimethylphenol	0.193	-7.9473	0.52	-0.034	3.131
25	4-Chlorophenol	-0.046	-7.7284	0.411	0.005	3.652
26	4-Ethylphenol	0.021	-6.9028	0.515	0.018	3.965
27	4-Methylphenol	-0.102	-8.6817	0.518	0.019	2.956
28	4-Nitrophenol	-0.218	-8.7434	0.5	-0.125	4.065
29	4-tert.Butylphenol	0.228	-4.3251	0.508	0.018	5.405
30	2,3-Dichlorophenol	0.076	-2.3124	0.061	4.443	4.311

31	2,3-Dimethylphenol	0.048	-7.4572	0.395	-0.305	4.311
32	2,4-Dibrompphenol	0.215	-7.88	0.032	-0.245	3.786
33	2,4-Dichlorophenol	0.093	-8.3698	0.092	-0.568	3.57
34	2,4-Dimethylphenol	0.053	-9.1499	0.413	-0.569	3.471
35	2,5-Dichlorophenol	0.111	-5.2384	0.095	2.569	3.567
36	2,5-Dimethylphenol	0.053	-8.9715	0.421	-0.413	3.455
37	2,5-Dinitrophenol	-0.06	-11.8895	-3.297	-0.231	5.473
38	2,6-Dichlorophenol	0.188	-5.2487	-0.006	2.014	4.17
39	2,6-Dichlorophenol	0.093	-5.6573	0.061	1.961	3.851
40	2,6-Dimethylphenol	0.09	-9.2379	0.446	-1.138	3.835
41	2,6-Dinitrophenol	-0.061	-11.2474	-3.82	-0.201	6.381
42	3,4-Dichlorophenol	0.117	-4.3459	0.502	2.276	4.01
43	3,4-Dimethylphenol	-0.013	-8.4724	0.524	0.173	3.396
44	3,5-Dichlorophenol	0.21	-10.3934	0.506	-2.808	3.377
45	3,5-Dimethylphenol	-0.013	-9.2857	0.529	-0.075	2.947
46	2,3,4-Trichlorophenol	0.25	-0.9624	0.045	4.356	5.504
47	2,3,5-Trichlorophenol	0.32	-4.1111	0.058	2.383	4.537
48	2,3,5-Trimethylphenol	0.165	-6.931	0.612	-0.462	3.916
49	2,3,6-Tricholorophenol	0.25	-1.336	0.023	4.955	4.815
50	2,3,6-Trimethylphenol	0.201	-6.3945	0.451	-0.972	5.232
51	2,4,5-Trichlorophenol	0.299	-4.1613	0.087	2.426	4.455
52	2,4,6-Trichlorophenol	0.324	-10.6086	0.052	-3.234	4.067
53	2,4,6-Trimethylphenol	0.217	-10.0801	0.443	-1.37	3.82
54	Pentachlorophenol	0.627	3.5222	0.019	5.483	8.687
Model-phase	-	4539.932	0	-161.685	1421.672	
Continued						
	FS	HB	ES	VW	aMIHB	aMIES
1	4524.3566	-1.477	-161.679	1424.08	1.26	1.793
2	4526.3172	0	-161.687	1423.826	0	0
3	4523.4393	0	-161.695	1422.641	0	0
4	4525.9811	0	-161.702	1424.623	0	0
5	4523.4174	0	-161.697	1422.222	0	0
6	4522.6071	0	-161.69	1421.186	0	0
7	4517.5654	0	-161.683	1418.835	0	0
8	4521.3436	-3.017	-161.681	1423.057	2.312	3.251
9	4518.7406	-2.949	-161.659	1418.041	2.434	3.251
10	4508.667	-1.658	-161.687	1422.341	1.175	1.611
11	4525.4771	-1.906	-159.845	1424.482	1.275	3.224
12	4519.7963	-1.442	-159.047	1417.373	1.179	4.717
13	4525.7946	-1.915	-159.624	1423.226	1.284	3.141
14	4523.623	-1.383	-162.15	1425.346	1.04	2.159
15	4517.4673	-1.387	-162.128	1416.434	1.281	2.148
16	4521.8246	-1.827	-161.891	1424.84	1.214	8.729
17	4521.1556	-1.475	-161.804	1422.198	1.235	4.486
18	4522.5517	-1.46	-161.794	1423.29	1.242	4.573
19	4519.8599	-1.468	-161.648	1418.647	1.242	2.181
20	4522.6151	-1.48	-161.663	1423.104	1.041	1.626
21	4521.1393	-1.491	-161.726	1423.228	1.273	7.667

22	4521.6493	-1.469	-161.742	1422.671	0.997	2.63
23	4522.5239	-1.375	-161.644	1422.991	1.25	2.25
24	4516.5275	-1.471	-162.993	1420.687	1.189	4.761
25	4522.1541	-1.466	-161.744	1423.128	1.236	3.581
26	4521.7959	-1.465	-161.678	1423.387	1.252	1.066
27	4522.3475	-1.461	-161.663	1423.07	1.03	2.037
28	4521.8571	-1.474	-161.732	1423.346	1.226	6.261
29	4525.6387	-1.455	-161.666	1422.403	1.231	1.472
30	4526.456	-1.923	-157.212	1422.439	1.301	6.224
31	4520.3934	-1.35	-162.026	1423.26	1.317	2.065
32	4517.5826	-1.904	-161.915	1419.139	1.23	4.149
33	4518.4952	-1.917	-162.244	1420.143	1.235	4.313
34	4520.311	-1.364	-162.254	1422.615	1.142	1.525
35	4523.9611	-1.913	-159.132	1422.74	1.263	0.232
36	4515.9516	-1.378	-162.086	1416.934	0.915	2.198
37	4516.2628	-4.109	-162.169	1423.579	1.241	15.176
38	4521.1061	-1.981	-159.648	1420.987	1.222	4.19
39	4523.2074	-1.965	-159.75	1422.369	1.268	5.54
40	4520.5631	-1.404	-162.854	1425.131	1.28	1.984
41	4518.1019	-1.468	-162.389	1425.669	1.255	13.424
42	4523.9433	-1.472	-159.37	1421.825	1.164	7.123
43	4520.8163	-1.471	-161.543	1421.093	0.982	1.529
44	4517.811	-1.477	-164.46	1421.594	1.154	4.37
45	4517.9459	-1.482	-161.785	1419.766	1.285	1.037
46	4527.7567	-1.916	-157.324	1423.792	1.29	7.351
47	4521.3492	-1.924	-159.274	1416.208	1.17	3.738
48	4517.4635	-1.507	-162.173	1419.147	1.308	1.377
49	4526.4971	-1.97	-156.716	1422.669	1.299	7.872\
50	4519.7589	-1.392	-162.651	1423.359	1.25	1.754
51	4521.9085	-1.913	-159.261	1420.392	1.266	7.183
52	4515.7196	-1.982	-164.916	1420.024	1.237	5.633
53	4517.9879	-1.38	-163.062	1421.036	1.276	1.71
54	4526.608	-1.993	-156.148	1422.308	1.168	8.612

fs, hb, es, vw: final (optimized) structure, hydrogen bonding, electrostatic, van der Waals energy values; aMIHB, and aMIES: molecular interaction energy values calculated using acetonitrile phase

7.2.2 Reversed-phase liquid chromatography for acidic compounds: The model phases are constructed employing the polysiloxane phase. The bonded groups are R-dimethylsilicones where R presents the pentyl- and hexenyl-, and octyl-groups, and the number of bonded groups is 54 for the shortest calculation hour. A flat model phase is suitable for phenolic compounds because the phenolic compounds analyzed were generally flat molecules and different from drugs. Therefore, the model phase possesses a pocket because these bonded phases are synthesized with porous silica gels, to maintain a similar shape and area, longer alkyl groups tighten the alkyl groups themselves and narrow the entrance area. Such a tightening interaction is causes by VW interaction of the alkyl groups. Therefore, some modification is required to construct suitable model phases for various compounds than the model phase of pentyl-bonded silica gels. Generally, three center groups among 54 groups are pulled down to form a pocket. Furthermore, three more groups are also slightly pulled down to from a better entrance for the octyl-bonded phase. Imagine a lily flower. When many groups are pulled down to form a deep dish, the model is suitable for large flat molecules, although it does not exhibit a selective interaction for a variety of compounds. The phenolic compound's structure is relatively flat; therefore, a flat sandwich type model supported the theoretical discussion of the retention mechanisms.

Drug chemical structures are complex, and docking analysis requires technical performance. Designing a suitable

pocket in model silica gel for docking drugs is based on a model of porous silica gels. The cone-shaped pocket can accommodate molecules of various sizes; however, a computer program cannot build a pocket for circular molecules. One solution is to pull down the center molecules to form a pocket. These two steps pull down to form a cone-type pocket, as shown in Figure 7.3. The initial location of salicylic acid docking onto a model octyl-bonded silica gel is shown. Figure 7.4 exhibits the complex conformation after optimizing the Figure 7.1 conformation where the docked salicylic acid exists inside the pocket.



FIgure 7.3: A model octyl-bonded silica gel phase. Atoms: red (black), yellow (light gray), large and small white: oxygen, carbon, silicon, and hydrogen.

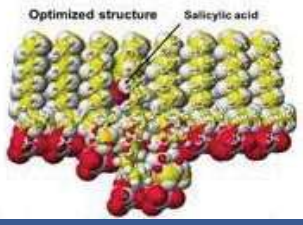


FIgure 7.4: Optimized structure of Figure 1. Atoms: red (black), yellow (light gray), large and small white: oxygen, carbon, silicon, and hydrogen.

Salicylic acid, located at the upper position, was dropped into the pocket after optimization using the MM2 program. Fixing the initial position of salicylic acid is critical. The surface of a corntype pocket is not smooth; therefore, if the initial position is incorrect, salicylic acid may not drop into the pocket center. In Figure 7.4, the front atom size is 0.2, and the back atom size is 1.0 to observe the optimized conformation. Red (black), yellow (light gray), large white, and small white balls are oxygen, carbon, silicon, and hydrogen. The simple docking approach prepares optimized conformations, then selects the conformation from tbased onalculated MI energy values. An autodocking program does not guarantee an optimized complex structure. Figure 7.5 is an overview of Figure 7.4, and Figure 7.6 indicates the blue-colored molecule, salicylic acid, for easy identification.

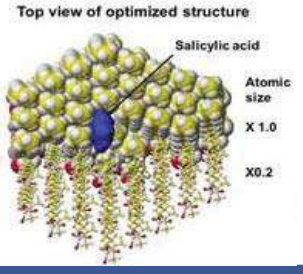


FIgure 7.5: Upper view of Figure 2 structure molecule.

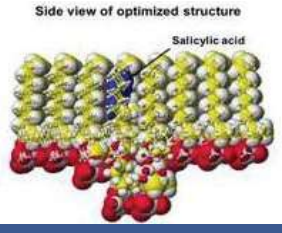


FIgure 7.6: A clear indication of salicylic acid as a blue molecule.

Calculated MI energy values of 19 acidic drugs using the model octyl-bonded silica gel are correlated to the log k values—Therwas0.336 (n=19).In addition, the solvent effect using a methanol phase was performed. Adding the solvent effect to the previous relation improved the *r* value from 0.336 to 0.919 (n = 19). The *r* value further improved to 0.941 (n = 18) when excluding the large molecular size of mefenamic acid. The results indicated that a larger, deeper pocket produced a better correlation, as the model performed better than a flat model. A combination of adsorption and desorption MI energy values supports that *in silico* modeling analysis can quantitatively analyze reversed-phase chromatographic retention time.

Further study used a model pentyl phase with a pocket for faster analysis. The log *k* values were measured using a pentyl-bonded silica gel column. The model pentyl-bonded silica gel was prepared by pulling down the center groups, as shown in Figure 7.7, with salicylic acid in the initial position. As shown in Figure 7.8, the optimized structure docked well in the high-density alkyl-bonded silica gel phase. Figure 7.9 shows the top view of Figure 7.8, and Figure 7.10 shows salicylic acid in blue at the prominent location.

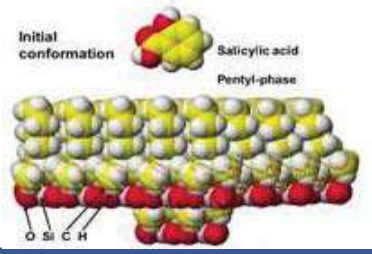


FIgure 7.7: Initial conformation of salicylic acid and a pentyl-phase. Atoms: red (black), yellow (light gray), large and small white: oxygen, carbon, silicon, and hydrogen

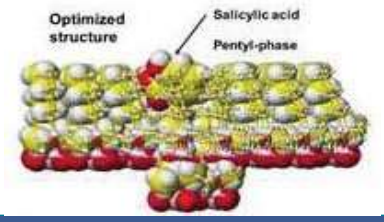


FIgure 7.8: The optimized conformation and a pentyl-phase. Atoms: red (black), yellow (light gray), large and small white: oxygen, carbon, silicon, and hydrogen

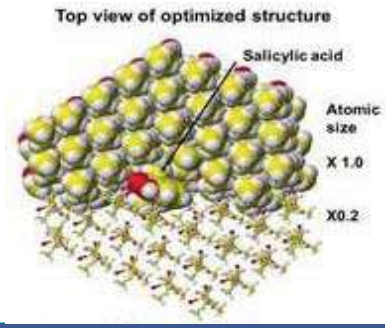


FIgure 7.9: Upper view of Figure 6.

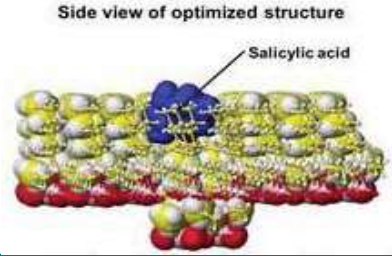


FIgure 7.10: Blue salicylic acid in the pocket.

The correlation between the measured log k values of acidic drugs and the calculated MIVW energy values was 0.531 (n = 19). Additional methanol solvent effect improved the *r* value to 0.919 (n=19).Eliminating mefenamic acid further improved these values, with *r* = 0.569 and 0.956 (n = 18), respectively. The results above suggest that calculating MI energy values using both bonded-silica gel and methanol phases is necessary to study chromatographic retention measured in reversed-phase mode.

Table 2: Molecular interaction energy values calculated using a pentyl- and a methanol-phase, and log *k* values of acidic drugs measured using a pentyl bonded silica gel.

Compound	MIHB	MIES	MIVW	mMIHB	mMIES	mMIVW	log *k*
Ammoxicillinum	5.106	0.393	26.636	28.758	5.153	15.981	-1.126
Barbital	0.586	-0.117	7.773	30.729	5.089	6.562	-1.574
Benzoic acid	0.015	-0.143	14.841	20.622	1.207	3.431	-0.048
Chloamphenicol	-0.199	-0.334	21.192	25.86	3.629	4.207	-0.078
Furosemide	0.253	0.049	19.413	25.556	1.319	8.118	-0.154
Ibuprophen	0.035	0.011	15.777	15.21	2.24	7.582	1.263
Indomethacin	0.195	-0.176	19.205	21.786	4.433	7.578	0.882
Iopanoic acid	0.066	-0.038	17.099	17.707	1.271	7.161	1.404
Mefenamic acid	6.484	-0.036	27.752	20.918	3.021	11.515	1.404
Nalidixiric acid	0.009	-0.058	15.193	20.846	3.045	7.117	0.035
Naproxen	-0.028	-0.182	25.271	19.422	2.148	8.814	0.609
Nicotinic acid	0.061	-0.146	13.917	27.974	2.934	5.25	-1.03
Phenylbutazone	0	0.088	18.849	17.079	4.297	7.676	0.837
p-Hydroxyl-benzoic acid	0.131	0.012	14.732	23.21	2.384	2.628	-0.099
Probenecid	0.007	0.085	21.66	21.173	2.558	11.656	0.586
Salicylic acid	3.843	0.157	14.228	22.265	2.889	3.997	-0.207
Sulfamethoxazole	0.996	0.013	19.084	26.851	1.633	5.704	-0.677
Tolazamide	0.456	0.32	22.257	23.66	5.993	12.675	0.461
Tolbutamide	0.351	0.11	22.531	23.264	5.4	13.139	0.407
Warfarin	-0.027	-0.356	21.504	19.337	2.52	6.208	0.759

Comparing acidic drug log *k* values (n = 17, at pH 3) measured using a hexenyl-bonded silica gel showed retention capacity equivalent to a pentyl-bonded silica gel and 70% of that of an octyl-bonded silica gel. The hexenyl-bonded silica gel has relatively high retention capacity for salicylic acid, furosemide, probenecid, and phenylbutazonene; the retention capacity of an octyl-bonded silica gel is 118% of that of the pentyl-bonded silica gel.

Comparing MI energy values indicates the primary interaction is van der Waals force. The pocket structure of the model phase was critical, and the smaller pore size suits small analytes. The complex structures of salicylic acid and a model phase are shown in Figures 7.11-14.

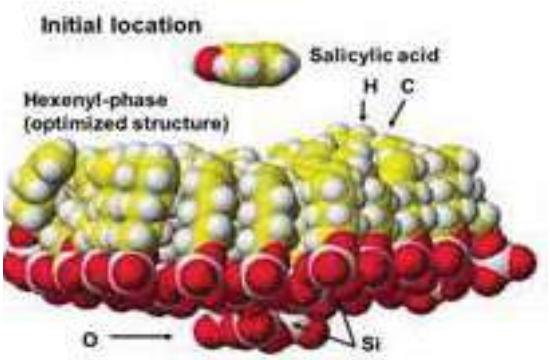


FIgure 7.11: The initial position of salicylic acid and model hexenyl phase.

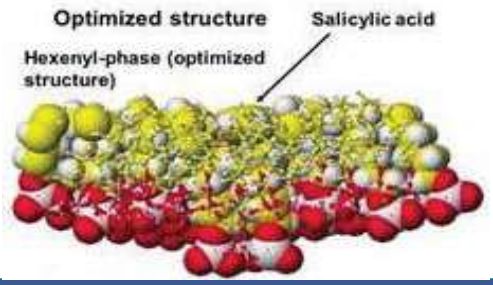


Figure 7.12: Optimized structure.

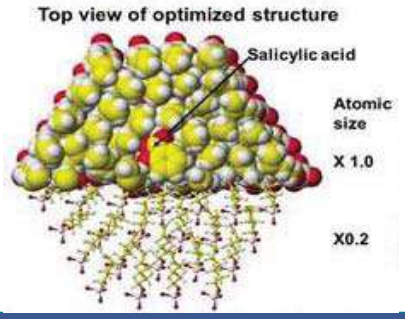


Figure 7.13: Upper view of Figure 7.12. Atoms: red(black), yellow(light gray), large and small white: oxygen, carbon, silicon, hydrogen.

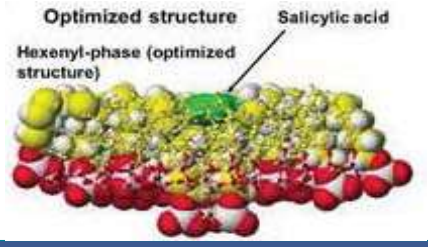


Figure 7.14: Precise conformation of blue salicylic acid in the hexenyl phase. Atoms: red(black), yellow(light gray), large and small white: oxygen, carbon, silicon, hydrogen.

The correlation coefficient between acidic drug log *k* values (n = 19) and MIVW energy values calculated using a model hexenyl phase was 0.248. Adding MIHB values calculated using the methanol phase (r = 0.830) to MIHB, MIES, and MIVW improved the r value to 0.967 (n = 19). The retention analysis in reversed-phase liquid chromatography requires only MIVW and mMIHB; however, the selectivity of a hexenyl phase requires additional MIHB and MIES to obtain a high correlation coefficient. Table 7.3 presents the calculated molecular properties of acidic drugs using a hexenyl phase with measured log *k* values.

Table 7.3: Molecular properties of Acidic drugs and molecular interaction energy values using hexenyl phase.

Chemicals	HB	ES	VW	MIHB	MIES	MIVW	mMIHB	log *k*
Amoxicillin	-7.44	14.514	4.814	3.94	9.402	29.829	28.758	-0.362
Barbital	-8.435	-75.19	4.532	5.162	0.158	14.588	30.729	-0.514
Benzoic acid	-5.701	-6.438	5.269	2.705	0.233	11.781	20.796	0.213
Chloropheniol	-8.459	25.75	7.412	3.45	-0.297	20.666	25.86	0.247
Furosemide	-7.664	-3.905	5.902	6.192	0.316	24.69	25.556	0.574
Ibuprophen	-5.805	-4.317	4.763	0.057	-0.08	18.649	15.21	1.346
Indomethacin	-5.967	-13.303	6.761	2.86	0.268	21.428	22.634	0.173
Iopanoic acid	-4.878	3.836	6.977	7.898	0.148	23.303	17.707	1.767
Mefenamic acid	0.272	-9.42	19.732	10.192	-0.26	30.373	20.918	1.696
Nalidixiric acid	-6.136	-39.589	12.072	1.997	0.447	16.705	20.846	0.373
Naproxen	-5.811	-4.3	6.879	3.179	-0.067	18.885	22.714	0.885
Nicotinic acid	-6.029	-9.676	3.879	2.585	-0.085	11.546	27.974	-0.265

Phenylbutazone	0	-10.94	18.105	0	20.851	25.917	17.079	1.337
p-Hydroxybenzoic acid	-5.198	-6.438	5.147	5.145	0.114	10.791	23.21	0.144
Probenecid	-5.704	-3.46	9.257	1.661	-0.002	23.735	21.173	1.123
Salicylic acid	-5.435	-6.148	5.988	5.322	0.152	14.738	22.265	0.754
Sulfamethoxazole	-1.028	2.724	3.083	8.147	14.012	28.59	26.851	-0.236
Tolazamide	-2.719	-12.84	8.645	6.572	2.073	20.625	23.66	0.673
Tolubutamide	-2.637	-25.652	5.029	5.542	0.785	16.744	23.264	0.588
Warfaein	-0.406	-5.761	8.878	0.096	0.422	17.767	19.345	1.03

HB, ES, VW: hydrogen bonding, electrostatic, van der Waals energy values; MI: molecular interaction; MIHB [24]; log *k* values measured using a hexenyl bonded silica gel and 40% methanol containing phosphoric acid (pH 3.0) at 40°C. Molecular interaction energy value unit: kcal mon^{-1}

Furthermore, we studied the selectivity of phenylhexyl-bonded silica gel for separating acidic drugs using reversed-phase liquid chromatography [25, 26]. The model phase shown in Figure 7.15 was modified into a pore-phase-bonded silica gel. Figure 7.16 shows a part of the model phase docked with salicylic acid. The measured capacity ratios were related to the MI energy values calculated using a model phenylhexyl phase and methanol phase. The solvent effect and interaction with methanol were

MIHB = -0.550 log k + 1.156, r = 0.531, n = 16,

MIVW = 3.388 log k + 14.555, r = 0.788, n = 16,

MIVW + 0.5 mMIHB = 5.886 log k – 23.36, r = 0.935, n = 16.

The contribution of MIES was closed to zero, and that of MIHB was minor, as indicated from the calculated data in Table 7.4. The fundamental molecular interaction was van der Waals, and solvation improved the correlation. These results were similar to those obtained for the pentyl-bonded phase [27]; MIHB contributed weakly to the interaction, but the overall contribution did not differ significantly from that of MIHB of the solvent (MeOH). The contribution of MIES was negligible, which was not expected for this phenylhexyl phase shown in Figures 7.15-18. The reason could be the complex formation between an analyte and the phenylhexyl-phase. MIES has already been observed in the case of a face-to-face complex between an analyte and a phenyl group [28]. Still, in this highly dense model, the analytes' aromatic groups did not form face-to-face complexes. However, chromatography using a graphitized carbon phase has shown weak hydrogen bonding [29]. In this experiment, tolbutamide (2.34/5.16: log *P*/p*K*a) and tolazamide (2.69/5.17: log *P*/p*K*a) were separated, as well as naproxen (3.18/4.15: log *P*/p*K*a) and probenecid (3.21/3.4: log *P*/p*K*a), but these separations were not achieved on pentyl- and octyl-bonded phases. These separations may depend not only on the hydrophobicity (log *P*) and dissociation constant (p*K*a) of the analytes but also on differences in contact surface area with the bonded phase, depending on molecular shape.

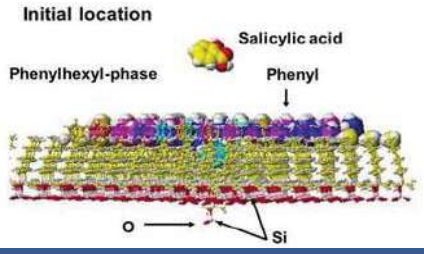


FIgure 7.15: The initial position of salicylic acid and phenylhexyl phase.

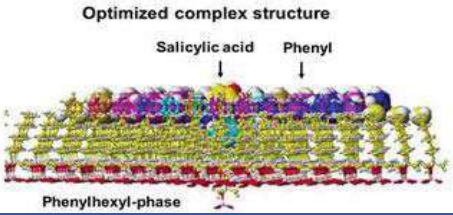


FIgure 7.16: The optimized structure.

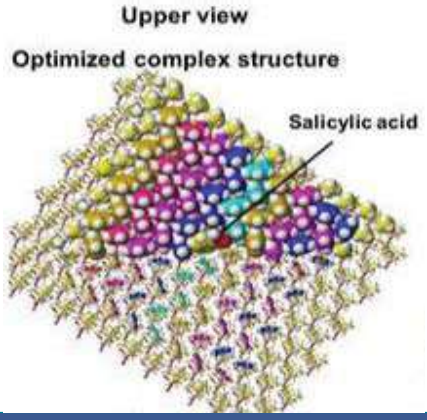


FIgure 7.17: Upper view of Figure 10.

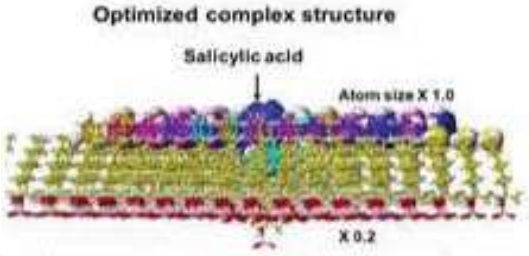


FIgure 7.18: Location of blue salicylic acid.

Sixteen acidic drug log*k* values were correlated to MIVW energy values with $r = 0.788$. The combined MIVW and MIHB (MeOH) improved the *r* value to 0.935. The contribution of MIES values was neglected; therefore, the primary interaction is van der Waals force. The retention capacity of the phenylhexyl phase was 80% of that of the octyl phase. However, tolazamide's MIVW was larger than that of tolbutamide, and these compounds were separated. Furosemide's MIVW was also larger than that of chloramphenicol. Their stereospecificity contributes to their separation.

Table 7.4: Molecular properties of Acidic drugs and molecular interaction energy values using phenylhexenyl phase.

Chemicals	log *k*	MIHB	MIES	MIVW	mMIHB
Benzoic acid	0.066	0.575	0.058	13.174	-72.34
Chloropheniol	0.175	0.375	-0.112	17.175	-80.336
Furosemide	0.358	0.93	0.011	18.228	-79.237
Ibuprofen	1.256	0.671	0.107	16.067	-67.032
Indomethacin	1.597	1.016	-0.261	20.79	-73.62
Mefenamic acid	1.603	0.639	0.036	18.325	-66.663
Nalidixiric acid	0.508	0.445	0.126	16.587	-72.999
Naproxen	0.874	0.063	-0.058	16.569	-71.25
Nicotinic acid	-0.678	1.193	-0.07	11.7	-80.02
Phenylbutazone	1.321	0	0.01	18.503	-63.096
p-Hydroxybenzoic acid	0.043	1.715	-0.055	12.617	-74.425
Probenecide	0.927	0.061	-0.113	19.943	-72.425
Salicylic acid	0.177	1.439	0.022	13.729	-73.717
Sulfamethoxazole	-0.241	2.643	3.781	13.402	-73.896
Tolazamide	0.752	0.739	-0.006	19.737	-72.396
Tolubutamide	0.608	0.856	0.027	18.023	-71.918

k measure using 150 x 4.6 mm, 5mm phenylhexyl bonded silica gel column with 50% methanol containing 10 mM formic acid at 40°C [25]; MIHB, MIESA, MIVW: molecular interaction energy values on hydrogen bonding, electrostatic, and van der Waals force interaction (unit: kcal mL^{-1}); mMIHB: molecular interaction hydrogen bonding energy values on methanol phase [28].

7.2.3 Reversed-phase liquid chromatography for basic compounds: Basic compounds were generally purified and analyzed by ion-exchange (IE) liquid chromatography. The introduction of high-performance (HP) liquid chromatography (HPLC) changed the chromatographic method. Generally, IELC packing materials are synthesized from organic polymers. Therefore, such packing materials are chemically stable in both strongly acidic and basic eluents. However, newly introduced HPLC packing materials are generally surface-modified silica gels and are limited in strongly acidic and basic eluents. Specifically, chemically modified silica gels resist eluents up to pH 8. Other limitations of basic compounds include free silanol groups on the surface, which form hydrogen bonds (HB) with nitrogen-containing compounds, and trace metals that form chelates with analytes. These molecular interactions could cause fronting and tailing peaks that deteriorate quality control.

Furthermore, peaks may not appear; therefore, several approaches have been applied: alumina, titania, and zirconia have been used instead of silica gels [30]; however, surface modification of these materials remains more challenging than with silica gels. Researchers evaluated the performance of surface-modified silica gels for basic compounds by modifying the eluent components. Peak symmetry for basic compounds depended on the manufactured columns [31]. Therefore, researchers added amine modifiers to the eluents to neutralize silanol groups and improve peak symmetry for basic compounds. To do so, they used 1,8-diamino octane. Another approach is to add counterions to form ion pairs that block hydrogen bonding in basic compounds [32, 33]. *N, N*-dimethyloctylamine was also a beneficial additive [34]. Other additives were triethylamine [35], perchlorate [36], ammonium hydrogencarbamate [37], butyl-, pentyl-, hexyl-, cyclopentyl-, cycloheptyl-, and *N, N*-dimethyloctylamine, tributylammonium chloride [38], and tetrabutylammonium [39].

Furthermore, chemically modified silica gels are generally employed as packing materials despite their chemical instability. Moreover, surface modification is critical for chromatography of nitrogen-containing (basic) compounds, even when silica gel purity is>99.999%. Further development of chemically stable, bonded silica gels enables easier chromatographic separation of basic compounds in reversed-phase [40, 41] and ion-exchange modes [42]. Researchers also developed a silica-based sulfonate-modified stationary phase [43, 44]. Propylsulfonic acid-modified silica gel with an eluent containing ammonium perchlorate was effectively employed for the chromatography of basic compounds [45]. A mixed-mode reversed-phase/weak cation exchange (carboxy-form ion-exchange) was demonstrated for chromatography of catecholamines and amphetamine related drugs [46]. Basic and acidic additives were used to separate some basic chiral drugs enantioselectively on polysaccharide-based chiral columns [47]. Furthermore, researchers synthesized polymethylsilsesquioxane microspheres for basic compounds as a low-silanol-activity chromatographic stationary phase [48].

Currently, bonded-phase silica gels with active silanol groups are expected to be inactivated, and their peak shapes are expected to improve for quantitative analysis. However, nitrogen-containing compounds behave differently from acidic compounds. For example, aniline retention in reversed-phase LC is weaker than that of benzoic acid because of its lower hydrophobicity (octanol-water partition coefficient, log *P*), and it is also lower than that of chlorobenzene in the bonded phase, which exhibits hydrogen-bond acceptance. The hydrogen-bonding capability of an amino group does not contribute to molecular interactions because of electron localization in the molecules. The electrons of chlorobenzene are well localized, as shown by the calculated atomic partial charge, compared with those of aniline. MOPAC calculations further examine these results as a substitute for the electron-localization effect. The electron localization effect on a chemical reaction is known as Hammett's σ constant obtained from thin-layer LC. When an electron is transferred to form a new compound, it is known as a chemical reaction. However, electron localization supports different retention times, resulting in chromatographic retention differences.

The following results show differences between the model phases and their ability to explain the behavior of basic compounds in reversed-phase LC quantitatively. The octyl- Pentyl-, hexenyl-, and octyl-bonded phases are shown in Figures 7.19 - 31, where scopolamine was contacted [1, 42, 49, 50]. The chromatographic retention times of basic compounds were analyzed using pentyl-, hexenyl-, and octyl-bonded silica gels. The chromatographic experiments were performed in semi-micro columns packed with 5 µm bonded silica gels. The eluent was a 50 mM sodium phosphate solution containing 50% methanol. The flow rate was 0.2 mL min^{-1} at 37 °C. Generally, fructose was utilized as the void volume marker [22]. However, we used the shortest elution time to calculate the relative retention time (*k*). Table 5 summarizes the log *k* values of the basic compounds measured using pentyl-, hexenyl-, and octyl-bonded silica gels, along with their log *P* and p*K*a values. We obtained these log*P* and p*K*a values from references [1, 49, 50]. Table 7.6 summarizes

the calculated properties of basic compounds and the molecular interaction energy values (MIHB, MIES, MIXW, mMIHB, mMIES). Figure 7.19 shows the initial position of scopolamine with an octyl-bonded silica gel model. Figure 7.20 shows the optimized structure, Figure 7.21 shows the upper view, and Figure 7.22 indicates blue (dark gray) scopolamine.

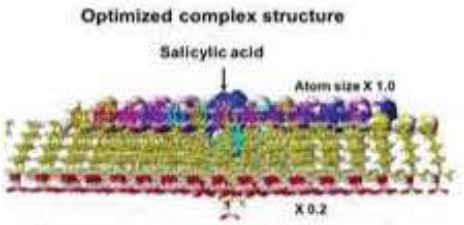


Figure 7.19: Scopolamine with a model octyl-bonded phase. Atoms: red (black), yellow (light gray), large and small white: oxygen, carbon, silicon, and hydrogen.

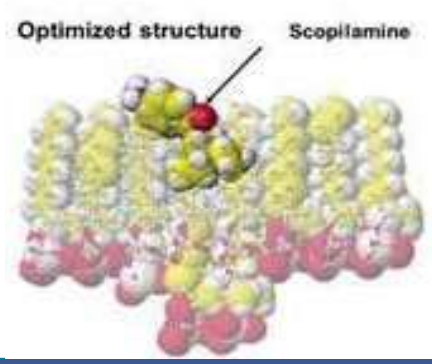


Figure 7.20: The optimized structure. Atoms: red (black), yellow (light gray), large and small white: oxygen, carbon, silicon, and hydrogen.

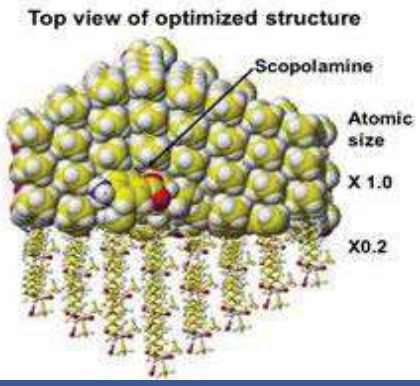


Figure 7.21: Upper view of Figure 7.19.

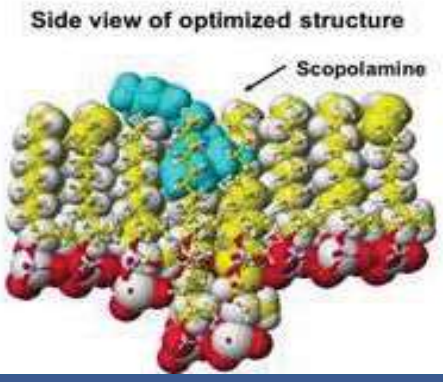


Figure 7.22: The prominent location of blue scopolamine.

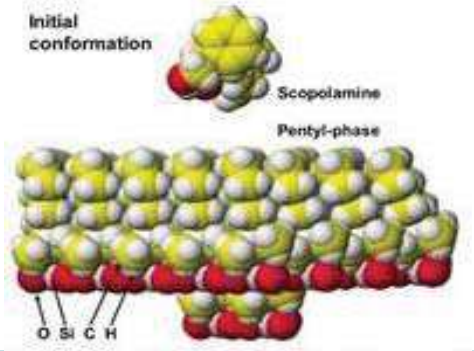


FIgure 7.23: Scopolamine with a model pentyl-bonded phase.

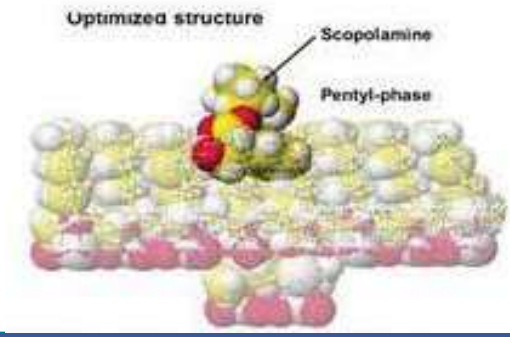


FIgure 7.24: The optimized structure.

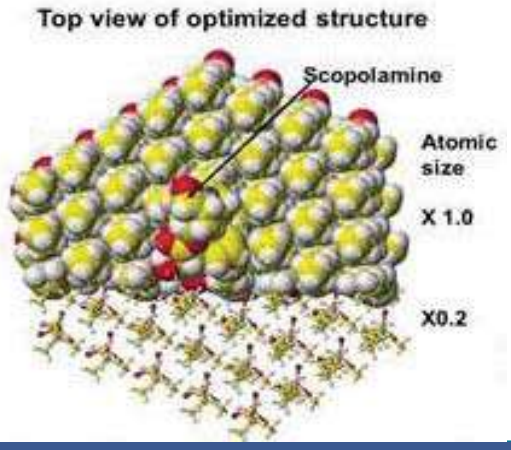


FIgure 7.25: Upper view of Figure 7.23.

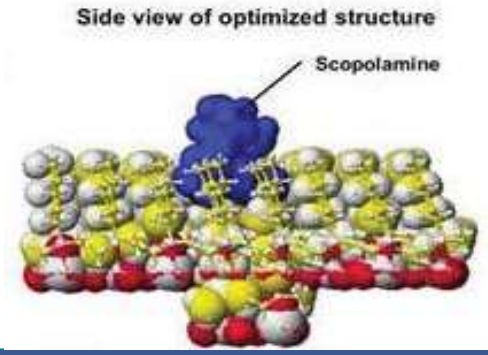


FIgure 7.26: The prominent location of blue scopolamine.

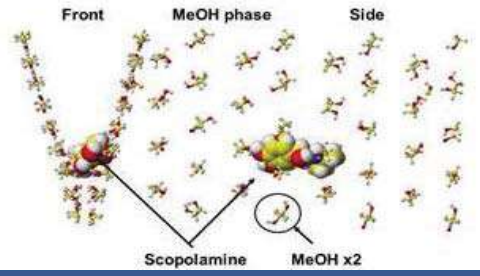


Figure 7.27: Front and side view of scopolamine on methanol phase. Atoms: red (black), yellow (light gray), large and small white: oxygen, carbon, silicon, and hydrogen

Figure 7.28 shows the initial position of scopolamine with a model hexenyl-bonded silica gel. Figure 7.29 shows the optimized structure. Figure 7.30 shows the upper view of Figure 7.28. - 31 indicates the optimized location of scopolamine.

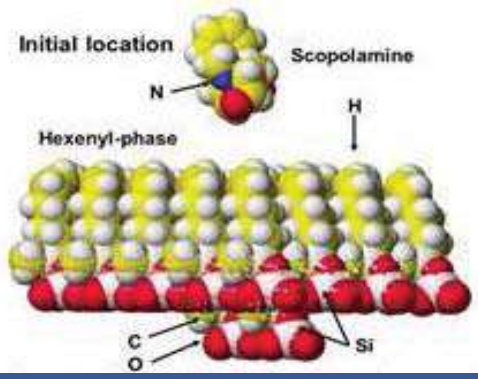


Figure 7.28: The initial position of scopolamine and hexenyl phase.

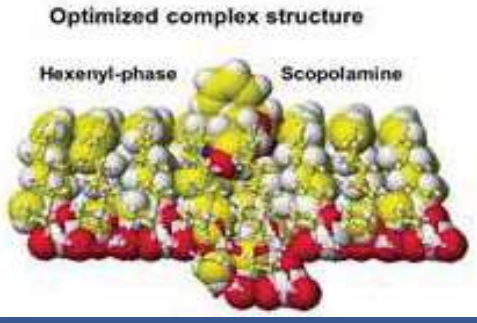


Figure 7.29: The optimized structure.

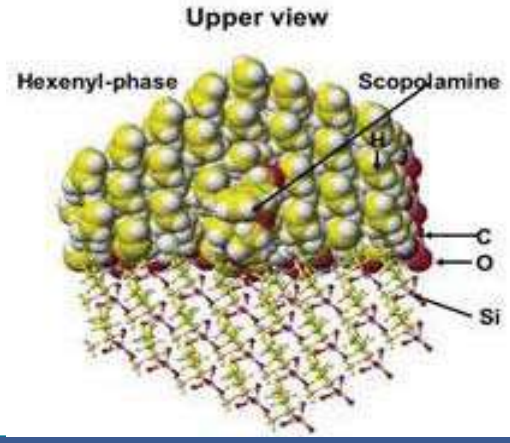


Figure 7.30: Upper view of Figure 29. Atoms: red(black), yellow(light gray), large and small white: oxygen, carbon, silicon, hydrogen.

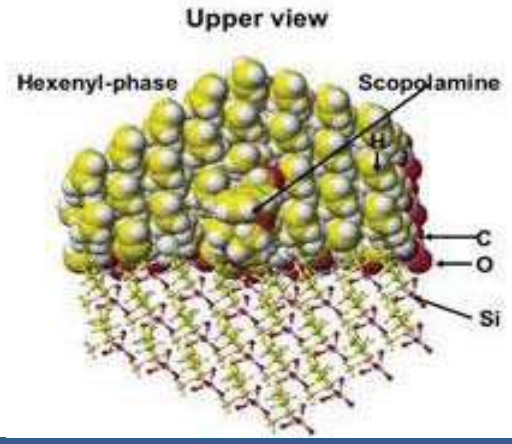


FIgure 7.31: Accessible location of blue scopolamine. Atoms: red(black), yellow(light gray), large and small white: oxygen, carbon, silicon, hydrogen.

The selectivity of these phases were analyzed employing log *k* value of the basic compounds that were measured in the same pH 10.00 eluent. These basic compounds were either in their molecular or ionized forms in pH 10.00 eluent at 37 °C. Their chemical structures in the eluent were determined based on their p*K*a values.

When the log *k* values measured with the octyl-bonded silica gel were employed as standard values, no selectivity was observed for the log *k* values measured with the pentyl bonded silica gel. The difference was the retention capacity. The following equation indicates the difference:

log *k* on pentyl phase = 0.910 log *k* (the octyl-phase) – 0.137, *r* = 0.998, n = 15.

The retention capacity of the pentyl-phase was 91% of the octyl-phase. The retention capacity of the hexenyl-phase was almost the same (97%) as that of the pentyl-phase, although it demonstrated selectivity.

log *k* (hexenyl-phase) = 0.974 log *k* (pentyl-phase) – 0.243, *r* = 0.991, n = 13.

The selectivity of the hexenyl-phase was observed at the log *k* values measured in pH 3,00 eluent, although the retention time times were very short in pH 3.00 eluent,

The selectivity for compared to the neutal compounds and benzoic acid. Further study was conducted employing the model pentyl-, octyl-, and hexyl-phases.

In the pH 3.00 eluent, these basic compounds expected to be in the ionized form, and their retention times were very short. The relation between the log *k* values of the octyl-phase and pentyl- or hexenyl-phases were evaluate:

log *k* (octyl-phase) = 0.987 log *k* (pentyl-phase) – 0.158, *r* = 0.991, n = 15

log *k* (octyl-phase) = 1.047 log *k* (hexenyl-phase) + 0.012, *r* = 0.856, n = 12.

These slopes indicated that the retention capacities of these bonded phases were like those of ionized basic compounds. However, the correlation coefficient indicated their selectivity. The hexenyl phase differed from the alkyl-chain bonded phases, although precision was uncertain because of their low log *k* values.

Table 7.5: Properties and log *k* values of basic compounds.

Chemicals	log *P*	p*K*a			log *k*			
Phase			hexenyl	pentyl	octyl			
		pH	3	10	3	10	3	10
Aniline	0.9	4.63	-0.866	-0.265	-1.143	-0.515	-0.995	-0.395
Atropine	0.16	9.6	-1.033	0.742	-0.901	0.449	-0.731	0.611
Caffeine	0.07	0.6	-0.271	-0.471	-0.714	-0.763	-0.668	-0.66
Carbamazepine	1.98	13.9	0.465	0.461	0.207	0.233	0.318	0.407

Dextormethorphan	3.99	8.3	-0.207	1.599	-0.079	1.292	0.077	1.625
Diazepam	3.18	3.3	-	1.001	0.701	0.753	0.873	0.994
Isoproterenol	0.08	8.6	-	-0.599	-	-0.767	-	-0.716
Lidocaine	1.98	7.9	-0.919	1.011	-0.635	0.878	-0.519	1.094
Prazosin	2.16	6.5	-0.815	0.433	-0.852	-0.048	-0.692	0.12
Procaine	2.24	8.01	-	0.513	-1.647	0.239	-1.512	0.41
Pyridine	0.65	5.19	-0.555	-0.212	-1.206	-0.361	-0.734	-0.37
Quinine	3.2	4.1	-0.347	1.116	-0.523	0.858	-0.294	1.134
Scopolamine	-0.2	7.75	-1.385	0.169	-1.149	-0.046	-0.965	0.097
Terbutaline	0.48	8.8	-	-	-2.29	-0.589	-2.242	-0.546
Theophylline	-0.02	3.5/8.81	-0.337	-	-0.797	-1.725	-0.766	-1.644
Log *P*, p*K*a from refs 1,42, 49, 50; log *k* measured in 50mM sodium phosphate solution containing 50% methanol at 37°C								

Table 7.6: Properties of basic compounds and molecular interaction energy values.

				Octyl phase			Methanol phase	
Chemical	**hb**	**es**	**vw**	**MIHB**	**MIES**	**MIVW**	**mMIHB**	**mMIES**
Aniline (I)	0	0	3.497	0	0.275	14.397	15.458	1.443
Aniline (M)	-1.334	0	3.416	0.003	0	14.44	17.017	-0.618
Atropine (I)	-3.435	-0.716	13.689	-0.513	-0.102	39.183	23.344	4.418
Atropine (M)	-3.451	-1.041	11.237	-0.143	-0.066	30.557	21.767	3.511
Caffeine (M)	0	-47.421	4.888	0	0.064	22.006	19.422	3.822
Carbamazepine (I)	-110.401	-7.183	19.781	-0.059	0.29	26.667	37.251	1.371
Dextromethorphan ((I)	0	0.12	14.724	0	0.284	37.33	14.153	1.683
Diazepam (I)	-4.187	7.476	13.611	0	-0.135	29.811	28.572	3.361
Diazepam (M)	0	0.675	15.243	0	-0.135	29.811	28.572	3.561
Isoproterenol (I)	-3.015	-0.041	6.071	-0.109	0.148	24.456	18.451	8.71
Lidocaine (I)	-2.146	-19.762	12.606	-0.007	1.377	27.698	22.064	3.183
Lidocaine (M)	-2.157	5.744	11.009	0.001	1.411	33.526	18.134	2.94
Prazosin (I)	0	4.104	13.136	0	0.225	30.8	24.863	3.961
Prazosin (M)	-1.257	0.633	13.8	0.008	0.003	26.098	27.836	3.303
Procaine (I)	0	-1.333	12.553	0	0.493	27.787	19.899	3.697
Procaine (M)	-1.334	-0.233	7.796	0	-0.031	28.8	19.392	2.614
Pyridine (I)	0	0	3.206	0	0.322	12.146	12.948	-1.064
Pyridine (M)	0	0	2.858	0	0.009	12.738	12.368	-0.691
Quinine (I)	-4.484	-1.001	12.917	-0.078	0.555	30.833	23.907	-0.127
Quinine (M)	-4.484	0.015	14.782	0.039	0.005	35.958	24.296	0.524
Scopolamine (I)	-3.624	-2.327	10.343	0.019	0.187	27.943	24.84	6.267
Scopolamine (M)	-0.436	-1.763	8.506	-0.034	-0.082	26.804	19.936	4.169
Terbutaline (I)	-3.028	-1.823	6.308	-0.054	-0.307	23.181	16.154	9.079
Theophylline (A)	-0.485	-47.408	6.3	0.011	-0.123	20.769	16.663	3.28
Theophylline (B)	0	-46.133	5.657	0	-0.294	22.086	15.781	5.488
	Pentyl phase			Hexenyl phase				
Chemical	MIHB	MIES	MIVW	MIHB	MIES	MIVW		
Aniline (M)	0.008	0.008	12.655	0.902	0.02	11.457		
Atropine (M)	-0.016	0.243	24.199	0.267	0.082	25.724		
Caffeine (M)	0	-0.073	15.237	0	-0.29	16.519		
Carbamazepine (I)	0.471	0.206	23.292	4.82	0.553	18.935		
Dextromethorphan (I)	0	0.235	30.468	0	0.54	29.188		

Diazepam (M)	0	0.079	27.351	0	-0.034	25.505		
Isoproterenol (I)	-0.067	-0.036	22.832	2.171	-1.152	19.705		
Lidocaine (M)	-0.01	1.613	25.32	0.238	1.098	25.184		
Prazosin (M)	0.003	0.109	26.141	0.192	0.862	27.029		
Procaine (M)	0	-0.036	19.938	0.226	-0.002	22.059		
Pyridine (M)	0	0.009	10.893	0	0.015	9.983		
Quinine (M)	-0.086	-0.008	26.651	0.541	-0.091	29.134		
Scopolamine (M)	0.025	-0.127	28.631	2.625	0.473	24.69		
Terbutaline (I)	-0.045	-0.406	24.288	2.851	-0.908	19.991		
Theophylline (B)	0	-0.167	15.232	0	-0.81	15.606		

hb, es, vw: hydrogen bonding, electrostatic, and van der Waals force energy values of analyte (kcal mol^{-1}); MIHB, MIES, MIVW: molecular interaction energy values between an analyte and a model-phase; mMIHB, mMIES: molecular interaction energy values between an analyte and a model methanol-phase (kcal ml^{-1}); M and I: molecular and ionized form; A and B: structure in acidic and basic solution.

The selectivity of these phases was analyzed using log *k* values for the basic compounds measured in the same pH 10.00 eluent. These basic compounds were in either their molecular or ionized form in the pH 10.00 eluent at 37°C. We determined their chemical structures in the eluent based on their p*K*a values. The log *k* value of basic drugs measured in the pH 10.00 eluent does not guarantee that we are describing the chromatographic behavior of the molecular form. Generally, basic drugs have dual ionic groups; therefore, the actual molecular form at pH 10.00 is unclear. The log *k* value at pH 3.00 is necessary to improve the theoretical analysis of chromatographic behavior.

Various packing materials with quantitatively known retention capability allow building a rapid separation system using a multi-column switching method with a single eluent instead of gradient elution. Multi-column, single-eluent systems provide fast analysis with a stable, flat baseline. A highly sensitive electrochemical detector can be used to chromatograph guanidyl compounds and catecholamine-related compounds. We measured these log *k* values using pentyl- and octyl-bonded silica gel columns.

These log *k* values were measured using pentyl- and octyl-bonded silica gel columns, with 50% methanol containing 50mM sodium phosphate (pH 3.00 -10.00) at 40°C.eluent. The results of the octyl-bonded silica gel column follow:

MIVW = 6.151 log *k* (pH 10.00) + 25.847, *r* = 0.750, n = 15,

MIVW – 2.2 mMIES = 8.052 log *k* (pH 10.00) + 22.325, *r* = 0.891, n = 15.

MIES, MIHB, and mMIHB contributed nothing. Van der Waals interactions between the octyl phase and the basic compounds were the primary interaction, and mMIES contributed to the desorption of the basic compounds from the octyl phase. These correlation constants improved to 0.931 and 0.933 (n = 14) after eliminating theophylline due to its very short retention time, with a log *k* value of -1.644.

From log *k* values measured using the pentyl-bonded phase:

MIVW = 5,125 log *k* (pH 10.00) + 22.247, *r* = 0.677, n = 15.

MIVW + MIES = 5.409 log *k* (pH 10.00) + 22.359. *r* = 0.702, n = 15.

MIVW + MIES – 1.58 mMIES = 7.911 log *k* (pH 10.00) + 17.061, *r* = 0.913, n = 15,

MIVW + MIES – 1.58 mMIES – 1.1 mMIHB = 7.654 log *k* (pH 10.00) – 14.783, *r* = 0.917, n = 15.

A reduced alkyl chain length of the bonded-phase silica gel appeared to be influenced by silicon dioxide oxygen. When an analyte penetrated silicon dioxide, the silicon dioxide oxygen affected the molecular interaction. This phenomenon is subsequently explained in the evaluation of bonded-phase inertness.

From the log *k* values measured using the hexenyl-bonded phase:

MIVW = 5.990 log *k* (pH 10.00) + 20.110, *r* = 0.737, n = 13,

MIVW + MIES = 6.486 log *k* (pH10.00) + 20.056, *r* = 0.767, n = 13,

MIVW + MIES – 1.16 mMIES = 8.260 log *k* (pH 10.00) + 15.913, *r* = 0.903, r = 13,

MIVW + MIES – 1.16 mMIES – 0.05 mMIHB = 8.184 log *k* (pH 10.00) + 15.093, *r* = 0.906, n = 13.

As expected for the hexenyl group, the ES energy contributed to retention in the hexenyl phase. Further, solvation effects with methanol indicated that the ES effect (mMIES) contributed significantly, while HB (mMIHB) contributed slightly.

The chromatographic behavior in acidic eluent was analyzed using log *k* values measured in pH 3.0 eluent.

From the log *k* values measured using the octyl-phae:

MIVW = 3.168 log *k* (pH 3.00) + 28.479, *r* = 0.316, n = 15,

MIVW – 4.4 mMIES = 11.319 log *k* (pH 3,00) + 19.706, *r* = 0.705, r = 15,

MIVW – 4.5 mMIES + 1.2 mMIHB = 16.184 log *k* (pH 3.00) + 46.283, *r* = 0.794, n = 15.

These results indicated the selectivity of the model phases: the longer the alkyl chain, the higher the VW contribution, and the shorter the alkyl chain, the higher the silica gel matrix contribution. ES solvation energy contributed more than HB energy to the retention of basic compounds in the pH 10.00 eluent in reversed-phase liquid chromatography. This differed from acidic drugs, where HB energy was predominant. The poor correlation coefficient of basic compounds was attributed to a mixture of both molecular and ionized forms.

7.2.4. Selectivity of Phenylhexyl-bonded siica gel: Another potential column selection is utilizing a PhHx-bonded silica gel column. The hydrophobicity of the PhHx column is similar to that of the C8 column. Still, it demonstrated selective separation between tolbutamide (9, log P: 2.34, pKa: 5.16) and tolazamide (10, log P: 2.69, pKa: 4.07) (Rs = 3.0); compared to the results obtained using the C8 column, no clear separation was observed (see Figure 32). The elution order of tolbutamide and tolazamide is related to their log P values (2.34/2.69). Resolution improves on the phenylhexyl-bonded phase because tolbutamide has a higher MIHB and tolazamide has a higher MIVW. (Table 7.4).

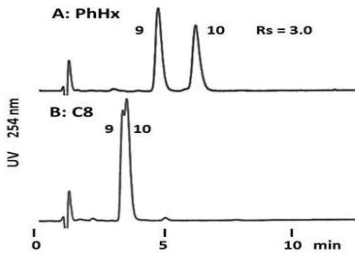


Figure 7.32-: Selective separation of tolbutamide (9) and tolazamide (10) on phenylhexyl-phase
Column A: Phenylhexyl 50 x 3.0 mm I.D., B: Octyl-phase, 50 x 3.0 mm I.D.; Eluent: 10 mM formic acid containing 50% methanol; Flow rate: 0.4 mL min-1 at 40°C.

The retention mechanism of basic compounds in reversed-phase liquid chromatography is van der Waals interaction, even when chromatography was performed using a pentyl-bonded silica gel with guaranteed inertness and long-term stability. The pentyl-bonded phase exhibited retention capacity, although it supported a greener operation. Quantitative analysis of the molecular interactions indicated that pentyl-bonded silica gel may contribute an ES interaction from the silicon dioxide oxygen. The hexenyl-bonded phase showed selectivity because of the double bond, although its retention capacity was similar to that of the pentyl-bonded phase. For the basic compounds, we observed a contribution of ES solvation energy with methanol. These results differed from those observed for acidic compounds, where the HB energy contribution was significant. This may be due to nitrogen lone-pair electrons. A limitation in studying the fundamental retention mechanism of basic compounds is the challenge of measuring the retention time of the molecular form. Silica gel-based packing materials can be resolved and analyzed. However, they are not stable in the high-pH eluents needed to measure the retention times of the molecular form of basic compounds. The log *k* value of basic drugs measured in a pH 10.00 eluent does not guarantee that we are describing the chromatography behavior of the molecular form. Generally, basic drugs have dual ionic groups; therefore, the actual molecular form at pH 10.00 is unclear. The log *k* value at pH 13.0 is necessary to improve the theoretical analysis of chromatographic behavior.

Quantitatively known retention capabilities of various packing materials permit building a rapid separation system using a multi-column switching method with a single eluent instead of a gradient eluent. The multi-column, single-eluent system provides fast analysis with a stable baseline. Highly sensitive electrochemical detection can be applied, such as for guanidyl compounds and catecholamine-related compounds.

7.3. Bio-mimic ion-exchange groups and chromatography

An ion-exchange liquid chromatography was developed using ion-exchange resins [51] as an amino acid analyzer [52]. Since then, ion-exchange resins have been used in several chromatographic modes, including stable adsorbents in normal-phase liquid chromatography. The chromatographic behavior of aromatic compounds on anion-exchange resins is similar to that on modified silica gels [53]. Chromatography using ion exchangers is called ion-exchange liquid chromatography; however, retention mechanisms are not purely ion exchange. All analytes are ionizable, either in molecular form in acidic eluent or in ionized form in basic eluent. Retention in acidic eluent should resemble Lewis acid-base interactions, and hydrogen bonding may predominate. Electron localization produces Lewis acid-base structures even when the analytes are neutral molecules.

Ion-exchanger properties were analyzed using spectroscopic methods and NMR spectra of the organic polymer gels were analyzed in various solvents to relate the water content outside and inside the resins to ion-exchange capacity was related, as water molecules contact the ion-exchange groups [**45**, 54,55]. Furthermore, a fundamental study of molecular interactions in chromatography used simple small molecules to analyze the chromatographic behavior of aromatic compounds on an anion-exchange resin with an aqueous eluent. The NMR spectra of a mimic anion-exchanger (trimethylammonium ion-exchange resin) with aniline or nitrobenzene in a deuterium solvent (ethanol-OD) were measured to investigate chromatographic molecular interactions. The probable signal of the trimethyl group of trimethylbenzylammonium shifted toward higher field with aniline and lower field with nitrobenzene. The chemical shift was larger with aniline than with nitrobenzene, and it was not observed with toluene. Chemical shift relates to electronegativity. The amino group of aniline faced the chloride ion of trimethyl benzyl-ammonium. The chloride ion repulsed thenitro-group ofnitrobenzene. Because the nitro group and chloride ions are electron-rich groups or atoms, these small molecules move freely in solution. Therefore, the contact conformation in the solution may not reflect the chromatographic interactions; spectra measured using ion-exchange resins were broad because the instrument was not used for solid-state NMR. However, the spectra supported chromatographic behavior [56].

Furthermore, electron spectroscopy for chemical analysis (ESCA) was used for measuring chemical shifts due to electron localization. The 12C signal shifted by 0.27 eV upon adsorption of αα-α-α-α-hydroxynaphthalene on the anion exchanger (CR400 Cl form), and by -0.26 eV upon adsorption of 1,8-dinitronaphthalene on the anion exchanger. The N1Schemical signal of the anion exchanger was -0.08 eV and -0.43 eV for α-hydroxynaphthalene and 1.8-dinitronaphthalene, respectively. NMR and ESCA results indicated that the chemical shifts resulted from interactions between the ion exchangers and the analytes. Although the shifts indicated stronger molecular interactions, the spectrometric resolution was insufficient at that time [57].

Numerous reports on ion exchangers have been published, but molecular interaction mechanisms and ion-exchange chemistry have not been quantitatively described [44, 58, 59]. A quantitative explanation of these retention mechanisms was studied *in silico* using model phases, proposing a cation exchanger for basic drugs in 2004 and an anion exchanger for acidic drugs in 2007 [1].

The relative retention time difference is based on the solubility factors commonly used to explain the retention mechanisms in liquid chromatography [22]. The mechanisms were quantitatively explained by in silico analysis using model compounds. The retention mechanisms combine van der Waals forces, electrostatic interactions, and hydrogen bonding. Different chromatography types reflect distinct molecular interaction forces. If the solubility factors can be quantitatively reconstructed, the chromatographic retention mechanisms can be analyzed quantitatively.

Computational chemical analysis using molecular mechanics software provides the molecular interaction (MI) energy values as the sum of mainly VW, HB, and ES energy values. VW energy relates to molecular size. Therefore, the contact surface area between analyte and adsorbent contributes to the MI energy. VW forces predominate in reversed-phase liquid chromatography. When HB exists between an analyte and an adsorbent, HB energy also contributes to the MI energy. HB is the primary molecular interaction in normal-phase liquid chromatography and plays a partial role in hydrophilic interaction liquid chromatography (aqueous normal-phase liquid chromatography). ES includes dipole-

dipole, π - π interactions, contact charge transfer, ion-dipole, and ion-ion interactions. These interactions help explain electron localization in organic reactions. Therefore, electrostatic energy values can also explain the degree of these interactions. Their MI energy values are the sum of the solute and model-phase energy values, yielding a complex energy value calculated as follows.

In chromatography, alkyl phases such as butyl- to dodecyl-bonded phases; electron-donor phases such as hexenyl- and phenyl-hexyl-bonded phases; hydrogen-bonding phases such as amino- and amide-bonded phases; and ion exchangers have been synthesized for various applications. Silica is the most common support because it is easy to handle, and other supports include synthesized polymer gels and natural polymers.

A quantitative explanation of the retention mechanisms of alkyl-bonded phases is relatively simple; however, retention mechanisms in non-aqueous systems are complex because both HB and ES must be considered. The inductive effect of ligands and analytes affects the quantitative explanation. Furthermore, the quantitative analysis of retention mechanisms in ion-exchange liquid chromatography is complicated, and modeling the ion-exchange phase is difficult because of the repulsion between ion-exchange groups. The fundamental phenomena were quantitatively analyzed using simple molecules [1], and a practical model is under development

The MI in chromatography was analyzed using single-bonded silicon oxides with model ligands such as octyl-, hexenyl-, hexylamine- and hexylguanidine-bonded trimethoxy-silicones. The HB, ES, and VW energy values use indices to characterize specific molecular interactions with the analyte [27]. This approach was applied to study the MI mechanisms of ion-exchange liquid chromatography of acidic drugs using hexylamine- and hexylguanidine-bonded silica gels [**60**/68]. We measured the retention times of acidic drugs in an aqueous eluent using a biomimetic ion exchanger, guanidine-bonded silica gel. We used the retention times for quantitative in silico analysis of the retention mechanisms. Furthermore, a simple method to measure human serum albumin-drug binding affinity (log n*K*) was demonstrated.

The precisely defined mechanism of ion-exchange liquid chromatography is based on ion exchange. This phenomenon is called ion chromatography. Developing ion-exchangers expanded the capability of ion-exchange liquid chromatography and permits the separation and purification of various compounds, including non-ionizable compounds. We call it ion-exchange liquid chromatography, but we use ion-exchanger more generally.

The strongest interaction in chromatography is ion-ion interaction, calculated at MIES using the MM2 program. The ES energy includes dipole-dipole interaction. The difference can be understood from the model comparison experiments, and amino acids contribute to the ion exchange *in vivo*; the amino acids are glutamine (p*K*a 4.25) and aspartic acid (p*K*a 3.65), whose carboxyl groups are cation exchangers, and arginine (p*K*a 12.48) guanidinium and lysine (p*K*a 10.53) ε-amino groups are anion exchangers.

The hexylamino group is a cation in a solution containing buffer components that hold molecularly neutral acidic compounds by hydrogen bonding and ionized acidic compounds by ion-ion interactions. Furthermore, the guanidinium group is an ion-exchange group of proteins. Protamine-coated silica gel was first used for liquid chromatography of saccharides. Thus, a guanidine-bonded phase was developed from a propylamine-bonded phase to achieve separation and quantitative recovery of saccharides comparable with that observed with a propyl-amine-bonded phase [61]. Poor recovery from the amino phase occurs because primary amines react with saccharides in vitro and form glycosides. Propylamine-bonded silica gel is unstable in buffer solutions; therefore, a hexylamine-bonded silica gel with a secondary silyl reaction was synthesized and used for saccharide chromatography after modifying the amino group to a guanidine group [62].

In contrast, the pentylcarboxyl group retains acidic compounds by hydrogen bonding and basic compounds by ion-ion interaction in acidic solutions. In neutral and basic solutions, the ionized carboxyl group retains ionized basic compounds by ion-ion interaction and basic molecular compounds by hydrogen bonding. However, retention times depend on the dissociation constant (p*K*a) of various compounds; therefore, modeling their structures is difficult, complicating quantitative explanations of retention mechanisms in ion-exchange liquid chromatography.

7.3.1. Cation-exchange liquid chromatography: The carboxyl group exists in molecular form in low-pH solution and ionizes as pH rises, elevating the eluent pH. The gradual change in chemical structure makes quantitative explanation of

retention mechanisms difficult. Titration measures ion-exchange capacity; however, the p*K*a of ion-exchange groups is not determined by structure. Benzoic acid p*K*a is 4.20; substituents affect the pKa of substituted benzoic acids. The substitute effect is known as Hammett's σ constant and indicates the electron localization degree. In liquid chromatography using a hexanoic acid-bonded silica gel, the ion-exchange group exists as the molecular form in very low-pH solution, where only phosphate-- or sulfate-substituted compounds are 100% ionized carboxy compounds, and ionized phenol compounds generally have p*K*a values above 10.

The relative retention (k) in an arbitrary pH is calculated using the following equation. $k = (k_m = ([K]/[H^+])/\{(1 + k_i ([K]/[H^+])\}$. The calculation requires k_m and k_i of the molecular and ionized from compounds, respectively, and the eluent pH (H^+ concentration) and the analyte's p*K*a. However, the chromatography measured p*K*a values are different from the reference values.

p*K*a (ion-exchange LC) = 0.612 (p*K*a reference) + 0.538, $r = 0.960$, n = 17

The p*K*a of aromatic acids measured using a propylamine-bonded silica gel (NH2) was smaller than that measured using an octadecyl-bonded silica gel (ODS), and the p*K*a measured using diethylaminoethyl-bonded silica gel (DEAE) was smaller. The p*K*a measured using a cation exchanger (SP) was shifted to a higher pH region [63]. The relations are given in the following equations.

p*K*a (NH2) = 0.744 (p*K*a (ODS) + 0.446, $r = 0.988$, n = 29,

p*K*a (DEAE) = 0.847 p*K*a (ODS) + 0.268, $r = 0.990$, n = 29,

p*K*a (SP) = 1.023 p*K*a (ODS) – 0.097, $r = 0.998$, n = 29.

We used 36 aromatic acids, but excluded seven that formed intramolecular hydrogen bonding from the calculation. We measured the retention times under the same experimental conditions with 20% acetonitrile. The organic modifier effect was 0.022 pH units of methanol or acetonitrile, experimentally [**64, 65**]. The organic concentration effect depended on the buffer components, even when pH was measured using standard buffers for pH-meter calibration. Furthermore, the p*K*a shift in the aqueous organic solvent depended on the analyte itself [**66**]. The organic modifier effect was observed for carboxylic acids in reversed-phase mode liquid chromatography [**67**] and for polar aromatic compounds in cation-exchanger and porous polymer gel [**68**]. Standardizing the organic modifier remains difficult because solvation is complex to predict. However, measuring pH before mixing with the organic modifier reduces experimental error, and deviations from standard values may reflect ion-exchanger properties. The slope indicates ion-exchanger selectivity.

The retention times of basic compounds measured in carboxy ion-exchange liquid chromatography are analyzed using molecular interaction energy values in molecular-mode phases. The molecular interaction energy values in acidic solutions are calculated using the molecular form of the carboxy phase (Figure 7.32), and those in basic solutions are calculated using the ionized form of the carboxy phase (Figure 7.33). The calculated using an ionized form of the carboxy phase (Figure 7.33). Table 7.7 lists the calculated MIFS values.

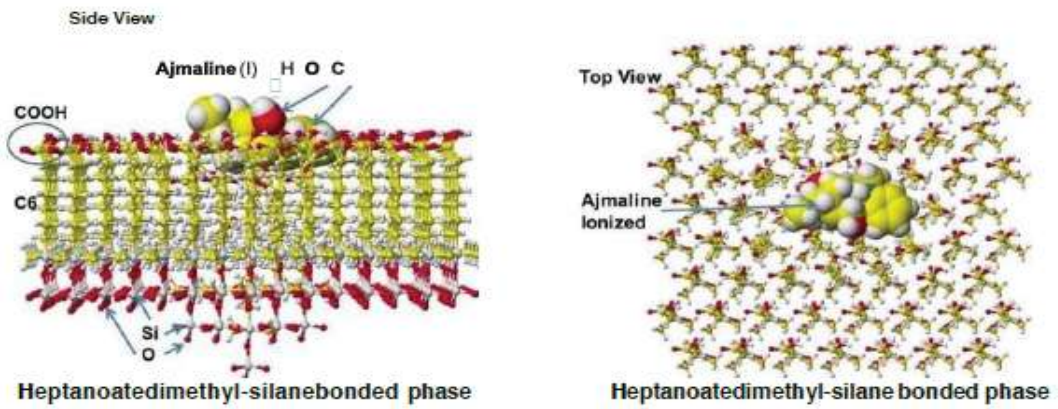


FIgure 7.32: SInteraction of ajmaline on the molecular form carboxy-phase

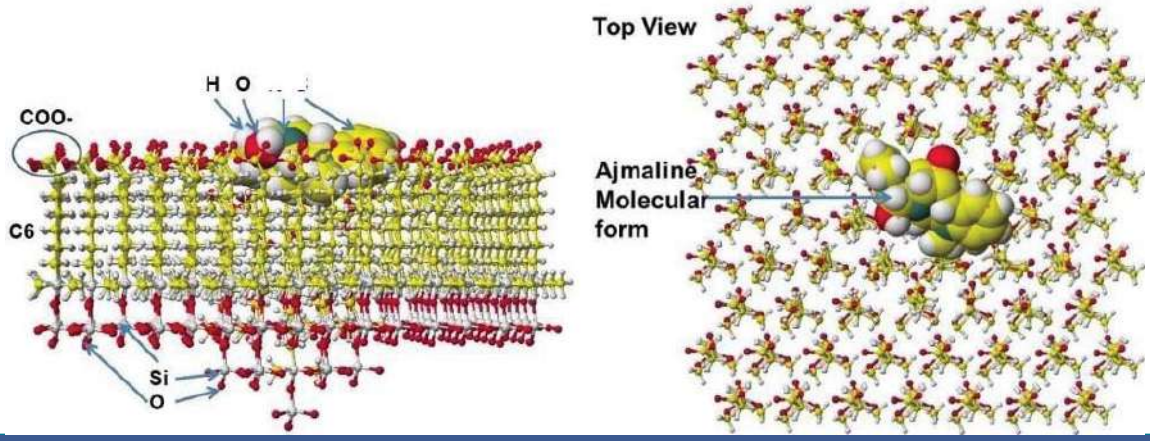


Figure 7.33: Interaction of ajmaline on the ionized form carboxy phase.

The MI energy value at an arbitrary pH is calculated using the following equation. The calculation requires the MI energy values for the molecular ($MIFS_m$) and ionized ($MIFS_i$) forms, respectively, the eluent pH (H^+), and the analyte's p*K*a.

$$MIFS = (MIFS_i + MIFS_m([K]/[H^+]) / (1 + ([K]/[H^+]))$$

The measured basic drug log *k* values in pH 6-8 were correlated to the calculated MIFS energy values with *r* values of 0.660 – 0.944 (n = 11). The correlation coefficients were 0.680 – 0.944 (n = 11) using p*K*a predicted from atomic partial charge [42].

Table 7.7: Molecular properties of basic compounds and their measured and calculated log *k* and molecular interaction energies.

Chemical	p*K*a	log *k*	log *k*	log *k*	log *k*	log *k*	MIFS	MIFS	MIFS	MIFS	MIFS
pH	pred.	3.2	6	7	8	9	3.2	6	7	8	9
Ajmaline	5.556	-0.306	0.971	1.17	1.163	1.13	83.745	58.984	46.998	45.136	44.939
Aniline	3.408	-0.944	-0.135	-0.206	-0.156	-0.185	65.838	10.476	10.146	10.116	10.112
Atropin	6.536	-0.878	0.463	0.663	0.784	0.796	77.126	66.175	40.142	28.609	26.868
Dextromethorphan	5.618	0.266	0.463	0.663	0.784	1.546	79.51	64.763	47.175	42.797	42.293
Imipramine	6.352	0.044	1.187	1.41	1.627	1.736	56.11	74.612	60.383	56.602	56.11
Isopretenol	5.801	-1.5*	-0.002	0.182	0.28	0.262	78.985	54.178	33.688	29.584	29.084
Lidcaine	5.373	-0.756	0.611	0.741	0.785	0.765	74.827	48.455	36.226	34.349	34.129
Pyridine	3.739	-0.335	-0.174	-0.219	-0.16	-0.188	61.594	8.857	8.719	8.705	8.703
Quinine	5.74	0.134	1.221	1.356	1.38	1.359	81.805	58.182	46.985	45.253	81.805
Scopolamine	5.281	-1.168	0.226	0.192	0.199	0.167	74.656	29.835	27.3	27.031	27.001
Terbutaline	5.924	-1.5*	0.019	0.19	0.263	0.257	74.246	48.125	30.378	27.18	26.796

-1.5*: temporary value the calculated log *k* value was less than -2.0 (due to ion-exclusion of inadequate V0 value.

7.3.2. Quantitative in silico analysis of acidic drug interactions on a bio-mimic guanidine ion-exchanger: A model saturated hexylamine-bonded phase was constructed based on a model bonded silica gel composed of 164 dimethyl-hexylamino-silicone tetraoxides. We converted the amino groups to guanidine groups to prepare a guanidine phase. The silicone tetra-oxide groups were locked as a model of silica gel. The distance between silicon atoms in the ligands was 6.2 Å, similar to that of the previously constructed polysiloxane phase [**60**]. Locked hexylguanidyl groups surrounded the free guanidyl groups to prevent the free hexylguanidine groups from bending outside the model phase. Figure 7.34 shows part of the model phase. Table 7.8 summarizes the MIFS energy values of molecular form acidic drugs, along with the measured log *k* and reference p*K*a values.

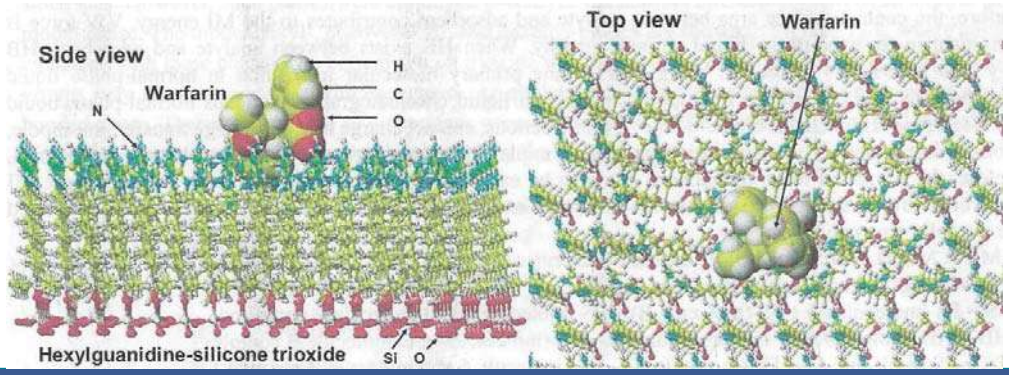


Figure 7.34: Retention of warfarin on hexylguanidine-phase. Yellow (gray), white, light blue (dark gray), and red (black) color balls: carbon, hydrogen (small) or silicone (large), nitrogen, and oxygen.

Table 7.8: Molecular properties of acidic drugs and their measured and calculated log *k* and molecular interaction energy values.

Chemical	n*K*	p*K*a	log *k*	log *k*	log *k*	MIFS	MIES	MIFS	MIFScal
			pH 3.0	pH 7.4	pH 9.0	pH 3.0	PO4	pH 9.0	pH 7.4
Benzoic acid	4.09	5.66	0.22	-1.002	-2.432	19.034	9.971	117.176	100.513
Furosemide	5.7	5.66	0.89	-0.248	-0.743	49.093	9.319	146.804	130.336
Ibuprofen	6.61	6.03	0.95	0.169	-0.117	33.604	4.137	142.257	119.082
Indomethacin	7.32	5.73	1.44	0.597	0.346	48.11	6.33	169.398	148.857
Iopanoic acid	7.84	6.05	1.47	0.684	0.409	41.959	2.583	155.032	131.022
Mefenamic acid	7.84	5.78	1.5	0.581	0.273	57.192	8.187	160.808	141.941
Nalidixic acid	4.18	6.48	0.36	-0.358	-0.977	43.075	21.968	135.883	101.024
Naproxen	5.75	5.94	0.78	-0.051	-0.459	35.996	3.543	142.513	121.509
Nicotinic acid	3.2	5.26	0.16	-1.818	-	17.229	6.754	115.902	104.541
Phenylbutazone	6.05	5.66	1.13	0.228	-0.124	35.648	0.55	143.089	126.867
p-Hydroxy	4.06	5.91	-0.03	-0.034	-0.735	22.095	11.02	128.685	106.438
benzoic acid									
Salicylic acid	4.81	5.23	1.12	-0.635	-1.202	31.734	1.388	129.97	119.764
Tolazamide	5.16	6.12	0.5	-0.064	-0.433	55.782	31.393	149.393	119.923
Tolubutamide	5.29	6.33	0.38	-0.191	-0.629	54.151	31.415	145.215	111.231
Warfarin	5.38	6.14	0.85	0.087	-0.314	49.625	11.463	150.341	124.771

The retention times: measured using hexyl-guanidine bonded silica gel. The eluent: aqueous 50% methanol solution containing 50mM sodium phosphate, and the column temperature: 37°C.

The relationship between the measured log *k* and calculated MI energy values of acidic drugs in ion-exchange liquid chromatography differed greatly from that in reversed-phase liquid chromatography. This was unsatisfactory compared with that obtained in reversed-phase liquid chromatography; however, the solvent effect improved the correlation. The relationship between log *k* by ion-exchange liquid chromatography and the calculated following equations express MI energy:

In pH 3.0:

MIFS = 12.774 log *k* + 29.630, *r* = 0.484, n = 15,

MIHB = 21.94 log *k* + 8.34, *r* = 0.322, n = 15,

MIES = 2.14 log *k* + 13.11, *r* = 0.156, n = 15,

MIVW = 6.33 log *k* + 9.10, *r* = 0.555, n = 15.

These results did not describe the chromatographic behavior of acidic drugs by ion-exchange liquid chromatograph. The relationship between log *k* and MI(MeOH) and MIVW(MeOH)energy due to solvation with methanol is shown by the

following equations. A combination of MIFS and MIFS(MeOH) and MIVW(MeOH) calculated in the methanol phase [**69**] did not improve the correlation coefficient between log k and the calculated energy values.

MIFS (MeOH) = 13.12 log k + 12.21, r = 0.725, n = 15

MIVW (MeOH) = 3.22 log k + 5.80, r = 0.443, n = 15,

MIFS – MIFS (MeOH) = 10.19 log k + 31.91, r = 0.131, n = 15,

MIFS -2xMIVW (MeOH) = 3.22 log k + 5.80, r = 0.370, n = 15.

The primary retention mechanism in ion-exchange liquid chromatography is the exchange of analytes and ions in the eluent. Therefore, we calculated the MI energy values between the analytes and a phosphate ion phase (PO_4). We constructed the phosphate phase by replacing MeOH with phosphate ions. Figure 7.35 shows the structure of the phosphate ion phase, with warfarin as the analyte.

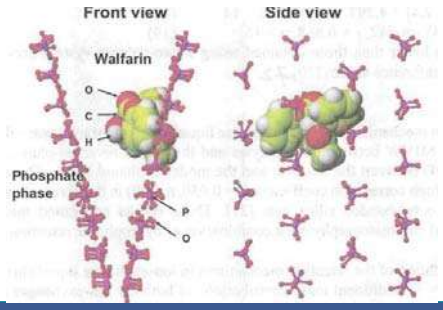


FIgure 7.35: Retention of warfarin on phosphate ion phase. Yellow (gray), white, magenta (dark gray), and red (black) balls: carbon, hydrogen, phosphate, and oxygen.

The MIES values of analytes with the phosphate ion phase MIES (PO_4) are collected in Table 7.8. The calculated results are given by the following equations:

MIES(PO_4) = -9.88 log k + 18.40, r = -0.496, n = 15,

MIFS(PO_4) = -2.38 log k + 30.65, r = -0.095, n = 15.

The negative slope indicates that MIES (PO_4) decreased retention times. These relationships show that ion replacement was the primary desorption mechanism. Combining MIFS with MIES(PO_4) or MIFS(PO_4), calculated using the phosphate ion phase, improved the correlation from 0.484 to 0.945 (n = 15), explaining the retention mechanism in ion-exchange liquid chromatography.

MIES – 1.34MIES (PO_4) = 26.01 log k + 4.98, r = 0.945, n = 15,

MIFS – 0.85MIFS (PO_4) = 14.797 log k + 3.58, r = 0.800, n = 15.

Furthermore, we analyzed the log k values measured at pH 9.0 and obtained the following equations. Ionized analytes were in contact with positive ion-exchange groups, and the correlation coefficient was 0.896 (n = 14), despite very short retention times under these conditions—the ionic effect calculated using a sodium ion phase (MIFS(Na^+)).

In pH 9.0 eluent:

MIFS = 16.59 log k + 153.19, r = 0.896, n = 14,

MIHB = 3.03 log k + 9.97, r = 0.896, n = 14

MIES = 7.08 log k + 123.73, r = 0.649, n = 14,

MIVW = 8.57 log k + 19.95, r = 0.856, n = 14,

MIFS(Na^+) = 13.73 log k + 96.07, r = 0.896, n = 14.

These model experiments demonstrates a quantitative explanation of ion-exchange chromatographic retentions.

7.4. Measurement of Albumin-drug binding affinity (log n*K*) using liquid chromatography

Human serum albumin (HSA) is the most abundant plasma protein and accounts for most drug binding in plasma. Because drug binding to HSA is readily reversible, the drug-HSA complex serves as a circulating drug reservoir that releases more drug as free drug is biotransformed or excreted. HSA's physiological function does not depend on specific interactions, but its broad, nonspecific physicochemical properties can prolong a drug's in vivo half-life. HSA also scavenges and clears unnecessary compounds. Several analytical methods measure HSA-drug binding affinity. Liquid chromatography is the most effective analytical method because it requires small sample amounts and is reproducible when comparing equilibrium dialysis and ultrafiltration. Several variants of liquid chromatography have been developed, including the Hummer-Dreyer method, frontal analysis, the vacancy peak method, retention analysis, and the immobilized protein column method, but the lack of pure HSA produces unacceptable data. A prediction method using a computational chemistry program was developed; however, several binding locations in HSA do not define the correct binding location for new compounds. A new liquid chromatography method was developed based on HSA's fundamental properties: hydrophobic and ion-ion interactions [70, 71].

A combination of reversed-phase and ion-exchange liquid chromatography produces the hydrophobic and ion-ion interactions separately. The measured log *k* values were correlated to log *K* values measured using the modified Hummer-Dreyer method [72]. Furthermore, the measured log *k* values were predicted *in silica* using model phases. We measured hydrophobic interactions using a pentyl-bonded silica gel, ion-ion interactions of acidic drugs using a guanidino-bonded silica gel, and those of basic drugs using a carboxy-bonded silica gel. The correlation between the combined log *k* values and log n*K* values measured using the modified Hummer-Dreyer method was 0.974 (n = 7) and 0.994 (n = 4) for acidic and basic drugs, respectively. The log *nK* values measured using the Hummer-Dreyer method are summarized. in Table 7.9.

Table 7.9: log n*K* values measured using the modified Hummer-Dreyer method.

Furosemide	5.54	Naproxen	5.81	Phenylbutazon	5.95
Salicylic acid	4.81	Sulfamethoxazole	4.02	Tolbutamide	5.26
Warfarin	5.63	Scopolamine	3.18	Isoplamine	3.76
Quinine	3.78	Dextromethorphan	4	Isoplamine	4.26
log n*K* values were 1neasured using a purified HSA. The purity is 97.3 % by chromatography					

These standard compounds are used to determine various compounds' log K values from log K values measured using the same pentyl-guanidine-bonded silica gel columns. Retention time in both reversed-phase and ion-exchange liquid chromatography is predictable from calculated molecular interaction energy values using model phases. The predicted log *k* values at pH 7.4 correlate with log n*K* values obtained using the modified Hummer-Dreyer method to predict log nK values for other compounds.

First, calculate molecular interaction (Ml) energy values for both the molecular (MIFSm) and ionized (MIFSi) forms of these compounds; then replace log *k*m and log *k* with MIFSm and MIFSi to obtain MIFS in MIFS values at pH 7.4. The following equation is the modified equation for this purpose.

MIFS = (MIFSm + MIFSi ([H⁺]/[*K*])/(1 + ([H⁺]/[*K*]) H⁺:$10_{7.4}$, *K*: 10^{pKa}

The correlation between MIFS(pH7.4) and the standard log n*K* values for acidic and basic drugs are 0.905 (n = 16) and 0.928 (n = 17),respectively. These *r* values are not close to 1.000 but are much better than the distributed reference values.

The distributed reference log n*K* values reflect the purity of the HSA used; a marketed Control V HSA contains more than 30% glycosylated albumin. We used 3.2% to 97.3% pure HSA obtained during purification to measure warfarin-HSA binding affinity and assess the effect of glycosylation. Warfarin -log n*K* was measured using HSA containing 30% glycosylated albumin and 97.3% pure HSA. This result means that the data measured using a marketed Control V albumin do not support the intended purpose. The difference in log nK2 means a 100-fold difference in binding affinity; the reference log n*K* values of naproxen and lidocaine vary by 2 and 3. These numbers exhibit 100- and 1000-fold differences in binding affinity.

The log *k* values of acidic drugs were measured by reversed-phase using a pentyl-bonded silica gel and ion-exchange liquid chromatography using a bio-mimic ion-exchanger (guanidino-bonded silica gel). The combined log *k* values were correlated with binding affinity (*log K)* for human serum albumin. The reference *log nK* values of the acidic drugs were measured using purified human serum albumin by the modified Hummel-Dreyer method [72]. Therefore, Table 13 gives the log n*K* values measured at pH 7.4. The correlation is shown in the following equation:

log n*K* = 2.614 log *k*(R) + 0.453log *k*(I)) + 3.1.20, *r* = 0.974 (n= 7).

Furthermore, the log n*K* values correlated well with the MIFS values calculated using the model propyl-guanidino-phase. MIFS (pH7.4) = 4.702 (log n*K*) + 14.314, *r* = 0.932 (n = 16) where MIFS (pH7.4) values were calculated using the following equation:

MIFS = (MIFSi + MIFSm([H^+]/[*K*a])/(1+[H^+]/[*K*a]),

Where MIFSi is the MIFS value of the ionic form analyte, MIFSm is the MIFS value of the molecular form analyte, and H^+ is hydrogenion concentration at pH7.4.The dissociation constants (p*K*a) are the values measured by ion-exchange liquid chromatography [73].

The above-mentioned approach used two columns (reversed-phase and ion-exchange). The hexyl-guanidino column is weakly hydrophobic; therefore, the log k values measured using the hexyl-guanidino-bonded silica gel column were correlated with the log K values. The following results were obtained for acidic drugs: log *nK* = 1.864 log*k* (mes.pH7.4) + 5.807, *r* = 0.862 (n = 15).Furthermore, the calculated log *k* (pH7.4) and MIFS (pH7.4) were related to acidic drugs log *nK* values.

log.n*K* = 2.248 log *k*(calc. pH7.4) + 4.397, *r* = 0.896, n = 14

log n*K* = 0.0814 FS_(pH7.4) - 4.742, *r* = 0.868, n = l5,

These correlation coefficients were lower than those obtained using a two-column system previously, but the reproducibility was higher than the reference value [72].

The *in silico* analysis of the retention mechanisms in reversed-phase liquid chromatography was relatively simple. The major retention force was the MIVW between a analyte and a model reversed-phase, and the major desorption force was MIHB (MeOH) between the analyte and the model methanol phase. The combination of MIVW and MIHB (MeOH) led to a high correlation coefficient (r = 0.950, n = 2020) in the chromatographic analysis of basic compounds using pentyl- and octyl-bonded silica gels [74]. These results confirmed that the retention mechanisms in reversed-phase liquid chromatography involve a combination of hydrophobic retention, hydrogen bonding and desorption.

However, quantitatively explaining retention mechanisms in ion-exchange liquid chromatography is complicated because it requires additional ionic contributions from both the ion exchanger and the eluent. In anion-exchange liquid chromatography, MIFS, MIHB, MIE, and MIVW could not explain the retention. Retention of acidic drags is in a pH 3.0 eluent. Neither solvation nor phosphate ions in the eluent provided a clear answer. However, the MI values between the analytes and the ion exchanger, and between the analytes and phosphate ions in the eluent, clearly described the retention mechanisms in anion-exchange liquid chromatography. These results indicated direct interaction between analytes and ion-exchange groups, and desorption due to replacement of acidic drugs with phosphate ions. At pH 9.0, both the acidic drugs and the ion exchanger are ionized, and retention is attributed to competition.

The hexylguanidine-bonded silica gel has two possible interaction sites: HB (hydrogen bonding) and ES (ion-ion interaction) sites; therefore, the contribution of HB and ES interactions varies with compound type. The retention time was quantitatively explained by combining analyte adsorption on the guanidino-phase and analyte desorption by replacement with phosphate ions. Furthermore, measuring the retention time at pH 7.4 is a simple analytical method to measure 0human serum albumin-drug binding affinity. Further improvement in the design of the ion-exchangers improves its precision. The MM2 software developed for protein analysis demonstrated strong ion-ion interactions and could not be used *in silico* analysis of ion-exchange liquid chromatography. Therefore, further development of the MM2 software also helps in handling new model phases.

7.5. Chromatography of saccharides

Saccharides are a key component of living organisms. Glucose is an energy source and a fundamental molecule to synthesize various molecules. Other saccharides are key components used to synthesize molecules ranging from small to large, such as DNA and glycoproteins. Molecular size varies from monomers to polymers. Here, we describe the fundamental structure-related molecular interactions.

Glycosylation occurs in the initial step of the Maillard reaction between proteins and saccharides. Glycosylation occurs non-enzymatically at lysine ε-amino groups and other amino groups. The reaction with glucose produces the smell and taste of food, and the brown color of pancakes is one example. Glucose, an energy saccharide, is a precursor of various enzymatic products. Natural saccharide structures look similar but are not the same; therefore, these saccharides are targets for chromatographic separation. First, saccharides were separated as borate complexes in ion-exchange liquid chromatography [**75**]. The retention mechanism is attributed to hydrogen bonding between the saccharide and the ion exchanger's borate. Later, saccharides were separated in high concentrated ethanol solution [**76**]. The latter method is considered the first hydrophilic interaction liquid chromatography. The retention mechanism is also hydrogen bonding between saccharides and ion-exchange groups. Later, propylamine-bonded silica gel was replaced with ion-exchange resins, using aqueous acetonitrile as the eluent.

However, glucose glycosylation is easy, and glucose recovery is not quantitative; therefore, amino silica gels are replaced with amide silica gels. Ion-exchange resins are also used for saccharide separation, and poly-, oligo-, and monosaccharides can be separated simultaneously using combination columns [**61**]. Saccharide recovery was improved by synthesizing a guanidine phase from an amino phase [**62**]. The guanidino group is part of arginine and an important ion-exchange group in proteins. Column stability improves when the propyl ligand is replaced with a hexyl ligand [**78**]. Figures 7.36 and 37 show models of hexylamino- and hexylguanidino-bonded silica gels with mannose retention. Red (black), blue (dark gray), yellow (light gray), large white, and small white atoms represent oxygen, nitrogen, carbon, silicon, and hydrogen, respectively. The atomic size of β-mannose is 100%, and the others are 20%.

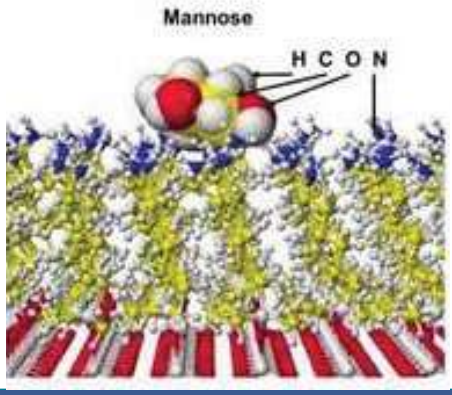


FIgure 7.36: Retention of mannose on a hexylamino-phase.

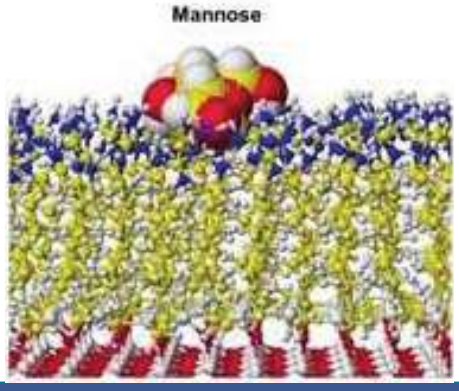


FIgure 7.37: Retention of mannose on a hexylguanidino-phase.

The structure of the mono-saccharide skeleton is like cyclohexane, whose one carbon is replaced with oxygen. The other replacement of hydrogen to hydroxyl group at the specific location produces various mono-saccharides, and their structure similarity puzzles the optimization of their separation condition. The most retention of the monosaccharide separation condition is complex due to their structural similarity. The most retentive saccharides contact via the many hydroxyl groups with the primary amino and quarternal amino groups. The correlation coefficient of monosaccharide retention time and the calculated MIHB, MIES, and MIVW energy values were 0.853, 0.356, and 0.035 (n = 9), The *r* value supported the hydrogen bonding is the primary interaction.

A glycoside forms instantly when glucose contacts a primary amine; then the Amadori rearrangement converts it to the Amadori compound, which produces superoxide in vivo. The Amadori rearrangement does not occur for mannose that produces mannoside. The chemical structures are complex, and four types of structures (αC1, α1C, βC1, β1C) should be considered; however, the database does not include these structures. Constructing these structures helps determine the NMR spectra using the spectrum prediction program. Converting an amine conjugated with a 1C carbon from β the β to the α-form is simple. Select the 1C carbon circle in Figure 7.38, and select invert chiral in a pull-down menu. This gives the α-form structure shown in Figure 7.38.

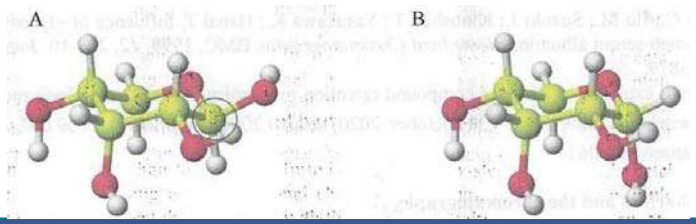


FIgure 7.38: Conversion of β-ribopyranose to α-ribopyranose.

Converting from chair to boat form requires a multi-step process. A catalyst helps the conversion in organic synthesis. Drawing a new molecule using a computational chemistry program is simple; use the methylene group to connect the 4th carbon to the 1st carbon hydroxyl-group oxygen, as shown in Figure 39B. Optimizing the structure in Figure 39B using the MM2 program produces structure 39C. We then removed the methylene (39D) and optimized it to produce the boat-type structure 39E.

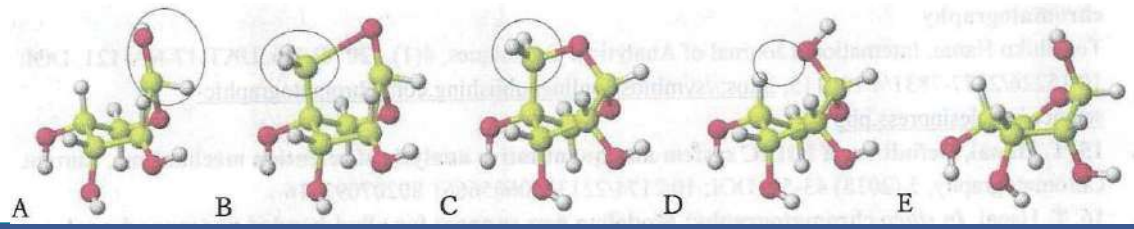


FIgure 7.39: Conversion of chair type β-ribopyranose to boat type β-ribopyranose.

Glycosylation may cause α- and β-conversion. Therefore, identifying chemical structures is challenging. High-resolution NMR and structure-prediction programs do not provide definitive answers. Therefore, constructing a possible structure and calculating the optimized energy supports estimating the measured spectrum, and computational chemical analysis also helps determine the components separated using chromatography.

7.6. Quantitative *in silico* analysis of reversed-phase ion-pair chromatography

Reversed-phase ion-pair liquid chromatography separates relatively polar compounds by forming ion pairs with relatively hydrophobic ions. The retention mechanism is like dynamic ion-exchange liquid chromatography. Hydrophobic ions first coat the surface of the hydrophobic phase and remain there. The technique is used to analyze amino acids with varying polarity, and separation requires a dynamic gradient elution; however, adding a relatively hydrophobic ion-pair reagent reduces the dynamic gradient range and shortens the separation time for ion-pair analytes.

7.6.1. Ion-pair liquid chromatography of free amino acid-copper complex: Free amino acids retain on a hydrophobic surface s the hydrophobic paired ion with hydrophobic ion-pair reagent. They also retain on a hydrophobic surface as the copper complexes in reversed-phase mode liquid chromatography. Further, the retention of the amino

acid-copper complexes is enhanced by ion-pair formation with hydrophobic ion-pair reagent[**79**]. In silico analysis quantitatively explains the retention mechanisms.

Copper forms a complex with three free amino acids. A complex structure of glycine-copper complex is shown in Figure 7.40. The positively charged amino group of an amino acid can form an ion pair with alkyl sulfate. Figure 7.41 shows the structure. The paired glycine-copper complex with three hexyl sulfate ions, shown in Figure 7.42, was docked with a dimethylhexylsilane-bonded silica gel, and molecular interaction energy values were calculated. Figure 7.43 shows the docked structure. The calculated the properties of free amino acid-copper complex and the paired ion with hexane-sulfate ion are summarized in Table 7.11.

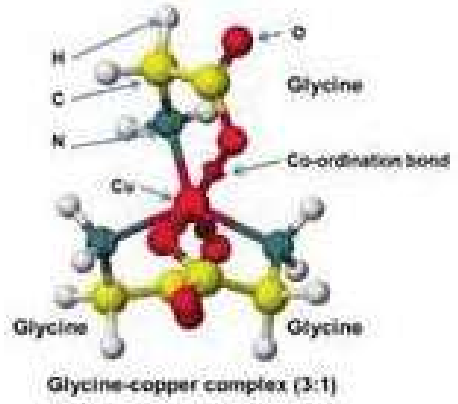


FIgure 7.40: Structure of glycine-copper complex.

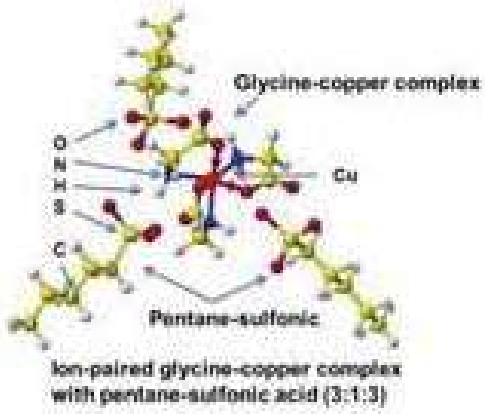


FIgure 7.41: Structure of ion-pair glycine-copper complex with pentane-sulfonic acid (3:1:3).

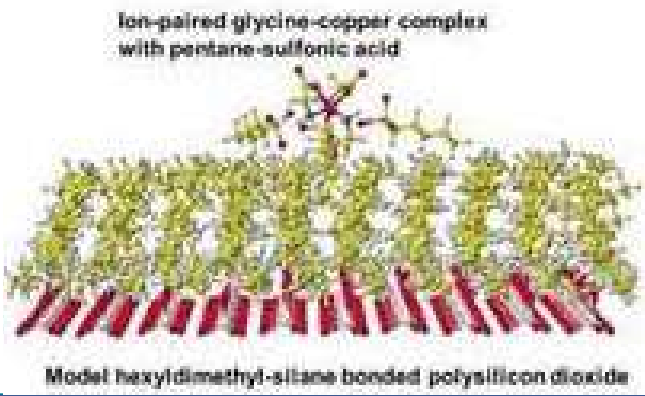


FIgure 7.42: Retention of ion-paired glycine-copper complex with pentane-sulfonic acid on a hexyl-phase.

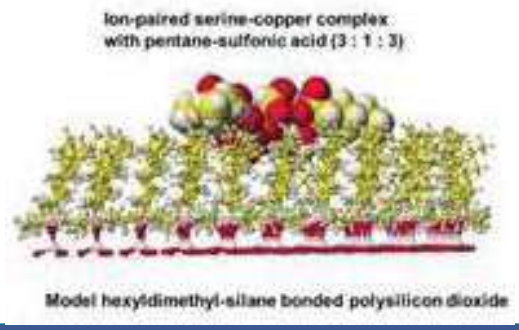


FIgure 7.43: Retention of ion-paired serine-copper complex with pentane-sulfonic acid on a hexyl-phase.

Table 7.11: Properties of free amino acid-copper complex and the paired ion with hexane-sulfate ion.

Compound	hb	es	vw	MIHB	MIES	MIVW
Glycine						
Glycine-copper complex	0	-172.406	-3.215			
Hexane sulfate ion	0	0	2.123			
Glycine-copper complex with hexane sulfate ion	0	-114.899	2.25			
Complex of paired ion of glycine C6-phase	0	-194.074	-5.1	0	-1.485	41.626
C6-phase	0	-250.732	-637.081			
Serine						
Serine-copper complex	-0.009	-123.749	-3.047			
Serine-copper complex with hexane sulfate ion	-6.231	-51.741	2.623			
Complex of paired ion of serine with C6-phase	-4.762	-146.255	-4.644	-0.215	-4.504	47.662

Increasing hydrophobicity of the ion-pair reagent and concentration enhanced retention. Amino acids range from very polar acidic amino acids to hydrophobic aromatic amino acids; however, the polarity range is narrowed in this system, permitting isocratic elution separation [79]. That is, the addition of hydrophobic ion-pair reagent in the eluent of reversed-phase liquid chromatography of polar compounds enhanced the retention time and made easier handling separation system—however, a drawback is the difficulty of removing ion-pair reagent from the efficient to recovery sample compounds.

7.6.2. Ion-pair liquid chromatography of Phenylthiohydantoin-amino acids: Quantitative in silico analysis of retention mechanisms in reversed-phase ion-pair liquid chromatography remains incomplete because the stationary phase structure is complex and the solid is coated with mobile-phase components. On the other hand, fast chromatographic analysis of amino acids is also of fundamentally importance. First, free amino acids were separated using ion-exchange liquid chromatography, followed by reversed-phase ion-pair liquid chromatography [80]. Furthermore, analysis of phenylthiohydantoin (PTH)-amino acids is an important process in protein chemistry. The chromatographic method was studied using reversed-phase ion-pair liquid chromatography [**81**]. The chromatographic data were used to study the retention mechanisms in reversed-phase ion-pair liquid chromatography via molecular mechanics calculations with model phases.

Generally, the retention of hydrophobic compounds, including acidic and basic drugs, is quantitatively related to MI energy values calculated using the MM2 program. Particularly, van der Waals energy values indicate hydrophobic interactions. First, we used a model pentyl-bonded silica gel phase to study the retention mechanisms of PTH-amino acids in reversed-phase ion-pair liquid chromatography; however, we deformed the model pentyl groups after optimization using MM2 calculations. Therefore, we used a model octyl-bonded silica gel phase to obtain the MI energy values (data are not provided here).

The hydrophobic MI energy values obtained using the model octyl-bonded silica gel phase were related to the log k values of 19 PTH-amino acids and the following equation was obtained:

MIVW = 3.630 log k + 25.253, r = 0.496, n = 19,

MIVW denotes the MI values of van der Waals energy calculated between the model octyl-bonded silica gel phase and the PTH-amino acids.

The correlation coefficient was less satisfactory than results previously obtained for aromatic acids, phenolic compounds, acidic drugs, and basic drugs [1]. We performed further studies to understand the solvent effects on these phenolic compounds. We used the same model acetonitrile phase as for phenolic compounds [82]. We obtained the solvent effects as MI energy values between the model acetonitrile phase and the PTH-amino acids. The calculated MI energy values are summarized in Table 7.12. We used the MI of hydrogen bonding and electrostatic energy values as the solvent effect, as for phenolic compounds. The calculated MI(HB + ES)a values were combined with the above results: y_2 = -2.855 log k + 9.346, r = 0.707, n = 19, where y is a combination of MIHBa and MIESa, calculated as the solvent effects using the acetonitrile phase:

MIVW + MI(HB + ES)a = -9.591 log k + 3.586, n = 19, (2),

Where MI(HB + ES)a represents the combined MI values of the hydrogen-bonding and electrostatic energies calculated between the model acetonitrile phase and the PTH-amino acids; Figure 7.44 shows an example of the complex conformation of PTH-alanine in the acetonitrile phase.

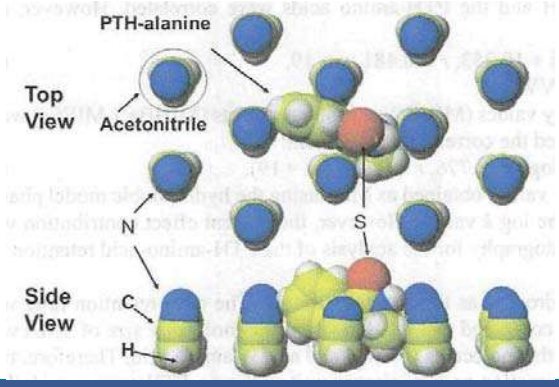


Figure 7.44: PTH-alanine in acetonitrile phase, blue (black), red(dark gray), yellow(carbon), and white balls are nitrogen, sulfer, carbon, and hydrogen atoms.

The above results indicated that further improvement of the correlation coefficient was necessary. Therefore, we constructed a model TBA phase and calculated the MI energy values of the PTH-amino acids. TBA is an ion-pair eluent and plays an important role in reversed-phase ion-pair liquid chromatography of PTH-amino acids. PTH-amino acids are generally not ionized; however, TBA may contribute to charge-transfer-like interactions. The hydrophobic alkyl groups of TBA coat the surface of the hydrophobic bonded phase. Therefore, we constructed a flat sheet of TBA using six TBA ions and calculated the MI energy values between the TBA phase and the PTH-amino acids. The MI energy values between the TBA phase and the PTH-amino acids showed the following correlation, where y is the MIVW value calculated between the model TBA phase and the PTH-amino acids. We further studied the effect of solvent by incorporating solvent effects into the calculation.

Adding the MI (HB + ES)a value to the MIVW values in equation 3 improved the correlation coefficient to 0.895: y = 5.771 log k + 2.724, r = 0.895, n = 19.

Further study was needed to obtain a better correlation coefficient. MI energy values calculated using a single TBA molecule and PTH-amino acids showed a very poor correlation coefficient (r = 0.118; n = 19). We further studied charge-transfer interactions between TBA hydroxide (OH) and PTH-amino acids. Initially, we studied the best complex structure of a TBA-PTH and PTH-alanine complex. Figure 7.45A shows the initial positions of PTH-alanine and TBA-OH. After several trial optimizations, we obtained the most stable, lowest-energy complex structure, as shown in Figure 7.45B. We then placed other PTH-amino acids at similar positions about 8å from the OH group and optimized their complex structures. Table 7.12 summarizes the calculated energy values of the complexes and the molecular properties of the PTH-amino acids. These values indicate that interactions between the OH groups and the aromatic rings of the PTH-amino acids are the primary molecular interactions in this chromatographic technique. Such interactions are called charge-transfer Lewis acid-base interactions.

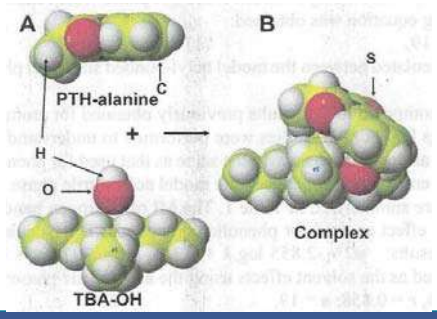


FIgure 7.45: Complex conformation of PTH-alanine with TBA-OH. Red (black), orange (dark gray), yellow (light gray), and white balls are oxygen, sulfur, carbon, and hydrogen atoms.

MI energy values between a model TBA-OH and the PTH-amino acids were correlated. However, the correlation coefficient was still not satisfactory:

$y_1 = 1.222 \log k + 10.253$, $r = 0.481$, n = 19, where y_1 is the MIVW.

Then, the above hydrophobic interaction energy values (MIVW) and solvent effects (MIHBa + MIESa) were combined. The combined MI energy values improved the correlation coefficient:

$y = y_1 + 0.8\, y_2 = 3.506 \log k + 2.776$, $r = 0.977$, n = 19.

Generally, the hydrophobic interaction energy values obtained as MIVW using the hydrophobic model phases mainly contributed to the quantitative analysis of the log *k* values. However, the solvent effect contribution was significant in reversed-phase ion-pair liquid chromatography for the analysis of the PTH-amino acid retention as shown in Figure 7.46.

The properties of TMA hydroxide was further studied as the ion-pair reagent. The total retention time was shorter because TMA is less hydrophobic than TBA. However, TMA's small size did not allow complete interaction between TMA and a PTH-amino acid. The optimized structure of two TMAOHs, determined using the MM2 program, is shown in Figure 7.46A. The TMA-OH pair then formed an ion pair with PTH-alanine. Table 7.12 summarizes the calculated values. Figure 7.46 B shows the structure.

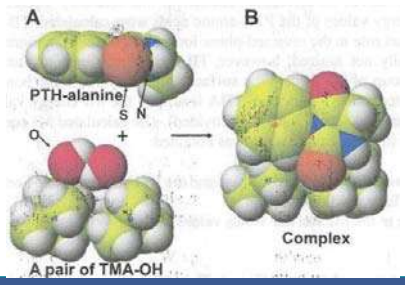


FIgure 7.46: Complex conformation of PTH-alanine with TBA-OH. Red (black), orange (dark gray), yellow (light gray), and white balls: oxygen, sulfer, carbon, and hydrogen.

The calculated MIVW values were related to the log *k* values of the PTH-amino acids. The correlation coefficient was 0.379 (n = 19). The correlation improved with the addition of the previously obtained solvent effects MI(HB + ES)a; the value was 0.979. A similar relationship was obtained, as shown in Figure 7.47.

The hydrophobic interaction between PTH-amino acids and a model octyl-bonded silica gel phase, TBA-OH or TMA-OH, did not significantly correlate with PTH-amino acid retention in reversed-phase ion-pair liquid chromatography. However, the MIs between the acetonitrile phase and the PTH-amino acids played an important role in quantitatively explaining retention in reversed-phase ion-pair liquid chromatography of the PTH-amino acids. The solvent effect contributed more than in reversed-phase liquid chromatography of phenolic compounds.

This chromatography was carried out using an eluent containing an ion-pair reagent. PTH-amino acids were not ionized except arginine, aspartic acid, glutamic acid, and histidine, depending on the eluent pH. However, the ion-pair reagent contributed significantly, resulting in fast, isocratic elution. The ion-pair reagent should be coated on the

hydrophobic phase surface. Therefore, the Lewis acid-base interaction between an OH group of the ion-pair reagent and an aromatic ring of PTH-amino acids was considered the main interaction.

Further study was carried out on the reversed-phase ion-pair liquid chromatography of free amino acids, in which the free amino acids formed ion-pairs with dodecyl sulfate ions. The chromatograph used was a homemade octadecyl-bonded silica gel column with an eluent containing 50 mM sodium-phosphate solution (pH 2.7), 25.6 mM sodium dodecyl sulfate, and 16% methanol at 45 °C. Free amino acids are polar compounds; therefore, they did not show a good correlation between log k values and MIVW values, as calculated with a model hydrophobic phase [**1**]. Even the paired ions of the free amino acids and the dodecyl sulfate ions did not demonstrate a meaningful correlation coefficient. The correlation coefficient was close to zero, and the slope was flat. The correlation improved to 0.935 with the addition of solvent effects (MIHB + MIES)m, where HBm and ESm indicate the hydrogen-bonding and electrostatic energy values calculated in a model methanol phase, similar to the model acetonitrile phase.

The retention mechanisms of PTH-amino acids in reversed-phase ion-pair liquid chromatography were quantitatively analyzed in silico. The most significant interaction driving retention was the Lewis acid-base interaction between the aromatic ring of a PTH-amino acid and the hydroxyl-group hydrogen of tetra-alkyl ammonium hydroxide. Solvent effects significantly improved the relationship between molecular interaction energy values calculated using a molecular mechanics program and log *k* values measured *via* chromatography. The correlation coefficient between the calculated molecular interaction energy values and the log *k* values was 0.98 (n = 19).

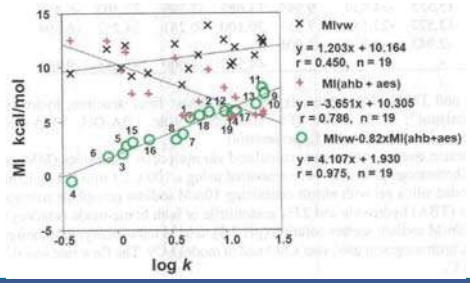


FIgure 7.47: Relation between calculated molecular interaction (MI) energy values (kcal mol-1) and measured log k values. Numbers beside symbols: see Table 7.12.

Table 7.12: Molecular properties of PTH-amino acids.

No.	Chemicals	log k_1	fs	hb	es	vw	TBAFS	TBAHB	TBAES	TBAVW
1	Alanine	0.671	-3.169	-0.282	-17.459	10.507	3.256	-8.028	-19.358	11.947
2	Arginine	0.851	-20.085	-0.293	-39.357	13.099	-16.567	-8.109	-40.458	10.589
3	Asparagine	0.053	-23.194	-3.589	-38.574	11.002	-16.805	-11.398	-40.557	12.422
4	Aspartic acid	-0.412	-5.849	-0.282	-21.665	10.837	0.579	-8.01	-23.966	12.66
5	Glutamine	0.091	-20.64	-3.289	-35.529	11.158	-16.848	-11.045	-37.833	10.493
6	Glutamic acid	-0.079	-2.284	-0.281	-17.325	11.089	1.571	-8.038	-19.854	10.706
7	Glycine	0.612	-4.639	-0.283	-17.459	10.441	2.766	-8.062	-19.811	13.383
8	Histidine	0.544	7.152	-1.061	-19.803	9.364	11.936	-9.066	-21.341	8.551
9	Isoleucine	1.359	0.994	-0.279	-17.519	12.259	4.887	-8.019	-19.391	11.191
10	Leucine	1.359	-0.5	-0.281	-17.476	11.469	3.672	-8.017	-19.343	10.602
11	Lysine	1.339	-0.668	-0.284	-17.42	11.469	3.672	-8.017	-19.343	10.029
12	Met4hionine	1.281	-11.725	-0.994	-17.754	12.807	-6.591	-8.779	-19.843	13.051
13	Phenylalanine	1.281	-11.725	-0.994	-18.011	12.807	-6.591	-8.779	-19.843	13.051
14	Proline	1.077	15.035	0	-17.229	14.448	20.727	-7.767	-19.129	15.341
15	Serine	0.145	-2.361	-0.5	-17.62	10.553	3.972	-8.216	-19.497	12.638
16	Threonine	0.3	-0.035	-0.562	-17.422	11.434	6.592	-8.296	-193451	13.266
17	Tryptophan	1.094	-6.646	-1.442	-18.698	10.98	-3.207	-9.597	-212.098	10.486
18	Tyrosine	0.763	-13.894	-2.46	-17.998	12.742	-8.742	-10.343	-10.821	12.935
19	Valine	1.059	-1.327	-0.281	-17.476	10.771	6.736	-7.358	-19.214	12.012

TBA-OH	-	22.59	0	-2.881	11.247	-	-	-	-	
No Chemicals	log k_2	TMAFS	TMAHB	TMAES	TMAVW	FSa	HBa	ESa	VWa	
1	Alanine	0.558	-22.823	-13.1	-24.248	8.009	28.296	-0.282	24.091	-6.401
2	Arginine	0.811	-41.574	-12.949	-45.861	8.51	5.929	-0.597	-1.733	-5.454
3	Asparagine	0.074	-14.224	-16.175	-46.01	7.62	3.446	-3.627	-1.503	-7.104
4	Aspartic acid	-0.632	-27.035	-13.345	-29.363	7.642	17.839	-0.282	12.922	-5.651
5	Glutamine	0.162	-42.218	-16.53	-43.142	7.743	3.505	-3.034	-0.114	-6.792
6	Glutamic acid	-0.215	-24.299	-13.282	-25.39	7.42	22.698	-0.281	17.352	-6.377
7	glycine	0.35	-24.651	-13.301	-24.531	7.975	27.818	-0.283	24.079	-5.427
8	Histidine	0.234	-14.426	-13.517	-27.62	5.615	33.302	-1.044	16.47	-7.709
9	Isoleucine	1.311	-21.521	-13.154	-26.01	8.582	30.512	-0.279	23.653	-6.084
10	Leucine	1.355	-21.354	-14.023	-23.175	7.418	30.031	-0.281	23.912	-6.269
11	Lysine	1.26	-21.577	-13.016	-24.392	7.721	30.01	-0.284	24.104	-6.139
12	Methionine	0.988	-24.067	-13.372	-25.045	6.848	25.445	-0.292	21.23	-7.81
13	Phenylalanine	1.206	-32.706	-13.741	-25.171	9.27	17.046	-0.896	23.417	-6.793
14	Proline	0.993	-3.307	-12.848	-24.351	11.494	46.097	0	24.374	-2.94
15	Serine	0.162	-23.119	-13.439	-24.418	7.774	28.41	-0.57	21.912	-6.183
16	Threonine`	0.162	-19.996	-13.617	-34.192	8.856	27.582	-0.69	22.088	-6.487
17	Tryptophan	1.079	29.307	-14.776	-26.452	6.942	20.11	-1.767	21.514	-9.261
18	Tyrosine	0.671	-34.294	-15.355	-24.929	9.949	13.685	-2.309	22.107	-6.858
19	Valine	0.993	-221.379	-13.527	-23.582	7.563	30.1	-0.281	24.252	-6.594
TMA-OH	-	-3.663	-2.943	-6.239	3.006	-	-	-	-	
ACN phase	-	-	-	-	-	44.57	0	47.055	-9.1	

logk_1 and logk_2: measured in TBA-OH and TMA-OH systems; fs, hb, es, vw: final structure, hydrogen bonding, electrostatic, and van der Waals energy values kcal mol^{-1}; TBA, TMA, (FS, HB, ES, VW)a: TBA-OH, TMA-OH acetonitrile phase with PTH amino acid complexes, kcal mon^{-1}; Experimental: Molecular modeling and molecular interaction energy values were calculated via molecular mechanics (MM) of CAChe™ program from Fujitsu, Tokyo. Chromatographic data are measured using a 100 x 2.1 mm ID column packed with homemade phenylhexyl-bonded silica gel with eluent containing 10mM sodium phosphate solution (pH 7.35), 0.001M tetrabutylammonium (TBA) hydroxide with 25% acetonitrile or with homemade octadecyl-bonded silica gel with eluent containing 10 mM sodium phosphate solution (pH 7.35), 0.001 M tetrabutylammonium (TBA) hydroxide and 25% acetonitrile or with homemade octadecyl bonded silica gel with eluent containing 10 mM sodium acetate solution (pH 7.3) 0.01M tetramethylammonium (TMA) hydroxide, and 30% acetonitrile. Chromatograph used was a Shimadzu model LC9. The flow rate was 0.2 mL min at 40°C.

The chromatographic behaviors of both free and derivatized amino acids in reversed-phase ion-pair liquid chromatography were the same. Amino acids formed ion pairs with hydrophobic counterions and were retained in the hydrophobic phase. The hydrophobic ions played a crucial role in retaining analytes that were not ionized in the system. The hydrophobic compounds contributed to MIVW, but solvent effects provided the main contribution, as calculated from both the model acetonitrile and metal phases. A combination of MIs between the hydrophobic ions and the PTH-amino acids, and the solvent effects, correlated well with the log k values, measured using the reversed-phase ion-pair liquid chromatography system. If we can predict solubility, we can develop a method to predict retention time.

7.6.3 Nitrobenzofurazan-amino acids in reversed-phase ion-pair liquid chromatography: A sensitive chromatographic analysis of amino acids is a fundamental requirement in biochemical studies. 4-Fluoro (chloro)-7-nitro-2,1,3-benzoxadiazole (NBD) was developed as a highly sensitive and easy-to-use reagent [**83**]. Based on computational chemical analysis, NBD produces highly sensitive derivatized amino acids. The absorption wavelength was relatively high, and the absorption intensity was relatively strong for various derivatizing reagents **[84]**. We used NBD for enantiomer analysis because it reacts with primary and secondary amino acids under mild conditions and generates stable derivatives with relatively long emission and excitation wavelengths. We evaluated chromatographic behavior using reversed-phase ion-pair liquid chromatography. We used the chromatographic data to study retention mechanisms in reversed-phase ion-pair liquid chromatography.

First, we studied the best complex structure of the TBVA-OH and NBD-alanine complex. After several optimization trials, we obtained the most stable, lowest-energy complex structure, as shown in Figure 7.48. We then placed other NBD-amino acids at similar positions above the OH group (> 8 Å) and optimized their complex structures.

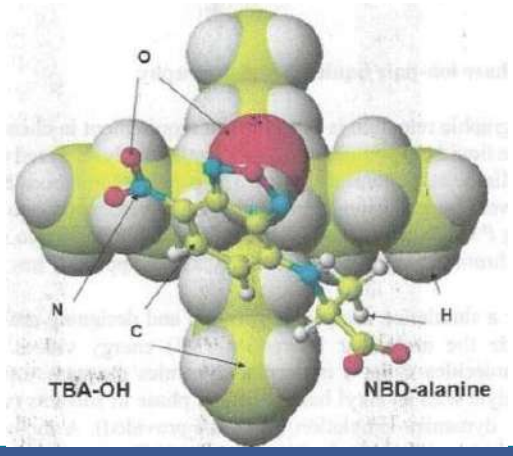


FIgure 7.48: Complex conformation of NBD-alanine with TBA-OH. Red (black), blue (dark gray), yellow (light gray) and white balls: oxygen, nitrogen, carbon, and hydrogen atoms.

Table 7.13 summarizes the calculated energy values of the complexes and the molecular properties of the NBD-amino acids. These values indicate that the interaction between the OH group and the aromatic ring of NBD-amino acids is the basic MI in this chromatography. Such interactions include charge-transfer and Lewis acid-base interactions. We correlated MI-energy values between a model TBA-OH and the NBD-amino acids; however, the correlation coefficient was very poor, and we obtained the following correlation.

MIVW = 0.486 log k_1 + 8.201, r = 0.27, n = 16, where MIVW is the MI van der Waals energy value calculated between the model TBA phase and the NBD-amino acids.

Further study was carried out by incorporating the solvent effect. The model acetonitrile phase was the same as that used for PTH-amino acids. We obtained the solvent effects as MI energy values between the model acetonitrile phase and the NBD-amino acids. The complex conformation with NBD-alanine is shown in Figure 7.49. We used the MI of hydrogen bonding and electrostatic energy values as the solvent effect of acetonitrile, a polar solvent. We correlated the calculated MIESa and MI(HB + ES)a values with log k_1 values.

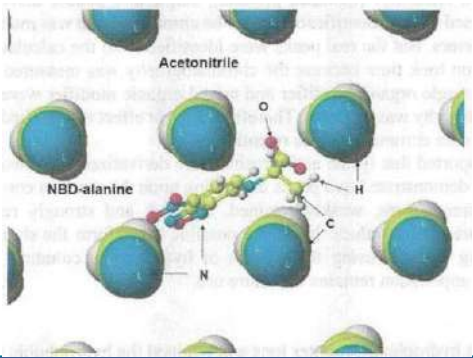


FIgure 7.49: NBD-alanine in acetonitrile phase, Red (black), blue (dark gray), yellow (right gray), and white balls: oxygen, nitrogen, carbon, And hydrogen

MIESa = -2.597 log k_1 + 123.863, r =0.658, n = 16,

MIHBa = -0.054 log k_1 + 0.128, r = 0.047, n = 16,

MI(HB + ES)a = -2.651 log k_1 + 12.863, r = 0.706, n = 16,

where MIESa and MIHBa are the MI electrostatic and hydrogen-bonding values calculated between the model acetonitrile phase and the NBD–amino acids. The MIHBa of serine was positive, but the MIHBa of other amino acids was close to zero. We then combined the hydrophobic interaction energy values (MIVW) with the solvent effects (MIHBa and MIESa).

Adding the MIESa value to the MIVW value improved the correlation coefficient to 0.958 {(MIVW – 0.72 MIESa) = 2.309 log k_1 – 1.045, n = 16}. But the combination of MIHBa did not improve the correlation. These values indicate that interactions between the OH groups and the aromatic rings of NBD-amino acids are the primary molecular interactions in this chromatography. These interactions include charge-transfer or Lewis acid-base interactions.

Generally, the hydrophobic interaction energy values obtained as MIVW using the hydrophobic model phases mainly contribute to the quantitative analysis of the log *k* values in reversed-phase liquid chromatography. However, the solvent-effect contribution was significant in reversed-phase ion-pair liquid chromatography for analyzing NBD-amino acid retention. We further studied relatively hydrophobic amino acids. Surprisingly, log k_2 values of hydrophobic NBD-amino acids demonstrated a quite high correlation coefficient with their MIVW. The correlation coefficient was 0.960 (n = 9).

The MI of hydrogen bonding and electrostatic energy values were used as the solvent effect. The calculated MIESa and MIHBa values were correlated with log k_2 values.

MIESa = 0.183 log k_2 + 9.645, r = 0.125, n = 9,

MIHBa = -0.739 log k_2 + 0.367, r - 0.734, n = 9,

MIESa + MIHBa = -0.556 log k_2 + 9.911, r = 0.338, n = 9.

These MIESa and MIHBa values were about the same, except MIHBa value of NBD-tyrosine. The combined MI energy value improved the correlation coefficient.

MIVW – 4.6 (MIESa + 5xMIHBa) = 7.140 log k_2 + 3.185, r = 0.989, n = 9.

The correlation between the calculated MI energy values and measured log *k* values improved when combining hydrophobic interaction energy values calculated using the TBA-OH model with hydrogen-bonding and electrostatic energy values calculated using the acetonitrile phase model. However, solvent effects were significant for the relatively polar NBD-amino acids. The results supported that polar compounds form hydrogen-bonding and electrostatic interactions under solvated conditions, while non-polar compounds form hydrophobic interactions in the solvent.

Hydrophobic interactions between the NBD-amino acids and the model TBA-OH did not significantly correlate with NBD-amino acid retention in reversed-phase ion-pair liquid chromatography. However, the MI between the acetonitrile phase and the NBD-amino acids played an important role in quantitatively explaining NBD-amino acid retention in reversed-phase ion-pair liquid chromatography, especially for relatively polar NBD-amino acids. Solvent effects contributed more than in general reversed-phase liquid chromatography.

This chromatography was carried out using an eluent containing an ion-pair reagent, which contributed significantly and enabled fast, isocratic elution. The ion-pair reagent should be coated on the hydrophobic phase surface. Therefore, the Lewis acid-base interaction between an OH group of the ion-pair reagent and an aromatic ring of an NBD-amino acid was considered the main interaction site.

Derivatization of amino acids with the NBD reagent produced compounds that appeared as peaks with different retention times, including the solvent peak, NBD-OH (oxidized product), and singly- and doubly-derivatized compounds. These chromatographic peaks complicated identification, even though we monitored the chromatograph using both UV-absorption and fluorescence detectors. However, we identified the true peaks using the calculated MI energy values. Chromatographic identification took time because we measured the chromatography under several conditions (data not shown). We used a single organic modifier and a mixed organic modifier; however, the elution order was similar, but the selectivity differed. Therefore, we studied the solvent effect using acetonitrile to assess its contribution to chromatographic retention.

In addition, the calculated MI energy values suggested that lysine and tyrosine were derivatized with two NBD reagents, and cysteine existed as a dimer. Lysine demonstrated two peaks depending on the reaction condition. The NBD-amino acids were classified into three groups, weakly retained, retained, and strongly retained compounds, by calculation MI values and measuring retention times using three types of hydrophobic columns, which succeeded for catechol amines [85]. The practical application remains for future use.

Derivatized amino acids formed ion pairs with hydrophobic counter ions and were retained on the hydrophobic phase. The hydrophobic ions played a crucial role in analyte retention. The hydrophobic compounds contributed to MIVW, but the main contribution came from solvent effects, as calculated from the model acetonitrile phase. A combination of MIs between hydrophobic ions and NBD-amino acids and solvent effects correlated well with the log k values measured by reversed-phase ion-pair liquid chromatography. If we can predict solubility, we can develop a method to predict retention time.

Computational chemical analysis of quantitative molecular interactions has been applied to different types of chromatography, such as ion-exchange separations, enantiomer separations, affinity separations, and chromatography detection mechanisms [1,22]. However, simple model studies indicate that current computational chemical calculation programs are far from perfect. These results will help improve the precision of such programs because chromatographic measurements of molecular interactions are highly reproducible. Precision should improve if quantitative solubility prediction becomes available.

We quantitatively analyzed the retention mechanisms of nitrobenzofurazan (NBD)-amino acids in reversed-phase ion-pair liquid chromatography in silico. The most important retention interaction is the Lewis acid-base interaction between the aromatic ring of NBD-amino acids and the hydroxyl-group hydrogen of tetrabutylammonium hydroxide coated on the hydrophobic phase. Solvent effects significantly improved the relationship between the calculated molecular interaction energy values from a molecular mechanics program and the log k values measured by chromatography. The correlation coefficient between the calculated molecular interaction energy values and the log *k* values was > 0.95.

Table 7.13: Properties of NBD-amino acids and the complexes with TBA-OH and acetonitrile phase

Amino acid	log k_1	log k_2	hs	hb	es	vw			
Gly	0.375	–	20.5852	0	20.137	5.183			
Ala	0.494	-	33.2427	-0.702	-29.464	5.44			
Arg	-0.146	-	5.8362	-0.055	-1.956	8.184			
Asp	-0.394	-	18.4126	-0.703	12.365	6.278			
Asn	0.129	-	-2.1193	-3.694	-6.678	5.775			
Cys-cys	-	1.135	26.5192	0	27.082	11.583			
Glu	0.001	-	23.7394	0	20.45	6.583			
Gln	0.091	-	4.2526	-3.016	1.133	6.691			
His	0.299	-	38.8507	-1.656	24.998	3.81			
Ile	1.347	0.292	24.9834	0	19.705	6.942			
Leu	1.374	0.292	26.515	0	19.912	7.284			
Lyn	1.123	-	24.1584	0	18.882	7.295			
Lyn*	-	0.7	23.8133	0	19.528	11.476			
Met	1.12	0.143	21.1342	0	19.932	6.457			
Phe	-	0.525	12.824	0	17.532	8.002			
Pro	0.296	-	22.2837	0	9.159	8.105			
Ser	0.279	-	23.651	-0.075	20.218	6.577			
Thr	0.428	-	24.9108	-0.075	20.218	6.577			
Trp	-	0.589	17.4171	-0.54	16.86	5.695			
Val	1.007	0.031	26.0136	0	20.218	6.294			
TBA-OH	-	-	22.5912	0	-2.879	11.267			
ACN-phase	-	-	44.5698	0	47.055	9.1			
Amino acid	FS	HB	ES	VW	aFS	aHB	aES		aVW
Gly	30.8716	-4.273	17.087	8.591	48.413	0	55.866	-9.675	
Ala	41.5628	-8.437	26.972	9.687	62.2925	-0.704	67.043	-9.939	
Arg	8.895	-8.126	-5.953	8.843	28.6895	-0.071	44.799	-6.537	
Asp	25.6166	-8.298	9.864	8.959	44.2673	-0.701	44.799	-6.537	
Asn	5.6925	-11.29	-8.927	9.277	24.8197	-3.253	28.284	-9.777	

Cys-cys	32.8194	-1.079	24.262	7.051	51.6453	0	63.85	-11.215	
Glu	30.0662	-7.757	17.487	9.153	49.4968	0	53.316	-10.177	
Gln	10.7142	-10.751	-1.422	9.041	31.9069	-2.818	34.366	-9.113	
His	44.9542	-10.463	21.694	7.652	69.6302	-1.511	61.75	-10.616	
Ile	33.598	-7.697	18.105	9.64	56.7291	0	57.933	-8.796	
Leu	31.8764	-7.686	17.549	8.699	53.9666	0	57.054	-10.173	
Lyn	30.6202	-7.712	16.891	8.125	47.7835	0	52.695	-11.279	
Lyn*	33.145	-2.479	17.912	10.658	53.0524	0	56.28	-3.473	
Met	28.4921	-7.699	14.939	8.861	50.0865	0	44.829	-7.234	
Phe	16.0161	-7.965	14.939	7.45	50.0189	0	67.137	-12.073	
Pro	30.4481	-7.741	6.705	11.269	50.0865	0	44.829	-7.234	
Ser	33.0153	-7.794	15.389	10.942	51.7949	-2.438	58.543	-9.756	
Thr	33.0329	-7.732	18.102	10.028	53.3582	-0.108	56.373	-9.136	
Trp	20.7816	-7.417	13.531	4.876	53.5405	-0.539	66.642	-15.756	
Tyr*	4.2798	-9.901	12.045	6.067	30.9242	0	52.917	-10.834	
Val	33.3816	-7.721	17.983	9.121	55.7023	0	56.484	-8.075	

fs, hb, es, vw: final (optimized) structure, hydrogen bonding, electrostatic, van der Waals energy of NBD-amino acids; FS, HB, ES, VW: final (optimized) structure, hydrogen bonding, electrostatic, van der Waals energy of NBD-amino acids and TBA-OH complexes; aFS, aHB, aES, aVW: final (optimized) structure, hydrogen bonding, electrostatic, van der Waals energy of NBD-amino acids and ACN phase complexes; *: Two NBDs were conjugated. unit: kcal mol^{-1}

Molecular modeling and molecular interaction energy values were calculated using molecular mechanics (MM2) in the CAChe™ (SciGress™) program (Fujitsu, Tokyo). Chromatographic data for strongly hydrophobic NBD-amino acids were measured using a 50 × 2.1 mm i.d. column packed with homemade octyl-bonded silica gel, with an eluent containing 20 mM sodium phosphate solution (pH 7.35), 20 mM tetrabutylammonium (TBA) hydroxide, and 10% acetonitrile and 15% tetrahydrofuran. For weakly hydrophobic NBD-amino acids, we measured retention time using a 150 × 4.6 mm i.d. column packed with homemade octyl-bonded silica gel, with an eluent containing 20 mM sodium phosphate (pH 7.0), 20 mM TBA-OH, 10% acetonitrile, and 7% tetrahydrofuran. Chromatography was performed on a Shimadzu LC9.

7.7. Evaluation of column test methods to study inactivation of chemically bonded silica gels

Since their inception by Kirkland, octadecyl-silanized silica gels have been the main packing materials in liquid chromatography [**86**]. The introduction of pure silica gel improved the quality of bonded-phase silica gels [**87**], and various quality test methods have been proposed and discussed [**88**].The chromatographic behavior of high p*K*a bases helped identify the different characteristics of bonded-phase silica gels: Pyridine was found to be a more sensitive compound than aniline for silanol detection, and the peak shape was affected by the components of the eluent[**89**]. A column evaluation methodology was described for the chromatography of basic compounds, and it was found that chromatograms obtained using marketed columns varied for the compounds tested with different eluents [**90,91**]. Several columns were tested for reversed-phase liquid chromatography, and the physico-chemical interactions were qua1itative1y described, and the results suggested the necessity of individual characterization [**92**].A method for the selection of a column for the chromatographic separation of basic compounds was proposed **[**93]; however, a description of the fundamental properties of bonded phase silica gels was lacking. A significant amount of metallic impurities is generally present in ordinary silica gels and they severely affect the activity of free silanol groups. It was found that washing the gels with an acid significantly reduced the negative effects of metal impurities [**88,94**].Therefore; a specific column testis required for general use. –A new type of packing material was introduced for reversed-phase liquid chromatography; and the performance was evaluated by comparing it wi than ordinary octadecyl-bonded silica gel [**95**]. Further test methods to be developed to study its ong-term stability with good peak shape for a variety of compounds.

Generally, the inactivation process:·is necessary to obtain stable and reproducibl packing materials, especially'for basic compounds, wherein the nitrogen-containing groups can easily··form hydrogen bonding with the silanol groups of the gels. Typically, the short alkyl groups such as trirnethy1-silan, are bonded to the free silanol groups as secondary silylation, where as the larger ligands are in capable of completely covering the silanols because of 'the restriction in physical contact. The atomic distance between the silanol groups is usually greater (5.37 Å) than that between the chloro or alkoxyl groups of silylation reagents (3.43 and 3.01 A, respectively) [1]. Iron, calcium, aluminum, sodium,

and magnesium are the common trace metals found in silica gels:·with the source of the metals being the water used in sieving process. The careful management of the reaction processes produces chemically inert bonded-phases and ensures a symmetrical peak shape and, as well, over two months of operation for quality control analyses [**96**]. However, the quality of marketed packed columns is not uniform, and the manufacturer demonstrates gel quality using specific chromatograms. The column test compounds are classified into two groups: one set tests for unreacted silanol groups. In contrast, the other set evaluates silica gel purity, which can contain trace metal impurities.

However, an experimental demonstration is not straight forward; consequently, quantitative assessment is performed by *in silica* analysis using model phases. Previous studies have examined the effect of alkyl-chain length on bonded silica gels. It was observed that, up to the butyl chain length, the silica gel was affected by silicon oxide; therefore, the analysis supported the instability of the butyl-bonded phase silica gel. The *in situ* analysis demonstrated electron localization and atomic partial charge at the end carbon of the butyl group [97]. Thus, we applied a similar approach using model alkyl phases from methyl to octyl. The solutes used here are aniline, pyridine, amitriptyline, 8-quinolinol, quinizarin, and hinokiol.

Initially, aniline was used to detect silanol groups based on acid-base interactions. Subsequently, pyridine was used because of its smaller molecular size and higher sensitivity for detecting silanols. Silica gels with a purity of > 99.999% were introduced and are now the common support material for analytical columns, as they offer guaranteed chemical stability and produce symmetrical peak shapes. This evolution in packing materials supports long-term, reproducible quality control in liquid chromatography. Critical test methods have been proposed to improve the long-term operation of these materials further. Amitriptyline is a compound that demonstrated a poor peak shape from those columns tha had previously demonstrated an excellent peak in the case of pyridine. The molecular mass of amitriptyline is higher than that of pyridine. The question then arises whether amitriptyline can access the free silanol groups that pyridine could not access. Ideally, amitriptyline should not interact with the free silanol groups, but this may indicate poor surface coverage of the alkyl ligands.

8-Quinolinol, quinizarin, and 1,10-phenanthroline are chelating reagents used to detect trace metals. Chemically bonded silica gels from pure silica should not contain trace metals on their surface. However, above mentioned compounds exhibited a tailing peak shape. This may be due to trace metals from solvents, including water, that can contaminate the silica gel and remain on the surface of the bonded phases. Alternatively, the tailing peak shape may result from indirect interactions between the compounds and the silica gels, as shown by the alkyl-chain effect of butyl-bonded silica gels. We studied the latter case by *in situ silica* analysis using model bonded phases.

7.7.1. Experimental: A constructed model dimethyl-alkyl mono-chlorosilane bonded phase is shown in Figure 7.50. The silicon dioxide connection was replaced with silicon atoms, and silicon trioxide was locked as part of the silica gel; the model phase size was chosen to minimize calculation time and match the molecular size of the analytes. The alkyl groups produce a tightly condensed phase. In practice, researchers do not synthesize such bonded phases using porous silica gels; instead, they use them to analyze indirect interactions between an analyte and a model phase. The bonded alkyldimethylsilane was kept free to enable contact between the analyte and the alkyl groups. The methyl group was changed to ethyl and soon up to octyl to study the effects of alkyl chain length.

These molecular interaction (MI) energy values (kcal mol^{-1}) are the sum of solute and model-phase energy values minus the complex energy value, calculated as per the following equations [**1**]. MIHB, MIES, and MIVW are the MI energy values for hydrogen bonding (HB), electrostatic (ES), and van der Waals (VW) interactions.

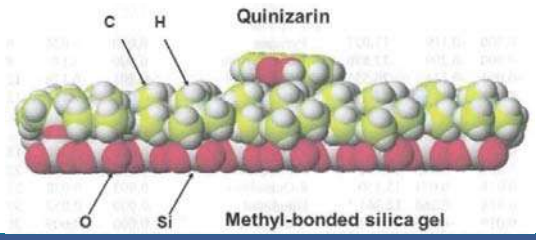


Figure 7.50: Adsorption of quinizarin on methyl-bonded silica gel phases.

MIHB = HB (molecule A) + HB (molecule B)-HB (molecule A and molecule B complex)

MIES = ES (molecule A)+ ES (molecule B) - ES (molecule A and molecule B complex),

and

MIVW·= VW (molecule A)+ VW (molecule B) -VW (molecule A and molecule B complex). The relative MIHB, MIES, and MIVW values indicate the contribt1tion level.

7.7.2. Results and discussion: The alkyl groups are condensed in the maximum-bonded phase to avoid free silanol groups. Therefore, all analytes can interact only with the alkyl groups, not the silanols. The analytes may indirectly contact silicon dioxide through the alkyl phase surface. If the alkyl phase is completely hydrophobic, molecular interactions between an analyte and the model phase should indicate MIVW, not MIHB and MIES [1].The properties of the standard eompounds are listed in Table 7.14.

Table 7.14: Properties of standard co1npounds.

Chemical		log *P*	p*Ka*
For silanol activity	Pyridine	0.7	5.23
	Amitriptyline	4.92	9.4
For trace metals	8- Quinolinol	2.02	5.017/9.812
	Hinokitiol	1.82	6.72
	Quinizarin	3.7	9.51

The docking process was followed. Analytes farther than 6 Å from the model phase were located, and the structure was optimized. The MI energy was calculated using the above equations. The calculated MI energy values are summarized in Table 7.15.

Table 7.15: Molecular interaction energy values of analytes with model alkyl-bonded silica gels.

Chem1cals	MIHB	MIES	MIVW		Chemical	MIHB	MIES	MIVW	
Model phase				**Model phase**					
Methyl phase				**Butyl phase**					
	Pyridine	0	0.068	6.635		Pyridine	0	-0.027	0.724
	Amitriptyline	0	0.091	25.652		Amitriptyline	0	-0.024	21.443
	8-Quininilnol	0.015	0.121	22.4		8-Quinolinol	0.009	0.041	28.766
	Hinokitiol	0.092	0.199	11.718		Hinokitiol	0	-0.056	34.453
	Quinizarin	0.147	0.272	8.613		Quinizarin	0.017	-0.03	29.576
Ethyl phase				Pentyl phase					
	Pyridine	0	-0.119	13.027		Pyridine	0	0.024	6.512
	Amitriptyline	0	-0.209	33.89		Amitriptyline	0	-0.146	9.169
	8-Quininilnol	-0.001	-0.114	26.551		8-Quinolinol	-0.001	-0.179	12.431
	Quinizarin	0.041	-0.176	27.315		Quinizarin	0.002	-1.111	15.992
Propyl phase				Hexyl phase					
	Pyridine	0	-0.028	8.759		Pyridine	0	-0.098	18.709
	Amitriptyline	0	-0.065	18.981		Amitriptyline	0	0.038	22.126
	8-Quininilnol	0.018	0.071	13.13		8-Quinolinol	0.003	-0.038	23.97
	Hinokitiol	0.014	-0.266	12.361		Hinokitiol	0	0.052	30.703
	Quinizarin	0.019	-0.045	11.791		Quinizarin	0	0.009	26.339

MIHB, MIES, MIVW: molecular interaction, hydrogen bonding, electrostatic, and van der Waals energy va1ues between an analyte and a model phase, kcal mol^{-1}

Pyridine and amitriptyline did not show any polar interaction with the methyl-phase. This implies that the methyl phase mimics inactivated silica gel. However, quinoline 1, hinokitiol, and quinizarin exhibited. polar interactions, although Metal atoms were not present on the surface. Such polar interactions ceased after interactions with the butyl

phase. This result suggested that although the surface modification is successfully performed based on the silanol activation test, themetal-sensitive compounds may demonstrate the poor performance of the chromatogram peaks. This is not due to trace metals but to insufficient hydrophobicity of the modified surface—the alkyl-chain-length effect on the hydrophobicity of alkyl-bonded silica gels was explained from the electron-density map [**97**]. This result suggested that first silanization of silica is important. Second, silanization cannot eliminate the poor chromatographic performance of metal-sensitive compounds. If the chromatographic behavior of metal-sensitive compounds is significant, manufacturers should perform trace metal analysis of their products and then analyze reagent quality.

Furthermore, the active silanol effect was studied using modified trimethylsilane-, pentyldimethylsilane-, and octyldimethylsilane-bonded silica gel models with pyridine and amitriptyline. Silanol active phases were constructed by removing one alkylsilane group located at the center of these model phases and keeping one silanol free forming a pinhole-like arrangement of these alkyl-bonded silica gels. These phases are shown with an analyte in Figures 7.51a-c, where silanols and analytes are indicated using large ball molecules for their easy identification and other molecules are shown as 20% of their original size.

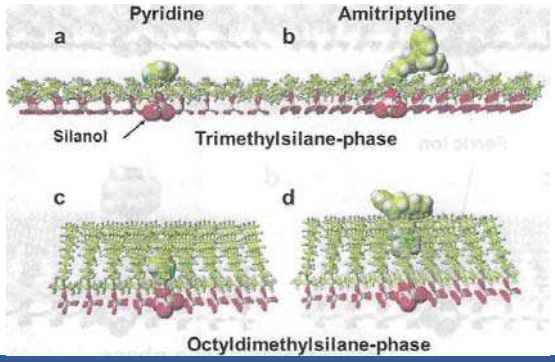


FIgure 7.51: a-d Hydrogen bonding interaction between analyte and silanol in trimethylsilane and octyldimethylsilane phases

Generally, column tests were performed using eluents without buffer components. The analytes were pyridine and amitriptyline; however, amitriptyline was ionized in a neutral aqueous eluent because of its p*K*a value (9.40). Therefore, the nitrogen of amitriptyline is sp^3-hybridized, not sp^2. We used both amitriptyline with sp^3 and sp^2 structures for the *in silico* MI analysis, considering uncertainty in the actual experimental conditions. Pyridine in both its molecular and· ionized forms was also used. Table 7.16 summarizes the calculated MIHB, MIES, and MIVW energy values.

Table 7.16. Silanol activity test results

Analytes	Methyl-phase	Pentyl-phase	Octy]-phase						
	MIHB	MIES	MIVW	MIHB	MIES	MIVW	MIHB	MIES	MIVW
Pyridine	0.403	0.257	7.165	0.31	0.048	13.327	0.91	0.277	18.63
Pyridine (I)	0.545	-0.493	12.824	0.26	-0.32	4.22	0.001	0.2	9.244
Amitriptyline	0.116	-0.422	19.998	1.014	-0.293	34.077	0.005	0.167	28.936
Amitriptyline (I)	0.048	0.446	24.143	0.014	-0.033	22.673	0.001	0.006	28.173

I: ionized form; unit: kcal $mo1^{-1}$

Pyridine showed weak MIHB energy in this model phase. The major interaction was the VW force between pyridine and the alkyl groups of this model phase. When pyridine was dropped into the octyl-phase hole and its conformation was optimized, it showed higher MIHB, as shown in Figure 2c. In contrast, amitriptyline showed weak MIHB only with the methyl phase, but due to steric hindrance, it could not reach the silanol in the octyl-bonded phase, as shown in Figure 7.51b,d. As the alkyl chain lengthens, the MIH for amitriptyline decreases because of steric hindrance.

These column tests with amitriptyline demonstrate silanol inactivity. Free silanol groups may remain on the surface of silica gels with high-density alkyl groups; therefore, small molecules are better suited for such a sensitive analysis. In addition, we studied the metal-ion effect using the model phases above. First, as an example, we adsorbed one ferric ion because ferric ions are commonly found in silica gels. We performed docking with the chelating reagents 8-quinolinol, quinizarin, and hinokitiol. Table 7.17 summarizes the calculated MIHBB, MIES, and MIVW energy values7.

Both 8-quinolinol and quinizarin should exist in their molecular forms at pH 7 due to their p*K*a values. The nitrogen of 8-quinolinol (pKa = 5.019) can be ionized in acidic conditions, and quinizarin is ionized in a high-pH eluent (pKa = 9.51). We used both the molecular and ionized forms to study their chromatographic behavior.

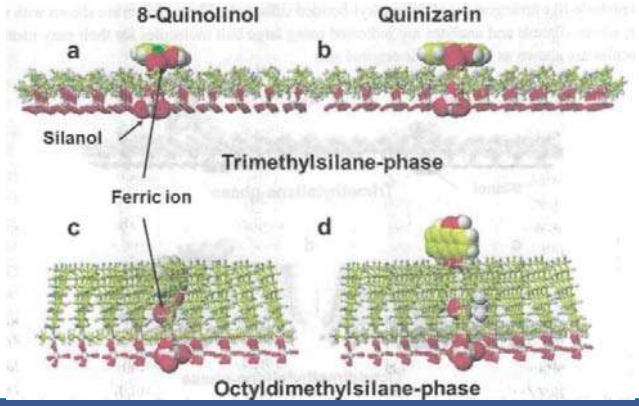


FIgure 7.52: a-d. Complex formation between the chelating reagent and ferric ions on the model phases.

8-Quinolinol, a common chelating reagent for various metal ions, forms a complex with ferric ions on the surface of methyl-bonded silica gel, as shown in Figure 7.52a. Silanol, ferric ion, and 8-quinolinol are represented shown ·1arge balls for-their easy identification. The chelate formation is demonstrated by MIES values, and MIVW values indicate the VW interaction between the analyte mid the model phase (Table 7.17). Quinizarin also formed a chelate with the ferric ion on the ethyl-phase, as show in Figure 3b. These ionized chelating· reagents formed stronger chelates, known. phenomenon in chelate chemistry. However, although 8-quinolinol demonstrated strong contact with the ferric ion). in the octy1phase, quinizarin did not because of its larger molecular size, preventing its entry into the octyl-phase hole for direct contact with the ferric ion. Steric hindrance made approaching the ferric ion located at the bottom of the hole in the highly dense octyl phase difficult, as shown in Figure 7.52c,d.

Table 7.17: Metal activity.

Analyte	Methyl-phase	Pentyl-phase	Octyl-phase						
	MIHB	MIES	MIVW	MIHB	MIES	MIVW	MIHB	MIES	MIVW
Hinokitiol	0.067	1.312	13.762	0.192	4.181	12.174	0.017	4.938	11.884
Hinokitiol (I)	0.247	2.326	14.692	0.046	11.265	8.919	0.003	11.045	12.618
9-Quinolitiol	0.107	1.663	10.184	0.277	1.256	13.619	0.022	-0.422	16.485
8-Quinokitiol (I)	0.019	9.438	9.887	0.025	9.087	9.904	0.001	9.419	5.952
Quinizarin	0.171	1.101	14.67	0.369	0.501	19.821	0.001	0.046	9.33
Quinizarin (I)	0.044	12.341	13.836	0.041	11.889	10.717	0.001	11.942	8.376

I: ionized form; unit: kcal mol^{-1}

This ferric ion did not closely contact silanol, but 8-quinolinol removed the fellic ion from the hole of the pentyl-bonded phase and extracted it (Figure 7.53a). This phenomenon was also observed.in the octyl phase, where the ferric ion was lifted from the bottom but did not completely form a chelate. 8-quinolinol and quinizarin are the molecular forms at pH 7, and hinokitiol is ionized. As can be seen from the Ml energy values in Table 4, ionized chelating reagents form a stronger chelate than their molecular forms. Therefore, hinokitiol should be a suitable chelating reagent to detect trace metals in bonded-phase silica gels, as shown in Figure 7.53b, where hinokitiol was pulled into the pinhole of the octyJ phase and formed a chelate with ferric ion.

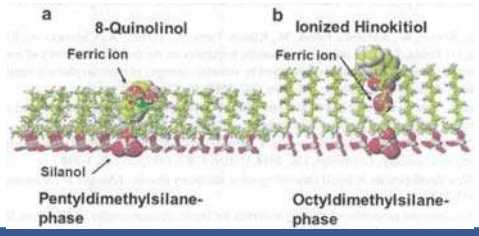


FIgure 7.53: a,b, Complex formation of chelating reagent with ferric ion in model phase.

Figure 7.53a,b, mechanisms of these analytes on bonded phases that were not completely silanized (end-apped). Because metal ions are contained within the matrix of inorganic silica gels, the acid-wash step cannot remove them completely. Detecting such metal ions on the silica gel surface requires a small chelating reagent. As shown in this study, chelating reagents can extract adsorbed metal ions from pure silica gels synthesized from organic silicons; however, the process is tedious. Generally, alkyl groups are not highly condensed, as shown in these models. Therefore, silanol and metal-chelate formation activity can be easily observed.

7.8. Gas chromatography, Retention mechanisms, Boiling point, and Enthalpy

Gas chromatography is a powerful separation tool; capillary columns have a high theoretical plate number, and capillary-column GC-MS has excellent identification power. A weakness of GC is the tedious derivatization process required for non-volatile compounds. GC is also used to measure physicochemical properties such as boiling point, enthalpy, entropy, and free energy. In gas chromatography, an inert gas is generally used as a mobile phase (carrier) to deliver gaseous molecules (analytes) to the column. Contact between the analytes and the liquid phase (stationary phase) slows their movement. Retention time depends on the analyte (solute) volatility and the interactions between the analyte and the stationary phase. Retention mechanisms can be explained quantitatively and can also predict boiling point and enthalpy.

7.8.1. Methyl-silicone phase and the selectivity: The methyl silicone phase is inert; therefore, analyte interactions are van der Waals forces. The elution order depends on analyte volatility. Conversely, you can predict analyte boiling points from retention time using a calibration curve of standard compounds. We construct a model methyl silicone phase using methyl silicone fibers.

The docking process to obtain the MI energy values is the same as for the graphitized carbon models—the obtained MIHB, MIES, and MIVW energy values are correlated to the gas-chromatographic retention times. Table 7.18 summarizes the calculated molecular properties and the collection of log *k* values. The **fsp** (p: pair) is the optimized energy value of a molecule complex. The **hbp**, **esp**, and **vwp** are the hydrogen-bonding, electrostatic, and van der Waals energy values of complexes.

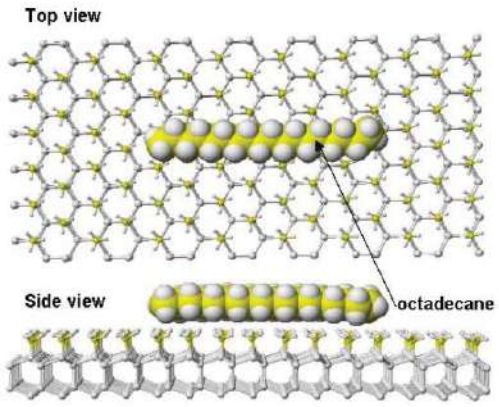


Figure 7.54: Optimized docked octadecane on a model methyl-phase.

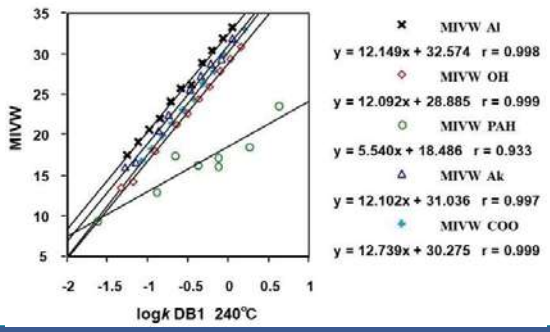


Figure 7.55: log *k* related to van der Waals interaction energy (MIVW) values.

The relation of MIVW and log k measured using a CPSil5 column at different temperatures follows:

MIVW = 14.178 (log *k* 280°C) + 34.366, *r* = 0.999, n =17.

MIVW = 10.207 (log k 220°C) + 25.112, *r* = 0.997, n = 16,

MIVW = 8.052 (log k 160°C) + 19.753, *r* = 0.999, n = 11.

The log *k* values of alkane(Al), alkylalcohol(OH), alkene (Ak),andfatty acidesters (COO) demonstrated high correlation coefficients; the relations are parallel. PAHs demonstrated exceptional relations. Considering benzene, naphthalene, and anthracene as the standard, the different behavior of PAHs from others is due to desorption (Δdes) from the methyl-silicone phase. The Δvap is a sum of fsp, 200xhbp, and esp, and exhibits a high correlation with des. The following equations show the correlation.

Δdes 280°C = -0.175 (Δvap) + 0.849, *r* = 0.989, n = 20, CPSil5,

Δdes 220°C = -0.146 (Δvap) + 10.644, *r* = 0.973, n = 19, CPSil5,

Δdes 160°C = -0.148 (Δvap) + 0.475, *r* = 0.997, n = 14, CPSil5.

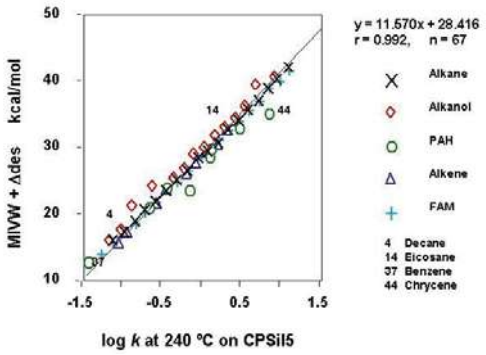


FIgure 7.56: IRelation between calculated MIVW + Δdes and measure boiling point at 240°C..

A combination of the above results with MIVW provides an excellent correlation with log k values. The results show as following equations.

log *k* 280°C = 0.070 (MIVW + Δdes) – 2.359, *r* = 0.993, n = 65, CPSil5,

log *k* 220°C = 0.096 (MIVW + Δdes) – 2.445, *r* = 0.995, n = 61, CPSil5,

log *k* 160°C = 0.129 (MIVW + Δdes) – 2.497, *r* = 0.994, n = 42, CPSil5.

Using methyl-silicone phases, the MIVW and Δvap calculated *in silico* achieved a quantitative explanation of gas chromatographic retention time.

Table 7.18: Calculated molecular properties and measured log *k* values

No Chemical	fsp[1]	hbp[1]	esp[1]	vwp[1]	MIFS[2]	MIHB[2]	MIES[2]	MIVW[2]	
1	Heptazne	1.9218	0	0	-0.197	11.5612	0	0	11.658
2	Octane	2.2065	0	0	-0.278	13.5452	0	0	13.717
3	Nonane	2.503	0	0	-0.335	15.3358	0	0	15.549
4	Decane	2.7874	0	0	-0.403	16.5148	0	0	16.725
5	Undecane	3.0924	0	0	-0.437	18.1734	0	0	18.431
6	Dodecane	3.3718	0	0	-0.539	20.0847	0	0	20.329
7	Tridecane	3.6846	0	0	-0.575	21.1949	0	0	21.47
8	Tetradecane	3.9351	0	0	-0.675	22.834	0	0	23.108
9	Pentadecane	4.2462	0	0	-0.747	24.62	0	0	24.854

10	Hexadecane	4.5375	0	0	-0.807	25.9265	0	0	26.308
11	Heptadecane	4.8088	0	0	-0.877	27.845	0	0	28.23
12	Octadecane	5.1196	0	0	-0.94	28.9292	0	0	29.363
13	Nonadecane	5.4176	0	0	-1.006	30.5334	0	0	30.533
14	ERicosane	5.7045	0	0	-1.071	32.3747	0	0	32.712
15	Heneicosane	5.9943	0	0	-1.136	33.6032	0	0	34.062
16	Docosane	6.2869	0	0	-1.205	35.2645	0	0	35.81
17	Tricosane	6.5729	0	0	-1.271	36.8734	0	0	37.188
18	Tetracosane	6.8666	0	0	-1.336	39.4414	0	0	39.007
19	Pentacosane	7.1545	0	0	-1.409	39.9656	0	0	40.511
20	Hexacosane	7.457	0	0	-1.472	41.7582	0	0	42.33
21	Pentanol	0.921	-0.079	-0.066	-0.479	9.7935	0	0.008	9.952
22	Hexanol	1.2063	-0.083	-0.057	-0.562	11.4458	0	0.037	11.566
23	Heptanol	1.4933	-0.077	-0.061	-0.628	12.776	0	0.037	32.802
24	Octanol	1.7802	-0.083	-0.059	-0.701	14.101	0	0.054	14.248
25	Decanol	2.3693	-0.081	-0.06	-0.833	17.685	0	-0.02	17.963
26	Dodecanol	2.9418	-0.081	-0.057	-0.973	20.735	0	0.032	21.003
27	Tridecanol	3.2485	-0.081	-0.059	-1.023	21.823	0	0.031	22.168
28	Tetradecanol	3.5447	-0.081	-0.061	-1.096	23.381	0	0.021	23.723
29	Pentadecanol	3.8276	-0.092	-0.06	-1.154	25.286	0	0.01	25.635
30	Hexadecanol	4.1157	-0.083	-0.06	-1.21	26.518	0	0.035	26.835
31	Heptadecanol	4.4004	-0.087	-0.059	-1.288	27.317	0	0.054	28.588
32	Octadecanol	4.7121	-0.094	-0.06	-1.386	29.257	0	-0.011	29.747
33	Nonadecanol	4.9819	-0.081	-0.062	-1.425	31.1395	0	0.009	31.516
34	Eicosanol	5.2751	-0.082	-0.061	-1.497	33.0836	0	0.008	33.398
35	Docosanol	5.8543	-0.087	-0.059	-1.624	35.9133	0	0.013	36.436
36	Tricosanol	6.1514	-0.086	-0.06	-1.697	37.4116	0	0.007	37.662
37	Benzene	-19.655	0	0	2.511	8.514	0	0	8.555
38	Naphtalene	-43.7744	0	0	5.151	12.93	0	0	12.947
39	Biphenyl	-42.1636	0	0	6.883	17.475	0	0	17.194
40	Fluorene	-35.8723	0	-0.003	-1.493	16.67	0	-0.013	16.718
41	Phenanthrene	-58.7912	0	0	10.503	17.939	0	0	18.031
42	Anthracene	-68.0926	0	0	7.639	17.892	0	0	17.927
43	Pyrene	-77.3877	0	0	9.374	19.496	0	0	19.577
44	Chrycene	-72.6256	0	0	16.693	22.288	0	0	22.44
45	1-Heptacene	0.9522	0	0.005	-0.064	11.7012	0	-0.005	10.52
46	1-Nonene	1.5297	0	0.005	-0.187	15.973	0	0.001	14.86
47	1-Decene	1.8176	0	0.005	-0.248	17.349	0	-0.002	16.408
48	1-Tridecene	2.6873	0	0.005	-0.461	21.771	0	0.001	21.054
49	1-Tetradecene	2.9782	0	0.005	-0.521	23.742	0	-0.002	22.95
50	1-Hexadecene	3.5613	0	0.005	-0.645	26.339	0	-0.002	25.477
51	1-Heptadecene	3.8544	0	0.005	-0.725	27.673	0	-0.003	27.209
52	1-Octadecene	4.1467	0	0.005	-0.791	29.349	0	0	28.86
53	1-Nonadecene	4.4338	0	0.005	-0.856	30.984	0	0.003	30.076
54	1-Eicocene	4.735	0	0.005	-0.907	33.118	0	-0.001	32.32
55	Methylpentanoate	-3.9406	0	-5.675	1.987	11.3533	0	0.129	11.335
56	Methylhexanoate	-3.5518	0	-5.609	1.947	13.2176	0	0.06	13.259
57	Methyloctanoate	-3.0185	0	-5.711	1.833	16.234	0	0.079	16.177

58	Methylnonanoate	-2.7649	0	-5.713	1.738	17.613	0	0.038	17.795
59	Methyldecanoate	-2.4539	0	-5.679	1.658	19.271	0	0.078	19.506
60	Methylundecanoate	-2.1841	0	-5.748	1.632	21.163	0	0.073	21.383
61	Methyldodecanoate	-1.8738	0	-5.52	1.589	22.307	0	0.069	22.582
62	Methyltridecanoate	-1.6012	0	-5.735	1.515	24.156	0	0.051	24.44
63	Methyltetradecanoate	-1.305	0	-5.752	1.435	25.912	0	0.069	26.17
64	Methylpentadecanoate	-1.0143	0	-5.756	1.372	27.024	0	0.069	27.396
65	Methylhexadecanoate	-0.7154	0	-5.735	1.296	28.781	0	0.077	29.117
66	Methylheptadecanopate	-0.4336	0	-5.789	1.268	30.174	0	0.067	30.461
67	Methyloctadecanoate	-0.1298	0	-5.757	1.178	31.709	0	0.06	32.072
68	Methylnonadecanoate	0.1444	0	-5.709	1.071	33.4139	0	0.047	33.677
69	Methyleicosanoate	0.4368	0	-5.717	1.013	34.7206	0	0.052	35.107
70	Methylhenicosanoate	0.7264	0	-5.723	0.949	36.4853	0	0.06	37.044
71	Methyldocosanoate	1.0219	0	-5.789	0.939	37.8673	0	0.062	38.249
72	Methyltricosanoate	1.3187	0	-5.869	0.909	39.3747	0	0.063	39.896
73	Methylytetracosanoate	1.6069	0	-5.731	0.755	41.19	0	0.059	41.76
No	280*3	260*3	240*3	220*3	200*3	180*3	160*3		
1	-	-	-	-	-	-	-0.988		
2	-	-	-	-1.189	-0.856	-0.925	-0.767		
3	-	-	-1.111	-1.026	-0.734	-0.736	-0.557		
4	-1.253	-1.11	-0.974	-0.869	-0.606	-0.549	-0.353		
5	-1.121	-0.981	-0.839	-0.571	-0.469	-0.368	-0.156		
6	-1.045	-0.863	-0.708	-0.423	-0.322	-0.188	0.044		
7	-0.897	-0.742	-0.575	-0.277	-0.173	-0.008	0.741		
8	-0.79	-0.622	-0.44	-0.133	-0.02	0.17	0.738		
9	-0.672	-0.503	-0.309	-0.016	0.132	0.346	0.633		
10	-0.555	-0.384	-0.176	0.156	0.288	0.522	0.828		
11	-0.441	-0.266	-0.045	0.296	0.442	0.697	1.021		
12	-0.329	-0.149	0.084	0.433	0.597	0.87	-		
13	-0.22	-0.033	0.211	0.578	0.753	1.021	-		
14	-0.112	0.082	0.339	0.716	0.905	-	-		
15	-0.004	0.196	0.469	0.855	1.06	-	-		
16	0.102	0.911	0.596	0.992	-	-	-		
17	0.205	0.424	0.722	1.125	-	-	-		
18	0.317	0.538	0.85	-	-	-	-		
19	0.42	0.649	0.945	-	-	-	-		
20	0.523	0.76	1.099	-	-	-	-		
21	-	-	-	-1.22	-0.992	-1.043	-0.893		
22	-	-	-	-1.066	-0.853	0.849	-0.663		
23	-1.185	-1.115	-1.152	-0.914	-0.714	-0.653	-0.467		
24	-1.071	-1.011	-1	-0.787	-0.563	-0.463	-0.256		
25	-0.87	-0.763	-0.864	-0.469	-0.257	-0.096	0.144		
26	-0.655	-0.529	-0.601	-0.176	0.051	0.264	0.54		
27	-0.548	-0.415	-0.339	-0.032	0.206	0.443	0.736		
28	-0.441	-0.293	-0.207	0.111	0.364	0.62	0.942		
29	-0.335	-0.176	-0.076	0.254	0.52	0.793	1.137		
30	-0.23	-0.059	0.053	0.396	0.675	0.967	-		
31	-0.123	0.057	0.182	0.538	0.833	-	-		

32	-0.018	0.173	0.312	0.676	0.988	-	-		
33	0.087	0.288	0.436	0.816	-	-	-		
34	0.192	0.402	0.566	0.956	-	-	-		
35	0.399	0.631	0.691	-	-	-	-		
36	0.502	0.743	0.944	-	-	-	-		
37	-1.616	-1.427	-1.418	-1.284	-1.243	-1.043	-1.032		
38	-0.902	-0.754	-0.649	-0.492	-0.335	-0.164	0.036		
39	-0.711	-0.557	-0.423	-0.244	-0.058	0.145	0.378		
40	-0.455	-0.293	-0.137	0.058	0.268	0.494	0.752		
41	-0.238	-0.065	0.107	0.318	0.549	0.799	1.079		
42	-0.226	-0.055	0.12	0.333	0.564	0.814	1.097		
43	0.102	0.291	0.493	0.735	0.995	-	-		
44	0.411	0.627	0.858	-	-	-	-		
45	-	-	-	-	-	-	-		
46	-1.128	-1.263	-1.034	-1.025	-0.794	-1.331	-1.013		
47	-1.079	-1.11	-0.921	-0.87	-0.653	-0.834	-0.583		
48	-0.849	-0.745	-0.549	-0.431	-0.205	-0.626	-0.374		
49	-0.743	-0.626	-0.426	-0.286	-0.051	-0.054	0.223		
50	-0.529	-0.391	-0.185	0.001	0.259	0.127	0.419		
51	-0.423	-0.274	-0.048	0.143	0.415	0.483	0.807		
52	-0.317	-0.158	0.083	0.285	0.567	0.658	1.001		
53	-0.211	-0.042	0.21	0.426	0.722	0.832	-		
54	-0.106	0.073	0.336	0.565	0.875	1.015	-		
55	-	-	-1.258	-1.147	-0.914	-0.939	-0.743		
56	-	-1.159	-1.1	-0.99	-0.78	-0.748	-0.542		
57	-1.003	-0.98	-0.823	-0.694	-0.489	-0.363	-0.141		
58	-0.929	-0.844	-0.691	-0.549	-0.338	-0.187	0.058		
59	-0.811	-0.723	-0.558	-0.401	-0.181	-	-		
60	-0.705	-0.602	-0.425	-0.257	-0.027	-0.007	-		
61	-0.606	-0.483	-0.296	-0.114	0.127	0.171	0.256		
62	-0.501	-0.365	-0.164	0.03	0.284	0.348	0.452		
63	-0.397	-0.248	-0.032	0.17	0.44	0.523	0.648		
64	-0.294	-0.133	0.098	0.314	0.595	0.698	0.843		
65	-0.187	-0.024	0.226	0.458	0.753	0.872	1.036		
66	-0.082	0.091	0.354	0.596	0.918	-	-		
67	0.023	0.208	0.481	0.736	1.075	-	-		
68	0.125	0.33	0.609	0.875	-	-	-		
69	0.228	0.444	0.737	1.014	-	-	-		
70	0.317	0.663	0.862	-	-	-	-		
71	0.434	0.775	0.991	-	-	-	-		
72	0.537	0.887	1.117	-	-	-	-		
73	0.639	-	-	-	-	-	-S		

#1: fsp, hbp, esp, vwp: final structure, hydrogen bonding, electrostatic and van der Waal energy value of a pair of compounds; #2: MIFS, MIHB, MIES, MIVW: final structure, hydrogen bonding, electrostatic and van der Waals interaction energy values calculated using a model methylsilicone phase; #3: log *k* values measured 280 – 160 °C on [98]

7.8.2. Boiling point and Enthalpy: Gas chromatography can be used both for separation and to measure physicochemical properties. Significantly, specific molecular interactions are negligible with non-polar columns. Boiling point relates to the Kovats retention index and van der Waals volume. Gas chromatography permits the measurement of enthalpy (ΔH).The log *k* value demonstrates linear relation with Trouton'sequation [(ΔH/Tb)=21] [99]. However, the

conversion of boiling points measured under low pressure to that at environmental conditions. The conversion equation is known as Hass & Newton equation [100]. The equations are the following equations.

$$Tb = t + \Delta t$$

$$\Delta t = \{(273.1 + t)(2.8808 - \log P)\}/\{P + 0.15(2.8808 - \log P)\}$$

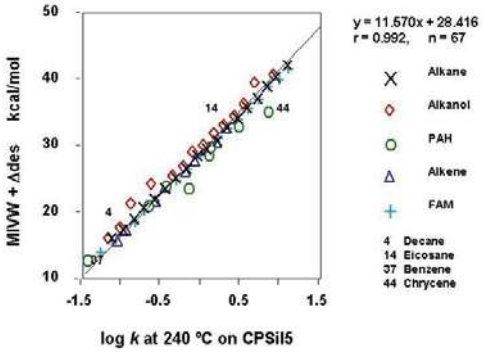


FIgure 7.57: Relation between log k and reversed absolute temperature.

The estimated boing point (y) is related to Enthalpy (x), and the result is given as the following equation.

$y = -103.79 + 2.909 \times 10^{-2}x$ $\quad (r^2 = 0.997)$

The correlation coefficient of the predicted boing point calculated above equation and the Enthalpy is 0.998 (n = 16). The Hass & Newton 's Φ was changed from 1.973 to 3.65.

The predicted alkyl-alcohol boing point was calculated using the following equation: $y = 20.967 + 2.021 \times 10^{-2}\ x$ ($r^2 = 0.997$) [102]. The predicted and measured boiling point is summarized in Table 7.19. The calculated van der Waals volume (VWV), Enthalpy, and calc(300) values are different from the program used. Use the same program with the same version to avoid confusion.

Table 7.19: Properties of standard compounds.

No	Analyte	vwv Å	DH calc mol^{-1}	bp °C	Prop			
	calc (300K)	GC	760mm Hg	Normalized	Measured	°C		
1	Pentane	95.97	5175	–	36.1	-	-	43.68
2	Hexasne	112.79	6048	-	68.7	-	-	69.29
3	Heptane	129.55	6919	6480	98.5	-	-	94.82
4	Octane	146.41	7794	7020	125.6	-	-	120.49
5	Nonane	163.23	8668	7860	150.9	-	-	146.1
6	Decane	180.01	9539	8480	174.1	-	-	171.65
7	Undecane	196.8	10411	9160	196.7	-	-	197.22
8	Docecane	213.65	11286	9860	216.3	231.95	91.5(10)	222.88
9	Tridecane	230.55	11286	9860	216.3	253.4	107(10)	248.62
10	Tetradecane	247.26	13032	11120	253.7	274.07	121.9(10)	274.06
11	Pentadecane	264.06	13904	11850	270.6	293.7	136(10)	299.63
12	Hexadecane	280.87	14777	12570	287	311.6	149(10)	325.73
13	Heptadecane	297.67	15650	13310	301.8	329.2	161.7(10)	350.81
14	Octadedecane	314.51	16524	14040	316.1	319.36	173.5(10)	376.45
15	Nonadecane	331.17	17390	14600	329.7	356.5	193(15)	401.82
16	Eicosane	348.09	18268	15220	343	376.3	195.7(10)	427.59
17	1-Butylalcohol	87.31	5042	-	117.3	-	-	122.87
18	1-Pentylalcohol	104.06	5911	6700	138.5	-	-	140.43

19	1-Hexylalcohol	120.92	6786	7520	157.9	-	-	158.11
20	1-Heptylalcohol	137.8	7661	7650	176.8	-	-	175.8
21	1-Octylalcohol	154.65	8535	8120	195	-	-	193.46
22	1-Nonylalcohol	171.44	9406	-	213.5	-	-	211.06
23	1-Decylalcohol	188.27	10279	9896	229	-	-	228.7
24	1-Undecylalcohol	205.2	11157	-	243.5	-	-	246.45
25	1-Docecylalcohol	221.85	12020	10930	-	255.99	153.5(25)	263.9
26	1-Tridecylalcohol	238.67	12880	11760	-	270.74	152(14)	281.27
27	1-Tetradecylalcohol	255.39	13760	12620	-	295-295.8	283.12-340.79	299.06
28	1-Pentadecylalcohol	272.28	14636	13420	296.8, 299	-	-	316.76
29	1-Hexadecylalcohol	289.22	15515	13790	344	316.58-320.84		334.52
30	1-Heptadecylalcohol	306.22	16396	14340	-	-	-	352.33
31	1-Octadecylalcohol	322.85	17259	15080	-	343.34	210.5(15)	322.07
32	1-Nonadecylalcohol	339.67	38131	15420	-	396.64	166.7(0.32)	387.4
33	1-Eicocylalcohol	356.5	19004	16210	-	408.51	220.5(3)	405.04

VWV, -DHcalc: calculated using CAChe MOPAC BlogP; -DH(GC) from reference 3; measured pressure are indicated in (Hg); Prop: predicted values

Figure 7.58 shows the log *k* measured using a methyl-silicone phase with the normalized boiling point, boiling point (Tb), and the heat of vaporization (vap). The high correlation coefficient demonstrates the possibility of predicting boiling point from the measured log *k* values using a methyl-silicone phase.

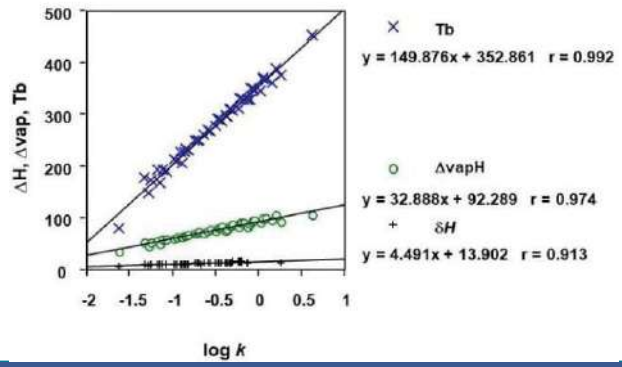


FIgure 7.58: Relation between log k and ΔH, Δvap, Tb.

7.8.3. Ethylene glycol-phase and the selectivity: A polar phase among various phases for gas-chromatography is the ethylene-glycol (Carbowax) phase.

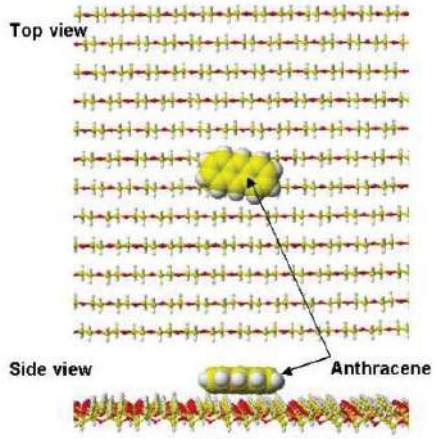


FIgure 7.59: A model polyethylene oligomer Figure 7.60. Molecular interaction energy (MIFS) and log *k*.

Phase measured on a polyethyleneglycol phase

Analyze a relation between log *k* and calculated MI values listed in Table 7.20 [103]. The difference obtained using the methylsilicone phase is the contribution of hydrogen bonding and electrostatic interaction, and the MIVW contributes significantly to the retention of analytes on the methyl-silicone phase. But MIFS is used for hydrogen bonding and electrostatic interaction to analyze the selectivity of the polyethylene glycol phase. The relations between MIFS and log *k* values measured using a CPWAX column are shown in Figure 7.60

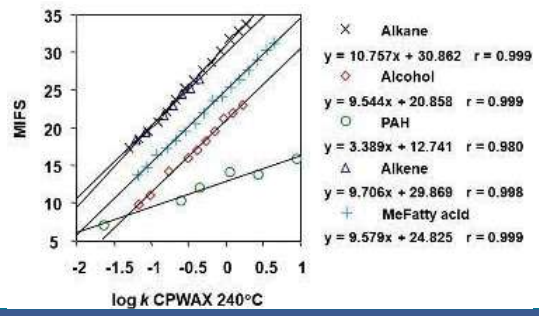


Figure 7.60: AMolecular interaction energy (MIFS) and log *k* measured on a polyethyleneglycol phase.

Each group shows a high correlation, but all groups exist independently. The result is different from that observed for a methyl-silicone phase in which all groups are lined together. The relation for alkanes used as the standard compounds shows in the following equations.

$MIFS_{240°} = 10.757 \log k + 30.862$, $r = 0.999$, n = 14 (CPWAX),

$MIFS_{200°} = 8.3829 \log k + 25.948$, $r = 0.999$, n =16 (CPWAM).

Vaporization used in the discussion for the methyl-silicone phase is considered to analyze the difference of alkanes from other compounds. The difference (Δdes) can be related to Δvap calculated as the sum of fsp + 350hbp + 2esp. The relation between Δdes and Δvap is shown in the following equations with the significant contribution of hbp.

$\Delta des_{240°} = -0.289\ (\Delta vap) + 1.557$, $r = 0.997$, n = 17 (CPWAX),

$\Delta des_{200°} = -0.293\ (\Delta vap) + 1.521$, $r = 0.993$, n = 19 (CPWAX).

The addition of Δdes to MIFS produces the final equations to explain the retention time measured using the ethylene glycol phase.

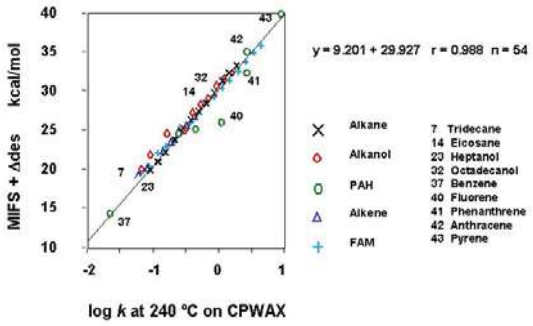


Figure 7.61: Relation between MIFS + Δdes and log *k* measured at 240°C on CPWAX

$\log k_{240°} = -0.105\ (MIFS+\Delta des) - 3.130$, $r = 0.986$, n = 54, (CPWAX),

$\log k_{200°} = -0.127\ (MIFS+\Delta des) - 3.232$, $r = 0.988$, n = 56 (CPWAX).

The above analysis exhibits that the ethylene glycol phase's retention time can be predicted for the methyl-silicone phase.

Table 7.20: Molecular properties and molecular interaction energy values calculated using a model ethyleneglycol phase.

No	Chemical	MIFS*1	MIHB*1	MIES*1	MIVW*1	240*2	200*2
1	Undecane	14.727	0	-1.15	14.976	-	-1.312
2	Dodecane	16.4348	0	-1.15	16.737	-1.478	-1.168
3	Tridecane	17.7929	0	-1.15	17.575	-1.358	-1.024
4	Tetradecane	18.3794	0	-1.15	18.619	-1.221	-0.88
5	Pentadecane	19.472	0	-1.15	19.694	-1.093	-0.733
6	Hexadecane	20.6851	0	-1.15	20.886	-0.968	-0.589
7	Heptadecane	22.0013	0	-1.15	22.287	-0.844	-0.445
8	Octadecane	23.7104	0	-1.15	23.975	-0.723	-0.301
9	Nonadecane	25.2255	0	-1.15	25.549	-0.605	-0.158
10	Eicosane	26.1911	0	-1.15	26.584	-0.484	-0.017
11	Heneicosane	27.5137	0	-1.15	27.944	-0.366	0.124
12	Docosane	28.6643	0	-1.15	29.024	-0.249	0.265
13	Tricosane	30.1168	0	-1.15	30.57	-0.133	0.404
14	Tetracosane	31.7059	0	-1.15	32.402	-0.017	0.542
15	Pentacosane	32.8353	0	-1.15	33.176	0.097	0.68
16	Hexacosane	33.7937	0	-1.15	34.176	0.211	0.817
17	Pentanol	7.5361	0.048	-1.124	7.572	-	-1.13
18	Hexanol	8.6249	0.056	-1.127	8.621	-	-0.969
19	Heptanol	9.7138	0.054	-0.134	9.675	-1.134	0.814
20	Octanol	10.9677	0.056	-1.133	10.905	-1.025	-0.66
21	Decanol	14.0514	0.058	-1.129	14.13	-0.761	-0.362
22	Dodecanol	15.911	0.059	-1.131	15.93	-0.397	-0.067
23	Tridecanol	16.9538	0.058	-1.134	16.947	-0.278	0.078
24	Tetradecanol	18.1744	0.059	-1.131	18.203	-0.159	0.222
25	Perntadecanol	19.473	0.06	-1.129	19.658	-0.041	0.366
26	Hexadecanol	21.1032	0.055	-1.138	21.106	0.076	0.712
27	Heptadecanol	21.8017	0.055	-1.138	21.838	0.193	0.907
28	Octadecanol	22.9217	0.055	-1.14	22.9	0.309	1.082
29	Benzene	6.9931	0	-1.15	6.998	-1.758	-1.426
30	Maphthalene	10.2538	0	-1.15	10.254	-0.59	-0.226
31	Biphenyl	11.3366	0	-1.15	10.654	-0.346	0.061
32	Fluorene	14.0677	0	-1.134	14.094	0.058	0.51
33	Phenanthrene	13.7446	0	-1.15	13.854	0.462	0.951
34	Anthracene	13.762	0	-1.15	13.767	0.449	0.957
35	Pyrene	15.895	0	-1.15	15.926	0.97	-
36	1-Tridecene	18.2859	0	-1.163	16.955	-1.286	-0.951
37	1-Tetradecene	18.2859	0	-1.163	18.016	-1.152	-0.808
38	1-Hexadecene	21.5834	0	-1.164	20.251	-0.9	-0.515
39	1-Heptadecene	22.8993	0	-1.164	21.693	-0.778	-0.37
40	1-Octadecene	24.4546	0	-1.163	23.094	-0.656	-0.227
41	1-Nonadecene	25.1489	0	-1.163	23.769	-0.536	-0.084
42	1-Eicocene	26.3361	0	-1.164	24.973	-0.418	0.057
43	Methylhexanoate	11.4103	0	-1.086	11.576	-	-1.19
44	Methyloctanoate	13.6755	0	-1.087	13.718	-1.174	-0.849
45	Methylnonanoate	14.6557	0	-1.1	14.812	-1.048	-0.706
46	Methyldecanoate	16.3692	0	-1.102	16.605	-0.923	-0.56

47	Methylundecanoate	17.2585	0	-1.103	17.406	-0.803	-0.412
48	Methyldodecanoate	18.298	0	-1.098	18.428	-0.682	-0.268
49	Methyltridecanoate	19.4004	0	-1.098	19.5	-0.56	-0.125
50	Metyltetradecanoate	20.5876	0	-1.099	20.685	-0.44	0.017
51	Methylpentadecanoate	21.8825	0	-1.091	21.984	-0.322	0.159
52	Methylhexadecanoate	23.4636	0	-1.102	23.569	-0.199	0.301
53	Methylheptadecanoate	24.1648	0	-1.102	24.274	-0.082	0.442
54	Methyloctadecanoate	25.3375	0	-1.102	25.443	0.034	0.582
55	Methylnonadecanoate	26.3548	0	-1.101	26.457	0.146	0.721
56	Methyleicosanoate	27.6285	0	-1.101	27.819	0.262	0.86
57	Methylhenicosanoate	28.9478	0	-1.1	29.253	0.378	0.998
58	Methyldocosanoate	30.2597	0	-1.101	30.412	0.491	-
59	Methyltricosanoate	31.1002	0	-1.101	31.413	0.606	-

1: MIFS, MIHB, MIES, MIVW: final structure, hydrogen bonding, electrostatic and van der Waals interaction energy values calculated using a model ethyleneglycol phase; 2: log *k* values measured 240, 200C on DBWAX

7.8.4. 50% phenylmethyl silicone phase and the selectivity: The selective phases for gas chromatography are liquid crystal, ion-exchange, chiral, and phenylmethyl-phases. A popular selective phase is some phenylmethyl silicone phases whose selectivity depends on the mixture ratio of phenyl and methyl groups. A 50% phenylmethyl silicone phase is selected because of the firm π-electron selectivity.

The standard parameter used for gas chromatographic retention that is active for the retention prediction using methyl-silicone phases is the Kovats retention index; however, the index is powerless for analyzing retention in phenylmethyl phases. It requires additional factors for phenylmethyl silicone phases. The retention time on the phenylmethyl silicone phase does not relate to the analyte's boiling point. The properties of the 50% phenylmethyl silicone phase are achieved by *in silico* analysis [104].

Increases the number of fibers and lays these parallel without space between these fibers. The organic polymer coats altogether to avoid not appearing the tube material properties during the gas chromatographic operation. Another approach to preparing a 50% phenylmethyl silicone phase is converting the methyl group of methyl-silicone phase prepared previously to a phenyl group. They constructed a 50% phenylmethyl silicone phase, which is shown in Figure 7.62.

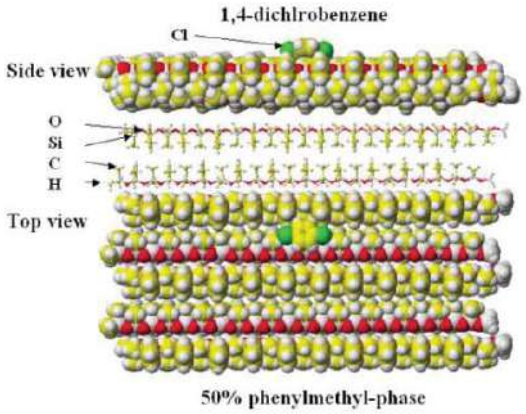


Figure 7.62: A model 50% phenylmethyl silicone phase binds 1,4-dichlorobenzene.

The MI energy values for various compounds were achieved, like for methyl and ethylene glycol phases. The relation between MIVW and log *k* measured using a 50% phenylmethyl phase is exhibited in Figure 7.63.

MIVW (Alkane) = 8.399 log $k_{200°C}$ + 24.614, r = 0.997, n = 9,

MIVW (alcohol) = 8.190 log $k_{200°C}$ + 19.296, r = 0.999, n = 13,

MIVW (alkylbenzene) = 8.427 log $k_{200°C}$, r = 0.997, n = 6.

MIVW (methylbenzene) = 6.744 log $k_{200°C}$ + 15.547, r = 0.984, n = 4,

MIVW (chlorobenzene) = 3.483 log $k_{200°C}$ + 11.528, r = 0.985, n = 5,

MIVW (PAH) = 2.603 log $k_{200°C}$ + 10.638, r = 0.977, n = 5.

The behavior of these compounds on the 50% phenylmethyl silicone phase is very different from those observed for methyl silicone and polyethylene glycol phases. Especially, PAH and polychlorobenzenes demonstrated their specificity. Use alkanes as the standard compounds added vaporization factor Δvap (fsp + 200hbp -2esp). The results are shown in Figure 7.64.

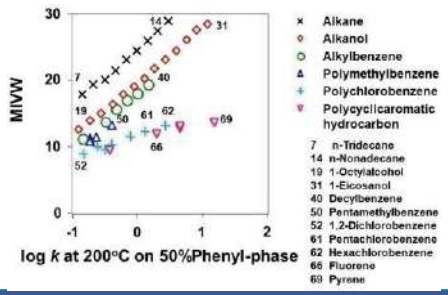


Figure 7.63: Van der Waals interaction energy values and log *k* measured on 50% phenylmethyl silicone phase.

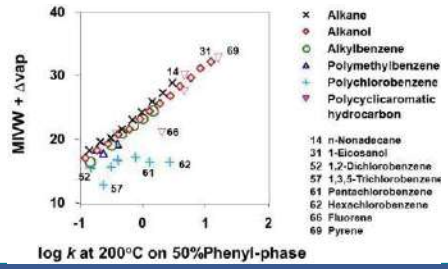


Figure 7.64: log *k* and MIVW plus Δvap

The previous approach could not handle the chromatographic behavior of polychlorobenzenes. The specificity of polychlorobenzenes depends on electron localization. Therefore, the degree of electron localization (HOMO and LUMO energy) is calculated using a MOPAC program. Adding HOMO and LUMO energy values to the above results improved the correlation, as shown in Figure 5. The final equation is: MIVW + Δvap + LUMO + 0.6HOMO = 7.706 log k + 23.240, r = 0.979, n = 44.

When fluorene, which includes one sp^3 carbon, is not a perfect PAH structure, was removed from the calculation, the correlation coefficient improved to 0.99 (n = 43). Such imperfect resonance structure of fluorene demonstrates inhomogeneous electron distribution as learned for 13PAH in the previous chapter.

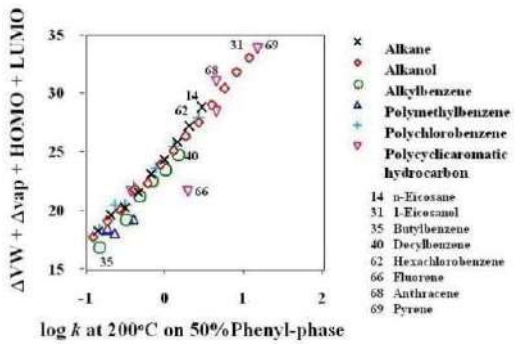


Figure 7.65: log *k* and sum of properties

Table 7.21: Molecular properties, molecular interaction energy and log k values on 50% phenylmethyl and methylsilicone phases.

No Chemical	fs	hb	es	vw	fsp	hbp	esp	vwp	
1	Heptane	4.1135	0	0	3.07	1.921	0	0	-0.204
2	Octane	4.7556	0	0	3.537	2.2087	0	0	-0.275
3	Nonane	5.3984	0	0	3.998	2.5031	0	0	-0.336
4	Decane	6.041	0	0	4.461	2.7874	0	0	-0.403
5	Undecane	6.682	0	0	4.925	3.0892	0	0	-0.468
6	Dodecane	7.324	0	0	5.386	3.3701	0	0	-0.548
7	Tridecane	7.966	0	0	5.85	3.6684	0	0	-0.593
8	Tetradecane	8.608	0	0	6.313	3.9591	0	0	-0.672
9	Pentadecane	9.25	0	0	6.776	4.2726	0	0	-0.752
10	Hexadecane	9.893	0	0	7.239	4.5397	0	0	-0.8
11	Heptadecane	10.535	0	0	7.701	4.8519	0	0	-0.866
12	Octadecane	11.177	0	0	8.16	5.1253	0	0	-0.945
13	Nonadecane	11.819	0	0	8.625	5.41	0	0	-1.002
14	Eicosane	12.461	0	0	9.088	5.0998	0	0	-1.072
15	Butylalcohol	2.129	0	0	1.566	0.6058	-0.078	-0.053	-0.427
16	Pentylalcohol	2.7786	0	0	2.038	0.9217	-0.07	-0.061	-0.482
17	Hexycylalcohol	3.4226	0	0	2.505	1.2104	-0.079	-0.057	-0.559
18	Heptylalcohol	4.0668	0	0	2.964	1.4962	-0.081	-0.061	-0.625
19	Octylalcohol	4.7082	0	0	3.425	1.7813	-0.081	-0.058	-0.702
20	Nonylalcohol	5.3503	0	0	3.889	2.0721	-0.08	-0.061	-0.764
21	Decanol	5.99	0	0	4.355	2.365	-0.081	-0.06	-0.829
22	Undecanol	6.638	0	0	4.811	2.6688	-0.086	-0.059	-0.883
23	Dodecanol	7.274	0	0	5.275	2.95	-0.07	-0.061	-0.957
24	Tridecanol	7.917	0	0	5.744	3.242	-0.081	-0.059	-1.028
25	Tetradecanoll	8.559	0	0	6.197	3.53	-0.081	-0.061	-1.1
26	Pentadecanolol	9.201	0	0	6.669	3.82	-0.077	-0.06	-1.158
27	Hexadecanol	9.843	0	0	7.125	4.116	-0.078	-0.061	-1.226
28	Heptadecanolol	10.485	0	0	7.593	4.4	-0.08	-0.061	-1.29
29	Octadecanolol	11.127	0	0	8.058	4.7	-0.078	-0.062	-1.365
30	Nonadecanol	11.7843	0	0	8.513	4.9819	-0.078	-0.061	-1.429
31	Eicosanol	12.4114	0	0	8.986	5.2751	-0.082	-0.061	-1.498
32	Toluene	-8.6003	0	0	3.03	-22.096	0	0	1.177
33	Ethylbenzene	-6.7841	0	0	4.054	-19.285	0	0	2.362
34	Propylbenzene	-6.0921	0	0	4.534	-18.772	0	0	2.461
35	Butylbenzene	-5.467	0	0	4.995	-18.583	0	0	2.292
36	Hexylbenzene	-4.1871	0	0	5.916	-18.0058	0	0	2.142
37	Heptylbenzene	-3.5456	0	0	6.382	-17.7167	0	0	2.053
38	Octylbenzene	-2.9034	0	0	6.845	-17.4332	0	0	1.976
39	Nonylbenzene	-2.2614	0	0	7.312	-17.1515	0	0	1.91
40	Decylbenzene	-1.6193	0	0	7.772	-16.8498	0	0	1.855
41	1,2-Dimethylbenzene	-6.3631	0	0.123	4.14	-22.6282	0	0.269	1.153
42	1,3-Dimethylbenzene	-9.2552	0	-0.125	3.061	-24.8721	0	-0.227	-0.155
43	1,4-Dimethylbenzene	-9.133	0	0.024	3.044	-24.1888	0	0.072	0.251
44	1,2,3-Trimethylbenzene	-4.9532	0	0.129	5.287	-22.591	0	0.32	1.398
45	1,2,4-Trimethylbenzene	-8.5581	0	0.027	3.683	-25.7387	0	0.112	-0.589
46	1,3,5-Trimethylbenzene	-10.0815	0	-0.377	3.042	-27.9339	0	-0.688	-1.543

47	1,2,3,4-Tetramethylbenzene	-3.3472	0	0.162	6.576	-21.2391	0	0.38	2.766
48	1,2,3,5-Tetramethylbezxene	-5.8268	0	-0.098	5.233	-25. 7257	0	-0.101	-0.049
49	1,2,4,5-Tetramethylbenzene	-8.0667	0	0.054	4.26	-27.2349	0	0.244	-1.402
50	Pentamethylbenzene	-1.9233	0	0.068	7.956	-20.4707	0	0.244	3.85
51	Chlorobenzene	-7.8015	0	0	3.214	-20.0071	0	0.105	1.926
52	1,2-Dichlorobenzene	-4.049	0	2.499	4.097	-13.5793	0	4.957	2.807
53	1,3-Dichlorobenzene	-10.094	0	-2.551	3.431	-25.2583	0	-4.43	1.129
54	1,4-Dichlorobenzene	-6.924	0	0.613	3.408	-18.8957	0	1.82	1.164
55	1,2,3-Trichlorobernzene	-2.5852	0	2.517	5.297	-11.0233	0	5.91	3.996
56	1,2,4-Trichlorobenzene	-5.7288	0	0.566	4.315	-16.9752	0	2.336	1.946
57	1,3,5-Trichlorobenzene	-14.9554	0	-7.654	3.657	-35.2035	0	-13.706	0.405
58	1,2,3,4-Tetrachlorobenzene	-0.4196	0	3.179	6.609	-7.4736	0	5.995	7.066
59	1,2,3,5-Tetrachlorobenzene	-6.8239	0	-1.97	5.542	-20.0373	0	-4.31	5.174
60	1,2,4,5-Tetrachlorobenzene	-3.9163	0	1.14	5.245	-13.304	0	3.411	3.901
61	Pentachlorobenzene	-0.7935	0	1.29	8.007	-8.429	0	2.323	9.524
62	Hexachlorobenzene	-3.2093	0	2.125	11.222	-0.7244	0	4.236	15.327
63	Benzene	-8.077	0	0	3.006	-19.6699	0	0	2.497
64	Naphthalene	-18.688	0	0	5.767	-43.7745	0	0	5.152
65	Biphenyl	-13.819	0	0	11.084	-42.1616	0	0	6.895
66	Fluorene	-13.344	0	0	3.841	-34.9013	0	0	-0.6
67	Phenanthrene	-24.636	0	0	9.988	-58.7896	0	0.026	10.506
68	Anthracene	-29.36	0	0	8.49	-68.0926	0	0	7.639
69	Pyrene	-33.178	0	0	10.19	-77.3879	0	0	9.376
70	Chrycene	-29.986	0	0	14.628	-78.3872	0	0	9.376
71	Tetracene	-40.0415	0	0.062	11.201	-92.4331	0	0	10.097
72	Benzpyrene	-39.0794	0	0	14.453	-92.3571	0	0.063	14.778
73	Pentacene	-50.7229	0	0	13.911	-116.7744	0	0.059	12.564
50%phenyl-phase	5315.5643	0	-528.095	-423.658	-	-	-	-	

fs, hb, es. vw: final (optimized) structure, hydrogen bonding, electrostatic, and van der Waals energy values of analyte. fsp, hbp, esp, vwp: fs, hb, es, vw energy values of a pair of analytes. unit: kcal mol^{-1}

No	HOMO	LUMO	FS*	HB*	ES*	VW*			
1	-10.303	0.2995	5308.7639	0	-528.096	-433.295			
2	-10.285	2.936	5307.939	0	-528.096	-435.333			
3	-10.283	2.89	5307.0138	0	-528.096	-435.466			
4	-10.275	2.851	5306.627	0	-528.097	-436.271			
5	-10.278	2.821	5306.0953	0	-528.095	-436.944			
6	-10.272	2.794	5305.3124	0	-528.099	-437.958			
7	-10.28	2.773	5304.418	0	-528.099	-438.985			
8	-10.271	2.754	5303.909	0	-528.097	-439.187			
9	-10.274	2.738	5303.1089	0	-528.097	-440.117			
10	-10.273	2.725	5302.3329	0	-528.098	-441.318			
11	-10.274	2.713	5301.8078	0	-528.098	-442.131			
12	-10.273	2.703	5300.9036	0	-528.098	-443.261			
13	-10.273	2.694	5300.0389	0	-528.098	-444.238			
14	-10.275	2.686	5299.8046	0	-528.097	-445.326			
15	-10.188	1.803	5308.7278	-2.38	-528.227	-431.243			
16	-10.212	1.778	5308.025	-2.372	-528.228	-431.969			
17	-10.19	1.701	5307.7142	-2.335	-528.225	-432.346			

18	-10.195	1.7	5307.052	-2.238	-528.221	-433.351			
19	-10.208	1.699	5306.1666	-2.203	-528.217	-434.546			
20	-10.227	1.757	5305.59	-2.284	-528.225	-435.505			
21	-10.191	1.773	5305.1369	-2.256	-528.222	-436.041			
22	-10.265	1.685	5304.3702	-2.25	-528.221	-436.957			
23	-10.212	1.76	5303.565	-2.199	-528.225	-438.03			
24	-10.191	1.771	5302.9514	-2.248	-528.222	-438.743			
25	-10.211	1.761	5302.2365	-2.247	-528.217	-439.54			
26	-10.215	1.758	5301.4158	-2.248	-528.219	-440.562			
27	-10.204	1.764	5300.8946	-2.235	-528.215	-441.338			
28	-10.198	1.767	5300.0283	-2.244	-528.215	-442.349			
29	-10.194	1.77	3299.1578	-2.241	-528.216	-443.432			
30	-10.215	1.757	5298.8552	-2.226	-528.225	-444.446			
31	-10.214	1.758	5298.3764	-2.225	-528.224	-444.986			
32	-8.839	0.648	5299.3286	0	-528.09	-429.725			
33	-8.789	0.653	5298.7005	0	-528.109	-430.948			
34	-8.857	0.617	5298.6774	0	-528.11	-431.229			
35	-8.819	0.632	5298.0573	0	-528.105	-431.62			
36	-8.826	0.633	5296.8959	0	-528.105	-433.268			
37	-8.828	0.681	5295.7618	0	-528.107	-434.823			
38	-8.829	0.848	5294.9679	0	-528.106	-435.748			
39	-8.83	0.655	5292.6038	0	-528.105	-436.285			
40	-8.829	0.64	5293.853	0	-528.106	-437.184			
41	-8.712	0.864	5296.7472	0	-527.979	-431.912			
42	-8.68	0.889	5296.8039	0	-528.24	-431.515			
43	-8.533	0.843	5297.2093	0	-528.06	-431.361			
44	-8.582	0.909	5298.3562	0	-527.95	-430.1			
45	-8.487	0.897	5296.8719	0	-528.041	-431.009			
46	-8.538	0.911	5294.9164	0	-528.493	-432.494			
47	-8.848	0.877	5298.0242	0	-527.918	-430.327			
48	-8.385	0.921	5296.1499	0	-528.178	-431.434			
49	-8.345	0.89	5295.5617	0	-528.016	-431.991			
50	-8.369	0.891	5297.471	0	-528.003	-430.709			
51	-9.184	0.355	5299.2714	0	-528.124	-430.403			
52	-9.244	0.085	5302.2409	0	-525.608	-430.281			
53	-9.368	-0.077	5296.1089	0	-530.734	-430.927			
54	-9.302	-0.108	5299.8245	0	-527.375	-430.437			
55	-9.566	-0.229	6302.2194	0	-528.529	-430.457			
56	-9.344	-0.312	5299.8062	0	-527.543	-430.683			
57	-9.639	-0.631	5290.0737	0	-535.887	-431.785			
58	-9.517	-0.531	5303.4072	0	-524.828	-430.368			
59	-9.531	-0.746	5297.3525	0	-529.961	-430.804			
60	-9.475	-0.658	5299.2928	0	-526.867	-432.859			
61	-9.565	-0.939	5301.909	0	-526.675	-429.764			
62	-9.751	-1.161	5305.0973	0	-525.79	-437.445			
63	-9.051	0.791	5301.0197	0	-528.096	-428.539			
64	-8.008	-0.2	5286.5644	0	-528.092	-429.186			
65	-8.305	-0.097	5286.7384	0	-528.094	-428.98			

66	-8.009	-0.057	5289.7174	0	-528.085	-433.457			
57	-7.916	-0.305	5277.2909	0	-528.09	-428.144			
58	-7.395	-0.839	5272.8776	0	-528.092	-429.948			
69	-7.396	-0.851	5288.0696	0	-528.091	-428.824			
70	-7.657	-0.597	5259.3662	0	-528.091	-426.164			
71	-7.702	-1.269	5259.7113	0	-528.069	-429.341			
72	-7.164	-1.571	-	-	-	-			
73	-6.762	-	-	-	-	-			
HOMO, LUMO energy (unitJ), FS*,HB*, ES*, VW*: fs, hb, es, vw energy values of analyte and phenyl-phase complex.									
No Chemical			160	170	180	190	200	210	220
1 Heptane	-	-	-	-	-	-	-	-	
2	Octane	-	-	-	-	-	-	-	-
3	Nonane	-	-	-	-	-	-	-	-
4	Decane	-0.7959	-0.8962	-1.0269	-	-	-	-	-
5	Undecane	-0.5918	-0.699	-0.8239	-	-	-	-	-
6	Dodecane	-0.3851	-0.5045	-0.6271	-0.7235	-0.8297	-	-	-
7	Tridecane	-0.1805	-0.3089	-0.4377	-0.5452	-0.6576	-0.7595	-0.8962	-
8	Tetradecane	0.0216	-0.1169	-0.2366	-0.3605	-0.4895	-0.5986	-0.7282	-0.8013
9	Pentadecane	0.2307	0.0799	-0.064	-0.1959	-0.3171	-0.4377	-0.567	-0.6536
10	Hexadecane	0.432	0.2714	0.1199	-0.0205	-0.1494	-0.2807	-0.4123	-0.5045
11	Heptadecane	0.6273	0.4579	0.2995	0.1511	0.0124	-0.1267	-0.2573	-0.3635
12	Octadecane	0.8201	0.6421	0.4763	0.3201	0.1714	0.0365	-0.1096	-0.2255
13	Nonadecane	1.0163	0.8289	0.6544	0.4902	0.3328	0.1807	0.0378	-0.0804
14	Eicosane	1.2035	1.0097	0.8266	0.6546	0.4867	0.31	0.1821	0.0461
15	Butylalcohol	-	-	-	-	-	-	-	-
16	Pentylalcohol	-	-	-	-	-	-	-	-
17	Hexycylalcohol	-0.8928	-	-	-	-	-	-	-
18	Heptylalcohol	-0.6778	-0.7852	-	-	-	-	-	-
19	Octylalcohol	-0.4647	-0.5841	-0.6757	-0.762	-0.8928	-	-	-
20	Nonylalcohol	-0.2557	-0.3851	-0.4881	-0.585	-0.7144	-0.8013	-	-
21	Decanol	-0.0482	-0.1878	-0.301	-0.4101	-0.5406	-0.6383	-0.7481	-
22	Undecanol	0.1562	0.0099	-0.1073	-0.2277	-0.3645	-0.4711	-0.5884	-0.6968
23	Dodecanol	0.3716	0.2038	0.0766	-0.0521	-0.1952	-0.308	-0.433	-0.5482
24	Tridecanol	0.5674	0.3934	0.2543	0.1159	-0.0315	-0.1524	-0.284	-0.4012
25	Tetradecanoll	0.7597	0.5806	0.4296	0.2817	0.129	-0.0013	-0.1361	-0.2596
26	Pentadecanolol	0.9497	0.7669	0.6025	0.4456	0.288	0.1483	0.0103	-0.1192
27	Hexadecanol	1.1541	0.9576	0.787	0.6213	0.4548	0.3081	0.1605	0.0241
28	Heptadecanolol	1.3435	1.1422	0.959	0.7843	0.6117	0.4562	0.0304	0.1617
29	Octadecanolol	-	1.3334	1.1471	0.9642	0.7827	0.6208	0.4576	0.3084
30	Nonadecanol	-	-	1.311	1.1186	0.9316	0.7599	0.5937	0.4381
31	Eicosanol	-	-	-	-	1.0938	0.914	0.7393	0.5769
32	Toluene	-	-	-	-	-	-	-	-
33	Ethylbenzene	-0.8386	-	-	-	-	-	-	-
34	Propylbenzene	-0.6198	-0.6925	-0.8386	-	-	-	-	-
35	Butylbenzene	-0.4045	-0.4989	-0.6234	-0.7212	-0.7327	-	-	-
36	Hexylbenzene	0.0141	-0.1163	-0.2457	-0.3655	-0.4881	-0.5918	-0.7033	-0.8013
37	Heptylbenzene	0.2148	0.0737	-0.0615	-0.1858	-0.3206	-0.4353	-0.5513	-0.6556

38	Octylbenzene	0.4161	0.2641	0.1219	-0.097	-0.15	-0.2757	-0.3979	-0.5114
39	Nonylbenzene	0.574	0.4329	0.2794	0.1464	0.0103	-0.1146	-0.2343	-0.3429
40	Decylbenzene	0.7794	0.613	0.457	0.3139	0.17	0.039	-0.0867	-0.202
41	1,2-Dimethylbenzene	-	-	-	-	-	-	-	-
42	1,3-Dimethylbenzene	-	-	-	-	-	-	-	-
43	1,4-Dimethylbenzene	-	-	-	-	-	-	-	-
44	1,2,3-Trimethylbenzene	-0.6144	-	-	-	-	-	-	-
45	1,2,4-Trimethylbenzene	-0.4401	-	-	-	-	-	-	-
46	1,3,5-Trimethylbenzene	-0.5376	-	-	-	-	-	-	-
47	1,2,3,4-Tetramethylbenzene	-0.1605	-0.2865	-0.4001	-0.4815	-0.6163	-	-	-
48	1,2,3,5-Tetramethylbezxene	-0.2652	-0.3883	-0.4949	-0.5735	-0.7122	-	-	-
49	1,2,4,5-Tetramethylbenzene	-0.2652	-0.3883	-0.4949	-0.5735	-0.7122	-	-	-
50	Pentamethylbenzene	0.1011	-0.0329	-0.1537	-0.2449	-0.383	-	-	-
51	Chlorobenzene	-1.2518	-	-	-	-	-	-	-
52	1,2-Dichlorobenzene	-0.3354	-0.4401	-0.5575	-0.6536	-0.8182	-	-	-
53	1,3-Dichlorobenzene	-0.7959	-0.8928	-1.0269	-	-	-	-	-
54	1,4-Dichlorobenzene	-0.4353	-0.5287	-0.6556	-	-	--	-	-
55	1,2,3-Trichlorobernzene	0.063	-0.0545	-0.1746	-0.2652	-0.3809	-0.4724	-0.5686	-
56	1,2,4-Trichlorobenzene	-0.0453	-0.163	-0.2823	-0.3645	-0.4828	-0.5702	-0.6615	-
57	1,3,5-Trichlorobenzene	-0.1884	-0.2993	-0.4191	-0.4895	-0.6073	-0.8827	-0.9747	-
58	1,2,3,4-Tetrachlorobenzene	0.4014	0.2697	0.1449	0.0302	-0.0964	-0.3179	-0.4214	-0.5157
59	1,2,3,5-Tetrachlorobenzene	-	-	-	-	-	-	-	-
60	1,2,4,5-Tetrachlorobenzene	-	-	-	-	-	-	-	-
61	Pentachlorobenzene	0.6599	0.5173	0.384	0.3043	0.1284	-0.149	-0.098	-0.2027
62	Hexachlorobenzene	1.0245	0.8685	0.7219	0.5831	0.4444	0.3195	0.197	0.0831
63	Benzene	-1.2757	-	-	-	-	-	-	-
64	Naphthalene	0.037	-0.0857	-0.2041	-0.2858	-0.4112	-0.4949	-0.5654	-0.7033
65	Biphenyl		-	-	-	-	-	-	-
66	Fluorene	0.8594	0.7098	0.5678	0.4362	0.3077	0.1836	0.0748	-0.0487
67	Phenanthrene	1.2788	1.1153	0.9598	0.8118	0.6698	0.5395	0.416	0.2862
68	Anthracene	1.2814	-	0.9697	0.8186	0.6724	0.5408	0.4195	0.2916
69	Pyrene	-	-	-	1.3688	1.2038	1.0554	0.9162	0.7736
70	Chrycene	-	-	-	-	-	-	1.3816	1.2271
71	Tetracene	-	-	-	-	-	-	-	1.2429
72	Benzpyrene	-	-	-	-	-	-	-	-
73	Pentacene	-	-	-	-	-	-	-	-
50%phenyl-phase	5315.5643	0	-528.095	-423.658	-	-	-	-	

References

1. T. Hanai, (ed) Quantitative in silico chromatography, Computational modeling of molecular interaction, Royal Society of Chemistry, Cambridge, 2014, pp.338.
2. E. Riccardi, J-C. Wang, A.I. Liapis, A molecular dynamics study on the transport of a charged biomolecule in a polymer adsorbent medium and its adsorption onto a charged ligand, Journal of Chemical Physics, 2010, 133: 084904.
3. P. Peluso, V. Mamane, E. Aubert, S. Cossu, Insights into the impact of shape and electronic selectors stereo selective halogen bonding interactions, Journal of Chromatography A, 2014, 1345, 182-192.
4. B-H. Kim, S.U. Lee, D.C. Moon, Enantiomer separation of N-t-BOC and N-CBZ a-amino acids and their esters on polysaccharide derived chiral stationary phases, Journal of Liquid Chromatography and Related Technology, 2013, 36, 1899-1914.
5. B-H. Kim, S.U. Lee, D.C. Moon, Chiral recognition of N-phthaloyl, N-tetrachorophthaloyl, and N-naphtaloyl z-amino acids and their esters on po1ysaccharide-derived chiral stationary phases, Chirality, 2012, 24, 1037-1046.

6. B. Natalini, N. Giscche, P. Sardella, F. Ianni, A. Macchiarulo, Computational studies for the elucidation of the enantio1ner elution order of·amino acids in chiral ligand-exchange chromatography, Journal of Chromatography A, 2010, 1217, 7523-7527.
7. L. Cuckovic, IO.M. Hodzic, S.R. Niketic, Computational study of the chromatographic enantio-separation of tris(acetylacetonato)cobalt (Ill) complexes on an arginine complex of cobalt (Ill) acting as a chiral selector, Journal of Serbian Chemical Society, 2002, 67, 735-744.
8. P. Peluso, V. Mamane, E. Aubert, S. Cossu, Insights into the impact of shape and electronic properties the enantio-separation of polyhalogenated 4,4'-bipyridines on polysaccharide-type selectors. Evidence of streoselective halogen bonding interactions, Journal of Chromatography A, 2014, 1345, 182-192.
9. E. Brena, S.L. Cosi, E.E. Ferradi, F. Parmeggiani, A. Sacchetti, Substrate scope and synthetic s of the enantioselective red11ction of D-alkyl-0-arylenones mediated by old yellow enzymes, Biomolecular Chemistry, 2013, 11, 2988-2996.
10. M.M.C. Ferreira, M. Trsic, The influence of R and S configurations of a: series of derivatives on quantitative structure-activity relationship models, Analitica Chimica Aeta, 2013, 759, 43-52.
11. C. Caballotti, C. Salvalaglie, Molecular 1nodeling of the affinity chromatography of' proteins -Status and perspectives, Chimica Oggi-Chemistry Today, 2012, 30, 16-19.
12. I. Noji, A. Oda, K. Kobayashi, O. Takahashi, Computational mvestigation of the substrate recognition mechanisms of protei11 D-aspartyl (L-isoaspartyl) O-methyltransferase by docking and molecular dynamics simulation. studies and application to interpret size exclusion chromatographic data, Journal o,f Chromatograph),B, 2011, 879, 3310-3316.
13. G. Zydek, E. Brzezinska, Normal and reversed-phase thin layer chromatography data in quantitative structure-activity relationship study of compounds with affinity for serotonin (5-HT) receptors, Journal of Chromat9graphy B, 2011, 879, 1764-1772.
14. M. Bonnet, J.U. Flanagan, D.A. Chan, A.J. Giaccia, M.P. Hay, Identifying novel targets in renal cell carcinoma: Design and synthesis of affmity chromatography reagent, Bioorganic and Medicinal C'hemistry, 2014, 22, 711-720.
15. C. Andre, L. Ping, M. Thomassin, J.F. Robert, Y.C. and Guillaume, Modeling of the association mechanisms of a series of rodenticide molecules with lipid membrane investigated by computational chemistry and biochemistry, Analitica Chimica Acta, 2005, 542,]99-206.
16. F. Li, C.D. Nandini, T. Hattori, X. Bao, D. Murayama, T. Nakamura, N. Fukushima, K. Sugahara, Structure of pleiotrophin- and hepatocyte growth factor-binding sulfated hexasaccharide determined by bioche1nical and computational approaches, .J. Bio. Chem., 2010, 285, 27673-27685.
17. M. Koba, T. Baczek, M.P. Marszall, Importance of retention data from affinity and reverse-phase high-performance liquid chromatography on antitumor activity prediction of imidazoacridinon.es using QSAR strategy, J. Pharm. Biom. Anal. 2012, 64-65, 87-93.
18. V. Voicu, I. Sora, C. Sarbu, V. David, A. Medvedovici, Hydrophobicity/hydrophilicity, Descriptors obtained from extrapolated chromatographic retention data as modeling tools for biological distribution: Application to some oxime-type acetylcholinesterase activators, J. Pharm. Biomed. Ana. 2010, 52, 508-516.
19. L. Mao, L.M. Colosi, S. Gao, Q. Huang, Understanding ligninase-mediated reactions of endocrine disrupting chemicals in water: Reaction rates and quantitative structure-activity relationships, Environ. Sci.Technol. 2011, 45, 5966-5972.
20. J. Srividhya, M.J. Mourao, E.J. Crampin, S. Schnell, Enzyme catalyzed reactions: From experiment to computational mechanism recognition, Computationa1Biology and Chemistry, 2010, 34, 11-18.
21. R.A. Friesneer, M-H. Baik, B.F. Gherman, V. Guallar, M. Wirstam, R.I. Murphy, S.J. Lippard, How iron-containing proteins control dioxygen chemistry: a detailed atomic level description via accurate quantum chemical and mixed quantum, mechanics/molecular mechanics calculations, Coordination Chemistry Reviews, 2003, 238-239, 267-290.
22. T. Hanai, HPLC, A Practical Guide, Royal Society of Chemistry, Cambridge, UK, 1999; (ISBN: 0-.85404-515-5),
23. D.J. Pietrzyk, C.H. Chu, Separation of organic acids on Amberlite XAD copolymers by reversed-phase high pressure liquid chromatography, Anal. Chem., 1977, 49, 860-867.
24. T. Hanai, Quantitative explanation of retention mechanisms in reversed-phase mode liquid chromatography, and utilization of typical reversed-phase liquid chromatography for drug discovery, Current Chromatography, 2019, 6, 52-64. DOI: 10.2174/2213240606666190619061912.07.33.
25. T. Hanai, F. Ahmed, I. Rustamov, D. Babusis, Selectivity of phenylhexyl-bonded silica gel for liquid chromatography, J. Liq. Chrom. & Rel. Technol. 1999, 22, 501-511.
26. T. Kurita, Precision of quantitative analysis performed by a combination of isocratic and· column switch elution, vs gradient elution, 28th Chromatography Symposium, Kyoto, 2017,_Nov.15.P-08.
27. T. Hanai, Definition of HILIC system and quantitative analysis of retention 1:ri.echanisms, CC, 2018, 5, 43-52.
28. T. Hanai, .In silica chromatography modeling a new support for alkyl-bonded phases and a solvent phase, J. Anal. Bioanal. Sep. Tech. 2017, 2(2), 111-117.
29. T. Hanai, Separation-of polar compounds-using carbon columns, J. Chromatogr. A, 2003, 989, 183-196
30. A. Kuigariov, U. Trudinger, T. Isaeva, K. Unger, Native and modified alumina, titania and zirconia in normal and reversed-phase high-performance liquid chromatography, Chromatagraphia, 1996, 42, 217-222.
31. McCalley, D.V. Effect of organic solvent modified and nature of solvente on the performance of bonded silica reversed-phase colnmns for the analysis of strongly basic compounds by high-performance liquid chromatography. J Chromatogr. A, 1996, 7B8, 169-179, ibid: 1997, 769, 169-173
32. V. Andrisano, H. Makatnba, E. Ovini, Y. Cavrini, S. Zappoli, HPLC analysis of basic organic compounds in a multi-component ion-interaction system:

a mechanistic study, Chromatographia, 1998, 47, 493-500.

33. M. Anderssoh, U-K. Hultin, A. Sbko1bwski, Effects of amine additives on the resolution of antipsychotic and antidepressant drugs on a cyanoalkyl HPLC co1umn, Chromatographia, 1998, 48, 770-776.
34. R.J.M. Vervoort, E. Ruyter, A.J.J. Debets, (...), C.A. Cramers, G. De Jong, Characterization of reversed-phase stationary phases for the liquid chromatographic analysis of basic pharmaceuticals by thermodynamic data, J Chromatogr. A, 2002, 964, 67-76.
35. A-B.Wu, M-C. Huang, I.F.L. Ho, G-C. Yeh, M-T. Sheu, Investigation on liquid chromatographic separation of basic compounds using silica column with aqueous/organic mobile phase containing triethylamine and acetic acid, Biomed. Chromatogr. 2004, 18, 443-449.
36. X. Wang, P.W. Carr, An unexpected observation concerning the effect of anionic additives on the retention behavior of basic drugs and peptides in reversed-phase liquid chromatography, Journal of Chromatography A., 2007, 1154, 165-173.
37. L. Peng, T. Farkas, Analysis of basic compounds by reversed-phase liquid chromatography-electrospray mass spectrometry in high-pH mobile phases, / Chromatogr. A, 2008, 1179, 131-144.
38. S. Calabuig-Hernandez, M.C. Garcia-Alvarez-Coque, M.J. Ruiz-Angel, Performance of amines as silanol suppressors in reversed-phase liquid chromatography, J Chromatogr. A, 2016, 1465: 98-106.
39. S. Manetto, G. Mazzoccanti, A. Ciogli, C. Villani, F. Gasparrini, F. Ultra-high performance separation of basic compounds on reversed-phase columns packed with fully/superficially porous silica and hybrid particles by using ultraviolet transparent L1ydrophobic cationic additives, J Sep. Sci. 2020, 43, 1653-1662.
40. T. Hanai, Chromatography in silica for basic drugs, J Chromatogr. Rel. Technol. 2005, 28, 2163-2177.
41. C. Stella, S. Rudaz, M. Mottaz, P-A. Carrupt, J-L. Veuthey, Analysis of basic compounds at high pH values·by reversed-phase liquid chromatography, J. Sep. Sci., 2004, 27, 284-292.
42. T. Hanai, Y. Masuda, H. Homma, H. Chromatography in silica; retention of basic compounds on a carboxyl ion exchanger, J. Liq. Chromatogr. Rel. Technol., 2005, 28, 3087-3097.
43. H. Luo, L. Ma, Y. Zhang, P.W. Carr, Synthesis and characterization of silica-based hyper-crosslinked su1fonate-modified reversed stationary phases, J Chromatogr. A, 2008, 1182, 41-55.
44. H. Luo, L. Ma, C. Paek, P.W. Carr, Application of silica-based hyper-crosslinked. sulfonate-modified reversed stationary phases for separating highly hydrophilic basic compounds, J Chromatogr. A, 2008, 1202, 8-18.
45. P.E. Morgan, V. Manwaring, R.JK. Flanagan, HPLC of basic drugs using non-aqueous ionic eluents: Evaluation of a 3 mm strong cation-exchange material, Biomed. Chromatogr. 2010, 24, 318-323.
46. Y. Zhang, P.W. Carr, Novel ultra-stable silica-based stationary phases for reversed-phase liquid chromatography-Study of a hydrophobically assisted weak acid cation exchange phase, J Chromatogr. A, 2011, 1218, 763-777.
47. L. Mosiashvili, L. Chankvetadze, T. Farkas, B. Chankvetadze, On the effect of basic and acidic additives on the separation of the enantiomers of some basic drugs with polysaccharide-based chiral selectors and polar organic mobile phases, J: Chromatogr. A, 2013.1317,167-174.
48. Z. Huo, Q. Wan, L. Chen, Synthesis and evaluation of porous polymethylsilses-quioxane microspheres as low silanol activity chromatographic stationary phase for basic compound separation, J Chromatogr. A, 2018, 1553, 90-100.
49. T. Hanai, H. Hatano, N. Nimura, T. Kinoshita, Molecular recognition in chromatography aided by computational chemistry, Supramol. Chem. 1994, 3, 243-247.
50. P.N. Craig, Drug compendit1m, in Comprehensive Medicinal Chemistry: the Rational Design, Mechanic study and therapeutic, Application of Chemical compounds, ed. C. Hansch, P.G. Sammes J.B. Taylor, Pergamon Press, Oxford, 1990, vol. 6, 237-965.
51. B.A. Adams, R.L. Holmes, Synthetic ion-exchange resins, J. Soc. Chem. Ind. 1935, 54, I-6T.
52. D.H. Spackman, E.H. Stein, S. Moore, Automatic recording apparatus for use in the chromatography of amino acids, Anal. Chem., 1958, 42, 1190-1206. doi: org/10.1021/ac60139a006
53. W. Funasaka, T. Ando, K. Fujimura T. Hanai, T. Non-aqueous solvent\ chromatography. I. Liquid chromatography of mono and disubstituted benzene derivatives with anion exchange resin and ethanol. Bunseki Kagaku 1971, 20(4), 427-30. Doi.org/10.2116/bw-isekikagaku.20.427
54. T.W. Creekmore, C.N. Reilley, Nuclear magnetic resonance study of ion-exchange resins. Anal/ Chem. 1970, 42, 570-575. doi: 10.1021/ac60288a014.
55. T.E. Gough, H.D. Sharma, N. Subramanian, Proton magnetic resonance studies of ionic solvation in ion-exchange resins. Part 1-. Sulfonated cation-exchange resins, Can. J. Chem. 1970, 48, 917-923. doi: 1O.l 139/v70-l 5l.
56. W. Funasaka, T. Hanai, Estimation of adsorption mechanisms using NMR and ESCA, Proceeding of the annual autumn symposium of Chubu Kagaku Kanrenkyokai, Nagoya, September·1974, IE04.
57. T. Hanai, H. Hatano, N. Nimura, T. Kinoshita, Computational cb,e1nical analysis of retention on an ion-exchange resin in normal-phase liquid chromatography, Editors H. Hatano, T. Hanai, International symposium on chromatography, Yokohama, World Sci. Singapore, Jan. 1995, 97-103. ISBN 981-02-2104-5
58. H.F. Walton, Ion-exchange chromatography, Editor Heftman E. Chromatography fundamentals and applications of chromatographic and electrophoretic methods, Elsevier, Amsterdam, 1983, A225-A255, ISBN 0-444-42043-6
59. O.B. Aikara, Ion-exchange chromatography and its applications, Column chromatography, Chapter 2, Intechopen, London, UK, 201.3, 32-58, http://

dx.doi.org/0.5772/55744.

60. T. Hanai, Polysiliconedioxide phase Fundamental Properties of Packing Materials for Liquid Chromatography, Separation, 2019, 6(2), l-20, doi: 10.3390/separations6010002 www.1ndpi.com/journal/separations

61. T. Hanai, Liquid chromatography of carbohydrates, Adv. Chromatogr. 1986, 25, 278-307

62. T. Hanai, R. Miyazaki, J. Suzuki, T. Kinoshita, Computational chemical analysis of newly developed guanidino-phase for quantitative analysis of saccharides in liquid chromatography, J. Liq. Chromatogr. Rel. Technol. 1997, 20, 2941-2948.

63. T. Hanai, J. Hubert, Chromatography of aromatic acids on ion-exchangers, J. Chromatogr. A, 1984, 316, 261-265.

64. T. Hanai, J. Hubert, J. Chromatographic behavior of acids on macroporous polystyrene gels, Chromatographia, 1983, 17, 633-639.

65. T. Hanai, K.C. Tran, J. Hubert, Prediction of retentions for aromatic acids in liquid chromatography, J. Chromatogr., 1982, 239, 385-394.

66. M. Rose, E. Bosch, Influence of mobile phase acid-base equilibria on the chromatographic behavior of protolytic compounds, J. Chromatogr. A, 2002, 982, 1-30.

67. J.L. van de Verne, H.M. Hendrikx, R.S. Deelder, Retention behavior of carboxylic acids in reversed-phase column liquid chromatography, J. Chromatogr., 1987, 167, 1-16.

68. T. Hanai, H. Walton, J.D. Navratil, D. Warren, Liquid chromatography of polar aromatic compounds on cation exchange resins and porous polymer gels, J. Chromatogr., 1978, 155, 264-271.

69. T. Hanai, In silico chromatography: Modeling new support for alkyl-bonded phases and a solvent phase, J. Anal. .Bioanal. Sep. Tech. 2017, 2, 111-117. doi:10.15436/2476-1869.17.1743 OMEGA Pub. 2017-12-29

70. T. Hanai, A. Koseki, R. Yoshikawa, M. Ue.no, T. Kinoshita, H. Homma, Prediction of human serum albumin-drug binding affinity without albumin. Analytica Chimica Acta 2002, 454 (I), 101-108. doi.org/10.1016/50003-2670(01)01515-X

71. T. Hanai, R. Miyazaki, T. Kinoshita, Quantitative analysis of human serum albumin-drug interactions using reversed-phase and ion-exchange liquid chromatography, Anal. Chim. Acta, 1999, 378, 77-82.

72. K. Koizumi, C. Ikeda, M. Ito, J. Suzuki, T. Kinoshita, K. Yasukawa, T. Hanai, Influence of glycosylation on the drug binding ofl1uman serum albumin, Biomedical Chromatography: BMC, 1998, 12, 203-10. Journal code: 8610241. ISSN:0269-3879.

73. T. Hanai, Chromatography and computational chemical analysis for drug discovery. Current Medicinal Chemistry, 2005, 12, 501-525. doi:10.2174/0929867310504050501

74. T. Hanai, Quantitative explanation of basic compound retention mechanisms in reversed-phase mode liquid chromatography, Separations, 2020, 7, 61 (30 October 2020) doi:10.20977/preprints202009.007.vl,1-11, doi.org/10.3390/separations7040061

75. J.X. Khym, L.P. Zill, The separation of sugars by ion exchange, J. Am. Chem. Soc. 1952, 74, 2090-2094.

76. B. Arwidi, O. Sa1muelson, Partition chromatography of sugars on ion-exchange resins, Svensk Kemish Tidskift, 1965, 77, 2.

77. R.H. Marchessault, S. Coulombe, T. Hanai, H. Morikawa,. Monomers and oligomers from wood. Transactions of the Technical Section (Canadian Pulp and Paper Association), 1980, 6(2), TR52-TR56.

78. T. Hanai, Hydrophilic interaction liquid chromatography for LC-MS, Mass Spectrom. Purif. Tech. 2018, 4, 1, doi: 10.4172/2469-9861.1000123, Properties of amino and guanidino groups

79. M. Hirukawa, M. Maeda, A. Tsuji, T. Hanai, Separation of free amino acids by reversed-phase ion-pair chromatography with column switching and isocratic elution, J. Chromatogr,. 1990, 507, 95-101.

80. T. Hanai, Quantitative in silico analysis of retention of phenylthiohydantoin-amino acids in reversed-phase ion-pair liquid chromatography, J. Chromatogr. Sci. Advance access published, Jan, 13, 2016, 1-5, 54, 2016, 604-608.

81. T. Hanai, Quantitative in silico analysis of organic modifier effect on retention in reversed-phase liquid chromatography, J, Chromatogr, Sci. 2014, 52, 75-80.

82. T. Hanai, M. Sekine, H. Homma, Quantitative In Silico Analysis of Retention of Nitrobenzofurazan-Amino Acids in Reversed-Phase Ion-Pair Liquid Chromatography, J Chromatogr Sci. 2016, 54 (10):1723-1726. doi: J. Chromatogr. Sci. Advance access published, Sept. 27, 2016, 1-5, Doi: 10.1093/chroma/sci/bmw128.:54, 2016,1723-1726.

83. K. Imai, Method of detection, separation and identification for expressed trace protein/peptide, EPO5482 A2, 2003.

84. M. Sekine, H. Fukuda, N. Nimura, T. Furuchi, H. Homma, Automated column-switching high-performance liquid chromatography system for quantifying N-methyl-D- and L-aspartate, Anal. Biochem. 2002, 310, 114-121.

85. T. Hanai, K. Kaneko, H. Homma, Semi-micro liquid chromatography of aromatic amino acid metabolites using isocratic elution and Column switching, Biom. Chromatogr., 2002, 03 September, https://doi.org/10.1002/bmc.176Digital Object Identifier (DOI)

86. J.J. Kirkland, J.H. DeStefano, Controlled surface porosity supports with chemically-bonded organic stationary phases for gas and liquid chromatography, J. Chrom. Sci. 1970, 8, 309-314.

87. M. Ohhira, F. Ohmura, T. Hanai, Inertness of bonded silica gel packings, J. Liq. Chromatogr. 1989, 12, 1065-1074.

88. T. Hanai, Synthesis and properties of stable bonded silica gel packings and the performances, T. Hanai, H. Hatasno, H, (eds), Advances in liquid chromatography, World Sci. Pub. Singapore, 1996, 307-329.

89. D.V. MaCally, Effect of organic modifier and nature of solute on the performance of bonded silica reversed-phase columns for the analysis of stroi\ ng basic compounds by high-performance liquid chromatography, J. Chromatogr. A, 1996, 738, 169-179.

90. K.I. Mapihan, J. Vial, A. Jardy, Reversed-phase liquid chromatography column testing robustness study of the test, J. Chromatogr, A, 2004, 1061, 149-158.

91. C. Stella, S. Rudaz, J.H. Gauvrit, P. Lanteri, A. Huteau, A. Tchapla, J.I. Veuthey, Characterization and comparison of the chromatographic performance of different types of reversed-phase stationary phases, J. Pharm. Biomed. Anal. 2007, 43, 89-98.

92. K.I. Mapihan, J. Vial, A. Jardy, A. Reversed-phase liquid chromatography column testing and classification: Physicochemical interpretation based on a wide set of stationary phase, J. Chromatogr. A, 2007, 1144, 183-196.

93. D.V. MaCally, The challenge of the analysis of basic compounds by high performance liquid chromatography; Some possible approaches for improved separations, J. Chromatogr. A, 2010, 1217, 858-880.

94. R.L. Gwada, W. Szwere, M. Aletanska-Kozak, A. Klimek-Turek, A. Torbicz, A. Chomicki, R. Kocjan, D. Matosiuk, T.H. Dzido, The influence of metallic impurities on the free silanol activity of commercial thin-layer chromatography adsorbents demonstrated by retention changes of basic/amphoteric compounds such as peptides, J. Planar Chromatogr. – Modern TLC, 2017, 30, 375-385.

95. Huo, L. Chen, Base-deactivated and alkaline-resistant chromatographic stationary phase based on functionalized polymethylsilsesquioxane microspheres, J. Sep. Sci. 2020, 43, 389-397. https://doi.org/10.1002/jssc.201900634

96. T. Hanai, New developments in liquid chromatographic stationary phases, Adv. In Chromatogr. 2000, 40, 315-357.

97. T. Hanai, Fundamental properties of packing materials for liquid chromatography, Separations, 2019, http://creativecommons.org/lisenses. by/4.0/

98. T. Hanai, C. Hong, Structure-retention correlation in CGC, J. HRC, 1989, 12, 327-332.

99. R.L. Laub, R.L.. Pecsok, (eds), "Physicochemical applications of gas chromatography," 1978, John Wiley & Sons, New York.

100. D.R. Lide, (ed), Handbook of Chemistry and Physics, 71st Edition, p.15, CRC Press, Boca Raton, 1991-1991.

101. T. Hanai, H. Hatano, N. Nimura, T. Kinoshita, T. Enthalpy and boiling point in capillary column gas chromatography, Anal. Sci. 1993, 9, 43-46.

102. T. Hanai, Quantitative in silico analysis of retention time on methylsilicone and polyethyleneglycol phases in capillary gas chromatography, Internet-Chromatography, 2010, 15 pages, http://www.internet-chromatography.com/html/toshihikbeitrage.html.

103. T. Hanai, Quantitative in silico analysis of retention time on methylsilicone and polyethyleneglycol phases in capillary gas chromatography 2, Internet-Chromatography, 2011, 4 pages, http://www.internet-chromatography.com/html/toshihikbeitrage.html.

104. T. Hanai, Quantitative in silico analysis of retention time on 50% phenylmethyl phases in capillary gas chromatography, Internet-Chromatography, 2012, 12 pages, included in the book, http://www.internet-chromatography.com/html/toshihikbeitrage.html.

Chapter 8: Enantiomer Recognition, Introduction of Fundamental Enantiomer Recognition Mechanisms

Instrumental development of chromatography has advanced well. The combination of chromatography and mass spectrometry has also succeeded. No further dynamic instrumental development seems exciting; however, the chemistry of chromatography has not been well developed. If we understand the chemistry of chromatography, we may separate target compounds using a column with a few theoretical plates. Especially, designing and preparing affinity phases require a wider range of chemical knowledge. How to design and develop of one chiral phase, which we can use for the separation of a variety of compounds, is not simple. So, called Pirkle-type phases have separation power in normal-phase conditions, but many compounds are mainly in aqueous conditions. Polysaccharide phases can be used in aqueous conditions, but the separation power is not satisfactory. We have to develop practical phases for biochemistry's requirements. On the other hand, the so-called affinity phase, based on proteins, is powerful for the biomedical field. Still, its synthesis is not easily developed, and it costs a lot to prepare for preparative-scale requirements.

Since different types of chiral selectors were reviewed, Oi [1] reviewed small-molecule, so-called Pirkle-type chiral selectors; Yashima and Okamoto [2] summarized the developed polysaccharide-related chiral selectors; and Oda and Miwa [3] described protein-related chiral selectors. Furthermore, the first quantitative explanation of enantiomer recognition mechanisms was summarized in 2014 [4]; the fundamental approaches were later published online as textbook chapters for teaching and self-learning for undergraduate students [5], and numerous reports have been published as research papers, reviews, and books. Based on a Scopus search, the total publications have exceeded 8000 since 2017.

8.1 Introduction of fundamental enantiomer recognition mechanisms

Most public data show that the recognition mechanism is a combination of hydrogen bonding and steric hindrance. Primary enantiomer recognition is generally hydrogen bonding at the contact center, and steric hindrance affects contact affinity. Another contact center is due to ligand formation [6, 7].Here, the *in silico* analyzed results are demonstrated. The molecular recognition mechanisms in chiral and affinity chromatography are the same. They combine van der Waals forces, hydrogen bonding, and electrostatic interactions, excluding ion-ion interactions and steric effects. Present Pirkle-type bonded phases are not perfect for the quantitative analysis of the retention mechanism due to the existence of silanol groups on the surface of bonded-phase silica gels. Silanol groups may interact with analytes through hydrogen bonding, which is considered the most important molecular interaction in normal-phase liquid chromatography. The contact surface area on the twisted polymers is the critical molecular interaction force with the derivatized polysaccharide, including cellulose and amylose phases. A simple example is the chiral recognition of cyclodextrin-phase, where the inside of cyclodextrin-phases can be considered a screw nut, and analytes can be considered a screw bolt. The nut-and-bolt fit was the main difference in chiral recognition [4].

On the other hand, proteins have very complicated structures and can show selectivity in their activity, including enantiomer recognition. The enzyme from the yeast has less selectivity than that of humans. However, engineers prepare enzymes from yeast because they are readily available. Structural information from thermostable enzymes from high-temperature environments is very helpful in designing engineered enzymes.

8.2 Pirkle type chiral selectors

The chiral recognition of chiral separation phases depends on the fitting affinity. One chiral compound contacts the chiral recognition phase well, while another does not contact it as tightly. Usually, the contact center forms hydrogen bonds, and steric hindrance affects contact tightness. Non-aqueous liquid chromatography is used to utilize hydrogen bonding effectively. Two types of chiral phases are commonly used: derivatized amino acids and polysaccharides and proteins. Polymer-type chiral phases have low resolution, but they do not require analyte derivatization; derivatized amino acid chiral phases have high resolution, but a single column cannot separate multiple compounds. The silica gel support is unstable in aqueous solution.

Pirkle developed derivatized amino acid-bonded silica gel for enantiomer separation. Several amino acid-derivatized phases have been developed to expand the enantiomer separation capability. Figure 8.1 shows the chemical structure of *N*-(*S*)-1-(α-naphthyl)ethylaminocarbonyl-(*S*)-valylaminobutane. The enantiomer selectivity cannot be understood from this 2D structure. Figure 2 shows the enantiomer-recognition structure, with complex structures of *R*-acetylalanine

and *S*-acetylalanine. The atomic sizes of acetylalanine and the chiral recognition molecules are 0.3 and 0.2, respectively. Red (black), blue (dark gray), yellow (light gray), and white represent oxygen, nitrogen, carbon, and hydrogen. Viewing the structure from one direction does not clarify enantiomer recognition; however, viewing the rotation clarifies the conformation, in which two amino hydrogens of the enantioselector contact the amino acid carbonyl oxygen to form hydrogen bonding. The calculated molecular interaction energy values support enantiomer recognition [6,7].

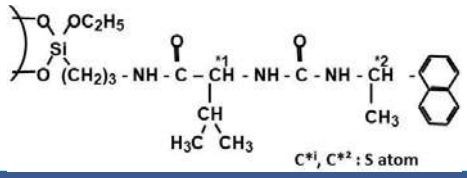


FIgure 8.1: Structure of enantiomer recognition

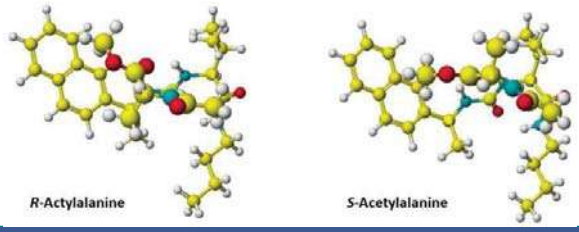


FIgure 8.2: Stereo structures of R- and S- acetylalanine group recognition.

The recognition mechanisms are considered as a combination of hydrogen bonding, dipole-dipole interaction, and hydrophobic interaction. The molecular interaction energy values calculated from Figure 8.2 structures provide a clear answer. The feasibility of tight contact depends on their structure difference. These two molecules pull each other at the strongest contact center; however, the steric hindrance affects the tight contact. We do not need to consider three-point contact sites; one hydrogen site and steric hindrance are fundamentally required.

The derivatized amino acid is bonded to silica gel *via* an alkyl ligand. The alkyl chain length affects enantiomer recognition because it determines the available molecular recognition space. Usually, these derivatized amino acids are bound to propylamino-bonded silica gels. Propylamine-bonded silica gels are not prepared by secondary silylation; therefore, free silanol groups that form hydrogen bonds exist on the silica gel surface. Figure 8.3 shows the location of silanol groups around the bonded enantioselector. Only one of the three ethoxy groups of the silyl reagent can bind with silica gel silanol. Figure 8.3 shows the propylamine bound by an enantioselector. The atomsize of these enantioselectors is 1.0, and that of othersis 0.2 for the easy recognition of the coverage of enantioselectors on the silica gel surface. One enantioselector covers at least seven silanol groups in Figure 8.4. Although the bonding reaction of derivatized amino acids is complete, free propylamine exists; therefore, the textbook's explanation of enantiomer recognition is doubtful.

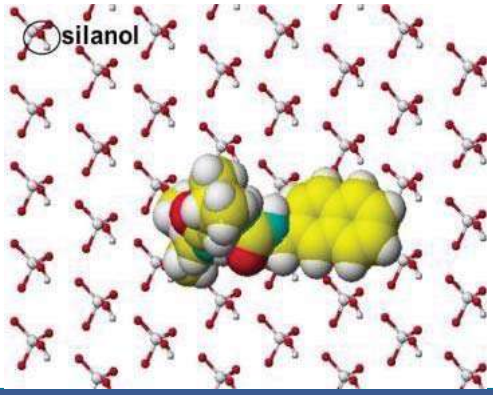


FIgure 8.3: Enantiomer selector bonded silica gel.

The unreacted amino groups may contribute to retention via hydrogen bonding. The calculated molecular interaction energy using model phases may not relate to the separation factor α. The theoretical analysis of enantiomer recognition

mechanisms requires the development of new types of alkyl ligands. Figure 8.5 demonstrates the alkyl chain length effect: acetylalanine contacts the derivatized amino acid and silica gel silanol (B). When end-capped hexylamine is used to bind the enantioselector, contact between acetylalanine and the silanol group is avoided (C).

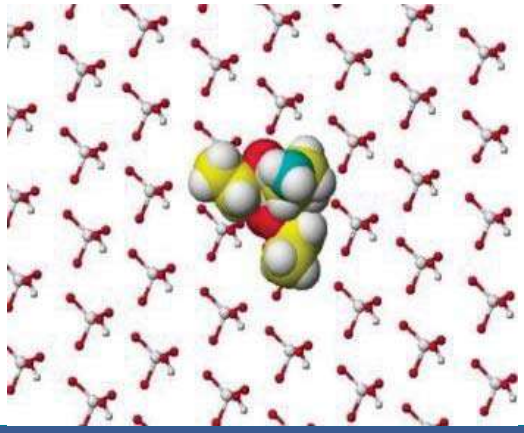


FIgure 8.4: Enantiomer selector bonded propylamino- silica.

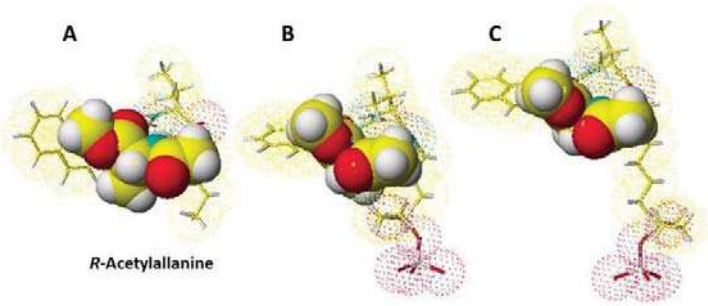


FIgure 8.5: Alkyl ligand length effect for enantiomer recognition A: complex conformation with *R*-acetylalanine, B: Aminopropyldiethoxy bonded chiralselector. Unreacted ethoxy contact with R-acetylalanine, C: diethylhexylamine bonded enantioselector. R-acetylalanine is free from active hydrogen-bonding silanol.

A precise explanation of enantiomer recognition mechanisms requires a bonded phase without extra silanol and methoxy or ethoxy effects; otherwise, the analyte contacts silanol and unreacted methoxy or ethoxy groups via hydrogen bonding. Figures 8.5 and 6 show model chiral bonded groups with end-capped hexylamine-bonded silica gel demonstrated [8]. The molecular size of the chiral selector indicatesthatall enantioselectors can not bind with amino groups; therefore, low-density hexylamine bonded silica gel is demanded. The alkyl ligand length contribution is studied by comparing propylamine- and hexylamine-bonded chiral selectors from their *R*-acetylamine complexes. The aceylalanine does not geometrically contact the silanol of the hexylamine-bonded enantioselector. We calculated the molecular interaction energy values for these enantioselectors with *R*- and *S*-acetylalanines. The calculated interaction energy values are summarized in Table 8.1.

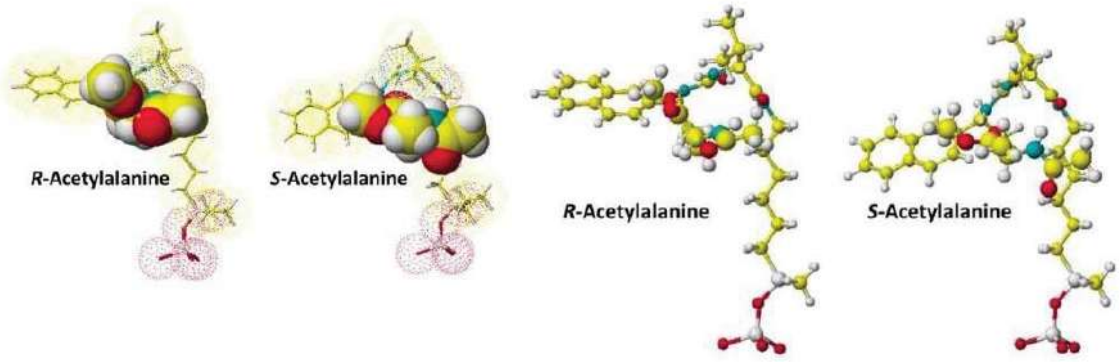


FIgure 8.6: Acetylalanine enantiomer recognition of propylamine and hexylamine bonded enantioselectors.

Table 8.1: Ligand length effect to enantiomer recognition.

Ligand	Aminopropyldiethoxy	Aminohexyldimethyl				
	MIHB	MIES	MIVW	MIHB	MIES	MIVW
R-Acetylamine	9.111	7.872	11.183	9.145	7.65	9.438
S-Acetylamine	10.734	5.907	12.261	10.352	5.472	9.613
unit: kcal·mol^{-1}						

The above-calculated results show that these chiral selectors' enantiomer-recognition power is identical if silanol and ethoxy oxygen do not contact these analytes; therefore, ligand length does not directly affect enantiomer recognition. The longer the ligand length, the easier the model analysis. Considering the mass of the chiral selector, silica gel silanol groups, and silyl-reagent oxygen suggests designing enantiomer-selectively bonded silica gels. Dinitrobenzoyl derivatization, instead of acetylation, is also performed for enantiomer separation. Figure 8.7 shows the structures of dinitrobenzoyl-derivatized alanine enantiomers.

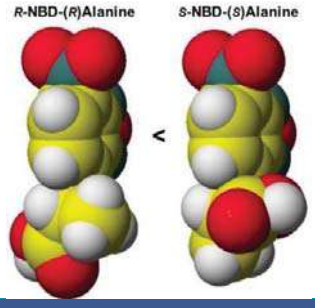


Figure 8.7: Structures of NBD derivatized alanine enantiomers.

The enantiomers of *N*'-nitrosonornicotine in human urine [9] were separated using a Pirkle column (1-(3,5-dinitrobenzamido)-1,2,3,4-tetrahydrophenanthrene bonded silica gel), and the separation mechanisms are the same as those of acetylation compounds. The chiral sector was used to synthesize preparative scale columns for a chiral derivative of xanthone and anti-flammatory drug naproxen, even though this type of chiralselector usually requires pre-derivatization of analytes to enhance enantiomer recognition. However, the high enantiomeric resolution shortens analysis time. [10]. Considering *N*'-nitrosonornicotine, the enantiomer recognition center is the cyano group (circles in Figure 8.8). We calculated the electron localization of the cyano group and showed the electrophilic superdelocalization in Figure 8.9. The nitrogen of the cyano group exhibited higher electrodensity.

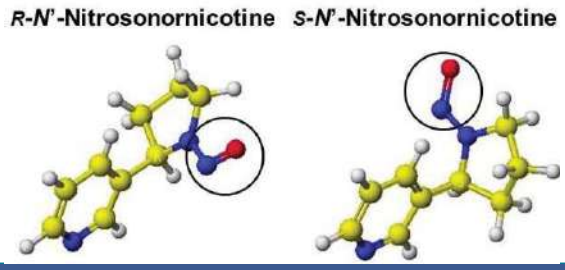


Figure 8.8: Structures of *R*- and S-Nitrosonornicotine.

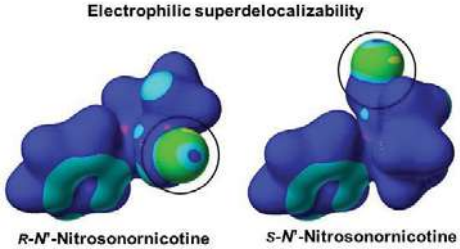


Figure 8.9: Electrophylic superdelocalizability of nitrosonornicotine, the cyano group is circled: light color: high electondencity.

Analysis of electro-localized points in analytes supports identifying the enantiomer recognition center of both analytes and the chiral selectors. Figure 8.10 shows the docked and optimized structures of these analytes with the Pirkle-type chiral selector Whelk-01.

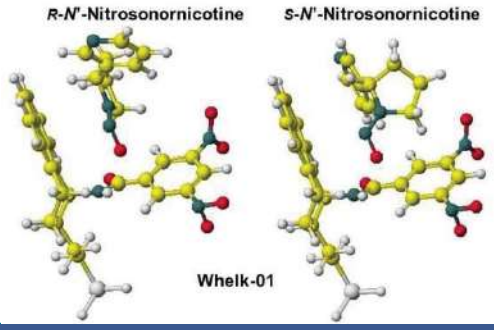


Figure 8.10: Structures of *N'*-nitrosonornicotine enantiomers with a chiral selector Whelk-01.

This chiral selector separated enantiomers of derivatized xanthone. Figure 8.11 shows the complex with s-xanthone, which demonstrates the hydrogen-bonding site between the NH hydrogen and the CO oxygen. The calculated molecular interaction energy values summarized in Table 8.2 support the enantioseparation.

Table 8.2: Enantiomer recognition of Whelk-01 unit: kcal·mol^{-1}.

	fs	hb	es	vw	MIFS	MIHB	MIES	MIVW
R-N'- nitrosonornicotione	6.697	0	-0.817	4.596	10.983	2.645	0.068	8.295
S-N'- nitrosonornicotione	7.539	0	-0.814	4.765	12.847	2.721	0.03	10.045
R-Xanthone	-26.744	-5.519	-13.009	11.459	26.508	7.452	3.737	16.781
S-Xanthone	-25.811	-4.641	-15.696	16.865	27.769	8.474	1.194	16.242
Whrek-01	-28.266	-4.591	-16.124	15.158				

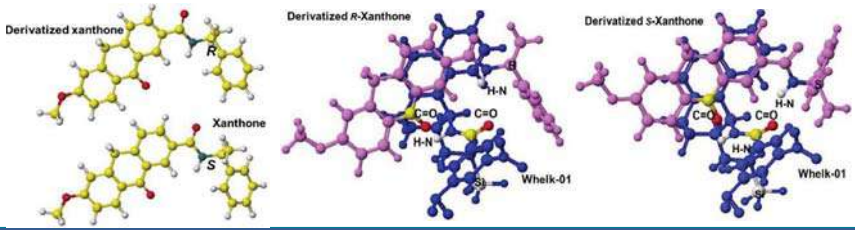


Figure 8.11: The structure of and S-derivatized xanthone and Whelk-01 complex.

The calculated molecular interaction energy values indicated thaton is van der Waals forces were the major molecular interaction forces; however, hydrogen-bonding energy values indicated the recognition center.

8.3. Enantiomer separation as diastereomers

Total amino acid enantiomer separation is performed as derivatized diastereomers using reversed-phase liquid chromatography. Examples of derivatization reagents are *o*-phthalaldehyde-*N*-acetyl-*L*-cysteine and *N*-*t*-butylthiocarbonyl-*L*-cysteine [11]. However, these reagents are unstable and should be prepared before derivatization. Figure 12 shows the structures of (+)-1-(9-fluorenyl)ethyl (FLE)- derivatized *R*- and *S*-arginine.

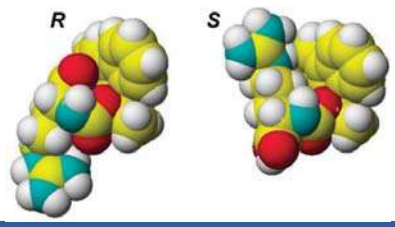


Figure 8.12: FLE derivatized R- and S-arginine.

The FLE derivatized *S*-amino acids retain longer than that of *R*-amino acids, and the MI energy values calculated using a model phase demonstrated the correlation coefficient of 0.938 (n = 14) with measured log *k* values. 4-Fluoro-7-nitrobenzofuran was used as a highly sensitive derivatization reagent at low reaction temperature [12]. Figure 8.13 shows the structures of derivatized 4-amino-3-(4-chlorophenyl)benzoic acid and 2-amino-3-phenylpropanoic acid.

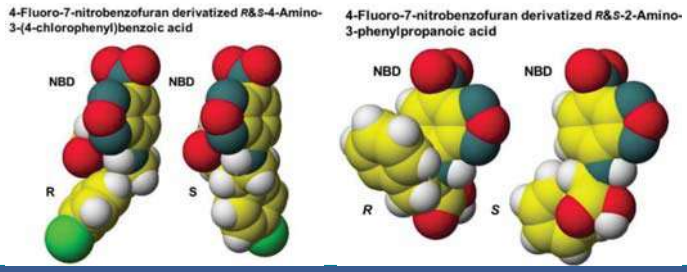


FIgure 8.13: Stereo structures of derivatized *R*- and *S*-aspartic acids.

Two axially chiral reagents were derived from 6,6'-dimethyl-2,2'-biphenyl diamine and evaluated for separating *R*- and *S*-amino acids with high sensitivity. Derivatized *R*-Amino acid was eluted before *S*-amino acid suitable method to analyze a trace amount of *R*-amino acids. Atto mole detection limits were demonstrated in the range of 7.0-127 amol [13]. The stereo structures of derivatized arginine are shown in Figure 8.14.

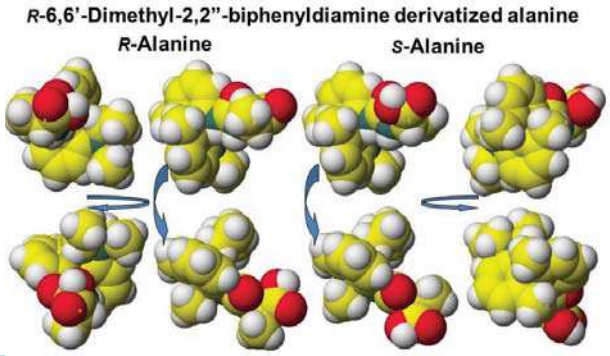


FIgure 8.14: Structures of alanine diastereomer derivatized dimethyl-2,2'-biphenyldiamine.

(*S*)-1-(5-(4-Methylpiperazine-1-yl)-2,4-dinitrophenyl)pyrrolidine-2-carboxylic acid was used for analyzing(*R*)-1-aminoindan metabolites [14].2,3,4,6-Tetra-*O*-acetyl-β-glucopyranosyl isothiocyanate was used for chiral derivatization of Ammuxetine (a novel chiral antidepressant candidate compound) [15].

8.4. Chiral derivatization for gas chromatographic analysis

Diastereomer derivatization has been developed for amino acid enantiomers analysis using liquid chromatography. Such diastereomer derivatization was also applied to gas-chromatographic enantiomer analysis of perfluorooctanoic acid in river water [16]. The (*S*)- 1-phenethyl esters of perfluorooctanoic acids were detected usingamass-spectrophotometer, but these compounds should be detected using an electron-capturedetector with high sensitivity. The structure of *S*-1-phenetyl derivatized 3-methylperfluoroheptanoic acid diastereomer is shown in Figure 8.15. (−)-Camphanic acid derivatives of dextrodropropizine enantiomers were analyzed as highly sensitive detection [17]. A visual chiral-recognition colorimetric sensor of ketoprofen enantiomers was developed using *S*-cysteine-capped silver nanoparticles (*S*-Cys-AgNPs), with a detection limit of 4.52 μM [18]. Enantiomeric profiling of amphetamines in wastewater was analyzed by gas chromatography-tandem mass spectrometry using *S*(-)-α-methoxy-α-(trifluoromethyl) phenylacetyl chloride as a derivatizing agent [19].

8.5. Ligand exchange chiral selector

Amino acid enantiomers are also separated using ligand-exchange liquid chromatography with an aqueous eluent. The structure of the *R*- and *S*-tyrosine complex with a binuclear Cu (II) derivative of *N*-salicylidene-(*R*)-2-amino-1,1-bis(2-butoxy-5-*tert*-butylphenyl)-3-phenyl-1-propanol is shown in Figure 8.16. The enantiomer recognition can be identified from their structures; however, the calculated MI energy values clarify the difference [20].

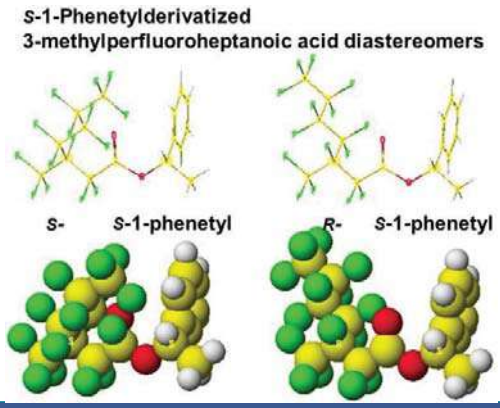


FIgure 8.15: Optimized structures of S-1-phenetyl derivatized 3-methylperfluoroheptanoic acid diastereomers.

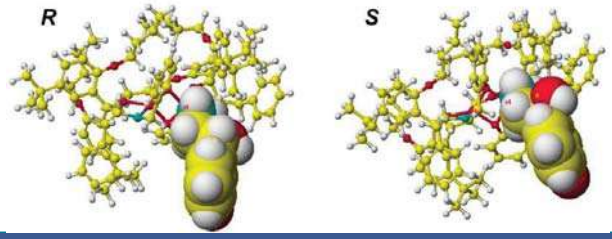


FIgure 8.16: Structure of ligand exchange complexes of R- and S-tyrosines. Green (gray), red (black), blue (dark gray), yellow (light gray), and white are copper, oxygen, nitrogen, carbon, and hydrogen atoms.

Tryptophan enantiomers were separated using *S*-cysteine-modified $ZnFe_2O_4$ nanoparticles via a Cu^{2+} ligand-exchange mechanism [21]. Glutathione-covered copper-platinum nanoparticles were shown to be a chiral selector for tyrosine enantiomers [22]. Ofloxacin and related enantiomers were separated using chiral ligand exchange liquid chromatography [23]. Atenolol enantiomers and their acid/alkaline degradation impurities were analyzed using chiral ligand exchange stationary phases [24]. Diastereo selective synthesis of an amidine-bridged biaryl ligand was achieved. The ring-closing reaction of racemic Atropos biphenyl 6,60-dimethoxy-[1,10-biphenyl]-2,20-dicarboxylic acid with (*R, R*)-diaminocyclohexane yields the diastereomerically and enantiomerically pure cyclic (Sax, *R, R*)-BIPOL, which can be used as a versatile chiral ligand. [25].

8.6. Crown ether as chiral selector

Crown ether is like a king's crown, and oxygen atoms circle inside the crown; therefore, the center of the crown is anionic. The anionic degree can be understood from the apc values of the inside oxygen calculated by the MOPAC program. The specific structure of crown ethers makes them selective 1A alkali-metal trappers. A large-ring crown ether can trap a cesium ion, as shown in Figure 8.17.

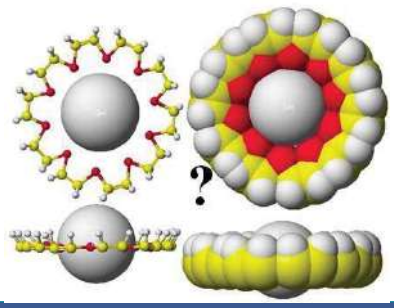


FIgure 8.17: Cesium trapped crown ether

As the crown ether traps cesium as a cation, the positively charged amino group is trapped inside the crown ether, and the amino acid carboxy oxygen forms hydrogen bonding with the crown ether oxygen, as shown in Figure 8.18, which shows the crown ether structure and its complex with *R*- and *S*-alanine. In addition, amino acid carboxy hydrogen contacts

with the near phenyl group produce high molecular interaction energy for the *S*-form, leading to longer retention time. Free amino acid enantiomers are separated using a crown ether bonded phase [26]. Supercritical fluid chromatography (SFC) for the analysis of chiral amino acids was performed using a CROWNPAK CR-I (+) column [27].

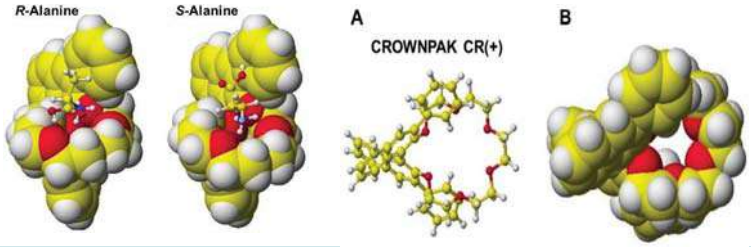


FIgure 8.18: Crown ether as enantio-separator and their complexes with R- and S-alanine.

8.7. Cyclodextrin derivatives as chiral selectors

The need for enantioselective properties, especially in drug development, has accelerated the development of enantiomer separation methods; therefore, various enantiomer-selective phases have been developed for liquid chromatography. Amino acids and saccharides are natural enantiomers; therefore, proteins and polysaccharides have been used as chiral selectors.

Derivatized celluloses can separate enantiomers of various molecules. However, the separation capability is less than that of derivatized amino acids, and the enantiomer recognition mechanisms are not well explained. Cellulose fibers are twisted, and the molecules twisted in the same direction contact tightly compared to the molecules twisted in the opposite direction. The contact surface area is related to the MI energy values. In the case of cyclodextrin, if cyclodextrin is a nut, the nut accepts the same spiral bolt. In chromatography using cyclodextrin, molecules with the same spiral screw retain longer, and molecules with opposite spirals elute first [28]. Figure 8.19 shows the structure of enantioselective phenylcarbamated β-cyclodextrin; the analyte is *S*-*N*-(3,5-dinitrophenyl)-2-aminomethylpropanoate. The front atom size is 0.2 for easy recognition of the internal structure. The oxygen (red or black) atoms indicate the screw structure. The blue molecule is *S*-*N*-(3,5-dinitrobenzoyl)-2-aminomethylpropanoate for easy identification—the top view of Figure 8.19 is shown in Figure 8.20.

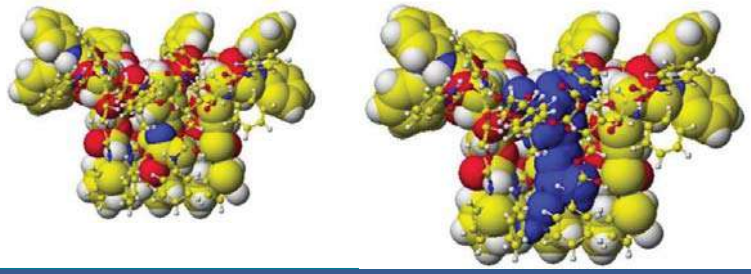


FIgure 8.19: The conformation of S-N-(3,5-Dinitorbenzoyl)-2-aminomethylpropanoate trapped inside of phenylcarbamated β-cyclodextrin; Right Figure indicates blue color analyte .

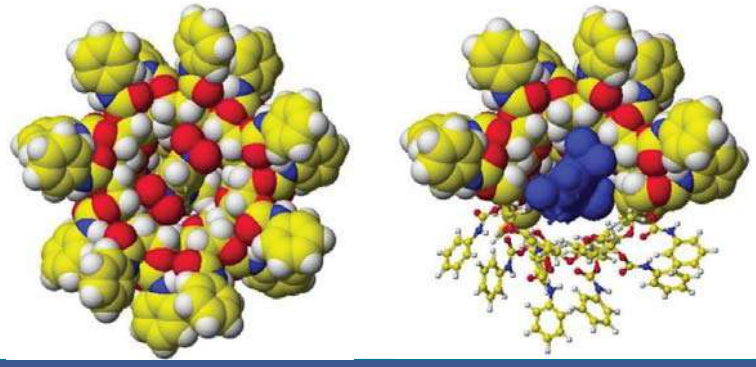


FIgure 8.20: Upper view of Figure 8.19, Right figure indicates blue color analyte

Cyclodextrin can recognize enantiomer-paired ions. Mandelic acid enantiomers are separated as paired ions with trifluoroacetic acid—the structure is shown in Figure 8.21indicates thelocation of these three molecules.

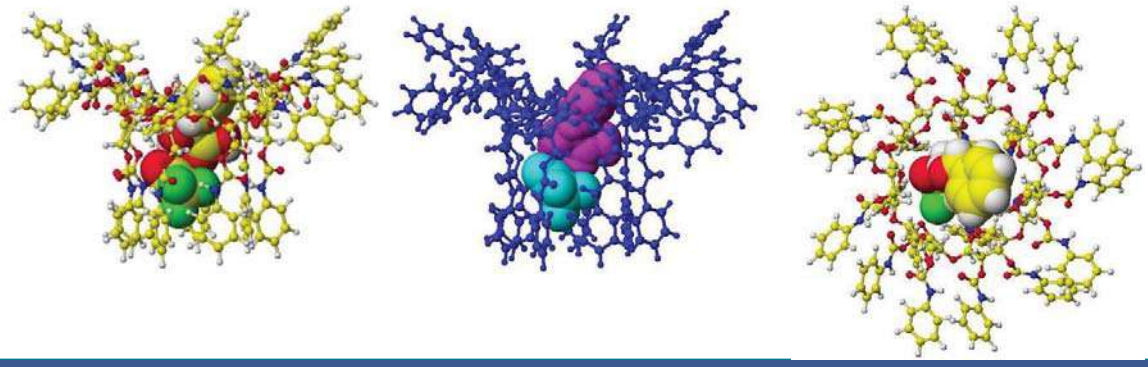


FIgure 8.21: Enantioreconition of derivatized cyclodextrin as paired ion of S-mandelic acid.

R- and *S*-Phenyl-1,2-ethanediol, *R, R*- and *S, S*-hydrobenzoin, and *R*- and *S*-1,1,2-triphenyl-1,2-ethanediol were separated as chromium complexes using cyclodextrin phase [29]. The complex structures of hydrobenzoin are shown in Figure 8.21. A chiral electrochemical sensor separated Tryptophan enantiomers as copper complexes [30, 31]. Tetrahydrozoline enantiomers were also analyzed using a carrier solution containing a cyclodextrin-chiral selector [32]. Catechin and epicatechin enantiomers were analyzed using β-cyclodextrin [33]. Ethylenediamine-β-cyclodextrin-modified graphene oxide nanocomposite membranes were developed to analyze tryptophan and propranolol enantiomers [34]. Sulfobutylether--cyclodextrin embedded in carbon nanofibers was developed to analyze amlodipine, metoprolol, and clenbuterol enantiomers [35]. Separation and determination of amino acid enantiomers in fruit juice by open-tubular nano-liquid chromatography were developed. The chiral selector was prepared by *in situ* polymerization of 3-chloro-2-hydroxypropylmethacrylate, ethylenedimethacrylate, and β-cyclodextrin [36]. Phospholipids with glycerol 1-phosphate and glycerol-3-phosphate enantiomers were determined in bacteria, eukarya, and archaea membranes [37]—the *R*and *S*enantiomers of diacyl-andalkenyl-acyl-glycerolsinasponge, beerspoilagebacteria Pectinatus and Megasphaera were identified bypositive ESI [38]. Effective extraction of hexabromocyclododecane enantiomers from soils and sediments was performed based on halogen bonding [39]. Hepta-*kis*-(2,6-di-*O*-methyl)-β-cyclodextrin was used as a component of the carrier solution in capillary electrophoresis for enantiomer separation of baclofen and phenylalanine [40]. Methamphetamine precursors ephedrine and pseudoephedrine enantiomers were also analyzed using capillary electrokinetic chromatography with cyclodextrin additives [41]. Microfluidic separation of baclofen and phenylalanine enantiomers was achieved using cyclodextrin electrokinetic chromatography [42].

Cyclodextrin-bound phases were used for gas-chromatographic enantiomer analysis and hydroxyglutarate enantiomers in serum without pre-derivatization [43] and α-ionone [isomers [44]. Enantiomers of volatile organic compounds in Slovak Tokai wine were analyzed using modified cyclodextrin phases in gas chromatography [45]. The enantiomers of three typical chiral congeners (PCB-95, PCB-132, and PCB-149) were measured in 24 serum samples from ε-waste workers using gas chromatography coupled to triple quadrupole tandem mass spectrometry [46]. Aromatic profiles and chiral odorants in fresh tea leaves and corresponding baked green teas with five levels of the tenderness of two representative cultivars were analyzed using stir bar sorptive extraction-gas chromatography-mass spectrometry [47]. The enantiomeric composition of chiral compounds in botrytized wines was analyzed by GC [48]. The enantiomeric composition within the complex volatilome of Corylus avellana L. belonging to different cultivars (Tonda Gentile Romana, Tonda Gentile Trilobata, Anakliuri) in different geographical areas (Italian and Georgian) was analyzed using headspace solid-phase micro extraction combined with enantioselective gas chromatography-mass spectrometry, enabling accurate tracking and annotation of about 150 compounds across many samples. [49]. Twelve commercial Juniperus communis fruit essential oils were analyzed by chiral GC-MS.α-Pinene showed considerable variation in enantiomeric distribution, depending on geographical location [50].

8.8. Derivatized polysaccharides as chiral selectors

8.8.1. β-*D*-glucopyranose derivatized chiral selectors: Naturally, saccharides are *R*(*D*)-enantiomers, and the derivatized natural polysaccharides have been used as chiral selectors. A popular enantioselective cellulose derivative model is constructed from a single saccharide. First, convert hydroxyl hydrogens to acetyl or benzoyl groups. Then, two derivatized β-*D*-glucopyranoses bind at their 1 and 4 positions after rotating 180 °. Figure 8.22 shows the structures of

the single benzoyl β-*D*-glucopyranose and the dimer. Repeat the 1-4 bonding and construct the longer β-*D*-glucopyranose fiber.

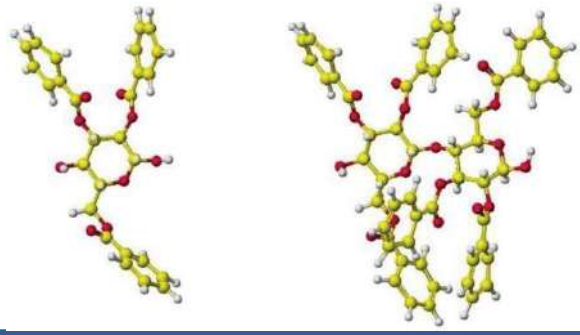


FIgure 8.22: Benzoyl β-*D*-glucopyranose and the 1-4 bond dimer.

The oligomer length depends on the analyte's molecular size. Both end saccharides are not homogeneous and bent. As the oligomer gets longer, it becomes more circular, while the acetylated oligomer becomes relatively flat. The shape depends on the derivatization method. Place an analyte at the oligomer center, optimize the charge-transfer contact structure, and determine which one lasts longer based on molecular interaction energy values. Figure 23 shows phenyl groups lined, and the only narrow channel exists behind the decamer. The location of the narrow channel should not be the location where an analyte contacts tightly. Indeed, a complex at the behind location produces weak interaction energy values.

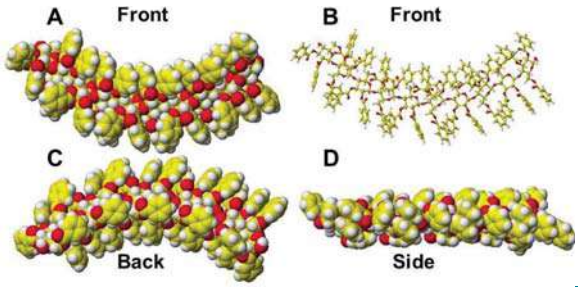


FIgure 8.23: Model benzoyl cellulose oligomer. A: Docking channel, B: 0.2 atomic size molecule, C and D: back and side view.

The enantiomer recognition of the benzoyl-β-*D*-glucopyranose decamer demonstrates the 4-phenyl-2-butanolbenzoate (Figure 8.24) and 1,3-diacetoxy-butane (Figure 8.25) enantiomers.

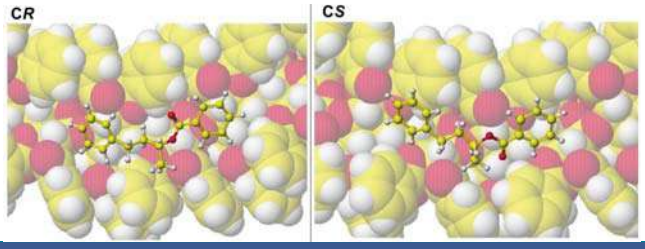


FIgure 8.24: Conformations of 4-phenyl-2-butanolbenzoate enantiomer and the oligomer complex, CR, CS: R- and S-4-phenyl-2-butanolbenzoate.

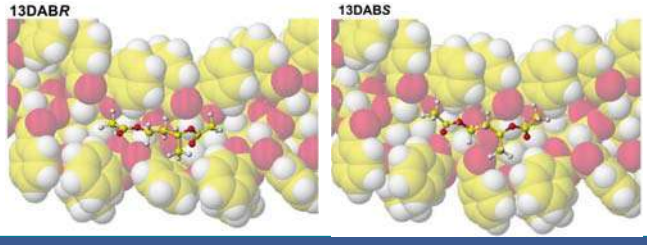


FIgure 8.25: Conformations of 1,3-diacetoxy-butane enantiomers and the oligomer complex, 13DABR, 13DABS: *R*- and *S*-1,3-diacetoxy-butane.

Table 8.3 summarizes the calculated molecular interaction energy values in this model phase. The calculated analyte properties support that enantiomers have identical molecular properties; however, differences in molecular shape produce different MI energy values. Van der Waals forces predominantly drive enantiomer selection. Avoid using a short oligomer for this docking analysis. The endo-side saccharides are bent and contacted with an analyte and produce unexpected, very high MIHB energy values. The elution order is the same as observed for cyclodextrin chiralselector; *R*-compound elutes before *S*-compound due to saccharides being *R*-compound.

Table 8.3: Analyte's properties and the molecular interaction energy values.

Analyte	fs	hb	es	vw	MIFS	MIHB	MIES	MIVW
R 13DAB	0.239	0	-4.79	5.14	18.49	0	1.05	18.48
S 13DAB	0.232	0	-4.57	5.17	20.9	0	1.76	20
R SC	-10.76	0	-2.62	10.88	23.77	-0.01	1.01	25.7
S SC	-10.76	0	-2.62	10.88	24.37	0	1.43	26.01

kcal·mol^{-1}

The structure of a model *p*-methylbenzoylcellulose is shown in Figure 8.26, and the complexes with *R*- and *S*-Ethotoin with *R*- and *S.*- methxiamide are shown in Figures 8.27 and 28. The molecular interaction energy values with ethotoin and methsuximide enantiomers are summarized in Table 8.4.

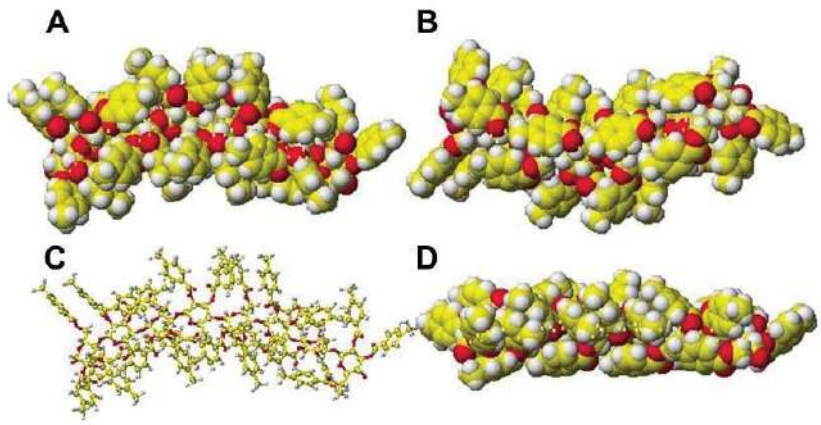


Figure 8.26: Structure of model p-methylbenzoylcellulose, A: possible docking channel, B: back view, C: 0.2 atomic size view, D: side view.

Table 8.4. Analyte's properties and the molecular interaction energy values with p-methylbenzoylcellulose

Analyte	fs	hb	es	vw	MIFS	MIHB	MIES	MIVW
R Ethotoin	-17.41	-2.46	-16.86	3.07	24.66	8.95	-0.79	16.93
S Ethotoin	-17.42	-2.43	-16.86	3.07	29.04	8.95	1.49	17.80
R Methxiamide	-16.44	0.00	-16.42	4.09	21.51	0.33	2.57	20.17
S Methxiamide	-16.44	0.00	-16.42	4.08	22.87	0.30	2.02	20.83

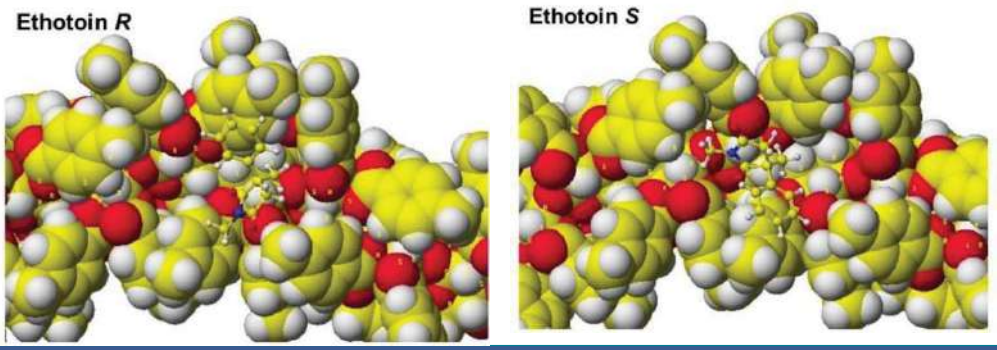


Figure 8.27: Ethotoin enantiomer complex with p-methylbenzoylcellulose.

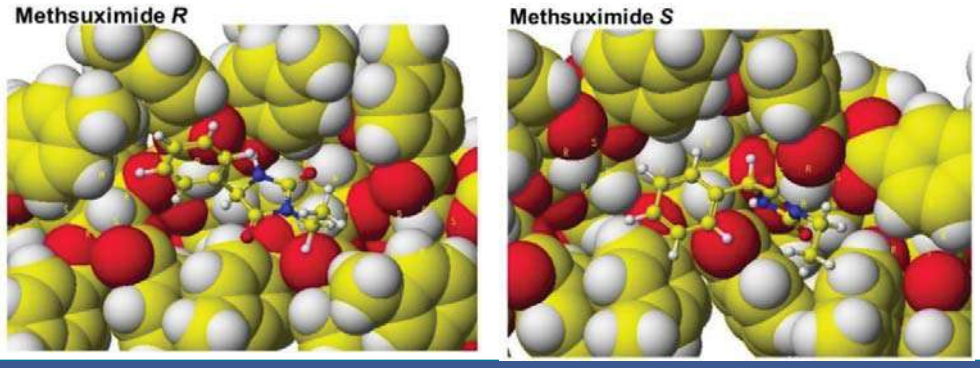


FIgure 8.28: Methsuximide enantiomer complex with p-methylbenzoylcellulose.

The molecular interaction energy values of the contact charge-transfer complexes of ethotoin and methsuximide enantiomers support the possible enantiomer elution order, and their *S*-form MIVW energy values are higher than those of the *R*-form. Their polarizations should determine their elution order; however, complex analysis using model chiral selectors helps understand the enantioselectivity of the enantioselective phases. Total amino acid enantiomer analysis requires further improved model phases.

A high-resolution enantiomer separation can be achieved by the free movement of analytes on the chiral-phase surface. Therefore, we studied the physical structure of the support materials. Generally, the pore size of silica gels was considered, and larger pore-size silica gels were used as an effective support material. A superficially porous support was prepared by cellulose tris(3,5-dimethybiphenylcarbamate) coating. The chiral phase demonstrated the high resolution of benzoin, flavanone, and trans-stilbene oxide enantiomers [51]. They used 450- and 1000-Å porous silica gels coated with cellulose derivatives and demonstrated high enantiomer resolution of several benzamide derivative enantiomers [52]. 18 derivatized cellulose chiral selectors have been studied for 14 sulfoxide enantiomer resolutions. The methanol concentration in the eluents also affected the enantiomer resolution [53]. Second-generation anticoagulant rodenticide enantiomers were analyzed from biological matrices using derivatized cellulose chiral selectors [54]. Enantiomers of a highly selective 5-HT4 receptor agonist, (*R, S*)-4-amino-5-chloro-2-ethoxy-*N*-[3-(4-fluorobenzylamino)-2-hydroxypropyl] benzamide, an active metabolite of mosapride, were analyzed, and the analytical method was validated [55]. Fluindapyr enantiomers in cucumber and tomato were analyzed by supercritical fluid chromatography [56]. A preparative-scale separation of praziquantel enantiomers was studied using Fisherian and Bayesian approaches, and enantiomer purity was predicted [57]. Flumequine enantiomers in multiple food matrices were analyzed using chiral liquid chromatography coupled with tandem mass spectrometry[58].The chromatographic behavior of five popular cannabinoids (including the cannabichromeneracemate, CBC) was studied to investigate the chiral selective column selectivity [59]. Synthesized amino, thio, and oxo derivatives of monoterpenelactones, amides, and esters were investigated for enantiomer separation using various polysaccharide columns [60]. Stilbenedimer enantiomers (pallidol, leachianol, restrytisol, and acyclic dimers) were isolated to determine their absolute configuration and assess whether stereochemistry could affect their biological properties [61]. Five butenolides, including two pairs of enantiomers, (+)-asperteretal G, (−)-asperteretal G, (+)-asperteretal H, (−)-asperteretal H, asperteretal I, and a para-hydroxybenzaldehyde derivative, (*S*)-3-(2,3-dihydroxy-3-methylbutyl)-4-hydroxybenzaldehyde (14), were isolated together with ten known butenolides from the coral-derived fungus Aspergillus terreus SCSIO41404. [62].

8.8.2 Amylose derivatized chiral selectors: Another popular polysaccharide chiral selector is prepared from amylose. Amylose is a polymer of αα-glucose, and cellulose is a polymer of β-glucose—mono-saccharide has four types of stereo structures, namely α1,α,β1, and 1β. The hydroxy group at carbon 1 indicates whether αit is the - or β-form. In the β-structure, the hydroxy group is on the upper side, and in the α-structure, it is on the lower side, as shown in Figure 8.29. The reactivity of these stereoisomers in glycosylation reactions was described [8]. Amylose chiral selectors are polymerized derivatized α-glucose 1-4 conjugation. One example, the structure of phenylcarbamyl α-*R*-glucopyranose, is shown in Figure 30/48. The dimer is also shown in Figure 8.30. Once the derivatized α-glucose was bound straight, the hexamer was the maximum length due to the mass of derivatization groups shown in Figure 8.31. The β-conjugated glucose demonstrates the twisted fibers shown as cellulose chiral selectors. When α-conjugation is favored, the monomer binds together as a twisted fiber; that is, the shape of the enantiomer recognition valley demonstrates analyte selectivity.

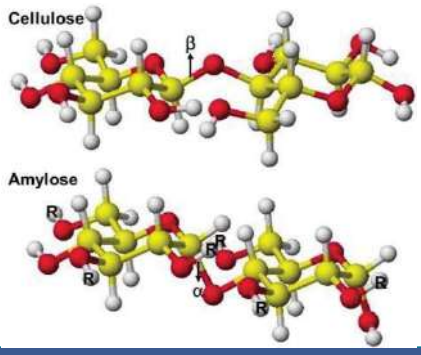


FIgure 8.29: Dimer of β-glucose (cellulose) (amylose) and α-glucose. R indicates the binding location of the derivatizing reagent.

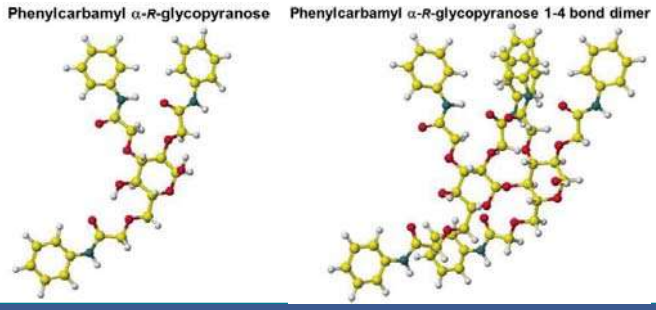


FIgure 8.30: Monomer and dimer of phenylcarbamyl and α-R-glucopyranose.

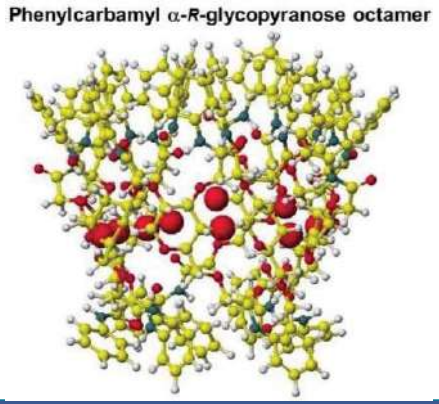


FIgure 8.31: Amylose Polymerization glucose α1 binding.

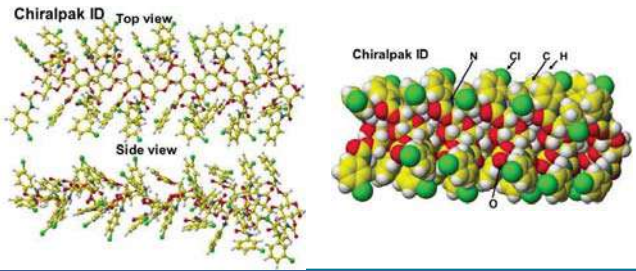


FIgure 8.32: Octamer of 3,5-dichlorophenylcarbamyl of derivatized α-glucose.

3,5-Dimethylphenylcarbamoyl (Figure 8.33) derivatized amylose is an early amylose chiral selector, and the elution order of enantiomers followed the general rule that the *R*-enantiomer elutes before the *S*-enantiomer [63]. Figure 8.34 shows the complex conformations of *R*- and *S*-carvedilol. The major contribution of molecular interaction is van der Waals force (MIVW), and hydrogen bonding contributes to the retention (MIHB). Table 8.5 summarizes the calculated MI values.

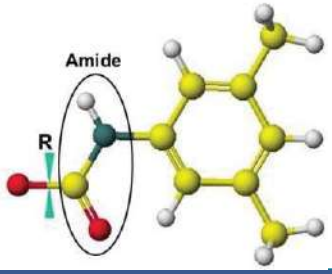


Figure 8.33: 3,4-Dimethylphenyl-carbamyl group.

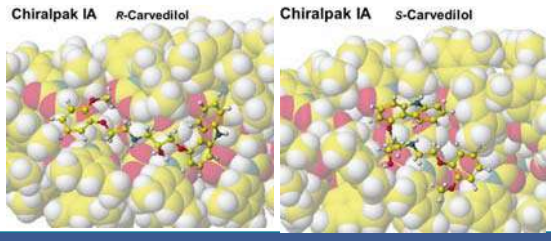


Figure 8.34: Complex conformations of *R*- and *S*-carvedilol with Chiralpak I.

Table 8.5: Analyte's properties and the molecular interaction energy values with Chiralpak IA.

Analyte	fs	hb	es	vw	MIFS	MIHB	MIES	MIVW
R Carvediol	-3.44	-5.37	3.64	9.5	43.93	8.3	1.93	35.71
S Carvediol	-0.58	-1.75	3.58	5.6	47.46	8.45	-0.59	37.35

3,5-Dichlorophenylcarbamyl-derivatized amylose phase (Chiralpak ID) demonstrated an interesting elution order [64]. Usually, the *S*-enantiomer is eluted before the *R*-enantiomer, but the elution order is reversed. The selectivity is caused by the polar carbamyl group of the 3,5-dichlorophenylcarbamyl group (Figure 8.35) and the relatively polar eluent components. The calculated MIFS energy value indicates *R*-ketoprofen should elute before *S*-ketoprofen; however, the experimental result demonstrated that *S*-ketoprofen eluted before *R*-ketoprofen. Figure 8.36 shows these complex conformations. The eluent was aqueous acetonitrile; therefore, we studied the solvent effect using a general aqueous eluent, excluding pure ion-exchange chromatographic conditions. The calculated solvent effect indicated that *S*-ketoprofen was highly solvated with acetonitrile. The interaction with the acetonitrile phase is shown in Figures 8.37 and 38. The calculated molecular interaction energy values are summarized in Tables 8.6 and 7. The stronger solvation of *S*-ketoprofen contributed to the early elution.

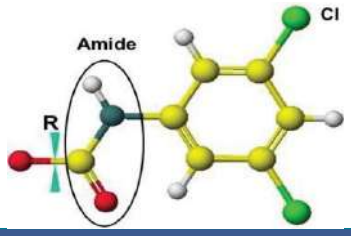


Figure 8.35: Structure of 3,5-dichloro-Phenylcarbamyl.

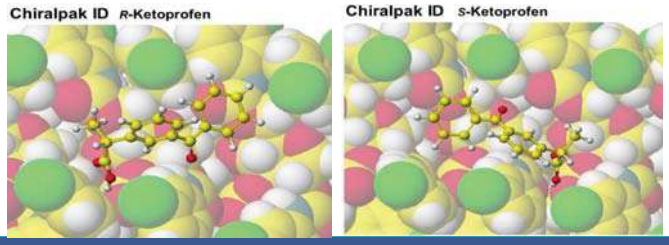


Figure 8.36: Complex conformations of R- and S-ketoprofen with Chiralpak ID.

Table 8.6: Analyte's properties and the molecular interaction energy values with Chiralpak ID.

Analyte	fs	hb	es	vw	MIFS	MIHB	MIES	MIVW
R Ketoprofen	-14.13	-3.78	-4.95	9.38	39.61	12.27	7.82	13.07
S Ketoprofen	-12.89	-3.65	-4.85	9.69	40.92	11.89	3.19	22.04

Table 8.7: Analyte's properties and the molecular interaction energy values with acetonitrile-phase

Analyte	fs	hb	es	vw	MIFS	MIHB	MIES	MIVW
R Ketoprofen	-14.13	-3.78	-4.95	9.38	17.81	-0.17	-49.56	9.43
S Ketoprofen	-12.89	-3.65	-4.85	9.69	20.15	-0.02	-48.46	10.25

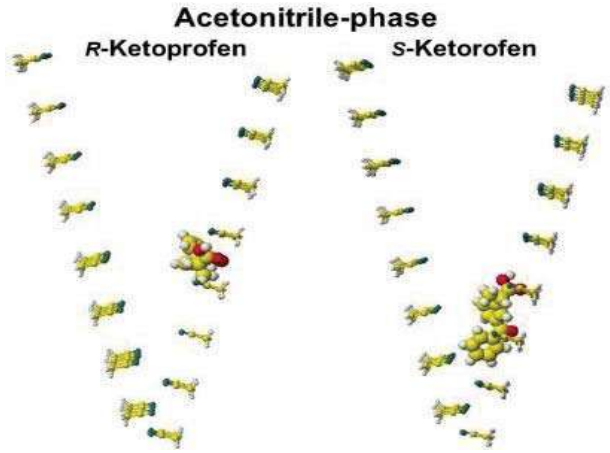


FIgure 8.37: Complex conformations.

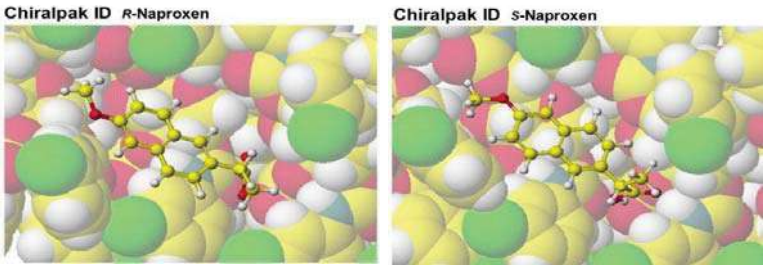


FIgure 8.38: Complex conformations.

Further analys is of the elution order of *R*- and *S*-naproxen was performed. Figure 8.56 shows the optimized complex conformations. The calculated MIFS energy value of the *S*-compound was higher than that of the *R*-compound (Table 8.8), and the solvation energy values were identical (Table 8.9). The results support their experimental result. The enantioseparation in hydrophobic conditions is quite simple, but adding a polar liquid to the eluent enhanced the separation selectivity [65].

Table 8.8: Analyte's properties and the molecular interaction energy values with Chiralpak ID.

Analyte	fs	hb	es	vw	MIFS	MIHB	MIES	MIVW
R Ketoprofen	-26.34 -3.76 -5.13 7.14	41.12 9.60 5.01 19.90						
S Ketoprofen	-12.89	-3.65	-4.85	9.69	40.92	11.89	3.19	22.04

Table 8.9: Analyte's properties and the molecular interaction energy values with Chiralpak ID.

Analyte	fs	hb	es	vw	MIFS	MIHB	MIES	MIVW
R Naproxen	-26.34 -3.76 -5.13 7.14 15.30 -0.17 -54.14 11.26							
S Naproxen	-26.34 - 3.76 -5.03 7.14 15.00 -0.14 -54.47 10.85							

Another interesting result was found in the results of ChralpakIG, which is the 3-chloro-5-methylphenylcarbamyl derivatized amylose phase. The structure of 3-chloro-5-methylphenylcarbamyl is shown in Figure 8.39. The complex conformation of naringenin with Chiralpak I and the methanol phase are shown in Figure 8.40 and 8.41, respectively. *S*-Naringenin eluted before *R*-naringenin [66]. This result opposes the general rule for polysaccharide chiral selectors—the calculated MI energy values support that *R*-naringenin should elute before *S*-naringenin (Table 8.10). The aqueous eluent components should control the elution order found in Chiralpak ID. Therefore, we calculated the solvent effect using a methanol phase (Table 8.11). The higher MIFS value of *S*-naringenin supports the elution order. These results suggest that the elution order of enantiomers does not depend on the chiral selector in the aqueous eluent. Analyte solubility is a significant factor controlling elution order, as generally observed in aqueous-mode liquid chromatography. Therefore, we need an enantiomer-selective detector to analyze unknown enantiomer mixtures.

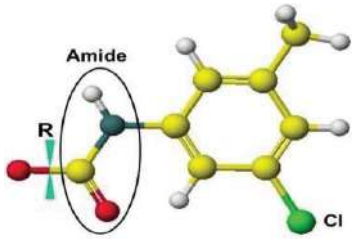


Figure 8.39: Structure of 3-chloro-methylphenylcarbamyl.

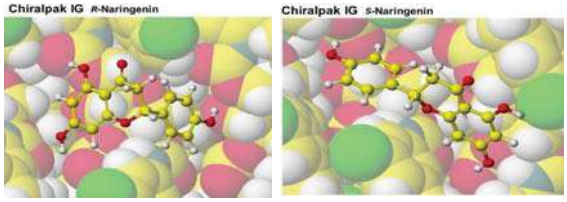


Figure 8.40: Complex conformations of *R*- and *S*-naringenin with 5-Chralpak IG.

Table 8.10: Analyte's properties and the molecular interaction energy values with Chiralpak IG.

Analyte	fs	hb	es	vw	MIFS	MIHB	MIES	MIVW
R Naringerin	-18.83	-4.86	-3.43	8.95	55.19	24.48	3.08	16.85
S Naringerin	-19.63	-4.82	-3.4	8.78	59.45	19.07	5.48	22.37

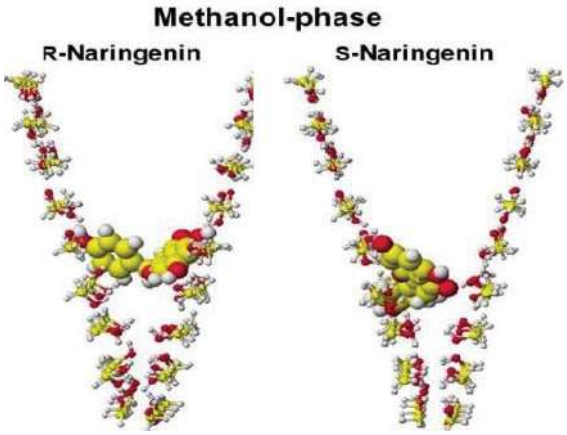


Figure 8.41: Complex conformations of *R*- and S-naringenin with methanol phase.

Enantiomer separation and identification are critical subjects in various fields. Direct enantiomeric separation is the preferred tool; therefore, derivatized polysaccharide chiralselectors have been applied in several fields. Several examples are followed. Zoxamide enantiomers were separated to study the enantioselective degradation process in agriculture plants

[67]. An antihypertensive and antianginal activities drug (Carvedilol enantiomers) was separated on a semipreparative scale[63]. Seven psychoactive drug enantiomers were analyzed in the range of 1–250 ng g^{-1} [68]. Naringenin enantiomers in citrus peel and pulp were determined [66]. Researchers analyzed non-steroidal anti-inflammatory drug enantiomers in fish tissues using chiral liquid chromatography coupled with tandem mass spectrometry [64]. Four stereoisomers of sulfoxaflor in zebrafish were separated, and the bioaccumulation experiment demonstrated that the bioconcentration of sulfoxaflor in zebrafish was enantioselective, and the four enantiomers accumulated in zebrafish in the elution order (+)-2*S*,3*S*-sulfoxaflor > (−)-2*R*,3*R*-sulfoxaflor > (+)-2*R*,3*S*-sulfoxaflor > (−)-2*S*,3*R*-sulfoxaflor [69]. A novel chiral fungicide sedaxane contained four enantiomers *S*,2*S*-(+)-sedaxane, *R*,2*R*-(-)-sedaxane, *R*,2*S*-(+)-sedaxane, and 1 *S*,2*S*-(+)-sedaxane. The stereoselective bioactivity, toxicity, and degradation of sedaxane were studied [70].

Supercritical fluid chromatography time-of-flight mass spectrometry was used to analyze basic drug enantiomers, such as climbazole, venlafaxine, tramadol, propranolol, miconazole, sertaconazole, tioconazole, and fenticonazole in sewage. Eight pharmaceuticals, considered emerging environmental pollutants and belonging to two different chemical classes, were analyzed in wastewater and sludge samples using supercritical fluid chromatography combined with time-of-flight mass spectrometry [71]. The spatial distribution of the predominant usnic acid enantiomer in lichens was characterized [72]. Supercritical fluid chromatography was used to separate β-blocker enantiomers [73]. Stereoselective metabolism of chloramphenicol by bacteria isolated from wastewater was analyzed using supercritical-fluid chromatography coupled with mass spectrometry [74]. Various selectors have been developed, and possible enantiomer-recognition mechanisms were proposed in supercritical fluid chromatography [75].

Furthermore, the specificities of cellulose and amylose chiralselectors have been analyzed for their effective uses. The superiority of cellulose- and amylose-based chiral selectors was studied after synthesis using different types of silica gels for benzoin, etozoline, trans-stilbene, and Troger's base. Superficially porous silica coated with polysaccharides was demonstrated as a better chiral selector [76]. The suitability of cellulose and amylose-based chiralselectors was analyzed for several β-agonist enantiomers [77]. Derivatized groups of cellulose and amylose affected the enantiomer resolution. The substituent selectron-donor and acceptor groups affected the solvation of the chiral selector, then the enantiomer resolution [78].

Organic modifier concentration affected the elution order of enantiomers as observed in reversed-phase liquid chromatography. This phenomenon likely stems from the relative hydrophobicity of chiral selectors and analytes [79]. Insecticide fipronil enantiomers and their major transformation products were determined by high-performance liquid chromatography interfaced with mass spectrometry [80]. Nano-liquid chromatography was applied to enantiomer separations [81]. A preparative-scale separation of planar-chiral cyclic molecules was achieved using polysaccharide phases [82].

Agrochemical enantiomers were analyzed using nano-liquid chromatography and capillary electrochromatography with amylose tris(3-chloro-5-methylphenylcarbamate) covalently immobilized onto silica [83]. 8 DBZ-related enantiomers were analyzed by supercritical fluid chromatography [84]. A series of 10 pharmaceutically relevant enantiomeric mixtures was analyzed using a parallel multicolumn SFC [85]. Two phenyltetrahydroimidazothiazole enantiomers, levamisole (*S*) and dexamisole (*R*), were analyzed, and it was found that steadily increasing (*R*)/(*S*)-ratios helped estimate the time of cocaine consumption. [86]. The *in vitro* phase I metabolism of prothioconazole, aprofungicide to *D*-PTC in human liver microsomes and human CYP450 forms, was studied [87]. Chiral pesticides were determined in hemp seeds using online coupling of supercritical fluid extraction with enantioselective supercritical fluid chromatography-triple quadrupole mass spectrometry. [88]. The enantiomeric composition of amphetamine, methamphetamine, and 3,4-methylenedioxy-*N*-methylamphetamine (MDMA) in seized street drug samples from southern Germany was determined because enantioselective monitoring of seized specimens was crucial for legal and forensic casework [90].

8.9. Protein as chiral selectors

8.9.1. Glycoprotein as chiral selector: Most amino acids are *L*(*S*)-form enantiomers, and saccharides are *D*(*R*)-form. Therefore, *S*-enantiomer elutes first from protein columns, and *R*-enantiomer elutes first from saccharide columns. The elution order from glycoproteins is *R*- then *S*-enantiomers because proteins coat the silica gel, and saccharides remain on the surface of the chiral selector. First, α1-acid glycoprotein was used as a chiral selector [90]. Synthetic opioid methadone enantiomers in plasma and saliva were quantitatively analyzed using an α1-acid glycoprotein chiral phase [91]. A glycoprotein structure (PDB 3kq0) was downloaded, and the complex structure was optimized with a substitute, (2*R*)-

2,3-dihydroxypropylacetate, which is shown in Figures 8.42 and 43. A key residual amino acid linked to the substitute was arginine (90), and its conformation is shown in Figure 8.44. The enantiomer recognition of methadone [92] was analyzed by replacing the original substitute with methadone enantiomers. Figures 8.45 and 8.46 show the stereo structures of the protein and *R*- and *S*-methadone, respectively, and Table 8.12 summarizes the calculated molecular interaction energy values.

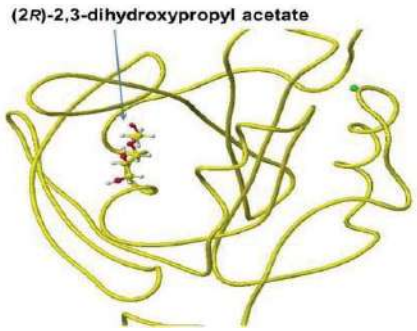


FIgure 8.42: Optimized structure of down-loaded α1-acid glycoprotein.

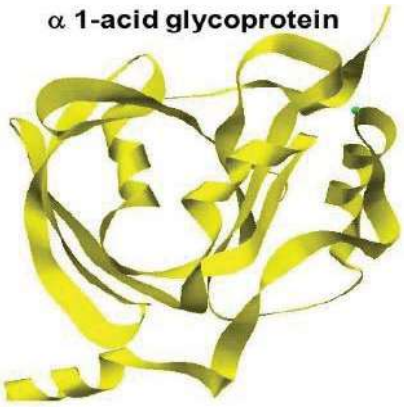


FIgure 8.43: Optimized stereo structure residues with (2R)-2,3-dihydroxypropylacetate.

FIgure 8.44: Contacted amino acid residue with glycoprotein with (2R)-2,3-dihydroxypropylacetate.

Table 8.12: a-acid glycoprotein enantiomer recognition of *R*- and *S*-methadone.

	Fs	hb	es	vw	MIFS	MIHB	MIES	MIVW
R Methadone	10.067	0	2.517	15.187	61.182	45.099	-36.436	50.354
S Methadone	7.012	0	2.544	12	37.66	36.137	-45.089	41.331
a1-Acid glycoprotein	-4187.849	-2677.046	-2290.557	2.562				

FIgure 8.45: Structures of *R*- and *S*-methadone glycoprotein enantio-center is circled.

FIgure 8.46: Complex conformation of α1-acid with R- and S-methadone.

8.9.2. Cellobiohydrolase: Another example is the enantioseparation of cellobiohydrolase-phase (Chiralpak CBH). In the study of organic cation transferase, *R, R*- and *S, S*-fenoterol were separated using cellobiohydrolase-phase [92]. Therefore, we downloaded one structure (PDB 1cel), replaced the original substrate with *R, R*- and *S, S*-fenoterol, and optimized the complex structures to obtain their MI energy values. The optimized structures of fenoterol and cellobiohydrolase are shown in Figures 8.47 and 8.48, respectively.

FIgure 8.47: Structure of *R*- and *S*-fenoterol.

FIgure 8.48: Optimized structure of 1cel.

The optimized complex structures are shown in Figure 8.49, and the calculated MI energy values are summarized in Table 8.13.

FIgure 8.49: Optimized complex conformations of cellobiohydrolase with R,R- and S,S- fenoterol.

Table 8.13: Enantiomer recognition of cellobiohydrolase.

	fs	hb	es	vw	MIFS	MIHB	MIES	MIVW
RR Fenoterol	-11.83	-2.99	1.75	9.24	58.87	88.1	14.22	-1.44
SS Fenoterol	-12.28	-2.74	2.01	9.67	84.54	117.77	11.89	-1.9
Cellobiohyddrolase	-4591.58	-5657.49	-243.23	-391.98				

Proteins are polymers of *S*-amino acids; therefore, *R*-form compounds are generally held tightly. However, *S,S*-form compound was eluted after *R,R*-form compound. We have to carefully determine the analyte structure either using standard compounds or a selective detector.

8.10 Natural organic compounds

Figure 64 shows the optimized complex structures of the protein with *R*- and *S*-methadone, and Table 8.18 summarizes the calculated MI energy values. Amino acid polymers (proteins) have a twisted *S*-structure; therefore, *R*-form compounds fit tightly inside the proteins. The contact surface area relates to MIVW, and specific interaction relates to MIHB—these calculated MIVW and MIHB values demonstrated the selective molecular interaction of proteins.

Figure 8.50 shows the stereostructure of vancomycin, and the enantiomer recognition center is circled; Figure 8.51 shows the optimized complex structures of vancomycin with R- and S-clenbuterol. The calculated MI energy values are summarized in Table 8.14.

FIgure 8.50: Stereo structure of vancomycin and the possible chiral selection location (circled)

FIgure 8.51: Optimized complex conformations of vancomycin with R- and S-clenbuterol.

Table 8.14: Enantiomer recognition of vancomycin.

	fs	hb	es	vw	MIFS	MIHB	MIES	MIVW
R Clenbuterol	9.83	-4.85	10.6	9	31.97	18.9	1.93	13.35
S Clenbuterol	9.89	-4.98	9.79	8.98	36.24	18.25	2.29	15.24
R Salbuterol	-5.58	-5.15	-0.31	7.68	48.84	37.59	4.59	12.49
S Salbuterol	-5.56	-5.33	-0.13	7.71	49.15	38.27	3.64	9.16
Vancomycin	-18.75	-80.49	5.43	37.1				

Natural compounds are generally enantiomer selective. Amino acid-related supra-molecular compounds selectively collect *R*-form compounds, and saccharide-related supra-molecular compounds selectively collect S-form compounds. Vancomycin is a combination of a peptide chain, saccharide, and phenolic compounds. These parts are abundant in nature; the structure is very complex and has a stereoselective capability.

8.11 Other enantiomer separation phases

Two covalently bound organic framework (COF) triazine membranes were synthesized, and the membranes demonstrated crown ether- and cyclodextrin-like chiral selectors for drug intermediates and drug enantiomers [96]. A chiral covalent organic framework was prepared as a chiral monolith phase and demonstrated for the enantiomer separation of Fmoc-amino acids [97]. The separation mechanisms are seemed similar to the above phase, even if their supporter's physical structures are different. A covalent organic framework was prepared; first, the 1,3,5-triformylphloroglucinol was functionalized with chiral (+)-diacetyl-*L*-tartaric anhydride to form the chiral functionalized monomer CTp, then bound with 1,4-phenylenediamine, 2,5-dimethyl-*p*-phenylenediamine. The COF-bound capillary columns using capillary gas chromatography demonstrated enantiomer separation of (±)-1-phenylethanol [98].The triazinecircle structure was constructed, and the enantio-selectivity of phenylethanol [96] was analyzed. Figure 8.52 shows the complex conformations of the triazine-circle structure with *S*- and *R*-phenylethanol. The calculated MI energy values are summarized in Table 8.15.

Figure 8.52: Optimized complex structure of chiral selector triazine with R- and S-phenylethanol.

Table 8.15: Enantiomer recognition of triazine-flame.

	fs	hb	es	vw	MIFS	MIHB	MIES	MIVW
R Phenylethanol	-10.48	-2.99	-0.99	3.98	12.41	0.02	-0.19	12.41
S Phenylethanol	-10.48	-2.99	-0.99	3.99	13.31	-0.02	-0.08	13.22
Triazine flame	219.94	-0.07	-62.28	91.58				

The enantio-selectivity of the circled triazine was like a polysaccharide phase, and the main interaction force is related to the contact surface area. Different types of supramolecules have been developed as chiral selectors. Saccharides are *R*(*D*)-form compounds, and cyclodextrin and polysaccharides have been prepared as enantioselective phases. Amino acids are generally *S*(*L*)-form, and proteins are used as chiralselectors. Therefore, glutamic acid bonded graphene was developed as a chiral selector for tryptophan [99]. Another candidate is a liquid crystal [100]. Novel chiral ionic liquid stationary phases were prepared, and the retention mechanisms of chiral acids were described by high-performance liquid chromatography [101]. The need for enantiomer separation drives the development of practical, selective chiral selectors.

8.12 Biological enantiomer selectivity

Enzyme (protein) reactions are highly selective and can recognize enantiomers. A simple example enzyme is *D*-amino acid oxidase, which selectively oxidizes *R(D)*-amino acids but not *S(L)*-amino acids. The evidence is explained quantitatively, and the enzyme-amino acid complex demonstrate exhibits of electron localization. Chapter 9 explains the details. Another piece of evidence is the existence of racemase, which produces a suitable enantiomer from the opposite amino acid. The mechanism is explained quantitatively for several racemases in the following Chapter 9 (Physical biochemistry of enzyme reactions).

Conclusion

Enantiomers are fundamentally separated using chiral selectors in liquid chromatography, supercritical fluid chromatography, gas chromatography, and electrophoresis. In some cases, pre-derivatization is necessary for specific chiral selectors and for diastereomeric separation. Generally, pre-column derivatization is avoided because the reaction process can cause racemization. Various chiral selectors have been developed, and molecular interaction mechanisms have been discussed. These mechanisms combine hydrogen bonding, dipole-dipole interaction, halogen bonding, ionic interaction, and van der Waals interaction. The π−π interaction, dipole-dipole interaction, and halogen bonding, and these interactions have been described as Lewis acid-base interaction, and the substitute effects have been demonstrated as Hammet's sigma constants. Lewis acid-base interactions, including substitute effects, are obtained as electrostatic energy values in *in silico* analysis. The ionic interaction is presented as electrostatic energy values. The difference is latter case exhibits high energy values. Van der Waals energy values related their contact surface area of analytes with chiral selectors. Natural supra-molecular compounds are chiral selectors, and the original and modified compounds have been used for enantiomer separations. The addition of a polar liquid quantitatively explained the separation selectivity as a solvent effect. The selection of eluent components was an important factor in handling enantio-separation. Quantitative *in silico* analysis of various enantio-separation methods should provide a clear guide for further analysis of enantiomers.

References

1. N. Oi, Recent progress of chiral stationary phases for HPLC, Y. Hanai, H. Hatano, (Eds) Advances in liquid chromatography, 35 years of column liquid chromatography in Japan, World Scientific Pub, Singapore, 1996, pp. 213-230. ISBN:9810219067
2. E. Yashima, Y. Okamoto, Chiral synthetic polymer packings, T. Hanai, H. Hatano, (Eds) Advances in liquid chromatography, 35 years of column liquid chromatography in Japan, World Scientific Pub, Singapore, 1996, pp. 231-254. ISBN:9810219067
3. Y. Oda, T. Miwa, T. Protein-bonded chiral packings and their application, T. Hanai, H. Hatano, (Eds) Advances in liquid chromatography, 35 years of column liquid chromatography in Japan, World Scientific Pub, Singapore, 1996, pp. 255-288. ISBN:9810219067
4. T. Hanai, Quantitative in silico chromatography, Computational modeling of molecular interactions, Royal Society of Chemistry, Cambridge, 2014, pp. 338. ISBN: 978-1-84973-991-7
5. T. Hanai, Quantitative in silico analytical chemistry (Toward A.I. Analytical Chemistry), 28 Chiral recognition 1, Feb. 07, 2021, and 29 Chiral recognition 2, Feb. 14, 2020, http://www.hanai-toshihiko.net
6. T. Hanai, H. Hatano, N. Nimura, T. Kinoshita, Computational chemical analysis of chiral recognition in liquid chromatography, selectivity of N-(R)-1-(α -naphthyl)ethylaminocarbonyl-(R or S)-valine and N-(S)-1-(α -naphthyl)ethylaminocarbonyl-(R or S)-valine bonded aminopropyl silica gels. Anal. Chim. Acta, 1996, 332(2-3), 213-224. https://doi.org/10.1016/0003-2670(96)00275-9
7. T. Hanai, H. Hatano, N. Nimura, T. Kinoshita, Computational chemical analysis of the separation of derivatized R- and S-amino acid enantiomers on N-(tert-butylaminocarbonyl)-(S)-valylaminopropylsilica gel and (R)-1-(α -naphthyl)-ethylaminocarbonyl -glycylaminopropylsilica gel by liquid chromatography. J. Liq. Chromatogr. Rel. Technol. 1996, 19(8), 1189-1204. https://doi.org/10.1080/10826079608006312
8. T. Hanai, K. Shimada, N. Koyama, Y. Nohara, H. Takayanagi, (late) T. Kinoshita, Quantitative analysis of selective glycosylation of saccharides with aromatic amines. Carbohydrate Research, 2021, 498, 108171, http://doi.org/10.1016/j.carres.2020.108171 Actual contributors: T. Hanai, K. Kato, E. Furukoshi, M. Hennmi, S. Imoto, A. Kotaka, K. Shimada, M. Tohma, M. Ishikawa, T. Watanabe,E. Ohgawara, N. Koyama, K. Furuhata, K. Nagahara, H. Takayanagi, Y. Nohara, T. Kinoshita,
9. J. Yang, S.G. Carmella, S.S. Hecht, Analysis of N'-nitrosonornicotine enantiomers in human urine by chiral stationary phase liquid chromatography-nanoelectrospray ionization-high resolution tandem mass spectrometry J. Chromatogr. B, 2017, 1044-1045, 127-131, http://dx.doi.org/10.1016/j.jchromb.2017.01.008
10. L. Goncalves, S. Cravo, C. Fernandes, M.E. Tiritan, Development and evaluation of Pirkle-type chiral stationary phase for flash chromatography, J. Chromatogr. A, 2022, 1675, 463156, http://doi.org/10.1016/j.chroma.2022.463156
11. N. Nimura, T. Kinoshita, o-Phthalaldehyde-N-acetyl-L-cysteine as a chiral derivatization reagent for liquid chromatographic optical resolution of amino acid enantiomers and its application to conventional amino acid analysis, J. Chromatogr. 1986, 352, 169-177. https://doi.org/10.1016/50021-9673(01)83377-X

12. C. Aoyama, T. Santa, M. Tsunoda, T. Fukushima, C. Kitada, K. Imai, A fully automated amino acid analyzer using NBD-F as a fluorescent derivatization reagent, Biomed. Chromatogr. 2004, 18, 630–636, DOI: 10.1002/bmc.365A

13. M. Harada, S. Kawahara, N. Yamada, H. Miyano, K. Shimbo, Biaryl axially chiral derivatizing agent for simultaneous separation and sensitive detection of proteinogenic amino acid enantiomers using liquid chromatography-tandem mass spectrometry, J. Chromatogr. A, 2019, 1593, 91-101. https://doi.org/10.1016/j.chroma.2019.01.075, https://doi.org/10.1016/j.chroma.2019.01.075

14. Y. Jin, Y. Pan, C. Zhang, (S)-1-(5-(4-Methylpiperazine-1-yl)-2,4-dinitrophenyl)pyrrolidine-2-carboxylic acid as a derivatization reagent for ultrasensitive detection of amine enantiomers by HPLC-MS/MS and its application to the chiral metabolite analysis of (R)-1-aminoindan in saliva, J. Pharm. Biomed. Anal. 2021, 194, 113815. https://doi.org/10.1016/j.jpba.2020.113815,

15. J. Yu, X. Li, J. Zhou, X. Xie, M. Chen, X. He, Y. Tang, Y. Zhang, A. Zheng, X. Mei, Y. Li, Chiral analysis of ammuxetine enantiomers in dog plasma using online SPE/liquid chromatography with tandem mass spectrometric detection after precolumn chiral derivatization Chirality, 2017, 29, 193-201, https://doi.org/10.1002/chir.22692

16. J. Zhu, K.H. Harada, X. Zou, C. Sun, C., investigating isomers/enantiomers of perfluorooctanoic acid in river water by gas chromatography-mass spectrometry with chiral derivatization, Chemosphere, 2020, 238, 124617, https://doi.org/10.1016/j.chemosphere.2019.12.124617

17. C. Zhang, Y. Liu, R. Liu, W. Li, C. Liu, L. He, Chiral probe for mass spectrometric identification and quantitation of levodropropizine and its enantiomer, dextrodropropizine, Chirality, 2022, 34, 955-967,

18. A. Obaid, A. Khairani, M. Jamil., S.M. Saharin, S. Mohamad, L-cysteine capped silver nanoparticles, as chiral recognition sensor for ketoprofen enantiomers, Chirality, 2021, 33, 810-823. https://doi.org/10.1002/chir.23354

19. T. Verovšek, D. Heath, E. Heath, Enantiomeric profiling of amphetamines in wastewater using chiral derivatization with gas chromatographic-tandem mass spectrometric detection, Sci. Total Environ. 2022, 835, 155594, http://dx.doi.org/10.1016/j.scitotenv.2022.155594

20. T. Hanai, H. Hatano, N. Nimura, T. Kinoshita, Computational chemical analysis of the chiral recognition of binuclear copper (II) of N-salicylidene (R)-2-amino-1,2-bis(2-butoxy-5-tert-butylphenyl)-3-phenyl-1-propanol in liquid chromatography. J. Liq. Chromatogr. 1994, 17(20), 4327-34. https://doi.org/10.1080/10826079408013620,

21. K. Deng, S. Chen, H. Song, Chiral recognition of tryptophan enantiomers with UV-VIS spectrophotometry approach by using L-cysteine modified ZnF22O4 nanoparticles in the presence of Cu2+, Spectrochimica Acta A: Molecular and Biomolecular Spectroscopy, 2022, 270, 120847. https://doi.org/10.1016/j.saa.2021.120847, https://doi.org/10.1016/j.saa.2021.120847

22. Q. Ye, Z-Z. Yin, ,...; Y. Kong, Decoration of glutathione with copper-platinum nanoparticles for chirality sensing of tyrosine enantiomers, Electrochem. Commun. 2022, 110, 106635. https://doi.org/10.1016/j.elecom.2019.106638,

23. X. Liang, L. Zhao, M. Deng, L. Liu, Y. Ma, X. Guo, Separation of Ofloxacin and Its Six Related Substances Enantiomers by Chiral Ligand-Exchange Chromatography, Chirality, 2015, 27, 843-849. https://doi.org/10.1002/chir.22527

24. H. Bai, L. Chen, Simultaneous separation of atenolol enantiomers and its acid/alkaline degradation impurities on mixed-mode chiral ligand exchange stationary phases, Chirality, 2021, 33, 710-721, https://doi.org/10.1002/chir.23353

25. S.Auras, O. Trapp, Diastereoselective synthesis of a cyclic diamide-bridged biphenyl as chiral Atropos ligand, Chirality. 2022, 34, 813–819. DOI: 10.1002/chir.23434

26. Daicel Chemical Industries, Application guide for chiral column selection, 2nd edition

27. Y. Konya, Y. Izumi, T. Bamba, Ultrafast simultaneous chiral analysis of native amino acid enantiomers using supercritical fluid chromatography/tandem mass spectrometry, J. Chromatogr. A, 2022, 1677, 463301, https://doi.org/10.1016/j.chroma.2022.463305

28. T. Hanai, F. Tazerouti, B-H. Ahmed, A. Yacine, Analysis of the mechanism of retention on a modified β-cyclodextrin/silica chiral stationary phase using a computational chemical method, J. Liq. Chromatogr. Rel. Technol. 2007, 30(20), 3043-3057. https://doi.org/10.1080/10826070701632345

29. Y. Liu, F. Xu, > Wu, H. Wang, Z. Liang, C-F. Ding, Chiral distinction of phenyl-substituted ethanediol enantiomers by measuring the ion mobility of their ternary complexes, Microchem. J. 2022, 178, 107389, https://doi.org/10.1016/j.microc.2022.107.389

30. J. Ji, L. Qu, Z. Wang, G. Li, W. Feng, G. Yang, A facile electrochemical chiral sensor for tryptophan enantiomers based on multiwalled carbon nanotube/hydroxypropyl-β-cyclodextrin functionalized carboxymethyl cellulose. Microchem. J., 2022, 175, 107133, https://doi.org/10.1016/j.microc.2021.107133

31. T. Li, Y. Wang, X. Kan, Electrochemical chiral recognition of tryptophan enantiomers based on copper-modified β-cyclodextrin, J. Electroanal. Chem., 2021, 902, 115817. https://doi.org/10.1016/j.elechem.2021.115817

32. A. Gogolashvili, K. Lomsadze, B. Chankvetadze, Separation of tetrahydrozoline enantiomers in capillary electrophoresis with cyclodextrin-type chiral selectors and investigation of chiral recognition mechanisms, J. Chromatogr. A, 2021, 1643, 462084. https://doi.org/10.1016/j.chroma.2021.462084

33. H. Terasima, M. Seki, S. Kodama, Chiral separation of catechin and epicatechin by reversed-phase high-performance liquid chromatography with β-cyclodextrin stepwise and linear gradient elution modes, J. Chromatoigr. A, 2022, 1673, 463029, https://doi.org/10.1016/j.chroma.2022.463029

34. X. Bai, J. Ke, ...J. Chen, Ethylenediamine-β-cyclodextrin modified graphene oxide nanocomposite membranes for highly efficient chiral separation of tryptophan and propranolol enantiomers, Sep. Purif. Technol. 2022, 290, 120833, https://doi.org/10.1016/j.seppur.2022.120833

35. P.K. Kalambate, S.S. Upadhyay, ... Y. Huang, Chiral nanocomposite to sulfobutyl ether-β-cyclodextrin embedded in carbon nanofibers for enantioselective electrochemical discrimination of amlodipine, metoprolol, and clenbuterol enantiomers, J. Meter. 2021, 7, 226-235, https://doi.org/10.1016/j.mat.2020.09.004

36. C. Aydogan, Chiral separation and determination of amino acid enantiomers in fruit juice by open-tubular nano liquid chromatography, Chirality, 2018, 30, 1144-1149, https://doi.org/10.1002/chir.23006

37. A. Palyzováa, I.A. Guschina, T. Rezanka, Chiral analysis of glycerol phosphates - can bacteria biosynthesize heterochiral phospholipid membranes?, J. Chromatogr. A, 2022, 1676, 463267, https://doi.org/10.1016/j.chroma.2022.463267

38. T.Rezanka, A.Palyzová, M.Vítová, T.Brányik, M.Kulišová, J.K.Irena, Article Structural Characterization of Mono- and Dimethylphosphatidylethanolamines from Various Organisms Using a Complex Analytical Strategy including Chiral Chromatography, Symmetry 2022, 14, 616, https://doi.org/10.3390/sym14030616

39. A.B. Lara, C. Caballo, M.D. Sicilia, S. Rubio, Speeding up the extraction of hexabromocyclododecane enantiomers in soils and sediments based on halogen bonding, Anal. Chem. Acta, 2018, 1027, 47-56, https://doi.org/10.1016/j.aca.2018.15.002

40. A.M. Zeid, J.J.M. Nasr, F. Belal, M. Walash, N. Kaji, Y. Baba Y. Midrofluidic fast chiral separation of baclofen and phenylalanine enantiomers based on cyclodextrin-electrokinetic chromatography, Microchem. J. 2021, 160, 105770, https;//doi.org/10.1016/J.microc.2020.105770

41. M. Protti, R. Mandrioli, L. Mercoline, Enantioselective analysis of the methamphetamine precursors ephedrine and pseudoephedrine by capillary electrokinetic chromatography using cyclodextrins as chiral selectors, J. Chromatogr. Open, 2022, 2, 100032. https://doi.org/10.1016/j.coa.2022.100032

42. A.M. Zeid, J.J.M. Nasr, Y. Baba, Microfluidic fast chiral separation of baclofen and phenylalanine enantiomers based on cyclodextrin-electrokinetic chromatography, Microchem. J. Part B, 2021, 160, 105770, https;//doi.org/10.1016/j.micro.2020.105770.

43. S.K. Strain, M.D. Croves, K.L. Olino, M.R. Emmett, Measurement of 2-hydroxyglutarate enantiomers in serum by chiral gas chromatography-tandem mass spectrometry and its application as a biomarker for IDH mutant gliomas, Cin. Mass Spectr. 2020, 15, 16-24. https://doi.org/10.1016/j.clinms.2019.11.002

44. F. Quattrini, G. Biressi, M. Juza, M. Mazzotti, C. Fuganti, M. Morbidelli, Enantiomer separation of a-ionone using gas chromatography with cyclodextrin derivatives as chiral stationary phase, J. Chromatogr. A, 1999, 865, 201-210, https://doi.org/10.1016/50021-9673(99)00998-X

45. L. Khvalbota, A. Machynakova, J. Cuchorova, K. Furdikova, L. Spanik, Enantiomer composition of chiral compounds present in traditional Slovak tokay wines, J. Food Comp. Anal., 2021, 96, 103719. Httop://doi.org/10.1016/j.fca.2020.103719.

46. S. Ma, G. Ren, J. Cui, M. Lin, J. Wang, J. Yuan, W. Yin, P. Peng, Z. Yu, Chiral signatures of polychlorinated biphenyls in serum from e-waste workers and their correlation with hydroxylated metabolites, Chemosphere, 2022, 304, 135212, https://doi.org/10.1016/j.chemosphere.2022.135212

47. C-Y. Shao, Y. Zhang, H-P. Lv, Z-E. Zhang, J.M. Zeng, Q-H. Peng, Y. Zhu, Z. Lin, Aromatic profiles and enantiomeric distributions of chiral odorants in baked green teas with different picking tenderness, Food Chemistry 2022, 388, 132969, https://doi.org/10.1016/j.foodchem.2022.132969

48. O. Vyviurskaa, N. Koljanci, A.A. Gomes, I. Špánik, Optimization of enantiomer separation in flow-modulated comprehensive two-dimensional gas chromatography by response surface methodology coupled to artificial neural networks: Wine analysis case study, J. Chromatogr. A 2022, 1675, 463189, https://doi.org/10.1016/j.chroma.2022.463189

49. F. Federico Stilo, M.C. Rosso, S. Square, C. Bicchi1, C. Cordero, C. Cagliero, L. Corylus avellana, Natural Signature: Chiral Recognition of Selected Informative Components in the Volatilome of High-Quality Hazelnuts, Front. Plant Sci. 2022, 13, 844711, doi: 10.3389/fpls.2022.844711

50. K. Swor1, A. Poudel, P. Satyal, W.N. Setzer, Enantiomeric Distribution of Terpenoids in Juniperus Essential Oils: Composition of Juniperus horizontalis and Juniperus scopulorum Leaf Essential Oils From Southwestern Idaho, Natural Product Commun. 2022, 17, 1–6, DOI:10.1177/1934578X221091006.

51. L. Bezhitashvili, A. Bardavelidze, T. Ordjonikidze, L. Chankvetradzem, M. Chitty, T. Farkas, B. Chankveradze, Effect of pore-size optimization on the performance of polysaccharide-based superficially porous chiral stationary phases bor the separation of enantiomers in high-performance liquid chromatography, J. Chromatogr. A, 2017, 1482, 32-38. http://dx.doi.org/10.1016.chroma.2016.12.055

52. S. Pantsulaia, K. Targamadze, N. Khundadze, Q. Kharaishvili, A. Volonterio, m. Chitty, T. Farkas, B. Chankveradze, J. Chromatogr. A, 2020, 1625, 461297. https://doi.org/10.1016/j.chroma.2020.461297.

53. Z. Shedania, R. Kakava, A. Volonterio, T. Farkas, B. Chankvetadze, J. Chromatogr. A, 2018, 1557, 62-74. https://doi.org/10.1016/j.chroma.2015.05.002.

54. I. Fourel, Enantiomer fraction evaluation of the four stereoisomers of second-generation anticoagulant rodenticides in biological matrices with polysaccharide-bassed chiral selectors and liquid chromatography-tandem mass spectrometry, J. Chromatogr. A, 2022, 1076, 463209. 55. https://doi.org/10.1016/j.chroma.2022.463209.

55. C. Wang, H. Sun, S. Wang, Z. He, L. Zhao, Z. Xiong, F. Qin, Development and validation of a chiral liquid chromatography method for the determination of MP 3950 enantiomers, a high selective 5-HT4 receptor agonist, in rat plasma and its application to stereoselective pharmacokinetic study, J. Chromatogr. B, 2016, 1033-1034, 49-54, http://dx.doi.org/10.1016/j.jchromb.2016.08.012

56. P. Guo, X. An, W. Chen, X. Pan, R. Li, J. Xu, X. Wi, Y. Zheng, F. Dong, Separation and determination of fluindapyr enantiomers in cucumber and tomato and by supercritical fluid chromatography-tandem mass spectrometry, Food Chem., 2022, 395, 133571, fttps://doi.org/10.1016/j.foodchem.2022.133571.

57. R. Cavalcante dos Santon, F.C. Cunha, C.F.C. Marcellos, M.S. Lima de Mello, F.W. Tavares, N. Pereira, Jr; A.G. Barreto, Jr, Adsorption of praziquantel enantiomers on chiral cellulose tris 3-chloro, 4-methylphenylcarbamate by frontal analysis: Fisherian and Bayesian parameter estimation and inference, J. Chromatogr, A, 2022, 1676, 463200, https://.doi.org/10.1016/j.chroma.2022.463200.

58. S. Li, B. Liu, X. Gto, Enantioseparation and determination of flumequine enantiomers in multiple food matrices with chiral liquid chromatography coupled with tandem mass spectrometry, Chirality, 2019, 31, 968-978, https://doi.org/10.1002/chir.23125

59. C. De Lucaa, A. Buratti, W. Umsteadb, P. Francoc, A. Cavazzini, S. Felletti, M. Catani, Investigation of retention behavior of natural cannabinoids on differently substituted polysaccharide-based chiral stationary phases under reversed-phase liquid chromatographic conditions, J. Chromatogr. A 2022, 1672, 46307, https://doi.org/10.1016/j.chroma.2022.463076.

60. A. Bajtai, G. Németi, T.M.. Le, Z. Szakonyi, A. Péter, I. Ilisz, Enantiomeric separation of newly synthesized amino, thio, and oxy derivatives of monoterpene lactones, amides, and ester applying polysaccharide-based chiral stationary phases in normal-phase mode, J. Chromatogr. A 2022, 1672, 463050, https://doi.org/10.1016/j.chroma.2022.463050

61. R. Huber, L. Marcourt, L-M. Quiros-Guerrero, A. Luscher, S. Schnee, E. Michellod, V. Ducret, T. Kohler, K. Perron, J-L. Wolfender, K. Gindro, E,F. Queiroz, Chiral Separation of Stilbene Dimers Generated by Biotransformation for Absolute Configuration Determination and Antibacterial Evaluation, Frontiers in Chemistry, 2022, 10, 912396, doi: 10.3389/fchem.2022.912396

62. Q. Peng, W. Chen, X. Lin, J. Xiao, Y. Liu, X. Zhou, Butenolides from the Coral-Derived Fungus Aspergillus terreus SCSIO41404, Mar. Drugs, 2022, 20, 212. https://doi.org/10.3390/md20030212

63. C. Panella, R. Ferretti, A. Casulli, R. Cirilli, Temperature and eluent composition effects on enantiomer separation of Carvedilol by high-performance liquid chromatography on immobilized amylose-based chiral stationary phases, J. Pharm. Anal. 2019, 9. 324-331. https://doi.org/10.1016/j.jpha.2019.04.002

64. M. Li, X. Liang, X. Guo, X. Di, Z. Jiang, Enantiomeric separation and enantioselective determination of some representative non-steroidal anti-inflammatory drug enantiomers in fish tissues by using chiral liquid chromatography coupled with tandem mass spectrometry, Microchem. J., 2020, 153, 104511, https://doi.org/10.1016/j.microc.2019.104511

65. S. Aslani, M.F. Wahab, M.E. Kenari, A. Berthod, Armstrong, D.W. An examination of the effects of water on normal phase enantioseparations, Anal. Chim. Acta, 2022, 1200, 339603, https://doi.org/10.1016/j.aca.2022.339608.

66. Z. Yao, S. Wu, H. Zhang, X. Feng, Z. Wang, M. Lin, Chiral determination of naringenin by ultra-performance liquid chromatography-tandem mass spectrometry and application in citrus peel and pulp. Front. Nutrition, 2022, 20, doi:10.3389/fnut.2022.906859

67. X. Pan, F. Dong, Z. Chen, J. Xu, X. Liu, X. Wu, Y. Zheng, The application of chiral ultra-fast-performance liquid chromatography tandem mass spectrometry to the separation of the zoxamide enantiomers and the study of enantio-selective degradation process in agriculture plants, J. Chromatogr. A, 2017, 1525, 87-95. https://doi.otg/10.1016/j.chroma.2017.10.016

68. B. Zhu, S. Li, L. Zhou, Q. Li, X. Guo, Simultaneous enantioselective determination of seven psychoactive drugs enantiomers in multi-specie animal tissues with chiral liquid chromatography coupled with tandem mass spectrometry, Food Chem., 2019, 300, 125241. https://doi.org/10.1016/j.foodchem.2019.125241.

69. Y. Deng, R. Wang, B. Song, Y. Yang, D. Hu, X. Xiao, X. Chen, P. Ping Lu, Enantioselective bioaccumulation and toxicity of rac-sulfoxaflor in zebrafish (Danio rerio), Sci.Total Environ. 2022, 817, 153007, http://dx.doi.org/10.1016/j.scitotenv.2022.153007

70. Z. Tong, Y. Chu, H. Wen, B. Li, X. Dong M. Sun, D. Meng, M. Wang, T. Tongchun Gao, J. Duan, Stereoselective bioactivity, toxicity and degradation of novel fungicide sedaxane with four enantiomers under rice-wheat rotation mode, Ecotoxicology and Environmental Safety 2022, 241, 113784, https://doi.org/10.1016/j.ecoenv.2022.113784

71. M. Cobo-Colpe, M. Ramil, R. Cela, I. Rodriguez, Supercritical fluid chromatography time-of-flight mass spectrometry enantiomeric determination on basic drugs in sewage samples. J. Chromatogr. A., 2022, 1673, 463088, https://doi.org/10.1016/j.chroma.2022.463088.

72. M. Xu, E. Oppong-Danquah, X. Wang, S. Oddsson, A. Abdelrahman, S.V. Pedersen, M. Szomek, A.E. Gylfason, B.S. Snorradottir, E.A. Christensen, D. Tasdemir, C.J. Jameson, S. Murad, O.S. Andresson, K.P. Magnusson, H.J. de Boer, M. Thorsteinsdottir, S. Omarsdottir, S. Heidmarsson, E.S. Olafsdottir, Novel methods to characterize spatial distribution and enantiomeric composition of usnic acids in four Icelandic lichens, Phytochemistry 2022, 200, 113210, https://doi.org/10.1016/j.phytochem.2022.113210

73. I. Ali, S.D. Alam, M. Silllanpaa, Chiral separation of β-blockers by supercritical fluid chromatography using Chiralpak-IG and Chiralpak IBN-5 columns, Chirality 2022, 34, 848-855 https://doi.org/10.1002/chir.23440

74. F.C.T. Elder, B. Pascoe, B.; Wells, S.; Sheppard, S.K.; Snape, J.; Gaze, W.H.; Feil, E.J.; Kasprzyk-Hordern, B. Stereoselective metabolism of chloramphenicol by bacteria isolated from wastewater, and the importance of stereochemistry in environmental risk assessments for antibiotics, Water Research 2022, 217, 118415, https://doi.org/10.1016/j.watres.2022.118415

75. Q. Kharaishvili, G. Jibuti, T. Farkas, B. Chankvetadze, Further proof to the utility of polysaccharide-based chiral selectors in combination with superficially porous silica particles as effective chiral stationary phases or separation of enantiomers in high-performance liquid chromatography, J. Chromatogr. A, 2016, 1467, 163-168. http://dx.doi.org/10.1016/j.chroma.2016.08.1419.

76. M. Gumustas, S.A. Ozkan, B. Chankvetadze, Separation and elution order of the enantiomers of some β-agonists using polysaccharide-based chiral columns and normal phase eluents by high-performance liquid chromatography, J. Chromatog. A, 2016, 1467, 297-305. http://dx.doi.org/10.1016/j.chroma.2016.08.011.

77. I. Matarashvili, A. Chelidze, G. Dolidze, G. Kobidze, N. Zaqashvili, A. Dadianidze, I. Bacskay, A. Felinger, T. Farkas, Separation of enantiomers of chiral basic drugs with amylose- and cellulose-phenylcarbamate-based chiral columns in acetonitrile and aqueous-acetonitrile in high-performance liquid chromatography with a focus on substituent electron-donor and electron-acceptor effects. J. Chromatogr. A, 2020, 1624, 461218, https://doi.org/10.1016/j.chroma.2020.461218.

78. I. Matarashvile, D. Ghughunishvili, L. Chankvetadze, N. Takaishvili, K. Khatiashvili, M. Tsintsadze, T. Farkas, B. Chankvetadze, B. Separation of enantiomers of chiral weak acids with polysaccharide based chiral columns and aqueous-organic mobile phases in high-performance liquid chromatography: Typical reversed-phase behavior? J. Chromatogr. A, 2017, 1483, 86-92. http://dx.doi.org/10.1016/j.chroma.2016.12.064.

79. L. Paolini, N. Haussern, T. Zhang, Chiral resolution of the insecticide fipronil enantiomers and the simultaneous determination of its major

transformation products by high-performance liquid chromatography interfaced with mass spectrometry. Chirality, 2022, 34, 473-483, https://doi.org/10.1002/chir.23412

80. S. Fanali, Nano-liquid chromatography applied to enantiomers separation, J. Chromatogr. A, 2017, 1486, 20-34, http://org.doi/10.1046/j.chroma.2016.10.028
81. K. Igawa, K. Uehara, Y. Kawasaki, K. Tomooka, Stereochemical study on planar-chiral cyclic molecules using polysaccharide-based column chromatography, Chirality, 2022, 34, 824-832, https://doi.org/10.1002/chir.23429
82. M.G. De Cesaris, G. ,D'Orazio, C. Fanali, A. Gentili, N. Takaishvili, B. Chankvetadze, S. Fanali, Enantioseparation of selected chiral agrochemicals by using nano-liquid chromatography and capillary electrochromatography with amylose tris(3-chloro-5-methylphenylcarbamate) covalently immobilized onto silica, J. Chromatogr. A, 2022, 1673, 463128, https://doi.org/10.1016/j.chroma.2022.463128
83. Y. Sun, P. Jia, J. Wei, Y. Bai L. Yang, Y. Bai, X. Zheng, Simultaneous and rapid analysis of chiral Danshensu and its ester derivatives by supercritical fluid chromatography, J. Pharm. Biom. Anal. 2022, 219, 114884, https://doi.org/10.1016/j.jpba.2022.114884
84. G.L. Losaccoa, J.O. DaSilvaa, I.A.H. Ahmada, I. Mangiona, T.A. Berger, E.L. Regalado, Parallel chiral sub/supercritical fluid chromatography screening as a framework for accelerated purification of pharmaceutical targets, J. Chromatogr. A, 2022, 1674, 463094, https://doi.org/10.1016/j.chroma.2022.463094
85. M. Losacker, M. Hundertmark, S. Zörntlein, J. Röhrich, C. Hess, Chiral pharmacokinetics of tetramisole stereoisomers— Enantioselective quantification of levamisole and dexamisole in serum samples from users of adulterated cocaine, Drug Test Anal. 2022, 14, 1053–1064, DOI: 10.1002/dta.3227
86. I.S. Perovani, M.F.S. Barbetta, R.M. da Silva, N.P. Lopes, A.R.M. de Oliveira, In vitro-in vivo correlation of the chiral pesticide prothioconazole after interaction with human CYP450 enzymes, Food Chem. Toxic. 2022, 163, 112947, https://doi.org/10.1016/j.fct.2022.112947
87. M. Zoccali, M. Russo, M.R.T. Camillo, F. Salafia, P.Q. Tranchida, P. Paola Dugo, L. Mondello, On-line coupling of supercritical fluid extraction with enantioselective supercritical fluid chromatography-triple quadrupole mass spectrometry for the determination of chiral pesticides in hemp seeds: A proof-of-principle study, Food Chem. 2022, 373, 131418, https://doi.org/10.1016/j.foodchem.2021.131418.
88. M. Losacker, S. Zörntlein, B. Schwarze, S. Staudt, J. Röhrich, C. Hess, Determination of the enantiomeric composition of amphetamine, methamphetamine and 3,4-methylenedioxy-N-methylamphetamine (MDMA) in seized street drug samples from southern Germany, Drug Test Anal. 2022, 14, 557–566. DOI: 10.1002/dta.3118
89. J. Hermansson, Direct liquid chromatographic resolution of racemic drugs using a1-acid glycoprotein as the chiral stationary phase, J. Chromatogr. A, 1983, 269, 71-80. 93. https://doi.org//10.1016/S2011-96373(01)90787-3
90. R. George, M. Lobb, A. Haywood, S. Khan, J. Hardy, P. Good, S. Hennig, R. Norris, Quantitative determination of the enantiomers of methadone in human plasma and saliva by chiral column Chromatography coupled with mass spectrometric detection, Talanta, 2016, 149, 142-148, https://doi.org/10.1016/j.talanta.2015.11.044
91. L. Lukas Gebauer, N.A. Murugan, O. Jensen, J. Brockmoller, M. Rafehi, Molecular basis for stereoselective transport of fenoterol by the organic cation transporters 1 and 2, Biochem. Pharmacol. 2022, 197, 114871, https://doi.org/10.1016/j.bcp.2021.114871
92. R. Liu, X. Tang, R. Xiong, L. Li, X. Du, L. He, Simultaneous determination of fourteen β2-agonist 97. enantiomers in food animal muscles by liquid chromatography coupled with tandem mass spectrometry, J. Chromatogr. B, 2022, 1193, 123169. https://doi.org/10.1016/j.jchromb.2022.123160
93. M.S. Arnipalli, N. Nimmu, … A.E. Kola, New enantioselective liquid chromatography method development and validation of dipeptidyl peptidase IV inhibitors using a macrocyclic glycopeptide (vancomycin) chiral stationary phase under polar ionic mode condition, Chirality, 2022, 34, 989-998. https://doi.org/10.1002/chir.23448
94. R. Liu, X. Tang, R. Xiong, L. Li, X. Du, L. He, Simultaneous determination of fourteen β2-agonist enantiomers in food animal muscles by liquid chromatography coupled with tandem mass spectrometry, J. Chromatogr. B 2022, 1193, 123169, https://doi.org/10.1016/j.jchromb.2022.123169.
95. C.R. Smith, M.J. Swartwood, Chiral separation and quantification of d,l-methylphenidate, d,l-ethylphenidate, and ritalinic acid in blood by LC-MS/MS, Forensic Chem. 2022, 27, 100400, https://doi.org/10.1016/j.forc.2022.100400
96. Y. Chen, I. Xia, Z. Lu, G. Li, Y. Hu, In situ fabrication of chiral covalent triazine frameworks membranes for enantiomer separation, J . Chromatogr. A, 2021, 1654, 462475. https;//doi.org/10.1016/l.chroma.2021.462475.
97. H-L. Qian, F. Liu, X. Liu, C. Yang, X-P. Yan, Chiral covalent organic framework-monolith as stationary phase for high-performance liquid chromatographic enantioseparation of selected amino acid, Anal. Bioanal. Chem. 2022, 414, 5255-5262. DOI: 1007/s00216-021-03574-3
98. H-L. Qian, C-X. Yang, X-P. Yan, Bottom-up synthesis of chiral covalent organic frameworks and their bound capillaries for chiral separation, Nature Commun. 2016, 2, DOI: 10.1038/ncomms12104
99. H. Pei, J. Wang, X. Jin, X. Zhang, W. Liu, R. Guo, N. Liu, Z. Mo, An electrochemical chiral sensor based on glutamic acid functionalized graphene-gold nanocomposites for chiral recognition of tryptophan enantiomers, J. Electroanal. Chem.,2022, 913, 116283. https://doi.org/10.1016/j.elechem.2022.116283.
100. P/ Vankatova, A. Kubickova, K. Kalikova, Enantioseparation of liquid crystals and their utilization as enantiodiscrimination materials, J. Chromatogr. A, 2022, 1673, 463074. https://doi.org/10.1016/j.chroma.2022.463074
101. S. He, Y. He, L. Cheng, Y. Wu, Y. Ke, Novel chiral ionic liquids stationary phases for the enantiomer separation of chiral acid by high-performance liquid chromatography, Chirality, 2018, 30, 670-679, https://doi.org/10.1002/chir.22839

Chapter 9: Physical biochemistry of enzyme reactions

This chapter begins with equations that describe phenomena in general terms; readers may struggle to understand specific phenomena from these equations. Computational chemistry can provide values that describe molecular properties for quantitative comparison. Consequently, we first obtain (calculate) molecular properties, combine them with the equations, and explain these phenomena quantitatively. Alternatively, we can simplify the process by directly calculating properties from the drawn molecules. The latter method lacks an understanding of the biochemical mechanisms but can explain these phenomena quantitatively and advance research projects. Biochemistry describes biological reactions as part of chemistry, where enzymes convert precursors into target molecules (metabolism) through selective molecular interactions with substrates. Enzyme reactions show selectivity different from chemical reactions; biochemical reactions are slow, while organic reactions are generally rapid. However, they require complex purification procedures for mixed products, while slow reactions require simpler purification.

Quantitative *in silico* analysis of enzyme reactions enables effective drug design and the development of mutants to prepare practical immunoassays. It also reduces animal testing. Molecular engineering approaches to generate improved molecules for use in various industrial production and medical settings are increasingly in demand. Designing proteins fundamentally requires a quantitative understanding of enzyme reaction mechanisms. In this context, we have developed a quantitative analysis of enzyme reactivity. Auto-docking programs are not satisfactory for this purpose mainly because they recognize molecular shape rather than the priority of the reaction center. Enzymatic reactions are typically simple chemical reactions in specific chambers where electron transfer can occur under low-energy conditions. One possible approach to finding an effective compound is to replace the original substrate used to obtain a protein crystal with a new substrate, then quantitatively analyze the resulting conformations. Quantitative methods for analyzing enzyme activity are critical for developing precise diagnostic methods, drug discovery, and reducing the number of animal tests. However, the specific affinity of an enzyme reaction can be analyzed *in silico*, even though generalizing the selectivity of an enzyme reaction remains an insoluble research target. However, we cannot automatically use downloaded protein structures from PDB files; we must review the downloaded structure, search for strange bonds and amino acids, and then fix the structure correctly. Basically, the amino acid structures are fixed during reconstruction for the exhibition; however, the lysine ε-amino group nitrogen shows a sp^2-like atom or connects with an unexpected atom. A critical consideration is that the enzyme structure is not automatically corrected. The following demonstration describes this evidence and the correction procedure.

Proteins relax the three-dimensional structure, collect various substrates, and tighten the complex structure; then, they metabolize the substrates. Alternatively, substrates can tighten the complex and inhibit enzyme activity. These complex mechanisms, based on a combination of ion-ion interactions (Coulomb forces), hydrogen bonding, and van der Waals forces, were evaluated using molecular mechanics calculations, and steric hindrance affects feasibility. Ion-ion interaction, calculated as electrostatic energy, is the strongest molecular interaction force; therefore, we quantitatively analyzed the properties of ion-exchange groups by binding alkyl groups to avoid matrix effects associated with ion-exchange groups. This approach was applied to quantitatively analyze enzyme reactivity, including alanine racemase, serine racemase, alcohol dehydrogenase, cinnamyl alcohol dehydrogenase, and *D*-amino acid oxidase (DAO) and *D*-aspartic acid oxidase (DDO). Arginine is the key amino acid that binds to these oxidases and racemases because of its strongly basic guanidino group. Individual cases are described separately.

9.1. Alcohol Dehydrogenase

Alcohol dehydrogenase (ADH) belongs to the oxidoreductase family, a class of enzymes that catalyze biological oxidation-reduction reactions. ADH catalyzes the interconversion between alcohols and the corresponding aldehydes or ketones using nicotinamide-8-iodo-adenine-dinucleotide (NADH) as a coenzyme; therefore, the reaction selectivity is an interesting subject. A protein fluorescence-quenching study ruled out the need for product dissociation [1]. Proton release preceded NAD^+ reduction at neutral pH. After ternary-complex formation, the catalytic step forms the enzyme-NADH-aldehyde complex. The role of the zinc ions in catalysis remains unclear; however, they likely increase the acidity of the alcohol hydroxyl group, facilitating hydride transfer via a related mechanism [2-4]. The stoichiometry of the oxidation reaction has suggested the release of one proton from the alcohol. Furthermore, no free-radical reduction involving carbon-hydrogen bond cleavage was observed, as probed using halo ketones to test for a radical intermediate in the NADH/liver alcohol dehydrogenase reduction reaction. A three-step reaction mechanism was proposed rather than a direct release mechanism [5].

The alcohol binds to the zinc ion through the oxygen atom, and this inner-sphere binding induces ionization of the alcohol to the alkoxide form. Formation of a zinc-bound alkoxide ion is necessary to form the closed conformation of the NADH ternary complex before hydride transfer. The lower the alcohol p*K*a, the greater the inductive effect on the hydride-donor carbon atom. For alcohols with electron-donating substituents at the C2 atom, ionization occurs at a relatively higher p*K*a, and hydride transfer therefore occurs more quickly [6]. The catalytic efficiency of the amphibian alcohol dehydrogenase enzyme ADH8, the vertebrate ADH with coenzyme NADPH, is greater for medium- or long-chain substrates such as hexanal, *trans*-2-hexanal, and several retinoid isomers, and their corresponding alcohols or retinols [7]. Comparison of three-dimensional (3D) structures suggested that a zinc ion may mediate displacement of the zinc-bound water molecule by an alcohol or aldehyde. That water played no catalytic role [8]. Possible electron transfer can be inferred from the electron localization of the targeted atoms and the position of the alcohol hydroxyl group. The detailed crystal structure of the cinnamyl ADH from Saccharomyces cerevisiae has been determined [9]. Further, the crystal structure of the ternary complex of the slow-allele form of Drosophila melanogaster ADH with NADH and acetate has also been determined [10]. We compared the three-dimensional structure of Drosophila melanogaster ADH-S with a theoretically built homology model. Moreover, the differences in the crystal structures of five available Drosophila lebanonensis ADHs in multiple complex forms were evaluated, residue conservation at the active site was examined, and the mutagenesis data available for the enzymes were interpreted [11].

Quantitative analysis of an enzyme's activity enables the design of mutants needed to develop practical immunoassay methods, enzymatic biosensors, engineered enzymes, and new drugs. Researchers have studied the basic phenomenon of protein-mediated molecular recognition by quantitatively analyzing molecular interactions using chromatography. Alcohol dehydrogenase (ADH) belongs to the oxidoreductase family, a class of enzymes that catalyze biological oxidation-reduction reactions. ADH catalyzes the interconversion between alcohols and the corresponding aldehydes or ketones using NADH as a coenzyme. Two types of ADHs exist: one is zinc-dependent, and another is zinc-independent. They require the coenzyme NAD (Nicotinamide-8-iodo-adenine-dinucleotide); therefore, the reaction selectivity is an interesting subject. Drosophila melanogaster's H is zinc-independent; the downloaded crystal structure (PDB 1MG5) is shown in Figure 9.1.

Figure 9.1: Download PDB 1MG5 structure. Red (black), blue (dark gray), yellow (light gray), and white are oxygen, nitrogen, carbon, and hydrogen.

The structure in Figure 9.1 does not clearly show the ADH conformation; therefore, hydrogen is added to the oxygen atom of the water molecule using Valence. The result produced the structure in Figure 9.2. Figure 9.3 shows the selected water in the menu and the water removed, making the ADH structure clear. The original structure appears as a dimer, as shown in Figure 9.4. Figure 9.5 shows the rotating structures to demonstrate their clarity. Figure 9.6 shows the location of coenzyme NAD and the substrate aldehyde. The structures of NAD and the aldehyde do not represent their actual molecular structures. Generally, we should question the downloaded coenzyme and substituent structures.

FIgure 9.2: Addition of hydrogen using Valence. Red (black), blue (dark gray), yellow (light gray), and white are oxygen, nitrogen, carbon, and hydrogen.

FIgure 9.3: 1MG5 removed the water molecules.

FIgure 9.4: Single thread structure.

FIgure 9.5: Location of two sets of molecules.

FIgure 9.6: An original molecular view of Figure 9.5.

FIgure 9.7: Extracted one ADH complex.

FIgure 9.8: Threaded pods view of ADH.

In the fixing process of a downloaded protein structure, lysine appears as an unusual molecular structure whose ε-amine hydrogen connects to a strange oxygen far from the lysine. The ε-amino nitrogen should be a positively charged sp^3 atom, but it appears as an sp^2 amine. Carefully examine aspartic and glutamic acid carbonyl groups. The double bond appears as a single bond, and the sulfur atom of cysteine also appears incorrectly. Usually, residual amino acids are presented as corrected structures; however, we must carefully examine their structure before further analysis. Select an amino acid on the sequence chart, view the enlarged structure, follow the step-by-step instructions, and correct the structure. Figure 9.9 shows an extracted structure of coenzyme NAD and the fixed structure.

FIgure 9.9: Downloaded and extracted NAD (A) and corrected NAD (B), Red (black), Blue (dark gray), yellow (light gray), white, and large magenta (black) are oxygen, nitrogen, carbon, hydrogen, and phosphorus..

After correcting the protein structure, the thread structure presents the location of the coenzyme and substrate. Then, optimize the structure using the MM2 program. Now, replace the original substrate with a target analyte and optimize the new complex structure. Repeat the process and analyze enzyme specificity. Figures 9.10 and 11 show the optimized structures for isopropyl alcohol and acetaldehyde.

FIgure 9.10: Optimized structures of isopropyl alcohol oxidation and acetaldehyde reduction reaction.

FIgure 9.11: Extracted conformations of isopropyl alcohol and acetaldehyde locations with NAD..

After optimizing the complex structure, extract molecules within 3 Å of the substrate, as shown in Figure 9.11. Lock the extracted complex; then, optimize it using MOPAC PM5 or a more recent program to analyze substrate specificity. Read the atomic partial charge (APC) of target atoms and assess the balance relative to the original values. The change in apc indicates reactivity: the larger the value, the stronger the reaction. The balance (Δ) apc values of the α-carbon were related to reactivity, suggesting the enzyme's substrate specificity. The Δapc values of ethyl alcohol, propyl alcohol, butyl alcohol, pentyl alcohol, isopropyl alcohol, isobutyl alcohol, furfural, allyl alcohol, and cinnamyl alcohol correlated with their *V*max/*K*m ($min^{-1}.mg^{-1}$) values (r = 0.838; n = 9). In the oxidative reaction, *V*max/*K*m ($min^{-1}.mg^{-1}$) values correlated with the Δapc values of the fifth carbon of the pyridine ring (r =915 (n = 9). The substrates are formaldehyde, acetaldehyde, propyl aldehyde, butyl aldehyde, pentyl aldehyde, benzyl aldehyde, furfural, acrolein, and cinnamyl aldehyde.

The structure in PDB 4W6Z of zinc-dependent ADH (ADHZ) from yeast is shown in Figure 9.12. The thread structure indicates that the downloaded structure appears to be a dimer. It looks like two molecules, as shown in Figures 9.12 and 13; rotation of the structure indicates a tetramer (Figure 9.14). Figure 9.15 shows the selected dimer. The complex on the left did not include coenzyme; therefore, the complex on the right was used. Figures 9.16 and 9.17 show one set of the enzyme, including a coenzyme and a substitute. Figures 9.18 and 9.19 indicate the precise location of zinc, the coenzyme, and the substrate.

FIgure 9.12: Downloaded ADHZ, 4W6Z.

Figure 9.13: Thread structure of Figure 9.12.

Figure 9.14: Rotated structure of Figure 9.12

Figure 9.15: A pair of 4W6Z structure2

Figure 9.16: A set of enzyme ADHZ..

Figure 9.17: Location of coenzyme, zinc, and substitute.

FIgure 9.18: Optimized locations of isopropyl alcohol and propyl aldehyde.

FIgure 9.19: Extracted conformations around isopropanol and propyl aldehyde.

The structure of protein ogenic amino acids in yeast ADHZ (PDB 4W6Z) was corrected. After correcting the coenzyme and substrate structure, the complex structure was optimized using the MM2 program. We replaced the original substrate with the target alcohol and optimized the structure. This procedure was repeated as performed for the 1MG5 complex, and the reaction selectivity was analyzed. Then, molecules within 3 Å of the locked molecules (Figure 9.19) were selected and optimized using MOPAC PM5 (or a more recent program). The optimized locations of NAD, Zn, iPrOH, NADH, Zn, and propanal are shown in Figure 9.20. We determined the α-carbon apc values of ethyl alcohol, propyl alcohol, butyl alcohol, pentyl alcohol, isopropyl alcohol, isobutyl alcohol, furfural, allyl alcohol, and cinnamyl alcohol, and calculated the difference from the original values. The Δapc values indicated the enzyme's substrate specificity. The correlation coefficient with their *V*max/*K*m (min^{-1} .mg^{-1}) values was 0.869 (n = 9). In the oxidative reaction, the correlation between the Δapc values of the fifth carbon of the pyridine ring and *V*max/*K*m (min^{-1} .mg^{-1}) was r = 0.915 (n = 9). The substrates were formaldehyde, acetaldehyde, propionaldehyde, butanal, pentanal, benzaldehyde, furfural, acrolein, and cinnamaldehyde.

FIgure 9.20: Further extracted conformations of coenzyme, zinc, and substitute.

Studying an enzyme's substrate specificity is easy if the protein's three-dimensional structure is listed in the PDB file. Download a structure, carefully correct the molecule's structure; then, optimize the complex structure using an MM2 program. Then replace the original substrate with the target substrate by superimposing the structures and optimizing the new complex. Extract molecules within 3 Å of the substrate, and lock them for further optimization using MOPAC PM5 (or a more recent program) to obtain apc values. Calculate the changes in apc values and correlate it with the measured reactivity.

9.2. Cinnamyl-alcohol Dehydrogenase (CAD) ELI3-2

CAD, a YMR318C gene product, is specific for NADPH and shows activity for a wide variety of substrates. In CAD, aldehydes are processed with 50-fold higher catalytic efficiency than the corresponding alcohols [12]. The apo and holo structures of an NADPH-dependent CAD from Saccharomyces cerevisiae were reported. The Saccharomyces cerevisiae ScAdh6p is structurally a heterodimer composed of one subunit in the apo conformation and the other subunit in the holo

conformation. ScAdh6p specificity for NADPH mainly arises from tripod-like interactions between the NADPH terminal phosphate group and the enzyme's S-210, R-211, and K-215 residues. The size and shape of the substrate-binding pocket correlated well with ScAdh6p specificity for cinnamaldehyde and other aromatic compounds. The function of CAD enzymes in bacteria and yeast needs to be clearly established [10]. CAD enzymes were originally discovered in plants, where they catalyze lignin precursor biosynthesis. Transgenic trees with reduced CAD activity are easier to delignify; therefore, this enzyme family is a favored target for biotechnological modification [13]. However, one member of the CAD family, ELI3, shows different enzymatic activities unrelated to lignin synthesis. Mannitol dehydrogenase, found in celery, oxidizes mannitol to mannose. Mannitol dehydrogenase is the ELI3 pathogenesis-related protein from parsley and Arabidopsis [14]. The biochemical function of Arabidopsis thaliana defense-related protein ELI3-2, found in Escherichia coli, is an aromatic alcohol: NADP+ oxidoreductase. This enzyme strongly prefers various aromatic aldehydes over the corresponding alcohols; however, no mannitol dehydrogenase activity was detected [15].

These reports do not clearly explain the ADH reaction mechanism. A cofactor activates a protein by either changing its 3D structure or participating in the overall reaction mechanism. Researchers have studied zinc's contribution to the ADH mechanism using a model compound under non-aqueous conditions; however, the effects of zinc catalysis on rate enhancement or product yield were small and did not clarify this important enzymatic process [16,17]. Therefore, we used the crystal structures of a zinc-dependent Saccharomyces cerevisiae ADH (4W6Z in PDB) and a zinc-independent Drosophila melanogaster ADH (1MG5 in PDB) as model enzymes and evaluated their binding affinities after replacing the substrate with various alcohols and aldehydes to study the ADH reaction mechanism. We also quantitatively analyzed enzyme reactivity of CAD ELI3 [18].

The biochemical function of Arabidopsis thaliana defense-related protein ELI3-2, found in Escherichia coli, is an aromatic alcohol: $NADP^+$ oxidoreductase. This enzyme strongly prefers various aromatic aldehydes over the corresponding alcohols; however, we detected no mannitol dehydrogenase activity. The downloaded cinnamyl alcohol dehydrogenase (CAD-2CP5) did not include coenzyme $NADP^+$; therefore, we downloaded 1PIW and used it as a model. The amino acid sequences of ELI3 and 1PIW differ, with 33.4% sequence similarity. However, if the enzyme reaction mechanisms are the same for both enzymes, they should have similar three-dimensional conformations. Therefore, we replaced the amino acid residues of 1PIW with those of ELI3 and optimized the conformation by MM2 calculations. Figure 9.21 shows the downloaded 1PIW structure, and Figure 9.22 shows the ELIS-3 modified from 1PIW.

Figure 9.21: Structure of downloaded 1PIW.

Figure 9.22: Constructed ELIS from 1PIW.

Figure 9.23: ELIS3 with high molecular mass substrate.

Figure 9.24: ELIS3 with 2- methoxybenzaldehyde substrate.

The 1PIW-modified ELIS3 structure retained the fundamental three-dimensional structure of 1PIW. ELIS3 handles large molecules; therefore, we modified the original substrate to increase its molecular mass to facilitate docking with large compounds, as shown in Figure 9.23. Then, the temporary substrate was replaced with a target substrate. Figure 9.24 shows the optimized ELIS3-2-methoxybenzaldehyde complex. Figure 9.25 shows the ELIS3 and 4-Coumaraldehyde complex, and Figure 9.26 shows the we extracted molecules within 3 Å from the substrate.

Figure 9.25: ELIS3 and 4-coumaraldehyde complex.

Figure 9.26: Location of amino acids, Zn, and NADP+

In the modification process from the template protein to a target protein, step-by-step optimization is necessary. Figure 9.27 shows the optimized ELIS3 structure after replacing all amino acids. The optimized structure retained the helical regions, but the coil-coil interactions failed, and the coenzyme separated.

FIgure 9.27: Directly optimized ELI3 structure after replacing whole amino acids.

Technically, replacing amino acids and optimizing the process is crucial for modifying the original protein into a mutant. We first locked all amino acids during structural replacement to avoid affecting the original three-dimensional structure. Subsequently, selected amino acids at the beginning and end of the protein were replaced with these residues unlocked because changes to these amino acids do not disrupt the protein's three-dimensional structure. The resulting structure was then optimized by MM2 calculations. In the second step, we selected an amino acid within a helix and replaced it with the desired amino acid. The whole structure was optimized, while the new amino acid was kept unlocked. Furthermore, the conformation of the replaced amino acid was analyzed to make sure that this amino acid was independent of other amino acids. Consequently, the newly replaced amino acid and both side amino acids were unlocked, and the protein structure was optimized. The entire three-dimensional structure was optimized again by unlocking all amino acids. If needed, we unlocked amino acids in helices before final optimization using MM2.

First, the helix amino acids were replaced, then the connected ribbon high-freedom peptide amino acids. Replacing both end amino acids is simple; these amino acids may not contribute to the enzyme reaction. Further attention should be given to replacing the large-mass substrate with the small original substrate used to make the crystal because the steric hindrance may cause unacceptable conformation. The three-dimensional structure of ELIS3 shown in Figure 9.28 indicates that the reaction chamber space is very narrow for large mass substrates. Therefore, the trifluoroalcohol fluorine on the substrate is converted to a methyl group to enlarge the reaction chamber, as shown in Figure 9.22. The position of the reaction-center group must be maintained; added groups may cause steric hindrance to argement converts one methyl hydrogen.

Now, replace the original substrate with a target analyte by superimposing their alcoholic hydroxy or aldehyde carbonyl groups; optimize the new complex structure. Repeat the process and analyze enzyme specificity. Figure 9.28 demonstrates the optimized structure of 2-methoxybenzaldehyde, zinc, NADP+, and S45 conformation with their interatomic distances and apc values. This approach can analyze enzyme reactivity related to substrate reactivity (electron localization); however, the cinnamaldehyde reactive group is located against the coenzyme after optimizing the Amber program with the automated docking method using the 1PIW enzyme. The automatic operation using an automated docking program should be doubted.

FIgure 9.28: Location of 2-methoxybenzaldehyde and their atomic distance and apc.

The nearest atom to the aromatic aldehyde oxygen was the threonine hydrogen, but the reactive hydrogen was the fourth carbon-hydrogen of the pyridine ring. The enzyme reactivity of the aromatic aldehydes (*V*max/*K*m) correlated well with the apc on the analyte aldehyde carbon, the fourth carbon, and the fourth hydrogen of the pyridine ring. The correlation coefficients were 0.785, 0.730, and 0.754 (n = 6), respectively. The highest correlation coefficient (0.899; n = 6) was obtained for the atomic distance between the aldehyde oxygen and the fourth carbon of the pyridine ring. The substrates were 2-methoxybenzaldehyde, 3-methoxybenzaldehyde, salicylaldehyde, benzaldehyde, cinnamaldehyde, and 4-coumaraldehyde. The oxygen of cinnamaldehyde and 4-coumraaldehyde existed near zinc; therefore, the zinc should contribute to the reaction. The above results support the feasibility of the modified ELIS3 structure from 1PIW.

9.3. Alanine Racemase

The racemization mechanism of amino acids was studied using arylglycines as the model amino acids. The zwitterion had the greatest reactivity—the inductive effect of the NH3+ group stabilizes the incipient carbanion and reduces the electron density of the α-carbon; removal of the proton attached to the α-carbon leaves behind a planar carbanion [19]. Introducing an electron-withdrawing substituent on the α-carbon atom or the amino group promotes racemization. Ionic strength modestly affects this reaction. The push-pull mechanism was proposed for the racemization of arylglycines in sodium phosphate buffer [20]. Alanine racemase is thought to racemize alanine via initial trans-aldimination, followed by -hydrogen (αH) abstraction to give a resonance-stabilized carbanion. Deprotonation on the opposite face yields the antipodal aldimine, followed by release of the isomerized alanine moiety. The differential active sites for *R*- and *S*-alanine have been proposed. The detailed mechanistic features, however, remain unclear [21]. The crystal structures of alanine racemase bound to reaction-intermediate analogs, *N*-(5'-phosphopyridoxyl)-*S*-alanine and *N*-(5'-phosphopyridoxyl)-*R*-alanine, were determined.Tyrosine-265' (Y265') and lysine-39 (K39) are the catalytic bases for abstracting the α-proton from *S*- and *R*-alanine. The alanine carboxyl group directly contributes to mediating proton transfer between the two catalytic bases K39 and Y265'. The protonated carboxylic group is readily formed to stabilize the α-carbanion [21]. PLP enzymes exist in their resting state as Schiff bases with an active site lysine residue. The incoming amine-containing substrate displaces the lysine ε-amino group from the internal aldimine. Y265 and K39 are likely to be the two acid/base catalysts in a two-base mechanism of racemization [22]. The results indicate that the amino group of the substrate amino acid should be close to the binding site. The efficient catalysis of *S*-alanine deprotonation by PLP and alanine racemase was studied using a computational chemical method. Large solvation effects of the external aldimine cofactor lower the p*K*a of the α-amino acid. Unprotonated PLP increases the acidity of the α-amino acid [23]. Co-enzyme PLP contributes to the racemization reaction process. The electron delocalization in PLP is affected by R136 and R219 [24].

Racemization occurs *in vitro* without an enzyme [19, 25]. If the reaction follows the same scheme *in vivo*, ionized alanine should be near the PLP aldehyde, where it competes with lysine (K39) for binding and replaces K39. Racemization occurs when substrate alanine competes with K39 to bind the PLP aldehyde. An αH on the substrate alanine indicates the possibility of deprotonation inside the alanine racemase. Here, the reaction selectivity of alanine racemase mutants was quantitatively studied based on the above-reported results, and the selectivity of a mutants was compared according to the three-dimensional structure of the alanine racemase. The selective reactivity was determined from data obtained using a mutants arginine-219-lysine (R219K), arginine-219-alanine (R219A), and arginine-219-glutamic acid (R219E) to investigate the role of R219 in catalysis [26]. Different conformations, including K39-conjugated PLP, were constructed to form complexes with either *S*- or *R*-alanine, and optimized the structures, then the alanine conformation to study mutant reactivity was examined. The PLP ring nitrogen forms an intermolecular O-H hydrogen bond with an aspartic acid (Q222) side chain, and the phosphate group forms three hydrogen bonds with other amino acid residues of aspartate aminotransferase from *Escherichia coli* [27].

R-amino acids were not believed to be residual; however, improved analytical methods found small amounts of *R*-amino acids in various locations. In particular, anadromous fish store large amounts of R-amino acids in the sea and convert them to *S*-amino acids in the river. *R*-amino acid is not trace amounts; therefore, it is easily detected without analytical error. Because the conversion is enzymatic, racemase activity has been studied in many systems. Racemase requires pyridoxal 5'-phosphate (PLP) as the coenzyme. Quantitative analysis of reaction mechanisms is not simple because the precursor and reaction products are very similar. Oxidation and reduction reactions produce different molecules; therefore, identifying these compounds is easier than identifying optical isomers. Usually, the racemization mechanisms are believed to occur dynamically by removing can α-hydrogen from one side and adding hydrogen from the other side. Another possible mechanism is that the amino acid adopts a planar structure and then turns over inside the reaction chamber.

The alanine racemase [281L6G structure] whose substrate is *R*-alanine was downloaded from the RCSB Protein Data Bank, and any irregular residues and atoms were corrected. We then separated the PLP-alanine complex into individual molecules. We constructed mutants by replacing R219 with different amino acids; the three-dimensional structure of the complexes was optimized using molecular mechanics force-field parameters (MM2). Furthermore, the apc of key atoms was calculated using MOPAC PM5 after extracting the *R*-alanine, PLP, and surrounding amino acid residues within 3 Å of the *R*-alanine. Figure 9.29 shows the downloaded 1l6g. Figure 9.30 shows water molecules by adding hydrogen to oxygen atoms using the Valence menu.

FIgure 9.29: Downloaded alanine racemase1l6g.

FIgure 9.30: Addition of hydrogen to erase water.

Figure 9.31 exhibits the distribution of water molecules; However, water molecules do not exist between coenzyme PLP and *R*-alanine. Figures 9.31 and 32 show the thread structure, and further correction of the molecule is necessary. The K129 ε-amino group nitrogen should be an anionized sp^3 atom and should not bind the water molecules circled in Figure 9.33. Cut the bond between *R*-alanine and PLP, and the structures of PLP and *R*-alanine. The alanine amino group should be an amino ion, and the carbonyl group should be recovered after replacing carbon with oxygen. The single bonds of the PLP pyridine ring were converted to double bonds, and sp^3carbon was fixed to sp^2 carbon, then used Valence to adjust the number of hydrogens. In addition, the hydroxy oxygen atom should be $sp^{2,}$ and atomic distances should be fixed.

FIgure 9.31: Distribution of water molecules.

FIgure 9.32: Protein (1l6g) spread structure.

Figure 34 shows the corrected structure of Figure 32 left-handside. When correcting unrealistic molecules, lock the whole molecule to preserve the stereostructure, and unlock only the molecule to be corrected. After one correction, lock the molecule; then, move to correct the following molecule. Repeat this process to provide a molecule for further study. After the correction, optimize the complex structure using the MM2 program.

FIgure 9.33: Extracted circled unrealistic molecules.

FIgure 9.34: Left-hand side structure of Figure 9.32.

FIgure 9.35: Optimized complex structure with *R*-alanine.

FIgure 9.36: Optimized complex structure with *S*-alanine.

Figure 9.35 shows the optimized structure with R-alanine; then, lock the structure in Figure 35, and replace *R*-alanine with *S*-alanine after superimposing their carboxy groups. Figure 9.36 shows the optimized structure with *S*-alanine. After optimizing structures in Figures 35 and 36 extracted molecules within 3Å from *R*- and *S*-alanines. Then, locked the structures and optimized using the PM5 program to obtain atomic distance and apc value of target atoms. Figures 9.37 and 38 show their extracted complex structures for *R*- and S-alanines.

FIgure 9.37: Molecules within 3Å from *R*-alanine.

FIgure 9.38: Molecules from *S*-alanine.

Figure 9.37 shows the properties of original *R*- and *S*-alanines and Figure 38 shows the properties of extracted *R*- and *S*-alanines from their complexs tructures for analyzing the balance. Figures 39 and 40 show the atomic angles of these *R*- and *S*-amino acids.

FIgure 9.39: The original structure of *R*- and *S*-alanine.

FIgure 9.40: Extracted structure of *R*- and *S*- alanine.

When the trigonal pyramid structure conversion process from *R*-alanine to *S*-alanine passes the flat conformation, α-hydrogen (αH) properties should differ from the original valuess. Therefore, the atomic angle related to αH and apc should be changed. In Figure 39, the sum of atomic angle was 322.29°,and apc of αH and α-carbon (αC) were 0.186 and -0.240 au for both *R*- and *S*-alanines. In Figure 9.40, the sum of the atomic angles was 320.39°, and apc of αH and αC were 0.185 and -0.166 au for *R*-alanine. However, the sum of the atomic angles was 340.50°, and the apc of H was 0.221 au for *S*-alanine. The racemization produced such a change in the atomic angle and apc.

In addition, the same analysis was performed using the downloaded 1l6f file where *R*-alanine is free from PLP. Deprotonation of the αC and the formation of an imine are the basic mechanisms underlying alanine racemase reactivity, the atomic distance between H and C and the apc of H changed little in the conformations of the molecular structures of PLP and tyrosine. The apc of the alanine αC correlated well with reactivity, and the value was high for *R*-alanine. The difference between 1l6g and 1l6f is that the structures of PLP and *R*-alanine produced slightly different conclusions. Therefore, we used the *S*-alanine complex of optimized 1l6g and reversed the process. We then analyzed the conformation of *R*-alanine. The apc of αH and αC were 0.202 and 0.102 au, respectively, and differed from the original valuess.

The substrate alanine could not bind with PLP or replace K39 bound to PLP; instead, alanine formed a complex with PLP. The calculations were performed without solvent (water). The results may not be directly comparable with those *in vitro*. However, the Lewis acid-base interaction is the strongest. Because water molecules cannot interrupt the Lewis acid-base interaction, this may help bridge the gap. Quantitatively analysis of the selective reactivity of alanine racemase is demonstrated. The *R*-form of alanine was stable in complexes with this enzyme because the enzyme structure favored it. The probability depends on the reality of the three-dimensional structure. The downloaded secondary structures of monomer pairs did not match. The computer system cannot construct the actual three-dimensional structure by itself. Which structure is the right structure? Remain as the fundamental question.

9.4. Human Serine Racemase

Researchers discovered substantial levels of *R*-serine in the mammalian brain in 1992 [29]. Researchers first purified mammalian SR (HSR) from rat brains and functionally characterized it in 1999 [30]. Serine racemase synthesizes *R*-serine from *S*-serine and controls *R*-serine levels by oxidizing *R*-serine to pyruvate. *R*-serine is the main endogenous coagonist of the *N*-methyl-*D*-aspartate (NMDA)-type glutamate receptor (NMDAR). It is involved in important functions such as synaptic plasticity, learning, memory, and excitotoxicity. The X-ray crystal structures of mammalian and rat serine racemase were determined to provide a molecular basis for rational drug design. The racemization reaction critically depended on the proximity of the catalytic S82 to the substrate, as shown by the closed ligand-bound structures [31]. SR was most active as a noncovalent dimer containing one or more free sulfhydryls in the enzyme's active center or a modulatory site. The recombinant HSR was sensitive to oxidative stress *in vivo,* perhaps consistent with a scenario in which such modification plays a role in feedback or other forms of regulation [32]. A decrease in *R*-serine concentration was reported in psychiatric diseases such as schizophrenia and bipolar disorder: association studies had linked DAO and the primate-specific gene 72 (pLG72) with schizophrenia susceptibility. The opportunity to regulate DAO activity opened the way to *R*-serine levels *in vivo* and thus to act on different pathological states involving alterations in NMDAR function. *R*-serine levels decreased in cells overexpressing HDAO, while cotransfection with pLG restored *R*-serine levels and decreased HDAO activity. The results highlight the cellular function of HDAO in *R*-serine catabolism and confirm the role of pLG72 as a negative effector of the flavo enzyme. The Interaction of pLG72 with HDAO on the cytosolic side of the outer mitochondrial membrane induced enzyme inactivation and sped up its degradation. In this way, cytosolic *R*-serine was preserved, and cells were protected from oxidative stress by hydrogen peroxide generated by the flavoprotein in

the cytosol. pLG72 inhibited HDAO and highlighted the specificity of class C compounds, as they did not inhibit glucose oxidase or DDP [33]. The potential involvement of *R*-serine in neurodegenerative diseases relates to impaired DAO activity, which could be developed as a therapeutic agent in Amyotrophic Lateral Sclerosis. *R*-serine up-regulation is caused either by impaired DAO metabolism or increased biosynthesis by SR [34]. Serine racemase is a PLP-dependent enzyme that catalyzes the racemization of *L*-serine to *D*-serine; however, the enzymatic racemization reaction was not fully understood [35]. Therefore, we quantitatively analyzed the bifunctional reaction mechanisms of mammalian SR *in silico,* as with DAO [25, 33, 34] and alanine racemase [28].

R-Serine was believed not to exist in mammalian tissue; however, improved analytical methods detected it in the mammalian brain. Since then, *R*-serine has been considered the main endogenous coagonist of the *N*-methyl-*D*-aspartate (NMDA)-type glutamate receptor (NMDAR), which is involved in essential functions such as synaptic plasticity, learning, memory, and excitotoxicity. Serine racemase (SR) is a pyridoxal 5'-phosphate (PLP)-dependent enzyme that catalyzes the racemization of *S*-serine to *R*-serine and the oxidation of *R*-serine to pyruvate. The bifunctional reaction is supposed to occur at a single site. Given the reaction efficiency, converting *S*-serine to *R*-serine and oxidizing it at the same location is unlikely to produce a measurable amount of *R*-serine. However, manganese exists near PLP, as in zinc for alanine racemase. Therefore, we considered the possibility of a bifunctional reaction at separate locations. The downloaded three-dimensional structures of *Rattusnorvegicus* (PBDID:3hmk) and mammalian(PDBID: 3l6r and 3l6b [28]) SR were optimized using molecular mechanic (MM2) calculation. Furthermore, the three-dimensional structure of mammalian SR was constructed using 3hmk and the amino acid sequence data. PDB files 316b and 316r lack some amino acids (circled in Figures 41 and 42). Therefore, human SR was constructed from *Rattusnorvegicus* SR (PDF: 3hmk) following the human SR (hSR) amino acid sequence. The downloaded three-dimensional structures of 316b, 316r, and 3hmk are shown in Figures 9.41-43.

FIgure 9.41: Downloaded 316b.

FIgure 9.42: Downloaded 316r.

FIgure 9.43: Downloaded 3hmk.

Figures 9.41 and 9.42 indicated a lack of peptides, and the locations are circles in these Figures. Amino acid sequences of 3hmk and HSR are very similar. Both sides of lacked peptides in 316b,316r, and 3hmk are identical; the R58–V68 (RGALNAVRSLV) and P76 –A90 (PKAVVTHSSGNHGQA) are the same.The difference is only T71(A71) and G74(T74) in the latter peptide. Their secondary structures are the same in the ribbon diagram. Therefore, replacing two amino acids is straight forward.

After removing water molecules, Figures 9.44 and 9.45 show the three-dimensional structures of 316b and 316r. The missing peptide is far from these reaction centers, and the reconstructed three-dimensional structure helps evaluate enzyme specificity. The molecular components in Figure 9.44 are malonic acid (used to produce the complex crystal), coenzyme PLP, and manganese. An additional molecule in Figure 45 is deformed methionine.

FIgure 9.44: Downloaded and water removed 316b.

FIgure 9.45: Downloaded and water removed 316t.

316b lacks 5 amino acids (P69 – E73), and 316r lacks 7 amino acids (P69 – K75). Both structures hold malonic acid and PLPK56 binds PLP in 316r, and PLPK56 binds PLP in 316r; the bound molecule is indicated as an unknown molecule. Furthermore, M150, M189, M227, and M279 are also indicated as unknown molecules.

FIgure 9.46: Corrected structure of human serine racemase.

FIgure 9.47: Location of PLP and Mn.

Deprotonation of the α-carbon and imine formation are the basic mechanisms underlying racemase reactivity. The serine carboxamide and amine groups contact the oppositely charged cation and anion of the residue to transfer electrons. The substrate serine formed a complex with PLP. The bond angles of the serine substitute indicated the location of oxidation and racemization. Therefore, bond angles can be used to quantify racemization

In the DAO reaction, the arginine guanidyl group contacts the *D*-amino acid carboxyl group via ion-ion interaction; then, the coenzyme FAD carbonyl contributes to electron localization. Amino acids located within 3 Å of malonic acid are K56, N86, G185, G187, G188, and S313. In the case of *D*-amino acid oxidase, the locations of the FAD flavin ring carbonyl and the substrate amino groups are essential; therefore, the HSR substrate is replaced with *R*-serine to optimize the structure. The optimized structures with *R*- and *S*-serine are shown in Figures 9.48 and 49, respectively.

FIgure 9.48: Location of *R*-serine, PLP, and Mn in hSR.

FIgure 9.49: Location of *S*-serine, PLP, and Mn is hSR.

FIgure 9.50: Molecules within 3Å from *R*-Serine.

FIgure 9.51: Atomic distance from *R*-Serine.

FIgure 9.52: Molecules within 3Å from *S*-Serine.

FIgure 9.53: Atomic distance from *S*-Serine.

Figures 9.51 and 9.53 show that the corresponding arginine of *D*-amino acid oxidase is lysine (K56), whose ionized ε-amino group lies within 2 Å of the serine carboxyl group. The glutamine amino group (Q155) may contribute to racemization. The αC apc value of *R*- and *S*-serine increased to -0.192 and -0.186 from -0.397 and -0.384, respectively. The nitrogen apc of *R*- and *S*-serine decreased from 0.076 and 0.077 to -0.017 and -0.025 au, respectively. Therefore, deamination should occur in this location as *D*-aminoacidoxidase. When the original apc value (-0.384au) of *S*-serine was used, the Δapc of *R*-serine was smaller (0.19au) than that of *S*-serine. The result supported the conclusion that SR oxidized *S*-serine at the site. Normally, hSR favors *S*-serine elimination activity over SR activity [36]. Manganese forms a complex using the hydroxyl group as a ligand [37], and the possible conformation indicates that the hydroxyl group of serine may indeed contribute as a ligand. Serine was non-enzymatically oxidized to pyruvate at metal sites. However, the schematic shows the metal ion near the PLP carbonyl group. Manganese is located opposite the oxidation reaction center in the enzymatic reaction. Furthermore, manganese's catalytic activity is weaker than that of aluminum, copper, and iron, which are involved in serine deamination but not racemization [38]. Manganese forms multi-ligand complexes with water molecules [39-41].

On the other hand, amino acids within 3Å of Mn are E210, A214, and D216; the carbonyl groups of glutamic acid (E210) and aspartic acid (D216) may contribute to complex formation with Mn. Put *S*-serine at the location and optimize the complex structure. Figure 9.54 shows the optimized structure, and Figure 9.55 shows amino acids within 3Å of *S*-serine. Figure 9.56 shows the extracted conformation of *S*-serine with Mn and PLP.

FIgure 9.54: Optimized structure of S-serine and Mn complex.

FIgure 9.55: Amino acids within 3 Å from S-serine.

FIgure 9.56: Extracted conformation of S-serine and Mn complex.

The optimization makes the flat serine structure. The atomic angle of the carboxy group-αC-αH expanded from 328 to 342°. However, the optimized structures of *R*-serine and alanine do not indicate a possible flat structure. This structural change occurs only for *S*-serine, indicating that racemization should occur near Mn. I remember that Dr. Tanaka (Queen-Mary Hospital, Montreal) mentioned the possibility of Mn as an essential element that may contribute to nervous system disorders in 1979 Montreal. Mn may contribute to serine racemase activity. [42].

9.5. Aspartate Racemase

S(L)-amino acids represent the most common amino acid form, most notably as protein residues, whereas *R(D)*-amino acids, despite their rare occurrence, play significant roles in many biological processes. Amino acid racemases catalyze the interconversion of *S(L)*- and/or *R(D)*-amino acids. *R(D)*-Aspartate is abundant in the developing brain, and the source of *R(D)*-aspartate has been investigated. Researchers identified a cloned mammalian aspartate racemase in the brain and neuroendocrine tissues [43]. The aspartate racemase complex conformation differs from that of *R(D)*-aspartate oxidase [44]. In *R(D)*-aspartate oxidase, two guanidyl groups contact two carboxy groups of aspartate to hold aspartate in a precise position, and the aspartate amino group faces the coenzyme FAD flavine carbonyl group. The amino group is oxidized, and the aspartate is converted to α-keto acid. The location of two alginic guanidinyl groups is critical in the selective reaction.

The downloaded three-dimensional structure PDB 5wxz (Crystal structure of Microcystis airuginosa PCC 7806 aspartate racemase in complex with *R(D)*-aspartate without coenzyme) was optimized, then the original aspartate was replaced with *S(L)*-aspartate, and the complex structures were optimized using an MM2 program. Extracted *R(D)*- and *S(L)*-aspartate atomic angles were compared with the original angles; generally, the rotation of the amino acid, racemization, occurs in the smallest atom (hydrogen). Indeed, the complex formation with the racemase flattened the original structures inside the protein. The optimized complex structure and the extracted structure, which clearly exhibited the complex conformation, are shown in Figures 9.57 and 58. The *R(D)*-aspartate β-carboxy group is in close contact with R53 and K167 via ion-ion interactions. The α-amino group is in close contact with E197 via an ion-ion interaction, but the α-carboxy group is weakly contacted by the L99 peptide-bond amino group and the T88 hydroxy group *via* a hydrogen bond. The angles of *S(L)*- and *R(D)*-aspartates are given to describe the structural changes in Figure 9.59. Table 9.1 summarizes the atomic angles of aspartate before and after complex formation.

In aspartate racemase, only the E197 carbonyl group tightly contacts the aspartate amino group via ion-ion interaction, and the α-carboxy contacts S87, S89, and S128 via hydrogen bonding. The β-carboxy group binds to the R53 guanidino group and the K165 amino group via ion-ion interactions. By the way, *R*- and *S*-aspartate were flattened inside the racemase. The total angle of *R*- and *S*-aspartate expanded by 2.28 and 6.81 °, respectively. Electro-localization also supported the conformational change. The enzyme appeared to favor racemization of *S(L)*-aspartate.

Table 9.1: Properties of aspartate before and after complexing with aspartate racemase (5wxz).

	R(D)-Aspartate					S(L) Aspartate				
	Angle °		apc (au)			Angle °		apc (au)		
	Before	After	DaH	DaC	DaN⁺	Before	After	DaH	DaH	DaN
CO_2^- - CH – CH_2	113.07	111.13	0.004	0.054	-0.062	113.11	116.31	-0.074	-0.053	0.003
NH_3^+ - CH – CO_2^-	99.74	101.32	-	-	-	99.74	103.78	-	-	-
NH_3^+ - CH – CH_2	110.46	113.1	-	-	-	110.5	110.07	-	-	-
Total	323.27	323.55	-	-	-	323.35	330.16	-	-	-
Change	-	2.28	-	-	-	-	6.81	-	-	-

FIgure 9.57: Optimized Structure. of aspartate racemase 5wxz with aspartate.

FIgure 9.58: Extracted R(D)-aspartate with surrounded residues.

FIgure 9.59: Extracted R(D)- and aspartates with measured angle.

The proposed reference racemization mechanism did not match the one obtained in this *in silico* analysis. In particular, the reference did not mention E197's contribution. McyF is an aspartate racemase and a pyridoxal 5′-phosphate (PLP)-independent amino acid racemase that produces the substrate *R(D)*-aspartate for microcystin biosynthesis in the cyanobacterium microcystin *aeruginosa* PCC7806. Structural analyses indicate that McyF and its homologs have highly conserved residues involved in substrate binding and catalysis. In addition, residues C87 and C195 were assigned as the key catalytic residues of the "two bases" that deprotonate *R(D*)-Asp and *S(L*)-Asp. Further, site-directed mutagenesis combined with enzymatic assays revealed that G197 also participates in the catalytic reaction. The findings provide structural insights into the catalytic mechanism of aspartate racemase and microcystin biosynthesis [45]. However, the aspartate amino group should contact a carboxy group for a strong ion-ion interaction. These enzymes do not require a coenzyme. However, other racemases (alanine racemase and serine racemase) require the coenzyme pyridoxal-5'-phosphate (PLP), and aspartate racemase requires the coenzyme PLP the coenzyme PLP.

9.6 Glutamate Racemase

Glutamate racemase is essential to bacterial cell wall biosynthesis and has been considered a target for antibacterial drug discovery. Three distinct regulatory mechanisms for the glutamate racemase family have been described: allosteric activation by metabolic precursors, kinetic regulation through substrate inhibition, and *R(D)*-glutamate recycling using an *R(D)*-amino acid transaminase. They found a series of uncompetitive inhibitors that bind to a cryptic allosteric site [46]. Glutamateracemase, a member of the cofactor-independent, two-thiol-based family of amino acid racemases, has been implicated in producing and maintaining sufficient *R(D)*-glutamate [47].

The three-dimensional structure PDB 1zuw (Human Mitochondrial Aldehyde Dehydrogenase Asian Variant, ALDH272, Apo Form, [48]) was downloaded, and the small molecules (1,2-ethanediol and guanidine) were replaced with *R(D)*- or *S(L)*-glutamate; the resulting complex structures were then optimized. The measured atomic angles of the extracted *R(D)*- and *S(L)*-glutamate and described the differences from the original angles. Generally, amino acid rotation (racemization) occurs by moving the smallest atom (hydrogen). Indeed, the original structures were flattened, and the total angles changed by about 7 degrees, as in the enzyme complex. The optimized complex structure and the extracted structure, which clearly exhibit the complex conformation, are shown in Figures 9.60 and 61. Figure 9.62 shows the angles of *S(L)*- and *R(D)*-glutamate to describe the structural changes. Table 9.2 summarizes the atomic angles of glutamate before and after complex formation. This enzyme seemed to favor the racemization of *S(L)*-glutamate.

Table 9.2: Properties of glutamate before and after in complex with glutamate racemase (1zuw).

	***R(D)*-Glutamate**					**S(L)-Glutamate**				
	Angle °		**apc (au)**			**Angle °**		**apc (au)**		
	Before	**After**	**DaH**	**DaC**	**DaN⁺**	**Before**	**After**	**DaH**	**DaH**	**DaN**
COc- - CH – CH2	110.33	112.26	0.052	0.009	-0.031	110.23	111.21	0.023	0.048	-0.038
NH3+ - CH – CO2-	99.76	104.81	-	-	-	99.72	105.91	-	-	-
NH3+ - CH – CH2	112.84	109.97	-	-	-	113.44	113.44	-	-	-
Total	322.93	637.04	-	-	-	323.39	330.56	-	-	-
Change	322.93	327.04	-	-	-	-	7.17	-	-	-

The complex conformation of glutamate racemase is similar to that of aspartate racemase. In glutamate racemase, only the D10 carbonyl group tightly contacts the glutamate amino group via an ion-ion interaction. Still, the α-carboxyl group contacts the N74 amino group and the T76 and T186 hydroxyl groups. Theγ-carboxy group does not demonstrate a strong binding site. By the way, *R(D)*- and *S(L)*-aspartate were flattened inside the racemase. The total angle of *R(D)*- and *S(L)*-aspartate expanded by 4.11 and 7.17°. Electro-localization also supported the conformational change. The exchange of contact sites of α- and γ-carboxy groups may not be possible due to the possible strong binding of the α-amino group and D10 carboxy group.

FIgure 9.60: Optimized structure of glutamate racemase 1zum with *R(D)*-glutamate.

FIgure 9.61: Extracted *R(D)*-glutamate with measured angle.

FIgure 9.62: Extracted S(L)-glutamate with measured angle.

The proposed conformation at the racemization site differs from that proposed in references 48 and 50, where two thiols contact an *S(L)*-glutamate amino group; however, flexibility around the α-carbon is the key factor. The final decision will be made using a computer system that can calculate the transition state of large molecules.

9.7. Human *D*-Amino acid Oxidase (DAO)

D-Amino acids are found in various tissues; however, they are not proteinogenic and are enzymatically oxidized. Improvements in analytical methods have highlighted the importance of *D*-amino acids in maintaining living creatures. Initially, the three-dimensional structure of human *D*-amino acid oxidase was not reported; therefore, the three-dimensional structure was constructed from the yeast three-dimensional structure of *D*-amino acid oxidase.

Reference 49 describes the step-by-step process for correcting the downloaded protein structures. Proteins naturally recognize enantiomers. The study of protein recognition of enantiomers was applied to analyze the reactivity of DAO, which selectively oxidizes *D*-amino acids (*D*-AAs). DAO was the second flavoenzyme to be discovered. Krebs first detected DAO activity in tissue specimens in 1935 [50]. This enzyme is present in various organisms, such as bacteria, yeast, fungi, mollusks, insects, fish, amphibians, reptiles, birds, and mammals. Although the total number of amino acid residues differs slightly, the amino acid sequences are highly conserved. The physiologic function has been reviewed [51]. The catalytic activity varies for *D*-AAs. DAO has broad substrate specificity, with a preference for *D*-AAs bearing hydrophobic side chains of up to four carbon atoms, followed by those carrying polar and aromatic groups [52]. The physiological role, stereostructure, and reaction mechanism of DAO were reviewed, including the mutants [53].

Many crystallographic structures of DAO are readily available from the Protein Data Bank [54]. The substrates of the DAO complexes were varied. We replaced the substrates with an amino acid. We then optimized the conformation of the DAO-amino acid complex using MM2 calculations to identify which DAO amino acid residue was directly involved in binding, based on atomic distances and electron transfer determined from the atomic apc of neighboring atoms. Furthermore, we estimated the three-dimensional structure of human DAO from the sequence data NP001908 [55] and the three-dimensional structure of pig kidney DAO 1VE9 [54] because of the similarity of these sequences; we then analyzed the selectivity of the estimated human DAO. The selectivity of DAO mutants was also analyzed after docking with various amino acids [56-58].

Downloaded DAO 3cuk is shownin Figure 9.56. The downloaded structure indicates that it is not a single enzyme; Figure 9.63 shows one enzyme with a long, bald bond. The modified bond indicates an unrealistic structure in the downloaded model. The bond represents missing peptides at S57, D58, P59, N60, and N61. Further analysis of the structure based on the amino acid sequence indicates missing amino acids at P297, T198, G299, P300, S301, K337, and S340. These amino acids are far from the reaction chamber and may not affect reactivity; however, they may sterically hinder substrate binding. The correction may be completed by cutting irregular bonds, but adding amino acids may be required.

Figure 9.63: Downloaded HDAO 3cuk.

Figure 9.64: Single structure of 3cuk.

The downloaded human *D*-amino acid dehydrogenase (2e49) is a tetramer that binds 3-hydroxy-2-iminopropanoic acid to form the crystal, as shown in Figure 9.64. After removing water molecules, the monomer is optimized, as shown in Figure 9.65, where the location of 3-hydroxy-2-iminopropanic acid and coenzyme FAD are indicated. However, the structures of FAD and substrate 3-hydroxy-2-iminopropanoicacid structures are not acceptable. The 3-hydroxy-2-iminopropanoic acid carboxy group connects with the arginine (R283) guanidyl group via ion-ion Interaction. However, the *D*-amino acid oxidation location is the same.

Figure 9.65: Downloaded HDAO 2e49.

Figure 9.66: Optimized HDAO 2e49

Another HDAO uses a high-mass 3-hydroxyquinoline-2(1H)-one to make the crystal (3g3e). Comparison of the additional molecule mass shows different numbers of regional amino acids: Figures 9.67 and 68 show the extracted conformations of 3g3e and 2e49, respectively. Eight molecules lie within 3Å of high-mass 3-hydroxyquinoline-2(1H)-one, while only four lie within 3Å of low-mass 3-hydroxy-2-iminopropanoic acid. The structure of 3g3e is highly dense, while that of 2e49 has more open space. These Figures indicate that the structures of the coenzyme and the crystallization-contributing molecule are not precisely shown.

Figure 9.67: Downloaded and extracted 3g3e.

Figure 9.68: Downloaded and extracted 2e49.

Figure 69 shows the extracted coenzyme FAD from 2e49, with the original and corrected FAD structures. The circle parts are not the right structure; therefore, these structures are corrected, and the entire structure is optimized. Figure 9.70 shows the molecules extracted within 3å of 3-hydroxy-2-iminopropanoic acid, where the total number of molecules increases from four to seven.

Figure 9.69: Correction of coenzyme structure.

Figure 9.70: Extracted molecules from the corrected 2e49.

The 3-hydroxy-2-iminopropanoic acid is replaced with *D*-alanine, and the complex is optimized after superimposing their carboxy groups. Figure 9.71 shows the optimized structure of the *D*-alanine complex, and Figure 9.72 shows the molecules extracted within 3Å of *D*-alanine.

Figure 9.71: *D*-alanine complex with 2e49.

Figure 9.72: Extracted molecules within 3Å from *D*-alanine.

When a three-dimensional structure of a human enzyme is unreported, the three-dimensional structure must be constructed from a known structure and human sequences; when the yeast protein structure is used, it does not directly construct the human protein structure and instead uses a relatively close mammalian structure as an intermediate. This process does not require replacing many amino acids or maintaining the three-dimensional structure without large deformation. The similarity of yeast and pig residual amino acids is 26% to human residual amino acids is 26% and 85%, respectively, and the similarity between pig and human amino acids is 90%.

Figure 9.73: Yeast *D*-amino acid oxidase.

Figure 9.74: Constructed human *D*-amino acid oxidase.

The difference between yeast *D*-amino acid oxidase and the constructed human *D*-amino acid oxidase is the visibility of the coenzyme FAD. FAD is hidden in human *D*-amino acid oxidase and clearly visible in yeast *D*-amino acid oxidase. This visual difference may support the high selectivity of human *D*-amino acid oxidase, while yeast *D*-amino acid oxidase more readily accepts and oxidizes various *D*-amino acids.

There is no guarantee that an auto-docking program correctly replaces substrates. The simple method is to superimpose these carboxy groups to face the arginine guanidyl group and replace them. Extract molecules within 3 Å of the amino acid after optimizing the entire structure. Then, the extracted complex is locked and optimized using MOPAC-PM5 (or the latest version) to obtain atomic partial charge values. This approach is an advanced method of studying chromatographic retention mechanisms. This enzyme reacts with the following amino acids: *D*-aspartic acid, *D*-glutamic acid, *D*-alanine, NMDA, *D*-glutamic acid, and methionine.

The calculated 14 *D*-amino acids α-carbon apc of HDAO, constructed from pig DAO (1ve7) and HDAO (3znn, 3g3e, 2du8), correlated with enzyme reactivity (U mg^{-1} protein) with $r > 0.8$. Even without an experimentally determined structure, the constructed three-dimensional structure, based on different spacing and amino acid sequences, supports further analysis of enzyme specificity. The substrate amino acids are *D*-aspartate, *D*-glutamate, *D*-alanine, *D*-phenylalanine, *D*-methionine, *D*-valine, *D*-leucine, *D*-serine, *D*-threonine, *D*-tryptophan, *D*-cysteine, *D*-arginine, *D*-lysine, and *D*-histidine. When sheep DAO is necessary, the three-dimensional structure can be derived from pig DAO. The calculated pig DAO and sheep DAO α-carbon apc were corrected for their relative oxidation reactivity with $r = 0.92$ (n = 7) and 0.83 (n = 7), respectively. The substrate amino acids are *D*-alanine, *D*-serine, *D*-aspartic acid, *N*-methyl-*D*-aspartic acid, *D*-glutamic acid, and γ-butyric acid.

Further analysis examined the selective inhibition of amino acid oxidation by kojic acid. The inhibition can be explained by the electron localization of the oxygen contacting the R283 guanidyl group. The inhibition ratio and these Δapc values were correlated (r = 0.98, n = 4). Selective enzyme reactivity can be quantitatively analyzed based on the apc of the reaction-center atoms obtained by forming a complex within the enzyme three-dimensional structure.

9.8. Human acidic *D*-amino acid oxidase (DDO)

The oxidation reactivity of DAO was quantitatively analyzed *in silico* [56-58] because *D*-amino acids exist in mammal

tissues, especially in the brain [59-61]. DAO is a catabolic enzyme that acts stereospecifically on several neutral and basic *D*-amino acids (but not on acidic *D*-amino acids), including free *D*-serine [62]. *D*-serine plays an essential role in regulating brain function by acting as an endogenous ligand for the *N*-methyl-*D*-aspartate (NMDA) receptor subtype of the *L*-glutamate receptor family and the α2-glutamate receptor [63-65]. Besides *D*-serine, free *D*-aspartic acid has also been studied extensively. Unlike the tissue (brain)-specific expression of *D*-serine, substantial amounts of *D*-aspartic acid are present in a wide variety of tissues and cells in mammals, particularly those that make up the central nervous, neuroendocrine, and endocrine systems. Several lines of evidence suggest that *D*-aspartic acid plays an important role in regulating developmental processes, hormone secretion, and steroidogenesis [66,67]. Acidic *D*-amino acids, such as *D*-aspartic acid, *D*-glutamic acid, and NMDA, are degraded by another *D*-amino acid-specific enzyme, *D*-aspartateoxidase (DDO). DAO and DDO are flavin adenine dinucleotide (FAD)- containing flavoproteins that catalyze the oxidative deamination of *D*-amino acids to generate 2-oxo acids, along with hydrogen peroxide and ammonia. The mammalian DAO and DDO are presumed to regulate the levels of several endogenous and exogenous *D*-amino acids, including *D*-serine and *D*-aspartic acid, in various organs [68]; however, their physiological roles *in vivo* remain to be fully clarified.

Previously, the role of Ser-308 in mouse DDO was investigated using site-specific mutational analysis of this residue [69]. Here, alanine-, glycine-, and tyrosine-substitution mutants (S308A, S308G, and S308Y, respectively) were prepared, and their enzyme properties were characterized [69]. The three-dimensional structures of these mutants, in addition to a double-point mutant of mouse DDO (S308G-G309Y mutant), were constructed in silico and optimized using MM2 calculations (shown in Figure 36). Furthermore, the apc of key atoms was calculated using the MOPAC-PM5 program, and then the reactivity of these mouse DDO mutants was analyzed [70,71].

Acidic *D*-amino acids, such as *D*-aspartic acid, *D*-glutamic acid, and NMDA, are degraded by another *D*-amino acid-specific enzyme, DDO.DDO is also a flavin adenine dinucleotide (FAD)-containing flavoprotein that catalyzes the oxidative deamination of *D*-amino acids to generate 2-oxo acids, along with hydrogen peroxide and ammonia. DDO selectively oxidizes acidic amino acids, and three guanidyl groups exist near FAD to trap an acidic *D*-amino acid via ion-ion Interaction with the two carboxy groups.

Mouse DDO (MDDO) was constructed from pig DAO (PDB1k1f) and the MDDO amino acid sequence (NCGI: NM 027442.5) to study MDDO specificity. The similarity and analogy are 43 and 56%, respectively. The constructed human DDO (HDDO), rat DDO (RDDO), cow DDO (CDDO), and mouse DDO (MDDO) have *D*-aspartic acid as the substrate; these complexes are then optimized. These structures are shown in Figure 9.75. Reaction selectivity can be inferred from their openness to capture various *D*-amino acids. The most selective HDDO exhibits a small FAD and *D*-aspartic acid, and the least selective MDDO shows a wide opening for trapping substrates.

Figure 9.75: Optimized structures of HDDO, PDDO, RDDO, CDDO, and MDDO with FAD and D-aspartic acid.

Figures 9.76 and 77 show the conformation of PDDO and MDDO. These conformations demonstrate the feasibility of their modified three-dimensional structures, where the fundamental structures of their reaction sites are very similar. We constructed five MDDO mutants (S308A, S308Gn, S308D (wild), S308G-G309Y, S308Y) and analyzed their reactivity with *D*-aspartic acid and NMDA. Their correlation between α-carbon apc and their reactivity (*V*max/*K*m) is 0.85 (n = 5) and 0.90 (n = 5), respectively.

Figure 9.76: Original PDAO structure.

Figure 9.77: Constructed MDDO from PDAO.

The higher reactivity of S308G than S308Y depends on the steric hindrance, and a larger residual amino acid inhibits the contact of aspartic acid with the FAD ring. The mutation of S308 affects the contact tightness of *D*-aspartic acid with the FAD ring. Figures 9.78 and 79 visually demonstrate the tyrosine's conformation covering the FAD ring and inhibiting *D*-aspartic acid contact.

Figure 9.78: Location of MDDO S308G.

Figure 9.79: Location of MDDO S308Y.

HDDO PDF: 6rkf is downloaded to study HDDO specificity. The downloaded 6rfc is a hexamer, as shown in Figure 9.80. The single-complex structure contains the substrate (2-amino-2-hydroxymethyl-propane-1,3-diol), and three arginines are within 3Å of the substrate. After replacing the substrate with *D*-aspartic acid, the complex is optimized, and the optimized structure, including *D*-aspartic acid, is shown in Figure 9.81. The peptide Y141-G143 differs from the sequence data (C143–C141) in UniProt KB-Q99489 (OXDD_HUMAN); however, we used the 6rkf structure for further HDDO analysis. In addition, the constructed MDDO and RDDO from 6rkf show no irregularities. Figure 9.82 shows HDDO constructed from PDDO with *D*-aspartic acid.

Figure 9.80: Downloaded HDDO.

Figure 9.81: Optimized 6rkf with D-aspartic acid.

Figure 9.82: HDDO from PDDO 6ekf.

The molecules within 3 Å of *D*-aspartic acid are shown in Figure 9.83. Figure 9.84 shows the contact atoms with *D*-aspartic acid: two guanidyl groups, R237 and R278, contact the *D*-aspartic acid β-carboxy groups via ion-ion interaction, and the R216 guanidyl group contacts the *D*-aspartic acid α-carboxy group via ion-ion Interaction. The multiple ion-ion interactions of DDO differ from DAOO, which forms only one ion-ion interaction. RDDO is constructed by replacing amino acids for studying species specificity, and the structure is shown in Figure 9.85. Figure 9.86 shows RDDO constructed from PDDO. Both structures are very similar.

Figure 9.83: Molecules within 3Å from D-aspartic acid. Red (black), blue (dark gray), yellow (light gray), white, and magenta: oxygen, nitrogen, carbon, hydrogen, phosphorous.

Figure 9.84: Contact atoms with D-aspartic acid. Red (black), blue (dark gray), yellow (light gray), white, and magenta: oxygen, nitrogen, carbon, hydrogen, phosphorous

Figure 9.85: RDDO structure from 6rkf

Figure 9.86: RDDO structure from PDAO.

Figure 9.87 shows molecules within 3Å from *D*-aspartic acid, and Figure 9.88 shows contact atoms with *D*-aspartic acid. The protein arginine R237 and R278 contact the β-carboxy group, and R218 contacts the α-carboxy group of *D*-aspartic acid, similar to the HDDO conformation.

Figure 9.87: Molecules within 3Å from *D*-aspartic acid.

Figure 9.88: Contact atoms with *D*-aspartic acid.

In addition, MDDO is constructed by replacing amino acids of 6rkf for studying species specificity, and the structure is shown in Figure 9.89. Figure 9.90 shows MDDO constructed from PDDO.

Figure 9.89: MDDO structure from 6rkf.

Figure 9.90: MDDO structure from PDAO.

Figure 9.91 shows molecules within 3å of *D*-aspartic acid, and Figure 9.92 shows contact atoms with *D*-aspartic acid. The protein arginine R2188, R2, and R2788 co-bind the β-carboxy group, and FAD contacts the α-carboxy group of *D*-aspartic acid. These three DDO structures look similar, but the conformations of these reaction centers differ slightly. Minor differences in residual amino acids affect arginine's position and its degree of electron localization.

FIgure 9.91: Molecules within 3Å from *D*-aspartic acid.

FIgure 9.92: Contact atoms with *D*-aspartic acid.

Quantitative analysis of enzyme reactivity can be performed by replacing the substrates, even when the three-dimensional structure is unknown. The necessary three-dimensional structure can be constructed from a known three-dimensional structure and the target compound's amino acid sequence data. The three-dimensional structures constructed from other species are similar, but there is no guarantee that the newly constructed structures reflect the species' actions. One selection difficulty is the definition of secondary structure indications between right-handed alpha (H) and 310 helices (G), which are defined for the same spiral peptides. For example, the last spiral peptide of HDDO, consisting of 16 amino acids (W315–H330), is shown using the right-handed alpha and 310 helix definition in Figure 9.93. The threads form structures that indicate a tight, soft tube; the secondary structure definitions are not identical for similar amino acid positions in the actual amino acid sequences. The residual amino acid differences produce slight differences in three-dimensional structure due to steric hindrance. The crystal structures do not show how the protein holds the substrate.

FIgure 9.93: Different spiral structures are defined by different secondary structures

The comparison of HDAO 3ch8 from 2e49 and 2du8 clarifies the lack of five amino acids (S57–N61) and six amino acids (R296–S301) in 3ch8. The secondary structure of T43–A48 is a 310 helix and right-handed alpha for 2e49 and 2du88. That of W185–Q190 is a right-handed alpha, and that A186–Q190 of 2e49 is 310 helix, and G183–L186 of 2du8 is 310helix. D218–G222 of 2e49 is a 310 helix, but the secondary structure is for 2du8 and 3cuk. In addition, several amino acids differ under the same secondary indication, and these differences in secondary structure should affect reaction selectivity. The molecular mass of compounds used for crystallization also affects the steric conformation of enzymes. The comparison of the amino acid sequencer of 6rkf, HDAO 4qfc holds 4-hydroxy-6-[2-(7-hydroxy-2-phenyl-2H-chromene-6-yl)ethyl]pyridazine-3(2H)-one lacks many amino acids: S25–P29, D58–P62, L296–T303, D2, T3, A4, T55, T59, I61, T63, P102, V106, Q287, T288, L290, L291, A292, C328, H330,and A335.The two missing peptides are shown as bold bonds in Figure 9.94. Molecules within 3 Å of this large mass compound are shown in Figure 9.95. HDAO 4qfc cannot be used to construct an HDDO.

FIgure 9.94: Stereo structure of HDAO 4qfc.

FIgure 9.95: Molecules within 3Å from the compound.

Another similar structure, 4qfd, which contains 3-(7-hydroxy-2-oxo-4-phenyl-2H-chromene-5-yl) propanoic acid, also lacks many amino acids, such as L56–P62, H24–L30, and others. Whether such large-mass compounds are naturally present in the enzyme is unclear. 4qfc and 4fd are prepared from the same enzyme, but their secondary structures are not identical. Therefore, we must carefully evaluate the downloaded three-dimensional structure by comparing the amino acid sequence data.

9.9. Aspartate Oxidase

S(L)-aspartate oxidase (α flavoenzyme) converts aspartate to imino-aspartate using either molecular oxygen or fumarate as electron acceptors; the structure was determined, and the binding site was proposed [73]. *S(L)*-Aspartate oxidase from the thermophilic archaea Sulfolobus Tokodaii was produced as are combinant protein in E.coli in the active form of a holoenzyme. High thermal stability biocatalyst for producing *R(D)*-aspartate[73].Recombinant thermo stable aspartate oxidase was used enantiomerically pure *R(D)*-aspartate [74].

The downloaded three-dimensional structure of PDB 1knr (*S(L)*-aspartate oxidase [75]: R386L mutant of Escherichia coli) was optimized after a mutation of L386R and fixing the structure of the FAD flavine ring. Two possible locations are where *S(L)*-aspartate is oxidized around the FAD flavine ring. The strongest molecular interaction (ion-ion interaction) is between the substrated aspartate carboxyl group and the residual protein arginine guanidyl group of *R(D)*-aspartate oxidase [56]; however, the key guanidyl group does not exist at the same location in *R(D)*-aspartate oxidase. Another is

located near the flavine carbonyl group, and another is located near the FAD flavin ring methyl group. One guanidyl group is located near the flavine carbonyl group. Another is near the FAD hydroxy group and is too far to form a binding with the aspartate β-carboxy group, as shown in Figure 9.96, where the β-carboxy group contacts the R386 guanidyl group and the α-carboxy group contacts the R290 guanidinyl group (Figure 9.97). *S(L)*-glutamate also formed a complex at this location in the in silico analysis, compared with *S(L)*-aspartate. The α-amino group is located near a different flavin carbonyl group in *R(D)*-aspartate oxidase. The possible 2nd complex conformation is shown in Figure 9.98, where the β-carboxy group contacts the H351 ring, but no guanidyl group is present at this location (Figure 9.99) .In this locationB, *S(L)*-alanine, and *R(D)*-aspartate might be oxidized; however, a nearby carboxy group (E121) contacted their amino group even if the amino group was located near the flavine carbonyl group. The electron localization of the amino acid α-carbon may indicate the possibility, as the value supported the selective oxidation of *R(D)*-amino acid oxidase [56]. The optimized (final structure) energy values of conformations A and B (Figures 9.96 and 98) were - 9078.9 and -8594.4 kcal mol^{-1}.

The apc of the extracted *S(L)*-aspartate alpha carbon changed from -0.265 to -0.157 au at location A (Figure 9.97), and from -0.265 to -0.135 au at location B (Figure 9.99). Location B is a favorite complex like that of *R(D)*-aspartate oxidase; however, the location is not specific for *S(L)*-aspartate based on the electron localization.

Figure 9.96: Aspartate oxidase, conformation A. residues.

Figure 9.97: *S(L)*-aspartate and tightly bound in conformation A.

Figure 9.98: Aspartate oxidase, conformation B. residues.

FIgure 9.99: *S(L)*-aspartate and tightly bound in conformation B.

The above approach was based on the reaction process of *R(D)*-aspartate oxidase, but not the same as that reported, where the succinate complex was the major reaction process to produce fumarate [72,75]. Their initial complex conformations were the same, with two residual arginine guanidinyl groups contacting the two aspartate carboxy groups. Conformation A, in which two guanidinyl groups contacted two aspartate carboxyl groups, was more stable than conformation B, in which one guanidinyl group contacted one aspartate carboxyl group. However, the apc of the α-carbon indicated that the diamino reaction was a favor in conformation B. The paper described *S(L)*-aspartate oxidase catalysis for a succinate-formate reaction, but estimated and proposed the *S(L)*-aspartate oxidase reaction mechanism in conformation A. The aspartate amino group was far from the proposed flavin ring nitrogen in conformation A. *S(L)*-aspartate oxidase involved succinate formation from fumarate in cyanobacteria, but the diamino reaction was not described [76]. This FAD-dependent enzyme differs from most amino acid oxidases and more closely resembles the succinate dehydrogenase/fumarate reductase family than the prototyped *R(D)*-amino acid oxidases [77]. This conclusion is based on the conformation around *S(L)*-aspartate. In *R(D)*-aspartate oxidase, the two carboxy groups of *R(D)*-aspartate are held by two guanidyl groups of the enzyme. This conformation is possible, but the amino group is located differently, as shown in Figure 9.97. The conclusion of the referenced work can be supported by conformation B shown in Figure 9.99.

9.10. Glutamate Oxidase

Glutamate oxidase has been used for the selective analysis of glutamate in food and pharmaceuticals, and various analytical systems have been developed [78,79]. Glutamate oxidase was purified, and the reaction products were determined spectrophotometrically. Reaction selectivity of purified *S(L)*-glutamate oxidase was studied [80]. *S(L)*-glutamate oxidase was immobilized for the enzyme assay [81-88]. The sensor was used for monitoring glutamate from cultured nerve cells [89-94]. A combination of glutamate racemase and oxidase censors permitted continuous analysis of both *R(D)*- and *S(L)*-glutamates [95]. Glutamate oxidase was used to selectively analyze the neurotoxic amino acid 3-*N*-oxalyl-L-α, β-diamino-propionic acid [96]. A recombinant *S(L)*-glutamate oxidase was developed for a stable biosensor [97].The amino acid (*S(L)*-glutamate) is prevalent throughout the mammalian brain, with an estimated 60-70% of synapses using it as their neurotransmitter. A Pt/glutamate oxidase-based sensor was developed and demonstrated reliable detection of physiological glutamate changes in response to rats' behavioral/neuronal activation [98].of glutamate physiological changes in response to rats' behavioral/neuronal activation [98].

α-Ketoglutarate, employed to treat mild chronic renal insufficiency, was obtained through enzymatic oxidation of monosodium glutamate catalyzed by *S(L)*-glutamate dehydrogenase coupled with NADH oxidase for the regeneration of NADH back to NAD^+[99]. Glutamate reuptake by dedicated transporters prevents its accumulation at the synapse, as well as non-physiological spillover. Indeed, extracellular glutamate increases the incidence of aberrant synaptic signaling, leading to neuronal excitotoxicity and cell death [100]. We performed a quantitative in silico analysis of the reaction mechanisms.

The three-dimensional structure PDB 7e0d (Structure of *S(L)*-glutamate oxidase R305E mutant in complex with *S(L)*-arginine of Streptomyces sp. X-119-6) was downloaded and optimized using the MM2 program after E305 was replaced to R305 and the FAD structure was fixed. Figure 9.100 shows the optimized structure. Considering the stereostructure of acidic *S(L)*-amino acid oxidase, the α-carboxy group contacted the R124 guanidyl group via ion-ion interaction, and the γ-carboxyl group contacted the guanidyl group of R305. The α-amino group was located near the flavine carbonyl group and contacted the carboxyl group of E617. Furthermore, we studied the possibility of *R(D)*-glutamate oxidation.

FIgure 9.100: Optimized structure of 7e0d E305R with *S(L)*-glutamate with *S(L)*-glutamate.

FIgure 9.101: Extracted *S(L)*-glutamate with bound molecules.

The oxidation mechanism is fundamentally the same as that of *R(D)*-aspartate oxidase. The glutamate α-carboxy group contacted the R124 guanidyl group, but the γ-carboxy group contacted N301, H312, and R305. However, the strong interaction with the R304 guanidyl group was not observed (Figure 9.101). The apc of the extracted *S(L)*-glutamate α-carbon changed from -0.202 to -0.192 apc in the optimized three-dimensional structure.

9.11. Arginine Oxidase

S(L)-Arginine oxidase was discovered in Pseudomonas sp.TPU7192 is a FAD-dependent enzyme that catalyzes the oxidative deamination of *S(L)*-arginine and converts *S(L)*-arginine to 2-ketoarginine. The cloned enzyme demonstrated high selectivity for *S(L)*-arginine [101]. The enzyme selectivity of ancestral and native *S(L)*-arginine oxidase was extensively analyzed. The native enzyme is Oceanobacter kriegii *S(L)*-arginine oxidase. The designed ancestral *L*-arginine oxidase was thermostable and exhibited very high selectivity. They found that *S(L)*-arginine oxidase may have evolved from a thermostable and promiscuous *S(L)*-amino acid oxidase [102]. The mutation of S*(L)*-glutamate oxidase (R305E) from Streptomyces sp. X-119-6 developed an enzyme to catalyze *S(L)*-arginine [103]. The three-dimensional structure of *L*-arginineoxidase was PDB 7e0d (Structure of *S(L)*-glutamateoxidase R305E), and a substrate *S(L)*-arginine was installed instead of *S(L)*-glutamate, and the complex structure was optimized.

S(L)-Amino acid oxidase/monooxygenase from Pseudomonas sp. AIU 813 catalyzes the oxidative deamination of the *S(L)*-amino acid α-amino group to produce a keto acid. Therefore, we determined the conformations of *S(L)*-lysine, arginine, and ornithine by preparing these complex structures. Furthermore, the mutation effect of D238 was performed by preparing D238A, D238F, and D238E.The key residual amino acids are D238 and Q258, which tightly contact the α-amino group of the substrated amino acids; D238 also tightly contacts the basic group of the substrated amino acids via ion-ion interactions [104], as found for *R(D)*-amino acid oxidase [105]. Therefore, the complex arginine structure (RSCBPDB5yb8, *S(L)-amino acid oxidase*/mono-oxygenase was downloaded, and conformational analysis was performed. The corrected and optimized structure is shown in Figure 9.102, and the detail is shown in Figure 9.103.

FIgure 9.102: Optimized structure of arginine oxidase with *S(L)*-arginine.

FIgure 9.103: Conformation of around *S(L)*-arginine.

The shortest distance between the arginine amino group and the FAD flavine ring was 3.1 Å, and the α-carboxy group was within 2.6 Å. The apc value of the α-carbon changed from 0.263 to 0.2266 au. An engineered *S(L)*-arginine oxidase was developed by mutating R305E in the initially created *S(L)*-lysine oxidase (RSCB PDB 7e0c) from *S(L)*-glutamate oxidase from Streptomyces sp. X-119-6 (RSCB2e1m). We determined the protein structure by X-ray crystallography and deposited it as PDB 7e0d. The conformation analysis demonstrated the highly selective *S(L)*-arginine oxidase [103]. Further *in silico* analysis of 7e0d was performed. Figure 9.104 shows the corrected and optimized structure, and Figure 9.105 shows the details.

FIgure 9.104: Optimized structure of arginine oxidase.

FIgure 9.105: Conformation of around *S(L)*-arginine 7e0d..

The original *S(L)*-arginine structure was significantly deformed in the optimized *S(L)*-arginine oxidases, as shown in Figure 9.104. The atomic distance between the substrated arginine amino group and the FAD flavine ring was less than 3.1 Å in 5yb8 and less than 2.9 Å in 7e0d. The apc of the arginine α-carbon changed from -0.263 au to -0.180 in 5yb8. In 5yb8, the arginine guanidyl group contacts D238, and the carboxy group contacts R612 by ion-ion interaction. In 7e0d, the substrate arginine carboxy group contacts R124 by ion-ion interaction, and the guanidyl group contacts S313, M302, and N301 by hydrogen bonds with their peptide connection carbonyl oxygen and hydroxyl groups. These differences suggest that their reaction rates may differ, even though these enzymes selectively oxidize *S(L)*-arginine. The selective oxidation of *S(L)*-arginine was high in 7e0d. Similar results were obtained for 7x7k ancestral lysine oxidase [106]. Figure 9.106 shows the optimized structure, and Figure 9.107 shows the conformation in detail.

FIgure 9.106: Optimized structure of 7x2k lysine oxidase.

FIgure 9.107: Extracted conformation around substitute *S(L)* -arginine.

The atomic distance between the substrated lysine carboxy oxygen and the flavine ring was 2.7 Å, and between the residual lysine α-amino group and the flavine ring was 3.7 Å. Both oxygen and amino hydrogen contacts the flavine ring; however, monooxygenase activity seemed stronger. The atomic partial charge of αthe α-carbon was 0.000, from -0.263 au. 7eij ancestral *S(L)*-Lys oxidase K387A variant with *S(L)*-arginine was also oxidized *S(L)*-arginine. Figure 9.108 shows the optimized structure, and Figure 9.109 shows the conformation around *S(L)*-arginine.

FIgure 9.108: Optimized structure of arginine oxidase.

FIgure 9.109: The conformation around *S(L)*- arginine.

The residual arginine αα-carboxy and α-amino groups were located at 3.1 and 3.9Å from the FAD flavine ring, respectively. The apc of αthe α-carbon was changed from -0.263 to -0.217 au. These results indicate that the enzyme 7eii is not favorable for arginine oxidation.

9.12. Lysine Oxidase

Lysine oxidase (LOX), also known as protein-lysine 6-oxidase, is an enzyme encoded by the LOX gene in humans. It catalyzes the conversion of lysine molecules into highly reactive aldehydes that form cross-links in extra cellular matrix proteins. Lysyl oxidase is an extracellular, copper-dependent enzyme that catalyzes the formation of aldehydes from lysine residues in collagen and elastin precursors. These aldehydes are highly reactive and undergo spontaneous chemical reactions with other lysiloxidase-derived aldehyde residues or with unmodified lysine residues. This cross-linking of collagen and elastin is essential for stabilizing collagen fibrils and maintaining the integrity and elasticity of mature elastin [105].

The Structure of *S(L)*-Amino acid oxidase/monooxygenase from Pseudomonas sp. AIU 813, which catalyzes both oxidative deamination and oxidative decarboxylation of the α-group of *S(L)*-lysine to produce an α-keto acid and an amide, was determined and revealed substrate recognition.[104]. The kinetic characteristics of the homodimeric enzyme *S(L)*-lysine α-oxidase from *Trichoderma, cf. aureoviride RifaiVKMF-4268D,* were investigated, taking allosteric effects into account. It was a highly selective allosteric enzyme with positive cooperativity for *S(L)*-lysine and was responsible for the biosynthesis of 2,6-diaminopimelic acid, *S*-ornithine, and *S*-arginine. [106]

The downloaded PDB 3x0v*S(L)*-lysine alpha-oxidase from Trichoderma does not include a lysine substitute; therefore, we based the lysine-substitute position on results from *R(D)*aspartate oxidase. First, we fixed the FAD structure and removed 4-(2-hydroxyethyl)-1-piperazine ethanesulfonic acid. The α-carboxy group should contact the α-guanidino or ε-lysine amino group *via* a strong ion-ion interaction (Coulombic force). The α-amino group should be near the carbonyl group of the coenzyme flavin ring for oxidation. The ε-amino group of the substrated lysine should contact the carboxy group of either glutamate or aspartate in the enzyme. Finally, the carboxy group of the substrate contacted the arginine (R68) guanidino group, and the ε-amino group of the enzyme contacted the carboxy group of aspartate D63). Figure 9.110 shows the complex structure, and Figure 9.111 shows the conformation details.

FIgure 9.110: Optimized structure of 3x0v with *S(L)*- arginine.

Figure 9.111: Extracted conformation structure of *S(L)*- arginine.

The electrons (atomic partial charge) of the α-carbon of the substrated lysine shifted from -0.262 to -0.1300 au. The electron localization supported the possible oxidation. The residual lysine α-amino group was 2.5 Å from the FAD flavin ring, and the carboxy group was 2.6 Å from the residual R68 guanidyl group. The results indicated that this enzyme favors oxidation of the lysine amino group.

Furthermore, we analyzed the ancLLys conformation to compare results with other oxidases, using the structure of downloaded lysine oxidase 7eii from the RCSB PDB. Ancestral *S(L)*-Lys oxidase K387A variant with *S(L)*-Lys [107] was optimized using an MM2 program. Figures 9.112 and 9.113 show the optimized and extracted structures.

Figure 9.112: Optimized structure of 7eii with *S(L)*- arginine.

Figure 9.113: Extracted conformation around the *S(L)*- arginine.

The substitute *S(L)*-lysine α-carboxy and γ-amino groups were in close contact with R36 and E383 *via* ion-ion interactions, respectively. However, the α-amino group contacted G553, Y254, and Y268 *via* hydrogen bonds. Y516 intercepted the substrated *S(L)*-lysine, contacting the FAD flavin ring. The α-amino and carboxy groups of substituted *S(L)*-lysine were located at 5.3 and 4.6 Å from the FAD flavin ring, and the apc α-carbon was 0.184 Å. The result indicated that the diamine oxidation reaction might not occur smoothly. However, the α-amino and carboxy groups of substitute *S(L)*-Lysine were located at 2.9 and 3.2 Å from the FAD flavin ring before complex optimization. Therefore, we studied the 7eii mutation using Y516A to reduce molecular size. The optimized conformation was the same, and the substrate *S(L)*-lysine was located near the FAD flavine ring. The substituent *S(L)*-lysine α-carboxy and α-amino groups were 3.1 and 3.8 Å from the FAD flavine ring. The result indicated that monooxygenase is the favored reaction. Further analysis was performed on the possible *R(D)*-lysine oxidation based on the conformation.

Similar results were obtained for 7x7j ancestral lysine oxidase [108]. The α-amino and carboxy groups of the substrate *S(L)*-lysine were located at 3.0 and 2.8 Å from the FAD flavine ring, respectively, as shown in Figures 9.114 and 115.

FIgure 9.114: Optimized structure of 7x7j lysine the oxidase.

FIgure 9.115: Extracted conformation around substitute *S(L)* -arginine.

These nearest atoms were in contact; however, monooxygenase reactivity may be stronger than that of the oxidase based on atomic distance. The apc of -carbon was changed from -0.262 to -0.194 au.This enzyme seems to digest more arginine than lysine. The atomic distance between the substrated lysine carboxy oxygen and the flavine ring was 2.8 Å, and that between the lysine α-amino group and the flavine ring was 3.0 Å. Both oxygen and amino hydrogen contacted the flavine ring; however, monooxygenase activity seemed stronger. The apc of α-carbon was -0.194 au from -0.000au.

Another anc*L*Lys was reported, and the specificity was reported. *Researchers developed a selective S(L)*-lysine oxidase (AncLLysO2) using ancestral sequence reconstruction and studied its specificities. AncLLysO2 exhibited strong oxidase

activity and high specificity for *S(L)*-Lys [107]. The stereo structure is 5yb7 PDB of RSDB. We fixed and optimized the downloaded structure to analyze selectivity. We analyzed the conformation based on the specificity of 5yb7 lysine oxidase. The optimized structure and the extracted structures are shown in Figures 9.116and 117.

FIgure 9.116: Optimized structure of 5yb7 lysine.

FIgure 9.117: Extracted conformation around Oxidase substitute S(L)-lysine.

The nearest substitute arginine α-amino group was located at 3.8 Å from the FAD flavine ring. The α-carboxy group was located at 4.3 Å from the FAD flavine ring, but it contacted the residual R102 guanidyl group.The apc of α-carbon was changed from -0.262 to 0.000 au for the lysine complex, and the change was from -0.211 to 0.000 au for the arginine complex. The apc value change indicates that this enzyme is a favor for the selective oxidation of *S(L)*-lysine.

Discussion

Quantitative analysis of enzyme reactions enables effective drug design and mutant development for practical immuno-chromatography; the above experiments were conducted using a desktop computer with MM2 software, using corrected human enzyme structures from amino acid sequence data and the stereochemistry of other spaces. Careful substitution and complex optimization, along with electron localization using the MOPAC PM5 program at the reaction centers, provided a quantitative explanation of this enzyme selectivity. The dehydrogenase enzyme activity was analyzed using the MOPAC-2012 RM1 program. The key descriptors were ionization potential, HOMO/SOMO, LUMO energy, dipole moment, and carbon-halogen atom distance. We used the same approach to quantitatively analyze other enzymes because the available current auto-docking program performed poorly.

The inhibitory peptides as antihypertensive effects for Angiotensin1 converting enzyme were quantitatively analyzed, and the different species' peptides exhibited different efficacy [110]. If the docking site of ACE1 and these peptides is clear, we may analyze amino acid effects at the binding site, like the quantitative analysis of ACE2 inhibition effects of SARS-CoV-2 SRB mutants, where manual docking was performed by replacing the S-SRB in the original conformation [111]. The number of targeted molecules should be reduced if the biological system can be engaged in a synthetic sequence.

When appropriate reactive molecules are provided, a small-molecule inhibitory candidate can be selected at the center of the enzyme's site. Analytical challenges in screening large numbers of combinations have changed, and surface science, chromatography, and other areas offer endless possibilities as fundamental knowledge accumulates across experimental and theoretical databases that validate clinical predictability. X-ray has an exemplary impact on process and analytical chemistry by determining three-dimensional structure, even though NMR can also determine three-dimensional structure and advanced computer programs can construct it from amino acid sequence data.

Further improvements to docking programs that incorporate pharmacological effects may simplify the analytical process, and molecular dynamics simulations [112,113] will improve precision in determining the best design strategy if the program provides binding energy values with reactivity.

Conclusion

We constructed optimized three-dimensional structures of various human enzymes, including alcohol dehydrogenase, Cinnamyl-alcohol dehydrogenase ELI3-2, Alanine racemase, Human serine racemase, Human *D*-amino acid oxidase DAO, Human acidic *D*-amino acid oxidase DDO, Aspartate racemase, Glutamate racemase, Aspartate oxidase, Glutamate oxidase, Arginine oxidase, and Lysine oxidase. We quantitatively analyze the selectivity of these enzyme reactions using a molecular mechanics program. This approach should provide further chemical information about enzyme-structure fitness, reaction mechanisms, and the design of drug candidates (reaction inhibitors) and new enzymes (artificial enzymes for industrial uses). The enzyme selectivity depends on the substrate's molecular shape and electron localization. This fundamental information should provide a basis for drug design. Drugs are either accelerators of enzyme reactions, like coenzymes and cofactors, or inhibitors of enzyme reactions, which are affinity-attached enzymes but not metabolized. One example is trifluoroacetic acid, an inhibitor of *D*-amino acid oxidase. It easily replaces the amino acid, but the enzyme reaction mechanism is amino-oxidation; therefore, the enzyme traps trifluoroacetic acid but cannot release it. This means that a good substitute well trapped in the enzyme is an excellent model structure for designing reaction inhibitors, and the active reaction center groups should be replaced with a new group that is not metabolized but has the same electron localization. This approach may apply to finding inhibitors for other enzymes based on fundamental chemistry. The fundamental chemistry of molecular interactions includes ion-ion, Lewis acid-base, hydrogen bonding, and van der Waals (hydrophobic) forces; ion-ion interaction, provided as an electrostatic energy value, is the strongest interaction force, followed by hydrogen bonding, and van der Waals is the weakest. Still, steric hindrance is not clearly provided as an energy value and requires personal analytical skill. Determining the racemization mechanism is not simple because no new compounds (metabolites) are found; it only changes molecular shape through the flexible three-dimensional structure of enzymes. The difference arises from a small change in the optimization energy value; therefore, careful handling of the three-dimensional structure is required.

However, the downloaded three-dimensional structures cannot be used directly in this process; they must be corrected using amino acid sequence data. The most problematic correction is for coenzymes and cofactors, and molecular orbitals must be carefully fixed and optimized within the protein. The most serious issue is the location of coenzymes and cofactors, and several downloaded structures lack these molecules; therefore, modifying other species' structures is easier than obtaining the final structures from downloaded human enzymes. Replacing one substitute with another cannot be done automatically; we must carefully adjust the location of contact-center atoms based on molecular interaction strength.

References

1. J.H. Shore, H.A. Theorell, Kinetic study of ternary complexes in the mechanism of action of liver alcohol dehydrogenase, Arch. Biochem. Biophys. 1966, 116, 255-260.
2. J.D. Shore, R.L. Brooks, Kinetic evidence for a binary complex isomerization in the liver alcohol dehydrogenase reaction mechanism, Arch. Biochem. Biophys. 1971, 147, 825-827.
3. J.D. Shore, H. Gutfreund, R.L. Brooks, D. Santiago, P. Santiago, Proton equilibria and kinetics in the liver alcohol dehydrogenase reaction mechanism, Biochemistry, 1974, 13, 4185-4190. [
4. L.D. Shore, H.R. Halvorson, K.D. Lucast, The role of conformational changes in the liver alcohol dehydrogenase reaction mechanism, FEBS-Symposium, 1977, 49, 416-425.
5. D.D. Tanner, A.R. Stein, On the mechanism of reduction by reduced nicotinamide adenine dinucleotide dependent alcohol dehydrogenase. A-Halo ketones as mechanistic probes, J. Org. Chem. 1988, 53, 16421646.
6. Y. Pocker, J.D. Page, Zinc-activated alcohols in ternary complexes of liver alcohol dehydrogenase, J. Biol. Chem. 1990, 265, 22101-22108.
7. A. Rosell, E. Valencia, X. Pares, I. Fita, J. Farres, W.F. Ochoa, Crystal structure of the vertebrate NADP(H)dependent alcohol dehydrogenase (ADH8), J. Mol. Biol. 2003, 330, 75-85.

8. S.B. Raj, S. Ramaswamy, B.V. Plapp, Yeast alcohol dehydrogenase structure and catalysis, Biochemistry 2014, 53, 5791-5803.
9. E. Valencia, C. Larroy, W.F. Ochoa, X. Pares, I. Fita, J.A. Biosca, Apo and Holo structure of NADP(H)dependent cinnamyl alcohol dehydrogenase from Saccharomyces cerevisiae, J. Mol. Biol. 2004, 341, 10491062.
10. J. Benach, J.O. Winberg, J.S. Svendsen, S. Atrian, R. Gonzalez-Duarte, R. Ladenstein, Drosophila alcohol dehydrogenase: Acetate-enzyme interactions and novel insights into the effects of electrostatics on catalysis, J. Mol. Biol. 2005, 345, 579-598.
11. T. Hanai, Quantitative in silico analysis of alcohol dehydrogenase reactivity, J. Drug Design Res., 2014, 2(1), 1006 (1-7).
12. C. Larroy, R.M. Fernandez, E. Gonzalez, X. Pares, J.A. Biosca, Characterization of the Saccharomyces cerevisiae YMR318C (ADH6) gene product as a broad specificity NADH-dependent alcohol dehydrogenase: relevance in aldehyde reduction, Biochem. J. 2002, 361, 163-172.
13. G. Pilate, E. Guiney, K. Holt, M. Petit-Conil, C. Lapierre, J.C. Lepl, B. Pollet, I. Mila, E.A. Webster, H.G. Marstorp, D.W. Hopkins, L. Jouanin, W. Boerjan, W. Schuch, D. Cornu, C. Halpin, Field and pulping performances of transgenic trees with altered lignification, Nature Biotechnology, 2002, 20, 607-612.
14. J.D. Williamson, J.M.H. Stoop, M.O. Massel, M.A. Conkling, D.M. Pharr, Sequence analysis of a mannitol dehydrogenase cDNA from plants reveals a function for the pathogenesis-related protein ELI3, Proc. Natl. Acad. Sci. USA, 1995, 92, 7148-7152.
15. I.E. Somssich, P. Wernert, S. Kiedroqwski, K. Hahlbrock, Arabidopsis thaliana defense-related protein ELIS3 is aromatic alcohol:NADP+ oxidoreductase, Proc. Natl. Acad. Sci. USA, 1996, 93, 14199-14203. 63
16. R. Waltz, H. Vahrenkamp, Functional modeling of alcoholdehydrogenase with pyrazoylborate-zinc complexes, Inorganic Chimica Acta, 2001, 314, 58-62.
17. Y.H. Zhang, H. Vahrenkamp, Zinc complexes of a macrocyclic N3O2 ligand for the functional modeling of alcoholdehydrogenase, Inorganic Chimica Acta. 2003, 351, 201-206.
18. Uniprot (Q02972), www.ncbi.nlm.nih.gov/entrez/query.fcgi?CMD
19. G.G. Smith, T. Sivakus, Mechanism of the racemization of amino acids. Kinetics of racemization of arylglycines, J. Org. Chem. 1983, 48, 627-634.
20. E.S. Faraci, C.T. Walsh, Racemization of alanine by the alanine racemases from Salmonella typhimurium and Bacillus stearothermophilus: Energetic reaction profiles, Biochemistry, 1988, 27, 3267-3276.
21. A. Watanabe, T. Yoshimura, B. Mikami, H. Hayashi, H. Kagamiyama, E. Esaki, Reaction mechanism of alanine racemase from Bacillus stearothermophilus, J. Biol. Chem, 2002, 277, 19166-19172.
22. Toney, M.D. Reaction specificity in pyridoxal phosphate enzyme, Ach. Biochem. Biophys. 2005, 433, 279287.
23. D.T. Major, K. Nam, J. Gao, J. Transition state stabilization and α-amino carbon acidity in alanine racemase, J. Am. Chem. Soc. 2006, 128, 8114-8115.
24. P. Jeffrey, J.P. Shaw, G.A. Petsko, D. Ringe, Determination of the structure of alanine racemase from Bacillus stearothermophilus at 1.9 Å resolution, Biochemistry, 1997, 36, 1329-1342.
25. A. Troiani, F. Gasparrini, F. Grandinetti, M. Speranza, Chiral ions in the gas phase. 1. Intramolecular racemization and isomerization of O-protonated (S)-trans-4-hexen-3-ol, J. Am. Chem. Soc. 1997, 119, 45254524.
26. S. Sun, M.D. Toney, Evidence for a two-base mechanism involving tyrosine265 from arginine219 mutants of alanine racemase, Biochemistry, 1999, 38, 4058-4065.
27. S. Sharif, D.R. Powell, D. Schagen, T. Steiner, M.D. Toney, E. Fogle, H-H. Limbach, X-ray crystallographic structures of enamine and amine Schiff bases of pyridoxal and its 1:1 hydrogen-bonded complexes with benzoic acid derivatives: evidence for coupled inter- and intra-molecular proton transfer, Acta Cryst. 2006, B62, 480-487.
28. T. Hanai, Quantitative in silico analysis of alanine racemase reactivity, In P. Watkins, (Ed.), Molecular Mechanics and Modeling. Nova Science: New York, 2015, Chapter 3, 49-71. (ISBN: 978-1-63483-388-2)
29. A. Hashimoto, T. Nishikawa, T. Hayashi, N. Fujii, K. Harada, T. Oka, K. Takahashi, The presence of free D-serine in rat brain. FWBS Let. 1992, 296, 33-36, DOI: 10.1016/0014-5793(92)80397-Y.
30. H. Wolosker, K.N. Sheth, M. Takahashi, J.P. Mothet, R.O. Brady, Jr. C.D. Ferris, S.H. Snyder, Purification of serine racemase: biosynthesis of the neuromodulator D-serine. Proc. Natl. Acad. Sci. U S A. 1999b, 96, 721–725.
31. M.A. Smith, V. Mach, A. Ebneth, O. Moraes, B. Felicetti, M. Wood, D. Schonfeld, O. Mather, A. Cesura, J. Barker, The structure of mammalian serine racemase, Evidence for conformational changes upon inhibitor binding, J. Bio. Chem. 2010, 285, 12873-12881. doi: 10.1074/jbcM109.050062.
32. W. Wang, S.W. Barger, Roles of quaternary structure and cysteine residues in the activity of human serine racemase, BMC Biochem. 2011, 12, 63. doi: 10.1186/1471-2091-12-63.
33. L. Pollegioni, L. Piubelli, G. Molla, E. Rosini, D-amino acid oxidase-pLG72 interaction and D-serine modulation, Front. Mol. Biosci., 2018, 5, 1-12. doi: 10.3389/fmolb.2018.00003.
34. Kondori, N.R.; Paul, P.; Robbins, JP; Liu, K.; Hilyard, J.C.W.; Wells, D.J.; De Belleroche, J.S. Focus on the role of D-serine and D-amino acid oxidase in Amyotrophic Lateral Sclerosis/motor neuron disease (ALC), Front. Mol. Biosci., 2018, 5, 1-7. doi: 10.3389/fmolb.2018.00008.
35. N. Nitoker, D.T. Major, Understanding the reaction mechanisms and intermediate stabilization in mammalian serine racemase using multiscale quantum-classical simulation, Biochem., 2015, 52(2), 516-527.
36. D.L. Nelson, G.A. Applegate, M.I. Beio, D.I. Graham, D.V. Berkowitz, Human serine racemase structure/activity relationship studies provide

mechanistic insight and point to position-84 as a hotspot for -elimination function, J. Biol. Chem., published on July 10, 2017, 1-35. doi:10.1074/jbc.M117.777904.

37. H. Wu, Y.B. Qi, J. Kong, F. Kou, F. Jia, X.F. Dan, Y. Wang, A seven-coordinate manganese (II) complex formed with the tripodal tetradentate ligand tris(N-methylbenzimidazol-2-ylmethyl)amine, Z. Naturforsch. 2010, 65b, 1097-1100.
38. D.E. Metzler, E.E. Snell, Deamination of serine: 1. Catalytic deamination of serine and cysteine by pyridoxal and metal salts, J. Biol. Chem., 1952, 198, 353-361.
39. L. Gorgannezhad, G. Dehghan, S.Y. Ebrahimipour, A. Nasen, J.E.N. Dolatabadi, Complex of manganese 64 (II) with curcumin: Spectroscopic characterization, DFT study, model-based analysis and antiradical activity, J. Mol. Struc., 2016, 1109, 139-145. doi: org/10.1016/jmoistruc.2015.12.051.
40. K. Islam, Manganese complex of ethylenediaminetetraacetic acid (EDTA)-benzothiazole aniline (BTA) conjugate as a potential liver-targeting MRI contrast agent, J. Med. Chem., 2017, 60(7), 2993-3001. doi: 10.1021/acs.jmedchem.6b01799.
41. D.W. Gohara, E.D. Cera, Molecular mechanisms of enzyme activation by monovalent cations, J. Biol. Chem. 2016, 291(40), 20840-20848. doi: 10.1074/jbc.R116.737833.
42. T. Hanai, Quantitative in silico analysis of mammalian serine racemase activity, Int. J. Chem. Math. Phy. (IJCMP), 2018, 2 (6), 53-58, https;//dx.doi.org/10.22161/ijcmp.2.6.1
43. P.M. Kim, X. Duan, A.S. Huang, C.Y. Liu, D-I. Ming, H. Song, S.H. Snyder, Aspartate racemase, generating neuronal D-aspartate, regulates adult neurogenesis, PNAS, 2010, 107, 3175-3179, www.pnas.org/cgi/doi/s0.1073/pnas.0914706107
44. T. Hanai, Quantitative in silico analysis of molecular recognition and reactivity of D-amino acid oxidase. Internet Electron. J. Mol. Des. 2006, 5, 247–259, http://www.biochempress.com.
45. D.D. Cao, C.P. Zhang, K. Zhou, Y.I. Jiang, X.F. Tan, J. Xie, Y.M. Ren, Y. Chen, C.Z. Zhou, W.T. Hou, Structural insights into the catalysis and substrate specificity of cyanobacterial aspartate racemase McyF. Biochem Biophys Res Commun, 2019, 514, 1108-1114, DOI: 10.1016/j.bbrc.2019.05.063
46. T. Lundqvist, S.L. Fisher, G. Kern, R.H.A. Folmer, Y. Xue, D.T. Newton, T.A. Keating, R.A. Alm. B.L. M. de Jonge, Exploitation of structural and regulatory diversity in glutamate racemase, Nature, 2007, 447, 817-822.
47. S.L. Fisher, Glutamate racemase as a target for drug discovery, Microbial Biotechnol. 2008, 1, 345-350, doi: 10.1111/j.1751-7915.2008.00031.x
48. H.N. Larson, H. Weiner, T.D. Hurley, Disruption of the coenzyme binding site and dimer interface revealed in the crystal structure of mitochondrial aldehyde dehydrogenase "Asian" variant, J. Biol. Chem. 2005, 280, 30550-30556, DOI: 10.1074/jbc.M502345200
49. T. Hanai, Basic properties of a molecular mechanics program and the generation of unknown three-dimensional structures of proteins for quantitative analysis of enzyme reactions, in Priscilla Watkins (ed) Molecular Mechanics and Modeling, Nova Science Publishers, 2015, New York, (ISBN: 978-1-63483-388-2) pp.25-48.
50. H.A. Krebs, Metabolism of amino acids III. Determination of amino acids, Biochem. J. 1935, 29, 1620-1644.
51. R. Konno, Y. Yasumura, D-Amino-acid oxidase and its physiological function, Int. J. Biochem. 1992, 24, 519-524.
52. D. Malcolm, K. Kjell, D-Amino acid oxidase II, Specificity, competitive inhibition and reaction sequence, Biochem. Biophys. Acta, 1965, 96, 368-382.
53. M.S. Pilone, D-Amino acid oxidase: new findings. Cell. Mol. Life Sci. 2000, 57, 1732-1747.
54. RCSB Protein Data Bank, www.rcsb.org/pdb/
55. NP 001908, D-amino acid oxidase [Homo sapiens], www.ncbi.nlm.nih.gov/entrez/query.fcgi?CMD
56. T. Hanai, Quantitative in silico analysis of molecular recognition and reactivity of D-amino acid oxidase. Internet Electronic Journal of Molecular Design, 2006, 5(5), 247-259. http://www.biochempress.com
57. T. Hanai, Quantitative in silico analysis of enzyme reactions: comparison of D-amino acid oxidase and monoamine oxidase. American Biotechnology Laboratory, 2007, 25(11), 8, 10, 12-13.
58. T. Hanai, Quantitative in silico analysis of D-amino acid oxidase reactivity and inhibition, Current Bioactive Compounds, 2017, 13, 312-317, doi:10.2174/1573407212666161014133246 (2016).
59. S. Nithya, T.S. Shanmugarajam, D-Amino acid oxidase: A review. Asian J. Pharm. Clin. Res., 2016, 9, 3336.
60. S. Panthis, H-J. Chung, J. Jung, N.Y. Jeong, Physiological importance of hydrogen sulfite: Emerging potent neuroprotector and neuromodulator. Oxid. Med. Cell. Longev., 2016, 9049781.
61. H. Kimura, Signalino molecules: Hydrogen sulfide and polysulfide. Antioxid. Redox. Signal., 2016, 22, 362-375.
62. H. Ohide, Y. Miyoshi, R. Maruyama, K. Hamase, R. Konno, D-Amino acid metabolism in mammals: biosynthesis, degradation and analytical aspects of the metabolic study. J. Chromatogr. B, 2011, 879, 31623168.
63. T. Nishikawa, Analysis of free D-serine in mammals and its biological relevance. J. Chromatogr. B, 2011, 879, 3169-3183.
64. H. Wolosker, NMDA receptor regulation by D-serine: new findings and perspectives. Mol. Neurobiol. 2007, 36, 152-164.
65. W. Kakegawa, Y. Miyoshi, K. Hamase, S. Matsuda, K. Matsuda, K. Kohda, K. Emi, J. Motohashi, R. Konno, K. Zaitsu, M. Yuzaki, D-Serine regulates cerebellar LTD and motor coordination through δ2 glutamate receptor. Nature Neurosci. 2011, 14, 603-611.

66. M.M. Di Fiore, A. Santillo, G.C. Baccari, Current knowledge of D-aspartate in glandular tissues, Amino Acids, 2014, 46, 1805-1818.

67. M. Katane, H. Homma, D-Aspartate – an important bioactive substance in mammals: a review from an analytical and bioanalytical point of view. J. Chromatogr. B. 2011, 879, 3108-3121.

68. M. Katane, H. Homma, D-Aspartate oxidase: the sole catabolic enzyme acting on free D-aspartate in mammals. Chem. Biodivers, 2010, 7, 1435-1449.

69. M. Katane, T. Hanai, T. Furuchi, M. Sekine, H. Homma, Hyperactive mutants of mouse D-aspartate oxidase: mutagenesis of the active site residue serine 308. Amino Acids, 2008, 35, 75-82.

70. M. Katane, Y. Saitoh, T. Hanai, M. Sekine, T. Furuchi, NB. Koyama, I. Nakagome, H. Tomoda, S. Hirono, H. Homma, Thiolactomycin inhibits D-aspartate oxidase: a novel approach to probing the active site environment, Biochim, 2010, 92, 1371-1378.

71. T. Hanai, M. Katane, H. Homma, Quantitative in silico analysis of selective enzyme reaction of mammalian D-amino acid oxidase and acidic D-amino acid oxidase mutants, SDRP J. Comp. Chem. Mol. Model. (JCCMM), 2018, 2 (3), 1-9. DOI: 10.25177/JCCMM.2.3.2

72. A. Mattevi, G. Tedeschi, L. Bacchella, A. Coda, A. Negri, S. Ronchi. Structure of L-aspartate oxidase; implications for the succinate dehydrogenase/ fumarate reductase oxidoreductase family, Structure, 1999, 7, 745-756. http://biomednet.com/elecref/0969212600700745,

73. D. Bifulco, L. Pellegrini, D. Tessaro, S. Servi, G.A. Molla, Thermostable L-aspartate oxidase: a new tool for biotechnological applications, Appl. Microbiol. Biotechnol. 2013, 97, 7285-7295, doi: 10.1007/s00253-013-4688-1,

74. P. D'Arrigo, C. Allegretti, A. Fiorati, L. Piubelli, E. Rosini, D. Tessaro, M. Valentino, L. Pollegioni, Immobilization of L-aspartate oxidase from Sulfolobus tokodaii as a biocatalyst for resolution of aspartate solutions, Catal. Sci. Technol. 2015, 5, 1106-1114, https://doy.org/10.1039/C4CY00968A

75. R.T. Bossi, A. Negri, G. Tedeschi, A. Mattevi, Structure of FAD-bound L-aspartate oxidase (1knr): insight into substrate specificity and catalysis. Biochemistry, 2002, 41, 3018-3024, DOI: 10.1021/bi015939r

76. K. Kukil, J.A. Hawkes, C. Bliksrad, P. Lindberg, L-Aspartate oxidase provides new insights into fumarate reduction in anaerobic darkness in Synechocystis sp. PCC6803, BioRxiv, Oct.19, 2022, https://doi.org/10.1101/2022.10.19.512830

77. C. Chow, S. Hegde, J.S. Blanchard, Mechanistic characterization of Escherichia coli L-aspartate oxidase from kinetic isotope effects, Biochemistry 2017, 56, 4044-4052, doi: 10.1021/acs.biochem.7b00307,

78. H. Ishikawa, H. Masaki, N. Muto, L-Glutamic acid oxidase and its use for analytical methods, Ger. Offen, 1983 DE 3307607

79. H. Kusakabe, Y. Midorikawa, T. Fujishima, Methods for determining L-glutamate in soy sauce with L-glutamate oxidase, Agric. Biolog. Chem. 1984, 48, 181-184.

80. T. Yao, H. Yamamoto, T. Wasa L-Glutamate enzyme electrode involving amplification by substrate recycling, Anal. Chim. Acta, 1990, 236, 437-440.

81. K. Kihara, S. Yasukawa, Measurement of transaminase activities with enzyme electrode, Jpn. Kokkai Tokkyo Koho, 1986, JP 61081799 A 19860425

82. K. Nagata, K. Kurosawa, K. Tomita, Apparatus for measurement of glutamate concentration, Shokuhin To Kagaku, 1987, 29, 93-95.

83. A. Boehmer, A. Mueller, M. Passage, P. Liebs, H. Honeck, H.G. Mueller, A novel L-glutamate oxidase from Streptomyces endus, Purification and Properties, Europ. J. Biochem. 1989, 182, 327-332

84. P.D. Hale, H.S. Lee, Y. Okamoto, T.A. Skotheim, Glutamate biosensor based on electrical communication between L-glutamate oxidase and a flexible redox polymer, Anal. Letters, 1991, 24, 345-356.

85. B.A.A. Dremel, R.D. Schmid, O.S. Wolfbeis, Comparison of two fiber-optic L-glutamate biosensors based on the detection of oxygen or carbon dioxide, and their application in combination with flow-injection analysis to the determination of glutamate, Anal. Chim. Acta, 1991, 248, 351-358.

86. E. Tamiya, Y. Sugiura, Y. Amou, I. Karube, A. Ajima, R.T. Kado, M. Ito, Direct monitoring of glutamate released from cerebellar neurons using platinized carbon disk microelectrode modified with glutamate oxidase-bound membrane, Sensors and Materials, 1995, 7, 249-259.

87. O. Niwa, K. Torimitsu, M. Morita, P. Osborne, K. Yamamoto, Concentration of extracellular L-glutamate released from cultured nerve cells a small-volume online sensor, Anal. Chem. 1996, 68, 1865-1870.

88. O. Niwa, T. Horiuchi, K. Torimitsu, Continuous monitoring of L-glutamate released from cultured nerve cells by an online sensor coupled with micro-capillary sampling, Biocencor & Bioelectronics, 1997, 12, 311-319.

89. K. Murakami, M. Kakemoto, H. Ogawa, Simultaneous determination of lactic acid, glutamic acid, and glucose by HPLC using an enzyme sensor with a photo-cross-linkable polymer support, Nippon Kagaku Kaishi, 1996, 457-461.

90. T. Oikawa, M. Watanabe, H. Makiura, H. Kusakabe, K. Yamada, K. Soda, Production of D-glutamate from L-glutamate with glutamate racemase and L-glutamate oxidase, Biosci. Biotechnol. Biochem. 1999, 63, 2168-2173.

91. K. Nakajima, T. Yamagiwa, A. Hirano, M. Sugawara, A glass capillary microelectrode based on capillary and its application to the detection of L-glutamate release from mouse brain slices, Anal. Sci. 2003, 19, 55-60.

92. A. Hirano, N. Moridera, M. Akashi, M. Saito, M. Sugawara, Imaging of L-glutamate fluxes in mouse brain slices based on an enzyme-based membrane combined with a difference-image analysis, Anal. Chem. 2003, 75, 3775-3783.

93. M. Ghirma, W. Negussie, G. Lo, Y. Yirgalem, K. Yirgalem, B. Abebaw, A. Girma, N.M. Baboo, T. Solomon, Glutamate oxidase advances the selective bioanalytical detection of the neurotoxic amino acid β-ODAP om grass peas: a decade of progress, Pure Appl. Chem. 2004, 76, 765-775.

94. B.Y. Lee, S.M. Seo, D.J. Lee, M. Lee, J. Lee, J-H. Cheon, H. Lee, I-Y. Ching, Y.J. Park, Biosensor system-on-a-chip including CMOS-based signal processing circuits and 64 carbon nono-tube-based sensors for the detection of a neurotransmitter, Lab on a Chip, 2010, 10, 894-898.

95. A. Hirano, M. Asakawa, N. Kido, M. Sugawara, Detection and imaging of L-glutamate released from mouse-brain slices with an enzyme-based membrane, Anal. Sci. 2000, 16, 25-29.

96. S. Upadhyay, N. Ohgami, H. Kusakabe, H. Mizuno, J. Arima, T. Tamura, K. Inagaki, H. Suzuki, Performance characterization of recombinant L-glutamate oxidase in a micro GOT/GPT sensing system, Sensors Actuators, B: Chemical, 2006, B119, 570-576.

97. A. Morales-Villagran, C. Sandoval-Salazar, L. Medina-Ceja, An analytical flow injection system to measure glutamate in microdialysis samples based on an enzymatic reaction and electrochemical detection, Electroanalysis, 2008, 20, 1032-1034.

98. K.P. Bermingham, M.M. Doran, F.B. Bolger, J.P. Lowry, Design optimization and characterization of an amperometric glutamate oxidase-based composite biosensor for neurotransmitter L-glutamate, Anal. Chim. Acta, 2022, 1224, 340205, https://doi.org/10.1016/j.aca.2022.340205

99. P. Odman, W.B. Wellbotn, A.S. Bommarius, An enzymatic process to a-ketoglutarate from l-glutamate; the coupled system l-glutamate dehydrogenase/NADH oxidase, Tetrahedron: Asymmetry, 2004, 15, 2933-2937, https://doi.org/10.1016/j.tetasy.2004.07-055

100. L. Lovino, M.F. Tremblay, L. Civiero, Glutamate-induced excitotoxicity in Pirkinson's disease: The role of glial cells, J. Pharmacol. Sci. 2020, 144, 151-164, https://doi.org/10.1016/j.jphs.2020.07. 11

101. F. Matsui, A. Terai, Y. Asano, L-Arginine oxidase from Pseudomonas sp. TPU 7192: Characterization, gene cloning, heterologous expression, and application to L-arginine determination, Enzyme and Microbial Technology, 2016, 82, 151-157. https://doi.org/10.1016/j.enzmictec.2015.10.002

102. S. Nakano, M. Niwa, Y. Asano, S. Ito, Following the evolutionary track of a highly specific L-arginine oxidase by reconstruction and biochemical analysis of ancestral and native enzymes, Applied and Environmental Microbiology, 2019, 85, aem.asm.org1-12. https://doi.org/10.1128/aem.00459-19

103. Y. Yano, S. Matsuo, N. Ito, T. Tamura, H. Kusakabe, K. Inagaki, K. Imada, A new L-arginine oxidase engineered from L-glutamate oxidase. Protein Sci. 2021, 30, 1044-1055, DOI: 10.1002/pro.4070

104. D. Im, D. Matsui, T. Arakawa, K. Isobe, Y. Asano, S. Fushinobu, Ligand complex structures of L-amino acid oxidase/monooxygenase from Pseudomonas sp. AIU 813 and its conformational change, FSBS Open Bio, 2018, 8 (3) 314-324, https://doi.org/10.1002/2211-5463.12387

105. M. Amano, H. Mizuguchi, T. Sano, H. Kondo, K. Shinyashiki, J. Inagaki, T. Tamura, T. Kawaguchi, H. Kusakabe, K. Imada, K. Inagaki, Recombinant expression, molecular characterization, and crystal structure of antitumor enzyme, L-lysine alpha-oxidase from Trichoderma viride. J. Biochem. 2015, 157, 549-559, DOI: 10.1093/jb/mvv012

106. V.L. Krupyanko, A.G. Medentsev, E.V. Lukasheva, Kinetic characteristics of L-lysine a-oxidase from Trichoderma cf. Aureoviride, Rifai VKM F-4268D: Substrate specificity and allosteric effects, Biochemistry Biophysics Reports, 2017, 9, 9-12, https://dx.doi.org/10.1016/j.bbrep.2016.11.003

107. S. Sugiura, S. Nakano, M. Niwa, F. Hasebe, D. Matsui, S. Ito, Catalytic mechanism if ancestral L-lysine oxidase assigned by sequence database mining, J. Biol. Chem. 2021, 297(3) 101043, 1-15, https://doi.org/10.1016/j.jbc.2021.101043

108. T. Motoyama, Y. Yamamoto, C. Ishida, F. Hasebe, Y. Kawamura, Y. Shigeta, S. Ito, S. Nakano, Reaction mechanism of ancestral L-Lys α-oxidase from Caulobacter species studied by biochemical, structural, and computational analysis, ACS Omega, 2022, 7, 44407-44419, https://doi.org/10.1621/acsomega.2c06334

109. R. Satpathy, B. Konkimalla, J. Ratha, In-silico rational protein engineering and design approach to improve thermostability of α haloalkane dehalogenase enzyme, Am. J. Bioinform. 2015, 4 (2): 34.46 DOI: 10.3844/ajbsp.2015.34.46

110. V. Vermeirssen, A. van der Bent, J. van Camp, A. van Amerongen, W. Verstraete, A quantitative in silico analysis calculates the angiotensin I converting enzyme (ACE) inhibitory activity in pea and whey protein digests, Biochimie, 2004, 86, (3), March 231-239, https://doi.org/10.1016/j.biochi.2004.01.003.

111. T. Hanai, Quantitative in silico analysis of SARS-CoV-2 S-RBD omicron mutant transmissibility, Talanta, 2022, 240, 123206, https://doi.org/10.1016/j.talanta.2022.123206

112. T. Hanai, Further quantitative in silico analysis of SARS-CoV-2 S-RBD Omicron BA.4, BA.5, BA.2.75, BQ.1, and BQ.1.1 transmissibility, Talanta, 2023, 254, 124127, https://doi.org/10.1016/j.talanta.2022.124127.

Chapter 10: Diagnosis and enzyme activity

10.1 Against Chronic Kidney Disease

Early detection of individual metabolic abnormalities and early treatment are simple, economical ways to keep people healthy. Personal health management is important for staying healthy. A typical example is diabetes in the USA. We can easily observe individuals with obesity and prediabetes in the USA. These unhealthy lifestyle patterns is spreading worldwide. Kidney disease may result from inadequate health management. Early monitoring of personal metabolism can prevent kidney disease.

HPLC analysis of guanidino compounds found a large quantity of arginine and creatine in kidney disease patients' sera. If people do not take arginine and creatine as supplements, poor production or third-party inhibition weakens the enzyme activity of glycine amidinotransferase (GAT) and creatine kinase (CK) [1]. Possible treatments include dosing RNA to restore expression or activating these enzymes with suitable compounds; therefore, we need to develop a rapid diagnostic for these enzymes [2]. The approach is either direct analysis of enzyme activity or analysis of precursors and metabolites. First, we must clarify the reaction mechanism to identify target compounds for developing rapid assays. The metabolism of arginine to creatine is a three-step enzyme reaction. The first reaction converts arginine to ornithine via glycineamidinotransferase; the second converts guanidinoacetate to creatine via guanidinoacetate *N*-methyltransferase; and the third converts creatine to 4-phosphocreatine via creatine kinase. The reaction scheme is shown in Figure 10.1. The details of these reactions are visualized in the following passages. The replacement of amino acids and the replacement and insertion of cofactors of downloaded PDB proteins are necessary to explain these human enzyme reactions. Each passage explains the details.

FIgure 10.1: Metabolic pathway of guanidine compounds.

These guanidine compounds are quantitatively analyzed by column-switching HPLC with isocratic elution within 15 min. An example of a chromatogram is shown in Figure 10.2. The chromatographic system switches between two columns using a single isocratic eluent. Columns: carbon column and ODS silica gel column; Eluent: 10 mM sodium citrate pH 4.5 containing 5 mM sodium octane sulfonate; Flow rate 1.0 mL min-1; fluorescence detection using post-column derivatization using ninhydrin; Standard compounds: GSA Guanidinosuccinic acid, TAU Taurocyamine,CT Creatine, GAA Guadininoacetic acid, GPA -Guanidinopropionic acid. CTN creatinine, G Guanidine, Arg arginine, MG Methylguanidine, GBA - Guanidinobutyric acid.

FIgure 10.2: Chromatograms of guanidine compounds in sera from nephritic patients. Chromatogram A is a standard mixture; Chromatogram B is sera of normal (control) patient; Chromatogram C is serum from continuous ambulatory peritoneal dialysis after renal transplantation; Chromatogram D is serum from membrane proliferative glomerulonephritis.

This HPLC system enabled baseline separation of ten guanidine compounds in serum within 15 min; it remained stable for over six months and was rapid enough for routine (clinical) analysis, handling 96 serum samples per day. This system was applied to monitor hemodialysis and to analyze different types of nephritic syndromes. Hemodialysis efficiency depended on individual differences, not to the properties of guanidine compounds. The concentrations of guanidino compounds in sera from patients with chronic glomerulonephritis were higher than those from subjects with diabetic nephropathy. The correlations among creatine, creatinine, and methylguanidine concentrations helped clarify the synthesis pathways of methylguanidine in different disease states. Methylguanidine was mainly synthesized from creatinine in diabetic nephropathy, and from both creatine and creatinine in chronic glomerulonephritis. Guanidinosuccinate may be synthesized from creatinine in diabetic nephropathy based on the observed correlation between guandininosuccinate/creatinine, but not arginine/guandininosuccinate, which is believed to be the major metabolic pathway. The results indicate that further analysis of guanidino compounds in serum can improve the diagnosis of diabetes [1].

10.1.1. Glycineamidino transferase: The reaction mechanism for the conversion of glycine to guanidinoacetate has been described as involving serine 355 (S355), in which serine contacts the arginine guanidino group and transfers the guanidino group to glycine [3]. However, the S355 hydroxyl group contacts the substrate arginine carboxyl group (4JDW) [4]; with other substrates, r-aminobutyric acid (6JDW) and norvaline (1JDX), the carboxyl group contacts the serine hydroxyl group, while their amino groups do not contact serine. An alternative proposed mechanism is that the glycine amino group contacts the substrate arginine guanidino group, and the guanidino group transfers to glycine [4,5]. We examined the reaction mechanism in silico using downloaded GAT structures.

Several three-dimensional structures of human GAT were downloaded from the RCSB PDB and selected 4JDW because it contains the substrate arginine, and the three-dimensional structure was optimized using the CACHE™ (SciGress™ from Fujitsu) MM2 program. Amino acid residues within 3Å were extracted for further analysis. A glycine molecule was placed near the arginine guanidino group and optimized it to assess the feasibility of electron transfer from the arginine guanidino group to glycine. The atomic distances and partial charges of the target atoms support the possibility of contact. Figure 10.3 shows the downloaded, corrected, and optimized structure of GAT (4JDW). The locations of arginine and glycine are shown as molecular models, and the protein is shown as a line model.

According to the GAT enzyme reaction mechanism report, the protein's serine removes arginine's guanidino group, transfers it to a glycine amino group, and produces guanidinoacetate. However, the stereo structure indicates that the carboxy and amino groups are located near the residual arginine guanidyl and serine hydroxy groups; the substrate arginine guanidino group is far from the molecular interaction site, and no serine exists near the substrate arginine guanidino group. The stereo structure indicates that rotation of the substrate arginine is difficult in the *in vivo* reaction. Therefore, the electron localization of the substrate arginine before and after being trapped in the enzyme reaction center was analyzed. Figure 10.4 shows the extracted substrate arginine and the original arginine, and shows the extracted conformation of substrate arginine with surrounding residual amino acids within 3Å of the substrate arginine. The feasibility of enzyme reactions is similar to that of chemical reactions. Localized electron density near the reaction center indicates reactivity; therefore, we calculated arginine's atomic partial charge (apc) before and after using the MOPAC PM5 program. The arginine carboxy group contacts residues S355 and R322, and the amino group contacts residue D298. The substrate arginine is tightly held by the residual amino acids S355, R322, and D295 and cannot be rotated inside the reaction chamber, and the guanidino group can contact glycine. The electron localization explains the binding tightness. The atomic partial charge values of target atoms shown in Figure 10.4 indicate the binding center.

FIgure 10.3: Downloaded and optimized stereo structure of Arginine Glycineamidinotransferase including arginine and glycine.

FIgure 10.4: Atomic partial charge of arginine heavy atoms: of free form (original) and optimized inside the enzyme.

FIgure 10.5: Extracted stereo structure of arginine and substitutes with residual amino acids within 3Å from the arginine (Arg) or ornithine (ORN). The key atom distances are indicated in the Figures. 10.3..

The complex structures of arginine and glycine complex and ornithine guanidinoacetate are shown in Figure 10.6. Initially, glycine contacts the arginine guanidino group (Figure 10.5A Pre), and the arginine guanidino group transfers to the glycine amino group; then, arginine is converted to ornithine, and the glycine becomes guanidinoacetate. Figure 5B shows electron localization. The atomic partial charge changes indicate the contact center and the feasibility of the reaction. Figure 10.7 shows the original structures of glycine and guanidinoacetate with atomic partial charges on heavy atoms to clarify the reaction center.

FIgure 10.6: Extracted conformations of pre- and post-reactions with heavy atom atomic partial charge values

The apc values of the substrate arginine carboxy oxygen are -0.628 and -0.481, and those held by the enzyme are -0.652 and -0.630 au; the strong negative values become slightly less negative upon complex formation with glycine. The apc value of the guanidino carbon changes from 0.286 to 0.365 au upon folding and is slightly recovered by complex formation to 0.324 au.

FIgure 10.7: Optimized structure and heavy atom atomic partial charge values of glycine and guanidinoacetate.

The reactivity can also be understood from the change in apc values of glycine and guanidinoacetate. The apc values of glycine carboxy oxygen atoms change from -0.490 and -0.662 to -0.616 and -0.650 au. The corresponding values for the carboxyl oxygen atoms of guanidinoacetate change from -0.620 and -0.549 to -0.724 and -0.501 au. These conformational changes and apc value shifts clarify the reaction center and the enzyme selectivity [Chapter 9].

10.1.2. Guanidinoacetate *N*-methyltransferase: Enzyme activity is reduced in both inherited disorders and acquired diseases. Early oral creatine supplementation may improve outcomes in patients with inherited disorders [6], and reduced GAT activity can be assessed by analyzing of guanidinoacetate (GAA) in urine and serum; however, a single-point analysis is affected by individual lifestyle factors and requires an assessment of metabolite balance. The next enzyme in the pathway after GAT is guanidinoacetate N-methyltransferase, which metabolizes guanidinoacetate to creatine. The coenzyme is *S*-adenosylmethionine (AdoMe), whose *S*-methyl group is transferred to the guanidinoacetate guanidyl group. A structure of human guanidinoacetate N-methyltransferase was downloaded from the PDB (3ORN), including *S*-adenosyl-*L*-homocysteine (AdoHey). Figure 10.8 shows the optimized structure, the extracted AdoHey structure with amino acid residues within 3Å, and the extracted AdoHey structures. The AdoHey carboxy group binds to the Aspartic acid (D135) carboxy group via an ion-ion interaction; the atomic distance between the amino nitrogen and carboxy oxygen is 2.2Å. AdoHey adenosine amino group binds to glutamic acid (E118) carboxy group; the atomic distance between the nitrogen and oxygen is 2.9Å. These bonds keep the AdoMe and AdoHey structures straight. The atomic partial charge of the key sulfur atom changed from 0.869 to 0.914 au, and that of the methyl group carbon changed from -0.447 to -0.572 au as a result of electron localization.

First, *S*-adenosyl-*L*-homocysteine is converted to *S*-adenosyl methionine, a guanidinoacetate molecule is inserted, and the chemical structures are corrected. Figure 10.9 shows the optimized complex structure, including amino acid residues within 3Å of AdoMe and the extracted AdoMe. AdoMe is held in the enzyme in the same manner as AdoHey. GAA was then inserted, and the complex structure was optimized. The GAA carboxyl group contacts the AdoMe sulfur. Constructing the transition state from GAA to creatine is difficult inside an enzyme. Therefore, we inserted creatine into the AdoHey complex and fully optimized the structure. The result is shown in Figure 10.10, including an extracted conformation with amino acid residues within 3Å of AdoHey.

FIgure 10.8: Downloaded and optimized structure of Guanidinoacetic acid N-methyltransferase, and extracted N-methyltransferase S-adenyl-L-homocysteine

Figure 10.9: Optimized structure of Guanidinoacetic acid N-methyltransferase with modified S-adenosylmethionine and the extracted conformation and S-adenosylmethionine.

Figure 10.10: Optimized structure of guanidinoacetic acid N-methyltransferase, S-adenosylmethionine, and guanidinoacetate extracted conformation, and S-adenosylmethionine guanidinoacetate complex.

After optimization, the extracted and modified AdoMe adopts a bent conformation outside the enzyme, as shown in Figure 10.11. Therefore, the docking process cannot be automated, and guanidinoacetate and creatine are carefully inserted and optimized as complex structures. Guanidinoacetate and creatine carboxy groups bind with the amino group of *S*-adenosylmethionine and *S*-adenosyl-*L*-homocysteine in vitro (Figure 10.12), but in vivo the amino group already binds to the residual amino acid carboxy group; therefore, the guanidinoacetate and creatine carboxy groups are positioned behind the sulfur atom of these coenzymes.

Figure 10.11: Optimized structure of guanidinoacetic acid N-methyltransferase with S-adenosyl-L-homocysteine and creatine complex, the extracted conformation, and S-adenosyl-L-homocysteine and creatine complex.

Figure 10.12: Optimized structure of S-adenosylmethionine, Complex of extracted S-adenosylmethionine and guanidinoacetic acid.

Chronic kidney disease is a major health concern, and resistance exercise can improve patient health; however, guanidinoacetate was not considered a diagnostic target [7]. This reaction converting guanidinoacetate to creatine requires the cofactor S-adenosyl methionine. Therefore, S-adenosyl methionine is a potential therapeutic candidate.

10.1.3. Creatine kinase: One potential diagnostic biomarker for kidney disease is creatine kinase, which metabolizes creatine to creatine phosphate, which is then metabolized to creatinine [8]. Therefore, creatine kinase activity can be determined by the ratio of creatine to creatinine concentrations. Because creatine is taken as a supplement and serum concentrations are affected by individual lifestyle factors, measuring the balance between creatine and creatinine is necessary to determine personal health status.

Several three-dimensional structures of human creatine kinase were downloaded from the RCSB PDB and corrected and then optimized using the MM2 program. Human brain creatine kinase PDB 3DRB [9] includes ADP, Mg, and nitrate; however, human brain creatine kinase 3DRE contains (-)-7-[(6-chloro-2-naphtalemyl)-1'-(pyridinyl)-spiro[5H-oxazolo[3,2-α]pyrazine-2(3H),4'-priperidin]-5-one instead of ADP even though the report indicates ADP as a cofactor. The stereostructure of 3DRE[3] appears distorted; therefore, we use the stereostructure of human creatine kinase PDB 7TUN [10] as the standard structure, based on comparisons with other human creatine kinases. An initial complex conformation with cofactors is critical for optimizing the complex structure; therefore, the PDB 4RF9 [11] structure is used as a reference structure.

Human sarcomeric mitochondrial creatine kinase 4ZPM includes ADP and uranium. It has 72.4% sequence similarity to human brain creatine kinase 7RUN, and T. Californica Creatine Kinase PDB 1VRP, containing ADP, guanidinoacetic acid, magnesium, and nitrate [12], has 89.3% sequence similarity to 7RUM, and their secondary structures are identical. Therefore, 7RUM is used as the standard for human brain creatine kinase, and 1VRP is used for further analysis to visualize the human creatine kinase reaction mechanism. Therefore, we carefully determine the positions of ATP and ADP by comparing several crystal structures. First, we converted ADP in 1VRP to ATP using the three-dimensional structure of Anthoplasma PDB 4RF9 [11], and replaced the remaining amino acids in 1VRP with those of 7TUM. The mutation process is the same as that used to create a human D-amino acid oxidase from yeast D-amino acid oxidase [13].

The optimized stereo structure of human brain creatine kinase is shown in Figure 10.13A. The stereo structure includes ATP, a creatine molecule, and an ionized magnesium (2+). Some magnesium binds the hydroxyl groups in reference structures, but in these structures, magnesium binds only the phosphate oxygen. Magnesium plays a crucial role in ATP activity [14, 15]; it binds three phosphate oxygens, then two remaining phosphate oxygens after releasing one phosphate to creatine. After releasing one phosphate to convert creatine to creatine phosphate, ATP converts to ADP. An optimized stereo structure of human creatine kinase with ADP and creatine phosphate is shown in Figure 10.13B—the extracted conformation of ATP, Mn^{2+}, and creatine and ADP. Mg^{2+} and phosphocreatine are shown in Figure 10.14.

Figure 10.13: Optimized structure of S-adenosylmethionine, Complex of extracted S-adenosylmethionine and guanidinoacetic acid.

Figure 10.14: Extracted conformations in human creatine kinase before and after the enzyme reaction.

The atomic partial charge of the γ-phosphorus atom of ATP changes from 1.629 to 1.002 au in the presence of creatine, and the atomic partial charge of the nitrogen atom of creatine increases from -0.569 to -0.531 au. This electron induction contributes to the molecular interaction. Changes in the atomic partial charges of key atoms can also explain the phosphorus transfer from ATP to creatine to produce 4-phosphocreatine. The β-phosphorus atomic partial charge decreases from 1.910 to 1.771 au, the γ-phosphorus of ATP increases from 0.876 to 1.145 au, and the nitrogen in 4-phosphocreatine decreases from -0.598 to -0.650 au. Optimization of the chemical structure with MM2 to calculate molecular interaction energies, together with MOPAC PM5 calculations of electron localization, helps clarify the enzyme reaction mechanisms.

Conclusion

Visualizing enzyme reaction processes helps us to understand the reaction mechanisms, develop the diagnostic methods, and design medicines. Chronic kidney disease is common, and resistance exercise can improve patient health. Visualizing enzyme reaction processes in kidney disease clarified the target enzymes and compounds for developing clinical analyses. The target enzymes are glycine amidinotransferase (GAT) and creatine kinase (CK). The glycineamidino transferase converts (metabolizes) arginine to ornithine and glycine to guanidinoacetate, which is not currently considered a diagnostic target.

Monitoring these enzyme activities may help prevent kidney disease. However, the easy availability of arginine and creatine as supplements complicates the interpretation of their concentrations for diagnostic purposes. Therefore, we need to measure the concentrations of these compounds and their metabolites, ornithine and 4-phosphocreatine. Alternatively, we can measure glycine, guanidinoacetic acid, and creatinine.

The second step, converting guanidinoacetate to creatine, requires the cofactor S-adenosylmethionine (AdoMet), which is both a drug candidate and a supplement. Supplementation with glycine and manganese should accelerate arginine metabolism. AdoMet can accelerate guanidinoacetate metabolism to creatine. Glycine, manganese, and AdoMet are available as supplements; therefore, we must measure their levels to avoid excessive intake.

Possible treatments include administering RNA for these enzymes to restore expression or dosing suitable cofactors to activate them; therefore, we need to develop a rapid and personalized assessment of enzyme status. This can be achieved either by directly analyzing enzyme activity or by measuring precursors and metabolites. However, we must clarify the reaction mechanism to identify the target compounds for developing rapid assays

Furthermore, enzyme-activating compounds and increasing enzyme production through RNA-based approaches are potential therapeutic strategies. If amino acid oxidase activity is too high, an inhibitor could be administered to keep glycine content constant. Glycine measurement is another potential diagnostic approach. Adenosine triphosphate (ATP) is unstable, and its precursor, adenosine diphosphate (ADP), is also unstable. Taking ATP and ADP is not recommended. The precursor of ADP is adenosine monophosphate (AMP), which is synthesized from adenine and phosphoribosyl 1-diphosphate using adenosine phosphoribosyl transferase with magnesium ions, an essential element in this synthesis process; further modification provides effective medicines. If an invading pathogen impairs enzyme activity, we should kill viruses and bacteria using antibacterial (antibiotic) and antiviral drugs. First, we need a precise diagnosis that clearly indicates individual enzyme activities. Furthermore, given the challenges of an aging society, early identification of biomarkers and the development of treatments for individuals in preclinical disease states (MIBYO) are important.

New technologies enable the development of mRNA therapeutics that produce proteins. Once a diagnostic assessment identifies reduced enzyme activity, whether due to low enzyme abundance or inactivation, mRNA therapeutics may be administered to normalize the enzyme activity in vivo. However, the solution is not simple. We must identify why enzyme activity is reduced. If endogenous enzyme production is reduced for a known reason due to the inactivation of either small molecules or proteins damaged by the synthesis environment, it may be possible to address the underlying cause. One problem is the presence of oxygen radicals, either from direct radiation or indirectly produced by the inventor's enzymes in vivo. We can use reactive oxygen species scavengers to catch oxygen radicals, but high doses may create additional problems for our immune system, which uses oxygen radicals to damage and kill the membranes of invading pathogens. We can tell a story through chemistry, but the action is complex. This illustrates the complexity of biological regulation.

Eating arginine and creatine to enhance physical strength may be a simple method, but excessive intake may cause metabolic disturbances. Taking L-methionine is one idea, but the enzyme S-adenosylmethionine synthetase requires

ATP as a substrate, and creatine kinase also requires ATP for its activity. Therefore, self-managing arginine and creatine metabolism is a risky approach to controlling our health. We should avoid self-control and consult a physician before taking these supplements.

10.2 Biomarker for senile dementia: Even when our metabolism is normal and we are healthy, some individuals develop health problems for reasons that are not yet understood. We can identify metabolic impairment caused by weakened enzymes by comparing it with normal metabolism. The precursor-to-metabolite ratio indicates a person's health status, and a weakened enzyme is a biomarker for the target condition. We should develop rapid, mass-based analytical methods for general use; furthermore, develop new medicines. One target is to identify individuals at risk of dementia (MIBYO persons) in our aging society. The key molecules for communication are catecholamines and serotonin; these are metabolites of aromatic amino acids (phenylalanine, tyrosine, and tryptophan) which our body cannot synthesize in vivo.

Phenylalanine metabolism is very complex, and several enzymes and coenzymes (cofactors) catalyze similar reactions. The number of enzymes is smaller than the number of metabolites; therefore, a weakened enzyme affects the overall metabolic balance. An HPLC chromatogram of metabolism may indicate a accumulation of several metabolites; however, the biomarker is one enzyme. We should also measure coenzyme concentrations that controls metabolism. Figure 10.15 indicates the metabolites and enzymes; those reactions will be visualized.

FIgure 10.15: Metabolic path ways of phenylalanine, tyrosince, and trypotophan.

An aging society faces a major challenge, even though the social system is well developed and lifestyles are convenient. The disease is senile dementia, whose patients' condition is complicated and cannot necessarily be treated with a single drug. Metabolic dysfunction in older adults has been proposed as a contributor to dementia. The concentration of catecholamine-related compounds, aromatic amino acid metabolites in body fluids, reflects sympathetic nerve functions, and thus, quantification of these compounds in the urine, plasma, and tissues has been informative in the diagnosis of many diseases, such as Alzheimer's, hypertension, Parkinson's disease, affective disorders, heart disease, neural crest tumors, hyper- and hypothyroidism, muscular dystrophy, and familial dysautonomia. Numerous chromatographic

studies of catecholamines have been reported. However, norepinephrine (NE), epinephrine (E), dihydroxyphenylalanine (*L*-DOPA), and dopamine (DA) have been the main targets because other metabolites are present at very low levels [16-19]. The *L*-DOPA/*L*-tyrosine ratio in human plasma was found to be a useful marker of metastatic malignant melanoma [20]. Plasma concentrations of 3-methyl-4-hydroxyphenethyleneglycol (MHPG) differed significantly between normal volunteers and hospital patients [21]. Although levodopa, a DA precursor, relieves many of the symptoms of Parkinson's disease, its effectiveness declines as the disease progresses [22]. The metabolism of catecholamine-related compounds is complex, and multiple enzymes contribute to it. One pathway begins with phenylalanine, and another begins with tryptophan. A lack of certain aromatic amino acids should cause this problem, but this condition is more common in meat-eating countries than in vegetarian countries. Poor diet is not the cause of senile dementia, and weakened enzyme activity does not damage normal metabolism. Is all enzyme activity weakened at a certain time? Each enzyme has a specific structure, and their production capacity depends on individual health conditions, such as lifespan. If we analyze only a limited number of catecholamines, we cannot identify which specific enzyme activity is reduced. First, we must find the target enzymes (biomarkers) using complicated analytical instruments.

We investigated detection and identification modes for rapid, selective, highly sensitive, and simultaneous determination of catecholamines, indoleamines, and related metabolites by liquid chromatography with a series of coulometric working electrodes. Oxidative single, redox, and redox-reductive screen modes were suitable for highly sensitive detection of catechol compounds. The total separation of catecholamine-related compounds has been studied to analyze metabolic mechanisms. The separation of 20 standard compounds was achieved within 25 min using reversed-phase ion-pair liquid chromatography with an electrochemical detector. Examples of three chromatograms monitored by these detectors for standard compounds are shown in Figure 10.1. This isocratic elution system with two column-switching valves is developed using three types of semi-micro columns for fast chromatographic analysis of catecholamine-related compounds [23, 24]. Measuring enzyme activity in these metabolic pathways will improve diagnosis, since these pathways are associated with a variety of symptoms.

FIgure 10.15: Column switching isocratic HPLC diagram.

FIgure 10.16: Chromatogram from 1st column.

Figure 10.17: Chromatogram of combined 1st and 2nd columns.

Figure 10.18: Chromatogram of combined three columns.

Chromatography condition: pentyl-, phenylhexyl-, and octadecyl-bonded silica gel semimiro columns. Eluent components are 21 g citric acid, 300 mg octanesulfonate, 3 mL diethylamine, and 70 mL acetonitrile L^{-1}. Flow rate 200 mL min, 35 °C.

We developed an isocratic solution system with two column-switching valves using three types of semi-micro columns: pentyl-, phenylhexyl-, and octadecyl-bonded silica gel. These columns were stable for over three months of operation in this reversed-phase ion-pair liquid chromatography system with electrochemical detection. In pig brain extract, 4-hydroxy-3-methoxyphenylglycol (or 4-hydroxy-3-methoxymandelic acid), 3,4-dihydroxyphenylalanine, norepinephrine, epinephrine, 3,4-dihydroxyphenylacetic acid, dopamine, 5-hydroxytryptophan, and 5-hydroxyindole acetic acid were quantified from their retention times. This highly sensitive method can be applied to serum samples to determine biomarkers. Because maintaining all metabolic processes through medication may require excessive dosing, we should determine which enzyme activity is weakened first and then treat most people in preclinical (MIBYO) states. This approach can be applied to other major diseases, except in individuals with uncontrolled lifestyles.

10.2.1 Human Phenylalanine -4- monooxygenase (phenylalanine hydroxylase): Deficiency of phenylalanine hydroxylase causes phenylketonuria. The toxic effects of accumulating phenylalanine metabolites cause severe intellectual disability [25]. Therefore, assessment of phenylalanine hydroxylase activity is an important diagnostic approach. Phenylalanine hydroxylase catalyzes the hydroxylation of L-phenylalanine to L-tyrosine. The reaction is described in the following equation [26,27].

(6*R*)-*L*-erythro-5,6,7,8-tetrahnydrobiopterin (**A**) + *L*-phenylalanine + O_2 = (4α*S*,6*R*)-4α-hydroxy-*L*-erythro 5,6,7,8-tetrahydrobiopterin (**B**) + *L*-tyrosine

A downloaded human phenylalanine hydroxylase includes cofactors of **A**, β(2-thienyl)alanine, and iron. The water molecules are removed, and the β(2-thienyl)alanine is converted to *L*-phenylalanine (Figure 10.18**a**). This phenylalanine

hydroxylase differs from that of human *Legionella pneumophila*, which plays a major role in synthesizing the pigment pyomelanin (a potential virulence factor). The reaction center of this phenylalanine hydroxylase is relatively hydrophobic, and residual amino acids within 5Å of the substituted phenylalanine are 20% aromatic amino acids, compared with 14% of the total 309 amino acids. The reaction center of later phenylalanine hydroxylase is hydrophilic [28]. Therefore, these human phenylalanine hydroxylases likely contribute differently to pathophysiology. A cofactor, iron (Fe^{2+}), forms a six-coordinate complex. The ion binds with two histidine ring nitrogens (H285, H290) and two glutamic acid oxygens (E330). The free ports should bind oxygen ligands to bridge with (6*R*)- *S*-erythro-5,6,7,8-tetrahydrobiopterin and *S*-phenylalanine. Therefore, two oxygen atoms were added and bound to the iron; then, the complex structure was optimized. The optimized structure is shown in Figure 10.18**b**. Then, (6*R*)-S-erythro-5,6,7,8-tetrahydrobiopterin was hydroxylated to (4α*S*, 4α-hydroxy-*S*-erythro-5,6,7,8-tetrahydrobiopterin), and phenylalanine was converted to *S*-tyrosine. The new complex is optimized. The optimized structure is shown in Figure 10.18**c**.

FIgure 10.18: a. Reaction scheme of phenylalanine hydroxylase; **b.** Optimized structure of phenylalanine hydrogenase complex with ligand oxygen atoms; c. Optimized structure of phenylalanine hydrogenase complex with tyrosine.

The cofactor conformations before and after the enzyme reactions are extracted from Figure 10.18 and are shown in Figure 10.19**a-c**. We examine the reaction processes using atomic partial charge changes (au) calculated with MOPAC PM5. The key atoms are circled in the Figure. The atomic partial charge values are summarized in Table 10.1.

FIgure 10.18: Reaction processes of phenylalanine hydroxylase.

Table 10.1: Atomic partial charge of key atoms (au)

Cofactor		A (free)	A+FeO_2	Δ	B	Δ	B (free)
Atom	C	-0.215	-0.196	(+0.019)	0.299	(-0.056)	0.355
	O	-0.512	-0.573	(+0.061)	-0.397	(+0.081)	-0.478
	H	-0.155	-0.138	(+0.017)	0.130	(-0.022)	0.152
Amino acid		PhAl (free)	PhAl+FeO_2	Δ	Tyr	Δ	Tyr (free)
	C	-0.155	-0.138	(+0.017)	0.130	(-0.022)	0.152

A: (6R)-S-erythro-5,6,7,8-tetrahnydrobiopterin; B: (4αS,6R)-4α-hydroxy-S-erythro-5,6,7,8- tetrahydrobiopterin; PhAl: phenylalanine; Tyr: tyrosine; Fe: iron; The atomic partial charge value of the "free" is calculated for the individual compounds.

The atomic partial charge values of key atoms indicate that the complex formation induces electron localization toward oxidation of compound A and reduction of compound B. The largest difference in the carbon (C) atomic partial charge (0.075 or 0.570 au) supports the reaction center.

Phenylalanine hydroxylase is the first enzyme in phenylalanine metabolism. When the activity of this enzyme is reduced, supplementation with these cofactors may reactivate the enzyme reaction. However, compound A, tetrahydrobiopterin, is biosynthesized from guanosine triphosphate (GTP) by three chemical reactions mediated by the enzymes GTP cyclohydrolase I, 6-pyruvoyltetrahydropterin synthase, and sepiapterin reductase [29]. Therefore,

reactivating phenylalanine hydroxylase is not straightforward. It requires iron and oxygen, and compound A, whose biosynthesis involves a complex pathway. Furthermore, compound A is a cofactor involved in the synthesis of serotonin, dopamine, and nitric oxide, which have all been implicated in the pathophysiology of schizophrenia. Compound A is considered an effective compound in treating all symptom domains of schizophrenia [30].

Computational chemists should know the fundamentals of pharmacology and organic synthesis to communicate with biochemists who prepare pure proteins (enzymes) and determine their stereostructures, and with organic chemists who synthesize new drug candidates. The time required for computational contributions may be short, depending on the researchers' expertise. The research team may shorten the drug discovery process if computational chemists know purification methods (chromatography) and the fundamental properties of drug candidates needed to run biological experiments. A major bottleneck in drug discovery is obtaining a three-dimensional structure of the target protein (enzyme). Computational chemists cannot design small-molecule drug candidates without the protein structure. If we want to develop mRNA-based medicines, computational chemists may have a more limited role. We have to develop biomarker diagnostics to prevent diseases. Computational scientists should participate throughout the drug discovery process.

10.2.2. Tyrosine hydrogenase: Tyrosine hydroxylase catalyzes the hydroxylation of *L*-tyrosine to *L*-3,4-dihydroxyphenylalanine (*L*-DOPA). The reaction is described by the following equation [29, 30].

(6*R*)-*L*-erythro-5,6,7,8-tetrahnydrobiopterin (**A**) + *L*-tyrosine + O_2 = (4α*S*,6_R)-4α-hydroxy-*L*-erythro-5,6,7,8-tetrahydrobiopterin (**B**) + *L*-DOPA

A downloaded human tyrosine hydroxylase structure (PDB 2XSN) contains only a zinc ion, whereas a rat tyrosine hydroxylase structure contains 7,8-dihydrobiopterin and an iron ion; however, the locations of these components are not adequate for analyzing the reaction mechanism. Tyrosine hydroxylase and phenylalanine hydroxylase use the same cofactors, and their three-dimensional structures are very similar. Therefore, the three-dimensional structure of tyrosine hydroxylase was constructed from the previously prepared phenylalanine hydroxylase structure [3]. The three-dimensional structure of tyrosine hydroxylase and the reaction scheme are shown in Figure 1.

Figure 10.19: Reaction scheme of tyrosine hydroxylase; Optimized structure of tyrosine hydrogenase complex with cofactor (A), iron, and tyrosine, and tyrosine hydrogenase complex with L-DOPA.

Figure 10.20: Reaction processes of tyrosine hydroxylase: The key carbon atoms are circled to explain the reaction.

The atomic partial charges of the atoms at the reaction center indicate electron localization influenced by the surrounding molecules; therefore, the initial positions of the cofactors are critical for analyzing the reaction mechanisms. We should carefully select a downloaded PDB file even if the species differ, because the fundamental conformation should be similar for the same reactions. Careful replacement of amino acid residues can produce the three-dimensional structures of human enzymes.

Tyrosine hydroxylase is the second enzyme involved in phenylalanine metabolism. Its reaction mechanism and cofactors are the same as those of phenylalanine hydroxylase. Therefore, we can use the same approach as that used for phenylalanine hydroxylase. When the activity of this enzyme is weakened, supplementation with these cofactors may reactivate the enzymatic reaction. However, compound A, tetrahydrobiopterin, is biosynthesized from guanosine triphosphate (GTP) through three reactions mediated by the enzymes GTP cyclohydrolase I, 6-pyruvoyltetrahydropterin synthase, and sepiapterin reductase [29]. Therefore, reactivation of tyrosine hydroxylase is not straightforward. It requires iron, oxygen, and compound A, whose precursor is not a simple chemical compound. Furthermore, compound A is a cofactor involved in the synthesis of serotonin, dopamine, and nitric oxide, all of which have been implicated in the pathophysiology of schizophrenia. Compound A is considered a potentially effective compound for treating all symptom domains of schizophrenia [30].

Remarks

Phenylketonuria (contribution by Eduardo Petazze): The enzyme phenylalanine hydroxylase catalyzes the conversion of phenylalanine to tyrosine. Phenylketonuria (PKU) is a congenital disease with an autosomal recessive inheritance pattern in which unmetabolized phenylalanine accumulates to toxic levels in the central nervous system (CNS), causing brain damage. Normal blood levels of phenylalanine are between 2 and 6 mg/dL. A lifelong low-protein diet allows patients with PKU to live normal lives.

In addition to PAH deficiency (encoded in cytogenetic band 12q23.2), the functional element LOC126861615 (CDK7 Strongly-Dependent Group 2 Enhancer), chr12: 103244689–103245888, an active group 2 enhancer identified by STARR-seq (Self-Transcribing Active Regulatory Region sequencing), is involved in PKU. This functional element depends on the cofactors BRD2, BRD4, P300/CBP, and MED14, with a strong dependence on CDK7 (cyclin-dependent kinase 7). https://www.malacards.org/card/phenylketonuria

Biomarkers (contribution by Mohammad Vaziri**)**

Understanding Biomarkers: Types and Their Importance:

Biomarkers are measurable indicators that provide information about the biological state or condition of an organism. They play a crucial role in fields such as medicine, research, and drug development. The following are some types of biomarkers and their significance:

Diagnostic Biomarkers: These biomarkers indicate the presence or absence of a disease. Examples include prostate-specific antigen (PSA) for prostate cancer and blood glucose levels for diabetes.

Prognostic Biomarkers: These biomarkers predict the likelihood of disease progression or the outcome of a disease. For instance, certain genetic markers can indicate the aggressiveness of some cancers.

Predictive Biomarkers: These biomarkers help determine how a patient will respond to a particular treatment. Genetic markers that predict responses to targeted therapies in cancer treatment are good examples.

Surrogate Biomarkers: Instead of directly measuring clinical outcomes, these biomarkers are used as substitutes to predict clinical benefit. For example, cholesterol levels can be used as a surrogate marker for cardiovascular risk.

Pharmacodynamic Biomarkers: These biomarkers measure the effects of a drug on the body. They can help us understand the drug's mechanism of action and its potential side effects.

Safety Biomarkers: These biomarkers indicate potential adverse effects or toxicity of a drug or treatment. Liver enzymes, for instance, can be monitored to assess potential liver damage due to medications. Activate to view larger images.

References

1. T. Hanai, Y. Inamoto, S. Inamoto, Analytical method to identify mal-function metabolites related to kidney diseases; Chromatography of guanidino compounds, J. Chromatogr. B. 2000, 747, 123-138. https://doi.org/10.1016/S0378-4347(00)00340-6

2. Y. Inamoto, S. Inamoto, T. Hanai, Y. Takahashi, K. Kadowaki, T. Kinoshita, Development of automated highly sensitive analytical system for guanidine sulfate in serum, J. Liq. Chrom. & Rel. Technol. 1997, 20, 2099-2108.s

3. E. Hanff, P. Hafner, A. Bollenbach, --, D. Tsikas, Effects of single and combined metformin and L-citrulline supplementation on L-arginine-related pathways in Becker muscular dystrophy patients: possible biochemical and clinical implications, Amino acids, 2018, 50, 6, DOI: 10.1007/s00726-018

4. E. Fritsche, A. Humm, R. Huber, The ligand-induced structural changes of human L-arginine: glycine amidinotransferase, J. Bio. Chem. 1999, 274, 3026-3032,

5. D. Tsikas, B. Redfors, Pilot study on acute effects of pharmacological intraperitoneal L-homoarginine on homeostasis of lysine and other amino acids in a rat model of isoprenaline-induced Taokotsubo cardiomyopathy, Int. J. Mol. Sci., 2022, 23, ,4734, https://doi.org/10.3390/ijms23094734

6. S. Stockler-Ipsiroglu, D. Apatean, R. Battini, S. DeBtpsse, K. Dessofy, S. Edvardson, F. Eichler, K. Johnston, D.M. Koeller, s. Nouioua, M. Tazir, A. Verma, M.D. Dpwing, K.J. Wierenga, a.M. Wierenga, V. Zhang, L.-J. C. Wong, Mol. Genet. Metab. 2015, 116, 252-259, 3. http://dx.doi.org/10.1016/j.ymgme.20015.10.003

7. C.-C. Chen, Y.-Y. Huang, H. Zhang, X. Liu, X.Q. Li, Y.-Q. Long, Z.W. Chen, T. Jin, Impact of resistance exercise on patients with chronic kidney disease, BMC Nephrology, 2024, 25, 115, http://doi.org/10.1186/10.1186/s12882-024-03547-5

8. Wikipedia

9. S.M. Bong, J.H. Moon, K.H. Nam, K.S. Lee, Y.M. Chi, K.Y. Hwang, Structural studies of human brain type creatine kinase complexed with the ADP-Mg2+-NO3—creatine transition-state analogue complex, FEBS Letters, 2008, 582, 3959-3965, doi: 10.1016/j.febs.2008.10.039, FEBS Letter, 2008, 582, 3959-3965

10. H.-S. Seo, S. Dhe-Paganon, Crystal Structure Analysis of human CKB complex with a covalent compound, to be published, PDB DOI: https://doi.org/10.2210/pdb7TUN/pdb

11. Z. Wang, Z. Qiao, S. Ye, R. Zhang, R., Structure of a double-domain phosphagen kinase reveals an asymmetric arrangement of the tandem domains.,(2015) Acta Crystallogr D Biol Crystallogr 71: 779-789, 12. SD. Lahiri, P.F. Wang, P.C. Babbitt, M.J. McLeish, G.I. Kenyon, K.N.. Allen, The 2.1 Structure of T. California Creatine Kinase Complexed with the Transition-State Analogue Complex, ADP-Mg 2+ /NO3- /Creatine, PDB DOI: https://doi.org/10.2210/pdb1VRP/pdb

12. The 2.1 A Structure of Torpedo Californica Creatine Kinase Complexed with the ADP-Mg(2+)-NO3(-)- Creatine Transition-State Analogue Complex, Biochemistry, 2002, 41: 13861-13867, DOI: https://doi.org/10.1021/bi026655p7.

13. T. Hanai (ed) Quantitative in silico Analytical Chemistry, Quantitative Analysis of Molecular from Chromatography Retention to Enzyme Selectivity, Chapter 9, Physical Biochemistry of Enzyme Reactions, 2024, p. 238-273, http://hanai-toshihiko.net/ quantitative in silico analytical chemistry/ pp.327, 43.5 MB.

14. F. P. Buelens, H. Leonov, B.L. de Groot, H. Grubmüller, ATP–Magnesium Coordination: Protein Structure Based Force Field Evaluation and Corrections J. Chem. Theory Comput. 2021, 17, 3, 1922–1930, https://doi.org/10.1021/acs.jctc.0c01205

15. C. Chinopoulos, G. Kiss, H. Kawamata, A. Starkov, Chapter Seventeen - Measurement of ADP–ATP Exchange in Relation to Mitochondrial Transmembrane Potential and Oxygen Consumption https://doi.org/10.1016/B978-0-12-416618-9.00017-0Get rights and content

16. K. Mori, Catecholamines. In Liquid Chromatography in Biomedical Analysis. J. Chromatogr. B. 2000, 747, 123-138.

17. B. Kagedal, D.S. Goldstein, Catecholamine and their metabolites, J. Chromatogr. 1988, 429, 177- 233.

18. Z. Deyl, I. Miksik, F. Biogenic amines, In Advanced Chromatographic and Electromigration Methods in Bioscience,. Elsevier Amsterdam. 1998, pp. 403.

19. M. Waksmundezka-Hajnos, Chromatographic separation of aromatic carboxylic acids, J. Chromatogr. B. 1988, 717, 93-118.

20. S. Letellier, J.P. Garmir, J. Spy, B. Bousquet, Determination of the L-DOPA/L-tyrosine ratio in human plasma by high-performance liquid chromatography, Usefulness as a marker in metastatic malignant melanoma, J. Chlomatogr. B. 1977, 696, 9-17.

21. E. Hollenbach, C. Schulz, H. Lehnert, Rapid and sensitive determination of catecholamines and the metabolite 3-methoxy-4-hydroxyphenetyleneglycol using HPLC following novel extraction procedures, Life Sci., 1988, 63, 737-750.

22. B.J. Hilman, The environment and Parkinson's, C & E News, 2001, 17, 35-37.

23. T. Hanai, Chromatography and Computational Chemical Analysis for Drug Discovery, Frontiers in Medicinal Chemistry, 2009, 4, 86-129.

24. T. Hanai, K. Kaneko, H. Homma, Semi-micro liquid chromatography of aromatic amino acid metabolites using isocratic elution and column switching, Biomed. Chromatogr. 2002, 16, 420-424,doi: 10.1002/bmc.176

25. H.L. Wilson, W. J. Roesler, CCAAT/enhancer binding proteins: do they possess intrinsic cAMP inducible activity? Molecular and Cellular Endocrinology, 2002, https://www.sciencedirect.com/science/article/pii/S0303720701007547; M. Kohlmeler, Amino acids and nitrogen compounds, Nutrient Metabolism, 2015, https;//www.sciencedirect.com/science/article/pii/B9780123877840000080; R.L.S. Russo, W.R. Wilcox, Amino acid metabolism, 3.1.2 Phenylalanine hydroxylase reaction, Emery and Rimoin's principles and practice of medical genetics and genomics, 2021, https://www.sciencedirect.com/science/article/pii/B9780128125359000030; K. de Meer, Inborn errors of metabolism, Overview, Hyperphenylalaninemia, Encyclopedia of Food Sciences and Nutrition, 2003, https://www.sciencedirect.com/science/article/pii/B012227055X006283; in Phenylalanine 4. Monooxygenase, Integrated review Biochemistry (2nd edition), Elsevier, 2012

26. 1MMK, PDB DOI: https://doi.org/10.2210/pdb1MMK/pdb

27. P00439.PH4H HUMAN, Phenylalanine-4-hydroxylase, UniProtKB (Swiss-Prot)

28. H-K.S. Leiros, M.I. Flydal, A. Martinez, Structural and thermodynamic insight into phenylalanine hydroxylase from the human pathogen Legionella preumophila, FEBS, Open Bio. 2013, 3, 370-378, http://dx.doi.org/10.1016/08.006

29. E. R Werner, N. Blau, B. Thöny, Tetrahydrobiopterin: biochemistry and pathophysiology, Biochem J, 2011 Sep 15;438(3):397-414. doi: 10.1042/BJ20110293.

30. Okusaga, 6R-L-erythro-5,6,7,8-tetrahydrobiopterin (BH4): a potential treatment for all symptom domains of schizophrenia, Medical Hypotheses, 2014, 82(3), 395-397. DOI: 10.1016/j.mehy.2014.01.011

Chapter 11: Protein-Protein Interactions: SARS-CoV-2 Variants Transmissibility and the Binding Inhibitors

Since the first COVID-19 virus was identified in 2019, various mutants have been identified, and the total number of variants was over 200 in spring 2022, but the number has exploded, and it has become difficult to count the actual number of variants. Several mutants are defined as VOC (Variants of Concern) and VIC (Variants of Interest), and others are just listed [1]. Severe Acute Respiratory Syndrome Coronavirus 2 (SARS-CoV-2) (COVID-19) virus variant have spread and rapidly throughout the entire world [1,2]. We cannot clean all mutants and target mutants to keep our healthy society. Therefore, people focus their research on finding infection mechanisms and prevention methods.

Numerous sublineages emerged from the continued evolution of the SARS-CoV-2 Omicron variants with different patterns of evasion from neutralizing antibodies. Various facts were observed such as human leukocyte antigen (HLA) class 1 and 2 presented T-cell epitopes in the spiked-glycoproteins were highly concerned across the entire evolution of SARS-CoV-2 suggesting that CD8+ and CD4+ T-cell recognition of Omicron, BQ.1.1, BA.2.75.2 and XBB might be largely intact. It is considered that Omicron sublineages effectively evaded B-cell immunity by altering neutralizing antibody epitopes [3], and N-acetyl cysteine covalent conjugation perturbed the stereo-specific orientations of the interacting key residues of spike protein, resulting in a threefold weakening in the binding affinity of spike protein with the ACE-2 non-receptor [4]. Persistent SARS-CoV-2 RNA was detected in multiple anatomic sites throughout the brain [5]. SARS-CoV-2 non-structural protein was sufficient to confer resistance to Natural killer cell killing [6]. Coldspot-guided antibody discovery reveals donor-derived neutralizing antibodies that were cross-reactive with Orthocoronavirine, including SARS-CoV-2 variants [7]. T cell epitope mapping across the SARS-CoV-2 proteome would allow us to understand better the risks presented by emerging SARS-CoV-2 variants and the mechanisms that drove viral evolution [8]. Adding adjuvants or changes in doses and more mechanistic interventions might be implemented, such as IL-7 [9].

Various side effects of vaccination have been reported capillary leak syndrome [10] and vaccine-induced myocarditis [11]. Furthermore, free spike antigen was detected in the blood of adolescents and young adults who developed post-mRNA vaccine myocarditis [12]. Fragment crystallizable-mediated effector functions are critical for antiviral immunity; therefore, the choice and timing of vaccination regimens using mRNA vaccines against SARS-CoV-I2 because the induction of IgG4 antibodies was not observed after homologous or heterologous SARS-CoV-2 vaccination with adenoviral vectors [13]. Live vaccines induce positive non-specific effects, whereas non-live vaccines induce several negative nonspecific effects. The-specific effects of mRNA vaccines on overall mortality should be studied in depth [14]. Therefore, there was a proposal that we should stop trying to prevent all symptomatic infections in healthy young people by boosting them with vaccines containing mRNA from strains that might disappear a few months later [15].

The BA.2.86 variant appeared and the effectiveness of a new monovalent XBB.1.5. vaccine showed good levels of neutralizing antibodies [16]. Further details of variants have been explored EG.5.1 and BA.2.86 sub-variants exhibited attenuated replication in hamsters' lungs as compared to the BA.5 variant. The XBB sub-variants showed enhancing transmissibility and ability to escape the adaptive immune response. The infectivity of BA.2.86 and EG.1 sub-variants was high compared to the BA.5, and the infections virus titers in the lungs of EG.5.1- and BA.2.86-infected animals were significantly lower than the BA.5-infected ones. The lung pathology scores of animals infected with EG.5.1 and BA.2.86 were also markedly lower than that of the BA.5 sub-variant [17]. The relative reproduction number of BA.2.86 is significantly higher than that of EG.5.1. The fusogenicity of the BA.2.86 spike is similar to that of the parent BA.2 spike, the intrinsic pathogenicity of BA.2.86 in hamsters were significantly lower than that of BA.2, The growth kinetics of BA.2.86 are also significantly lower than that of BA.2 both *in vitro* and *in vivo*. The attenuation pathogenicity of BA.2.86 is likely due to its decreased replication capacity BA.2.86 was more transmissible than EG.5.1, even if the sensitivity of BA.2.86 to antiviral drugs was comparable to that of EG.5.1. The replication efficiency of BA.2.86 *in vitro* and *in vivo* was lower than that of EG.5.1 [18].

The mutation of COVID-19 occurred too rapidly and caused a pandemic environment is our social system, following this, the analysis of transmissibility and estimation of the multiplications was delayed. Preventing infection was an urgent issue. Quickly developed vaccines cannot inhibit the infection. The vaccines were considered to protect patients; however, they have presented different problems. Therefore, an effective way to use available medicines to treat patients has been performed.

Proteins exhibit selective molecular recognition. The strongest molecular interaction force is ion-ion interaction, a part of electrostatic interaction, following hydrogen bonding, then hydrophobic interaction. The quantitative explanation method of molecular interactions was achieved based on a reproducible experiment, liquid chromatography with the stable bonded phase silica gels developed. The selective molecular interaction mechanisms was first explained by enantiomer recognitions that required with steric hindrance, The fundamental method was first applied for quantitative analysis of enzyme reactivity and was furthermore applied for protein-protein interactions. The developed method has been used for quantitative analysis of COVID-19 transmissibility and designing binding inhibitors [19].

The three-dimensional structure of the SARS-CoV-2 and Angiotensin-Converting Enzyme 2 (ACE-2) complex was determined and the binding site of SARS-CoV-2 with ACE-2 was clarified [20]. Increasing number of basic amino acids by mutation as the Spiked Protein Receptor Binding Domain (S-RBD) binding site enhanced the binding strength supported by increases in molecular interaction (ion-ion interaction) energy values calculated using an MM2 program between S-RBD and ACE-2 proteins [19]. Once the binding strength reaches the maximum by Omicron BA.2 developing vaccines and medicines do not protect against the infection but have scattered the infection even through the calculated binding strength of new variants weakened [21]. Variant XBB is becoming a major variant; therefore, the quantitative analysis of the binding strength was a great subject for studying the protein-protein interactions.

The conformation of the COVID-19 S-RBD and ACE-2 was identified [22]. Therefore, the inhibition compounds can be estimated from their structure's properties. The early-stage mutated S-RBD especially enhanced the binding affinity with ACE-2 by replacing acidic and neutral amino acids with basic amino acids. In addition, acidic amino acids are lined up at the binding site of ACE-2. These structures indicate that acid-base interaction enhanced the binding affinity. A fundamental study of the ion-ion interaction between acidic amino acids and other amino acids exhibited their binding strength difference. The simplest analysis does not include the steric hindrance of the protein's surface structures. The direct protein-protein interaction strength was quantitatively analyzed using a molecular mechanics program.

The binding of SARS-CoV-2 with ACE-2 causes more severe infection than influenza. The three-dimensional structures of SARS-CoV and SARS-CoV-2 are similar, and the ACE-2 binding mode of the SARS-CoV-2 S-RBD is nearly identical to that of the SARS-CoV RBD [22]; however, the external fusion proteins of influenza virus (SARS-CoV) are relatively rigid, and those of SARS-CoV-2 are widely flexible [23]. Comparison of amino acid sequences of bat-CoV, SARS-CoV, and SARS-CoV-2 determine the impact of the mutation and loopsd in RBD of SARS-CoV and SARS-CoV-2 are required in order to predict a possible zoonotic event in the future [24]. Furthermore, the family tree of SARS-CoV-2 was determined and predicted new variants [25-27], and the newly developed analytical method was applied for quantitative *in silico* quantitative analysis of the SARS-CoV-2 S-RBD mutant's binding affinity with ACE-2. The transmissibility can be analyzed based on the molecular structure of SARS-CoV-2 mutants. A computational chemical analysis of the molecular interaction of model compounds was performed to consider the binding site of amino acids of SARS-CoV-2 and ACE-2 [28].

The infection degree (transmissibility) is a combination of binding strength and virus multiplication. The calculated molecular interaction energy values indicated the binding strength. However, the energy values do not directly indicate the transmissibility of COVID-19 mutants. Our immune system can protect us from invaders and destroy viruses, but it cannot protect from an overwhelming number of viruses like a classic human battle, and our immune system has no specific against mass-attached viruses, Therefore, we need medicines to help our immune system. We can consider two types of medicines against COVID-19 infection, One is binding inhibitors, and another is multiplication inhibitors. The design of the binding inhibitors is relatively simple, but that of the multiplication is difficult due to finding the binding affinity location. The ideal medicine should have capability of both inhibit binding and multiplication.

11.1. Structure of COVID-19 S-RBD Mutants

The downloaded three-dimensional structure of SARS-CoV-2 with ACE-2 complex (RSC PDB:7mjk) indicates that the binding site of ACE-2 contains many acidic amino acids [29]. Figure 11.1 shows the downloaded COVID-19 protein 7mjk structure, which consists of a complex with saccharides. Figures 11.2 and 3 show one extracted molecule without adsorbed saccharides with the location of mutated amino acids indicated using 0.5Å atom size amino acids. The missing several amino acid residues are between L176 and Q185, V620, and N641, Q675 and S691, and T827 and N856. The location of mutated amino acids in S-RBD is shown in Figure 11.4. The ACE-2 binding site with the SD-RBD is indicated as ACE-2. The ACE-2 protein structure in Figures 11.5 and 6 where many acidic amino acids are lined up at the contact site with S-RBD, and these acidic amino acids are indicated as 0.5A atoms for the identification.

FIgure 11.1: Doiwnloaded protein complex 7mjk.

FIgure 11.2: Extracted one pair of complex.

FIgure 11.3: Key residual amino acids.

FIgure 11.4: S-RBD binding site amino acids.

FIgure 11.5: Structure of ACE-2 protein 7mjk.

FIgure 11.6: ACE-2 S-RBD binding site amino acids.

Mutations in the SARS-CoV-2 protein occurred rapidly, and over 200 mutants have been identified in three years. Several mutant structures of S-RBD (N331-K529) are shown in Figure 11.7. Mutated amino acids are indicated using large atom sizes. Mutants with high transmissibility replaced the acidic and neutral amino acids with basic amino acids. The reason for their transmissibility is clear from the previous demonstration. Analyzing ion-ion interactions using simple ion-exchange groups demonstrated the high electrostatic energy values between a cation and an anion interaction. The strong ion-ion interaction was the primary force that the proteins recognize a substrate for the selective enzyme reactions.

The S-RBD mutant amino acids of Beta and Gamma are the same; those of Eta, Iota, and Zeta, and those of Epsilon and another Iota are the same; therefore, these individual structures are not given. Considering the contact site mutated amino acids, the existence of basic amino acids enhanced their transmissible strength. The mutated amino acids are summarized in Table 11.1. The transmissibility strength was first analyzed based on the molecular interaction energy values between two amino acids for the simplest study. Omicron XD, XE, and F are hybrid Delta with Omicron BA.1, BA.2, and BA.3 are considered to cause severe infection, Both omicron BA.1 and BA.2 include T478K mutation but not the L452R mutation. Increasing numbers of basic amino acids increases the risk of severe illness.

Table 11.1: Mutated amino acids of SARS-CoV-2 S-RBD mutants.

WHO name	Linkage plus	Mutated amino acids .
WT		N501
Alpha	B.1.1.7	N501Y
Alpha plus	B.1.1.7+	E484K N501N, E484K*1
Beta	B-1.351	N417K, E484K, N-501Y
Delta	B.1.517.2	L452R, T478K
Delta plus	AY.1	K417N, L452R, T478K
Epsilon	B.1.427/B.1.429	L452R
Eta	B.1.525	E484K

Gamma	P.1	K417N, E484K, N501Y
Gamma	P.1	K417N, E484K, N501Y*2
Iota	B.1.526	E484k, (Eta B.1.525)
Iota	B.1.526.1	L452R
Kappa	B.1.617.1	L452R, E484Q
Kappa	B.1.620	S477N, E484K
Lambda	C37	L452Q, F490S
Mu	B.1.621	R346K, E484K, N501Y
Theta	P.3	E484K, N501Y, (Alpha B.1.7 + E484K)
Theta	B.1.616	V483A
Zeta	P.2	E484K, (Eta B.1.525)
Omicron	BA1	G339D, S371L, S373P, S375F, K417N, N440K, G446S, S477N, T478K,
		E484A, Q493R, G496S, Q498R, N501Y, Y505H,
Omicron	BA2	G339D, S371F, S373P, S375F, T376A, D405N, R408S, K417N, N440K,
		S477N, T478K, E484A, Q493R, Q498R, N501Y, Y505H,
Omicron	B.2.75	D339H, G446S, N460K, Q493R
Omicron	BA.4/5	L452R, F486V, Q493R
Omicron	BQ.1	K444T, N460K
Omicron	BQ.1.1	R346T, K444T, N460K
Omicron	XBB	R346T, V445P, G446S, N460K, F486S, F490S, Q493R
Omicron	XBB.1.5	F456L,N460K, F486P, F490S
Omicron	XBB.1.16	T478R, F486P
Omicron	FE.1	F456L, F486P, F490S
Omicron	EG.5	F456L, N460K, S486P, FS490S
Omicron	BA.2.86	I332V, D339H, R403K, V445H, G446S, N450F, L452W, N481K,483del, E484K, F486P
Omicron	BA.2.87.1	G339D, S371F, S373P, S376F, T376A, D405N, R408S,K417T, N471K,
		E484A, Q498R, N501Y, Y506H
Omicron	HV.1	R346T, L368I, T376A, D405N, K417N, N440K, V445P, G446S, L452R,
		V460K, S477N, T478K, E484A, F486P, F490S, Q493R, N501Y, Y505H
Omicron	JN.1	T332V, K356T, T376A, R403K, D405N, K417N, N440K, V445H,
		G446S, N450D, L452W, L455S, V460K, S477N, T478K, N481K, 483V,
		E484A, F486P, F490P, Q493R, N501Y, Y505H
Omicron	JN.1.17	T332V, K356T, T376A, R403K, D405N, K417N, N440K, V445H,
		G446S, N450D, L452W, L455S, V460K, S477N, T478K, N481K, 483V,
		E484A, F486P, F490P, Q493R, N501Y, Y505H, T572I
Omicron	JN.1.18	T332V, R346T, K356T, T376A, R403K, D405N, K417N, N440K,
		V445H, G446S, N450D, L452W, L455S, V460K, S477N, T478K, N481K,
		483V, E484A, F486P, F490P, Q493R, N501Y, Y505H,
Omicron	KP.2	T332V, K356T, R346T, T376A, R403K, D405N, K417N, N440K,
		V445H, G446S, N450D, L452W, L455S, F456L, V460K, S477N, T478K,
		N481K, 483V, E484A, F486P, F490P, Q493R, N501Y, Y505H, T572I
Omicron	KP.3	T332V, K356T, T376A, R403K, D405N, K417N, N440K, V445H,
		G446S, N450D, L452W, L455S, F456L, V460K, S477N, T478K, N481K,
		483V, E484A, F486P, F490P, Q493E, N501Y, Y505H, T572I-

FIgure 11.7: Structure of mutated COVIS-19 S-RBD.

FIgure 11.7: Structure of mutated COVIS-19 S-RBD.

Figure 11.7: Structure of mutated COVIS-19 S-RBD.

11.2. Fast Analysis of Transmissibility by Binding Strength between Two Amino Acids

SARS-CoV-2 tyrosine 501 (Y501), converted from N501, contacts the Y41 of ACE-2. However, the 449th, 453th, 489th, and 505th amino acids of SARS-CoV-2 are also tyrosine. On the other hand, many acidic amino acids are present at the contact site of ACE-2. Aspartic acid (Asp, D) is located on the 30th, 38th, and 355th, and glutamic acid (Glu, E) is located on the 23rd, 34th, and 329th. Other amino acids include Y41, R357, R393, K31, and K353. Therefore, a simple binding analysis was carried out. A selected amino acid in ACE-2 was glutamic acid (Glu, E). The corresponding amino acids of SARS-CoV-2 were amino acids reported in the mutants.

The Delta mutant, whose neutral amino acids are replaced with basic amino acids, exhibits very strong transmissibility. The basic amino acids of the Delta mutant bind strongly with the acidic amino acids of ACE-2 based on ion-ion interactions, and binding (transmissibility) strength is related to molecular interaction strength. Therefore, a one-to-one interaction of SARS-CoV-2 SRBD and ACE-2 amino acids was calculated as a simple model interaction. Some model interactions are shown in Figure 11.8, where A and B indicate the initial conformation and the optimized complex structure.

Figure 11.8: The molecular interaction between two amino acids. Yellow (light gray), red (black), blue (dark gray), and white balls: carbon, oxygen, nitrogen, and hydrogen.

The molecular interaction (MI) energy (kcal·mol-1) between Glu and an amino acid on the surface of SARS-CoV-2 was calculated using the same approach as that used for the MI energy calculation represented in chromatographic molecular interaction mechanisms [30]. The MI energy value of the final (optimized) structure is the sum of the energies of the individual molecules (one example: glutamic acid (Glu) and Alanine (Ala) minus that of the complex (Glu + Ala). The calculated MI energy values are presented in Table 11.2, where MIFS, MIHB, MIES, and MIVW are the MI energy values of the optimized structure, hydrogen bonding, electrostatic interactions, and van der Waals interactions, respectively. The MIHB, MIES, and MIVW indicate specific contributions to the interactions.

Table 11.2: Molecular interaction energy values between two amino acids kcal·mol^{-1}.

Amino acid	MIFS	MIHB	MIES	MIVW	Amino acid	MIFS	MIHB	MIES	MIVW
Glu + Ala (A)	10.48	0.07	11.35	-0.92	Glu + Pro (P)	5.32	-0.004	5	0.53
Glu + Arg (E)	84.05	25.29	64.31	-3.3	Glu + Thr (T)	25.17	9.29	16.69	0.08
Glu + Asn (N)	33.56	18.74	16.47	-2.17	Glu + Tyr (Y)	24.75	9.85	20.04	-0.26
Glu + Asp*(D)	-5.05	-0.05	-5.09	0.01	Glu + Phe (F)	12.61	0.07	9.41	2.91
Glu + Glu*(E)	-5.73	0.02	-5.75	-0.01	Glu + Ser (S)	22.53	9.68	14.34	-0.57
Glu + Gln (Q)	31.27	17.19	16.49	-2.4	Glu + Val (V)	13.26	0.28	13.97	-0.54
Glu + Gly (G)	16.41	-0.11	15.5	-1.06					
Glu + His (H)	21.2	4.3	17.04	0.25	Tyr + Asn (N)	-27.71	-14.69	-13.24	5.56
Glu + Leu (L)	8.16	0.11	7.15	1.06	Lys + Asn (N)	43.92	27.77	20.73	-4.65
Glu + Lys (K)	142.03	33.8	120.21	-8.67	Lys + Tyr (Y)	31.38	28.95	5.17	-3.52

MIFS, MIHB, MIES, MIVW: Molecular interaction energy values of final structure (FS), hydrogen bonding (HB), electrostatic interaction (ES), and van der Waals force (VW). *Repulsion, no MI energy. Unit: kcal·mol^{-1}.

The MI energy change by mutation was calculated using the above individual interaction energy values between two amino acids. The calculation was performed using only contact site amino acids to ACE-2. One example: MIFS energy y of a mutation from arginine (E) to lysine (K) is Glu+Lys (142.03) minus Glu+Arg (84.05) making 57.98 kcal mol^{-1}. The energy balance of other mutations for MIFS, MIHB, MIES, and MIVW are given the following equations.

MIFS energy values of mutation (kcal mol^{-1})

FS (D339H) = 21.20 - (-5.05) = 26.25

FS (R346K) = 142.03 - 84.05 = 57.98

FS (R346T) = 25.17 – 84.05 = -58.88

FS (K417N) = 33.56 – 142.03 = -108.67

MIHB energy values of mutation (kcal mol^{-1})

HB (D339H) = 4.30 - (-0.05) = 4.35

HB (R346K) = 33.80 - 25.29 = 8.51

HB (R346T) = 9.29 – 25.29 = -16.00

HB(K417N) = 18.74- 33.80= -15.06

FS (K444T) = 250.17 01420.03 =- -116.86
FS (V445P) = 5.32 -13.26 = -7.94
FS (G446S) = 22.53 – 16.21 = 6.32
FS (L452R) = 870.05 – 8.16 = 78.89
FS (F456L) = 8.16 – 12.61 = -4.45
FS (N460K) = 1420.03 - 33.56= 108.47
FS (S477N) = 33.56 – 22.53= 11.03
FS (T478K) = 142.03 – 25.17 = 116.86
FS (T478R) = 84.05 – 25.17 = 58.88
FS (V483A) = 10.48 – 13.26 = -2.78
FS (E484K) = 1420.03 – 0.00 = 1420.03
FS (E484Q) = 31.27 - 0.00 = 31.27
FS (E484A) = 10.48 - 0.00= 10.48
FS (F486P) = 5.32 – 12.61 = -7.29
FS (F486V) = 13.26 – 12.61 = 0.65
FS (F490S) = 22.53 – 12.61 = 9.92
FS (Q493R) = 84.05 – 31.27 = 52.78
FS (G496S) = 220.53 – 16.21 = 6.32
FS (N501Y) = 24.75 – 33.56 = -8.81

HB (K444T) = 9.29 – 33.80 = -24.51
HB (V445P) = -0.004 – 0.28 = -0.284
HB (G446S) = 9.67 - (-0.11) = 9.79
HB (L452R) = 25.29 – 0.11 = 25.18
HB (F456L) = 0.11 – 0.07 = 0.04
HB (N460K) = 33.80 – 18.74 = 15.06
HB (S477N) = 18.74 – 9.68 = 9.06
HB (T478K) = 33.80 - 9.29 – 24.51
HB (T478B) = 25.29 – 9.29 = 16.00
HB (V483A) = 0.07 – 0.28 = -0.21
HB (E484A) = 33.80 – 0.00 = 33.80
HB (E484Q) = 17.19 – 0.00 = 17.19
HB (E484A) = 0.07 – 0.00 = 0.07
HB (F486P) = -0.004 – 0.07 = -0.074
HB (F486V) = 0.28 – 0.07 = 0.21
HB (F490S) = 9.68 - 0.07 = 9.61
HB (Q493R) = 25.29 - 17.19 = 8.10
HB (G496S) = 9.68 – (-0.11) = 9.79
HB (N501Y) = 9.85 – 17.74 = -7.89

MIES energy values of mutation (kcal mol^{-1})

ES (D339H) = 17.04 – (-5.09) = 22.13
ES (R346K) = 120.21 – 64.31 = 55.90
ES (R346T) = 16.69 – 64.31 = -47.62
ES (K417N) = 16.47 -120.21 = -103.72
`ES (K444T) = 16.69 – 120.21 = 103.52
ES (V445P) = 13.97 – 5.40 = 8.57
ES (G446S) = 14.34 -15.50 = 1.16
ES (L452R) = 64.31- 7.15 = 57.16
ES (L452Q) = 16.49 – 7.15 = 9.34
ES (F456L) = 7.15 – 9.41 = 2.26
ES (N460K) = 120.21 – 16.47 = 103.74
ES (S477N) = 16.47 – 14.34 = 2.13

MIVW energy values of mutation (kcal mol^{-1})

VW (D339H) = 0.25 – 0.01 = 0.24
VW (R346K) = -8.67 – (-3.30) = -5.37
VW (R346T) = 0.08 – (-3.30) = 3.37
VW (K417N) = -2.17 –(-8.67) = 6.50
VW (K444T) = 0.08 –(8.67) = 8.75
VW (V445P) = 0.53 –(-0.54) = 1.07
VW (G446S) = -0.57 –(-1.06) = 0.49
VW (L452R) = -3.30 – 1.06 = -2.24
VW (F456Q) = -2.40 -1.06 = -3.46
VW (F456L) = 1.06 – 2.91 = -1.85
VW (N460K) = -8.67 –(-2.17) = -6.50
VW (S477N) = -2.17 – (-0.57) = -1.60

ES (T478K) = 120.21 – 16.69 = 103.52 VW (T478K) = -8.67 – 0.08 = -8.59

ES (T478R) = 64.31 -16.69 = 47.62 VW (T478R) = -3.30 – (-8.67) = 5.37

ES (V483A) = 11.35 – 13.97 = -2.62 VW (V483A) = -0.92 – (-0.54) = -0.38

ES (E484K) = 120.21 – 0.00 = 120.21 VW (E484K) = -8.67 – 0.00 = -8.67

ES (E484Q) = 16.49 – 0.00 = 16.49 VW (E484Q) = -2.40 – 0.00 = -2.40

ES (E484A) = 11.35 – 0.00 = 11.35 VW (E484A) = -0.92 – 0.00 = -0.92

ES (F486P) = 5.40 – 9.41 = 4.01 VW (F486P) = 0.53 – 2.941 = -2.38

ES (F486V) = 13.97 – 9.41 = 4.56 VW (F486V) = -0.54 -2.91 = -3.45

ES (F490S) = 14.34 – 9.41 = 4.93 VW (F490S) = -0.57 – 2.91 = -3.48

ES (Q493R) = 64.31 – 16.49 = 47.82 VW (Q493R) = -3.30 –(-2.40) = -0.90

ES (G496S) = 14.34 -15.50 = -1.16 VW (G496S) = -0.57 –(-1.06) = 0.49

ES (N501Y) = 20.04 – 16.47 = 3.57 VW (N501Y) = -0.26 –(-2.17) = 1.91

The variant's MI energy values were calculated as the sum of mutated amino acids using the data listed in Table 10.2, and the processes were achieved using the following equations.

For example:

WT (N501) = Glu + Asn (N) = 33.56

Alpha (N501Y) = (Glu + Tyr(Y)) – (Gln + Asn (N)) = 24.75 – 33.56 = -8.81 kcal mol^{-1}

Delta has two mutation sites, L452R and T478K, have been reported. The calculation of the MI energy change of L452R and T478K is as follows.

For MIFS: L452R = (Glu + Arg) – (Glu + Leu) = 84.005 – 8.16 = 75.89

T478K = (Glu + Lys) – (Glu + The) = 142003 – 25.17 = 116.86

Therefore, L452R + T478K = 75.89 + 116.86 = 192.75 for the Delta mutant. However, E484 is considered a reversed constant where S-RBD glutamic acid comes into contact with ACE-2 R357. The MI energy values of other mutants are listed in Table 11.3.

MIFS energy values of mutants (kcal mol^{-1})

WT (N501) = 33.56

Alpha (N501Y) = -8.81

Alpha + E484K (E484K + N501Y) = 142.03 – 8.81 = 133.22

Beta (K417N + E484K + N501Y) = -108.47 + 142.03 – 8.81 = 24.75

Gamma, P.1 (K417N + E484K + N501Y) = -108.67 + 142.003 – 8.81 = 24.75

Delta (L452R + T478K) = 78.89 + 116.86 = 195.75

Delta plus (K417N + L452R + T478K) = 108.67 + 78.89 - 116.86 = 87.08

Epsilon = (L452R) = 78.89

Eta (E484K) = 142.03

Iota B.1.526 (E484K) = 142.03

Iota B.1.526.1 (L452R) = 78.89

Kappa B.1.617.1 (L452R + E484Q) = 78.89 + 31.27 = 110.16

Kappa B.1.620 (S477N + E484K) = 11.03 + 31.27 = 42.30

Kappa B.1.621 (E484K + N501Y) = 142.03 – 8.81 = 133.22

Lambda (L452Q + F490S) = 23.11 + 9.92 = 33.03

Mu (E484K + N501Y) = 142.03 - 8.81 = 133.22

Theta P.3 (E484K + N501Y) = 142.03 – 8.81 = 133.22

Theta B.1.616 (V483A) = -2.78

Zeta (E484K) = 142.03

Omicron BA.1 (G446S + T478K + E484A+ Q493R + G496S + Q498R + N501Y) = 6.32 + 116.86 + 10.48 + 52.78 + 6.32 + 52.78 – 8.81 = 236.76

Omicron BA.2 (T478K + E484A + Q493R + Q498R + N501Y) = 16.86 + 52.78 + 52.78 – 8.81 = 224.47

Omicron B.2.75 (D339H + G446S + N460K + Q493R) = 26.25 + 6.32 + 108.47 + 52.78 = 193.82

Omicron BA.4/5 (L452R + F486V + Q493R) = 78.89 + 0.65 + 52.78 = 132.32

Omicron BQ.1 (K444T + N460K) = -16.86 + 108.47 = -8.39

Omicron BQ.1.1 (R346T + K444T + N460K) = 57.788 – 116.86 + 108.47 = 49.59

Omicron XBB (R346T + V445P + G446S + N460K + F486P + F490S + Q493R = -58.88 – 7.94 + 6.32 + 108.47 – 7.29 + 9.92 + 52.78 = 103.38

Omicron XBB.1.5 (N460K + F486P + F490S) = 108.47 – 7.29 + 9.92 = 111.1

Omicron XBB.1.16 (T478R + F486P) = 58.88 – 7.29 = 51.59

Omicron FE.1 (F456L + F486P + F490S) = -4.45 – 7.29 + 9.92 = -1.82

MIHB energy values of mutants (kcal mol^{-1})

WT (N501) = 18.74

Alpha (N501Y) = -8.89

Alpha + E484K (E484K + N501Y) = 33.80 – 8.89 = 24.91

Beta (K417N + E484K + N501Y) = -15.06 + 33.80 – 8.89 = 9.85

Gamma, P.1 (K417N + E484K + N501Y) = -15.16 + 33.80 -8.89 = 9.85

Delta (L452R + T478K) = 25.18 24.51 = 49.69

Delta plus (K417N + L452R + T478K) = -15.06 + 25.18 + 24.51 = 34.63

Epsilon = (L452R) = 25.18

Eta (E484K) = 33.80

Iota B.1.526 (E484K) = 33.80

Iota B.1.526.1 (L452R) = 25.18

Kappa B.1.617.1 (L452R + E484Q) = 25.18 + 17.19 = 42.37

Kappa B.1.620 (S477N + E484K) = 9.06 + 33.80 = 42.86

Kappa B.1.621 (E484K + N501Y) = 33.80 – 8.89 = 24.91

Lambda (L452Q + F490S) = 17.08 + 9.61 = 26.69

Mu (E484K + N501Y) = 33.80 – 8.89 = 24.91

Theta P.3 (E484K + N501Y) = 33.80 – 8.89 = 24.91

Theta B.1.616 (V483A) = -0.21

Zeta (E484K) = 33.80

Omicron BA.1 (G446S + T478K + E484A+ Q493R + G496S + Q498R + N501Y) = 9.79 + 24.51 + 0.07 + 8.10 +9.79 + 8.10 – 8.89 = 51.47

Omicron BA.2 (T478K + E484A + Q493R + Q498R + N501Y) = 24.51 + 0.07 +8.10 + 8.10 – 8.89 = 31.89

Omicron B.2.75 (D339H + G446S + N460K + Q493R) = 4.35 + 9.79 + 15.06 + 8.1 = 37.3

Omicron BA.4/5 (L452R + F486V + Q493R) = 25.18 + 0.21 + 8.1 = 33.49

Omicron BQ.1 (K444T + N460K) = -24.51 + 15.6 = -8.91

Omicron BQ.1.1 (R346T + K444T + N460K) = 16.0 - 24.51 + 15.06 = 6.55

Omicron XBB (R346T + V445P + G446S + N460K + F486P + F490S + Q493R = 16.00 – 0.284 + .79 + 15.06 – 0.074 + 9.61 + 8.1 = 58.202

Omicron XBB.1.5 (N460K + F486P + F490S) = 15.06 – 0.074 + 9.61 = 24.596

Omicron XBB.1.16 (T478R + F486P) = 16.0 - 0.074 = 15.926

Omicron FE.1 (F456L + F486P + F490S) = 0.04 – 0.074 + 9.61 = 9.496

MIES energy values of mutants (kcal mol^{-1})

WT (N501) = 16.47

Alpha (N501Y) = 3.57

Alpha + E484K (E484K + N501Y) = 120.21 + 3.57 = 123.78

Beta (K417N + E484K + N501Y) = -103.72 + 120.21 + 3.57 = 20.06

Gamma, P.1 (K417N + E484K + N501Y) = -103.72 + 120.21 + 3.57 = 20.06

Delta (L452R + T478K) = 57.16 + 103.52 = 160.68

Delta plus (K417N + L452R + T478K) = -103.72 + 57.16 + 103.52 = 56.96

Epsilon = (L452R) = 57.16

Eta (E484K) = 120.21

Iota B.1.526 (E484K) = 120.21

Iota B.1.526.1 (L452R) = 57.16

Kappa B.1.617.1 (L452R + E484Q) = 57.16 + 16.49 = 73.65

Kappa B.1.620 (S477N + E484K) = 2.13 + 120.31 = 122.34

Kappa B.1.621 (E484K + N501Y) = 120.21 + 3.57 = 123.78

Lambda (L452Q + F490S) = 9.34 + 4.93 = 14.27

Mu (E484K + N501Y) = 120.21 + 3.57 = 123.78

Theta P.3 (E484K + N501Y) = 120.21 + 3.57 = 123.78

Theta B.1.616 (V483A) = -2.62

Zeta (E484K) = 120.21

Omicron BA.1 (G446S + T478K + E484A+ Q493R + G496S + Q498R + N501Y) = 1.16 +103.52 + 11.354 + 47.82 – 1.16 + 47.82 + 3.57 = 210.51

Omicron BA.2 (T478K + E484A + Q493R + Q498R + N501Y) = 103.52 + 11.35 + 47.82 + 47.82 + 3.57 = 214.08

Omicron B.2.75 (D339H + G446S + N460K + Q493R) = 22.13 + 1.16 +103.74 + 47.82 = 175.85

Omicron BA.4/5 (L452R + F486V + Q493R) = 57.16 + 4.56 + 47.82 = 109.54

Omicron BQ.1 (K444T + N460K) = -103.52 + 103.74 = 0.22

Omicron BQ.1.1 (R346T + K444T + N460K) = -47.62 – 103.52 + 103.74 = -47.5

Omicron XBB (R346T + V445P + G446S + N460K + F486P + F490S + Q493R = -47.62 + 8.57 + 1.16 + 103.74 + 4.01 + 4.93 +47.82 = 122.61

Omicron XBB.1.5 (N460K + F486P + F490S) = 103.74 + 4.01 + 4.93 = 112.68

Omicron XBB.1.16 (T478R + F486P) = 47.62 + 4.01 = 51.63

Omicron FE.1 (F456L + F486P + F490S) = 2.26 + 4.01 + 4.93 = 11.2

MIVW energy values of mutants (kcal mol^{-1})

WT (N501) = -2.17

Alpha (N501Y) = 1.91

Alpha + E484K (E484K + N501Y) = -8.67 + 1.91 = -6.76

Beta (K417N + E484K + N501Y) = 6.50 – 8.67 + 1.91 = 0.26

Gamma, P.1 (K417N + E484K + N501Y) = 6.50 – 8.67 + 1.91 = 0.26

Delta (L452R + T478K) = -2.24 – 8.59 = -10.83

Delta plus (K417N + L452R + T478K) = 6.50 – 2.24 – 8.59 = -4.33

Epsilon = (L452R) = -2.24

Eta (E484K) = -8.67

Iota B.1.526 (E484K) = -8.67

Iota B.1.526.1 (L452R) = -2.24

Kappa B.1.617.1 (L452R + E484Q) = -2.24 – 2.40 = -4.64

Kappa B.1.620 (S477N + E484K) = -1.60 – 8.67 -10.27

Kappa B.1.621 (E484K + N501Y) = -8.67 + 1.91 = -6.76

Lambda (L452Q + F490S) = -3.46 – 3.48 = -6.76

Mu (E484K + N501Y) = -8.67 + 1.91 = -6.76

Theta P.3 (E484K + N501Y) = -8.67 + 1.91 = -6.76

Theta B.1.616 (V483A) = -0.92

Zeta (E484K) = -8.67

Omicron BA.1 (G446S + T478K + E484A+ Q493R + G496S + Q498R + N501Y) = 0.49 – 8.59 – 0.92 + 0.49 – 0.90 + 1.91 = -8.42

Omicron BA.2 (T478K + E484A + Q493R + Q498R + N501Y) = -8.59 – 0.92 – 0.90 – 0.90 + 1.91 = -9.40

Omicron B.2.75 (D339H + G446S + N460K + Q493R) = 0.24 + 0.49 – 6.50 -0.90 = -6.67

Omicron BA.4/5 (L452R + F486V + Q493R) = -2.24 – 3.45 – 0.90 = -6.69

Omicron BQ.1 (K444T + N460K) = 8.75 – 6.50 = 2.25

Omicron BQ.1.1 (R346T + K444T + N460K) = 3.37 + 8.75 – 6.5 = 5.62

Omicron XBB (R346T + V445P + G446S + N460K + F486P + F490S + Q493R = 3.37 + 1.07 + 0.49 – 6.50 – 2.38 - 3.48 – 0.90 = -8.33

Omicron XBB.1.5 (N460K + F486P + F490S) = -6.50 – 2.38 – 3.48 = -12.36

Omicron XBB.1.16 (T478R + F486P) = -8.59 – 2.38 = -10.97

Omicron FE.1 (F456L + F486P + F490S) = -1.85 – 2.38 – 3.48 = -7.71

These simple analyses clearly explain the binding mechanisms and demonstrate the significant contribution of electrostatic interaction; the supporting contribution of hydrogen bonding and van der Waals force did not affect the interaction. The mutation of lysine especially enhances the transmissibility. Arginine also enhances the binding. Some mutants changed one amino acid, and others changed multi-le amino acids of S-RBD proteins. The contribution of MI energy values of mutants was calculated between ACE-2 glutamic acid and S-RBD mutant's contacted amino acids, and the results are summarized in Table 11.3

Table 11.3: Molecular interaction energy values between ACE-2 and SARS-CoV-2 mutants.

Mutant Mutated amino acids	MIFS	MIHB	MIES	MIVW
WT N501	33.56	18.74	16.47	-2.17
WT N501#1	-27.71	-14.69	-13.24	5.56
Alpha N501Y	8.81	8.9	-3.58	-1.91
Alpha N501Y#2	52.57	36.29	14.85	-6.93
Beta, Gamma K417N, E*484K, N501Y	33.56	18.74	16.47	-2.17
Beta, Gama K417N, E*484K, N501Y#2	86.13	55.03	31.32	-9.1
Lambda L452Q, F490S	35.32	28.25	14.25	-6.72
Delta-plus K417N, L452R, T478K	84.28	34.6	56.94	-11.61
Delta L452R, T478K	192.75	49.65	160.69	-5.11
Mu R346K, E484K, N501Y	109.44	9.68	115.35	-8.6
Theta E484K, N501Y	51.46	1.17	59.45	-3.23
Kappa (B.1.617.1) L452R, E484Q	126.38	31.73	100	-5.49

Kappa (B.1.621) R346K, E484K, N501Y	109.44	9.68	115.35	-8.6
Lambda	33.03	26.69	14.27	-6.94
Mu	133.22	24.91	123.78	-6.76
Theta P.3	133.22	24.91	123.78	-6.76
Theta B!.616	-2.78	-0.21	-2.62	-0.92
Zeta	142.03	33.8	120.21	-8.67
Omicron BA.1	236.76	51.47	210.51	-8.42
Omicron BA.2	224.47	31.89	214.08	-9.4
Omicron BA.2.75	193.82	37.3	145.85	-6.67
Omicron BA. ¾	132.32	33.49	109.54	-6.59
Omicron BQ.1	-8.39	-8.91	0.22	2.25
Omicron BQ.1.1	49.59	6.55	-47.5	5.62
Omicron XBB	103.38	58.2	122.61	-8.33
Omicron XBB.1.5	111.1	24.6	112.68	-12.36
Omicron XBB.1.16	51.59	15.93	51.63	-10.97
Omicron FE.1	-1.82	9.5	11.2	-7.71

*Glu + Glu (E) is repulsed; therefore, MI values were considered zero for the calculation. #1Tyrosine of N501Y contacts with ACE-2 Y41. #2Tyrosine of N501Y contacts with ACE-2 K353. Unit: kcal·mol^{-1}

These MI energy values were calculated for the amino acids of SARS-CoV-2 in contact with ACE-2 glutamic acid. The order of the MIFS energy value of the mutants was Omicron BQ.1, Omicron BQ 1.1, Omicron 1.16, Alpha < Theta B.1.616 < Beta, Gamma < Lambda < WT (wild type) < Kappa B.1.620 < Epsilon, Iota B.1.526.1 < Delta plus < Kappa B.1.617.1, Omicron FE.1 < Alpha + E484K, Kappa B.1.621, Omicron BA.4, Mu, Omicron XBB.1.5, Theta P.3 < Eta, Iota B.1.526, Zeta < Delta < Omicron BA.2.75 < Omicron BA.2 < Omicron BA.1. Ion–ion interaction is the strongest interaction force, and the strength can be obtained as a large MIES value. The amides exhibited relatively strong hydrogen bonding. This simple approach can provide the strength of a mutant's transmissibility. The Alpha-MIFS value was smaller than that of WT, and the transmissibility, based on the calculation, seemed weaker than that of the wild type. The reference three-dimensional structure indicated that SARS-CoV-2 Y501 did not have head-to-head contact with ACE-2 Y41 and contacted the peptide bond nitrogen. However, SARS-CoV-2 N501 only contacted ACE-2 Y41, while SARS-CoV-2 Y501 contacted ACE-2 Y41 and K353. This mutation improved the contact site. Therefore, the MI energy was recalculated between ACE-2 Y41 and SARS-CoV-2 N501 and between ACE-2 K353 and SARS-CoV-2 Y501. The calculated MI energy values of the WT MIFS was a minus value (-27.71 kcal·mol^{-1}), and N501Y showed a positive value (52.27 kcal·mol^{-1}). This simple calculation provided the possible transmissibility of variants but did not include steric hindrance.

Actual protein-protein interactions should include steric hindrance at the contact site; therefore, the direct interaction between SARS-CoV-2 was quantitatively analyzed to determine the transmissibility using a method used for the quantitative analysis of enzyme reactivity [31]. Figure 11.9 shows the binding conformation of wild type S-RBD and ACE-2. The circled part of ACE-2 of the original conformation was removed to reduce the calculation hour. The calculation hour of the original conformation and the reduced size conformation was six hours30 minutes and one hour 30 minutes, respectively. This calculation used the S-RBD of SARSD-CoV-2 and two contact site peptides of ACE-2 (S-19 – S105 and E-329 – N394). However, the four end amino acids of the selected ACE-2 peptides were locked to maintain their three-dimensional structure. This modification was applied based on the calculation capability of a desktop computer. The calculated MI energy values are presented in Table 11.4.

Figure 11.9: The molecular interaction between two amino acids. Yellow (light gray), red (black), blue (dark gray), and white balls: carbon, oxygen, nitrogen, and hydrogen.

Table 11.4: Molecular interaction energy values between SARS-CoV-2 mutants and ACE-2.

Mutant	MIFS	MIHB	MIES	MIVW
WT	346.0675	284.725	186.499	-58.491
Alpha B.1.1.7	320.9545	233.255	155.734	-41.626
Alpha + E484K	442.3393	218.879	246.999	-4.801
Beta B .1.351	515.7918	340.56	302.832	-41.978
Gamma P.1		#NAME?		
Delta B.1.517.2	594.1785	321.588	426.31	-70.623
Delta plus AY.1	511.2668	353.568	264.584	-53.387
Epsilon B.1.427	465.3735	289.895	279.507	-18.675
Eta B.1.525	450.1992	199.843	295.278	-22.293
Iota	B.526		#NAME?	
Iota B.1.526.1		#NAME?		
Kappa B.1.617.1	544.5906	311.86	337.362	-64.514
Kappa B.1.620	382.5573	189.907	256.668	-27.934
Kappa B.1.621	524.7044	238.331	388.452	-76.51
Lambda C.37	345.3966	198.131	186.466	-33.126
Mu B.1.621		#NAME?		
Theta P.3		#NAME?		
Theta B.1.616	487.0045	296.061	279.185	-41.916
Zeta P.1		#NAME?		
Omicron BA.1	761.7122	389.186	484.065	-60.1
Omicron BA.2	904.3286	475.158	576.588	-73.122
Omicron BA.2.75	515.1229	288.025	282.777	-27.285
Omicron BA.4	344.6077	175.479	166.875	-62.349
Omicron BQ.1	424.6153	707.312	151.402	15.95
Omicron BQ.1.1	364.6192	300.761	114.112	-17.027
Omicron XBB	436.8711	314.14	208.562	-22.816
Omicron XBB.1.5	373.8973	300.913	90.35	11.886
Omicron XBB.1.16	443.7985	189.64	141.811	74.879
Omicron FE.1	350.551	219.398	173.155	-18.616
Omicron EG.5	420.3829	197.339	249.328	-9.865
Omicron BA.2.86	556.1528	167.982	434.817	-9.145
Omicron HV.1	702.6767	223.317	386.677	93.955
Omicron JN.1	632.3226	101.838	481.137	85.248

Original structure: PDB 7kmb. Unit: kcal mol^{-1}

Actual protein-protein interactions should include steric hindrance at the contact site. The calculated transmissibility order (MIFS) was Alpha < Lambda < WT < FE. < EG.5 < Alpha+E484K < Omicron XBB.1.16 < Epsilon < Delta plus < Beta, Kappa B..62 < Kappa B.1.67.1 < BA. 2.86 < Delta B.1.57.2 < Omicron HV.1 < Omicron JN.1 < Omicron BA.1 < Omicron BA.2. The contribution of electrostatic interaction was described using various experimental data [32-35]. The mutation to basic amino acids enhanced the ion-ion interaction, and the calculated results support the mutant's transmissibility. The Delta mutant had demonstrated the strongest transmissibility; however, the Omicron replaced the transmissibility strength. The higher transmissibility y should be caused by mutation from acidic amino acids to basic amino acids. Lysine and arginine are contained in meat. The calculation was performed using a part of these proteins but not the full size proteins, and further calculations using full size structures should improve the precision. In particular, other parts of SARS-CoV-19 are important for protein complex tightness. However, this simple calculation provides a quick estimation of ther transmissibility of the mutant and can be useful to study finding inhibitors.

The high transmissibility of Omicron was reported [36, 37], and the immunogenicity, immune escape, and pathogenicity

were described [38]. The analysis of the difference between the Omicron variant and Delta variant suggested the higher transmissibility of Omicron by computational studies [39]. Omicron binding affinity tohACE2 is similar to the prototype RBD; however, multi-mutations might affect immune escape and transmissibility [40, 41]. Pathophysiological differences between COVID-19 and HIV-1 were described, and antibody based therapeutics to treat comorbid –patients [42] were proposed. Scanning the RBD molecular interactions suggested omicron was more stable than WT [43]. The heavily mutated Omicron variants are highly susceptible to T-cell response; therefore, antibodies are likely less effective, but the activation of T-cells should improve against CO VID-19 viruses [44].

11.3. COVID-19 Transmissibility and the Binding Inhibitors

The mutation of neutral amino acids of S-RBD to basic amino acids, especially the Delta mutant (L452R, T478K), exhibited very strong transmissibility based on ion-ion interaction. The mutation of amino acids to basic amino acids such as arginine (K) of S-RBD increases the transmissibility of COVID-19. In the initial study, acidic compounds inhibited the docking of S-RBD with ACE-2 because acidic compounds are repulsed from acidic amino acids and form strong ion-pair with basic compounds but not basic compounds due to strong acid-base interactions.

As demonstrated in Chapter 11.2, a fast analysis of transmissibility by binding strength between two amino acids shows that many acidic amino acids are present at the binding site of ACE-2. The mutation of neutral two amino acids of S-RBD to basic amino acids exhibited very strong transmissibility based on ion-ion interaction. The mutation of amino acids to basic amino acids such as arginine (R) and lysine (K) of S-RBS increases the transmissibility of COVID-19. In the initial stud y, acidic compounds inhibited the binding of S-RBD with ACE-2 because acidic compounds are repulsed from ACE-2 acidic amino acids but form strong ion-pair with basic compounds.

Therefore, 82 compounds listed in Table 11.5 were investigated as potential binding inhibitors, including ingredients in flu medicines, food components, and proposed drugs in the literatures. First, the binding of these candidates with Alpha-S-RBD was performed. All candidates were bound at S-RBD binding site with ACE-2. Second, the binding of these candidates with the ACE-2 binding site with S-RBD was performed. Only compounds having ionized carboxy groups were repulsed from ACE-2 as the ionic form. Even if the molecular form compounds were bound with ACE-2 via hydrogen bonding. Phenolic hydroxyl and secondary amino groups were also formed by hydrogen bonding with ACE-2 carboxy oxygen. However, the initial analysis indicated that basic compounds, including basic drugs, bound tightly to the ACE-2 binding site; therefore, basic compounds are not included in the Table. The strength of ion-ion interaction is described in detail in Chapters 2 and 3. The results are indicated As “repulsed” in Table 11.5.

Table 11.5: Proposed compounds for anti-COVID-19.

Compound [ref]	MIHB	MIES	MIVW	XlogP	logP*	pKa*			
Acetaminophen	22.556	6.459	7.314	0.5	0.9(D), 0.46(S)	9.38(HS),-4.4(D)			
Adrenaline	1.879	-36.645	9.929	-1.4	-1.2(D,E),-1.37(H)	8.23(HS),8.59(D),			
								9.24(HS)	
Amentoflavone [45]	202.902	-2.314	-18.12	5					
Aminoquinoline [46]	nc	nc	nc	1.3	1.28(H)				
Ascorbic acid	114.66	13.562	-14.768	-			4.1,11.6(W)		
Aspirin (I)		repulsed		1.2	1.18(D),1.19(H,E) 3.47(Ch),3.49(HS)				
Aspirin-*O*-mannoside (M)	88.702	32.79	9.539						
Aspirin-*O*-mannoside (I)		repulsed							
AZD1061,8895 [47]		monoclonal antibody							
Azithromycin [46,48-50]	50.893	20.479	19.384	4	3.03(D),4.02(E)	8.5(D),8.75(HS)			
Bamlanivimab [51]		monoclonal antibody							
Baricitinib (Olumiant) [52]	160.67	-13.21	-15.38	-0.5					
Benzoic acid (I)		repulsed		1.9	1.87(H)		3.96, 4.2(Ch)		
b-Blocker	109.747	13.473	5.982						
Calcitriol [53]	144.948	-16.333	-9.458	5.1	5(D)				

Captopril [54]	82.331	24.944	-3.189	0.3	0.34(D,E)				
Casirivimab [55]		monoclonal antibody							
Cepharanthine [56]	nc	ne	nc	6.5					
N-Chloroacetylaniline [57]	nc	nc	nc	1.6	1.63(H)-				
N-Chloroacetyl-N'-sulfonamide-									
	Piperazine [57]	168.391	-11.246	-16.554	-0.5				
N-Chloroactyl piperidinyl-4-									
	carboxamide [57]	164.716	-1.666	-18.242					
Chlorophenylamine	57.639	5.753	3.635	1.9					
Chlorophenylamine-mannoside	117.796	26.983	-12.663 –						
Citric acid (M)	34.137	26.273	12.308	-1.7	-1.64(D,E)		2.79(D)		
Citric acid (I)		repulsed							
Citric acid dimethyl		repulsed							
Citric acid trimethyl	-31.569	-28.32	18.756						
Citric acid-*O*-mannoside		repulsed							
Citric acid di-*O*-mannoside		repulsed							
Citric acid tri-*O*-mannoside		repulsed							
Cytonic acid A (M) [58]	263.069	-3.168	-19.231						
Cytonic acid A (I)		repulsed							
Cytonic acid B (M) [58]	234.665	11.648	-7.886						
Cytonic acid B (I)		repulsed							
Ephedrine		-20.538	-36.343	16.908	0.9	1.13(D)	9.61(Ch), 10.3(D),9.65,		
									10.25(HS)
Etesevimab [51]		monoclonal antibody							
Ethionamide	78.667	23.403	-14.267	1.1	0.5(D) 4.49(HS)				
Euchrenone all [59]	176.775	-16.253	2.503	6.5					
Ferulic acid (I)		repulsed							
Ferulic acid (M)	102.862	25.208	-2.031	1.5	1.51(H)	4.42, 4.58(HS)			
Flavonoid	-19.046	-38.559	18.881						
Furosemide (M)	76.89	16.207	-5.917	2	2.03(S)	3.52,3.63(Ch) ,3.8,7.5(HS)			
Furosemide (I)		repulsed		-					
Gallic acid (M)	13.225	5.943	7.976	0.7	0.70(H)	4.21(Ch),4.40(HS.)			
Gallic acid (I)		repulsed							
Gallocatechin gallate [45]	191.495	-13.926	-21.252	1.2					
Gingerol	36.512	-20.758	22.002	2.5					
Glychylrrizic acid (M) [60]	48.689	17.6	23.219	6.4					
Glychylrrizic acid (I)		repulsed -							
Hydroxychloroaquine[46,48-50,61]	32.042	3.842	13.72	3.6		9.67(D)			
Ibuprophen (M)	-8.323	3.074	17.239	3.5	3.97(D,E)	4.45(Ch),5.3(D),4.47,			
							5.2(HS)		
Ibuprophen (I)		repulsed							
Isopropylantipyrine	2.452	-1.553	11.248	3.6					
Ivermectin [62,63]	169.012	-7.959	5.777	4.1					
Lactic acid	470.995	-41.16	-9.79	-0.7	-0.72(D,H)	3.86(D,HS)			
Lopinavir [46,49]	83.964	27.438	14.638	5.9					

Losartan [63]	166.159	1.967	1.794		4.3 1.19(D) 5.5(D),5.6(HS),4.07,4.29,				
								14.27(HS)	
Malic acid-*O*-mannoside (M)	203.675	52.086	1.901						
Malic acid-*O*-mannoside (I)		repulsed							
Mefenamic acid (M)	80.91	24.118	8.248	5.1	5.12(H),4.2(HM)	4.2(D),4.5(Ch)			
Mefenamic acid (I)		repulsed							
Mefloquine (Lariam) [64,65]	-15.651	-37.673	22.934	3.6	4.49(E)		9.46,13.79(HS)		
Molnupiravir (Lagevrio) [66,67]	6.149	10.703	18.641	-0.8					
Monoclonal antibodies [68]		monoclonal antibody							
N3 [49]	1.993	0.077	17.653						
Nalidixic acid (M)	44.072	-21.433	7.572	1.4	1.59 (D,E)	6.01(Ch),8.6(D,HS)			
Nalidixic acid (I)		repulsed							
Naproxen (M)	20.794	8.143	8.723	3.3	3.18(H)	4.18(Ch), 4.15(D,HS)			
Naproxen (I)		repulsed							
Oseltamivir (Tamiflu) [49,69]		repulsed		1.1 1(D)			7.7(HS)		
PF07321332(Nirmatrelvir,Paxlovid)[69b] -33.505 -27.398 13.497									
Probenecid (M)	17.869	8.963	13.656						
Probenecid (I)		repulsed							
Remdesivir (GS5734) [46,49,61,63,66,69,70]									
		-29.369	-34.957	26.6	1.9				
Ritonavir [49,61,71]	44.125	23.473	20.108	6	3.9(D)				
Sotrovimab [71]		monoclonal antibody							
Unifenovir (Arbidol) (M) [72,73]	60.178	14.744	9.711	4.4					
Unifenovir (Arbidol) (I)	-43.969	-39.268	29.022						
Xocova	44.028	10.506	21.466						
Zanamivir (Relenza) (M)[69,70]	83.668	33.302	3.367	-3.2	-3(D)				
Zanamivir (Relenza) (I)		repulsed							

(M), (I): molecular and ionized compounds; MIFS, MIHB, MIES, MUVW: Molecular interaction energy value of the final (optimized) structure, hydrogen bonding, electrostatic and van der Waals interaction (unit: kcal.mol^{-1}) *log*P* and pKa from PubChem: D(Drug Bank), E(E.P.A. DSSTox), H (Hansch log*P*), S(Sangster), Ch(ChEMBL), HS (Hazardous substance data bank)

Therefore, 55 compounds listed in Table 11.6, including ingredients in flue medicines and food components, were investigated as potential docking inhibitors and proposed drugs. First, the docking of these candidates with Alpha-S-RBD was performed. All candidates were bound at the S-RBD binding site with ACE-2, and the binding is indicated as "B" in Table 10.6. Second, the docking of these candidates with ACE-2 docking site with S-RBD was performed. The results are summarized in Table 11.6. "R" and "B" indicate repulsion and binding, respectively. Several repulsed compounds that rejected the binding from ACE-2 were selected and made complexes with Delta S-RBD. The surface of the docking site of both proteins is quite large; therefore, three Acidic molecules were used to prepare the complexes with one Delta-S-RBD. The structures of binding inhibitor candidates are shown in Figure 11.10.

Table 11.6: Inhibitor candidates for binding of S-RBD with ACE-2.

Compounds	S-RBD	ACE-2	C+A*	Compounds	S-RBD	ACE-2	C+A*
Acetaminophen	B	B	–	Furosemide	B	B	–
Adrenaline	B	B	–	Gallic acid	B	R	R
Ascorbic acid	B	B	–	Gingerol	B	B	–
Aspirin I	B	R	PB	Glycyrrhizinic acid	B	R	R
Aspirin-O-mannoside M	B	B	–	Hydroxychloroquine	B	B	–
Aspirin-O-mannoside I	B	R	–	Ibuprofen I	B	R	R

Azithromycin	B	B	–	Ibuprofen M	B	B	B
Benzoic acid I	B	R	PB	Isopropylantipyrine	B	B	–
β-Blocker	B	B	–	Lactic acid I	B	B	R
m-Carboxyl-L-tyrosine	B	R	R	Lactic acid M	B	B	R
m-Carboxyl-L-tyrosine N-mannoside	B	R	R	Lopinavir	B	B	–
Catechin	B	B	–	Malic acid D-mannoside M	B	B	–
Captopril	B	B	–	Malic acid D-mannoside I	B	R	R
Clofazimine	B	B	–	Mefenamic acid I	B	R	R
Mefloquine	B	B	–	Molnupiravir	B	B	B
Chlorophenyl amine-Malonate	B	B	–	N3	B	B	–
Citric acid	B	R	R	Nalidixic acid I	B	R	R
Citric acid dimethyl	B	R	R	Naproxen I	B	R	R
Citric acid trimethyl	B	B	PB	Oseltamivir	B	R	B
Citric acid O-mannoside	B	R	R	PF-07321332	B	B	B
Citric acid di-O-mannoside	B	R	R	Probenecid I	B	R	–
Citric acid tri-O-mannoside	B	B	–	Remdesivir	B	B	–
Ethionamide	B	B	–	Ritonavir	B	B	–
Ephedrine	B	B	–	Unifenovir	B	B	–
Favipiravir	B	B	–	Unifenovir I	B	B	–
Ferulic acid I	B	R	R	Xocova	B	B	B
Ferulic acid M	B	B	–	Zanamivir	B	R	B
Flavonoid	B	B	–				

*: Delta-SRBD+ACE-2 complex, M: molecular form, I: ionized form, B: bound, R: rejection,. PB: partly bound, -: not calculated because of rejection by ACE-2.

Figure 11.10: Binding inhibitor candidates. White, yellow (light gray), blue (dark gray), red (black) balls: hydrogen, carbon, nitrogen, oxygen.

11.4. Analysis of Binding Inhibitors as the S-RBD Complexes

The surface of the binding site of both proteins is quite large; therefore, three molecules were used to prepare the complexes with one Delta S-RBD. Selected compounds were marketed medicines, such as Aspirin, PF-07321332, Molnupiravir, and Xocova for further study.

11.4.1. Properties of Aspirin: Aspirin is a popular flu medicine and is used in curing COVID-19 patients: however, the effectiveness was mixed results, and the variant types were not provided in the reports [74-76]. The binding affinity of current spreading Omicron BQ.1 and Omicron XBB.1.5 (MIFS: 309.9 and 373.9 kcal mol^{-1}, respectively was weaker than that of the Delta variant (MIFS: 594.2 kcal mol^{-1}), and they do not contain extra basic amino acids at the binding site [20]. After optimization of these complexes using an MM2 program, the Aspirin-bound mBQ.1 and XBB.1.5 S-RBD complexes were repulsed from ACE-2. The initial conformation of BQ.1 S-RBD and three Aspirin and their complex (optimized)

structure and the initial conformation of BQ.1 with three Aspirin complexes and the ACE-2 are shown in Figure 10.11. After optimization, the Aspirin binding site is completely repulsed due to the ion-ion repulsing. The *in silico* analysis of molecular interactions indicated that Aspirin should also inhibit the binding like other carboxylic compounds among 82 compounds analyzed [19, 20].

FIgure 11.11: Initial conformation of BQ.1 S-RBD and three Aspirin, and ACE-2 and BQ.1 three Aspirin complex and their optimized (repulsed) structure..

Aspirin also inhibited the binding of Omicron XBB.1.16 S-RBD binding with ACE-2. The initial conformation of XBB.1.16 and three Aspirins and their complex structures shown in Figure 11.12, and the initial conformation of XBB.1.16 and three Aspirins complex and ACE-2 and their complex structure are shown in Figure 11.12.

FIgure 11.12: Initial conformation of XBB 1.16 and three Aspirin and their complex structure, XBB 1.16 and three Aspirin complex and ACE-2 and their complex structure.

Further analysis was performed for Delta S-RBD, which exhibited stronger binding affinity compared to that of BQ.1 and XBB 1.16. The initial location of Delta S-RBD. Three Aspirin molecules, and the optimized (complex) structure are shown in Figure 11.13. The initial conformation of the Delta S-RBD and Aspirin complex and ACE-2 are shown in Figure 11.13, where Aspirin is indicated as a molecular color for the easy identification. The *in silico* analysis demonstrated that it did not inhibit the binding of Delta S-RBD with ACE-2. The binding site was extracted, And the structure was detailed, where Delta K478 S-RBD should be rejected from the binding with SCE-2 R357, because both amino acids are basic. However, Aspirin connected these amino acids. This result indicated that a single carboxy group might not effectively inhibit the binding of these proteins (S-RBD and ACE-2).

FIgure 11.13: Initial location of Delta S-RPD and three Aspirin and the optimized complex structure of Delta-S-RPD and three Aspirin complex, and ACE-2 and three Aspirin optimized structure.

This *in silico* model analysis indicates that a flu medicine Aspirin may inhibit COVID-19 S-RBD binding with the ACE-2 if strong basic amino acids do not exist at the binding site of S-RBD. Such *in silico* analysis of molecular interactions should help to understand the feasibility of binding inhibitors. The actual experiment using viruses is required before studying animal tests. Overdose of medicines should be avoided, as overtaking vitamins and amino acids has caused health problem.

11.4.2. Lactic acid, performance of ionized carboxyl acid: An inhibitor candidate lactic acid was bound on the S-RPD binding site, as shown in Figure 11.14 where three molecular form lactic acids were used to cover the S-RBD binding site. The complex of Delta S-RPD and three lactic acids was located under the ACE-2 and optimized the conformation. The complex and the ACE-2 bound together. The lactic acid did not inhibit the binding. This is a pharmacological mistake. Lactic acid is ionized in physiological conditions. Therefore, ionized lactic acid should be used for the complex formation and binding inhibition study. Three ionized lactic acids were bound with Delta S-RPD, and the complex was located below the ACE-2 and optimized the conformation. Figure 11.15 shows that the ionized lactic acid inhibited the binding. This type of mistake was found in reports where an auto docking program was introduced.

Figure 11.14: Properties of docking inhibitor candidate of molecular form lactic acid.

Figure 11.15: Properties of docking inhibitor candidate of ionized form lactic acid.

11.4.3. Acidic Compounds as Inhibitor Candidates:

The feasibility of these acidic compounds-binding inhibition was analyzed using the Delta variant. Acidic inhibitor candidates are ionized m-carboxyl-*L*-tyrosine, m-carboxyl-*L*-**tyrosine** *N*-mannoside, citric acid, citric acid dimethyl, citric acid *O*-mannoside, citric acid di-*O*-mannoside, Ferulic acid, Gallic acid, Ibuprofen, Glycyrrhizic acid, mefenamic acid, nalidixic acid, naproxen, probenecid, and Cyonic acid. The residual amino acid of Delta S-RBD is K478, which binds one of these carboxy groups. These ionized form compounds inhibited the binding but not their molecular form compounds. The process of these compounds is shown in Figure 11.16a & b. However, the ionized carboxy group repulsed each other when these acids were located close together. One example is Nalidixic acid, which is repulsed, and only two Nalidixic acids are bound with Delta S-RBD.

Figure 11.16a: Performance of acidic compounds inhibited binding Delta and ACE-2.

The same analysis was performed for the Omicron BA.2.86 variant. The mutated amino acids of S-RBD are D339H, R403K, V445H, G446S, N450D, L452W, N481K, E484K, and R486P, and the mutation was complicated compared to the mutation of the Delta, whose spike mutations of interest were L452R, T478K, D614G, and P681R. The key amino acids

for binding of BA.2.86 are R403K, N481K, and E484K. Especially, E484K enhances the binding. However, many acidic compounds inhibited the binding of the Delta and the ACE-2 but failed to inhibit the binding of BA.2.86 and the ACE-2. The fundamental docking study demonstrated that natural multi-carboxy acids inhibit the docking of S-RBD protein with ACE-2 enzyme but not inhibit ACE-2 enzyme activity. Malic acid inhibits the docking of Delta S-RBD and ACE-2, summarized in Table 11.6. Further, malic acid inhibits the docking of Omicron BA.2, which exhibits the strongest docking power with ACE-2. The demonstration process follows: three malic acids are put above the Omicron BA.2 docking site, and the optimized structure is shown in Figure 10.16b. The complex faces ACE-2 and optimized the structure. The BA.2 malic acid complex is repulsed from ACE-2 (Figure 11.16b). The same result is exhibited for citric acid, which exhibits strong repulsion from ACE-2 (Table 11.5).

The osertrivir amino group is bound with a carboxy group of ACE-2 D38 and E329. It also bound peptide bridge carbonyl via hydrogen bond. Cytonic acid phenolic hydroxy group forms hydrogen bonds with both D36 carboxy and K353 amino groups. One Gallic acid contributes to the binding where a hydroxy group binds with the Q38 amino group. The other two Gallic acid hydroxy groups did not involve the binding. The Furosemide amino group binds with E35 and D38 carboxy groups via hydrogen bonding, and The ferulic acid phenolic hydroxy group binds to the D38 carboxy group. The last three compounds did not inhibit the binding, but these compounds mainly bound to ACE-2 via hydrogen bonding. The results indicated that these acidic compound carboxy groups bound tightly with the BA.2.86 S-RBD via ion-ion interactions, and the binding to ACE-2 was weak hydrogen bonding. That is, the steric hindrance is a crucial factor in the affinity of the protein substitute**.**

The optimized molecular interaction ion(MIF energy values showed that Omicron BA. 2's MIFS value was 1.4 times Delta MIFS and 2.7 times Alpha MIFS. The Omicron BA.2 S-RBD showed the highest transmissibility. These mutants' MIFS energy values increased from Alpha to Omicron BA.2. 14 proposed medical treatment compounds did not show as inhibitors of Omicron S-RBD and ACE-2 binding.

A popular Omicron JN.1 is further mutated valiant from Omicron XBB.1.5 and exhibited stronger binding affinity with ACE-2 than that of BA.2.86. The mutation L455S increases the flexibility of JN.1, and the R454 mutation contributes strong binding affinity of JN.1. The binding strength of current popular KP.2 and KP.3 is around that of Delta. The calculated binding strength (molecular interaction energy kcal mol-1) of variants is Alfa (321.0) < Lambda (345.4) < WT (346.1) < RE.1 (350.6) < XBB1.5 (373.9) < EG.5 420.4) ≈ BQ.1 (424.6) = Alpha+E484K (442.3) ≈ Omicron XBB.1.16 (443.8) ≈ Epsilon, Iota (465.4) < EG.5 (487.6) < Delta plus (511.3) ≈ Beta, Kappa B.1.621 (515.8) ≈ KP.3 (535.8) ≈ Kappa B.1.617.1 (544.6) ≈ Delta B.1.517.2 (594.2) < KP.2 (662.2) < BA.2.86 (726.1) ≈ JN.1 (737.5) ≈ HV.1 (756.0) ≈ BA.1 (761.7) < BA.2 (904.3) based on protein (S-RBD) and protein (ACE-2) interaction energy values, calculated using *in silico* analysis [21]. Malic acid and glycyrrhizinic acid inhibited the binding with ACE-2 except for Glycyrrhizinic and Krebs cycle acids. The analysis processes are shown in Figure 11.17 using JN.1 mutant, which demonstrated a similar binding affinity to ACE-2 to that of BA.2.86.

The results demonstrated that malic acid might inhibit the binding of the strongest binding capability, Omicron BA.2 with ACE-2. Citric acid was also exhibited as the binding inhibitor (Figure 11.16b). The possible reason why acidic compounds inhibited Delta S-RBD and ACE-2 binding did not inhibit BA.2.86 and ACE-2 binding is the conformation of R454. Delta R454 is buried inside, but BA.2.86 R454 is located in a relatively open space; therefore, the R454 guanidyl group can bind with ACE-2. Such steric hindrance contributes to the binding. Computational chemistry can analyze chemical interactions quantitatively, but it is difficult to analyze biological interactions.

In physiological conditions, the carboxy group and some polyphenol phenolic hydroxy groups are ionized, and these ionized acidic groups are effectively repulsed from the ACE-2 binding site. The ionization of a phenolic hydroxy group can be estimated from the atomic partial charge values (unit: au) calculated by the MOPAC AM1 program. The failed conformations to inhibit the binding of BA.2.86 S-RBD and ACE-2 are not due to the ion-ion interactions between the inhibitor candidates and ACE-2.

11.4.4. Natural Polyphenols as Binding Inhibitors: Green and black tea components inhibited the binding of S-RBD with ACE-2 [77-81]. The components EGCG (Epigallocatechin gallate), TFDG (Theaflavin digallate), and Catechin are polyphenols. Phenolic compounds are classified as acidic compounds, but the dissociation constant of common phenolic compounds is more than 9; therefore, common phenolic compounds are neutral in physiological conditions. Generally, ionized acidic compounds inhibit the binding of S-RBD with ACE-2, and basic amino acids enhance the binding

strength [20]. The molecular form phenolic compounds did not inhibit the binding and just adsorbed on the binding site; however, the dissociation constant (p*K*a) of EGCG, TFDG, and Catechin was not known. Therefore, the dissociation of these compounds was estimated from the atomic partial charge (apc) of their phenolic hydroxy groups. A p*K*a prediction method for acidic compounds used the apc value of the hydroxy group of oxygen and hydrogen calculated using the MOPAC AM1 program [82]. The method was applied to estimate the dissociation of green and black tea components. While the hydrogen partial atomic charge value exceeded 0.23 au, the p*K*a value was less than 7.5.

FIgure 11.16b. Performance of TCA acids binding inhibition: these binding inhibitors and indicated as color molecules for easy identification of their location with S-RBD.

FIgure 11.17. Inhibition of glycyrrhizic acid of BA 2.86, BA.2, and JN.1 binding with ACE-2, these binding inhibitors are indicated as color molecules for their easy identification of their binding locations with S-RBD.

The calculated apc value of several hydroxy group hydrogens of these three compounds was more than 0.23 au [20], and these Gallate hydroxy groups indicated the possible ionization because of their hydrogen apc values. The hydroxyl groups are circled in the Figure 11.18. Tea leaves' partly ionized acidic compounds were applied to binding inhibition analysis. First, the ionized compounds were docked at the S-RBD docking site, then the complex was faced to the ACE-2 docking site and optimized the structures. The processes are shown in the Figures 11.19. For the inhibitor search study, three inhibitor candidates were located above S-RBD; however, the necessary number if inhibitors was varied due to the molecular size and the repulsion between the inhibitor candidate. One Genistein, two (-) Catechin, (-) Epicatechin, and Quercetin were enough to inhibit the binding with ACE-2.

FIgure 11.18. Chemical structure of polyuphenols, 1: (-) Catechin, 2: (+) Catechbin, 3: (-) Epicatechin, 4: Apigenin, 5 : Apigetrin, 6: Daidzein, 8: Genistein, 9: Oleuropein, Red (black), yellow (gray), and shite balls are oxygen, carbon, and hydrogen.

These partly ionized phenolic compounds inhibited the binding of S-RBD with ACE-2. The Figure shows the inhibition of TFDG as an example. This *in silico* analysis supported that these phenolic compounds in tea indeed inhibit the binding of S-RBD with ACE-2. In addition, the binding strength of Omicron BA.2.86 was weaker than that of the Delta variant.

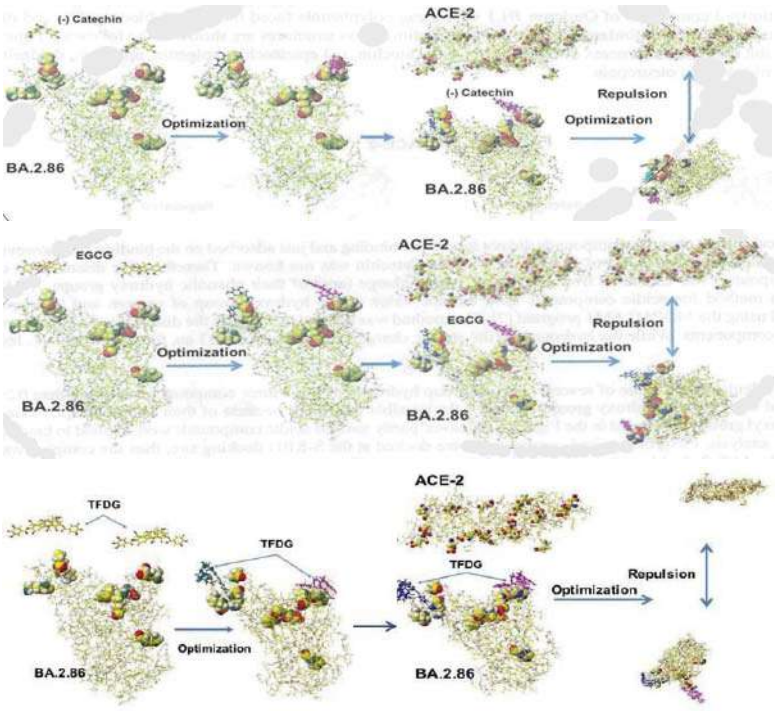


FIgure 11.19: Initial conformation of BA 2.86 and three tea components and their complex structures, (-) Catechin, EGCG, TFDG.

Polyphenols have been used for the oral glucose tolerance test as a way to diagnose diabetes. Tea leaf components (polyphenols) inhibit the binding of COVI-19 S-RBD with ACE-2. Therefore, the feasibility of several polyphenols, such as flavanols, isoflavones, and flavonols being contained in natural plants [83] has been annalyzed their feasibilit y as binding inhibitors of S-RBD with ACE-2, The structrures of used polyphenols are shown in Figure 11.18. The process was the same As that performed for tea polyphenols (Figure 11.18). While the phenolic hydroxy group is the molecular form, the phenolic compounds bind to AC2 via hydrogen bond, and the ionized hydroxy group is repulsed from acidic amino acids via ion-ion repyulsion.

The optimized complexes of Omicron JN.1 with these polyphenols faced the ACE-2 binding site, and the corformed structures were optimized. The pre and post-optimization structures are shown in the following Figure 11.20, which exhibit the reaction process of (-) Catechin, (+) Catechin, (+) Epicatechin, Apigenin, Apigetrin, Daidzein, Quercetin, Genistein, and Oleuropein.

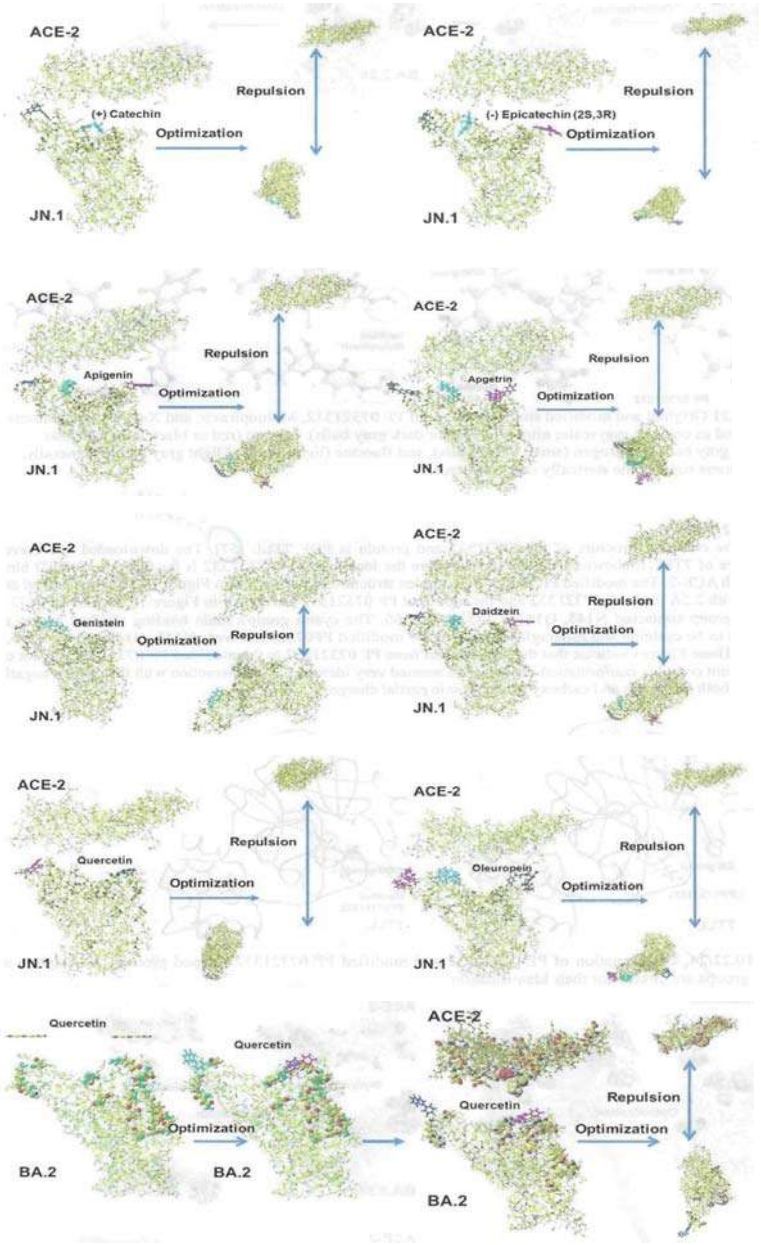


Figure 11.20: Optimization of ACE-2 and JN.1 and a polyuphenol complex. Color molecules are polyphenols.

Natuiral food components can protect against infection by COVID-19 in computational chemical analysis; however, the actual steric hindrance, the quantitative analysis of biologicval reactions, is still difficult. These phenolic compounds inhibited the binding of JN.1 S-RBD with ACE-2, In physiological conditions, natural compounds with ionized acidic groups (carboxy and phenolic hydroxy) may inhibit the binding of S-RBD with ACE-2. The in silico analysis quantitatively demonstrated that the natural polyphenols inhibited the binding of JN.1 S-RBD with AVE-2.

11.4.5. Modification of Medicines to Improve the Capability:

11.4.5.1. Properties of PF 07321332 (Nirumatrelvir) and Molnupiravir: The analysis of binding inhibitor candidates from binding strength with ACE-2 indicates that carboxy compounds were repulsed from the ACE-2 binding

site where acidic amino acids line up; therefore, further modification of medical treatment candidates may produce an effective binding inhibitor. The modified PF-07321332, whose cyano group was replaced with a carboxy group based on precursor search in organic reaction, rejected the binding from ACE-2. The chemical structure of PF07321352 and the modified compound is shown in Figure 11.21.

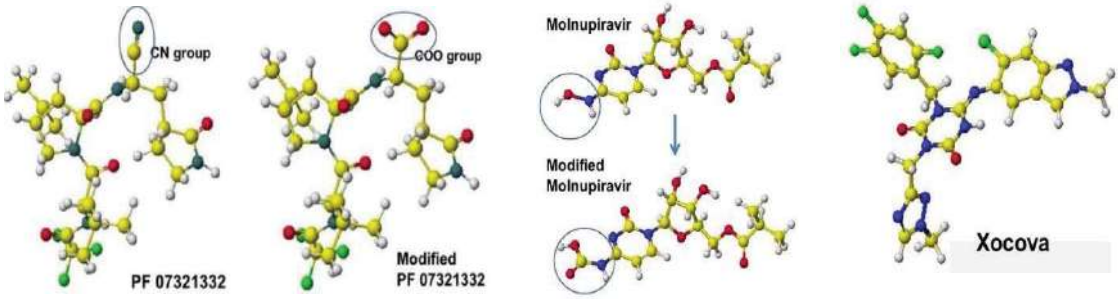


FIgure 11.21: Original and modified stereo structure of PF 07321332, Molnupiravir, and Xocova where atoms are indicated as color or gray scale; nitrogen (blue or dark gray balls), oxygen (red or black balls), carbon (yellow or gray balls), hydrogen (small white balls), and fluorine (light green of light gray balls). Generally, fluorine atoms support the steric stable structure.

PF07321332

The complex structure of PF 07321332 and protein is PDB 7TLL[56]. The downloaded and corrected structure of 7TLL is shown in Figure 10.22, where the location of PF07321332 is far from the S-RBD binding site with ACE-2. The modified PF 07321332 complex structure is also shown in Figure 11.22. The residual amino acids with 2.5Å from PF 07321332 and the modified PF 07321332 are shown in Figure 11.23. The PF07321332 cyano group contacted N143, G143, C145, and E166. The cyano group's main binding residual amino acids seemed to be cysteine and asparagine. Those of the modified PF07321332 were N142, G143, C145, E166, and H172. These Figures indicate that the replacement from PF 07321332 to the modified PF 07321332 did not cause significant complex conformation changes and seemed very identical. The interaction with the protein negatively shifted both the cyano and carboxy group atomic partial charge. The cyano and carboxy groups are circled for their identification.

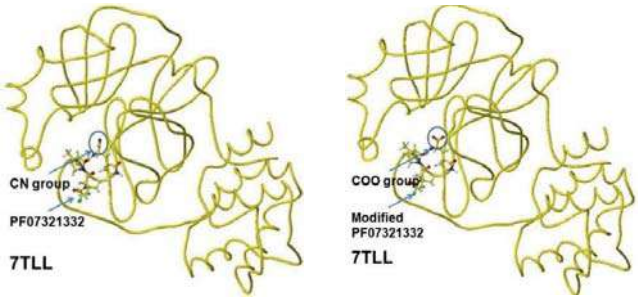


FIgure 11.22: Conformation of PF 07321332 and modified PF 07321332 trapped protein The cyano and carboxy groups are circled for their identification.

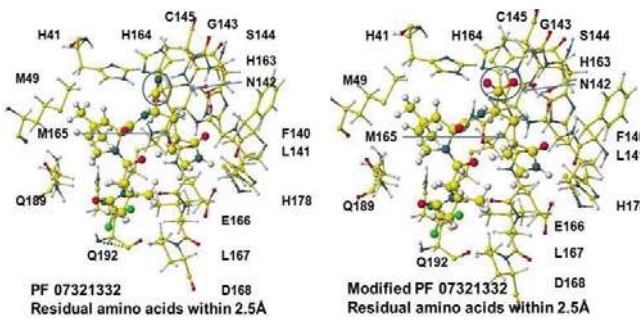


FIgure 11.23: Amino acid residues within 2.5 Å from PF 07321332 and modified PF 07321332. Cyano and carboxy groups are circles for their identification.

For the inhibition study, the feasibility of PF07321352 (PF) and the modified PF07321352 (mPF) was studied to determine whether these compounds inhibit the binding of Delta with ACE-2. The experimental protocol follows the constructed and optimized Delta and three PFs conformation (Figure 11.23). The optimized complex is located about 10Å below the part of ACE-2 and optimized these compounds to obtain their complex structure (Figure 11.24).

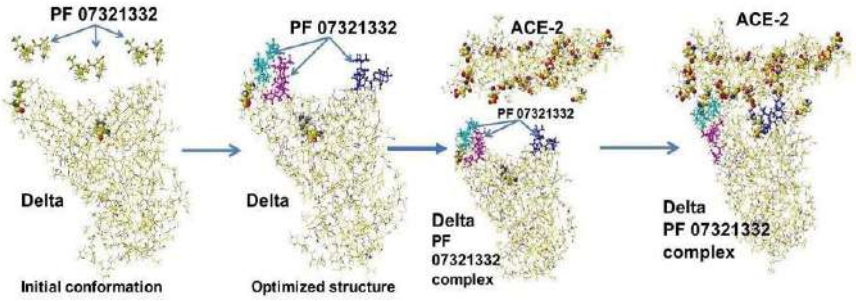


Figure 11.24: Initial conformation of Delta and three PF07321332 and their complex structure, Delta and three PF07321332 complex, and ACE-2 and their complex structure.

The same study was performed for modified PF 07321332. The initial conformation of Delta S-RBD, modified PF 07321332 complex, and ACE-2 and their optimized structures are shown in Figure 11.25.

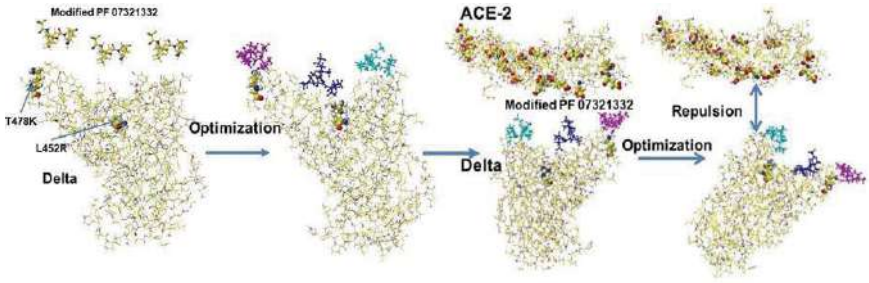


Figure 11.25: Initial conformation of Delta and three modified PF07321332 and their complex structure, Delta and three modified PF07321332 complex, and ACE-2 and their complex structure.

The original PF and Delta S-RBD complex was bound with ACE-2, but the modified PF 07321332 and Delta S-RBD complex was repulsed from ACE-2. The modification seems to be a promised approach for the effective use of PF 07321332. Omicron BA.2 has the strongest binding strength with ACE-2; therefore, the feasibility of modified PF 07321332 was studied. First, three m modified PF 07321332 molecules were located above Omicron BA.2 S-RBD, and the structure has optimized the structure where three modified PF 07321332 molecules were used to cover the binding site. The optimized complex of S-RBD and three modified PF 07321332 molecules faced an ACE-2 binding site, and these compounds were optimized. However, the complex was not repulsed and bound with the ACE-2, as shown in Figure 11.26. The result indicated that even the modification of PF by the addition of a carboxy group might not inhibit the binding to ACE-2.

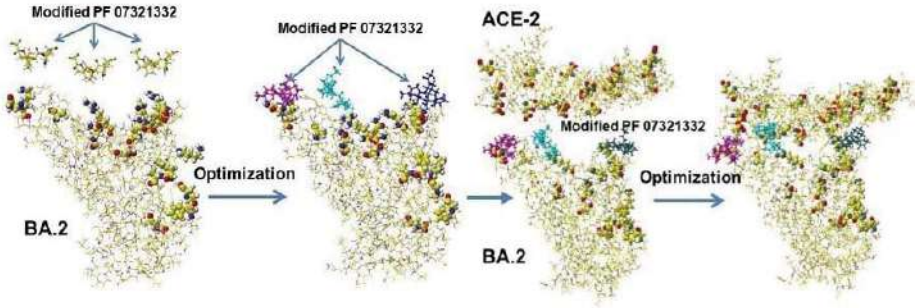


Figure 11.26: Initial conformations of BA.2 and three modified PF07321332 and their complex structure, BA.2 and three modified PF07321332 complex, and ACE-2 and their complex structure.

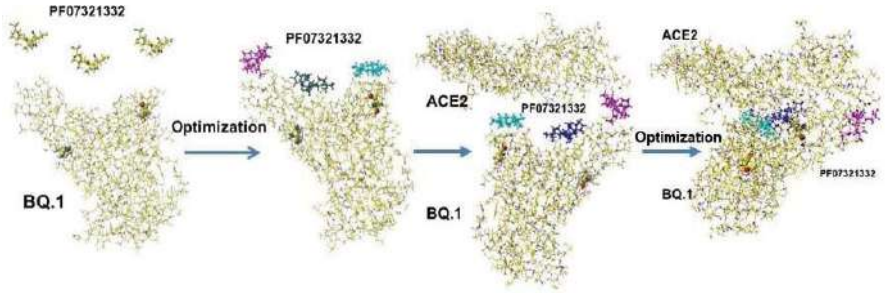


FIgure 11.27: Initial conformations of BQ.1 S-RBD with three PF 07321332 molecules, the complex (optimized) structure of BQ.1 S-RBD with three PF 07321332 molecules complex, and ACE-2 and their optimized structure.

Further study is carried out for Omicron BQ.1 mutant. Omicron BQ.1 bound ACE-2. Three PF 07321332 molecules were located at 10Å above BQ.1 for covering the BQ.1 binding site, and the structure was optimized (complex structure in Figure 11.27). Then, the PF07321332-bound complex was located below the ACE-2, and the complex structure was optimized. As a result, PF was sandwiched between BQ.1 and ACE-2, as shown in Figure 11.27. The same experiment was performed for the modified PF07321332 shown in Figure 11.28. The *in silico* analysis indicated that PF07321332 could not inhibit the binding of BQ.1 S-RBD binding with the ACE-2, but the modified PF 07321332 can inhibit the binding of S-RBD mutants having weak binding strength with ACE-2.

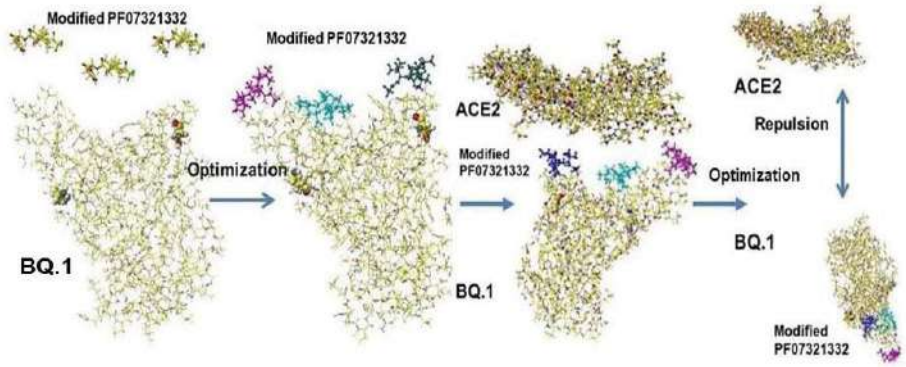


FIgure 11.28: The initial position of Omicron BQ.1-S-RBD and modified PF-07321332 and Omicron BQ.1 and modified PF-07321332 complex and ACE-2 and their optimized structure.

The original PF 07321332 and Delta S-RBD complex were bound with ACE-2, but the modified PF07321332 and Delta S-RBD complex were repulsed from ACE-2. Modification seems to be a promising approach for the effective use of PF07321332. The same approach was performed for modified Molnupiravir.

Molnupiravir (EIDD-2801)

Large molecular size acidic molecules may inhibit the docking of S-RBD with ACE-2, and nitrogen groups bind with ACE-2 acidic amino acids. Reported drug candidates adsorbed with ACE-2 even their docking position in SARS-CoV-2 protein is known. Therefore, the feasibility of another marketed medicine, Molnupiravir, was adsorbed on both Delta S-RBD and ACE-2. The experimental protocol was the same as that used for PF-07321332. The chemical structures of Molnupiravir and the modified compound are shown in Figure 11.21. Molnupiravir was modified; the hydroxy-amino group was replaced with a carbamate. The three original and modified Molnupiravir molecules are located about 10Å above the Delta S-SBD binding site, then optimized these complexes. Molnupiravir bound ACE-2 structure is shown in Figure 11.29. These complexes were located about 10Å below the part of ACE-2 and optimized these complexes. The complex with the original Molnuporavir bound with ACE-2 (Figure 11.29) and Molnupiravir did not inhibit the binding.

The same binding analysis was performed for modified Molnupiravir. The initial conformation of Delta S-RBD and three modified Molnupiravir molecules, their complex structure, and Delta S-RBD, modified Molnupiravir complex, and ACE-2 and their optimized structures are shown in Figure 11.30. The complex with the original Molnuporavir bound with

ACE-2 and Molnupiravir did not inhibit the binding, but the modified Molnupiravir inhibited the binding. The compound with an ionized carboxy group was rejected to bind with ACE-2 due to ion-ion repulsing.

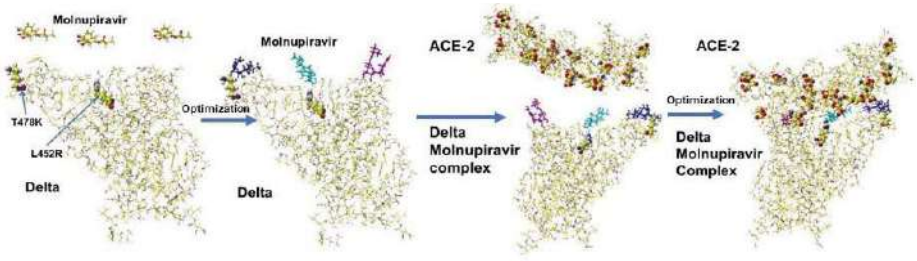


Figure 11.29: The initial position of Delta-S-RBD and Molnupiravir and Delta-s-RBD and Molnupiravir complex and ACE-2 and their optimized structure.

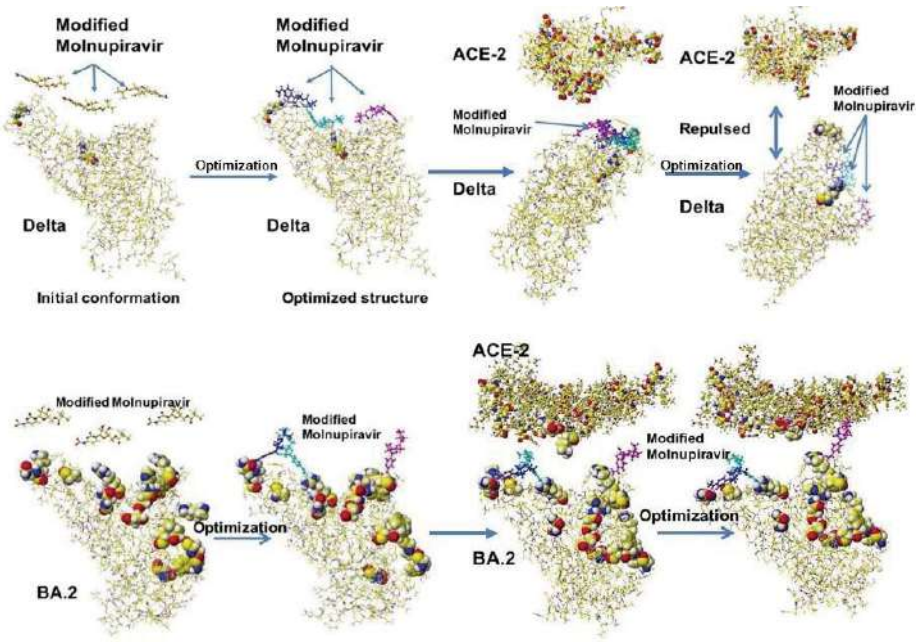


Figure 11.30: Initial conformations of Delta S-RBD and Omicron BA.2 with three modified Molnupiravir molecules, the complex (optimized) structure of Delta and BA.2 S-RBD with three modified Molnupiravir molecules complex and ACE-2 and their optimized structure.

The modified Molunupiravir bound side of Delta S-RBD was repulsed from ACE-2 and completely turned, as shown in Figure 11.30. This *in silico* analysis indicated that Molnupiravir could not inhibit Delta S-RBD binding with the ACE-2, but the modified compound can inhibit the binding. However, modified Molnupiravir bound BA.2 was not repulsed from ACE-2. Further analysis is carried out for Omicron BQ.1. The initial conformation of Molnupiravir and BQ.1 and their complex structures and The initial conformation of BQ.1 and Molnupiravir complex with ACE-2 and their optimized structure are shown in Figure 11.31.

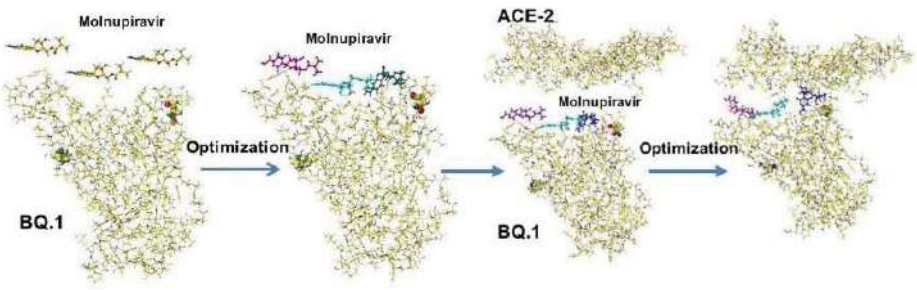


Figure 11.31: The initial position of BQ.1-S-RBD and Molnupiravir and BQ.1-S-RPF and Molnupiravir complex and ACE-2 and their optimized structure.

Molnupiravir did not inhibit the binding of weak binding affinity BQ.1 with ACE-2. Therefore, the same analysis was performed for modified Molnupiravir. The initial conformation of BQ.1 and three modified Monlunipiravir and their optimized (complex) structure are shown in Figure 11.32.

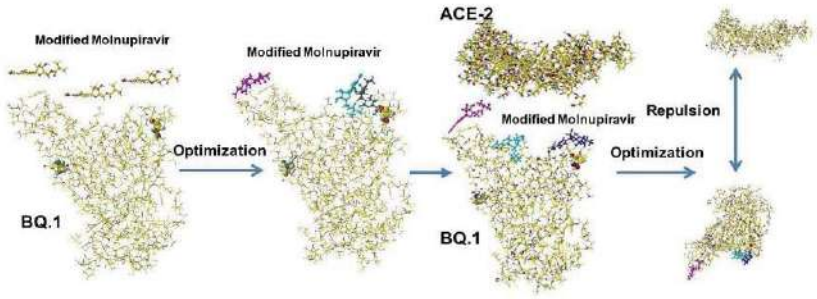


FIgure 11.32: The initial position of BQ.1-S-RBD and modified Molnupiravir and BQ.1 S-RBD and modified Molnupiravir complex and ACE-2 and their optimized structure.

The complex of BQ.1 with the modified Molnupiravir was repulsed from ACE-2. The compound with ionized carboxy compounds was rejected to bind with ACE-2 due to ion-ion repulsing. The Molnupiravir bound side was repulsed and completely turned. This *in silico* analysis indicated that Molnupiravir could not inhibit BQ.1 S-RBD binding with the ACE-2, but the modified compound can inhibit the binding.

11.4.6. Cocktail inhibitors: There are two types of drugs. One is trapped by proteins and is not metabolized by the protein (enzyme). This type of compound is a suicide helper, and various acidic drugs have been developed against enzyme activity. Basic compounds (drugs) bind with the phosphate of DNA and ACE-2 binding. If these compounds are not trapped by ACE-2 and keep ACE-2 enzyme activities, they ay work as active drugs. The modification is one solution, and a cocktail with another compound is another solution. Cocktail drugs consisting of a mixture of the drug candidate and acidic compounds may help the feasibility of the proposed compounds.

11.4.6.1. Barcitinib, Clofazimine, and Malic Acid Cocktail

Barcitinib and Malic Acid Cocktail: Barcitinib (Figure 11.33) is a medicine for treating COVID-19 patients but is not an officially recommended medicine for COVID-19 patients. This molecule has an electron-rich cyano group that may be modified to a carboxy group like a modified PF07321332. However, three Barcitinib molecules-bound Delta S-RBD were not repulsed from ACE-2 (Figure 10.34). These results were applied to a popular FE.1 mutant. The mutation of amino acids of FE.1 S-RBD is similar to those of XBB.1.5; therefore, the three-dimensional structure of XBB.1.5 was used for further analysis. Even XBB.1.5 has no strong binding (basic) amino acid with ACE-2 because K462 is located far from the binding site.

The Baricitinib malic acid complex bound Delta S-RBD was repulsed from ACE-2. Delta has a strong binding affinity to ACE-2 and Omicron XBB.1.5, which has no basic amino acid at the binding site with ACE-2. Therefore, the binding repulsion effect of Baricitinib was studied using Omicron XBB.1.5. The Baricitinib bound XBB.1.5 (Figure 11.34) was partly bound to ACE-2, and Baricitinib bridged between ACE-2 A387 and XBB.1.5 Q498 (Figure 11.34). However, this binding is not a strong interaction like ion-ion interaction; therefore, it may be interrupted by the addition of malic acid. Their malic acid complexes inhibited the binding even though only two complexes were used for the docking instead of three complexes (Figure 11.34).

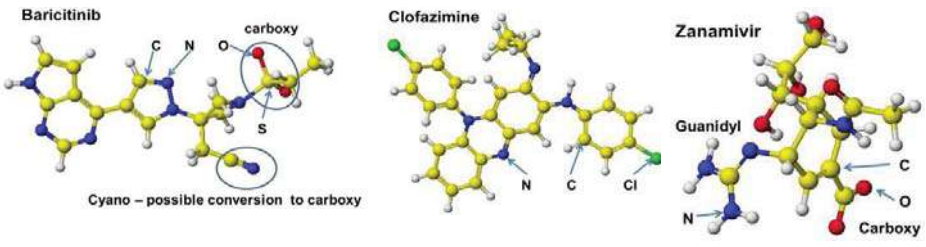


FIgure 11.33: Structure of Baricithinib, Clofazimine, and Zanamivir.

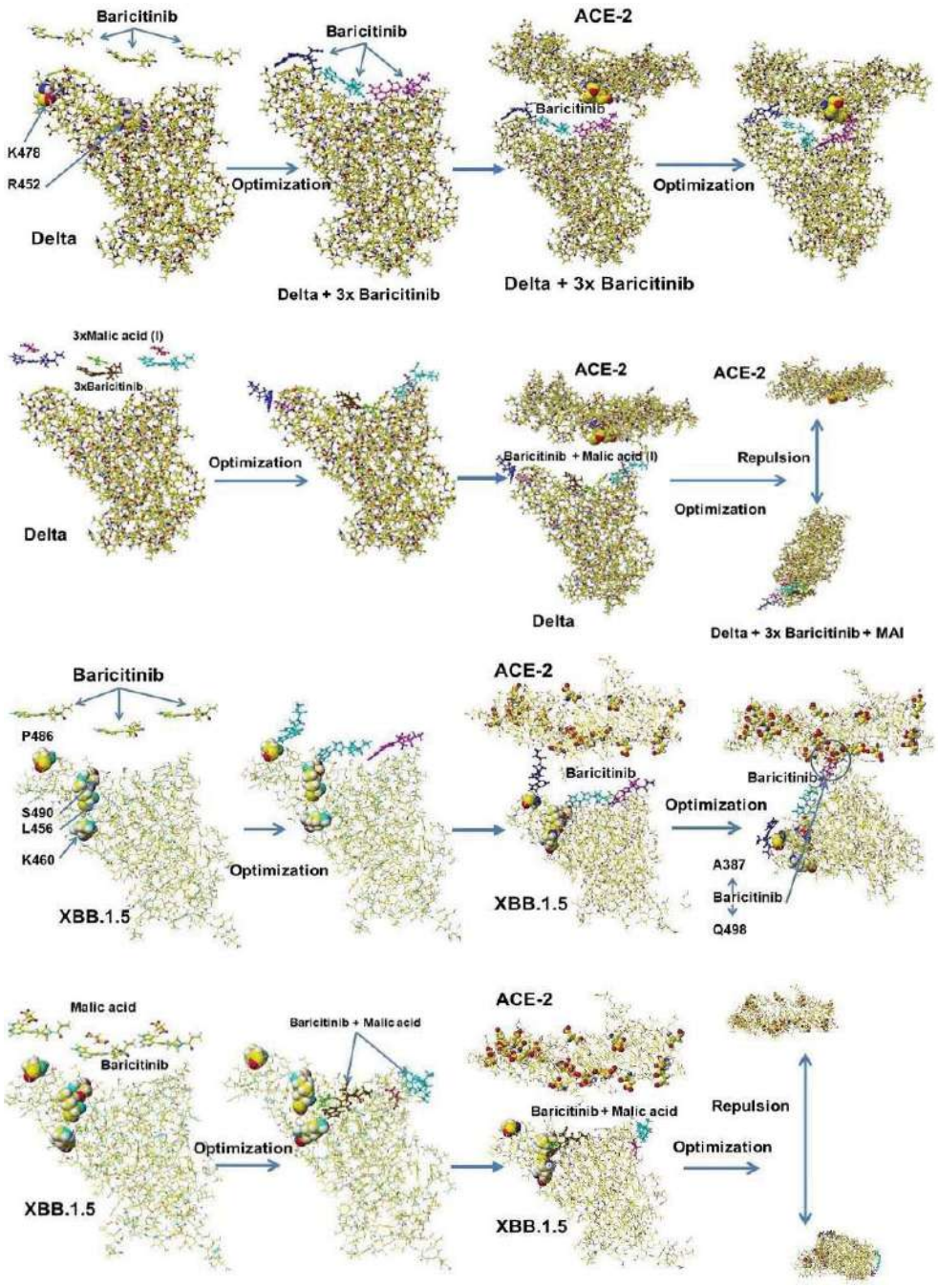


FIgure 11.34: Binding and repulsion process of Barcitinib.

Clofazimine and Malic Acid Cocktail: Clofazine (Figure 11.33) is an upper-limit compound of the rule of five and is used for the treatment of COVID-19 patients. This large-size molecule, Clofazimine, did not inhibit the Delta complexes to bind ACE-2.). The malic acid complexe inhibited the binding for the docking of Delta (Figure 11.35).

Zanamivir and Malic Acid Cocktail: Zanamivir (Figure 11.33) has dual ion of a basic guanidino and acidic carboxy groups. The carboxy group should be repulsed from ACE-2 acidic amino acids, and the guanidino group should bind with the ACE-2 acidic amino acids. Malic acid forms a complex with the guanidino group but not with malic acid. Therefore, the initial conformation produces different conclusions. Zanamivir is different from Baricitinib and Clofazimine; the carboxy group did not bind well to the XBB.1.5 S-RBD binding site and kick off from the binding site at the optimization process with ACE-2. The XBB.1.5 (also EG.5) exhibits weak binding power with ACE-2, but the binding cannot be inhibited using these compounds without the cocktail dose.

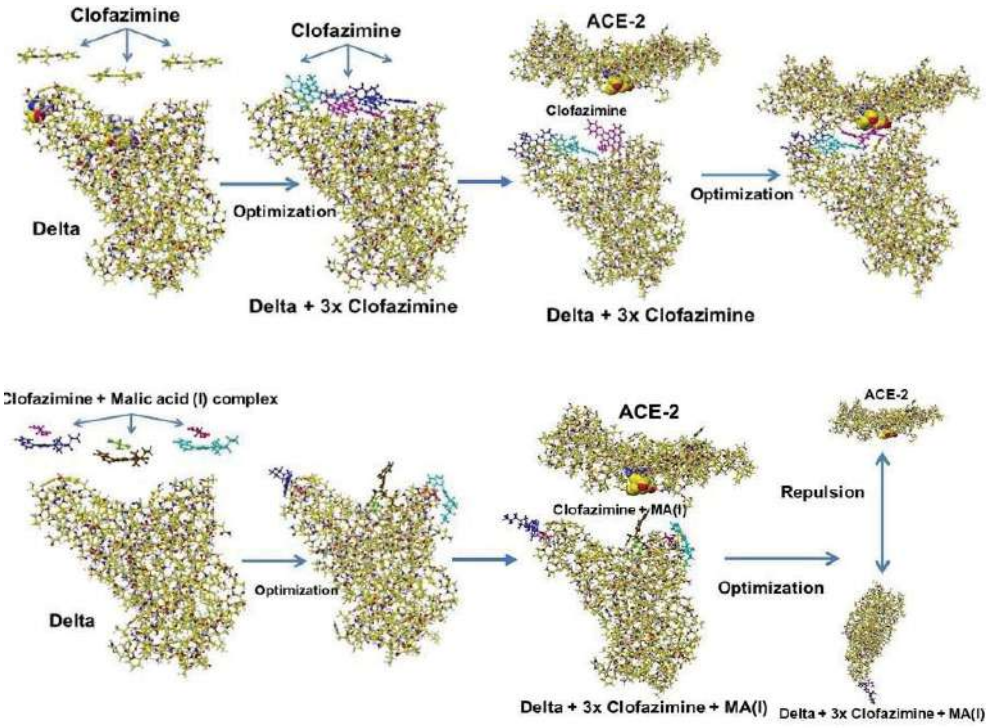


FIgure 11.35: Binding and repulsion process of Clofazimine.

Three molecules are used to cover the S-RBD binding site. The results of Zanamivir were different from those compounds. The Zanamivir carboxy group inhibited the binding but could not inhibit ACE-2 K313 and D-RBD K444 binding. The location is circled in Figure 11.36. However, the Zanamivir does not form a complex with a malic acid due to ion-ion repulsion. The Zanamivir may not inhibit the multiplication of mRNA. Further details of other medicines will be visualized to help you understand their binding mechanisms easily. The *in silico* analysis provides fundamental chemistry, but the actual biochemical experiments are required as real drug candidates.

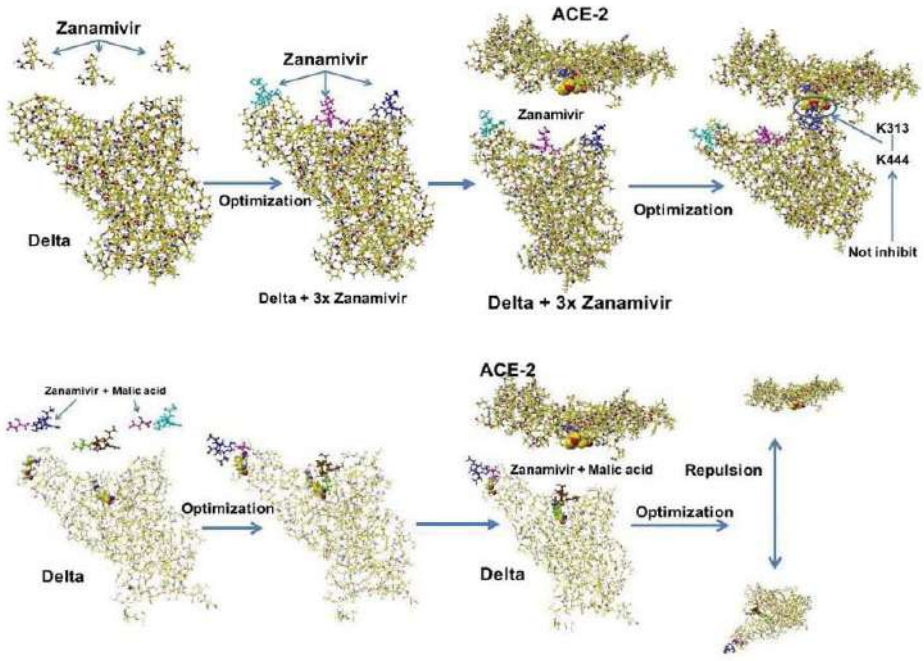


FIgure 11.36: Zanamivir.as a binding inhibitor.

11.4.6.2. Further Study of Cocktail Applications: Omicron BA.2.86 is a current VOC. The binding strength is about the Delta but below that of Omicron BA.1 and 2. However, the BA.2.86 binding strength with ACE-2 is still stronger than previous Omicron BA.4 and 5 variants. The key mutations of Omicron BA.2.86 are N481K and E484K among I332V, D339H, R403K, V445H, G446S, N450F, L452W, and F486P. R403K reduces the binding strength, but E484K (replacing an acidic amino acid with a basic amino acid) strengthens the binding. Therefore, the property of six medicine candidates was investigated. The selected compounds were Chloroquine, Dalcetrapib, Deguetin, Dolutegravir, Ebselen, and Etravine. The *in silico* analytical method is the same as that previously described. Figure 10.37 shows their optimized structures.

The binding sites of PF07321332 and Molnupiravir are known, but these six compounds have no similarity to replace these known compounds. Ensitrelvir has two basic groups that may bind two phosphates of DNA and RNA, like derivatized β-alanine, which was once an excellent target compound in medicines. These six compounds may not have the capability of PF07321332 and Molnupiravir. TCA-cycle acids can inhibit the binding of the variant and ACE-2, and medicine is required to inhibit the multiplication of the protein. If these six compounds inhibit the multiplication of COVID-19 protein, the cocktail with organic acid may improve medical activity.

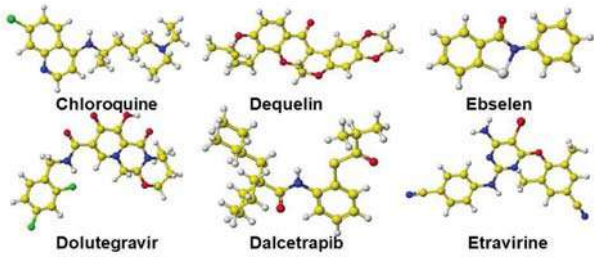


FIgure 11.37: Structure of Chloroquine, Dalcetrapib, Deguetin, Dolutegravir, Ebselen, and Etravine, where atoms are indicated as color or grayscale; nitrogen (blue or dark gray balls), oxygen (red or black balls), carbon (yellow or gray balls), hydrogen (small white balls), and fluorine (light green of light gray balls). Generally, fluorone atoms support the sterically stable structure.

These compounds did not inhibit the binding of BA.2.86 S-RBD binding with ACE-2. Considering the covering of basic amino acids, organic acid should face the ACE-2 binding site. Their malic acid complexes were prepared for their cocktail dose, and their malic acid complexes bound S-RBD were faced with an ACE-2 binding site, then optimized their conformations. The optimized structures of these six compounds are shown in Figure 11.38. These visualized Figures clearly exhibit the useful dose of cocktail medicines.

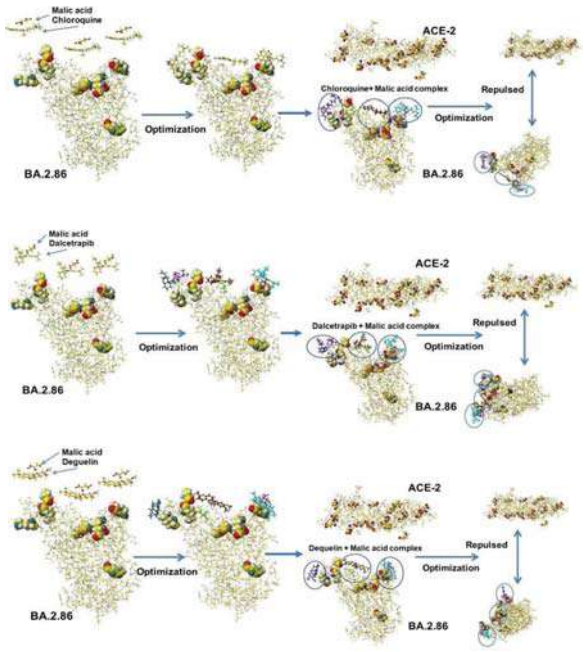


FIgure 11.38: Optimized bound structures of Chloroquine, Dalcetrapib, Deguetin, Dolutegravir, Ebselen, and Etravine.

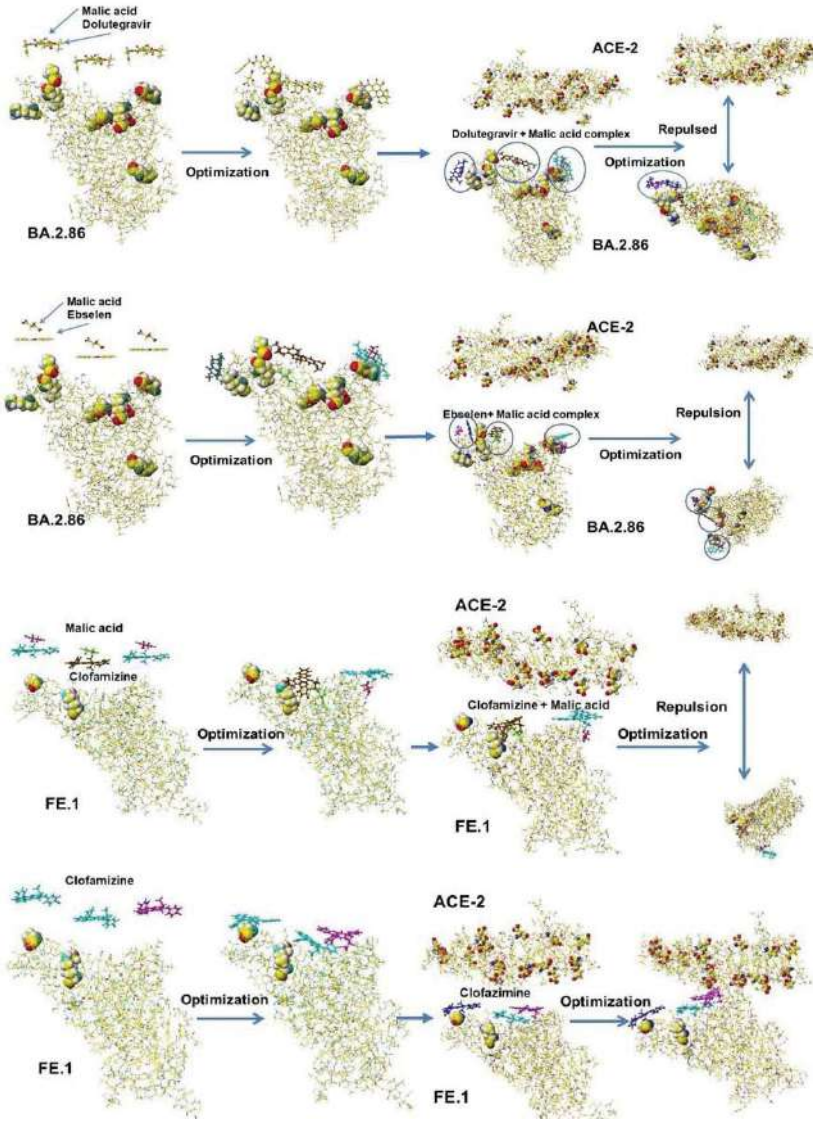


FIgure 11.38: Optimized bound structures of Chloroquine, Dalcetrapib, Deguetin, Dolutegravir, Ebselen, and Etravine.

11.5 Possible Approach to Improve the Known Medicine Activity: *Improving the Performance of PF 07321332, Molnupiravir, and Xocova*

This demonstration indicates that multi-carboxy acids can inhibit the binding of Omicron BA.2, which exhibited the strongest binding power binding to ACE-2 (Table 10.4). These acids are candidates for making cocktail drugs; citric acid is the strongest docking inhibitor, but the taste is not good for a drug additive. Therefore, the feasibility of malic acid was studied for PF07321332, Molnupiravir, and Xocova. First, PF07321332, Molnupiravir, and Xocova malic acid complexes were constructed, and the complexes were put above the Delta binding site and optimized for the structures. The initial conformation of the optimized complex and ACE-2 shown in Figure 11.39 was optimized. Omicron BA.2 malic acid Molnupiravir complex was repulsed from ACE-2 (Figure 11.39).

Xocova is also a medicine to treat COVID-19 patients. It is a very basic compound and easily binds to the ACE-2 binding site via ion-ion interaction. Furthermore, replacing a group with a carboxy group like PF07321332 is difficult. The basic property easily makes a complex with carboxyl acid. The structure of Xocova is shown in Figure 11.21, where three nitrogen (blue or dark gray) rings indicate strong basic properties and fluorine atoms support the sterically stable structure. The Xocova bound Delta S-RBD (Figure 11.39). The optimized structure exhibited that Xocova did not inhibit the binding. The effective use of Xocova may bind mRNA and inhibit multiplication but requires modification for cocktail use. Therefore, the feasibility of the cocktail with malic acid is studied.

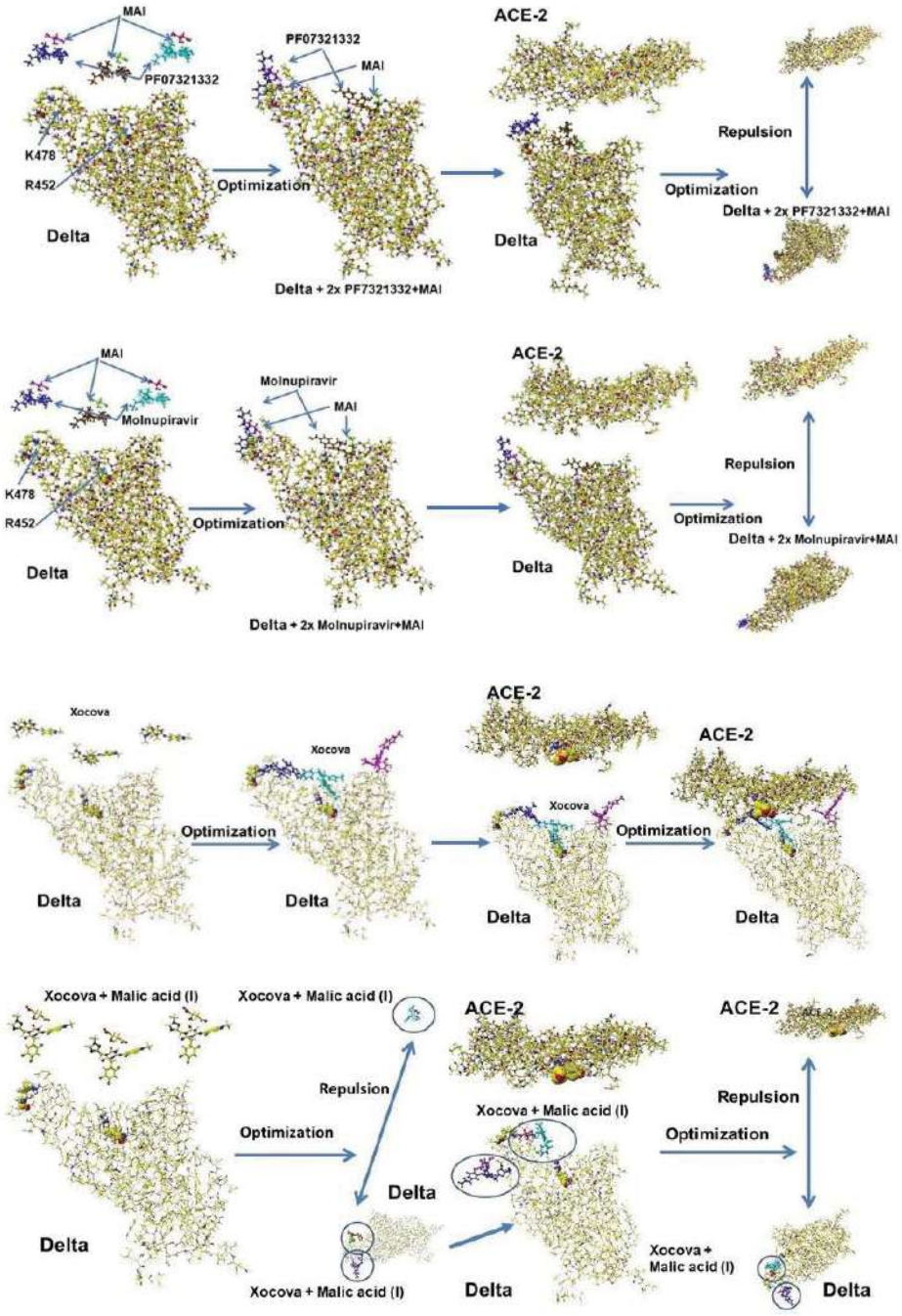


FIgure 11.39: Binding inhibition of PF07321332, Molnupiravir, and Xocova as malic acid cocktails.

Xocoba (Ensitrelvir Fumaric Acid) is like an extended β-alanine derivative and may bind RNA and/or DNA phosphate and inhibit the multiplication. Xocova was later modified as fumarate, and the drug activity improved (Ensitrelvir Fumaric Acid). It is a very basic compound and easily binds to the ACE-2 binding site via ion-ion interaction. Furthermore, replacing a group with a carboxy group like PF07321332 is difficult. The basic property easily makes a complex with carboxyl acid. Further study was carried out for Omicron BA.2.86 and BA.2. The Xocova bound Omicron BA.2 S-RBD. The complex faces ACE-2 and optimized the structure. The optimized structure exhibits that Xocova did not inhibit the binding. May bind mRNA and inhibit the multiplication but it is required the modification of the cocktail use. Therefore, the feasibility of the cocktail with malic aid was studied. The cocktail performance of PF07321332 and Molnupiravir was also exhibited in Figure 11.27 and 29. However, the PF07321332 and malic acid cocktail was not powerful enough to inhibit the binding and Molnupiravir and Xocova malic acid cocktails inhibited the binding as shown in Figure 11.40.

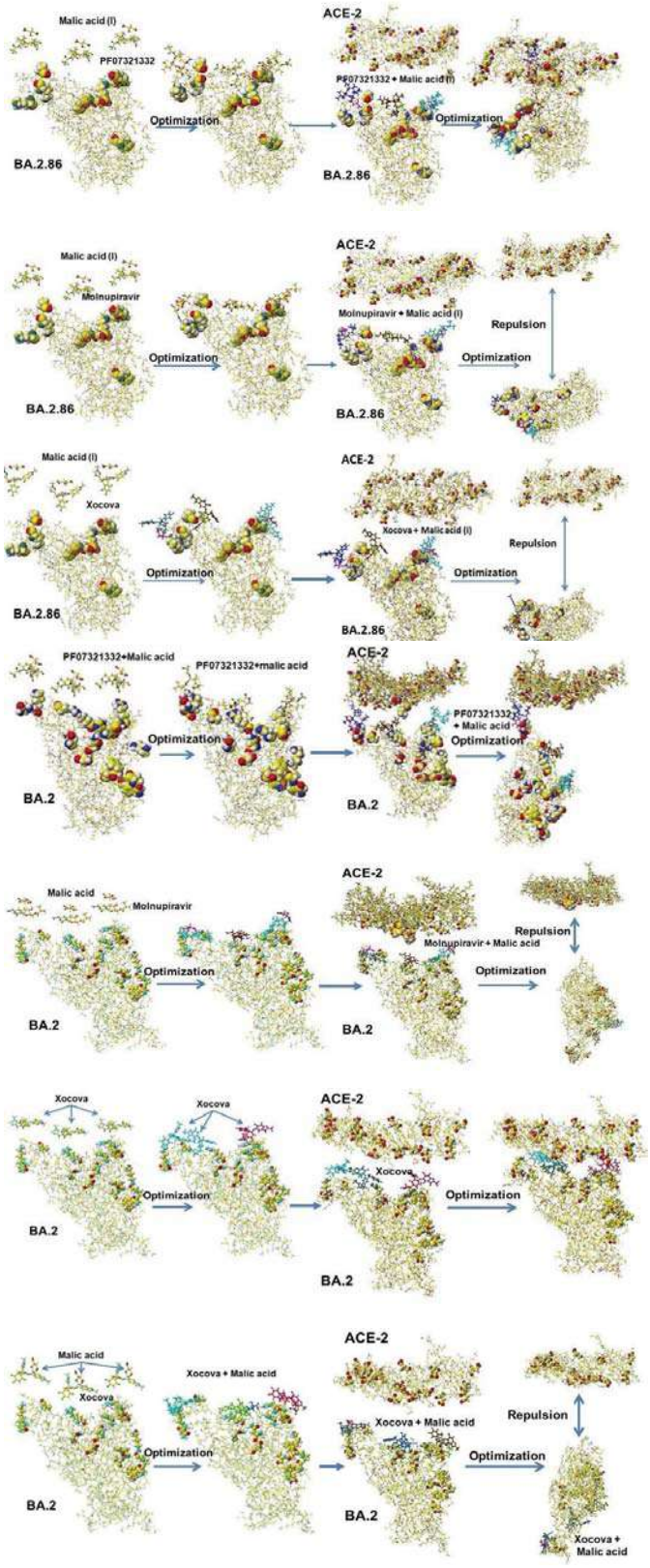


Figure 11.40: Effect of cocktail medicines with malic acid.

Officially recognized medicines, PF07321332, Molnupiravir, and Xocova did not inhibit the binding of BQ.1 with ACE-2; however, the modified PF07321332 and Molnupiravir inhibited the binding of BQ.1 with ACE-2 but not for BA.2 binding with ACE-2, The modified PF07321332 and Molnupiravir were effective for inhibiting binding of BQ.1 and the effectiveness was moderate for Delta, but not BA.2.; therefore the easy solution may be dosing cocktail medicine with TCA acids. Molnupiravir and Xocova cocktail with malic acid inhibited the binding with Omicron BA.2.86 and ACE-2; however, the PF07321332 with a malic acid cocktail was not strong enough to inhibit the binding with BA.2. Xocova did not inhibit the binding of BA.2 with ACE-2; however, the malic acid complex inhibited the binding. These visualized Figures clearly exhibit the useful dose of cocktail medicines except PF07321332 malic acid complex.

11.6. Further Proposal of Medicines against COVID-19

Ivermectin and Malic Acid Cocktail: Various drugs have been used for infected patients. Three of them are officially recommended. Many drugs have been applied, and the Pros and Cons of performance have been reported. According to Science-Direct, 1198 scientific reports related to Ivermectin and COVID-19 have been published since 2019. The total number of research and review articles is 405 and 352, respectively. The balance indicates that the conclusion does not produce a clear answer. Therefore, the quantitative interaction of Ivermectin with COVID-19 protein was studied, and the actual conformations were visualized for the discussions.

The original structure (PDB 7mjk) consists of trimmers; therefore, one protein with aspargine (N) bound saccharides that are eight 2-acetamido-2-deoxy-β-*D*-glucopyranose and four dimers (2-acetamide-2-deoxy-β-*D*-glucopyranose-(1-4)-2-acetamido-2-deoxy-β-*D*-glucopyranose (large size molecules) was picked up (Figure 11.41). Only one glucoside is located in the S-RPD, and the location indicates that the glucoside may not be directly involved in the infection. Structures of these saccharides and Ivermectin are shown in Figure 11.42. Generally, saccharides adsorb on glycoproteins and damage the activity [84, 85]. Ivermectin is a glycoside; therefore, the binding of Ivermectin on the surface of the protein was examined. Four Ivermectin molecules were adsorbed at different locations in the initial study (Figure 11.43). Many Ivermectin molecules seem to cover the surface and inhibit the enzyme activity. The observation is supported by glycocalyx damage COVID-19 activity.

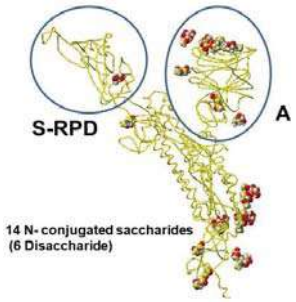


Figure 11.41: Structure of protein.

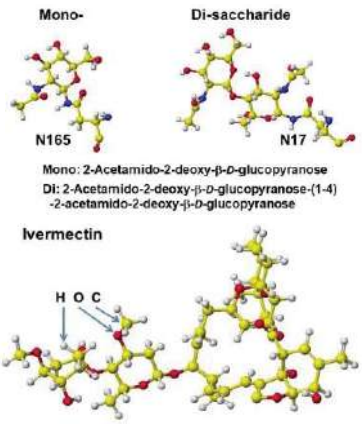


Figure 11.42: Structure of conjugated Saccharides and Ivermectin.

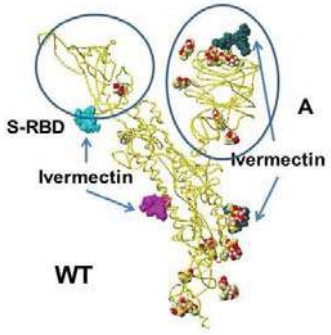


FIgure 11.43: Ivermectin bound WT.

Ivermectin-bound Delta S-RBD was not repulsed from ACE-2; therefore, the Ivermectin-malic acid complex was used to study the binding inhibition. The structure of the Ivermectin-malic acid complex adsorbed Delta S-RBD is shown in Figure 11.44. ACE-2 repulsed this complex. Ivermectin is adsorbed on both ACE-2 and the glycoprotein via hydrogen bonding but not strong ion-ion interaction. Therefore, the bind can be easily cut by other molecules like water.

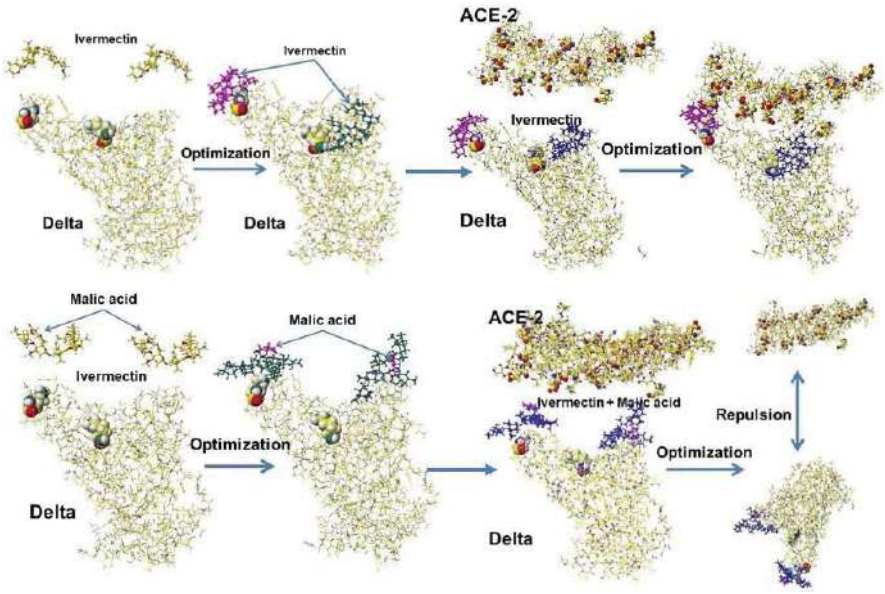


FIgure 11.44: Practical use of Ivermectin with malic acid as an inhibitor.

The key mutations of Omicron BA.2.86 are N481K and E484K among I332V, D339H, R403K, V445H, G446S, N450F, L452W, and F486P. R403K reduces the binding strength, but E484K (replacing an acidic amino acid with a basic amino acid) strengthens the binding. These compounds did not inhibit the binding of BA.2.86 S-RBD binding with ACE-2. Considering the covering of basic amino acids, organic acid should face the ACE-2 binding site. Their malic acid complexes were prepared for their cocktail dose, and their malic acid complexes bound S-RBD were faced with an ACE-2 binding site, then optimized their conformations.

Various compounds have been applied for COVID-19 treatment. Acidic compounds of cannabinoids did block the cellular entry of SARS-CoV-2 [86]. Pros and Cons results have been redported for Ivermectin because the saccharides adsorb glycoproteins and damage their Activity [87,88]. Effectiveness of several compounds such as Ursodeoxycholic acid [89], a combination of Nirmatrelvir and Ritonavir [90], fungal metabolites [91], Bruceine A [92], Gamabufotalin [92], VITAMIC BIOSEN [93], prophylactics [94], and Azvudine [95] was reported, and Sotrovimab remained weakly reactive and broadly neutralizing antibody SA55 was still highly effective [96]. However, Nirmatrelvir, Ritonavir, Bruceine A and D, Gamabufotalin, and Azvudine were adsorbed on the ACE-2 in the above experiment. Ursodeoxycholic acid was repulsed from the ACE-2. Further study is required for their practical use.

Omicron JN.1 is further mutated valiant from Omicron XBB.1.5 and exhibited stronger binding affinity with ACE-2 than that of BA.2.86. The JN.1 mutation of amino acid from leucine to serine (L455S) reduced the steric hindrance for the S-RBD binding with ACE-2 and enhanced the binding affinity [97,98]. The mutation L455S increases the flexibility of JN.1 R454. The mutation contributed to a strong binding affinity of JN.1; therefore, further extended study for JN.1 is necessary. Sweden experienced fewer deaths per population unit during pandemic seasons than most high-income countries and was comparable to neighboring Nordic countries [99], and the modified vaccine virus Anlara vector expressing the SARS-CoV-2 spike protein conferred full protection against SARS-CoV-2 cerebral infection may be a promising vaccine candidate against SARS-CoV-2 [100]; therefore, we should study our immune system capability and further practical use of current practice medicines.

Discussion

The mutation of COVID-19 is too fast, following the analysis of transmissibility and estimation of the multiplication are delayed. Preventing infection is an urgent subject. The previous analysis [28] suggested that the inhibitor candidates are citric acid and related Krebs cycle organic acids, synthesized from glucose as normal metabolic processes. Kids constantly produce these acids and then synthesize related amino acids and other important compounds for growing. Aging reduces such activity; therefore, adults must eat food containing essential metabolites. This known metabolisms may support the idea that kids are less infected [101]. Children's self-protection against COVID-19 was reported, even though children do not have a particular compound, and the fundamental defense mechanism should be the same as those of adults [102, 103]. It may be not have enough vital metabolites to protect from COVID-19 infection if they do not balanced foods. Food habits may affect the mortality of meat-eating and vegetable-eating populations by comparison to their food habits, Before vaccination became a common practice, the USA"s total death/ and infectibility/population ratio was approximately 14 and 10 times Japan's total death/ and infectibility/population ratio. American's relative intake of citric acid-related metabolites [104] is lower than Japanese. The "Healthy Eating" report presented the regional food habits [105], suggesting transmissibility and mortality are very high in certain countries. Excess dairy and animal protein eating seems to relate to the urgent problem. We have to analyze the evidence continuously based on quantitative analytical chemistry.

Myocarditis and/or pericarditis were observed after SARS-CoV-2 mRNA vaccination with a predilection for adolescent and young adult males [106]. We need temporary help with vaccines; however, we must maintain our daily health by exercising and eating balanced food. We should avid continuous vaccination to maintain our immune system as our normal condition against unpredictable viruses and bacteria. Continuous vaccination is like living in a greenhouse and eating supplements. People who used to live in such conditions are vulnerable outside of the greenhouse. The unbalanced habits seem to be clear evidence for COVID-19 transmissibility and mortality like diabetes. Understanding fundamental chemistry should help individuals reconsider their life style, including vaccination and drugs; therefore, the contribution of natural polyphenols as binding inhibitors was investigated.

Natural immunity is considered superior to vaccine-induced immunity. A growing body of literature provides evidence on natural immunity after COVID-19 infection that not only confers robust, durable, and high-level protection against COVID-19 [107]. Herbal medicine is exploring untapped therapeutic potential in neurodegenerative disease management [108], and various effective compounds have been identified in herbal medicines [109]. The *in silico* analysis of the binding inhibition by natural polyphenols supported the effect of food components that ma y inhibit the infection and help natural immunity. Several RNA vaccines are developing, mRNA vaccines produce new, toxic proteins ti viruses and bacteria; however, the products are new intruders to our immune system that may cause some side effects. While we are health y, our bodies can compete against intruders. However, aging and other incidents weaken our metabolic system, and our immune system is also weakened. Why not produce mRNA to recover our weakened metabolism? The best approach, now we can do, is to reconsider our eating habit and do certain exercises. One example against COVID-19 infection is eating certain foods containing compound that inhibit the SD-RBD binding to ACE-2. Therefore, eating balanced food habit can protect against COVID-19 infection. Remain question is how to inhibit virus multiplication. The possible compounds are oligosaccharides that bind glycoproteins and reduce their activity. The oligosaccharide effect may support Pros Ivermectin. Various oligosaccharides and polyphenol compounds are contained in natural foods. Therefore, eating colorful vegetables may protect us.

Conclusion

The fundamental study of ion-exchange group properties was achieved using bio-mimic ion-exchange groups. The

quantitative analytical method was successfully applied to the quantitative analysis of molecular interaction between a small molecule (substitute) and proteins (quantitative analysis of enzyme reactions). Furthermore, the method applied the quantitative analysis of protein-protein interaction for quantitative analysis of COVID-19 variant transmissibility.

Acidic amino acids lined up at the ACE-2 binding site, and highly transmissible valiant's S-RBD has mutated from acidic and neutral amino acids to basic amino acids. That is, ion-ion interaction enhanced the binding. Therefore, molecular interaction energy calculation between two amino acids supported the transmissibility. This calculation does not require a high-level computational chemical system. The direct calculation of molecular interaction energy values between valiant's S-RBD and ACE-2 improves the precision of molecular interaction energy difference due to the effect of the steric hindrance of protein stereo structure. The key mutated amino acids are L452R, T478K, N440K, L452R, T478K, E484K, Q493R, and Q498R, and these multi-mutations to basic amino acids further enhanced the transmissibility.

The number of mutated amino acids of variant's S-RBD was Alfa → Lambda → WT → FE.1 → XBB.1.5 → EG.5 → Delta plus → Beta → Kappa B 1.620 → KP.3 → Kappa B1.617.1 → Delta B.617.4 → KP.3 → BA.2.86 → JN.1 → HV.1 → BA.1 → BA.2 = 1 → 2 → 0 → 3 → 4 → 4 → 3 → 3 → 2 → 25 → 2 → 2 → 25 → 11 → 23 → 18 → 15 → 16 and the binding strength (affinity) was Alfa < Lambda < WT < FE.1 < XBB1.5 < EG.5 ≈ BQ.1 ≈ Alpha+E484K ≈ Omicron XBB.1.16 ≈ Epsilon, Iota < EG.5 < Delta plus ≈ Beta, Kappa B.1.621 ≈ KP.3 ≈ Kappa B.1.617.1 ≈ Delta B.1.517.2 < KP.2 < BA.2.86 ≈ JN.1 ≈ HV.1 ≈ BA.1 < BA.2. Delta has two mutated basic amino acids; however, BA.5, BQ.1.1, and XBB.1.16 have only one extra basic amino acid. This result indicates that the transmissibility is not due to the binding strength but the facile multiplication. Another possibility is that our immune system does not warn us that new viruses are as dangerous as we faced at the beginning. XBB.1.16 does not increase basic amino acid at the binding site, but the binding strength is enhanced. Worry-some will appear delta-related variants that have more basic amino acids at the binding site, and a few mutations are necessary (strong binding affinity with easy multiplication).

The current three medicines are considered to inhibit virus multiplication; however, S-RBDs bound with these medicines were not repulsed from the ACE-2 binding site. The replacement of a group with a carboxy group permitted the repulsion of a modified PF07321332 and a modified Molnupiravir. A common inhibitor was tricarboxylic acid cycle acids like citric acid and natural polyphenols; therefore, the cocktail dose with TCA acids should be effective in inhibiting infection. In addition, the capability of our killer cells has limitations to erase the invented viruses; therefore, compounds that inhibit the multiplication of viruses are required. The virus multiplication of strong binding affinity can be reduced by avoiding taking excess amounts of lysine and arginine used for their mutation. A modified oral drug seemed to inhibit the S-RBD binding with the ACE-2. Understanding the fundamental molecular interaction mechanisms can support designing new drug candidates. The binding strength is based on the mutation to basic amino acids. Acidic amino acids were repulsed from ACE-2 lined-up acidic amino acids. That is, the binding can be inhibited by the compounds having ionized acidic groups. Furthermore, the 82 medicine candidates were analyzed as binding inhibitors from binding with ACE-2. Only carboxy compounds were repulsed from the ACE-2 binding site, indicating that further modification of medical treatment candidates may convert to an effective binding inhibitor. The most effective binding inhibitors are TCA acids and natural polyphenols also inhibit the binding. The glycosides bind saccharides of glycoproteins and reduce the glycoprotein activities.

The fundamentally basic compounds bind phosphate ions of DNA and RNA via strong ion-ion interaction. Acidic compounds are selectively bound proteins (enzymes) and damage enzymatic activity. Therefore, we must carefully use basic compounds for medical treatment because of the non-selective binding, including normal DNA and RNA. TCA-cycle acids can inhibit the binding of the variant and ACE-2, and medicine is required to inhibit the multiplication of the COVID-19 protein.

We must consider finding effective ways to treat people who suffer from COVID-19 as an urgent and foremost priority. We need temporary help with vaccines; however, we must maintain our daily health by exercising and eating balanced food. We should avoid continuous vaccination to maintain our immune system as our normal condition against unpredictable viruses and bacteria. Continuous vaccination is like living in a greenhouse and eating supplements. People who used to live in such conditions are vulnerable outside of the greenhouse. The unbalanced habits seem to be clear evidence for COVID-19 transmissibility and mortality like diabetes. Understanding fundamental chemistry should help individuals reconsider their lifestyle, including vaccination and drugs; therefore, the contribution of natural polyphenols as binding inhibitors was investigated.

References

1. A. Katsnelson, What do we know about the novel coronavirus's 29 proteins? C&EN, 2020, April 1.
2. European Centre for Disease and Control, SARS-CoV-2 variants of concern as of June 3, 2021
3. A. Muik,B.G. Lui, H. Diao, Y. Fu, M. Bacher, A. Toker, J. Grosser, O. Ozhelvaci, S. Grikscheit, K. Hoehl, N. Kohmer, Y. Lustig, G. Regev-Yochay, S. Ciesek, K. Beguir, A. Poran, U. Türeci, O. Sahin, Progressive loss of conserved spike protein neutralizing antibody sites in Omicron sublineages is balanced by preserved T-cell recognition epitopes, BioRxiv 2022, preprint: https://doi.org/10.1101/2022.12.15.520569, Cell Reports, 2023, 42, (8), 112888, Aug. 29, 2023, pp.13, https://doi.org/10.1016/j.celrep.2023.112888.
4. U. Debnath, A. Mitra, V. Dewake, Y.S. Prabhakar, R. Tadala, K. Krishnan, P. Wagh, C. Velusamy, U. Subramani, S. Agarwal, S. Vrati, A. Baliyan, A.V. Kurpad, P. Bhattacharya, A.K. Mandal, Nacetyl cysteine: A tool to perturb SARS-CoV-2 spike protein conformation, http://chemorg/engage/apigateway/chemrxiv/ssets/ Preprint from ChemRxiv, 06 Jan 2021, pp.21 https://doi.org/10.26434/chemrxiv.12687923.v2,
5. S.R. Stein, S.C. Ramelli, A. Grazioli, J-Y. Chung, M. Singh, C.K. Yinda, C.W. Winkler, J. Sun, J.M. Dickey, K. Ylaya, S.H. Ko, A.P. Platt, P.D. Burbelo, M. Quezado, S. Pittaluga, M. Purcell, V.J. Munster, F. Belinky, M.J. Ramos-Benitez, E.A. Boritz, I.A. Lach, D.L. Herr, J. Rabin, K.K. Saharia, R.J. Madathil, A. Tabatabai, S. Soherwardi, M.T. McCurdy, A. Consortium, K.E. Peterson, J.I. Cohen, E. de Wit, K.M. Vannella, S.M. Hewitt, D.E. Kleiner, D.S. Chertow, SARS-CoV-2 infection and persistence in the human body and brain at autopsy, Nature 2022, 612, 758-763, http://doi.org/10.1038/s41586-022-65542-y
6. M.J. Lee, M.W. Leong, A. Rustagi, A. Beck, L. Zeng, S. Holmes, L.S. Qi, C.A. Blish, SARS-CoV-2 escapes direct NK cell killing through Nsp1-mediated downregulation of ligands for NKG2D, Cell Reports 2022, 41, 111892, Dec. 27, 2022, https://doi.org/10.1016/j.celrep.2022.111892,
7. F. Bianchini, V. Crivelli, M.E. Abernathy, C. Guerra, M. Palus, J. Muri, H. Marcotte, A. Piralla, M. Pedotti, R. De Gasparo, L. Simonelli, M. Matkovic, C. Toscano, M. Biggiogero, V. Calvaruso, P. Svoboda, T.C. Rincón, T. Fava, L. Podešvová, A.A. Shanbhag, A. Celoria, J. Sgrignani, M. Stefanik, V. Hönig, V. Pranclova, T. Michalcikova, J. Prochazka, G. Guerrini, D. Mehn, A. Ciabattini, H. Abolhassani, D. Jarrossay, M. Uguccioni, D. Medaglini, Q. Pan-Hammarström, L. Calzolai, D. Fernandez, F. Baldanti, A. Franzetti-Pellanda, C. Garzoni, R. Sedlacek, D. Ruzek, L. Varani, A. Cavalli, C.O. Barnes, D.F. Robbiani, Human neutralizing antibodies to cold linear epitopes and subdomain 1 of the SARS-CoV-2 spike glycoprotein, Sci. Immunol., 2023, 8,1-17, DOI:10.1126/sciimunol.ade0958. 2023
8. E.X.C. Tye, E. Jinks, T. Haigh, B. Kaul, P. Patek, H.M. Parry, M.K. Newby, M. Crispin, N. Kaur, P. Moss, S.J. Drennan, G.S. Tayloe, H.M. Long, Mutations in SARS-CoV-2 spike protein impair epitope-specific CD4+ T cell recognition. Nat. Immunol. 2022, 23, 1726-1736. https://doi.org/10.1038/s41590-022-01351-7.
9. T. Fulop, A. Larbi, G. Pawelec, A.A. Cohen, G. Provost, A. Khalil, G. Lacombe, S. Rodrigues, M. Desroches, K. Hirokawa, et al. Immunosenescence and Altered Vaccine Efficiency in Older Subjects: A Myth Difficult to Change, Vaccines 2022, 10, 607. https://doi.org/ 10.3390/vaccines10040607, 41
10. R. Ruggiero, N. Balzano, R. Di Napoli, A. Mascolo, P.M. Berrino, C. Rafaniello, L. Sportiello, F. Rossi, A. Capuano, Capillary leak syndrome following COVID-19 vaccination: Front. Immunol. 2023, 13, 956825. doi: 10.3389/fimmu.2022.956825,
11. C. Schwab, I.M. Domke, L. Hartmann, A. Stenzinger, T. Longerich, P. Schirmacher, Autopsy-based histopathological characterization of myocarditis after anti-SARS-CoV-2-vaccination, Clin. Res. Cardiol. 2023, 112, 431-440, https://doi.org/10.1007/s00392-022-02129-5,
12. L.M. Yonker, Z. Swank, Y.C. Bartsch, M. D. Burns, A. Kane, B. P. Boribong, J. P. Davis, M. Loiselle, T. Novak, Y. Senussi, C-A. Cheng, E. Burgess, A.G. Edlow, J. Chou, A. Dionne, D. Balaguru, M. Lahoud-Rahme, M. Arditi, B. Julg, A.G. Randolph, G. Alter, A. Fasano, D.R. Walt, Circulating Spike Protein Detected in Post–COVID-19 mRNA Vaccine Myocarditis, Circulation. 2023, 147, 867-876, DOI: 10.1161/CIRCULATIONAHA.122.061025
13. Irrgang, P., Gerling, J., Kocher, K., Lapuente, D., Steininger, P., Habenicht, K., Wytopi, M., Beileke, S., Schäfer, S., Zhong, J., Ssebyatika, G., Krey, T., Falcone, V., Schülein, C., Peter, A.S., Nganou Makamdop, K., Hengel, H., Held, J., Bogdan, C., Überla, K., Schober, K., Winkler, T.H., Tenbusch, M. Class switch towards non-inflammatory, spike-specific IgG4 antibodies after repeated SARS-CoV-2 mRNA vaccination, Sci. Immunol.2023, 8, 1-13, DOI: 10.1126/ sciimunol.ade2798
14. A. Rubio-Casillas, C.M. Rodrigues-Quintero, E.M. Redwan, M.N. Gupta, V.N. Uversky, M. Raszek, M., Do vaccines increases or decreases susceptibility to diseases other than those they protect against? Vaccine, available online Dec. 29, 2023.
15. P.A. Offit, Bivalent COVID-19 Vaccines — A Cautionary Tale, N. Engl. J. Med. 2023, 388, 481-483, doi: 10.1056/NEJMp2215780,
16. E. Topol. The BA2.86 variant and the new booster, Ground Truths, Sept. 9, 2023. pp.12.
17. R. Abdelnabi, R. Lassauniere, P. Maes, N.J. Weynand, Comparing the infectivity of recent SARS-CoV Omicron sub-variants in Syrian Hamsters, Viruses 2024, 16, 122. https://doi.org/10.3390/v160101212
18. T. Tamura, K. Mizuma, H. Nasser, S. Deguchi, M. Padila-Blanco, Y. Oda, K. Uriu, J.M.E. Tolentino, S. Tsujino, R. Suzuki, I. Kojima, N. Nao, R. Shimidzu, L. Wang, M. Tsuda, M. Jonathan, K. Kosugi, Z. Guo, A.A. Hinay, Jr., O. Putri, Y. Kim, Y.L. Tanaka, H. Asakusa, Viological characteristic of the SARS-CoV-2 BA.2.86 variant, Cell Host & Microbe, 2024, https://doi.org/10.1016/j.chrom.2024.pp12.
19. T. Hanai, Quantitative in silico analysis of SARS-CoV-2 S-RBD omicron mutant transmissibility, Talanta, 2022, 240, 123206, https://doi.org/10.1016/j.talanta.2022.123206
20. X. Zhu, D. Manner, S.S. Srivastava, A.M. Berezuk, J.P. Demers, J.M. Saville, K. Leoppold, W. Li, D.S. Dimitriv, K.S. Tuttle, S. Zhou, S. Chittori, S. Subramaniam, Cryo-electron microscopy structures of the N501Y SARS-CoV-2 spike protein in complex with ACE2 and 2 potent neutralizing antibodies, PloS Biol. 2021, 19(4): e3001237, http://doi.org/10.1371/jpurnal.pbio,3001237.
21. T. Hanai, Further quantitative in silico analysis of SARS-CoV-2 S-RBD Omicron BA.4, BA.5, BA.2.75, BQ.1, and BQ.1.1 transmissibility, Talanta, 2023, 254, 124127.

22. J. Lan, J. Ge, J. Yu. S. Shan, H. Zhou, S. Fan, Q. Zhang, X. Shi, Q. Wang, L. Zhang, X. Wang, Structure of the SARS-CoV-2 spike receptor-binding domain bound to the ACE2 receptor, Nature, 2000, 581, 215-220, https://doi.org/10.1038/s41586-020-2180-5

23. M. Scudellari, How SARS-CoV-2 infects cells – and why Delta is so dangerous, Nature 2021, 595, 640644, https;//doi.org/10.1038/d41586-021-02039-y

24. J.T. Ortega, F.J. Serrano, F.H. Pujol, F.R. Rangel, Rile of changes in SARS-CoV-2 spike protein in the interaction with the human ACE2 receptor, an in silico analysis, EXCLI Journal, 2020, 19, 410-417. http://dx.doi.org/10.17179/excil2020-1167.

25. W.A. Haseltine, Birth of the omicron family: BA.2, BA.2, BA.3. each different as alpha is from Delta, Coronavirus, 2022, Jan. 26.

26. W.A. Haseltine, Whither the omicron family: BA.1, BA.1.1, BA.2, BA.2.H78Y, BA.3? Coronavirus, 2002, Feb. 23.

27. J. Chen, R. Wang, M. Wang, G.W. Wei, Mutations strengthend SARS-CoV-2 infectivity, J. Med. Bio. 2020, 432, 5212-5226;

28. T. Hanai, SARS-CoV-2 transmissibility and the protein structures, HYAKUMANBEN-TSUSHIN, 181, July, 2021, pp. 4-12. & T. Hanai, COVID-19 transmissibility and food habitude, HYAKUMANBEN TSUSHIN, 182, Oct. 2021, 5-7.http://www.emeritusclub.jp

29. UniProtKBQ9BYF1 (ACE-2-Human) 4a ACE angiotensin-converting enzyme 2 [homo sapiens (human)]. Gene ID: 59272, 24-May-2021

30. Hanai, T. Introduction of in silico chromatography. J. Chromatogr. Sep. Tech. 2016, 7, 1-8, DOI: 10.4172/2157-70641.1000333

31. Pascarella, S., Ciccozi, M., Binchi, M., Benvenuto, D., et al. The electrostatic potential of the omicron variant spike is higher than in delta and delta-plus variants: a hint to higher transmissibility? J. Med. Virology, 2021, 94, 1277-1280, http://doi.org/10.1002/jmv.27528

32. Rath, S.L., Pahdi, A.K., Mandal, S.L., Scanning the RBD-ACE2 molecular interactions in omicron variant. Biom. Biophysis. Res. Commun. 2022, 592, 18-23.

33. Mandel, N., Padhi, A.K., Rath, S,.l. Molecular insights into the differential dynamics of SARS-CoV-2 variants, of concern. BioRxiv, 2021, https://doi.org/10.1101/2021.10.22.465272

34. Goher, S.S., Ali, F., Amin, M. The delta variant mutationed in the receptor-binding domain of SARS-CoV-2 show enhanced electrostatic interactions with the ACE2. Med. Drug Discov. 2022, 13, 100114, https://doi.org/10.1016/j.medodd.2021.100114

35. T. Hanai, Quantitative in silico analysis of mammalian serine racemase activity, J. Chem. Math. Phy. (IJCMP), 2018, 2, 53-58, https://dx.doi.org/10.22161/ijcmp.2.6.1

36. T. Koley, M. Kumar, A. Goswami, A.S. Ethyathulla, G. Hariprasad, Biochem. Biophys. Res. Commun. 2021, 592, 51-53. https;//doi.org/10.1016/j.bbrc.2021.12.082

37. S. Majumdar, R. Sarkar, Mutational and phylogenetic analyses of the two lineages of the Omicron variant, J. Med. Virology, Dec. 29, 2021, https://doi.org/10.1002/jmv.27558

38. V. Pierros, E. Kontopodis, D.J. Stravopodis, G.T. Tsangaris, Prediction of SARS-SoV-2 omicron variant immunogenicity, immune escape and pathogenicity, through analysis of spiked protein-specific core unique peptides, MedRxiv preprint Dec. 29, 2021, pp.10. :https;//doi.org/10.1101/2021.12.26.21268418; E. Kontopodis, V. Pierros, D.J. Stravopodis, G.T. Tsangaris, Prediction of SARS-CoV-2 omicron variant immunogenicity, immune escape and pathogenicity, through analysis of spiked protein-protein core unique peptides, Vaccines (Basel) 2022, Feb. 24, 10, 357, doi:10.3390/vaccines10030357

39. S. Kumar, T.S. Thambiraja, K. Kanruppanan, G. Subramaniam, Omicron and delta variant fo SARS-CoV2: A comparative computational study of spike protein, J. Med. Virology, 2021, 94, 1641-1649. http://dpo.org/10.1002/jmv.27526; S. Kumar, T.S. Thambiraja, K. Kanruppanan, G. Subramaniam, Omicron and Delta variant of SARS-CoV2: A comparative computational study of spike protein, BioRxiv preprint Dec. 3, 2021. doi: http://doi.org/10.1101/2021.12.02.470946,

40. P. Han, L. Li, S. Liu, Q. Wang, D. Zhang, Z. Xu, P. Han, X. Li, Q. Peng, C. Su, B. Huang, D. Li, R. Zhang, M. Tian, L. Fu, Y. Gao, X. Zhao, K. Lou, J. Qi, G.F. Gao, P. Wang, Receptor binding and complex structures of human ACE2 to spike RBD from omicron and delta SARS-CoV-2, Cell, 2022, 185, 630-640, http://doi.org/10.1016/cell.2022.01.001

41. S. Reardon, How well can Omicron evade immunity from Covid vaccines? News, 02 Feb. 2022, http://doi.org/10.1038/d41585-022-00283-4

42. P. Bose, Similarities and dissimilarities in immune responses and metabolism in SARS-CoV-2 and HIV-1 infections, 2022, https:www.news-medical.net/news/20220113,similarities-and-dissimilarities-in-immuneresponses-and-metabolism-in-SARS-CoV-2-and-HIV-1-infections.aspx

43. S.L. Rath, A.K. Padhi, N. Mandal, Scanning the RBD-ACE2 molecular interactions in Omicron variant, Biochem. Biophys. Res. Commun. 2002, 592, 18-23, https;//doi.org/10.1016/j.bbrc.2022.01.006

44. H. Ledford, Nature, 2022. 601, 307- & Nature, 2021, 590, 374-375

45. A. Swargiary, S. Mahmud, A. Saleh, Screening of phytochemicals as a potent inhibitor of 3-chymotrypsin and papain-like proteases of SARS-CoV-2: an in silico approach to combat COVID-19, J. Biomol. Struc. Dynamics, 2020, 1-15, doi; 10.1080/07391102.2020.1835729

46. A.N. El-Hoshoudy, Investigating the potential antiviral activity drugs against SARS-CoV-2 by molecular docking simulation, L. Mol. Liq. 2020, 318, 113968, pp.19, http://doi.org/10.1016/j.molliq.2020.11.3968

47. J.E. Dong, P. Gilchuk, J. Rodriguez, E. Armstrong, C. Gainza, R.S. Nargi, E. Binshetein, X. Xie, X. Zhang, P-Y. Shi, J. Logue, S. Weston, M.R. McGrath, M.B. Frieman, T. Brady, K.M. Tuffy, H. Bright, Y.M. Loo, P.M. McTamney, M.T. Esser, R.H. Carnahan, M.S. Diamond, J.D. Bloom, J.E. Crowe Jr, Genetic and structural basis for SARS-CoV-2 variant neutralization by a two-antibody cocktail, Nature Microbiology Letter, 2021, 6, 1233-1244.

48. M. Saleh, J. Gabriels, D. Chang, B.S. Kim, A. Mansoor, E. Mahmood, P. Maller, H. Ismail, B. Goldner, J. Willner, S. Beldner, R. Mitra, R. John, J. Chinitz, N.

Skipitaris, S. Mountantonakis, L.M. Epstein, Effect of chloroquine, hydroxychloroquine, and Azithromycin on the corrected Q.T. interval in patients with SARS-CoV-2 infection, Circ Arrhythm Electrophysiol, 2020 Jun;13(6):e008662. doi: 10.1161/CIRCEP.120.008662. Epub 2020 Apr 29.

49. S. Boopathi, A.B. Poma, P. Kolandaivel, Novel 2019 coronavirus structure, mechanism of action, antiviral drug promises and rule out against its treatment, J. Biomol. Struc. Dyn. 2020, 1-10, doi: 10.1080/07391102.2020.1758788

50. S.H. Basha, Coronavirus drugs – a brief overview of past, present and future, J. PeerScoentist, 2020, 2, e1000013.http://journal.peerscientist.com, pp.16

51. M. Shah, H.G. Woo, Omicron: A heavily mutated SARS-CoV-2 variant exhibits stronger binding to ACE2 and potently escapes approved COVID-19 therapeutic antibodies, BioTxiv 2021, preprint doi: http://doi.org/10.1101/2021.12.04.

52. S. Assadiasl, Y. Fatanhi, B. Moshamovahed, B. Mohebbi, M.H. Nickname, Baricitinib: From rheumatoid arthritis to COVID-19, J. Clin. Pharmacol. 2021, June 12, 1-17, DOI: 10.1002/jcph.1874

53. J. Oristrell, J.C. Oliva, I. Subirana, E. Casado, D. Dominguez, A. Toloba, P. Aguilera, J. Esplugues, P. Fafian, M. Grau, Association of calcitriol supplementation with reduced COVID-19 mortality in patients with chronic kidney disease: a population-based study, Biomedicines. 2021 May 5; 9(5):509. doi: 10.3390/biomedicines9050509

54. L.K. Boerner, Rethinking the role of blood pressure drugs in COVID-19, Once thought to boot levels of ACE2, the novel coronavirus's doorway into human cells, these widely used medicines are now contenders to treat the disease, C&EN, 2020, May 25, 28-33.

55. P. Indu, M.R. Rameshkumar, N. Arunagirinathan, N.A. Al-Dhahi, M.V. Arasu, S. Ignacimuthu, Raltegravir, Indinavir, Tipranavir, Dolutegravir, and Etravirine against main protease and RNA-dependent R.N.A. polymerase of SARS-CoV-2: A molecular docking and drug repurposing approach, J. Inf. Pub. Health, 2020, 13, 1856-186, http;//doi.org/10.1016/j.jiph.2020.10.015

56. C-R. Wu, W-C. Yin, Y. Jiang, H.E. Xu, Structure genomics of SARS-CoV-2 and its omicron variant: drug design templates for Dovid-19, Acta Pharm. Sinica, 2022, https://doi.org/10.1038/s41401-021-00851-w

57. A. Douangamath, D. Fearon, P. Gehrtz, T. Krojer, P. Lukacik, C.D. Owen, E. Resnick, C. Strain-Damerell, A. Aimon, P. Abranyi-Balogh, J. Brandao-Neto, A. Carbery, G. Davison, A. Dias, T.D. Downes, L. Dunnett, M. Fairhead, J.D. Firth, S.P. Jones, A. Keeley, G.M. Keseru, H.F. Klein, M.P. Martin, M.E.N. Noble, P. O'Brien, A. Powell, R.N. Reddi, R. Skyner, M. Snee, M.J. Waring, C. Wild, N. London, F. Von Delft, M.A. Walsh, Crystallographic and electrophilic fragment screening of the SARS-Cov-2 main protease, Nature Communications, 2020. pp. 1-11, http://doi.org/10.1038/s41467-020-18709-w 66

58. J. Prajapati, R. Patel, P. Rao, M. Saraf, R. Rawal, D. Goswami, Perceiving SARS-CoV2 Mpro and Plpro dual inhibitors from pool of recognized antiviral compounds of endophytic microbes: an in-silico simulation study, Res. Square, 2021, p.1-47, doi.org/10.21203/rs.3.rs-829046/v1

59. G. Jimenez-Avalos, A.P. VargasoRuiz, N.E. Delgado-Pease, G.E. Olivos-Ramirez, P. Sheen, M. Fernandez-Diaz, M. Quiliano, M. Zimic, COVID-19 Working group in Peru, Comprehensive virtual screening of 4.8K flavonoids reveals novel insights into allosteric inhibition of ASRS-CoV-2 Mpro, Scientific Reports, 2021, 1115452, pp. 1-18. www.nature.com/scienificreports, doi.org/10.1038/s41598-021-94951-6

60. Bryant, A., Lawrie, T.A., Dowswell, T., Fordham, D.J., Mitchell, S., Hill, S.R., Tham, T.C. Ivermectin for prevention and treatment of COVID-19 infection: A systematic review. meta-analysis, and trial sequential analysis to inform clinical guidelines, Am. J. Ther., 2021, 28(4) e434-e460, doi: 10.1097/mjt.0000000000001402

61. H. Cubuk, M. Ozbil, Comparison of clinically approved molecules on SARS-CoV-2 drug target proteins: a molecular docking study, Turk. J. Chem. 2021, 45, 35-41

62. Z. Wang, L. Yang, Turning the tide; natural products and natural-product-inspired chemicals as potential counters to SARS-Cov-2 infection, Front. in Pharmacol. 2020, 11, 1-12. Doi: 10.3389/fphar.2020.01013

63. K. Watashi, Mefloquine, a potent anti-severe acute respiratory syndrome-related coronavirus 2 (SARS-CoV2) drug as an entry inhibitor in vitro, Frontiers in Microbiology, 2021, doi: 10.3389/fmicb.2021.651403

64. VA(http://www.va.gov/) > Health Care (http://www.va.gov/health) ? Public Health (/index.asp) > Military Exposures (/PUBLICHEALTH/exposures/indec.asp) > Mefloquine (Lariam@)

65. M. Satyanarayana, Two COVID-19 antiviral pills advance to late-stage trials, C&EN, Sept.13, 2021

66. J. Yang, Z. Zhang, F. Yang, H. Zhang, H. Wu, F. Zhu, W. Xue, Computational design and modeling of nanobodies toward SARS-C0V-2 receptor binding domain, Chem Biol. Drug Design,202?, 98, 1-18

67. L.D. Manzanares-Meza, O. Medina-Contreras, SARS-Cov-2 and influenza: a comparative overview and treatment implications, Bol. Med. Hosp. Infant Med. 2020, 77(5), 262-273. Doi: 10.24875/bmhim.20000183.

68. D.C. Hall Jr. H.F. Ji, A search for medications to treat COVID-9 via in silico molecular docking models of the SARS-CoV-2 spike glycoprotein and 3CL protease, Travel Med. Inf. Disease, 2020, 35, 101646, pp.3, http;//doi.org/10.1016/j.tmaid.2020.101646

69. Z. Qiao, H. Zhang, H.F. Ji, Q. Chen, Computational view toward the inhibition of SARS-CoV-2 spike glycoprotein and the 3CL protease, Communication 2020, 8, 53-61; doi.0.3390/computation8020053

69b. K. Vandyuck, et al. Consideration for the discovery and development of 3-chymotrypsin-like cysteine protease inhibitors targeting SARS-CoV-2 infection, Current Opinion in virology, Available online, 2021

70. J. Mourani, Sotrovimab monoclonal antibody treatment effective at reducing severe disease from Omicron COVID-19 variant, 2022, http://www.pvhmc.org/blog/2022/january/

71. M. Peplow, AI finds alternative routes to CONID-19 drug candidates, C&E News, (Aug. 10/17, 2020) pp. 9. (T. Cernak, ChemRxiv 2020, doi: 10.26434/chemrxiv.12765410.Vl).

72. I.A. Darazam, S. Shokouhi, M. Mardanai, M.A. Pourhoseingholi, M.M. Rabiei, F. Hatami, M. Shabani, O. Moradi, F.J. Gharehbagh, S.S.N. Irvani, M. Amirdosara, M. Hajiesmaeli, O. Rezaei, A. Khoshkar, L. Lotfollahi, L. Gachkar, H.S. Dehbsneh, N. Khalili, A. Soleymaninia, A.H. Kusha, M.U. Shoushtani, P. Torabinavid, Umifenovir in hospitalized moderate to severe COVID-19 patients; A randomized Chlinical trial, Int. Immunopharmacol. 2021, 107969, doi: 10.1016/j.intimp.2021.107969

73. RCSB Protein Data Bank, 7TLL, www.rcsb.org/pdb/.

74. I. Kim, S. Yon, M. Kim, H. Lee, S. Park, W. Kim. S. Lee, Aspirin is related to worse clinical outcomes of COVID-19, Medicina (Kaunas), 2021, 57, s931, doi: 10.3390/medicina57090931

75. J. Bloom, Aspirin reduces ventilation and deaths in hospitalized. American Council on Science and Health, 2021, June, 15, https://www.acsh.org/news/2021/06/15/aspirin-reduces

76. A. Hui, Aspirin didn't improve survival for hospitalized COVID-19 Patients, Study, Finds, Coronavirus News, 2022, April 04, https://www.verywellhealth.com/aspirin-covid-treatment

77. T.E. Tallei, Fatimawali, N.J. Niode, R. Idroes, R.M. Zidan, S. Mitra, L. Celik, F. Nainu, D. Ağagündüz, T.B. Emran, R. Capasso, A Comprehensive Review of the Potential Use of Green Tea Polyphenols in the Management of COVID-19, Evid Based Complement Alternat Med. 2021, 7170736. Published online 2021 Dec 3. doi: 10.1155/2021/7170736

78. R. Ghosh, A. Chakraborty, A. Biswas, S. Chowdhuri, Evaluation of green tea polyphenols, as novel coronavirus (SARS CoV-2) main protease (Mpro) inhibitors – an in silico docking and molecular dynamics simulation study, J Biomol Struct Dyn. 2020, 1–13. Published online 2020 Jun 22. doi: 10.1080/07391102.2020.1779818

79. L. Henss, A. Auste, C. Schürmann, C. Schmidt, C. von Rhein, M.D. Mühlebach, B.S. Schnierle, The green tea catechin epigallocatechin gallate inhibits SARS-CoV-2 infection, J Gen Virol. 2021, 102(4), 001574. doi: 10.1099/jgv.0.001574.

80. J. Park, R. Park, M. Jang, Y-I. Park, Therapeutic Potential of EGCG, a Green Tea Polyphenol, for Treatment of Coronavirus Diseases, Life (Basel).2021, 10, 197. Published online 2021 Mar 4. doi: 10.3390/life11030197

81. H. Nishimura, M. Okamoto, I. Dapat, K. Katsumi, H. Oshitani, Inactivation of SARS-CoV-2 by Catechins from Green Tea, Jpn J Infect Dis. 2021, 74(5), 421-423, Sep 22 doi: 10.7883/yoken.JJID.2020.902. Epub 2021 Jan 29.

82. T. Hanai, (ed) Quantitative in silico chromatography, Computational modeling of molecular interactions, 2014, RSC, Cambridge, p.94-100. (T. Hanai, Quantitative structure-retention relationship of phenolic compounds without Hammet's equations, J. Chromatogr. A, 2003, 985, 343-349.)

83. G. Williamson, Effects of polyphenols on glucose-induced metabolic changes in healthy human subjects and on glucose transporters, Mol. Nutr. Food Res. 2022, 66, 2101113, doi: 10.1002/mnfr.202101113; 1.

84. D. Zha, M. Fu, Y. Qian, Vascular endothetial glycocalyx damage and potential targeted therapy in COVID-19, Cells, 2022, 11, 1972, https://doi.org/10.3390/cells11121972

85. G.T. Kissel, M. Rene, M. Toes, W. Thomas, J. Huizingal, W. Manfred, Glycobiology of rheumatic diseases, Nature Reviews Rheumatology, https://doi.org/10.1038/s41584-022-00867-4

86. R.B. Van Breemen, R.N. Muchiri, T.A. Bates, J.B. Weinstein, H.C. Leier, S. Farly, F.G. Tafesse, Cannabinoids block cellular entry of SARS-CoV-2 and the emerging variants, J. Nat. Prod. 2022, 85, 496-184. https://doi.org/10.1021/acs.jbaprof.1c00946

87. T. Brevini, M. Maes, G.J. Webb, B.V. John, C.D. Fuchs, G. Buescher, L. Wang, C. Griffiths, M.L. Brown, W.E. Scott III, P. Pereyra-Gerber, W.T.H. Gelson, S. Brown, S. Dillon, D. Muraro, J. Sharp, M. Neary, H. Box, L. Tatham, J. Stewart, P. Curley, H. Pertinez, S. Forrest, P. Mlcochova, FXR inhibition may protect from SARS-CoV-2 infection by reducing ACE2, Nature, 2023, 615, 134–142, https://doi.org/10.1038/s41586-022-05594-0

88. J. Hammond, H. Leister-Tebbe, A. Gardner, P. Abreu, W. Bao, W. Wisemandle, M-L. Baniecki, V.M. Hendrick, B. Damle, A. Simón-Campos, R. Pypstra, J.M. Rusnak, Oral Nirmatrelvir for High-Risk, Nonhospitalized Adults with COVID-19, N Engl J Med. 2022, 386, 1397-408. Doi: 10.1056/NEJMoa2118542,

89. J.A. Takahashi, B.V.R. Barbosa, M.T.N.S. Lima, P.G. Cardoso, C. Consigli, L.P.S. Pimenta, Antiviral fungal metabolites and some insights into their contribution to the current COVID-19 pandemic, Bioorg. Med. Chem. 2021, 46, 116366, https://doi.org/10.1016/j.bmc.2021.116366

90. J. Yang, Y. Xiao, P.V. Lidsky, C-T. Wu, L.R. Bonser, S. Peng, M.A. Garcia-Knight, M. Tassetto, C-I. Chung, X. Li, T. Nakayama, I.T. Lee, J.V. Nayak, K. Ghias, K.I. Hargett, B.K. Shoichet, D.J. Erle, P.K. Jackson, R. Andino, X. Shu, Fluorogenic reporter enables identification of compounds that inhibit SARS-CoV-2, Nature Microbiology, 2023, 8, 121–134, https://doi.org/10.1038/s41564-022-01288-5.

91. F.M.M. Cordero, Research study to evaluate the clinical effectiveness of the nutritional supplement VITAMIC BIOSEN®, Combination of Curcumin, Vitamin C, and Boswellia Serrata, on individuals with symptoms consistent with LONG COVID who have been vaccinated against the SARS-CoV2, Biomed J Sci & Tech Res. 2022, 47, BJSTR.MS.ID.007512, 38567-38581, doi: 10.26717/BISTR. 2022.47.007512

92. N.M. Bodie, R. Hashimoto, D. Connolly, J. Chu, K. Takayama, B.D. Uhal, Design of a chimeric ACE-2/Tc-silent fusion protein with ultrahigh affinity and neutralizing capacity for SARS-CoV-2 variants, Antib. Ther. 2023, 20, 59-74, https://academic.oup.com/abt/advance-article/doi/10.1093/abt/tbad001/6994056 by guest on Jan. 25, 2023

93. J-L. Zhang, Y-H. Li, L-I. Wang, H-Q. Liu, S-Y. Lu, Y. Liu, K. Li, B. Li, S-Y. Li, F-M. Shao, K. Wang, N. Sheng, R. Li, J-J. Cui, P-C. Sun, C-X. Ma, B. Zhu, Z. Wang, Y-H. Wan, S-S. Yu, Y. Che, C-Y. Wang, C. Wang, Q. Zhang, L-M. Zhao, X-Z. Peng, Z. Cheng, J-B. Chang, J-D. Jiang, Azvudine is a thymus-homing anti-SARS-CoV-2 drug effective in treating COVID-19 patients, Signal Transduction and Targeted Therapy, 2021, 6, 414, https://doi.org/10.1038/s41392-021-00835-6

94. C. Yue, W. Song, L. Wang, F. Jian, X. Chen, F. Gao, Z. Shen, Y. Wang, X. Wang, Y. Cao, ACE2 binding and antibody evasion in enhanced transmissibility of XBB.1.5, The Lancet Infectious Diseases, Lancet Infect Dis. 2023, Mar, 23(3):278-280. doi: 10.1016/S1473-3099(23)00010-5. Epub 2023 Feb

95. E. Topol, The virus takes a detour in its evolution arc, Ground Truths, On the evolution process, the difference of JN.1 from BA.2.86 is L455S mutation. https:/erictopod.substack.com/p/the-virus-takes-a-detour-in-its-evolution-arc/

96. Y. Kaku, K. Okumura, M. Padilla-Blanco, Y. Kosugi, K. Uriu, A.A. Hinay Jr, L. Chen, A. Plianchaisuk, K. Kobiyama, K.J. Ishii, J. Zahradnik, J. Ito, K. Sato, Virological characteristics of the SARS-CoV-2 JN.1 variant Lancet Infect Dis. 2024, Jan.3. 2024, https://doi.org/10.1016/51473-3099(23)00813-7

97. A. Bjorkman, M. Gisslen, M. Gullberg, J. Ludvigsson, The Swedish COVID-19 approach: a scientific dialogue on mitigation policies, Frontiers in Public Health, 2023, 20, 1-4, doi: 10.3389/fpubh.2023.1206732101.

98. J. Villadiego, J. García-Arriaza, R. Ramírez-Lorca, R. García-Swinburn, D. Cabello-Rivera, A.E. Rosales-Nieves, M.I. Álvarez-Vergara, F. Cala-Fernández, E. García-Roldán, J.L. López-Ogáyarl, C. Zamora, D. Astorgano, G. Albericio, P. Pérez, A.M. Muñoz-Cabello, A. Pascual, M. Esteban, J. López-Barneo, J.J. Toledo-Ara, Full protection from SARS-CoV-2 brain infection and damage in susceptible transgenic mice conferred by MVA-CoV2-S vaccine candidate, Nature Neuroscience, 2022, 26, 226-238,

99. S. Cheriyedath, Understanding immune responses to Sars-Cov-2 infections in children, News Med. Sci. Jan. 26, 2022, https://www.news-medical.net/news/202201125/Understanding-immune-responses-to-SARSCoV-2-infections-inchildren.aspx

100. S. Mallapaty, Kids Covid: Why young immune systems are still on top. Nature, 2021, 597, 166-168. Doi: 10.1038/d41586-02502423-8

101. S. Mallapaty, Kids show mysteriously low levels of COVID-19 antibodies. Nature, News, 2022, Mar.10. 42, Doi:10.1038/d41586-02200681-8.

102. J.J. Briere, J. Favier, A-P. Gimenez-Roqueple, P. Rustin, Tricarboxylic acid cycle dysfunction as a cause of human diseases and tumor formation, Am. J. Physiol. Cell Physiol. 2006, 291, C1114-C1120

103. K. Smith, Healthy eating, Nature News, Des. 10, 2021, (W. Willett et al. Food in the Anthropocene: the EAT-Lancet commission on healthy diets from sustainable food systems. Doi: 10.1016/s170-6736(18)31788-4; Lancet, 2019, 383, 447-492, B.K. Hirvonen et al. Affordability of the EAT-Lancet reference diet: a global analysis, Lancet Glob. Health, 2020, 8, e59-e66. http;//doi.org/10.1038/d41586-021.

104. A. Barmada, J. Klein, A. Ramaswamy, N.N. Brodsky, J.R. Joyucox, H. Sheikha, K.M. Nines, V. Habet, M. Campbell, T.S. Shimoda, A. Kontorovich, D. Bogunovic, C.R. Oliveira, J. Steele, E.K. Hall, M. Pena-Hernandev, V. Monteiro, C. Lucan, A.M. Ring, S.B. Omer, A. Iwasaki, I. Yildirim, C.L. Lucas, Cytokinopathy with aberrant cytotoxic lymphocytes and p[rofibrotic myloid responde in SARS-CoV-2 mRNA vaccine-associated myocarditis, Additional introduction. Sci. Immunol. 2023, 8, 1-18. Eadh3455.Epub2023, May 5. Doi: 10.1126/sciimmurol.adh3455.

105. S. Pavelic, K. Pavelic, Open questions over the COVID-19 pandemic, DOI: 10.5005/jp-hournals-11005-0027, Science, Art and Religion, 2023, 1, 211-220.

106. Y. Guan, G. Tang, L. Li, J. Shu, Y. Zhao, L. Huang, J. Tang, Herbal medicine and gut midrobiota: exploring untapped therapeutic potential in neurodegerative disease management, Achieves of Pharmaceutical Research, 2024, 47, 146-164. https://doi.org/10.1007/s12272-023-01484-9.

107. J. Tozser, S. Benko, Natural compounds as regulators of NLRP3 inflammasome-mediated IK-1b production, Mediator of Inflammation, 2016, Article ID: 5460302, pp.16, http://dx.doi.ortg/10.1155/2016/5460302